

Geotechnical Frontiers 2017: Foundations



Selected Papers from the
Proceedings of Geotechnical Frontiers 2017

GSP 279



Edited by
Thomas L. Brandon, Ph.D., P.E.
Richard J. Valentine, P.E.



**GEO-
INSTITUTE**

GEOTECHNICAL SPECIAL PUBLICATION NO. 279

GEOTECHNICAL FRONTIERS 2017

FOUNDATIONS

SELECTED PAPERS FROM SESSIONS OF
GEOTECHNICAL FRONTIERS 2017

March 12–15, 2017
Orlando, Florida

SPONSORED BY

Industrial Fabrics Association International

Geo-Institute of the American Society of Civil Engineers

EDITED BY

Thomas L. Brandon, Ph.D., P.E.
Richard J. Valentine, P.E.



Published by the American Society of Civil Engineers

Published by American Society of Civil Engineers
1801 Alexander Bell Drive
Reston, Virginia, 20191-4382
www.asce.org/publications | ascelibrary.org

Any statements expressed in these materials are those of the individual authors and do not necessarily represent the views of ASCE, which takes no responsibility for any statement made herein. No reference made in this publication to any specific method, product, process, or service constitutes or implies an endorsement, recommendation, or warranty thereof by ASCE. The materials are for general information only and do not represent a standard of ASCE, nor are they intended as a reference in purchase specifications, contracts, regulations, statutes, or any other legal document. ASCE makes no representation or warranty of any kind, whether express or implied, concerning the accuracy, completeness, suitability, or utility of any information, apparatus, product, or process discussed in this publication, and assumes no liability therefor. The information contained in these materials should not be used without first securing competent advice with respect to its suitability for any general or specific application. Anyone utilizing such information assumes all liability arising from such use, including but not limited to infringement of any patent or patents.

ASCE and American Society of Civil Engineers—Registered in U.S. Patent and Trademark Office.

Photocopies and permissions. Permission to photocopy or reproduce material from ASCE publications can be requested by sending an e-mail to permissions@asce.org or by locating a title in ASCE's Civil Engineering Database (<http://cedb.asce.org>) or ASCE Library (<http://ascelibrary.org>) and using the “Permissions” link.

Errata: Errata, if any, can be found at <https://doi.org/10.1061/9780784480465>

Copyright © 2017 by the American Society of Civil Engineers.
All Rights Reserved.
ISBN 978-0-7844-8046-5 (PDF)
Manufactured in the United States of America.

Preface

Geotechnical Frontiers 2017 was held in Orlando, FL, on March 12-15. It is the third conference co-sponsored by the Industrial Fabrics Association International (IFAI) and the American Society of Civil Engineers' Geo-Institute (G-I). Other supporting organizations are acknowledged below.

The conference includes topics which illustrate that our understanding of traditional subjects, such as the physical properties of soils, the stability of slopes, the details of mechanically-stabilized earth, the design of roadways and the efficacies of geosynthetics remains far from complete. It also includes topics that reflect the dynamic and evolving nature of our industry, such as thermal properties of soils, energy geostructures, coastal engineering and measures to process coal combustion residuals.

The conference was organized with eight concurrent technical sessions over a period of three days. Most sessions are 90-minutes-long, and ideally, contain five to six presentations. These constraints limited the total number of slots that are available for paper presentations, and consequently, the total number of papers that can be included in the proceedings. This is because, according to the conference rules, a paper must be presented in order to be published in the proceedings.

We received 893 abstracts for the conference. Each abstract was reviewed by the two technical session co-chairs and by at least one of the conference technical co-chairs. Of the 689 abstracts that were accepted, 583 resulted in draft manuscript submittals. Each manuscript received at least two reviews. At the end of this process, 361 manuscripts were recommended for publication in the six volumes of these proceedings. Unfortunately, the limited number of presentation slots made it necessary to decline many fine papers. We encourage the authors to submit at other venues.

Geotechnical Frontiers is also the venue for special presentations of invited and award lectures. Prof. Kerry Rowe presented the Terzaghi Lecture, Prof. Vaughan Griffiths presented the Seed Lecture, and Prof. Ning Lu presented the Peck Lecture. The inaugural Robert. M. Koerner Award and Lecture debuted at this conference and George Koerner was the speaker. There was also a special honorary symposium in recognition of the distinguished career and countless contributions of Professor Mike Duncan.

Thomas L. Brandon and Richard J. Valentine, Editors
Barbara J. Connett, Secretary General

Conference Organizing Committee

The conference organizing committee started planning in March, 2015. The individuals listed below have been actively involved in the planning and production of the conference.

Program Committee Co-Chairs

Elizabeth Dwyre, PE, DGE, Parsons Brinckerhoff, Inc.
Jorge Zornberg, PhD, PE, University of Texas at Austin

Secretary General / Event Manager

Barbara Connett, IFAI

Technical Program Co-Chairs

Thomas L. Brandon, PhD, PE, Virginia Tech
Richard J. Valentine, PE, Valentine Engineering Associates, Inc.

Conference Advisors

Jie Han, PhD, PE, University of Kansas
Robert Mackey, PE, S2L, Inc.

Exhibit Chair

Jennifer McKay, TenCate Geosynthetics

Short Course Chair

L. David Suits, North American Geosynthetics Society

Student Activities Chair

Aaron Budge, PhD, PE, GE, Minnesota State University

Student Programs Project Manager

Ashleigh Esselman, IFAI

Geo- Institute

Brad Keelor
Helen Cook

Additional Organizational Assistance

Many professional organizations contributed to the many components necessary to hold a conference like Geotechnical Frontiers 2017. These are listed below.

Supporting Organizations

Academy of Geo-Professionals (AGP)
International Association of Foundation Drilling (ADSC)
Association of Environmental and Engineering Geologists (AEG)

Association for Metallically Stabilized Earth (AMSE)
 American Society of Civil Engineers – FL Section East Central Branch Geo-Institute (ASCE FL)
 ASTM International (ASTM)
 Bombay Textile Research Association (BTRA)
 Business Co-ordination House (BCH)
 Canadian Geotechnical Society (CGS)
 Deep Foundations Institute (DFI)
 Erosion Control Technology Council (ECTC)
 Fabricated Geomembrane Institute (FGI)
 Federal Highway Administration (FHWA)
 GeoProfessional Business Association (GBA)
 Geosynthetic Institute (GSI)
 International Association of Geosynthetic Installers (IAGI)
 The Nonwovens Institute (NWI)
 Pile Driving Contractors Association (PDCA)
 Transportation Research Board (TRB)
 United States Universities Council on Geotechnical Education and Research (USUCGER)

Supported by

North American chapter of the International Geosynthetics Society (IGS-NA)

Under the Auspices of

International Geosynthetics Society (IGS)

Supporting Media

GeoChannel
 geoengineer.org
GEOSTRATA magazine
Geosynthetics magazine
Pile Buck magazine
 TechTex India

Session Co-Chairs and Paper Reviewers

Papers were reviewed by the technical session co-chairs and by a generous donation of time from volunteer reviewers. These individuals are listed below:

Technical Session Co-Chairs

Aaron Budge	Angel Palomino	Beena Ajmera
Aaron Goldberg	Anne Lemnitzer	Ben Leshchinsky
Adrian Rodriguez-Marek	Antonio Carraro	Bernardo Castellanos
Alec Marshall	Arvin Farid	Binod Tiwari
Alejandro Martinez	Ashley MacMillan	BooHyun Nam
Allen Cadden	Ashly Cabas-Mijares	Bora Cetin
Amr Morsy	Assaf Klar	Burak Tanyu

Charles Schwartz
 Cheng Lin
 Chris Richgels
 Chris Woods
 Christopher Meehan
 Corrie Walton-Macaulay
 Craig Benson
 Daniel VandenBerge
 David Frost
 Don Hullings
 Elizabeth Dwyer
 Eric Blond
 Fayun Liang
 Fei Wang
 Guney Olgun
 Ingrid Tomac
 Jack Montgomery

James McKelvey
 Jason Hertz
 Jie Huang
 John McCartney
 Jose Clemente
 Joseph Scalia
 Katerina Ziotopoulou
 Krishna Reddy
 Kristi Bumpas
 Kristin Sample-Lord
 Liu Huabei
 Mahmoud Enad
 Majid Khabbazian
 Majid Manzari
 Malay Ghose Hajra
 Maurice Morvant
 Mike Adams

Miriam Smith
 Morton Barlaz
 Mourad Zeghal
 Nathan Ivy
 Nazli Yesiller
 Neil Schwanz
 Nina Stark
 Qian Zhao
 Reinaldo Vega-Meyer
 Robert H. Swan, Jr.
 Rune Dyvik
 Ryan Corey
 Stacey Kulesza
 Tarek Abichou
 Victor Kaliakin

Paper Reviewers

Aaron Zdinak
 Abdolreza Osouli
 Ahmadreza Hedayat
 Ahmet Aydilek
 Alan Luetenegger
 Albert Kottke
 Alec McGillivray
 Alexander Reeb
 Alfonso Cerna Diaz
 Alfonso Rivera
 Ali Eliadorani
 Ali Soleimanbeigi
 Alireza Ayoubian
 Alissa Kendall
 Amro El Badawy
 Anand J. Puppala
 Andrea L. Welker
 Andrew Assadollahi
 Andrew Booth
 Anirban Mandal
 Anna Saindon
 Archie Filshill
 Armin Stuedlein
 Asli Yalcin Dayioglu
 Balasingam Muhunthan
 Behnam Golestani

Ben Bowers
 Ben Mason
 Ben North
 Billy Camp
 Bob Bachus
 Bogart Mendez
 Brad Wham
 Brandon Buschmeir
 Brendan Fitzpatrick
 Brendan Sheppard
 Brent McNeme
 Brent Robinson
 Brett Maurer
 Brian Albrecht
 Brian Cole
 Brian Diefenderfer
 Brian Ladd
 Brian Metcalfe
 Brian Sweeney
 Bulent Hatipoglu
 Carlos Englert
 Carmine Polito
 Chad Held
 Chadi El Mohtar
 Cheng Lin
 Chengzhi Xiao

Chloe Arson
 Cholachat Rujikiatkamjorn
 Chris Athanassopoulos
 Chris Sneddon
 Christopher Behling
 Christopher Krage
 Chrysanthos Steiakakis
 Clayton Cook
 Conrad Felice
 Curt Basnett
 D. Wanatowski
 D.A. Saftner
 Dale Biggers
 Daniel S. Rohe
 Daniele Cazzuffi
 David Airey
 David Chapman
 David Parr
 David White
 Debra Laefer
 Debra Reinhart
 Deepak K. Neupane
 Diego F. Fagundes
 Dipanjan Basu
 Douglas Crum
 Edward Kavazanjian, Jr.

Emad Gheibi	Jacquelyn Allmond	Kevin Earley
Eric Fitzsimmons	Jaewon Jang	Kevin Foye
Erik Loehr	James Hanson	Kevin Franke
Erin Yargicoglu	James Kaklamanos	Kimberly Mugg
Ernest Berney	James Niehoff	Knut H. Andersen
Eugene Lenhardt	James Tinjum	Kord J. Wissmann
Everett Litton	James W. Levis	Kyle Murrell
Fan Ri-Dong	Jason Curd	Lance Kitchens
Faraz Tehrani	Jason DeJong	Larry Johnson
Farshid Vahedifard	Jason Valeria	Lee Peterson
Fitsum Gebremariam	Jay Mezher	Lei Wang
Frank Rausche	Jean Audibert	Luis Garcia
Frederic Masse	Jeff Huffman	Luis Vallejo
Garland Likins	Jeff Kuhn	M. Giulliana
Gary Fuerstenberg	Jeff Locke	Magnus Soldal
Gavin Gautreau	Jeff Segar	Mandar Dewolkar
Geir Sandbækken	Jeff Sizemore	Manisha Rai
Gema Amaya-Santos	Jesse Rauser	Márcio S.S. de Almeida
Gemmina Di Emidio	Jesus Gomez	Maria Eugênia Gimenez
George Teetes	Jian Song	Boscov
George Zalachoris	Jianping Hu	Mark Knight
Gerry McShane	Jie Han	Mark Stephani
Giovanna Biscontin	Joaquin Wright	Mark Thompson
Girish Kumar	Joel Sprague	Mark Wayne
Glenn Rix	Joeng-Yun Won	Mary Nodine
Gokhan Saygili	John Delphia	Mason Ghafghazi
Greg Canivan	John Germaine	Matt Evans
Greg Hebler	John Seymour	Matt Goff
Gregg Sherry	Jon Bender	Matthew Wilcock
Hadi Khabbaz	Jonathan C. Pasco	Mehdi Veiskarami
Haitham Dawood	Jonathan Cheng	Mehran Mazari
Haiying Huang	Jorge Alba	Melissa Chappel
Hakan A. Oren	Jorge R. Parra	Menzer Pehlivan
Hamed Khodadadi	Jorge Zornberg	Merve Gizem Bozkurt
Tirkolaei	Joseph Labuz	Michael McGuire
Hanumantha Rao	Joseph T. Coe, Jr.	Michael A. Malusis
Hugo Aparicio	Juan Mayoral	Michael Gomez
Ilhan Chang	Julio Valdes	Michael Iten
Inthuorn Sasanakul	Julius Arop	Michael Maisel
Isaac Howard	Kalehiwot Nega	Michael P. McGuire
Isaac Stephens	Manahiloh	Michael Sharp
Itai Elkayam	Karl Higgins	Michéle Casagrande
Italo Gonzalez	Kenichi Sato	Mile Khire
Ivan Contreras	Kenneth P. Akins	Ming Xiao
J. Antonio H. Carraro	Kent von Maubeuge	Ming Zhu
J.P.A Hettiaratchi	Kerry Rowe	Mo Nasim

Mohamad Hussein	Russell Green	Tim(Xiaobin) Lin
Mohammad Khosravi	Ryan Beemer	Timothy O'Leary
Mohammed El-Shafie	Ryan Keiper	Timothy Stark
Morgan Race	S. Mehdi Mousavi	Timothy Wood
Muhannad T Suleiman	S.K. Bhatia	Tom Wesling
Mustafa Nalcakan	Saad Ullah	Tom Witherspoon
Nancy Straub	Sahadat Hossain	Tong Qiu
Nasir Massoudi	Sajjad Salam	Toraj Ghofrani
Nasser Hamdan	Sal Romero	Tran Nhan
Nathalie Boukpeti	Saleh Behbahani	Travis Deane
Navid Jafari	Sam Lasley	Travis Richards
Neil Dixon	Samuel Yniesta	Trevor Woodward
Nejan Huvaj	Santiago Caballero	Tuncer Edil
Neven Matasovic	Scott Brandenburg	Van Komurka
Nico Kuehn	Scott Deaton	Vincent Drnevich
Nik Okkels	Scott Mackiewicz	Vincente Quinteros
Nima Latifi	Scott Marr	Vishnu Diyaljee
Noah Vroman	Sean O'Donnell	Wenping Gong
Omer Bozok	Shaoshuai Gong	William Baker
Osama Abuhajar	Shawn Griffiths	William K. Petersen
Ozgur Ertugrul	Sheng Dai	Wing Shun Kwan
Pasquale Carotenuto	Shiaohuey Chow	Xiaohui Sun
Pat Fox	Siddharth Parida	Xiaomin You
Patricia Dolez	Sihyun Kim	Xinbao Yu
Paul C. Schmall	Sochan Jung	Xiong (Bill) Yu
Paul Mayne	Stanley Miller	Yanbo Huang
Peggy Hagerty Duffy	Steve Davidow	Yan-Jun Du
Philip Erbland	Sudheesh Thiyyakkandi	Yao Zhang
Qamar Kazmi	Sugeng Wahyudi	Yaurel Guadalupe-Torres
Qian Zhao	Sung-Hee Kim	Yazen Khasawneh
R.D. Fan	Thayanan Boonyarak	Yusuke Suzuki
Radoslaw Michalowski	Theresa Andrejack Loux	Zachary Spera
Rakesh Acharya	Thomas Dobrowski	Zahirul Islam
Ram Rathan Lal	Thomas Pennington	Zana Karimi
Ramin Motamed	Thomas Weinmann	Zhaohui Yang
Randy Post	Tim Bauters	Zhen Liu
Raymond J. Castelli	Tim Siegel	Zhibin Liu
Richard Armstrong		
Richard Morales		
Richard Thiel		
Rick J. Buffalini		
Robert Nyren		
Ronald Andrus		

Contents

Bridge and Offshore Structure Scour

Effect of the Level of Compaction on the Internal Erosion Potential for Granular Soils	1
J. Israr, B. Indraratna, and C. Rujikiatkamjorn	
Comparison and Estimation of the Local Scour Depth around Pile Groups and Wide Piers	11
Chen Wang, Xiong (Bill) Yu, and Fayun Liang	
Experimental Investigation of the Pier Streamlining Effect on Bridge Local Scour under Clear Water Conditions	20
Junhong Li and Junliang Tao	
Modified Strain Wedge Calculation of a Laterally Loaded Pile in Sand Considering Scouring	29
C. Zhang, X. Yang, M. Huang, and J. Yuan	
Study of the Particle Shape Influence on Soil Erodibility Using Coupled CFD-DEM Modeling	40
Y. Guo and X. Yu	
Two-Dimensional Soil Erosion Profile Using Electrical Resistivity Surveys	50
Md. Zahidul Karim and Stacey E. Tucker-Kulesza	

Geosynthetics in Foundations

Geofoam Inclusions for Reducing Passive Force on Bridge Abutments Based on Large-Scale Tests.....	59
Kyle M. Rollins, Eric Scott, and Aaron Marsh	
Observation of the Progressive Failure Mechanism of Reinforced Foundation Soil Using the Digital Image Correlation Technique.....	69
Mazhar I. Arshad, Monica Prezzi, and Rodrigo Salgado	
Numerical Modelling, Design, and Construction of a Geotextile-Reinforced Soil-Metal Buried Structure (GRS) under Deep Fills in Challenging Soil Conditions.....	80
Meckkey El-Sharnouby, Dave Worsley, Phil Carroll, and Calvin D. VanBuskirk	

Protecting Buried HDPE Pipes Subjected to Ground Subsidence Using Geosynthetics.....	92
Min Zhou, Fei Wang, and Yan-Jun Du	

Offshore Foundation Systems

Numerical Study of the Effect of Pile Driving on a Position of a Neutral Plane.....	101
Arindam Dey and Michael C. Koch	

Numerical Simulation of the Lateral Loading Capacity of a Bucket Foundation.....	112
Xu Yang, Xuefei Wang, and Xiangwu Zeng	

Three-Dimensional Finite Element Modeling for Spudcan Penetration into a Clayey Seabed	122
Volkan Emren, Nejan Huvaj, and Kagan Tuncay	

Offshore Anchor Penetration in Sands—Granular Simulations	132
Nan Zhang and T. Matthew Evans	

Drop Weight Dynamic Load Testing for Construction Monitoring and Quality Control of Offshore Drilled Foundations	143
Seth O. Robertson and Samuel G. Paikowsky	

Experimental Investigation of the Horizontal Resistance of Group Suction Piles with Different Pile Spacing	154
Juhyung Lee and Jinung Do	

Pile, Shaft, and Pier Foundations

Parametric Study for Understanding the Behavior of Integral Abutment Bridges	164
Karrthik Kirupakaran and Kanthasamy K. Muraleetharan	

Applications of the Continuous Wavelet Transform Method in Crosshole Sonic Logging Tests	174
Farnyuh Menq, Shin Tower Wang, and William Isenhower	

A Robust Method for a Lateral Loading Analysis of Large Diameter Piles	184
Bret N. Lingwall, Byron Foster, Omololu Ogunseye, and James Gingery	

Development of Empirical Models to Estimate the Increase in Pile Resistance (Set-Up) with Time	193
Md. Nafiul Haque and Murad Y. Abu-Farsakh	

Robust Geotechnical Design of Piled-Raft Foundations for Tall Onshore Wind Turbines.....	204
Shweta Shrestha, Nadarajah Ravichandran, and Parishad Rahbari	
Drivability and Performance of Steel H-Piles in Schist Saprolite.....	214
Lei Gu, Sarah E. McInnes, and Ara G. Mouradian	
Elastic Analysis of Differential Settlements for Steel Storage Tank Foundations	223
Suranga Gunerathne, Hoyoung Seo, William Lawson, and Priyantha Jayawickrama	
Sustainable Slope Protection and Cut-Off Wall Installation in Densely Populated Areas by the Press-In Piling Method	233
Takefumi Takuma and Shigeru Kambe	
Load-Carrying Capacity of Slab-on-Grade Foundations Supporting Rack Post Loads.....	242
Xiaochao Tang and Mohamad N. Jilati	
A Semi-Analytical Solution for the Analysis of Axially Loaded Pile Groups in Layered Elastic Soil.....	247
Faraz S. Tehrani, Rodrigo Salgado, and Monica Prezzi	
Laboratory Study of the Effect of Pile Surface Roughness on the Response of Soil and Non-Displacement Piles.....	256
Faraz S. Tehrani, Fei Han, Rodrigo Salgado, and Monica Prezzi	
The Sensitivity of Settlement Predictions for an Axially Loaded Drilled Shaft to ϵ_{50}	265
Kevin Stanton, Maryam Ostovar, and Ramin Motamed	
Multi-Level O-Cell Tests on Instrumented Bored Piles in the Mekong Delta	274
H. M. Nguyen, A. J. Puppala, U. D. Patil, L. Mosadegh, and A. Banerjee	
Use of High-Strain Dynamic Testing to Efficiently Design and Construct Bridge Foundations in Glacial Soils.....	284
Morgan Race, Bryan Field, and Matthew Glisson	
Underpinning a Boston Landmark for the Ages: The First Church of Christ, Scientist (TFCCS), the Original Mother Church (TOMC), Foundation Repairs	294
Giuliana A. Zelada and Sean M. Homem	

Augered Cast-in-Place Pile Foundation Design and Construction for the MLK Bridge, New Stadium Project, Atlanta	305
Graham Elliott, Natale Marini, Matthew Meyer, and W. Morgan NeSmith	
General Bearing Capacity Theory and Soil Extraction Method for the Mitigation of Differential Settlements	314
Rozbeh B. Moghaddam and Priyantha W. Jayawickrama	
Minimization of the Cost and CO₂ Emissions for Strip Footings under Dynamic Loading Using a Big Bang-Big Crunch Algorithm	324
Andrew Assadollahi	
Three-Dimensional Soil-Pile Group Interaction in Layered Soil with Disturbed Zone by the Boundary Element Analysis	334
Jeremy C. Ashlock and Zhiyan Jiang	
Discussion of Concrete Pier Foundation Design for Transmission Structures	345
Haijian Shi and Drew Pizzo	
Case History of a Full Scale Axial Load Test of Sheet Piles	355
Matthew B. Sylvain, Miguel A. Pando, Matthew J. Whelan, Corey D. Rice, Vincent O. Ogunro, Youngjin Park, and Thomas Koch	
Load Testing and Performance of Instrumented ACIP Piles in Texas Clays.....	366
Nasser Massoudi and Kenneth R. Bell	
Variability of Pile-Soil Interaction: A Comparison of Behavior Seen in Instrumented Pile Pairs at Three MnDOT Bridge Sites.....	379
Aaron S. Budge and Derrick D. Dasenbrock	

Effect of the Level of Compaction on the Internal Erosion Potential for Granular Soils

J. Israr, M.Sc.¹; B. Indraratna, P.E., F.ASCE²; and C. Rujikiatkamjorn, Ph.D.³

¹Doctoral Student, School of Civil, Mining and Environmental Engineering, Univ. of Wollongong, NSW 2522, Australia. E-mail: jahanzaib.israr182@gmail.com

²Distinguished Professor of Civil Engineering, Director, Centre for Geomechanics and Railway Engineering, Univ. of Wollongong, NSW 2522, Australia. E-mail: indra@uow.edu.au

³Associate Professor, School of Civil, Mining and Environmental Engineering, Univ. of Wollongong, NSW 2522, Australia. E-mail: cholacha@uow.edu.au

Abstract

Internal erosion occurs when the seepage forces wash out the fines of a non-uniform soil along the pre-existing openings (e.g., cracks and voids), resulting into substantial increase in permeability. Given that the drainage characteristics of soils are significantly influenced by the shapes, packing arrangement and size distribution of their particles, the erosion of fines can alter the drainage characteristics. The assessment for internal erosion potential is normally obtained based on grain size distribution ignoring the effect of compaction and particles' shapes. In this study, the experimental results of hydraulic gradient controlled erosion tests, conducted over a select range of compacted soils, were used to compare with the internal erosion assessments from some of the existing criteria. Consequently, a new approach that considers the shapes, packing arrangement and size distribution of particles for assessing their internal erosion potential is proposed that showed highest success rate compared to the rest.

INTRODUCTION

Internal erosion is generally exhibited by non-uniform soils with bimodal structures whereby the steady seepage forces accompanying finer fractions from the granular media cause their drainage characteristics to deteriorate to the extent that the soils can no longer be used as effective filters. For instance, the permeability of soils susceptible to internal erosion (unstable soils) increases substantially due to erosion, which may not be desirable. In literature, internal erosion has various terminologies such as piping (uniform sands), internal and external piping or erosion, segregation piping (bi-modal soils, i.e. broadly- and gap-graded sand gravel mixtures), tunnelling or jugging (dispersive silts and clays), suffusion and excessive washout (bi-modal soils) etc. (Lane 1934; Terzaghi 1922; Kezdi 1979; Kenney and Lau 1985; Indraratna et al. 2015). In reality, failures of up to 50% of all water impounding structures could be related to internal erosion (Richards and Reddy, 2007), that begins at hydraulic gradients that are much smaller than Terzaghi's critical hydraulic gradient ($i_{cr,t}$) for soil piping i.e. $1/5 - 1/2 i_{cr,t}$ (Skempton and Brogan, 1994).

Thus far, internal erosion is considered to be a function of soil gradation e.g. uniformity coefficient (C_u), percentage of fines ($f \leq 20-30\%$) and the slope of grain size distribution curve (GSD), based on which various criteria were proposed for assessing the potential for internal erosion. For instance, Kezdi (1979) and Sherard (1979) applied Terzaghi's (1939) criterion for filter design on a split GSD-curve and proposed that soils possessing $D_{15}^c/d_{85}^f > 4$ and 5, respectively, would suffer from this problem. Here, D_{15}^c and d_{85}^f define the particle sizes corresponding to 15% and 85% finer for coarse and fine fractions obtained from splitting the

GSD, respectively. Kenney and Lau (1985) assumed that a particle d could erode through the constrictions (the opening between adjacent pore spaces) formed by particles $\geq 4d$, while particle sizes between d and $4d$ would control the potential for internal erosion as given by $(H/F)_{min} < 1$, where F and H are the percentile finer corresponding to d and between d and $4d$, respectively. Notably, the non-erosion primary fabric constitutes a variety of constriction sizes based on the GSD and relative density (R_d) of soil. For example, the largest constriction is obtained by the four largest particles of soil in contact at $R_d = 0\%$, while the smallest constriction is constituted by three of the finest contacting particles at $R_d = 100\%$. The intermediate constriction sizes can be evaluated based on stochastic theory as a function of the GSD and R_d of soil (Locke et al. 2001).

In this study, a series of hydraulic gradient controlled erosion tests were conducted on six granular soils with varying C_u (from 1.2 to 40) and R_d (from 5 to 95%) and the results were reported. Consequently, a new approach that combined two well-accepted GSD and CSD based criteria for assessing the potential for internal erosion was proposed and subsequently verified with a large body of previously published experimental data.

LABORATORY INVESTIGATION

Test Material and Geometrical Assessments. The test material for the current study was consisted of sand and sand-gravel mixtures with a C_u ranging between 1 and 40 (Figure 1).

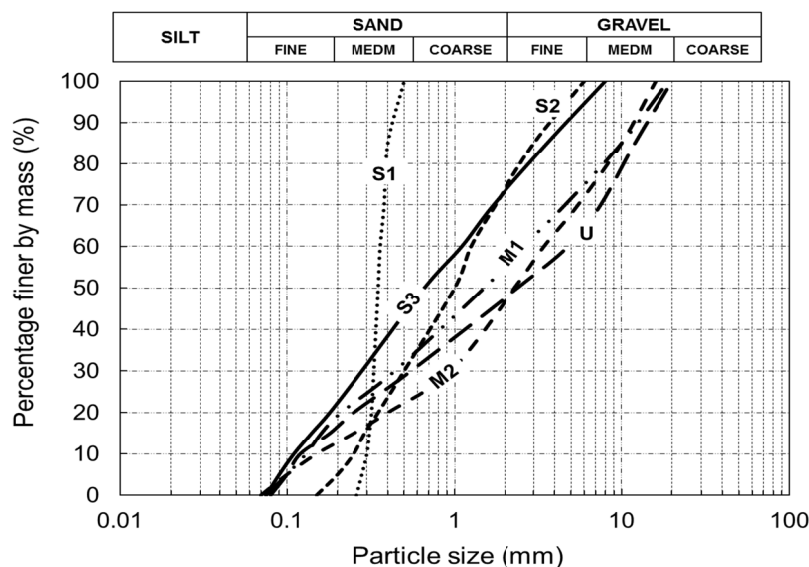


Figure 1. Grain size distribution (GSD) curves for test samples.

A total of 20 internal erosion tests was conducted on these samples that were prepared at levels of compaction varying from $R_d = 0$ to 100%, to evaluate the role of geometrical factors on their potential for internal erosion (e.g. f , C_u , GSD and R_d). Table 1 summarises the geometrical assessments from existing GSD based criteria (i.e. Kezdi, 1979; Sherard, 1979; Kenney and Lau, 1985), the physical properties, and the laboratory erosion test results for the tested soils. For instance, samples-S1, -S2 and -S3 were assessed as internally stable, sample-U was assessed as internally unstable by all the existing criteria, whereas samples-M1 and -M2 were assessed as stable by Kenney and Lau (1985), unstable by Kezdi (1979) and stable and unstable, respectively, by Sherard (1979).

Table 1. Physical soil properties and test results for current test samples.

Sample ID	Internal Erosion Potential Assessment Results			Computed Properties			Observed Properties			
	Kenney & Lau (1985)	Sherard (1979)	Kezdi (1979)	R_d (%)	i_{ct}	E_c (kJ/m ³)	C_u Pre-test	C_u Post-test	i_{cr}	Internal stability
S1-R7	S	S	S	7	0.97	26	1.2	1.2	1.07	S
S1-R52	S	S	S	52	1.07	263	1.2	1.2	1.18	S
S1-R94	S	S	S	94	1.18	564	1.2	1.2	1.29	S
S2-R7	S	S	S	7	0.94	26	5	5	1.0	S
S2-R52	S	S	S	52	1.03	263	5	5	1.05	S
S2-R93	S	S	S	93	1.13	564	5	5	1.10	S
S3-R6	S	S	S	6	0.93	26	10	10	0.9	S
S3-R47	S	S	S	47	1.01	263	10	10	1.0	S
S3-93	S	S	S	93	1.12	564	10	10	1.05	S
M1-R6	S*	S*	S*	6	0.92	26	20	23.7	0.45	U
M1-R51	S*	S*	S*	51	1.02	263	20	22.2	0.56	U
M1-R72	S	S	S	72	1.07	364	20	20	0.90	S
M1-R96	S	S	S	96	1.14	564	20	20	0.98	S
M2-R7	S*	U	U	7	0.93	26	23	18.2	0.62	U
M2-R32	S	U [#]	U [#]	32	0.98	157	23	23	0.79	S
M2-R63	S	U [#]	U [#]	63	1.05	313	23	23	0.94	S
M2-R94	S	U [#]	U [#]	94	1.13	564	23	23	1.03	S
U-R6	U	S*	U	6	0.92	26	40	10	0.28	U
U-R48	U	S*	U	48	1.02	263	40	11.2	0.31	U
U-R93	U	S*	U	93	1.14	564	40	12.5	0.37	U

Note: S, U, E_c , superscripts # and subscript * define stable, unstable, compaction energy, conservative (safe) predictions and non-conservative (unsafe) predictions, respectively.

Test Setup and Procedure. Figure 2 presents the test setup and schematic illustration of the test procedure that involved applying an upward flow to the test samples. The test setup consisted of a 150 mm diameter perspex cell that could accommodate a 200 mm long soil specimen with minimum boundary effects on erosion of fines (i.e. $D/d_{100} > 9$; D = diameter of the cell and d_{100} = largest size particle), e.g. the effects of preferential flow channels and friction at the cell wall (Zou et al. 2013).

For sampling, the moist soil was mixed beforehand and compacted in layers by applying a predetermined magnitude of compaction energy to achieve the target R_d -values. These samples were saturated under a back pressure of 100 kPa for a minimum of 24 hours. Details of sample preparation and assessments of their uniformity (i.e. with respect to particle size distribution and compaction) can be obtained from Indraratna et al. (2015). During erosion testing, an upwards flow of water was applied through the soil at a pre-requisite hydraulic pressure difference across the test sample (hence, the hydraulic gradient i). The increments in i -values i.e. Δi were applied at controlled rates e.g. $\Delta i \approx 0.05$ and 0.025 for 30 minutes (or until a steady flow condition was achieved) were adopted for the geometrically stable samples (from S1 to S3) and unstable samples (i.e. M2 and U), respectively.

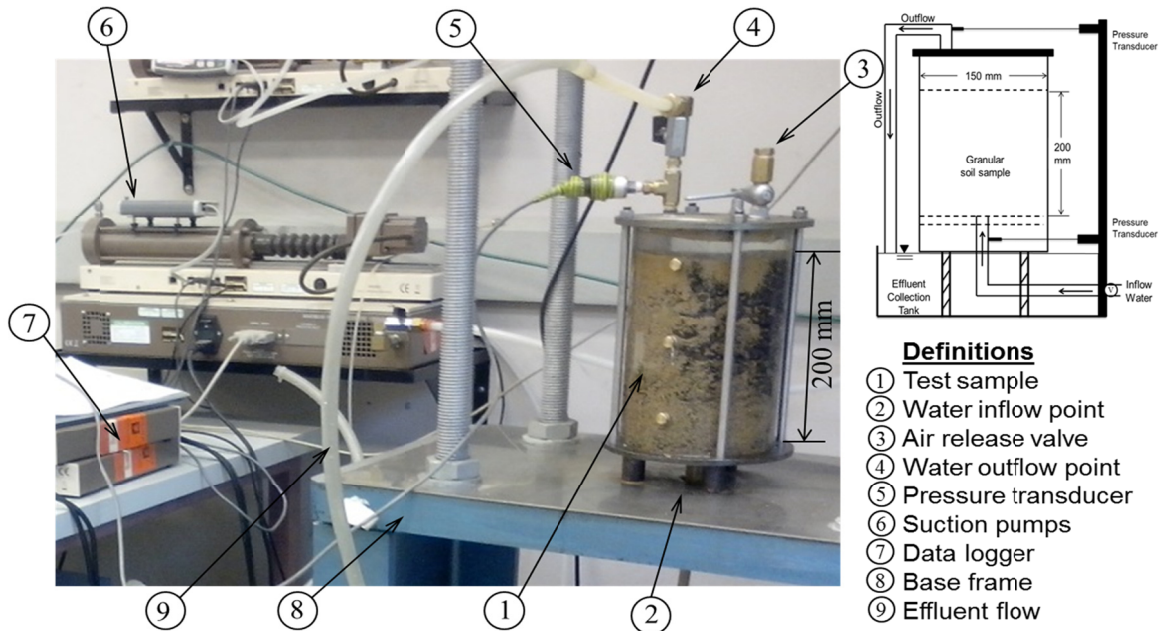


Figure 2. Visual and schematic illustrations of test setup.

TEST RESULTS AND DISCUSSIONS

Figure 3 shows the relationships between the flow rate of the effluent and hydraulic gradient applied (Q_f versus i) in the form of flow curves with companion effluent turbidity variations for the selected sample-M1 (marginally stable sample with $(H/F)_{\min} = 1$) compacted at $R_d = 6, 51, 72$ and 96%. The inception of internal erosion (critical onset) was identified by a sudden rise in effluent turbidity (> 60 NTU) with steepening flow curves and the corresponding values of hydraulic gradients that were reported as $i_{cr,0}$ (Indraratna et al. 2015). The development of heave in the stable S1, S2, and S3, the suffusion in the unstable M1-R6, M1-R51, and M2-R7, and the composite heave-piping in the marginal M1-R72, M1-R96, M2-R32, M2-R63, M2-R94, and U soil samples could be visually observed at the critical onsets.

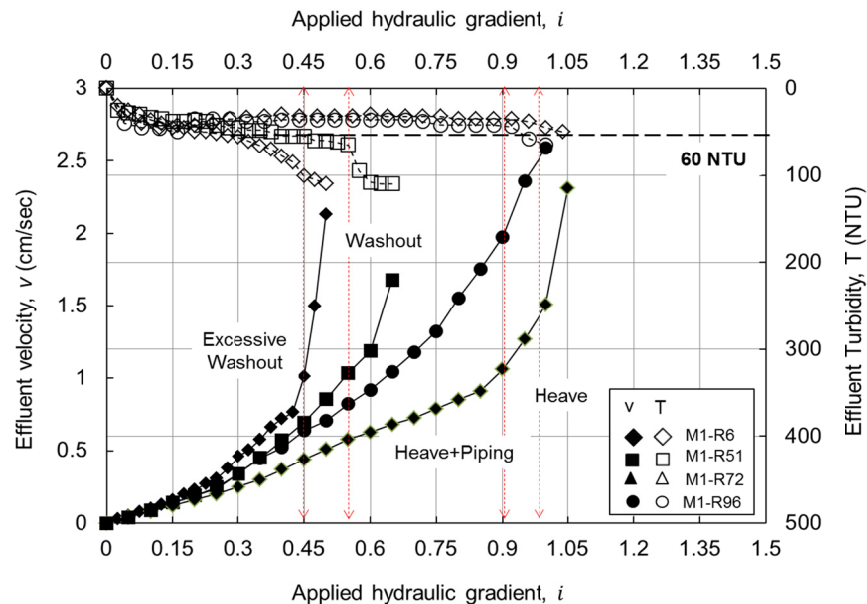


Figure 3. Hydraulic response of sample-M1 at $R_d = 6, 51, 71$ and 96%.

Figure 4 (a) shows the effects of increasing relative density on the magnitude of i_{cr} , which generally increased with the magnitude of R_d for all test samples. Interestingly, this increase was comparatively smaller for the highly stable and unstable samples S1, S2, S3 and U, respectively, than for the marginal samples M1 and M2, whereby an increase of up to two-fold was observed. This may be because the constrictions of a stable soil barely allow any erosion, which reduces further with the reduction in constriction sizes at higher R_d . Similarly, the constrictions of an unstable soil are already too large to retain any fines and further compaction may not reduce them sufficiently to reduce erosion. The stress reduction factor α ($= i_{cr}/i_{ct}$) (Skempton and Brogan 1994) could be deduced for the test results of this study and plotted against the respective R_d -values in Figure 4 (b), where i_{ct} is the ratio between unit weights of soil (γ') and water (γ_w). It was revealed that the increasing R_d could transform some of the erodible finer fraction into load carrying sustainable primary fabric, as reflected by an increasing magnitude of α . In particular, the marginal samples M1 and M2 showed a significant improvement in their response to the seepage flow, with a marked reduction in the amount of eroded fines (see Figure 4(c)) and increases in the companion $i_{cr,0}$ and α . Nevertheless, the increase in R_d increased the stability of all samples against internal erosion and these effects were prominent for the marginal soils.

For instance, there was no significant erosion of fines from either of the highly stable samples-S1, -S2, and -S3, whereby particles with almost identical sizes and shapes created a stable primary fabric with a negligible amount of erodible fines. Whereas the unstable sample-U consisted of particles of soil with a variety of sizes and shapes resulted in a bimodal system. The particles with larger surface areas could share mechanically active contacts while accommodating those with smaller surface areas within their pore spaces. However, the sizes and shapes of particles in marginal soils (M1 and M2) constituted constriction networks at a given R_d that could retain significant amounts of erodible fines that extended the primary fabric and made them internally stable at higher R_d . Figure 5 illustrates the inception of internal erosion in the selected samples, showing the development of heave in S2-R93 and S3-R93, heave-piping in M1-R72 and excessive washout in U-R95.

INTERNAL EROSION POTENTIAL ASSESSMENTS

Results from Existing Criteria. The GSD based criteria of Kezdi (1979), Sherard (1979), and Kenney and Lau (1985) were used to assess the potential of the current test samples for internal erosion, and the results are listed in Table 1. In summary, the criterion of Sherard (1979) yielded 8 incorrect assessments, i.e. 3 safe (conservative) and 5 unsafe, that of Kezdi (1979) resulted in 5 incorrect assessments, including 3 safe and 2 unsafe, while the approach of Kenney and Lau (1985) showed enhanced rigor with only 3 incorrect predictions (85% success), although unsafe. Notably, Indraratna et al. (2015) reassessed the criterion of Kenney and Lau (1985) for a larger database of 92 published experimental results and reported that this method yielded close to 90% success in assessing the potential for internal erosion, with only 8 incorrect predictions. However, none of the reported GSD based criteria could accurately capture the potential of the currently tested samples for internal erosion when their level of compaction was varied.

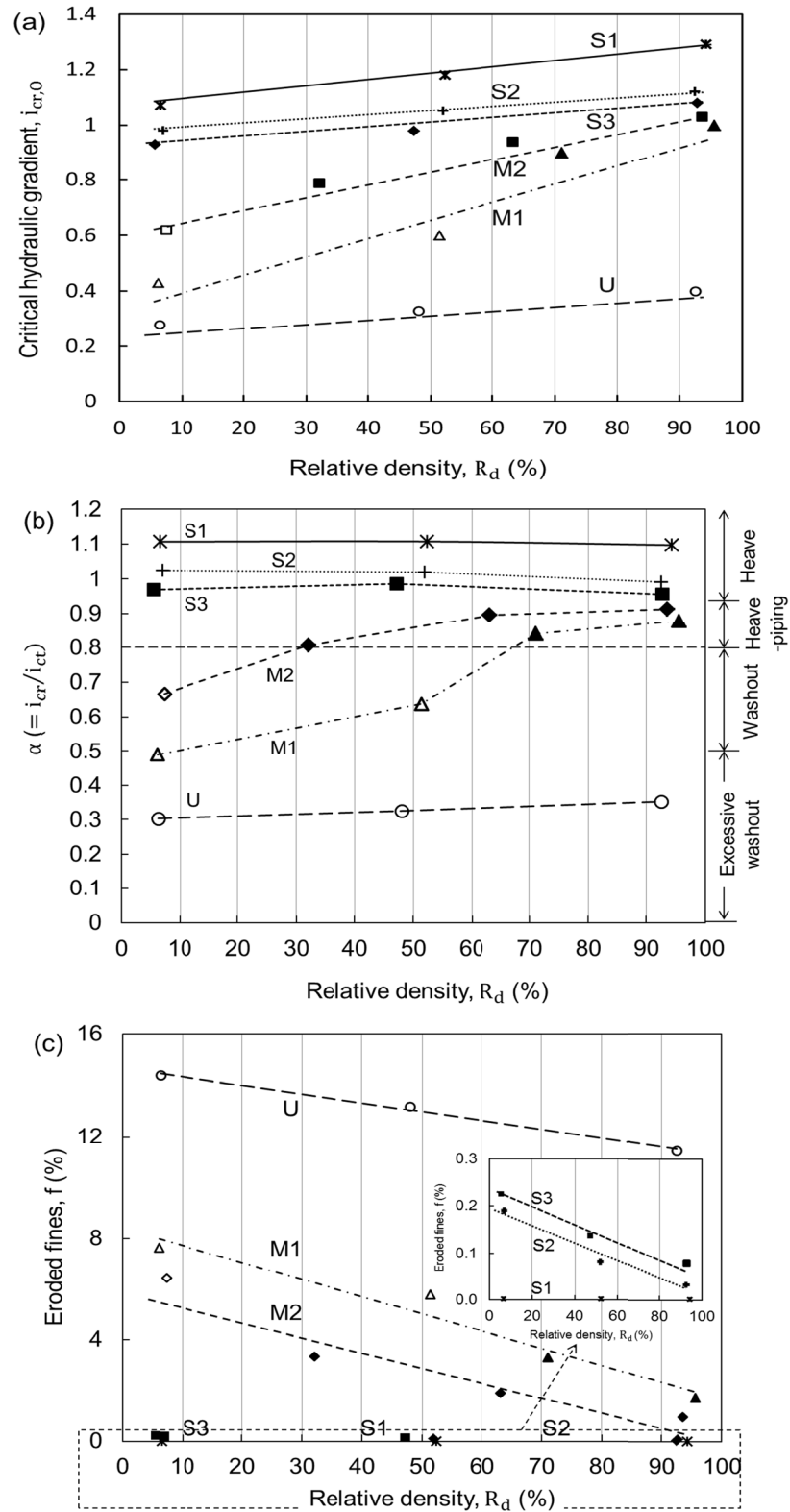


Figure 4. Effect of compaction on (a) stress reduction factor, (b) critical hydraulic gradient and (c) percentile eroded fines (after Indraratna et al. 2015).

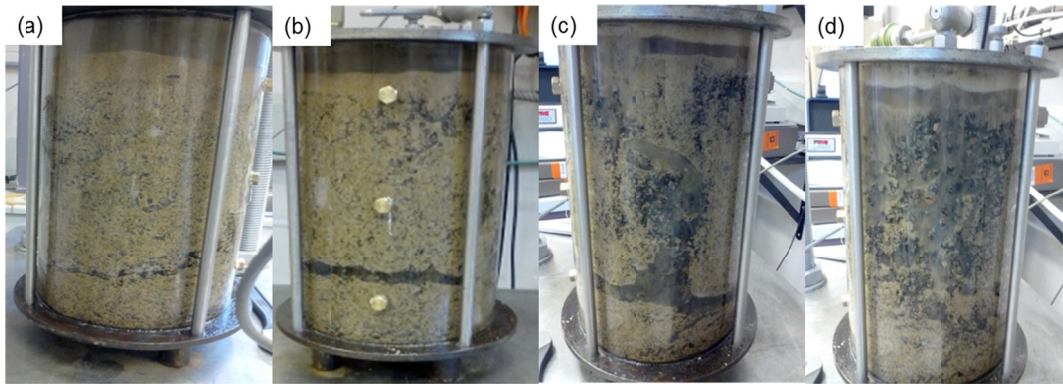


Figure 5. Visual illustrations of various seepage induced internal erosion failures; (a) development of heave in S1-R94, (b) onset of heave in S3-R93, (c) piping failure in M2-R72 and (d) onset of washout failure in C40-R93.

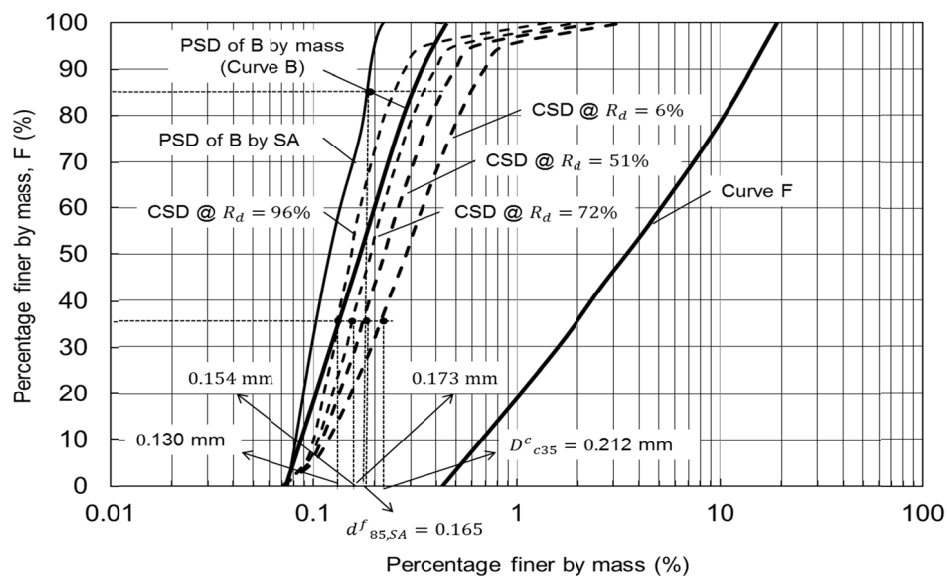


Figure 6. Effect of R_d on CSD of coarser fraction of sample-4 (M1).

The GSD by surface area is an acceptable measure of the shapes of soil particles (Trani and Indraratna 2010) that can adversely affect the potential of soils for internal erosion. Figure 6 shows the application of the proposed method for sample-M1 whereby the assessment results agreed with the experimental results, i.e. unstable at $R_d \leq 70\%$ and stable at $R_d > 70\%$, while the use of $d_{85(m)}$ instead of $d_{85(SA)}$, unsafely assessed it to be internally stable even at $R_d = 0\%$. The proposed criterion was initially tested for all 20 samples of this study, so the stable samples could be successfully separated from their counterparts (Table 1). This method was then applied to a larger dataset of 92 published test results compiled by Indraratna et al. (2015) and promising results were obtained, with only one incorrect assessment. This result corresponded to the soil gradation that defined the stability boundary of Kenney and Lau's criterion, i.e. Fuller curve and sample-M1 of this study, which was experimentally observed as stable at $R_d > 70\%$ (with no vibrations imparted while testing for internal erosion). One explanation for this discrepancy between the observed and predicted behaviour of the borderline sample M1 (i.e. corresponding to Fuller curve) could be that it is only partially stable at $R_d > 70\%$ with no vibrations (Indraratna et al. 2015), because vibrations can adversely affect the constriction size distribution of soils (Xiao et al. 2006) and hence the proposed criterion.

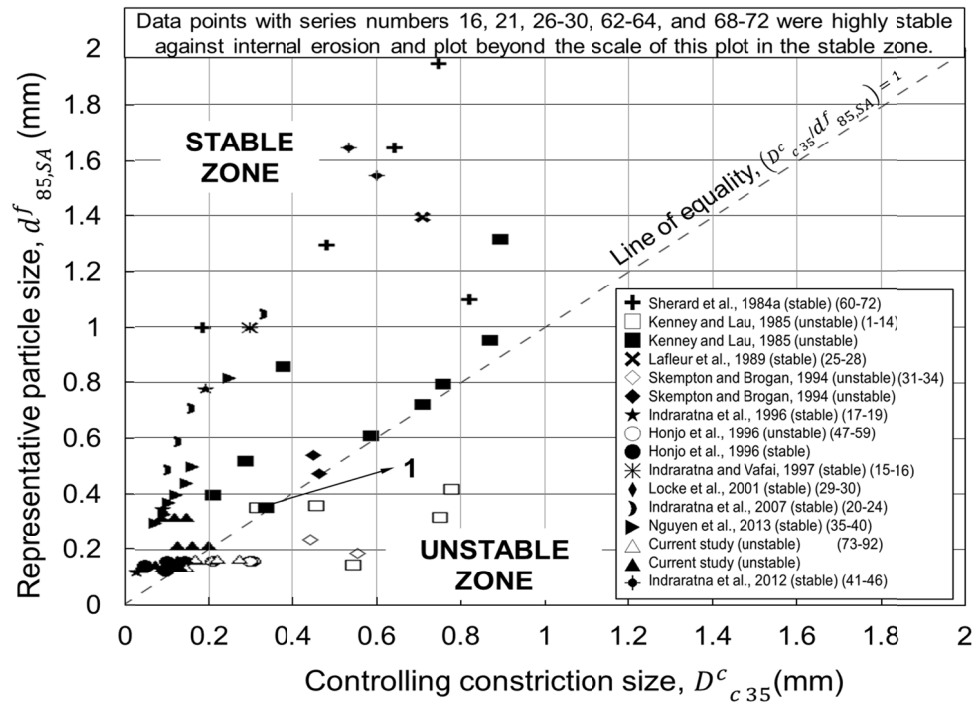


Figure 7. Validation of proposed criterion (after Indraratna et al. 2015).

CONCLUSIONS

In this study, the results from a series of erosion tests conducted to assess and interpret the potential of six granular soils for internal erosion at varying levels of compaction were reported. It was found that apart from the GSD of a soil sample, the R_d also influences the amount of fines eroded at a critical hydraulic gradient and that could significantly reduce the potential internal erosion of soils and transform marginal soils into internally stable ones. Therefore, in order to accurately assess the potential of a soil sample for internal erosion, it is imperative to consider its GSD and R_d together to elucidate the role of CSD too, and not just the GSD, as is considered in existing geometrical criteria.

A novel approach was proposed that couples two existing GSD and CSD based criteria to capture the role of R_d in assessing the internal erosion potential for granular soils. The proposed approach requires caution in demarcating the GSD at a specific division point on the curve that corresponds to the $(H/F)_{\min}$ ratio of Kenney and Lau (1985) for $F \leq 30\%$. The resulting idealised base-filter system should then be assessed by the CSD based retention criterion of Indraratna et al. (2007) to see whether the filter component can retain the base component. The proposed criterion correctly assessed the potential for internal erosion for a large body of published data in conjunction with the current results. It is advisable to use caution when applying the proposed criterion to soils with properties other than those tested in this study.

ACKNOWLEDGEMENT

Technical support from Hi-Bay laboratory staff of University of Wollongong and the financial supports from the Governments of Pakistan and Australia in the form of FDP and IPTA scholarships, respectively, are gratefully acknowledged.

REFERENCES

- Honjo, Y., Haque, M. A., and Tsai, K. A. (1996). "Self-filtration behaviour of broadly and gap-graded cohesionless soils." *Geofilters'96*, J. Lafleur and A. Rollin, eds., Bitech Publications, Montreal, 227-236.
- Indraratna, B., and Vafai, F. (1997). "Analytical model for particle migration within base soil-filter system." *J. Geotech. Geoenviron. Eng.*, 123(2), 100-109.
- Indraratna, B., Israr, J., & Rujikiatkamjorn, C. (2015). "Geometrical method for evaluating the internal instability of granular filters based on constriction size distribution." *J. Geotech. Geoenviron. Eng.*, (DOI: 10.1061/(ASCE)GT.1943-5606.0001343.).
- Indraratna, B., Nguyen, V. T., and Rujikiatkamjorn, C. (2012). "Hydraulic conductivity of saturated granular soils determined using a constriction-based technique." *Can. Geotech. J.*, 49, 607-613.
- Indraratna, B., Raut, A. K., and Khabbaz, H. (2007). "Constriction-based retention criterion for granular filter design." *J. Geotech. Geoenviron. Eng.*, 133(3), 266-276.
- Indraratna, B., Vafai, F., and Dilema, E. (1996). "An experimental study of the filtration of a lateritic clay slurry by sand filters." *Proc. Instn Civ. Engrs. Geotec. Eng.*, 119(2), 75-83.
- Kenney, T. C., and Lau, D. (1985). "Internal stability of granular filters." *Can. Geotech. J.*, 22, 215-225.
- Kezdi, A. (1979). *Soil physics*, Elsevier Scientific, Amsterdam, The Netherlands.
- Lafleur, J., Mlynarek, J., and Rollin, A. (1989). "Filtration of broadly graded cohesionless soils." *J. Geotech. Eng.*, 115(12), 1747-1768.
- Lafleur, J., Mlynarek, J., and Rollin, A. (1989). "Filtration of broadly graded cohesionless soils." *J. Geotech. Eng.*, 115(12), 1747-1768.
- Lane, E. W. (1934) "Security from under-seepage masonry dams on earth foundations." *Trans ASCE* 60(4), 929-966.
- Locke, M., Indraratna, B., and Adikari, G. (2001). "Time-dependent particle transport through granular filters." *J. Geotech. Geoenviron. Eng.*, 127(6), 521-529.
- Nguyen, V. T., Rujikiatkamjorn, C., and Indraratna, B. (2013). "Analytical Solutions for Filtration Process Based on Constriction Size Concept." *J. Geotech. Geoenviron. Eng.*, 139(7), 1049-1061.
- Richards, K. S. and Reddy, K. R. (2007). Critical appraisal of piping phenomena in earth dams. *Bulletin Eng Geology Eng.*, 66(4), 381-402.
- Sherard, J. L. (1979). "Sinkholes in dams of coarse broadly graded soils." *Proc. 13th Congr. Large Dams, New Delhi.*, 2, 25-35.
- Sherard, J., Dunnigan, L., and Talbot, J. (1984). "Basic properties of sand and gravel filters." *J. Geotech. Eng.*, 110(6), 684-700.
- Skempton, A. W., and Brogan, J. M. (1994). "Experiments on piping in sandy gravels." *Geotechnique*, 44(3), 449-460.
- Terzaghi, K. (1922). Failure of dam foundations by piping and means for preventing it (in German). *Die Wasserkraft, Zeitschrift fur die gesamte Wasserwirtschaft.*, 17(24), 445-449.
- Terzaghi, K. (1939). "Soil mechanics—A new chapter in engineering science." *J. Inst. of Civ. Eng. (UK)*, 12(7), 106-141.
- Trani, L. D. O. and Indraratna, B. (2010). "Assessment of Subballast Filtration under Cyclic Loading." *J. Geotech. Geoenviron. Eng.*, 136(11), 1519-1528.

- Unites States Army Corps of Engineers USACE. (1953). "Investigation of filter requirements for underdrains." *Tech. Memo. No. 3-360*, U.S. Waterways Experiment Station, Vicksburg, Miss.
- Xiao, M., Reddi, L.N., and Steinberg, S. (2006). "Effect of vibrations on pore fluid distribution in porous media." *Transport in Porous Media*, 62(2), 187-204.
- Zou, Y., Chen, Q., Chen, X., and Cui, P. (2013) "Discrete numerical modelling of particle transport in granular filters." *Comput. Geotech.*, 32(5), 340-57.

Comparison and Estimation of the Local Scour Depth around Pile Groups and Wide Piers

Chen Wang, S.M.ASCE¹; Xiong (Bill) Yu, Ph.D., P.E., M.ASCE²; and Fayun Liang, Ph.D.³

¹Research Assistant, Dept. of Geotechnical Engineering, Tongji Univ., Shanghai 200092, P.R. China; Currently, Research Scholar, Dept. of Civil Engineering, Case Western Reserve Univ., Bingham Bldg Room 203D, 2104 Adelbert Rd., Cleveland, OH 44106. E-mail: cxw492@case.edu

²Dept. of Civil Engineering, Courtesy with Depts. of EECS, MAE, Case Western Reserve Univ., 2104 Adelbert Rd., Bingham Building Room 206, Cleveland, OH 44106.

E-mail: xyy21@case.edu

³Dept. of Geotechnical Engineering, Tongji Univ., Shanghai 200092, P.R. China. E-mail: fyliang@tongji.edu.cn

Abstract

Experiments of local scour around pile groups and wide piers are carried out under steady currents. Piers with large diameter and pile groups were arranged properly so that the scour process and maximum scour depth could be compared. Although numerous empirical formulas have been proposed to predict equilibrium scour depth around various bridge piers, there is still no general formula that satisfies all conditions. In addition, the scour characteristics of different types of structures are not clearly understood. This study observed the dynamic scour process and the scour depth of every case was determined. Comparisons of pile groups and wide piers were made to aid in the determination of the influence of several foundation types.

INTRODUCTION

Local scour at bridge piers in alluvial rivers during large floods is identified as one of the key factors of bridge failures (Richardson and Davis 2001; Hunt 2009; Liang et al. 2015). Experiments and measurements of local scour at foundations have been carried out by many researchers over the last several decades (for example, Melville and Sutherland 1998; Sheppard et al. 1995; Melville and Coleman 2000; Atatie-Ashtiani and Beheshti 2006; Amini et al. 2012). Scour is a natural phenomenon caused by the erosive action of flowing stream on alluvial beds. It occurs in three main forms, namely, general scour, contraction scour and local scour. Local scour usually occurs at a pier, abutment, erosion control device, or other obstacles obstructing the flow. The obstructions cause flow acceleration and create vortexes that remove the surrounding sediments as briefly shown in Figure 1. Generally, depths of local scour are much larger than general scour depths, often by a factor of ten.

The mechanism of local scour has been studied by many researchers in the past decades. Numerous studies on local scour around vertical piles in steady currents have been carried out, and most of these studies are laboratory results. These efforts can be found in Richardson and Davies (2001), Whitehouse (1998), Sumer and Fredsøe (2002), Zhao et al. (2010) and Liang et al. (2012). The effects of flow can be divided into three aspects: (1) horseshoe vortex caused by acceleration of flow around the nose of pier winnows the sediments around piers; (2) down flow,

which rushes down to the riverbed, brings high-speed water which reaches incipient velocity of sediments; (3) wake vortex generated in the downstream area can also erode the soil behind the structures. However, it becomes more complicated for pile groups or large structures due to the arrangement and flow-obstruction interaction. Some types of pile groups were investigated and different methods of predictions were presented by Ataie-Ashtiani and Beheshti (2006). Liang et al. (2015) carried out flume test on pile groups and investigated the interaction between piles in steady currents. A measure, which combines other expressions for scouring respectively at uniform pier, caisson-founded piers, pile groups with debris rafts, and pile groups alone were presented by Coleman (2005). Zhao et al. (2012) carried out flume tests on the scour behavior of cubic caissons and explored the effect of flow attack angle. However, few works comparing scour between pile groups and caisson have been carried out. To make the bridge and other underwater structures stable, wide piers (e.g. Caissons) have been widely used in practice. Scour at wide piers was evaluated by Sheppard et al. (2011) by comparing the results of the existing predictive equations with collected in-situ and laboratory data. In the present study, flume tests were carried out on both pile groups and caisson. The results including the equilibrium scour depth and scour extents were compared for these two types of foundations. The mechanism of local scour around complex foundation types was discussed.

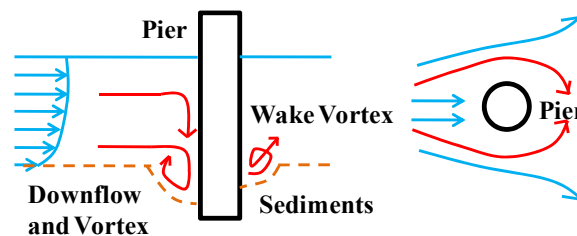


Figure 1. Bridge scour and vortices near a cylindrical pier.

EXPERIMENTAL SETUP

In total, eight experiments were carried out for different foundation configurations as shown in Figure 2. The diameter of the pile groups were designed to be equal to the side width of the caissons, namely 90 mm and 120 mm, so these piles (10 mm in diameter) were arranged with the pile spacing of 35 mm and 46 mm respectively. These experiments were carried out in a 50 m long, 0.8 m wide, and 1.2 m high flume as shown in Figure 3. As the flume width is relatively small, width of the model pile should be also small to prevent sidewall effects. Ataie-Ashtiani and Beheshti (2006) suggested that the blockage area of the models should not exceed 12% of the total flow section, while Whitehouse (1998) suggested that the ratio of flume width to model pile width should be greater than 6.0. As such, in the flume tests the diameter of model pile (D) equal to 0.09 and 0.12 m was used. According to Raudkivi and Ettema (1983) and Melville and Chiew (1999), D/d_{50} (d_{50} is mean particle size) should be greater than 50 in laboratory to reasonably reflect the scour extent in the full scale condition. Therefore, bed materials with the mean particle sizes of 0.15 mm were used, resulting in the D/d_{50} -ratio ranging from 600 to 1000. After trial and error, a flow velocity of 22.5 cm/s and a water depth of 25 cm were selected. The flow velocity was monitored by the Acoustic Doppler Velocimetry (ADV) installed upstream the testing area (Figure 2). In each group, the scour depth was measured mainly by a probe, which is made of a slender metal rod combined with a dial indicator. The Shields parameter θ_s is calculated by:

$$\theta_s = \frac{\tau_s}{\rho g (s-1) d_{50}}$$

where ρ is the water density, g is the acceleration due to gravity, s is the specific gravity of sand, d_{50} is the median particle size of sand, and τ_s is the shear stress, which is calculated by (Soulsby 1997).

$$\tau_s = \rho C_D \bar{U}$$

Here, $C_D = \{\kappa / [\ln(z_{0s}/h) + 1]\}^2$, κ (equals to 0.4) is the Karman constant, z_{0s} (equals to $d_{50}/12$) is the bed roughness and h is the water depth, and \bar{U} is the average flow velocity. The Shield parameter θ_s , which is always used to judge the onset of sediment motion, is 0.18 in present study.

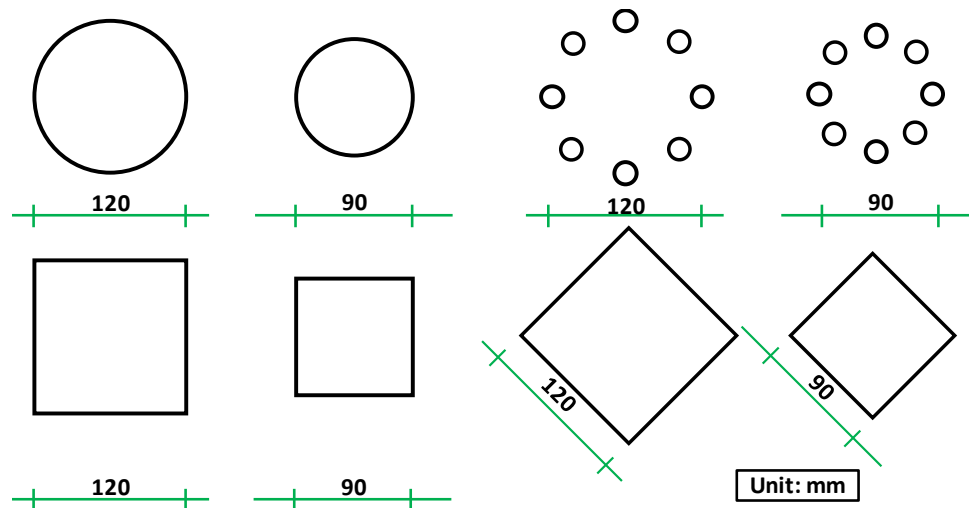


Figure 2. Experimental model arrangement.

RESULTS AND ANALYSIS

Pile groups. Scour around pile groups can be divided into two parts, namely integral scour and separate scour. An integral scour is developed when the coming flow creates a single scour hole at a pile group at a relatively small pile spacing. Separate scour is developed when at a larger pile spacing, independent scour holes are formed at piles within a pile group. Scour mechanism of pile groups has been studied by researchers before, and the shielding effect and jetting effect have been proposed by Liang et al. (2015). The upstream piles in a pile group act as a vortex shield for the downstream piles, which helps reduce the scour at downstream piles. This phenomenon also appears in the present pile group arrangement. The cross-section between piles is narrowed when piles exist in the channel side-by-side, in which case the flow will be accelerated and redirected in these area. This is called jetting effect, and appears in the present study as shown in Figure 4. However, this effect was less evident for the pile group patterns in Figure 2 because every two piles are aligned to the attack angle of the approach flow. When the pile spacing is large enough, these piles behaved as several single piles leading to the development of separate scour. In this study, scour at pile groups and circular and cubic caissons was investigated and the results for pile groups and circular caissons were compared.

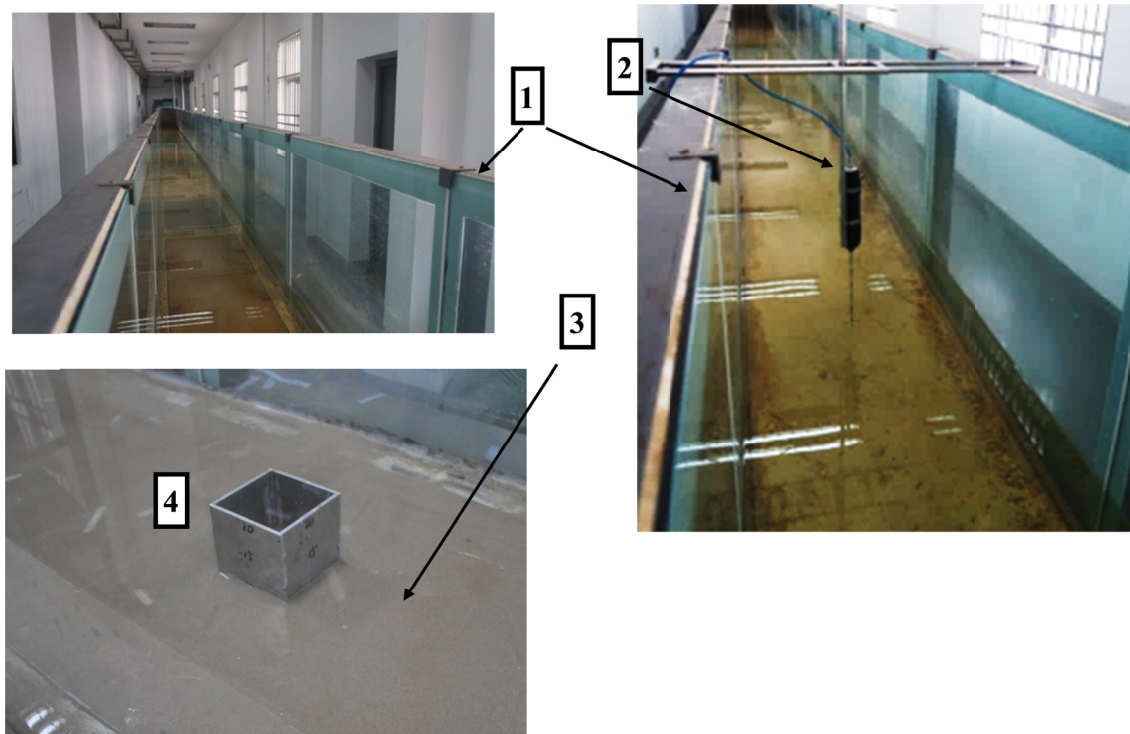


Figure 3. Experimental setup (1. Flume; 2. Acoustic Doppler Velocimetry (ADV) ;3. Sand Basin and Bed Material; 4. Model).



Figure 4. Scoured Pile Groups with the outer diameter of: (a) 120 mm; (b) 90 mm.

Circular caissons. Research on caissons has been carried out in previous studies in the past decades due to the proliferation of complex foundations used in bridge and coastal engineering recently. Coleman (2005) carried out flume tests on caissons with different embedded depths and the effects of the caisson embedment. Unlike a single pile, caissons always have large diameters, causing significant disturbance of flow structure around the foundations. Moreover, the scour process is quite different along the boundaries according to the local flow generated by the interaction between the caisson and the flow. The scour holes developed at two sizes of caisson models are shown in Figure 5. Scour initiated rapidly in the upstream. Then the scour rate was

reduced gradually and eventually arrived in the equilibrium. Based on the observed scour process, the boundary of caisson can be divided into three areas: clear-water area, live-bed area and deposition area. In clear-water area, with the development of scour, the riverbed was continually eroded and the scour hole eventually reached the equilibrium. In live-bed area, the riverbed changed due to the sediment transported from upstream, while the scour rate also changed with the bed elevation. In deposition area, the scour occurred slightly on both sides as shown in Figure 5. The holes were then connected with each other and were refilled with soil particles to become a dune.

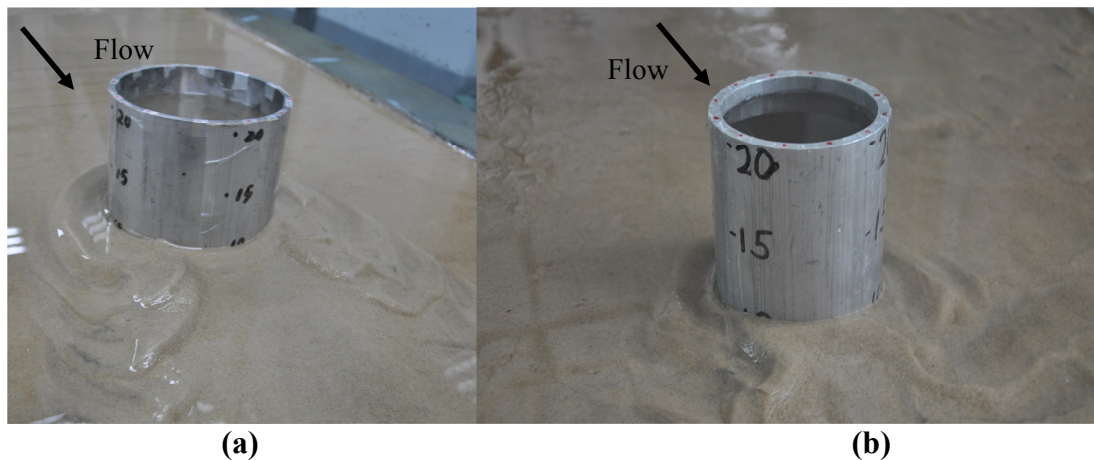


Figure 5. Scoured Caisson with the Diameter of 120 mm (a) and 90 mm (b).

Cubic caissons. In many cases, cubic caissons are used as the foundation of bridges, especially sea bridges. Zhao et al. (2012) studied the influence of caisson width and attack angle using flume tests. In the present study, the behaviors of corners were investigated and the dynamic process was observed. As shown in Figure 6, erosion occurred around the upstream corners, and the scour holes around corners were connected with the development of scour process. These corners can be divided into three categories: upstream frontier corners, upstream sides corners, and downstream corners. The frontier corners can redirect the coming flow and reduce its power, leading to a smaller scour hole. For the sides corners, vortices were developed due to the interactions between the flow and the caisson. Scour around these corners was more significant than others. In the case of downstream corners, flow power was decreased by the upstream corners and deposition and thus scour was least in this area. Figure 6 also indicates that the cubic caisson rotated by 45 degrees with respect to the flow direction experienced less scour, implying the importance of caisson skew angle.

Comparisons. The scour process and equilibrium scour depth for the above foundations are compared in this section. Generally speaking, foundations of the same type showed similar scour characteristics. As shown in Figure 7, a cubic caisson with an attack angle (45 degrees in present study) experienced the least scour. The erosion develops gradually from beginning to the equilibrium condition. The reason may be that the frontier corner, which can reduce the power of coming flow, plays an important role in the scour process. At the same time, pile groups can also redirect and reduce the coming flow, thus leading to a small local flow structure. Scour around pile



Figure 6. Scoured Cubic Caisson (a) and Caisson with Angle (b).

groups is more serious than the caisson with an attack angle because the flow can jet between two piles, which will bring separate scour to each pile. When compared with pile groups with the same outer diameter, the caisson has a stronger interaction with the coming flow, which provides significant scour for these large obstructions. For the same type of foundation, the larger diameter, the deeper the scour will be. This is because the local flow generated by an obstruction is influenced by the foundation width. For the pile groups and cubic caisson with an attack angle with a small diameter, the equilibrium scour depths can be alike because the interaction between foundations and flow is slight. However, the scour ratio (scour depth divided by foundation diameter) is not always the same. The relationship between scour depth and pier width is not a linear one, but always regarded as an exponential one (Richardson and Davis 2001; Melville and Coleman 2000; the Ministry of Communications of PRC 2002). But it varies with the change of diameter according to scour observed in laboratory and field tests. A comprehensive analysis of the relationship between the scour depth and pier diameter needs to be further investigated.

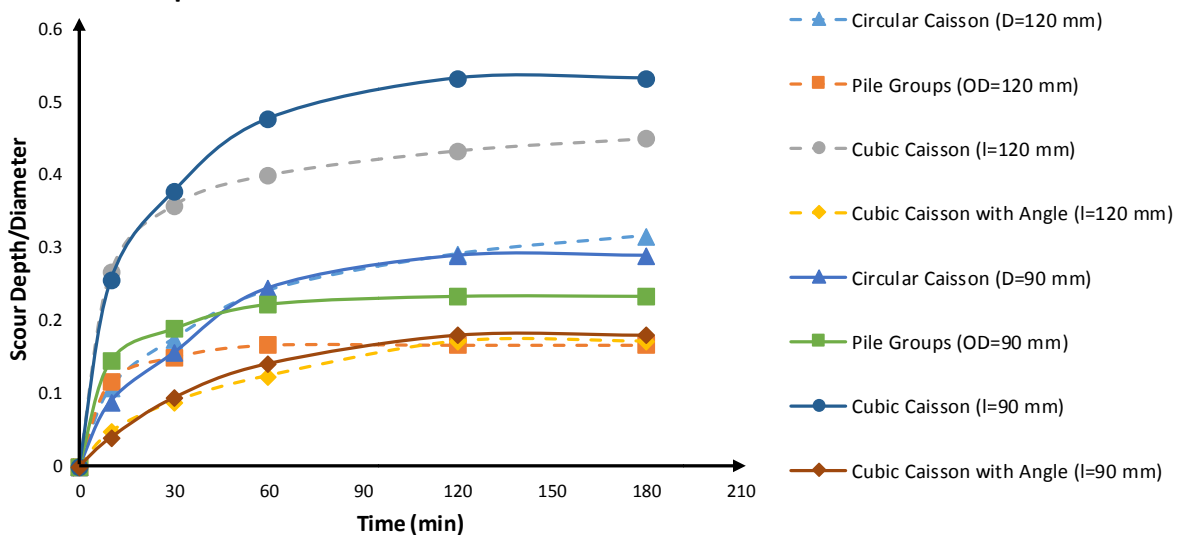


Figure 7. Comparison between pile groups and caissons.

Laboratory studies together with field observations of scour depth at wide piers indicate that the existing equations overestimate scour depths. Because of this limitation, the design methods lead to the use of costly foundations or countermeasures. The widely accepted HEC-18 equation can be used to predict both live-bed and clear-water pier scour. It is stated as:

$$\frac{h_b}{h_p} = 2.0K_1K_2K_3 \left(\frac{D}{h_p} \right)^{0.65} Fr^{0.43}$$

Here, h_b =scour depth; h_p =flow depth; D =pier diameter; K_1 =correction factor for pier nose; K_2 =correction factor for attack angle; K_3 =correction factor for bed condition; Fr = Froude Number.

When it comes to pile groups, the effective width of an equivalent full depth pier (D^*) is calculated to take the interaction of piles into consideration. It is stated as:

$$D^* = D_{proj}K_{sp}K_m$$

Here, D_{proj} =sum of non-overlapping projected widths of piles; K_{sp} =coefficient for pile spacing; S =spacing between columns of piles; D =pile diameter; K_m =coefficient for number of rows.

To better predict the scour depth around wide piers, Sheppard and Demir (2011) compared existing equations and recommended a melding and slight modification of equations as:

$$\frac{h_b}{a^*} = \begin{cases} 2.5f_1f_2f_3 & \text{for } 0.4 \leq \frac{V_1}{V_c} < 1.0 \\ f_1 \left[2.2 \left(\frac{\frac{V_1}{V_c} - 1}{\frac{V_{1p}}{V_c} - 1} \right) + 2.5f_3 \left(\frac{\frac{V_{1p}}{V_c} - \frac{V_1}{V_c}}{\frac{V_{1p}}{V_c} - 1} \right) \right] & \text{for } 1 \leq \frac{V_1}{V_c} \leq \frac{V_{1p}}{V_c} \\ 2.2f_1 & \text{for } \frac{V_1}{V_c} > \frac{V_{1p}}{V_c} \end{cases}$$

Here, V_1 is flow velocity, V_c is sediment critical velocity, V_{1p} is live-bed peak velocity, a^* is effective diameter, and f_1, f_2, f_3 is coefficient for calculation.

These two methods provide different results when compared with laboratory data herein as shown in Figure 8. The overestimation of wide pier is corrected in the NCHRP Report 682 method, which agrees better with the measured data. For pile groups, HEC-18 equation overestimates the results because the complex interaction between pile and particle size are not well considered. For cubic caissons, scour depths are influenced by the corners but both methods lack the analysis on these corners. For circular caissons, the overestimation is also evident for these methods. Overall, NCHRP Report 682 method is recommended for the large foundations.

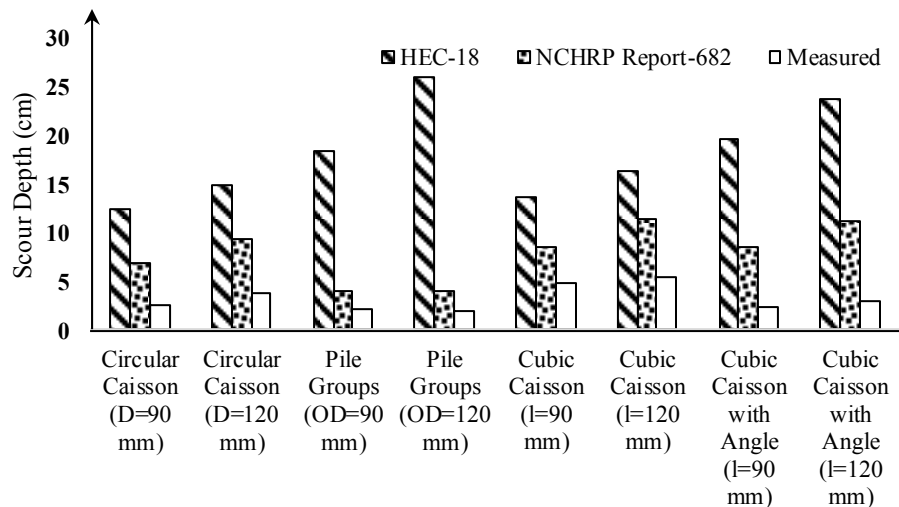


Figure 8. Comparison between measured and calculated results.

CONCLUSIONS

In the present study, eight experiments on four types of foundations were carried out. The scour process was observed and the mechanism of scour was discussed. The following conclusions are drawn from this study:

- (1) The local scour around pile groups can be divided into two parts: integral scour and separate scour. Both of them are affected by shielding and jetting effects. For a narrowly spaced pile group subjected to scour, the front piles can provide protection to the rear piles (shielding effects), while the narrowed spacing between side-by-side piles lead to more serious erosion.
- (2) Wide piers, such as caissons, are more complex than narrow piers because the interaction between flow and boundary is much more complicated. However, scour pattern varied with the types of foundations and skew angles, especially when the diameter is relatively large. Even with the same outer diameter, the scour characteristics are quite different for circular caisson (with and without angle), cubic caisson and pile groups.
- (3) Corners of cubic caissons play an important role in the scour process. Three different types of corners have their own characteristics at local scour, which varies with the attack angle. The local flow generated due to the structure reasons, including their shape, diameter, surface, etc., determines the equilibrium scour depth of underwater obstructions.
- (4) The scour extent for the foundations investigated in this study follows the order: cubic caissons normal to flow direction, the pile groups, circular caissons, and cubic caissons rotated 45 degrees to the flow direction. The normalized scour depth (to pier width) appears in a nonlinear relationship with test time.

REFERENCES

- Amini, A., Melville, B. W., Ali, T. M., and Ghazali, A. H. (2011). "Clear-water local scour around pile groups in shallow-water flow." *J. Journal of Hydraulic Engineering*, 138(2), 177-185.

- Ataie-Ashtiani, B., and Beheshti, A. A. (2006). "Experimental investigation of clear-water local scour at pile groups." *J. Hydraul. Eng.*, 132(10), 1100–1104.
- Coleman, S. E. (2005). "Clearwater Local Scour at Complex Piers." *J. Journal of hydraulic engineering*, 131 (4): 330-334.
- Liang, F., Wang, C., and Huang, M. (2015). "A preliminary experimental study on the mechanism of local scour at pile groups in steady currents." *In: The 3rd International Symposium on Frontiers in Offshore Geotechnics*, Oslo, Norway: 599-604.
- Hunt, B.E. (2009). *Monitoring scour critical bridges*. Washington, D.C.
- Liang, D., Gotoh, H., Scott, N., and Tang, H. (2012). "Experimental study of local scour around twin piles in oscillatory flows." *J. Journal of Waterway, Port, Coastal, and Ocean Engineering*, 139(5), 404-412.
- Liang, F., Zhang, H., and Huang, M. (2015). "Extreme scour effects on the buckling of bridge piles considering the stress history of soft clay." *J. Natural Hazards*, 77(2), 1143-1159.
- Melville, B.W., and Coleman, S. E. (2000). *Bridge scour*, Water Resources Publications, Highlands Ranch, CO.
- Melville, B.W., and Sutherland, A.J., (1988). "Design Method for Local Scour at Bridge Piers." *J. Proceedings of ASCE Journal of Hydraulic Engineering* 114 (10), 1210–1226.
- Arneson L. A., Zevenbergen L. W., Lagasse P. F., and Clopper P. E. (2012) "Evaluating scour at bridges", 5th Ed. Hydraulic Engineering Circular No. 18 (HEC-18), *Federal Highway Administration*, Washington, DC, USA.
- Sheppard, D. M., Demir, H., & Melville, B. W. (2011). *Scour at wide piers and long skewed piers* (Vol. 682). Transportation Research Board.
- Sheppard, D. M., Ontowirjo, B., and Zhao, G. (1995). "Local scour near single piles in steady currents." *Proc., 1st Hydraulics Engineering Conf.*, San Antonio.
- Sumer, B. M., and Fredsøe, J. (2002). "The mechanics of scour in the marine environment." *J. World Scientific*, Singapore. 536 pp.
- Whitehouse, R. (1998). *Scour at marine structures: A manual for practical applications*. Thomas Telford. 198 pp.
- Zhao, M., Cheng, L., and Zang, Z. (2010). "Experimental and numerical investigation of local scour around a submerged vertical circular cylinder in steady currents." *J. Coastal Engineering*, 57(8), 709-721.
- Zhao, M., Zhu, X., Cheng, L., et al (2012). "Experimental Study of Local Scour around Subsea Caissons in Steady Currents." *J. Coastal Engineering*, 60: 30-40.

Experimental Investigation of the Pier Streamlining Effect on Bridge Local Scour under Clear Water Conditions

Junhong Li¹ and Junliang Tao, A.M.ASCE²

¹Graduate Research Assistant, Dept. of Civil Engineering, Univ. of Akron, OH 44325. E-mail: jl175@ziips.uakron.edu

²Assistant Professor, Dept. of Civil Engineering, Univ. of Akron, OH 44325. E-mail: jtao2@uakron.edu

Abstract

A series of experimental tests were conducted to investigate the effect of pier streamlining on bridge local scour under clear-water conditions. A total of four testing cases were included in this study. Test conditions in all cases were kept the same except that the pier geometry in each case had sequentially increased extents of streamlining. These streamlining features were adopted from a previous numerical study by the authors. This paper compared the time evolution of local scour among cases. Contour maps of the scoured bed were obtained using the structure from motion (SfM) technique. The streamlined piers generally showed advantage over the traditional oblong pier in terms of the scour rate, the maximum scour depth and the total scoured volume at equilibrium. This study suggests that streamlining can be a viable scour countermeasure, but more real-life scenarios including variabilities in soil and flow properties need to be further investigated.

INTRODUCTION

Bridge local scour—the erosion, or specifically, the entrainment and transportation of the sediment materials in the vicinity of piers and abutments—is widely recognized as one of the most critical causes for bridge failure (Landers 1992). Consequently, development and effectiveness evaluation of scour countermeasures has become a primary interest of bridge engineers. Bridge scour countermeasures that are commonly used in practice nowadays, along with their design guidelines, are included in the Hydraulic Engineering Circular (HEC) No. 23 (Lagasse et al. 2009) and No. 18 (Arneson et al. 2012). However, most of these countermeasures are subject to a service life limitations and require periodic inspection, which increases the costs in the long run. Moreover, reports on failure of scour countermeasures such as for riprap are not uncommon. Consequently, persistent efforts have been made by researchers to seek more robust and cost-effective scour countermeasure alternatives. For example, Robie Bonilla (2010) recently proposed adding a sheath to the pier in order to give the ensemble a streamlined profile and enhance its anti-scour performance. The sheath can be freely rotated to align with flow direction so as to counteract the adverse influence of the flow attack angle. El-Ghorab (2013) suggested a modified method that involves designing an arrangement of openings in the pier body, to reduce the vortex strength and the scour depth in front of bridge piers. Other studies on the use of slotted piers as a scour control measure can be found (Grimaldi et al. 2009; Moncada-M et al. 2009). However, further research on structural safety and slot occlusion issues is needed before the slotted pier can be adopted in the field.

In a continuing effort to explore scour countermeasure, the authors proposed pier streamlining as a feasible alternative to reduce scour potential and identified a relatively optimal streamlined pier configuration using a Computational Fluid Dynamics (CFD) numerical model (Li and Tao 2015a; Li and Tao 2015b). In particular, streamlined piers were found to eliminate downward jet flow in front of the piers and reduce the horseshoe vortex strength as well as the maximum bed shear stress. These findings suggest that streamlined piers could potentially serve as an alternative scour control measure. However, it would be imprudent to apply the concept of pier streamlining to practice without experimental validation. Therefore, in the present study, a set of flume tests were conducted under clear-water conditions in the laboratory to investigate the scour pattern around four pier models, which had sequentially ascending streamlining features. A high speed camera was set up to record the local scour process. The Structure from Motion (SfM) technique was employed to generate the digital elevation model (DEM) of scoured bed around different pier shapes, from which the contour maps of scoured bed at various scour stages were generated. Comparisons were made of the time evolution of the maximum scour depth for different pier models as well as for the scour hole volume for each at equilibrium.

EXPERIMENTAL SETUP AND PROCEDURE

The flume. Experiments were carried out in a Plexiglas-sided recirculating flume with a length of 3m, a width of 0.3m and a depth of 0.45m. The flume was supported by a steel framework and was kept horizontal throughout the experiments. The setup included a tank, two pumps, and a network of pipes. A sand recess ($0.9\text{m} \times 0.3\text{m} \times 0.08\text{m}$) was positioned 1.2m downstream of the flume inlet to retain the standard Ottawa sand used as bed materials (specific gravity is 2.65; median diameter $d_{50}=0.60\text{mm}$; and critical bed shear stress $\tau_c \sim 0.3\text{Pa}$). The standard deviation (σ_g) of 1.38 for the sand implied that the sediment could be assumed as uniform. The top of the sand bed was constructed at the same elevation as the upstream planer bed, to ensure that the fully-developed turbulent flow would enter the sediment bed smoothly. Eroded sand was collected by a sediment trap at the downstream end of flume. A straw screen filter was installed at the inlet to encourage a uniform flow distribution and also to dampen fluctuations at the water surface. The discharging rate (Q) could be adjusted by the control valve of pipe connecting to water pumps, and the flow depth (h) could be adjusted using a tailgate fitted at the end of the flume. During experiments for all test cases, the approaching flow depth (h) was kept constant at about 10cm. This was to ensure that there were no significant influence of flow depth on the scour depth, as suggested by Melville and Sutherland (1988) as $h/b \geq 3.5$ for a uniform cylindrical pier (b is pier width).

The depth-averaged inlet velocity (U) was literally controlled as 0.21m/s for all tests. Such a magnitude was determined from Shields' diagram as 75% of the critical velocity for the Ottawa sand ($d_{50}=0.60\text{mm}$) used in this study, in order to satisfy clear-water conditions. This critical velocity (U_c) was also verified by conducting an experiment without pier. The depth-averaged inlet velocity was calibrated by using an acoustic Doppler velocimeter (ADV) to measure velocity profile of the approaching flow at about 0.8m upstream of the pier. A wooden screed was mounted on the flume to level the sand bed in the recess. A point gauge carrier, which could be freely moved in both longitudinal and transverse directions of the flume, was also mounted on the flume top. The Vernier point gauge with an accuracy of 0.1mm was used to measure the instantaneous maximum scour depth.

Test cases and pier models. A total of four test cases were conducted to investigate the scour patterns around four pier models with increased streamlining extents, as shown in Figure 1. These streamlining features were following those optimized in a previous numerical study by the authors (Li and Tao 2016), but all pier models were scaled down accordingly due to the small dimensions of the flume used for the experiments. For pier models used in this study, the pier width (b) was 30 mm, which was 20% of the width used in numerical study. The aspect ratio of pier width to length was kept constant at 1:4. Pier height and flow depth were 10 cm in the laboratory test while they were exactly 20 cm in the numerical study. Other geometric configurations of the pier, such as nose sloping and sidewall concaving curvature, followed the pier features in the previous optimization study. In both studies, the blockage ratio of pier at the flume transverse cross-section in all test cases was kept the same (10%) so that the results would be comparable. The blockage ratio of 10% in our study was below the maximum value of 16% suggested by Raudkivi and Ettema (1983), who recommended that the flume width should be no less than 6.25 times of pier width to avoid the wall friction effect in the flume. An alternative study suggested that the pier size should not be more than 10% of flume width so as to avoid the contraction effect in the flume (Sarker 1998). To keep it consistent with the previous numerical study, cases were named using the format “pier cross-sectional shape + nose + sidewall configuration”. In Case#3, for example, the pier’s horizontal cross-section had the optimal features determined in previous numerical optimization study (Li and Tao 2015a). Noses of the pier in Case#3 were sloped at V:H=4:3 and the sidewalls were vertically straight. For each test case, the pier models shown in Figure 1 were pier bodies above the initial sediment bed surface placed in the middle of recess, with its long axis aligned with the flow direction. The bottom cross-section of each pier model in Figure 1 was extruded vertically downward to form the embedded part of pier, which was fixed on bottom of the flume recess. All pier models were built in SolidWorks and printed out via 3D printing. The sediment bed in all test cases were prepared following the air pluviation technique (raining the sand).



Figure 1. Pier geometry in different cases.

Experimental procedure. All the experiments were conducted under steady turbulent flow and clear-water conditions in this study. First, the sediment bed was prepared by sprinkling Ottawa sand into the recess. A wooden screed, attached to a trolley mounted on the flume top, was

utilized to level the bed surface. Next, the sand bed was saturated for at least one hour. After sample saturation was achieved, the control valve was opened to gradually increase the inlet discharge to 0.21 m/s. To avoid initial bed erosion, a glass plate was firstly placed downstream of the sand recess to slow the flow of water; it was removed once an adequate water depth (10 cm) was achieved in the flume. For each test, a Vernier point gauge was used to measure the time evolution of maximum scour depth (at a higher frequency during the initial scour stage and less frequently at later stages). A high-speed camera was mounted near the pier models to record the side view of the local scour process as it developed.

Each test case was run for a period nominally expected to be sufficient to reach the equilibrium scour stage. The equilibrium condition was considered to be achieved when a negligible ($<0.5\text{mm}$) variation in max scour depth was observed at an interval of 2 hours after running the test for 24 hours. This time period is considered as sufficient based on the calibration run by Ataie-Ashtiani and Beheshti (2006), who found that 86% and 92% of the equilibrium scour depth were attained at times of 5.5 hours and 8 hours, respectively. When the equilibrium stage was reached, water was gently removed from the flume to avoid disturbing the final topography of the scoured bed. After the maximum scour depth was determined, each case was repeated in order to document the scoured bed morphology at intermediate stages.

RESULTS AND DISCUSSION

In this section, the general local scour developing process is described. Also presented are the time evolution of scour depth, the scoured volume at equilibrium and the scour pattern in different test cases. By comparing the results from the various cases, the effect of pier streamlining on local scour reduction is discussed.

Local scour development. Local scour is a result of complex interactions between the flow, pier and sediment particles. The downward flow along the pier nose and the horseshoe vortex upstream of pier are well known as the main agents responsible for sediment entrainment. The eroded sediment materials are then transported downstream by the vortex structure in the wake region. The local scour process follows a general pattern shown in Figure 2, which includes six representative snapshots of the development of instantaneous local scour around the oblong pier in Case#1. During the initial stage of local scour development (t_1), a small ring-like groove forms around the upstream pier nose due to the downflow and the corner vortex. The groove typically forms within a very short period of time (<1 minute). Scour of sand particles then presents a quasi-periodic character, which corresponds to the periodic shedding nature of the horseshoe vortex. During each cycle, sand particles in the scour hole near the pier corner are first ejected upstream into a suspension state and are then transported downstream along the pier flanks (t_2). As the scour process continues, the scour hole slope exceeds the angle of repose for the bed material. As a result, sand particles along the upper slope collapse into the bottom of scour hole, and the scour hole gradually develops upstream (t_3). This scour process is repeated (e.g., $t_4 \sim t_5$) until the equilibrium state is reached (t_6).

Local scour pattern. Firstly, the time evolution of maximum scour depth for all cases is presented in Figure 3, which shows that scour depth is significantly decreased as the extent of pier streamlining increases. Furthermore, the scour rates in Case#2, #3 and #4 are much smaller than that in Case#1. This may imply a potential for additional benefits from pier streamlining in

the case of a short-period flooding event. Figure 3 shows a large discrepancy between the first two trials of Case#4. In view of such an inconsistency, Case#4 was repeated for two additional times, the results of which generally agreed with that from the second trial. Therefore, results from the second trial for Case#4 can be considered as reliable. Reason for the discrepancy between the first two trials for Case#4 is uncertain. One hypothesis is that the pier model might be embedded a little into the original bed surface during the first trial. Since the embedded part of piers in both Case#3 and #4 were vertically lofted from the bottom cross-section as shown in Figure 1, the embedded part of pier#4 had a much larger pier width as well as a blunter pier nose than the other three cases. This hypothesis is supported by the scour evolution during the first hour of experiment. At early stage, scour hole around pier#4 was actually developed slower than pier#3. After the embedded pier body was exposed, scour depth developing rate dramatically increased. However, the influence of pier embedment for the most streamlined pier in Case#4 needs to be further investigated. So far as Figure 3 indicates, Case#3 has the smallest scour depth, which approximates 1/3 of the max scour depth in Case#1.

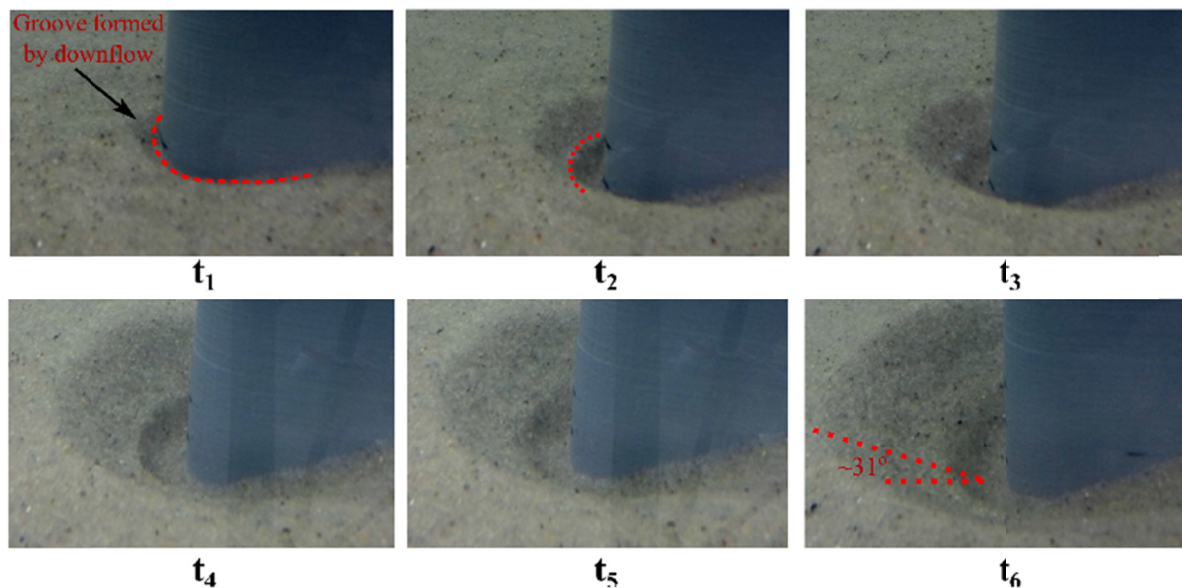


Figure 2. Instantaneous snapshots of local scour developing process in Case#1.

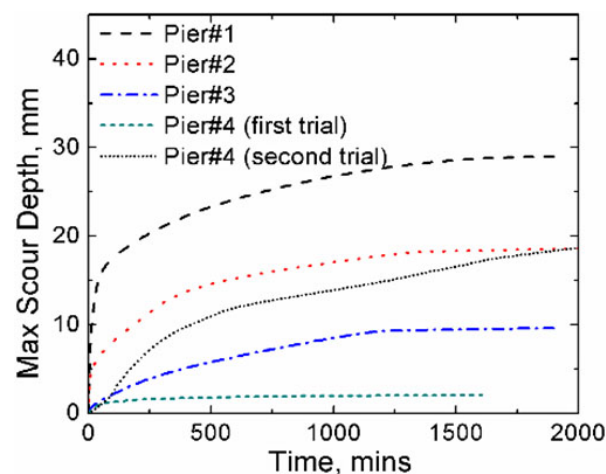


Figure 3. Time evolution of the maximum scour depth for all cases.

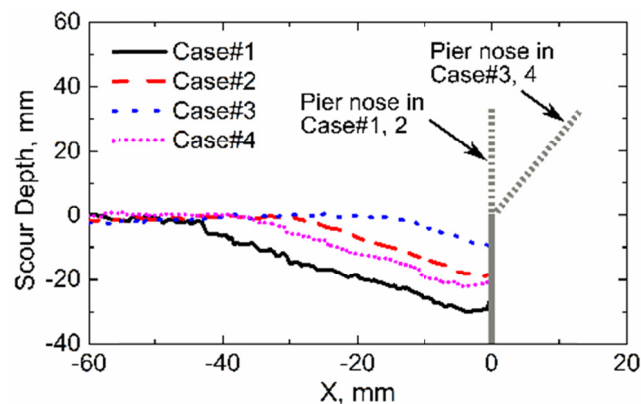


Figure 4. Scour Profile at equilibrium on the symmetry plane for all cases.

Time evolution of the bed morphology for all cases (shown in Figure 5) was reported using the Structure from Motion (SfM) technique (Westoby et al. 2012), which is able to reconstruct a 3-D scene using overlapping photos taken from different angles. Specifically, Figure 5 includes bed contour maps at four intermediate scour stages, equivalent to 30%, 60%, 80% and 100% of the maximum scour depth at equilibrium (d_{se}). Two open source software applications, VisualSfM (Wu 2013; Wu et al. 2011) and CloudCompare (2015), were employed to generate the digital elevation model from overlapping photos of the scour bed. Figure 5 shows that the scour hole was developed within a smaller region upstream of the streamlined piers, especially for the pier in Case#3. A certain amount of scoured sediment particles was deposited beside the piers in Case#1, #2 and #4. In comparison, sand particles eroded from upstream were deposited relatively uniformly downstream of the pier in Case#3. This indicates that a much weaker wake vortex formed in Case#3 than in other cases.

Figure 6 compares the volume of the sand eroded from the scour hole in front of the piers for all cases. From this figure, it can be noticed that the streamlined piers significantly reduce the volume of eroded bed material. In the previous numerical study by the authors (Li and Tao 2016), the presence of sediment particles was not considered, and the simulation results suggested that there was a 39% reduction in the maximum bed shear stress from Case#1 to Case#3. By comparison, in the present experiment study that takes into account the flow-sediment interaction, the maximum scour depth and the total eroded volume for Case#3 are only about 33% and 10% of those in Case#1, respectively. The benefits gained from pier streamlining are proven to be significant.

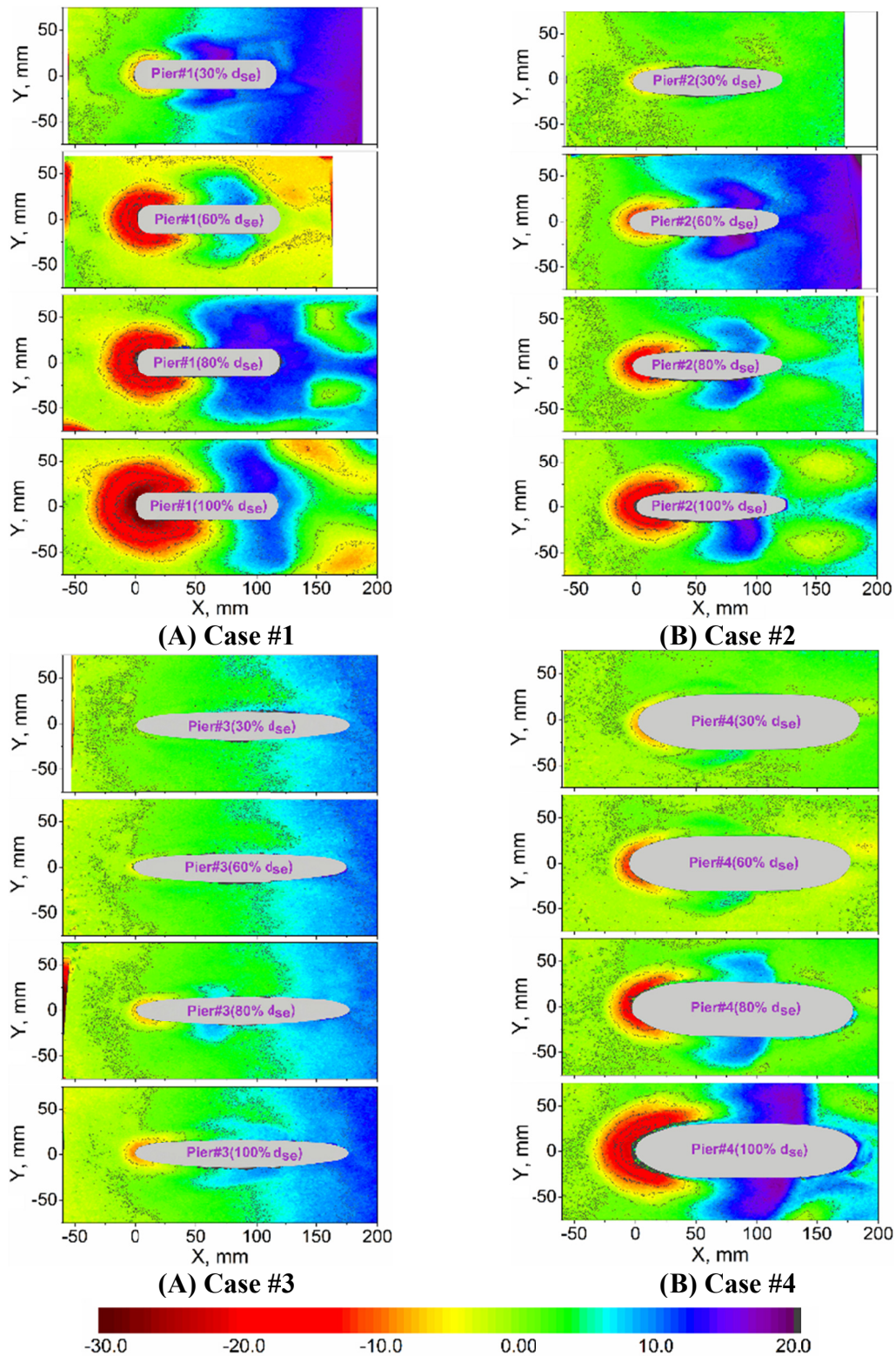


Figure 5. Time evolution of scour contour for all cases.

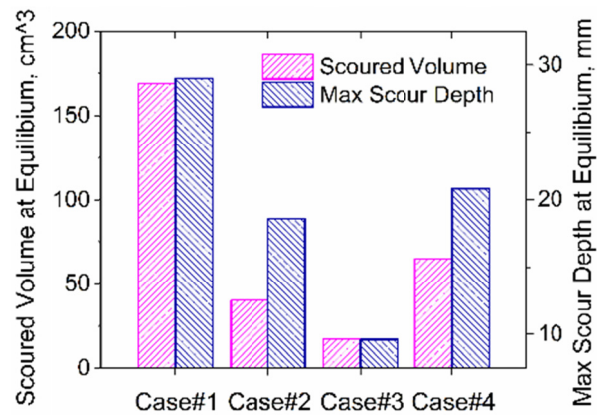


Figure 6. Comparison of the scour hole volume for all cases.

CONCLUSIONS

Bridge scour control is a big concern to engineers because of the detrimental damage scour issues may cause. Although HEC-18 and HEC-23 provide the design guidelines for a number of commonly-used scour countermeasures in practice, these countermeasures still have certain shortcomings, limiting their values in field application. Therefore, as part of the efforts to seek for more robust and cost-effective scour countermeasure alternatives, the authors proposed pier streamlining as a feasible alternative in a previous numerical study. In order to further validate the effectiveness of pier streamlining in reducing local scour potential, the present study performed a series of open-channel flume tests in the laboratory. A total of four pier models with sequentially increased streamlining extents were constructed following the streamlining features obtained in the previous numerical study. All the experiments were conducted under steady turbulent flow and clear-water conditions.

Experimental results showed that pier#3 (the pier with streamlined horizontal cross-section, sloped nose and vertically straight sidewalls) resulted in the lowest values of both maximum scour depth and scoured volume at equilibrium. In particular, the total scoured volume around the streamlined pier in pier#3 was only about 10% of that in pier#1 (the pier with a non-streamlined cross section, straight nose profile and straight side walls). From the time evolution of the maximum scour depth (Figure 2), it was also found that the scour rate was decreased around the streamlined piers. This indicated potentially further benefits from pier streamlining in case of a short-period flooding event. Finally, the contour maps of the scoured bed at equilibrium showed that the scour holes were developed within a smaller region upstream of the streamlined piers, especially for the pier in Case#3. Instead of being entrained and transported further downstream, the sediment particles began to settle from the middle of pier#3, indicating a much less wake vortex intensity in pier#3 than in other cases. In summary, this study further verified the results from a previous numerical study by the authors that pier streamlining could help reduce the local scour potential around bridge piers, and it can thus serve as an effective scour countermeasure alternative or at least a supplementary measure to existing scour control measures. However, since flow conditions and sediment properties in the present experimental study were not varied, pier streamlining warrants further investigation under different combinations of scour controlling variables. The feasibility of applying the streamlined pier to prototype bridges also needs to be further evaluated from the perspectives of structural design and economic benefit before it can be applied in the field with confidence.

REFERENCE

- Arneson, L. A., Zevenbergen, L. W., Lagasse, P. F., and Clopper, P. E. (2012). *Hydraulic Engineering Circular No. 18, Evaluating Scour at Bridges: Fifth Edition*, U.S. Department of Transportation, Federal Highway Administration.
- Ataie-Ashtiani, B., and Beheshti, A. (2006). "Experimental investigation of clear-water local scour at pile groups." *Journal of Hydraulic Engineering*, 132(10), 1100-1104.
- CloudCompare (2015). < (version 2.6) [GPL software], Retrieved from <http://www.cloudcompare.org/>.
- El-Ghorab, E. A. S. (2013). "Reduction of scour around bridge piers using a modified method for vortex reduction." *Alexandria Engineering Journal*, 52(3), 467-478.
- Grimaldi, C., Gaudio, R., Calomino, F., and Cardoso, A. H. (2009). "Countermeasures against local scouring at bridge piers: slot and combined system of slot and bed sill." *Journal of Hydraulic Engineering*, 135(5), 425-431.
- Lagasse, P. F., Clopper, P. E., Pagán-Ortiz, J. E., Zevenbergen, L. W., Arneson, L. A., Schall, J. D., and Girard, L. G. (2009). *Hydraulic Engineering Circular No. 23 - Bridge Scour and Stream Instability Countermeasures: Experience, Selection and Design Guidance, Third Edition*, U.S. Department of Transportation, Federal Highway Administration.
- Landers, M. N. (1992). "Bridge Scour Data Management." *Hydraulic Engineering: Saving a Threatened Resource, published by American Society of Civil Engineering*.
- Li, J., and Tao, J. (2015a). "Streamlining of Bridge Piers as Scour Countermeasure: Optimization of Cross Section." *Journal of Transportation Research Board*, No. 2521, 160-169.
- Li, J., and Tao, J. (2015b). "Streamlining of Bridge Piers as Scour Countermeasure: Effects of Curvature of Vertical Profiles." *Journal of Transportation Research Board*, No. 2521, 170-180.
- Li, J., and Tao, J. "DES Investigation of the Effect of Pier Streamlining on Coherent Dynamics of the Turbulence Structure around Piers." *Proc., Transportation Research Board 95th Annual Meeting (2016)*, In press.
- Melville, B., and Sutherland, A. (1988). "Design Method for Local Scour at Bridge Piers." *Journal of Hydraulic Engineering*, 114(10), 1210-1226.
- Moncada-M, A., Aguirre-Pe, J., Bolivar, J., and Flores, E. (2009). "Scour protection of circular bridge piers with collars and slots." *Journal of Hydraulic Research*, 47(1), 119-126.
- Raudkivi, A. J., and Ettema, R. (1983). "Clear-Water Scour at Cylindrical Piers." *Journal of Hydraulic Engineering*, 109(3), 338-350.
- Robie Bonilla, G. (2010). "Sheath for Reducing Local Scour in Bridge Piers." *Scour and Erosion*, 987-996.
- Sarker, M. A. (1998). "Flow measurement around scoured bridge piers using Acoustic-Doppler Velocimeter (ADV)." *Flow measurement and instrumentation*, 9(4), 217-227.
- Westoby, M. J., Brasington, J., Glasser, N. F., Hambrey, M. J., and Reynolds, J. M. (2012). "'Structure-from-Motion' photogrammetry: A low-cost, effective tool for geoscience applications." *Geomorphology*, 179, 300-314.
- Wu, C. "Towards linear-time incremental structure from motion." *Proc., 2013 International Conference on 3D Vision-3DV 2013*, IEEE, 127-134.
- Wu, C., Agarwal, S., Curless, B., and Seitz, S. M. "Multicore bundle adjustment." *Proc., Computer Vision and Pattern Recognition (CVPR), 2011 IEEE Conference on*, IEEE, 3057-3064.

Modified Strain Wedge Calculation of a Laterally Loaded Pile in Sand Considering Scouring

C. Zhang¹; X. Yang²; M. Huang³; and J. Yuan⁴

¹Dept. of Geotechnical Engineering, Tongji Univ., 200092 Shanghai, China; Key Laboratory of Geotechnical and Underground Engineering of Ministry of Education, Tongji Univ., 200092 Shanghai, China. E-mail: zcrong33@tongji.edu.cn

²Dept. of Geotechnical Engineering, Tongji Univ., 200092 Shanghai, China; Key Laboratory of Geotechnical and Underground Engineering of Ministry of Education, Tongji Univ., 200092 Shanghai, China.

³Dept. of Geotechnical Engineering, Tongji Univ., 200092 Shanghai, China; Key Laboratory of Geotechnical and Underground Engineering of Ministry of Education, Tongji Univ., 200092 Shanghai, China.

⁴Dept. of Geotechnical Engineering, Tongji Univ., 200092 Shanghai, China; Key Laboratory of Geotechnical and Underground Engineering of Ministry of Education, Tongji Univ., 200092 Shanghai, China.

Abstract

A modified strain wedge model is presented to calculate the effect of scouring on the responses of a laterally loaded pile. The strain wedge (SW) model is capable to derive a p-y curve for the analysis of a vertical beam on a nonlinear foundation. To improve the SW method, a modified strain wedge (MSW) model is developed by assuming a nonlinear lateral deflection of pile to get the nonuniform soil strain in the passive wedge. Treating the soil weight above the scour bottom as a vertical load, an equivalent depth is obtained in the MSW model to consider scour hole dimensions. The applicability of the MSW model in the problem of a pile under scouring is proved by comparing with a model test and also the FEM results. It is found that the deflection ratio at the ground surface maintains 1.8 and 3.0 under large load level for scour depth as $S_d = 3.2D$ and $6.4D$ respectively and the scour induced change on the soil reaction modulus under small load is obvious in the model test and MSW analysis, while negligible in the FEM analysis.

INTRODUCTION

Pile foundations are often designed to resist lateral loads in projects of bridges, ports and offshore platforms. The p-y method, treating the soil as a series of disconnected springs and the pile as a beam on a nonlinear Winkler foundation (BNWF), is the most popular due to its simplicity. For the pile in sandy soil, Reese et al. (1974) first proposed a p-y curve expression based on field tests. The strain wedge (SW) model is developed by Norris (1986) to derive the soil reaction modulus of the one-dimensional beam from the three-dimensional passive soil strain wedge in front of the pile, and extended by Ashour et al. (1998) for layered soils. Xu et al. (2013) compared the responses of a lateral loaded pile based on the hyperbolic stress-strain relationship of sandy soil as Duncan-Chang model and bilinear curve as Mohr-Coulomb model respectively. Based on the basic concept of the deflection profile of a laterally loaded pile, the soil strain in the wedge in fact varies with pile depth. Therefore, the use of soil strain that is constant with depth in the current SW approach would seem to involve significant compromise.

Scouring in the offshore area forms a local scour hole around the pile, leading to a degradation of the lateral capacity and stiffness of the pile foundation. Ni et al. (2012) evaluated the scour effect on the pile's behavior by removing the upper soil layer to the scour depth, obviously a conservative estimation. The FE simulation by Achums et al. (2010) and FLAC 3D analysis by Li et al. (2013) investigated several key factors on the responses of pile, such as scour depth, scour width and pile diameter. By considering three-dimensional scour hole dimensions, the limiting soil resistance in Reese et al. (1974)'s p-y curve is modified based on a wedge failure mode near ground in Lin et al. (2014).

The pile analysis presented herein is based on the concept of the SW model, in which nonuniform strain distribution is formed in the wedge and an equivalent vertical load is applied on the scour hole bottom to take place of the self-weight of remaining soil around scour hole. A model test are used to demonstrate the validity of the proposed approach in calculating the responses of a pile considering scouring hole dimensions, in which a finite element analysis is also presented.

MODIFIED STRAIN WEDGE (MSW) MODEL

The strain wedge model features the mobilization of the passive wedge in front of the pile (Norris 1986; Ashour et al. 1998) as shown in Fig. 1(a), characterized by a fan angle ϕ_m , a base angle β_m and a wedge depth H . Two basic assumptions associated with the SW model are:

- (1) The deflection pattern of the pile is taken to be linear over the controlling depth of the soil near pile top, resulting in a linearized deflection angle δ and a uniform soil strain to be assessed, as shown in Figure 1(b).
- (2) As the pile installation makes the lateral earth pressure coefficient K_0 as 1.0, the soil stress state in the strain wedge is similar to that in an isotropically consolidated drained triaxial test.

The loading direction of the pile is the axial direction in the triaxial test and the major principle stress change in the wedge is equivalent to the deviatoric stress change of the soil in the triaxial test.

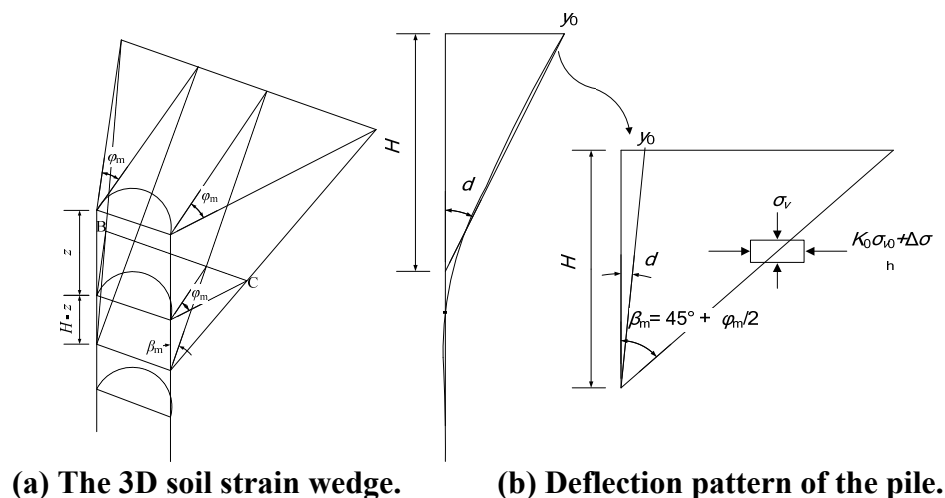


Figure 1. The basic strain wedge model (after Ashour et al. 1998).

The mobilized geometry of passive wedge change with the level of lateral load at pile head, in which the configuration of base angle β_m , and width \overline{BC} of the wedge face at any depth are related to the mobilized angle of internal friction of sand φ_m as:

$$\beta_m = 45^\circ + \frac{\varphi_m}{2} \quad (1)$$

$$\overline{BC} = D + 2(H - z)\tan\beta_m \tan\varphi_m \quad (2)$$

Here, D is the pile diameter or the width of the pile cross-section. φ_m also represents the fanning angle and is governed by stress level in the soil in which a nonlinear soil stress-strain curve can be introduced to determine the horizontal soil strain in the strain wedge. Based on horizontal equilibrium of stress for the horizontal slice and assumption of linear pile deflection, the soil reaction modulus from strain wedge is obtained with:

$$k = \frac{p}{y}$$

Here, p is soil reaction force per unit length of the pile.

Relationship between pile lateral deflection y and lateral soil strain ε . The SW model is modified in that a nonlinear deflection of the pile along the depth is assumed to derive a rational relationship between pile lateral displacement y and the horizontal soil strain ε in the strain wedge. The pile lateral displacement varies nonlinearly along the depth of the soil wedge in front of the pile, as shown in Figure 2. The loaded pile and strain wedge are divided into N sublayers of constant thickness h . For a horizontal slice i of the passive wedge, the lateral displacement at the upper and lower interface are y_{i-1} and y_i . Though the deflection pattern δ of the embedded pile is continuous, the value at the middle of the sublayer δ_i is treated as for the entire sublayer, which gives the relationship between pile displacement and pile rotation angle as

$$\tan\delta_i = \frac{y_{i-1} - y_i}{h} \quad (3)$$

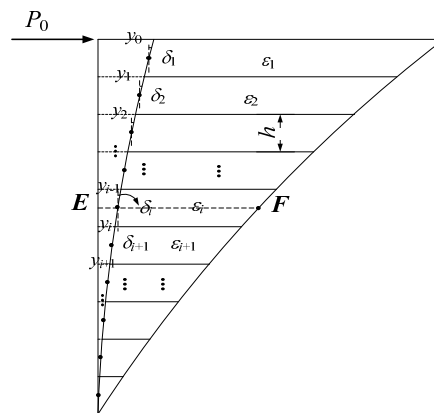


Figure 2. The nonlinear displacement of the pile in the MSW model.

The lateral soil strain ε in the strain wedge varies along the depth of the soil wedge, related to the location of the sublayer i as:

$$\varepsilon_i = \frac{y_{i-1} + y_i}{2EF_i} \quad (4)$$

Here, $\overline{EF_i}$ is the width of the wedge in the middle of layer i , as shown in Figure 2.

The relationship between pile deflection angle δ_i and lateral soil strain ε_i has been derived in Ashour et al. (1998) from the Mohr's circle for soil strain, as shown in the Figure 3.

$$\delta_i = \frac{\gamma_i}{2} = \frac{\varepsilon_i - \varepsilon_{v_i}}{2} \sin(2\theta_{mi}) = \frac{(1+\nu)\varepsilon_i}{2} \cos\varphi_{mi} \quad (5)$$

Here, vertical strain of soil $\varepsilon_{v_i} = -\nu\varepsilon_i$, ν = Poisson's ratio of soil and $\theta_{mi} = 45^\circ - \varphi_{mi}/2$.

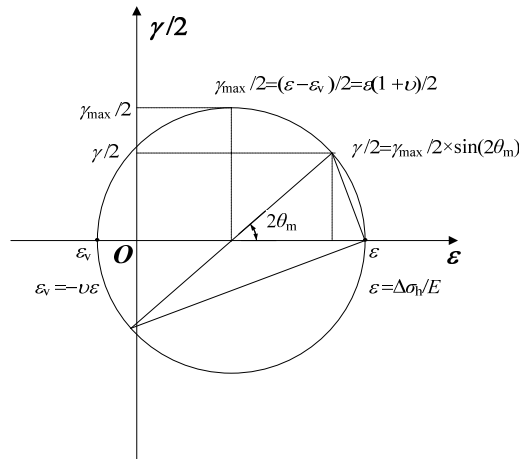


Figure 3. Mohr circle of soil strain (after Ashour et al. 1998).

Relationship between force p and $(\Delta\sigma_h, \tau)$. Corresponding to the horizontal slice(sublayer) of the passive wedge at depth z as shown in Figure 4, the horizontal equilibrium of horizontal and shear stresses is expressed as:

$$p = \Delta\sigma_h \overline{BC} S_1 + 2\tau D S_2 \quad (6)$$

Here, S_1 and S_2 are pile shape factors, $S_1=0.75, S_2=0.5$ for a circular pile, and $S_1=S_2=1.0$ for a square pile. The width of the wedge face \overline{BC} is calculated as:

$$\overline{BC} = D + 2\overline{EF} \tan\varphi_m \quad (7)$$

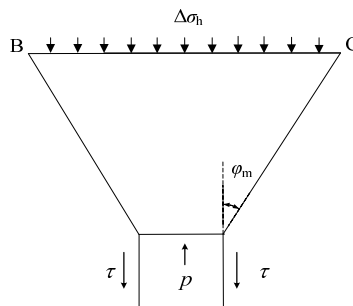


Figure 4. Slice of the strain wedge model at depth z .

A BNWF interactive process is performed by solving the governing equation of a bended beam with finite difference method, to determine the mobilized geometry of the passive wedge and the horizontal strain of the soil, in which the p-y curve is generated.

MSW ANALYSIS CONSIDERING SCOUR

The profile of a typical scour hole as shown in Figure 5, is described by a scour depth S_d , slope angle θ and scour widths (the top width as S_{tw} , the bottom width as S_w). Lin et al. (2014) developed a simplified method capable of considering scour hole dimensions by modifying the p-y curves by Reese et al. (1974). Although a wedge type of failure is assumed in Lin's method, only change of ultimate soil resistance is derived and the soil modulus is assumed unaffected. In this paper, the MSW model is used to analyze of the effect of scour on a lateral loaded pile, for its ability to evaluate the soil modulus with dependence on both soil and pile properties during the whole loading range. The effects of scour hole dimensions is considered by treating the soil weight above scour bottom as an additional vertical load and the change in the geometry of passive strain wedge is given by an equivalent soil depth h_s , as shown in Figure 6. The detailed derivation is given below.

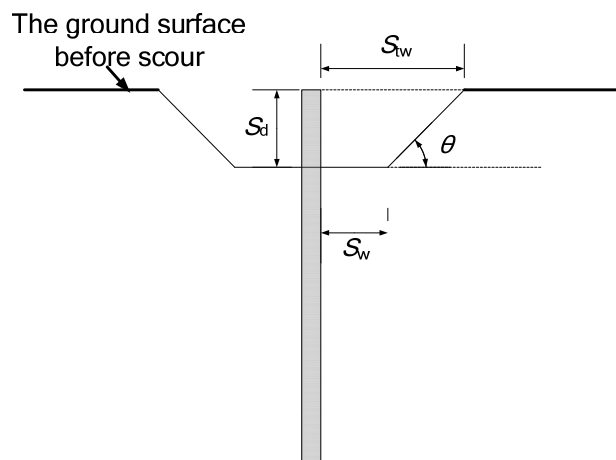


Figure 5. The profile of a scour hole (after Lin et al., 2014).

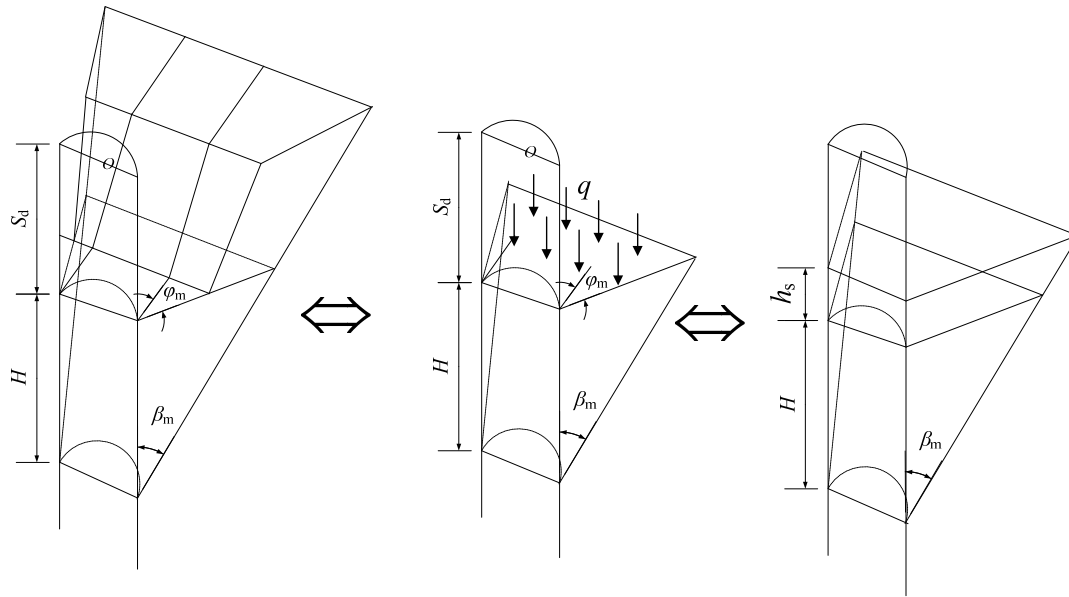


Figure 6. The equivalent wedge model under scouring.

The deduction of equivalent wedge height. According to the relationship between the base angle β_m of the wedge and the slope angle θ of the scour hole, the equivalent wedge height h_s can be determined respectively for two different cases.

(1) The case of $\theta < 90^\circ - \beta_m$

As shown in Figure 7 (a), the horizontal distance (OB) from pile axis to the vertex point of scour top is $T_w = S_w + D/2$ and the distance (O_1A_1) from pile axis to the vertex point of scour bottom is $T_w = S_w + D/2$. When the applied horizontal load is small with $0 < H \leq H_1$ ($H_1 = T_w / \tan \beta_m$), the wedge plane intersects with the scour plane at the bottom of the scour hole and equivalent wedge height $h_s = 0$, for the scour didn't affect the three dimensional pile-soil interaction here. With increased load leading to $H_1 < H \leq H_2$ ($H_2 = T_w / \tan \beta_m - S_d$), the wedge plane intersects with scour plane along the scour slope at point C (y_c, z_c), coordinates of which is expressed as:

$$\begin{cases} y_c = \frac{H - T_w \tan \theta}{\cot \beta_m - \tan \theta} \\ z_c = H + S_d - \frac{H - T_w \tan \theta}{1 - \tan \beta_m \tan \theta} \end{cases} \quad (8)$$

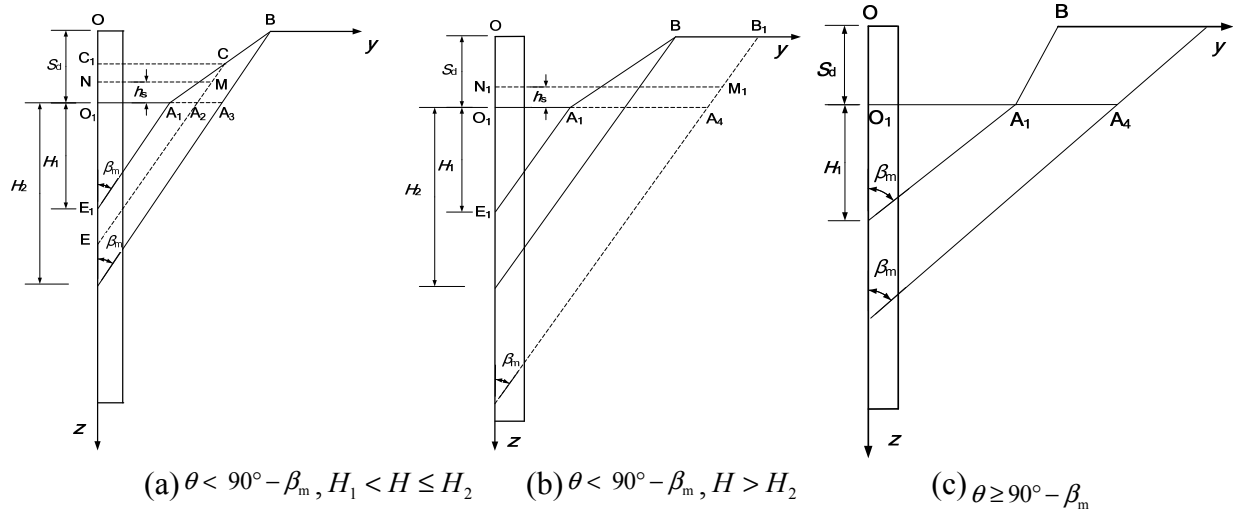


Figure 7. The wedge considering scour hole dimensions.

With homogeneous soil assumed above scour bottom, the soil weight which is treated as a vertical load above the scour bottom, is now related to the soil volume. The remaining soil volume above the scour bottom and involved in the strain wedge is calculated as:

$$V_{A_1A_2C} = V_{O_1A_2CC_1} - V_{O_1A_1CC_1} \quad (9)$$

where:

$$V_{O_1A_2CC_1} = (S_d - z_c) \left[\frac{y_c + H \tan \beta_m}{2} D + \frac{(y_c^2 + H^2 \tan^2 \beta_m + y_c H \tan \beta_m)}{3} \tan \phi_m \right] \quad (10)$$

$$V_{O_1A_1CC_1} = \left[\frac{(y_c^2 + T_w^2 + y_c T_w)}{3} \tan \phi_m + \frac{y_c + T_w}{2} D \right] (S_d - z_c) \quad (11)$$

By equating volume $V_{A_1A_2C}$ to the equivalent volume $V_{O_1A_2MN}$, the controlling point M (y_s, z_s) to affirm the geometry of the equivalent soil wedge is given by $z_s = S_d - h_s$ and $y_s = (H + h_s) \tan \beta_m$. Deducting the volume of pile as $\pi h_s D^2 / 8$, the equivalent soil strain wedge volume V can be rewritten with h_s as:

$$V = V_{O_1A_2MN} - \frac{\pi h_s D^2}{8} = \frac{(y_s^2 + H^2 \tan^2 \beta_m + y_s H \tan \beta_m) h_s}{3} \tan \phi_m + \frac{(y_s + H \tan \beta_m) D h_s}{2} - \frac{\pi h_s D^2}{8} \quad (12)$$

Combining Equation 9 with Equation 12, the equivalent height h_s is obtained.

As the load at pile top grows further with $H > H_2$ in Figure 9(b), the wedge plane interacts with the scour plane at scour top (ground surface) as B_1 , the actual soil volume involved in the wedge is:

$$V_{A_1A_4B_1B} = V_{O_1A_4B_1O} - V_{O_1A_1BO} \quad (13)$$

where:

$$V_{O_1A_4B_1O} = S_d \left[\frac{(y_1^2 + y_2^2 + y_1 y_2)}{3} \tan \phi_m + \frac{y_1 + y_2}{2} D \right] \quad (14)$$

$$y_1 = (H + S_d) \tan \beta_m \quad (15a)$$

$$y_2 = H \tan \beta_m \quad (15b)$$

$$V_{O_1A_1BO} = S_d \left[\frac{(S_{tw}^2 + S_w^2 + S_{tw} S_w)}{3} \tan \phi_m + \frac{S_{tw} + S_w}{2} D \right] \quad (16)$$

With similar procedure for $H_1 < H \leq H_2$ and combining Eq (12) with Eq.(13), the equivalent height h_s can be obtained.

(2) The case of $\theta \geq 90^\circ - \beta_m$

For the wedge plane will never interact with the scour plane along the scour slope in Figure 9(c), the calculation of h_s is similar to above analysis with $0 < H \leq H_1$ and $H > H_2$ respectively.

It should be emphasized that as the geometry of the strain wedge changed with the applied load, the β_m in the increment analysis should be checked every time to affirm its relationship with scour angle. As an equivalent wedge height h_s obtained, the following process is similar to the SW analysis without scouring.

CASE STUDY CONSIDERING SCOUR

A model test has been carried out by Gao (2015) to get a better understanding of the scour effect on the behavior of a laterally loaded pile in sand. The test soil is finely graded fine sand. Properties of this sand are presented in Table 1. The test pile consists of a hollow plastic tube with pile parameters in Table 2. It is buried with an embedment depth of 0.69m, and a lateral load is applied 0.16m above the ground surface. The shape of the scour hole is formed with excavation and the scour width ($S_w=0$) and scour hole slope angle ($\theta=20^\circ$) were maintained unchanged for the analysis here. Three tests are analyzed to account for the variation of scour depth S_d as $0D$ (no scour), $3.2D$ and $6.4D$, in which both the simplified MSW analysis and numerical FEM analysis are conducted. All tests are interpreted with model type. Pile displacements are measured with two LVDTs at pile top and the strain distribution of the pile is measured by ten pairs of strain gauges along the pile length which is then calculated to obtain p-y curves. Only half of the model is used considering symmetry as shown in Figure 8. The behavior of the pile is assumed linearly elastic, whereas the soil is assumed elastoplastic with Mohr-Coulomb criterion. An interface friction angle of $\phi/2$ between pile soil interface is used according to Lin et al. (2014). Due to the small model dimensions, a homogeneous soil is

assumed with a depth-independent elastic modulus $E=0.3\text{MPa}$ and Poisson's ratio $\nu=0.3$, which is obtained by comparing the FEM results with the test results for the case without scouring. A small value of cohesion as $c=0.5\text{kPa}$ is used for the sand to ensure convergence in the FEM calculation.

Table 1. Sand parameters.

effective unit weight $\gamma(\text{kN/m}^3)$	interface friction angle $\phi/^\circ$	relative density $D_r/\%$	maximum dry density g/cm^3	minimum dry density g/cm^3
14.33	32	60	1.573	1.322

Table 2. Parameters of the model pile.

pile length/m	out diameter/mm	Wall thickness/mm	Young's modulus/GPa
0.85	25	2.5	2.51

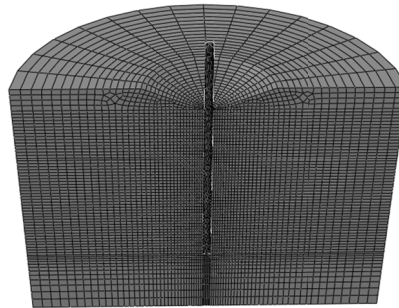


Figure 8. Finite element model considering the scouring.

The results from the simplified MSW method have been plotted with the test results and the results from the FEM simulation in Figure 9, including the load-deflection curves, the bending moment profile and the deflection profile along the pile length and p-y curves, under the lateral load of 11.76N . The responses of the pile change obviously with an increased scour depth, as a result of a decreased pile-soil stiffness, increased pile deflection and bending moment, and a deeper location with maximum bending moment. The p-y curves at a depth of $6.9D$ below the ground surface is given in Figure 9(d) under three scour depths. The FEM analysis shows that the soil reaction modulus didn't change with scour depth, which is consistent with Lin et al. (2014) conclusion, while the results measured in the model test and calculated by the proposed simplified both exhibit a remarkably degradation of soil reaction modulus by scouring even under small load level.

Figure 10 (a) shows the variation of the groundline displacement of the pile with scour depth under two lateral load. The three results agree well with each other at a small load as $P_0=11.76\text{N}$, while the MSW analysis overpredicted the deflection at pile head for $P_0=27.44\text{N}$ and in comparison, the FEM analysis gave a smaller prediction. Despite the discrepancy in the prediction for large load using the two methods, a conservative calculation is achieved with the simplified MSW method. The deflection ratio, which is defined as the ratio of groundline deflection of a pile under scouring to that without scour, has been shown in the Figure 10(b), in which the ratio is larger for scour depth as $6.4D$ than in the case with S_d as $3.2D$. It is interesting to observe that the change of the ratio is small when the load level is large. As such, when scour depth is $6.4D$ and $3.2D$, the pile deflection at pile head may be seen as three times larger and 1.8 times larger than the deflection without scour.

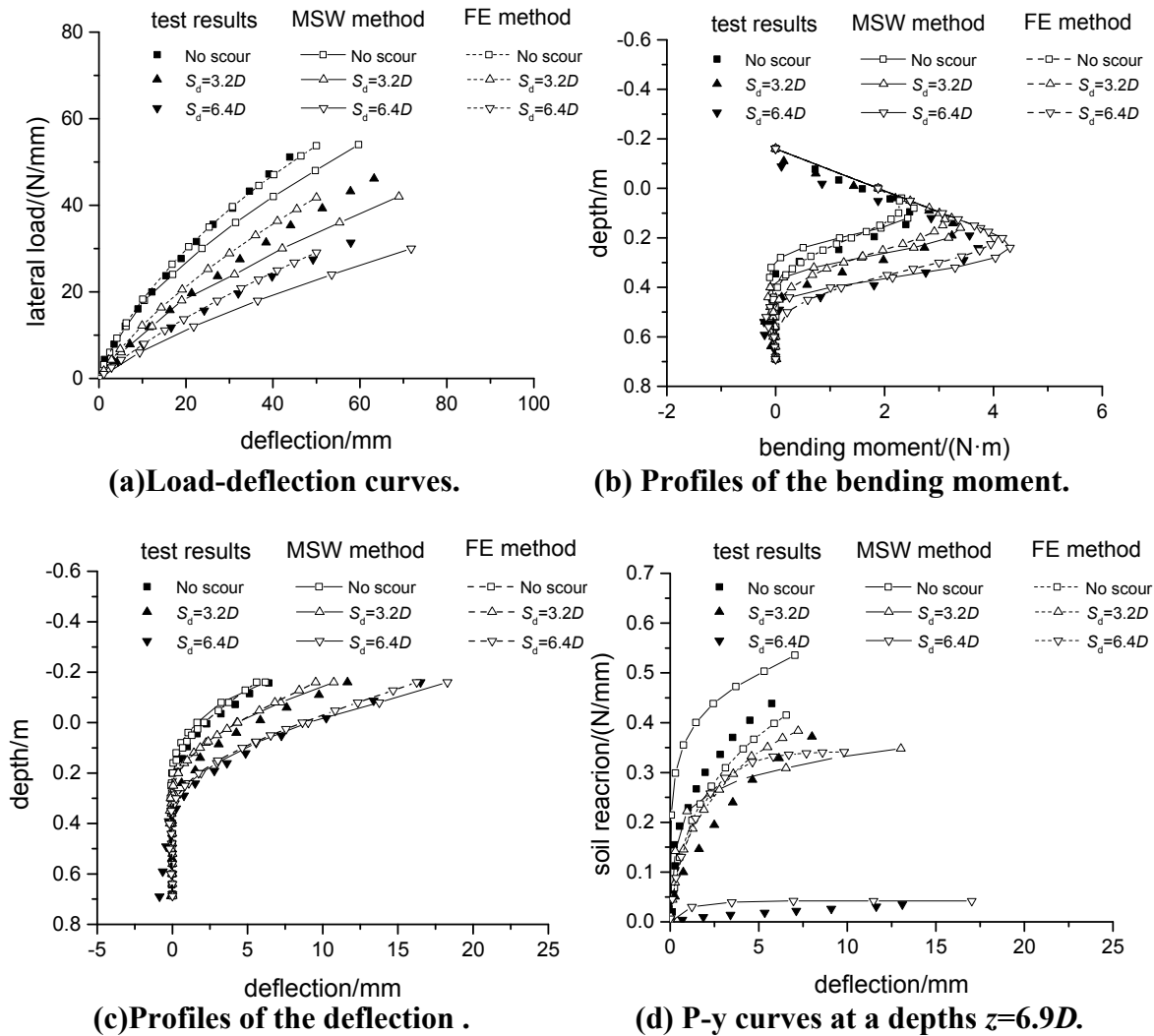


Figure 9. Comparisons of the responses of a laterally loaded pile under scouring.

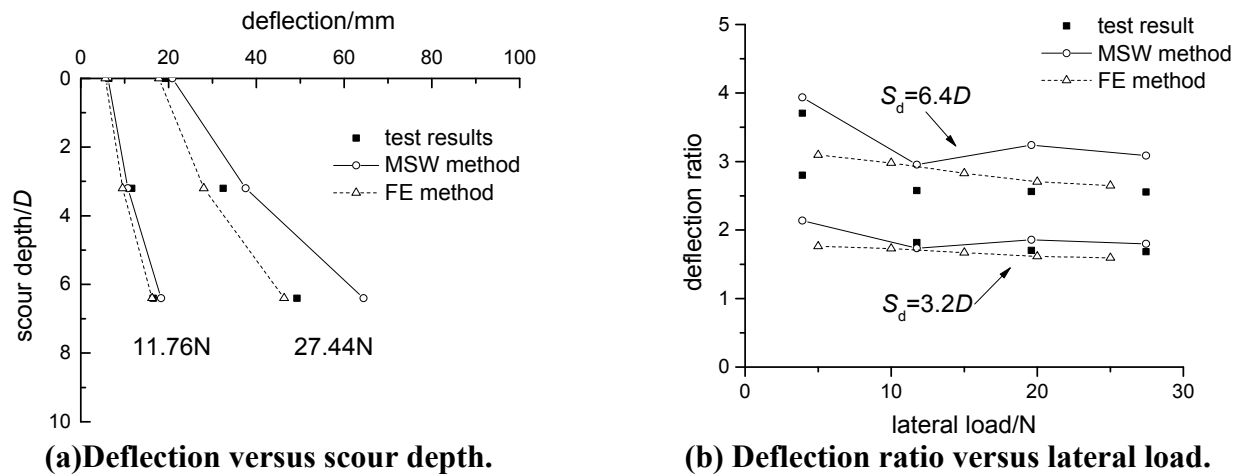


Figure 10. Groundline Displacements for two scour depths.

CONCLUSION

The strain wedge model gives an iterative procedure to derive the load-dependent soil reaction modulus for a laterally loaded pile. It is modified by calculating the uneven soil strain in the wedge with a nonlinear deflection pattern along the pile. Then the modified strain wedge method (MSW) is extended to the problem of a pile considering scour hole dimensions. A cases is studied to validate the rationality of the MSW model in analyzing the responses of a laterally loaded pile with scouring. The following conclusions can be obtained:

- (1) The effect of scour is remarkable for the performance of a lateral loaded pile, which induces a decreased stiffness, increased pile deflection and bending moment with increased scour depth. The deflection ratio at the ground surface maintains 1.8 and 3.0 under large load level for scour depth as $S_d = 3.2D$ and $6.4D$ respectively.
- (2) The scour induced change on the soil reaction modulus under small load is obvious in the model test and MSW analysis, and is negligible in the FEM analysis.

ACKNOWLEDGEMENTS

The authors thank the National Natural Science Foundation of China(Grant No. 51378392)for its financial support.

REFERENCES

- Reese, L.C., Cox, W.R. (1974) "Analysis of laterally loaded piles in sand." *Proc., 6th Annual Offshore Technol. Conf., OTC*, Houston, Texas, 473-485.
- Norris, G.M. (1986) "Theoretically based BEF laterally loaded pile analysis." *Proc., 3rd Int. Conf. on Numerical Methods in Offshore Piling*, Paris, France. 361-386.
- Ashour, M., Norris, G., Pilling, P. (1998) "Lateral loading of a pile in layered soil using the strain wedge model." *J. Geotech. Geoenviron. Eng.*, ASCE, 124:303-315.
- Xu, L.Y., Cai, F., Wang, G.X., et al. (2013) "Nonlinear analysis of laterally loaded single piles in sand using modified strain wedge model." *Comput. Geotech.*, 51: 60-71.
- Ni, S.H., Huang, Y.H., Lo, K.F. (2011) "Numerical Investigation of the Scouring Effect on the Lateral Response of Piles in Sand". *J. Perform. Constr. Fac.*, 26(3): 320-325.
- Achmus, M., Kuo, Y.S., Abdel-Rahman, K. (2010) "Numerical investigation of scour effect on lateral resistance of windfarm monopoles." *Proc., 20th Int. Offshore Polar Eng. Conf.*
- Li, F., Han, J., Lin, C. (2013) "Effect of scour on the behavior of laterally loaded single piles in marine clay." *Mar. Georesour. Geotec.*, 31(3): 271-289.
- Lin, C., Han, J., Bennett, C., et al. (2014) "Analysis of Laterally Loaded Piles in Sand Considering Scour Hole Dimensions." *J. Geotech. Geoenviron. Eng.*, 10161/(ASCE)GT.1943-5606.0001111, 04014024.
- Gao, B.L. (2015) "Model test and numerical simulation of the influence of scouring on the lateral response of pile foundations in sand." MS thesis, University of Tongji University, Shanghai, 2015.

Study of the Particle Shape Influence on Soil Erodibility Using Coupled CFD-DEM Modeling

Y. Guo, S.M.ASCE¹; and X. Yu, Ph.D., P.E., M.ASCE²

¹Graduate Research Assistant, Dept. of Civil Engineering, Case Western Reserve Univ., Cleveland, OH. E-mail: yxg223@case.edu

²Professor, Dept. of Civil Engineering, Case Western Reserve Univ., Cleveland, OH. E-mail: xiong.yu@case.edu

Abstract

Researches show erodibility of sand is mainly determined by the grain size, or the mass median diameter. The influence of particle shape on sand erodibility has been neglected for simplification. Here using a coupled CFD-DEM method, the influence of sand particle shape on soil erodibility has been analyzed. The model was built prototyping from the Erosion Function Apparatus (EFA) developed by Briaud, where soil sample inside a Shelby tube is extruded into a rectangular flow channel with an extrusion height of 1 mm, and subjected to the erosion of flowing water. Critical shear stress and erosion rate of the soil sample can be obtained through the EFA test. In the simulating cases, spherical particles and non-spherical particles with aspect ratios of 1.10, 1.20 and 1.30 have been tested and compared. The results show grain angularity plays an important role in the formation of erosion resistance. For spherical particles, due to the lack of rolling resistance, no critical velocity has been observed. For non-spherical particles, with the increase of aspect ratio, the critical velocity increases indicating a higher erosion resistance. Erosion rate increases linearly with flow velocity, which is consistent with experimental studies.

INTRODUCTION

Soil erosion is a critical issue in hydraulic and geotechnical engineering as it is regarded as one major cause of bridge failures in the US (Briaud 2001, 2015a). Accurate predictions of erosion rate and scour depth are still challenging due to the complex influencing factors on soil erodibility, which include its physical and geochemical properties as well as the surrounding biological activities (Tejada and Gonzalez, 2006; Wynn et al. 2008; Grabowski et al. 2011; Adams et al. 2013; Pan et al. 2015). For cohesionless soil, the erodibility model is relatively simple: the critical shear stress and erosion rate are related to soil density, porosity, and mean grain size (Stevens et al. 2007; Wei et al. 2014; Briaud 2015b; Sharif et al. 2015). The influence of grain shape on sand erodibility tends to be ignored for simplification.

It is widely accepted that grain angularity greatly influences the physical and mechanical properties of soils: increase of particle angularity leads to the increase of maximum and minimum void ratios (Cho et al. 2006), a larger tensile stress of grain particles (McDowell et al. 1996), and a higher shear resistance (Cavarretta et al. 2010; Yang and Luo 2015). Experiments of jet test on glass beads and crushed glass beads also show that particle angularity significantly changed the formation of crater: angular glass beads tend to form a smaller but deeper crater (LaMarche and Curtis 2015).

To better understand the influence of particle shape on sand erodibility, a coupled CFD-DEM method has been used to simulate spherical and non-spherical particles' erosion behaviors under fluid flow. This CFD-DEM method adopts locally averaged fluid velocity and pressure fields to provide a continuous solution for fluid phase (Anderson and Jackson 1967, 1969) and a discrete solid particles to describe the solid phase. Two phases exchange momentum during calculations through proper drag force model (Tsuji et al. 1992). This Eulerian-Lagrangian model was firstly proposed by Tsuji (1992, 1993) in his study of fluidized beds, and then widely used in chemical and mechanical engineering (Xu and Yu 1997; Limtrakul et al. 2003; Shan and Zhao 2014). In this paper, a CFD-DEM model has been built through a custom-build framework under Matlab environment combining with two general code: COMSOL and PFC3D. Erosion behaviors of different shape particles are compared. It is shown that erosion resistance increases significantly with the increase of particle angularity (or aspect ratio).

MATHEMATICAL FORMULATIONS

The mathematical formulations are provided in this section. The customized framework has been verified by the free settling of a single spherical particle experimentally and mathematically, which however will not discuss in details due to the space limitation of this paper. The fluid phase is solved under COMSOL with its weak form module, and the solid phase is solved with PFC3D. Momentum exchange and solving sequence are controlled by Matlab.

Fluid phase. The locally averaged Navier-Stokes equations are given below (Anderson and Jackson 1967). Fluid and solid phases exchange momentum through the interaction force term to maintain the momentum conservation of the whole fluid-solid system.

$$\begin{aligned}\frac{\partial np}{\partial t} + (\nabla \cdot n\mathbf{p}\mathbf{u}) &= 0 \\ \frac{\partial n\mathbf{p}\mathbf{u}}{\partial t} + (\nabla \cdot n\mathbf{p}\mathbf{u}\mathbf{u}) &= -n\nabla p + \nabla \cdot n\mathbf{K} + n\rho\mathbf{g} + \mathbf{f}^p\end{aligned}$$

Here, n is porosity from the solid phase; t is the simulation time; \mathbf{u} is the fluid velocity vector; ρ is the density of fluid; p is fluid pressure; \mathbf{K} is stress tensor of the fluid and $\mathbf{K} = \mu(\nabla\mathbf{u} + (\nabla\mathbf{u})^T)$; μ is the fluid dynamic viscosity; \mathbf{g} is gravitational acceleration and g_z equals to -9.80 m/s^2 ; \mathbf{f}^p is volumetric fluid-particle interaction force.

Solid phase. The movement of solid particles is governed by Newton's Laws of Motion. Constitutive models between two contacting particles include: linear springs and dashpots in both normal and tangential directions, and a slider in the tangential direction. It should be noted that the dashpots were used only to acquire the gravitational balance efficiently, and the damping coefficient is set as zero in the subsequent coupling calculations. Conservations of momentum and angular momentum of each particle read:

$$m_i \frac{d\mathbf{U}_i^p}{dt} = \sum_{j=1}^{n_i^c} \mathbf{F}_{ij}^c + \mathbf{F}_i^f + \mathbf{F}_i^g$$

$$I_i \frac{d\mathbf{w}_i}{dt} = \sum_{j=1}^{n_i^c} \mathbf{M}_{ij}$$

where m_i is the mass of particle i ; \mathbf{U}_i^p is the translational velocity of particle i ; t is the simulation time; n_i^c is the total number of contacts of particle i ; \mathbf{F}_{ij}^c is the contact force acting on particle i from particle j ; \mathbf{F}_i^f is the fluid interaction force acting on particle i , which has the same magnitude but opposite direction as \mathbf{f}^p ; \mathbf{F}_i^g is the gravitational force of particle i ; I_i is the moment of inertia of particle i ; \mathbf{w}_i is the angular velocity of particle i ; \mathbf{M}_{ij} is the torque applied from particle j to particle i .

Fluid-solid interaction force. Momentum exchange between solid and fluid is calculated according to the interaction force model. For fully saturated condition, only the buoyant force (or pressure gradient force) and the drag force are included in this model. Virtual mass force, lift force, capillary force are ignored considering their relatively small magnitudes compared with drag force. The drag force is determined by the Wen and Yu's equation (Wen and Yu 1966) including a voidage function term proposed by Felice (1994), $n^{1-\chi}$:

$$\mathbf{F}_i^f = \frac{1}{8} C_D \pi \rho_f d_p^2 |\mathbf{u} - \mathbf{U}| (\mathbf{u} - \mathbf{U}) n^{1-\chi}$$

Here, \mathbf{F}_i^f is the drag force acting on particle i ; C_D is the drag coefficient; ρ_f is the fluid density; d_p is the particle diameter; \mathbf{u}, \mathbf{U} are the fluid velocity and particle velocity. The drag coefficient is calculated through the equations below.

$$\begin{aligned} C_D &= \frac{24}{R_e} (1 + 0.15 R_e^{0.687}) \quad \text{for } R_e \leq 1000 \\ C_D &= 0.44 \quad \text{for } R_e > 1000 \\ \chi &= 3.7 - 0.65 \exp\left(-\frac{(1.5 - \log_{10} R_e)^2}{2}\right) \end{aligned}$$

Here, R_e is the particle Reynolds number and $R_e = n \rho_f |\mathbf{u} - \mathbf{U}| d_p / \mu$. For non-spherical clumps approximated by overlapped spheres, the drag force has been scaled according to their overlapping volumes.

MODEL DESCRIPTION

A soil erosion model has been built using the CFD-DEM framework described above. The numerical model prototypes from the Erosion Function Apparatus (EFA) proposed by Briaud (2001). Dimensions of the model are given in Figure 1. Soil sample is extruded from Shelby tube into the flow channel with a height of 1.0 mm and subjected to flow erosion. Different flow velocities are applied in order to plot the erosion rate curve.

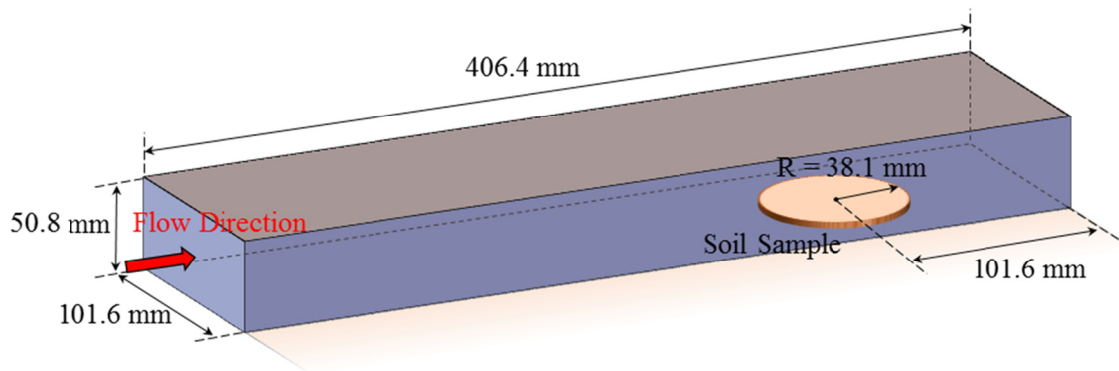


Figure 1. Dimensions of EFA numerical model.

Four different particle shapes are considered here (Figure 2), referred as Particle-1, Particle-2, Particle-3 and Particle-4. Particle-1 is spherical shape while the rest three types are ellipsoidal shapes approximated through three overlapped spheres. Aspect ratios of these four types of particles are: 1:1, 1:1.1, 1:1.2 and 1:1.3. The size of the four types of particles is scaled in order to maintain the same volume, as well as the same particle weight. The mean grain sizes (D_{50}) are 1.000 mm, 0.988 mm, 0.964 mm and 0.939 mm for Particle-1, Particle-2, Particle-3 and Particle-4, respectively (also given in Table 1).

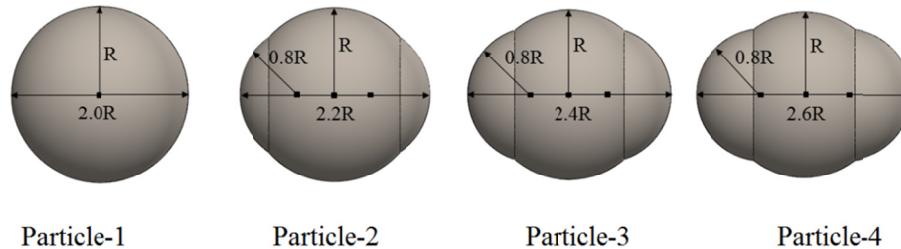


Figure 2. Shapes of four different types of particles.

The microscale parameters of particles are deduced through the inverse analysis by simulating the behaviors of triaxial test sand samples. These parameters characterize the sand with an internal friction angle of 26 degree and a Young's modulus of 9.7 MPa under 200 kPa confining pressure.

Overall this CFD-DEM model consists of 4545 spherical or ellipsoidal particles in DEM module and 11399 tetrahedral elements in CFD module. It should be noted that the compacted height of soil sample is 1.0 mm for spherical particles, but increases to around 1.2 mm for ellipsoidal particles due to the particle arrangement. Four seconds were simulated and it took about 90 hours of computation for each case in a desktop computer with a 3.40 GHz processor.

Table 1. Parameters used in the soil erosion model.

Parameter	Value
Particle diameter (Particle-1)	0.800~1.200 mm
Particle minor axis (Particle-2)	0.790~1.185 mm
Particle minor axis (Particle-3)	0.771~1.156 mm
Particle minor axis (Particle-4)	0.751~1.127 mm
Particle density	2600 kg/m ³
Normal stiffness	2.0×10^5 N/m
Shear stiffness	2.0×10^5 N/m
Wall normal stiffness	1.0×10^8 N/m
Wall shear stiffness	1.0×10^8 N/m
Particle friction coefficient	0.6
Water density	1000 kg/m ³
Water dynamic viscosity	0.001 Pa*s
DEM time step size	1.0×10^{-7} s
CFD time step size	5.0×10^{-4} s
Time step for coupling	1.0×10^{-3} s
Total time simulated	4.0 s

SIMULATION RESULTS

One simulation example has been plotted in Figure 3 with an inlet flow velocity of 0.6 m/s. The erosion behaviors of the four types of particles vary significantly. Spherical particles (Particle-1) show little resistance against flow erosion. While for ellipsoidal particles, the erosion resistance increases with the increase of particle angularity. For Particle-3 and Particle-4, the majority of sand grains remain in the sample area after two seconds erosion.

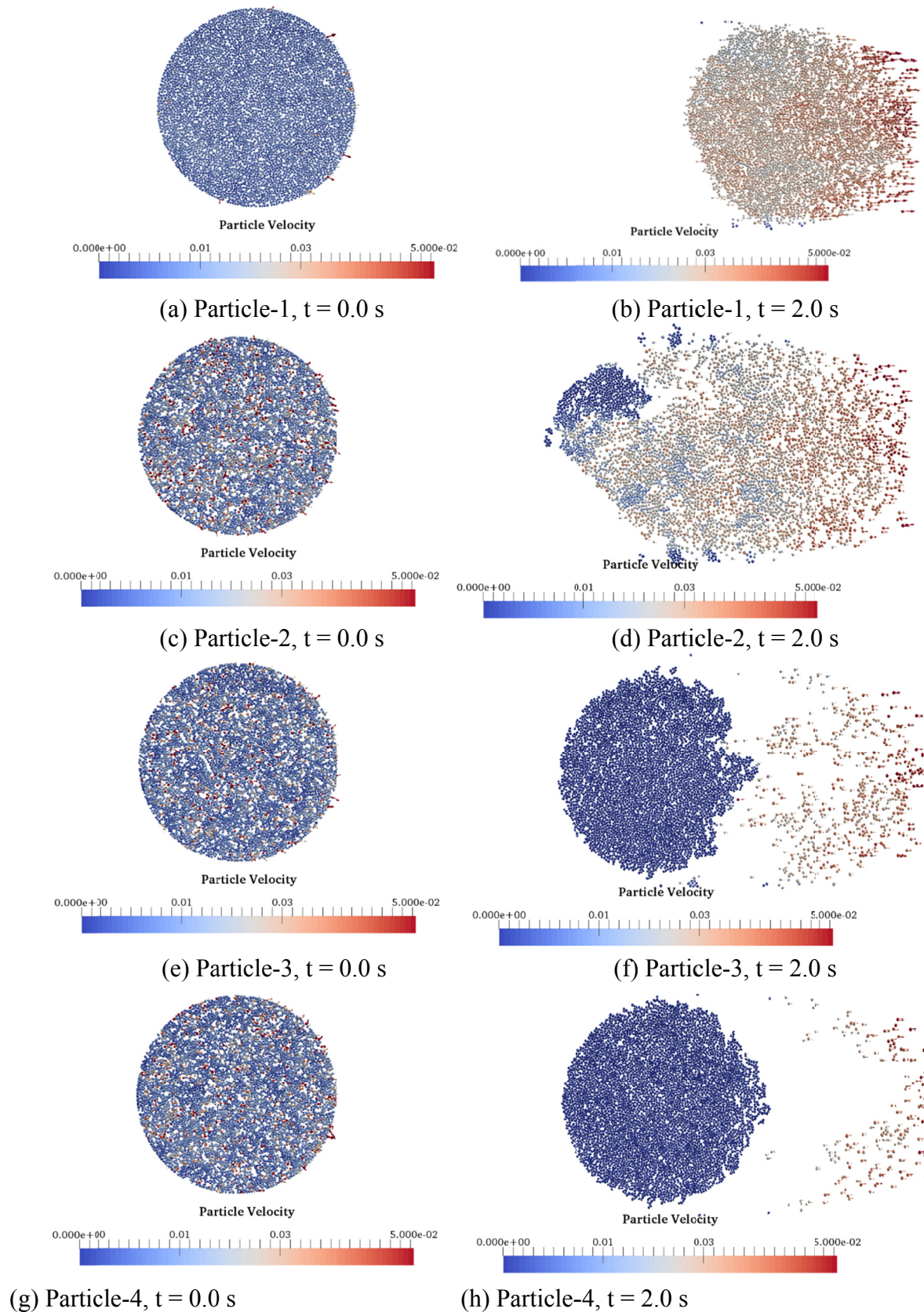


Figure 3. Erosion behaviors of different particles ($V_{\text{inlet}} = 0.6$ m/s).

Particle drag force in the beginning of erosion has been provided in Figure 4. As can be seen, the average drag force increases with the increase of particle angularity, which mainly results from the increase of packing height. It can be said that fluid drag force (or shear stress) distributes randomly but also uniformly on the soil surface.

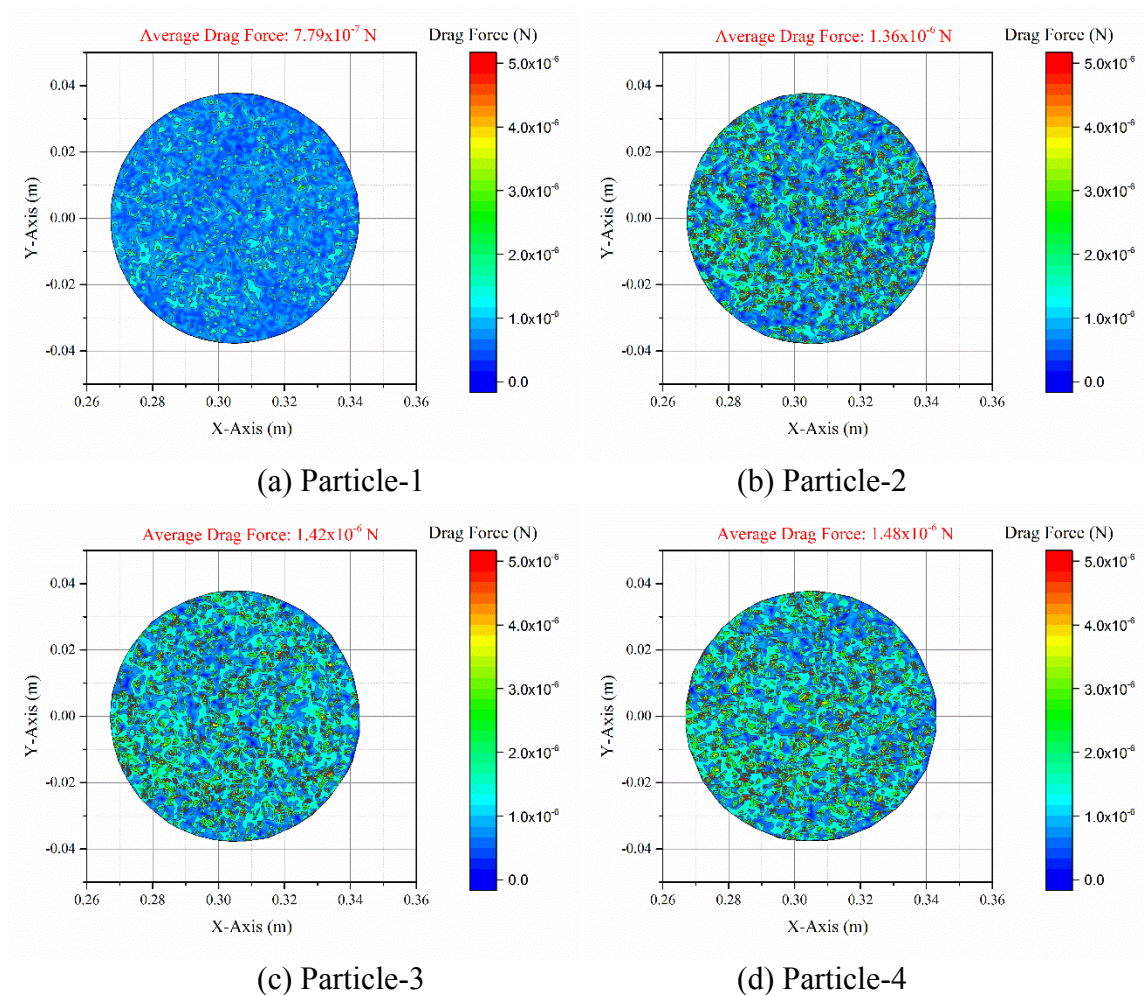


Figure 4. Particle drag forces at $t = 0.020$ s ($V_{\text{inlet}} = 0.6$ m/s).

Erosion rate can be calculated through counting the number of particles remaining in the sample zone. The mass percentage of sand particles remaining in the circular sample zone is shown in Figure 5. For ellipsoidal particles, as the flow velocity decreases to certain level, the mass percentage remains as a constant, indicating a final steady stage of erosion. Slope of these mass percentage curves are linearly related to the erosion rate.

Erosion rate curves of different types of particles are plotted in Figure 6. As discussed above, for spherical particles (Particle-1), due to their lack of rolling resistance, erosion curve is almost linear and back intercepts to the origin. For ellipsoidal particles (Particle-2, Particle-3 and Particle-4), there clearly exists a critical flow velocity above which erosion starts to occur. The critical flow velocity increases with the particle angularity. The simulation results of ellipsoidal particles are more consistent with the experimental observations.

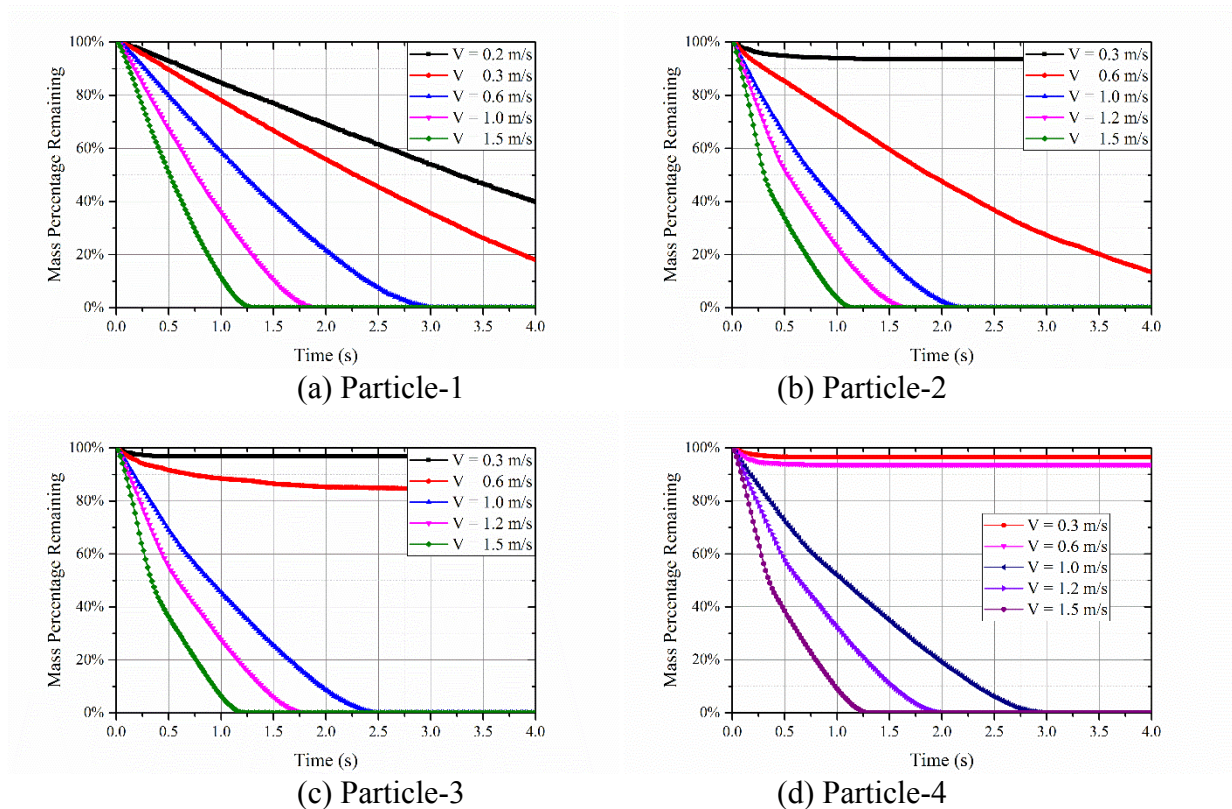


Figure 5. Mass percentage of different particles remaining in the sample area.

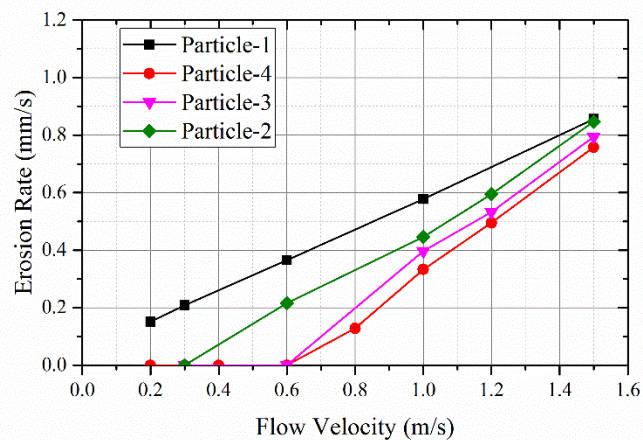


Figure 6. Erosion rate curve of four different particle shapes.

CONCLUSIONS

The influence of grain angularity on sand erodibility has been discussed in this paper using the coupled CFD-DEM method. A soil erosion model prototyping from the Erosion Function Apparatus proposed by Briaud was built and the erosion behavior of four different-shaped particles has been compared. The aspect ratios of the four types of particles are 1:1, 1:1.1, 1:1.2 and 1:1.3, respectively. The results show grain angularity greatly influences the erosion

resistance of sand particles. For spherical particles (Particle-1), since the external forces are acting on the centroids and no rolling resistance exists, particles are eroded away even with a small inlet flow. For ellipsoidal particles (Particle-2, Particle-3 and Particle-4), the non-spherical particle shape provides extra angular momentum against rolling, which largely increases their erosion resistance. A critical flow velocity can be observed in the simulating cases of the ellipsoidal particles, which is more consistent with experimental observations. Increase of particle angularity (or aspect ratio) could enhance the erodibility of sands. Further research will focus on the experimental validations of these observations.

REFERENCES

- Adams, B.T., Xiao, M., and Wright, A. (2013). "Erosion mechanisms of organic soil and bioabatement of piping erosion of sand." *Journal of Geotechnical and Geoenvironmental Engineering*, 139, 1360-1368.
- Anderson, T.B. and Jackson, R. (1967). "A fluid mechanical description of fluidized beds: equations of motion." *Industrial & Engineering Chemistry Fundamentals*, 6, 527-539.
- Anderson, T.B. and Jackson, R. (1969). "A fluid mechanical description of fluidized beds: comparison of theory and experiment." *Industrial & Engineering Chemistry Fundamentals*, 8, 137-144.
- Briaud, J.L., Ting, F., Chen, H.C., Cao, Y., Han, S.W., and Kwak, K.W. (2001). "Erosion function apparatus for scour rate predictions." *Journal of Geotechnical and Geoenvironmental Engineering*, 127, 105-113.
- Briaud, J.L. (2015a). "Scour depth at bridges: method including soil properties. i: maximum scour depth prediction." *Journal of Geotechnical and Geoenvironmental Engineering*, 04014104, 13.
- Briaud, J.L. (2015b). "Scour depth at bridges: method including soil properties. ii: time rate of scour prediction." *Journal of Geotechnical and Geoenvironmental Engineering*, 04014105, 13.
- Cavarretta, I., Coop, M., and O'Sullivan, C. (2010). "The influence of particle characteristics on the behaviour of coarse grained soils." *Géotechnique*, 60, 413-423.
- Cho, G.C., Dodds, J., and Santamarina, J.C. (2006). "Particle shape effects on packing density, stiffness, and strength: natural and crushed sands." *Journal of Geotechnical and Geoenvironmental Engineering*, 132, 591-602.
- Felice, R.D. (1994). "The voidage function for fluid-particle interaction systems." *International Journal of Multiphase Flow*, 20, 153-159.
- Grabowski, R.C., Droppo, I.G., and Wharton, G. (2011). "Erodibility of cohesive sediment: the importance of sediment properties." *Earth-Science Reviews*, 105, 101-120.
- LaMarche, C.Q. and Curtis, J.S. (2015). "Cratering of a particle bed by a subsonic turbulent jet: effect of particle shape, size and density." *Chemical Engineering Science*, 138, 432-445.
- Limtrakul, S., Chalermwattanatai, A., Unggurawirote, K., Tsuji, Y., Kawaguchi, T., and Tanthapanichakoon, W. (2003). "Discrete particle simulation of solids motion in a gas-solid fluidized bed." *Chemical Engineering Science*, 58, 915-921.
- McDowell, G.R., Bolton, M.D., and Robertson, D. (1996). "The fractal crushing of granular materials." *Journal of the Mechanics and Physics of Solids*, 44, 2079-2102.
- Pan, Y., Li, L., Amini, F., and Kuang, C. (2015). "Overtopping erosion and failure mechanism of earthen levee strengthened by vegetated hptrm system." *Ocean Engineering*, 96, 139-148.

- Shan, T. and Zhao, J. (2014). "A coupled CFD-DEM analysis of granular flow impacting on a water reservoir." *Acta Mechanica*, 225, 2449-2470.
- Sharif, Y.A., Elkholy, M., Chaudhry, M.H., and Imran, J. (2015). "Experimental study on the piping erosion process in earthen embankments." *Journal of Hydraulic Engineering*, 04015012, 9.
- Stevens, A.W., Wheatcroft, R.A., and Wiberg, P.L. (2007). "Seabed properties and sediment erodibility along the western Adriatic margin, Italy." *Continental Shelf Research*, 27, 400-416.
- Tejada, M. and Gonzalez, J.L. (2006). "The relationships between erodibility and erosion in a soil treated with two organic amendments." *Soil and Tillage Research*, 91, 186-198.
- Tsuji, Y., Tanaka, T., and Ishida, T. (1992). "Lagrangian numerical simulation of plug flow of cohesionless particles in a horizontal pipe." *Powder Technology*, 71, 239-250.
- Tsuji, Y., Kawaguchi, T., and Tanaka, T. (1993). "Discrete particle simulation of two dimensional fluidized bed." *Powder Technology*, 77, 79-87.
- Wei, G., Brethour, J., Grünzner, M., and Burnham, J. (2014). "Sedimentation scour model." *Flow Science Report 03-14*.
- Wen, C.Y. and Yu, Y.H. (1966). "Mechanics of fluidization." *Chemical Engineering Progress Symposium Series*, 62, 100-111.
- Wynn, T.M., Henderson, M.B., and Vaughan, D.H. (2008). "Changes in streambank erodibility and critical shear stress due to subaerial processes along a headwater stream, southwestern Virginia, USA." *Geomorphology*, 97, 260-273.
- Xu, B.H. and Yu, A.B. (1997). "Numerical simulation of the gas-solid flow in a fluidized bed by combining discrete particle method with computational fluid dynamics." *Chemical Engineering Science*, 52.
- Yang, J. and Luo, X.D. (2015). "Exploring the relationship between critical state and particle shape for granular materials." *Journal of the Mechanics and Physics of Solids*, 84, 196-213.

Two-Dimensional Soil Erosion Profile Using Electrical Resistivity Surveys

Md. Zahidul Karim, S.M.ASCE¹; and Stacey E. Tucker-Kulesza, Ph.D., M.ASCE²

¹Graduate Student, Dept. of Civil Engineering, Kansas State Univ., 1701 C Platt St, Fiedler 2118, Manhattan, KS 66506. E-mail: mdzahidulkarim@ksu.edu

²Assistant Professor, Dept. of Civil Engineering, Kansas State Univ., 1701 C Platt St, Fiedler 2118, Manhattan, KS 66506. E-mail: sekulesza@ksu.edu

Abstract

Various soil characteristics that affect the erosion of soil also influence in situ bulk electrical resistivity measurements. The objective of this study was to develop two dimensional soil erosion profiles correlating the in situ electrical resistivity of soil with the erodibility measurements from the Kansas State University Erosion Function Apparatus (KSU-EFA). Electrical resistivity surveys were conducted at ten bridge sites. Five samples were collected at each site and tested in the KSU-EFA. Erosion potential profiles were created using the subsurface electrical resistivity distributions. This study showed that the rapid in situ data obtained from an electrical resistivity survey can predict the presence of highly erosive soils. As such, electrical resistivity surveys may be used to identify where further testing is necessary to measure the scour potential or determine which existing bridges should be closed or closely monitored for scour potential during a flood event.

INTRODUCTION

The Federal Highway Administration (FHWA) defines scour as the result of erosive action of flowing water, excavating and carrying away material from the bed and banks of streams and from around the piers and abutments of bridges (Calappi et al. 2010). From 1965 to 2005, over 1,500 bridges collapsed in the United States and scour was responsible for nearly 60% of these failures (Calappi et al. 2010). Among these failures, the 1987 interstate highway bridge failure over Schoharie Creek in New York that killed ten people was one of the primary motivators for the FHWA to establish scour monitoring procedures (Lin et al. 2014). Responding immediately to this catastrophic failure, the FHWA published “Interim Procedures for Evaluating Scour at Bridges,” (FHWA 1988). In 1991, the FHWA updated the interim procedures to Hydraulic Engineering Circular 18 (HEC-18). HEC-18 remains the primary tool for predicting scour depth and prioritizing bridge monitoring schedules (Arneson et al. 2012). However, many have observed that HEC-18 scour equations tend to over-predict scour depth for most geologic and hydraulic conditions because these empirical equations were developed from regression analysis of laboratory test results using coarse-grained soils. For example, during the early 1990s’, the New Jersey Department of Transportation (NJDOT) analyzed nearly 2,400 state and county owned bridges using HEC-18 equations and identified 165 bridges as “scour critical”. In 2006, NJDOT launched a Plan of action for the state’s scour critical bridges and engaged the United States Geological Surveys (USGS) West Trenton office to conduct erosion monitoring of these bridges. The USGS found that these bridges were not scour critical and were placed in the list solely based on HEC-18 analysis method (Schuring et al. 2010). Although HEC-18 has served as a useful benchmark for scour prediction, a single manual based on granular soils is not

applicable to all geologic, geotechnical, and hydraulic circumstances. As such, site specific testing is necessary for accurately predicting erosion.

Numerous testing devices have been developed by researchers for directly measuring soil erosion in the laboratory and in the field. Some of the recent apparatuses for erosion measurements include the Sediment Erosion Rate Flume (Crowley et al. 2012), the FLUME (Ravens 2007), the Jet Erosion Testing (JET) apparatus (Hanson and Cook 2004), and the Erosion Function Apparatus (EFA) (Briaud et al. 2001). The EFA, utilized in this study, is a flume style apparatus that measures the erosion of undisturbed samples collected in Shelby tubes. While soil erosion measurements are valuable using these and other devices, they are often time consuming. In-situ electrical resistivity (ER) measurements are rapid compared to erosion testing and there are several common factors between ER and soil erosion (Abu-Hassanein et al. 1996, Kibria et al. 2012, Grabowski et al. 2011). Hence, correlating the erodibility of soil and ER can provide rapid, in-situ measurements of erodibility. Moreover, in all testing methods that require soil samples for laboratory tests (such as erosion testing in the EFA), only one area of the soil profile is measured. ER surveys yield continuous, two dimensional, subsurface profiles of erodibility. The objective of this study was to characterize two dimensional soil erosion profiles using ER. A brief overview of electrical resistivity follows this introduction, then methodology of the study including field and laboratory work are described. In the results and analysis section, the erodibility categorizing graph obtained from HEC-18 (Arneson et al. 2012) was used to identify erodibility levels. Based on the erodibility levels, two dimensional subsurface soil erosion profiles were produced using ER for three sites. This paper ends with conclusions and future work.

ELECTRICAL RESISTIVITY

Electrical resistivity (ER) is a measurement of the material's ability to oppose the flow of current which is measured in Ohm meters ($\Omega\cdot\text{m}$). Principal soil parameters that affect the bulk ER include water content, porosity, mineralogy (Zhou et al. 2001), particle size, index properties, unit weight, amount of dissolved ion, and soil temperature (Abu-Hassanein et al. 1996; Kibria et al. 2012). Generally, clays have ER between 1 to 20 $\Omega\cdot\text{m}$, and sands (wet to moist) have ER between 20 to 200 $\Omega\cdot\text{m}$. ER values of geologic materials can be as high as 1,000,000 $\Omega\cdot\text{m}$, for example, for igneous rocks (Everett 2013).

METHODOLOGY

Ten bridge sites around eastern Kansas were used for this study. Depending on the accessibility, samples were collected as close to the stream as possible. Five 0.6 m long soil samples were collected at each site with a drill rig continuously pushing from the surface to 3 m using 88.9 mm diameter thin-walled Shelby tubes. Each sample was tested in the KSU-EFA. The samples were designated according to their highway name and the order of sampling. For example, the top sample from US-400 site was designated as US-400 #1.

In the EFA, water flows through a rectangular flume using a pump to control the velocity. One end of the Shelby tube containing the sample is placed over a piston and the other end is passed through a circular opening in the bottom of the flume so that soil is in flush with the flume bottom. Water flows for an hour at a specific velocity and the sample is allowed to erode as water flows along the top of the sample. The erosion rate, ϵ_r , is measured at six different

velocities for each sample. Shear stress applied by the flowing water that causes the erosion is calculated using the following equation:

$$\tau = \frac{1}{8} f \rho v^2 \quad (1)$$

Here, f is the friction factor, ρ is the density of the flowing fluid (water), and v is the water velocity (Briaud et al. 2001). The friction factor is obtained from the Moody (1944) chart and is a function of relative roughness of the eroding surface (measured by calipers after testing under each velocity) and Reynold's number (function of flume and eroding fluid properties). Critical shear stress is an important parameter obtained from erosion tests and it is defined as the threshold shear stress that initiates erosion. In this study, critical shear stress was considered as the shear stress corresponding to 0.1 mm/hr erosion rate. For this purpose, the data in the erosion rate vs. shear stress graph were interpolated to obtain the shear stress at an erosion rate of 0.1 mm/hr similar to Bernhardt et al. (2011). After erosion testing, the remaining sample was used for classification using Unified Soil Classification System (USCS). For this purpose, sieve analysis was performed using ASTM standards C117 (ASTM 2013) and C136 (ASTM 2014); and hydrometer analysis was performed using ASTM standard D422 (ASTM 2007). Plasticity Index (PI) for classification was determined by measuring liquid limit and plastic limit according to ASTM standard D4318 (ASTM 2010).

ER surveys were conducted on the same day of sampling to maintain constant hydro-geological conditions. Because ER and soil erodibility are functions of moisture content an additional ER test was conducted at one site six months following the initial survey. Although moisture contents were not identical, particularly near the surface, the change in ER was negligible over time. As mentioned previously, total depth of sampling for five continuous samples was 3.0 m. As such, the array (configuration), spacing, and total number of electrodes were chosen in such a way that ER imaging covered more than 3.0 m into subsurface at an optimum resolution. The dipole-dipole array with 56 electrodes at a center-to-center spacing of 0.46 m was utilized for this study. A SuperSting R8 resistivity meter was utilized for data acquisition. The SuperSting R8 sends current into the ground and measures the voltage difference across up to eight channels reducing testing time. The measured data was inverted using EarthImager 2D (AGI 2008) software for interpretation.

RESULTS AND ANALYSIS

Categorizing Erodibility. The erosion tests for all sites were plotted with respect to the measured ER using the erodibility categorizing graph provided by HEC-18 (Figure 1). Six of the Shelby tubes from different sites were bent during sampling and could not be used for erosion testing. Each of the remaining 44 samples (from ten sites) were tested for erosion in EFA using six different velocities. Equation (1) was used to calculate shear stress for corresponding velocity. Note that prior to reaching critical shear stress, no erosion takes place; therefore, points with zero erosion rate are not visible in the logarithmic plot.

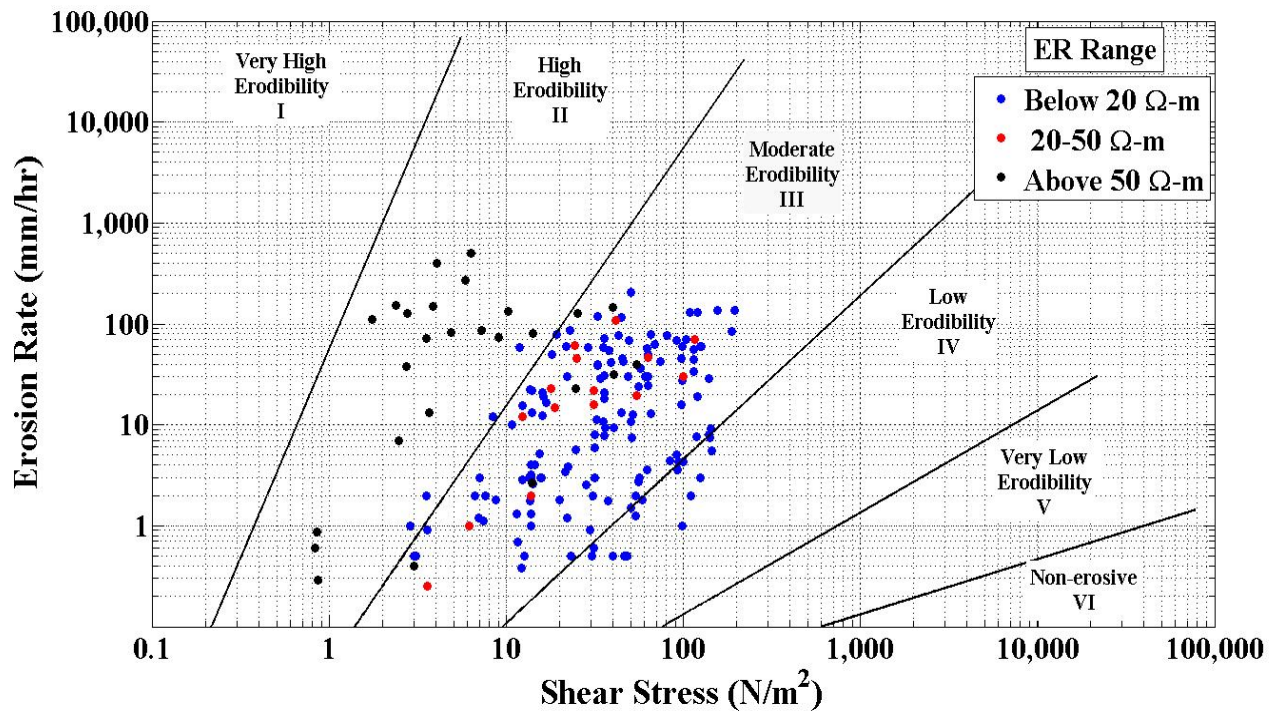


Figure 1. Erosion Rate vs. Shear Stress for varying ER for ten sites.

As seen in Figure 1, the majority of the data lie in the moderate erodibility zone (79.9%), surrounded by few in the low (7.6%) and high (12.5%) erodibility zones. ER values for all samples were divided into three different ranges: below 20 Ω -m, 20 to 50 Ω -m, and above 50 Ω -m, for analysis. The reason for selecting these three ranges follows the typical ER ranges for soils according to Everett (2013). An ER value below 20 Ω -m is typical of clays, which are more conductive than most geo-materials. The ranges of 20-50 Ω -m and above 50 Ω -m are likely sandy soils. The division of 20-50 Ω -m was included to reflect potential variations in moisture content or the inclusion of finer particles, which reduces ER and affects soil erodibility. The erosion test results of Figure 1 for all samples are summarized in Table 1 to associate erodibility levels with respect to the ER ranges.

Table 1. ER range and associated erodibility level based on erosion tests from ten sites.

ER Range	Points Falling in Different Erodibility Zones			Associated Erodibility Level
	High	Moderate	Low	
Below 20 Ω -m	2.8%	87.3%	9.9%	Low to Moderate
20 to 50 Ω -m	0%	100%	0%	Moderate
Above 50 Ω -m	73.1%	26.9%	0%	High

Only one site from this study, K-126, provided samples that had ER values over 50 Ω -m. Most of the samples from this site, although classified as sands, contained both fines and gravel. Visually it looked like a fine-grained soil but the ER survey identified the presence of gravel (as ER was more than 50 Ω -m) entrapped within the fines in the subsurface and it was highly erodible. This highlights how ER can be used to predict the erodibility.

Two Dimensional Soil Erosion Profiles. Based on the ER ranges discussed above and their associated erodibility levels, two dimensional erosion profiles were constructed for three bridge sites, US-400, US-24, and K-126. Table 2 contains the summary of test results and geotechnical properties of the soil samples; and results of erosion tests are given in Figure 2. Sample #3 from US-400 and #2 and #4 from US-24 were not tested in the EFA as the tubes were bent.

Table 2 shows that samples from US-400 have smaller grain size, higher plasticity index and higher critical shear stress for erosion. On the other hand, these properties are opposite (larger grain size, lower plasticity index and lower critical shear stress for erosion) for samples collected from K-126. Overall ER of US-400 samples were low and ER values were high for K-126 samples. US-24 soil properties fall in between these two sites. A direct impact of these properties is observed in the erodibility categorization graph using these three sites in Figure 2; as US-400 samples showed low to moderate erodibility, K-126 samples showed high erodibility, and points corresponding to US-24 fell in the middle.

Table 2. Summary of soil properties of the samples from three sites used in the analysis.

Sample Designation	Sampling Depth	Electrical Resistivity	Critical Shear Stress	Water Content	Mean Grain Size	Plasticity Index	USCS Classification
	m	ohm-m	N/m ²	%	mm	%	
US-400 #1	0.0-0.6	11.1	31.05	21	0.012	27	CL
US-400 #2	0.6-1.2	12.5	21.09	21	0.007	37	CH
US-400 #4	1.8-2.4	9.7	12.66	23	0.005	38	CH
US-400 #5	2.7-3.3	12.6	36.81	25	0.011	27	CL
US-24 #1	0.0-0.6	35.6	2.71	33	0.023	25	CL
US-24 #3	1.2-1.8	17.5	3.64	31	0.021	17	CL
US-24 #5	2.4-3.0	13.0	9.31	29	0.021	17	CL
K-126 #1	0.0-0.6	131.9	1.40	21	0.019	9	CL
K-126 #2	0.6-1.2	327.7	1.27	18	0.082	10	SC
K-126 #3	1.2-1.8	257.3	0.85	25	1.800	8	SC
K-126 #4	1.8-2.4	189.4	0.70	17	1.640	7	SC
K-126 #5	2.4-3.0	136.7	0.61	24	1.920	7	SW-SC

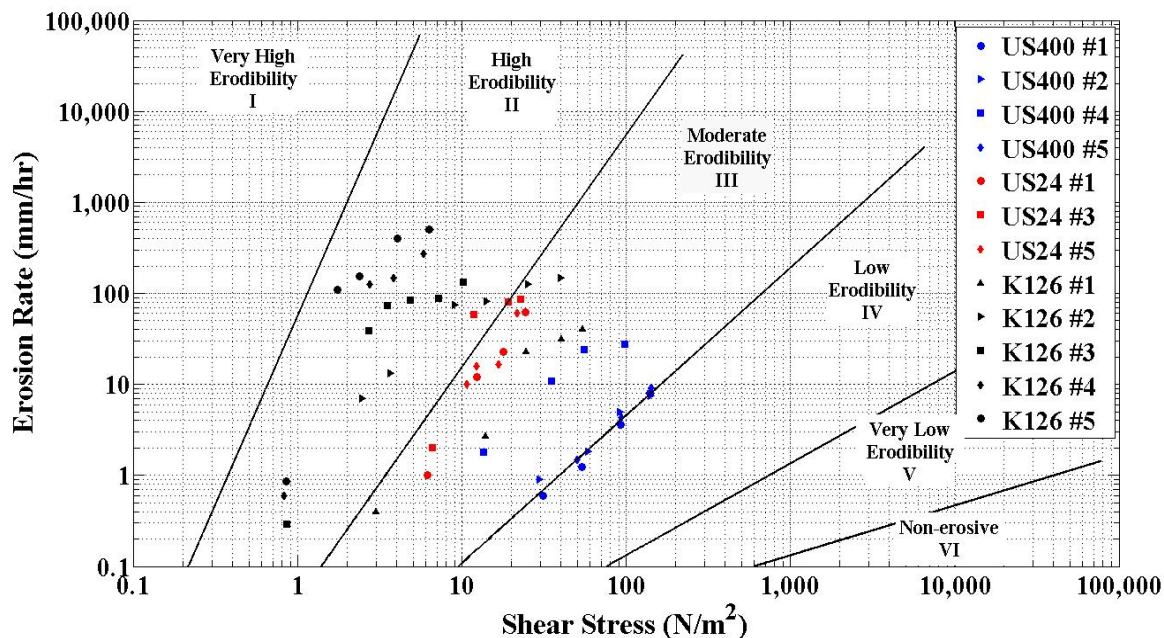


Figure 2. Erosion Rate vs. Shear Stress for varying ER for three sites

As shown in Table 1, 97.2% points corresponding to samples having ER below 20 Ω -m showed low to moderate erodibility; 100% samples corresponding to ER ranging between 20 to 50 Ω -m showed moderate erodibility; and lastly, 73.1% of the points corresponding to samples having ER more than 50 Ω -m were highly erodible based on the data in this study. Using the associated erodibility levels, subsurface ER distribution of these three sites were converted to a qualitative two dimensional erosion potential diagram (Figure 3). The rectangle drawn with dashed lines in each profile shows the location of sampling (corresponding to five samples). The ER values of these samples (averaged for each sample) is in Table 2. Note that the scale is different on K-126 to improve visualization of the profiles.

US-400, shown in Figure 3 (a), had ER below 20 Ω -m at the sampling location. Based on the current data set these soils were likely low to moderate erodibility. The advantage of these profiles is they give erosion potential of the entire survey area beyond the sampling location. Figure 3(a) shows that there were more erodible locations (indicated by the yellow zones) than the sampling location at US-400. The sampling location at US-24 (Figure 3(b)) should exhibit moderate (corresponding to yellow zone) and low to moderate (corresponding to blue zone) erodibility; confirmed by erosion tests as seen in Figure 2. The soil erosion potential also showed that the top layer was likely more erodible (yellow layer) as compared to deeper layers at US-24. Again, comparatively more erodible soils were identified from erosion testing with a lower measured critical shear stress at the top sample (US-24 #1) than other two samples from the site (shown in Table 2). Lastly, the erosion profile of K-126 (Figure 3 (c)), shows that the entire subsurface soil is highly erodible due to higher values (over 50 Ω -m) of ER. Using the ER distribution alone this site identified the higher erosion potential than other sites.

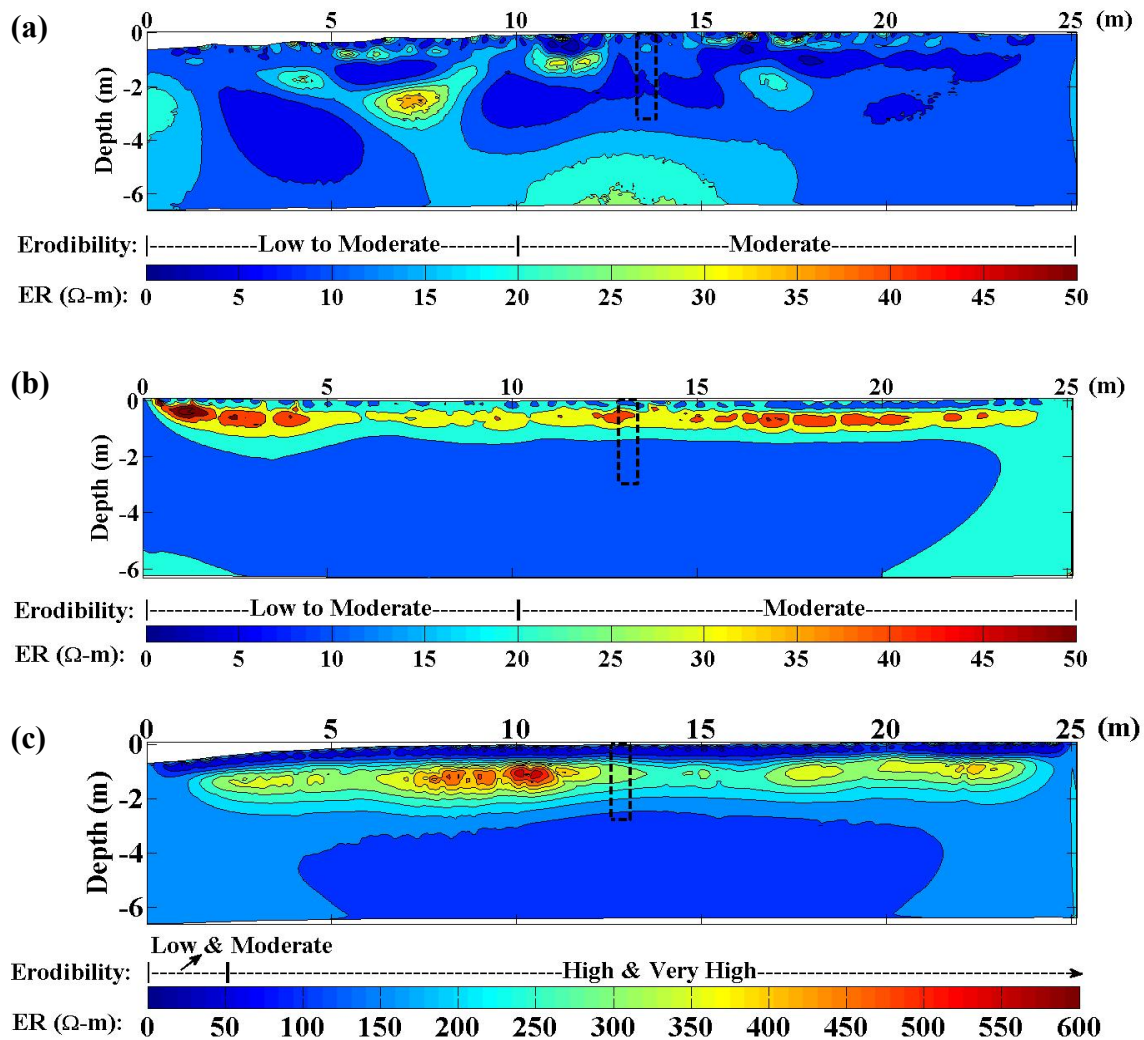


Figure 3. Two dimensional erosion potential using ER: (a) US-400, (b) US-24, (c) K-126 sites (scale of color bar is different for K-126 for better visualization).

CONCLUSION

This study showed that ER surveys may be used for identifying soil erosion potential without erosion testing. The correlation between ER and erosion potential in this data set indicated that if the measured ER was above 50 Ω -m for a site the soils were likely highly erodible. Based on these findings, transportation agencies can utilize ER to prioritize bridge sites for additional sampling and erosion testing as part of scour monitoring procedures. Five more bridges, or 25 more samples, remain in this project for characterization and erosion testing. Additionally, regression analysis based on the measured bulk ER and measured soil properties is on-going to predict several parameters such as critical shear stress and to develop a probability of exceedance for erosion characterization based on available data.

ACKNOWLEDGEMENTS

This research was funded by the Kansas Department of Transportation. The authors thank Bradford Rognlie, Mike Orth, James Brennan, Mike Noguera, and others with the Kansas Department of Transportation for supporting the project, providing feedback, selecting a variety of bridge sites, and collecting soil samples.

REFERENCES

- Abu-Hassanein, Z., Benson, C., and Blotz, L. (1996). "Electrical Resistivity of Compacted Clays." *J. Geotech. Engrg.*, 122(5), 397-406.
- AGI (Advanced Geosciences, Inc.). (2008). *Instruction Manual for EarthImager 2D Version 2.4.0 Resistivity and IP Inversion Software*, Advanced Geosciences, Inc., Austin, TX.
- Arneson, L. A., Zevenbergen, L. W., Lagasse, P. F., and Clopper, P. E. (2012). *Evaluating scour at bridges* (No. FHWA-HIF-12-003). NHI, Arlington, VA.
- ASTM D422-63 (2007). *Standard Test Method for Particle-Size Analysis of Soils*, ASTM International, West Conshohocken, PA.
- ASTM D4318-10 (2010). *Standard Test Methods for Liquid Limit, Plastic Limit, and Plasticity Index of Soils*, ASTM International, West Conshohocken, PA.
- ASTM C117-13 (2013). *Standard Test Method for Materials Finer than 75- μ m (No. 200) Sieve in Mineral Aggregates by Washing*, ASTM International, West Conshohocken, PA.
- ASTM C136/C136M-14 (2014). *Standard Test Method for Sieve Analysis of Fine and Coarse Aggregates*, ASTM International, West Conshohocken, PA.
- Bernhardt, M., Briaud, J., Kim, D., Leclair, M., Storesund, R., Lim, S., Bea, R. G., and Rogers, J. D. (2011). "Mississippi river levee failure: June 2008 flood." *International Journal of Geoenvironmental case history*, 2(3), 127-162.
- Briaud, J., Ting, F., Chen, H., Cao, Y., Han, S., and Kwak, K. (2001). "Erosion Function Apparatus for Scour Rate Predictions." *J. Geotech. Geoenviron. Eng.*, 127(2), 105-113.
- Calappi, T., Miller, C., and Carpenter, D. (2010). "Revisiting the HEC-18 Scour Equation." *Scour and Erosion*, ASCE, Reston, VA, 1102-1109.
- Crowley, R., Bloomquist, D., Shah, F., and Holst, C. (2012). "The sediment erosion rate flume (SERF): a new testing device for measuring soil erosion rate and shear stress." *Geotechnical Testing Journal*, 35(4), 1-11.
- Everett, M. E. (2013). "Electrical Resistivity Method." Chapter 4 in *Near-Surface Applied Geophysics*. Cambridge University Press, New York, NY, 70-102.
- Federal Highway Administration (FHWA). (1988). *Interim Procedures for Evaluating Scour at Bridges* (No. 1), U.S. Department of Transportation, Washington, D.C..
- Grabowski, R. C., Droppo, I. G., and Wharton, G. (2011). "Erodibility of cohesive sediment: the importance of sediment properties." *Earth-Science Reviews*, 105(3), 101-120.
- Hanson, G.J., and Cook, K.R. (2004). "Apparatus, test procedures, and analytical methods to measure soil erodibility in situ." *Applied Eng. In Agricul.*, 20(4), 455-462.
- Kibria, G., and Hossain, M. S. (2012). "Investigation of geotechnical parameters affecting electrical resistivity of compacted clays." *Journal of Geotechnical and Geoenvironmental Engineering*, 138(12), 1520-1529.

- Lin, C., Han, J., Bennett, C., and Parsons, R. L. (2014). "Case history analysis of bridge failures due to scour." *Climatic Effects on Pavement and Geotechnical Infrastructure*, ASCE, Reston, VA, 204-216.
- Ravens, T.M. (2007). "Comparison of Two Techniques to Measure Sediment Erodibility in the Fox River, Wisconsin." *Journal of Hydraulic Engineering*, 133(1), 111-115.
- Schuring, J. R., Dresnack, R., Golub, E., Khan, M. A., Young, M. R., Dunne, R., and Aboobaker, N. (2010). "Review of bridge scour practice in the US." *Scour and Erosion*, ASCE, Reston, VA, 1110-1119.
- Zhou, Q. Y., Shimada, J., and Sato, A. (2001). "Three-dimensional spatial and temporal monitoring of soil water content using electrical resistivity tomography." *Water Resources Research*, 37(2), 273-285.

Geofoam Inclusions for Reducing Passive Force on Bridge Abutments Based on Large-Scale Tests

Kyle M. Rollins, Ph.D. M.ASCE¹; Eric Scott, M.ASCE²; and Aaron Marsh, M.ASCE³

¹Dept. of Civil and Environmental Engineering, Brigham Young Univ., 368 CB, Provo, UT 84602. E-mail: rollinsk@byu.edu

²CKR Engineers, 1295 N State St., Orem, UT 84057. E-mail: escott1025@gmail.com

³DOWL, 4041 B St., Anchorage, AK 99503. E-mail: aaron.kirt@gmail.com

Abstract

To decrease lateral earth pressures on structures, a zone of compressible material or an “inclusion” can be used as a barrier to decrease lateral earth pressures on structures. The compressible material is typically expanded polystyrene or geofoam. Little guidance is available on the development of passive force with an inclusion. To explore this issue, large-scale passive force tests were conducted with and without a geofoam inclusion acting as a barrier between the backfill soil and a simulated bridge abutment. The presence of the geofoam inclusion reduced the passive force by 70% relative to the sand backfill alone. Although the measured force and failure geometry appeared to conform to a log-spiral mechanism when only sand backfill was used, the geofoam inclusion transforms the failure geometry to a Rankine failure mechanism. This suggests that the geofoam acted to reduce the interface friction between the wall and the backfill sand thereby reducing the passive resistance.

INTRODUCTION

A zone of compressible material or an “inclusion” has been proposed as a barrier to decrease lateral earth pressures on structures (Horvath 1997). The compressible material is typically expanded polystyrene (EPS), also known as geofoam. Although the influence of geofoam inclusions has been investigated for the case of active earth pressure (Ertugrul and Trandafir 2012; Ertugrul and Trandafir 2012; Horvath 1997), very few tests have previously been conducted to examine the effect of geofoam inclusions on passive earth pressure (Bathurst and Zarnani 2013; Horvath, 1997). In some cases, it might be desirable to isolate the bridge structure and abutment walls from the passive backfill force. For example, in the event of liquefaction in an underlying sand layer, lateral spread displacements could cause passive force to develop against the abutment as the overlying backfill soil slides towards the bridge abutment. Alternatively, dynamic forces from inertial earthquake loading could cause structural movement towards a soil backfill leading to large passive pressures on the backwall.

Current design codes and technical literature provide little guidance on passive force-deflection relationships with geofoam inclusions and no field test are available to define performance. To provide some basic information on the behavior of this system, large-scale passive force tests were conducted with and without a geofoam inclusion acting as a barrier between the backfill soil and a simulated bridge abutment. This report describes the properties of the backfill and geofoam materials and the testing procedures employed, and provides results

from the tests. Test results include passive force-deflection curves, lateral and vertical deformation of the geofoam and backfill soil, shear plane formation and surface cracking patterns, and backfill strain.

GEOMETRY OF SIMULATED ABUTMENT TEST

Figure 1 provides plan and profile drawings showing the layout of the pile cap which simulates a bridge abutment, the geofoam inclusion, the backfill soil and the loading system. The pile cap consists of a reinforced concrete block 3.35-m (11-ft) wide, 1.68 m (5.5-ft) high, and 4.57 (15-ft) long. The pile cap is supported by six 32.4 cm (12.75 in) OD steel pile piles filled with concrete. The piles extend to a depth of approximately 12.2 (40 ft) below the ground surface and ensure that the pile cap does not move vertically. The test layout used by Marsh et al (2013) was identical; however, the inclusion was not present. Load was applied using two MTS hydraulic actuators capable of applying a horizontal force of 5300 kN (1200 kips) in compression. The reaction for the actuators was provided by two 1.22 m (4 ft) diameter drilled shafts along with a 9.1 m (30 ft) deep sheet pile wall tied together by two deep beams as shown in Figure 1.

The backfill zone used for both the tests with and without the geofoam inclusion was approximately 6.4 m (21 ft) wide and 7.9 m (26 ft) long. The backfill was placed directly north of the pile cap and geofoam inclusions. To fully contain a potential log-spiral type failure surface, the soil backfill extended one foot below the pile cap. During placement of the backfill zone, two nuclear density gauge measurements were taken for each lift of soil placed to ensure compaction and to determine the moisture content and unit weight of the soil used. The backfill soil was poorly graded sand and classified as SP soil type according to the Unified Soil Classification System. The maximum density of the soil according to the modified Proctor compaction test (ASTM D1557) was 17.5 kN/m³ (111.5 lbs/ft³) with an optimum moisture content of 7.1%. Typical relative compaction was approximately 96%.

Pile cap load was the sum of the two actuator loads and pile cap deflection was the average of four string potentiometers attached to the back corners of the pile cap. Heave of the backfill was measured with a conventional survey level on a grid pattern before and after testing. Backfill displacement was measured using string potentiometers inserted into the geofoam at 0.15 m (0.5 ft) intervals and into the sand at 0.6 m (2 ft intervals). A number of vertical holes were excavated in the backfill and filled with red sand so that the shear plane could be identified.

The geofoam barrier that was placed between the pile cap and the soil backfill consisted of four blocks of expanded polystyrene (EPS), or geofoam. The bottom two blocks were 1.2 m (4 ft) tall while the upper blocks were 0.6 m (2 ft) tall as shown in Figure 1. These dimensions allowed the geofoam inclusion to extend beneath the pile cap while the top surface of the geofoam remained relatively level with the top of the pile cap. All blocks were 0.9 m (3 ft) thick in the direction of loading, and 2.44 m (8 ft) wide. Thus, the blocks spanned 4.88 m (16 ft) at the face of the backfill zone with a joint in the center of the cap. The geofoam blocks were designated EPS19 which is a medium density geofoam that provides some strength but is also readily compressible when loaded. Geofoam density typically ranges from 12 to 46 kg/m³. The “19” indicates that the geofoam has a density of 19 kg/m³ (1.15 lb/ft³) or about 1/90th of the dry unit weight of the backfill sand (Horvath 1997). The elastic modulus of the EPS19 geofoam is 4000 kPa (580 psi). These geofoam blocks offer 90 kPa (13.1 psi) of compressive resistance at 5% deformation or 16.0 psi at 10% deformation (EPS Geofoam 2012). The blocks were simply stacked on top of each other and not connected using any mechanical or geometric interlocking

system. The upper blocks weighed approximately 25 kN (55 lbs) while the lower blocks weighed approximately 50 kN (110 lbs).

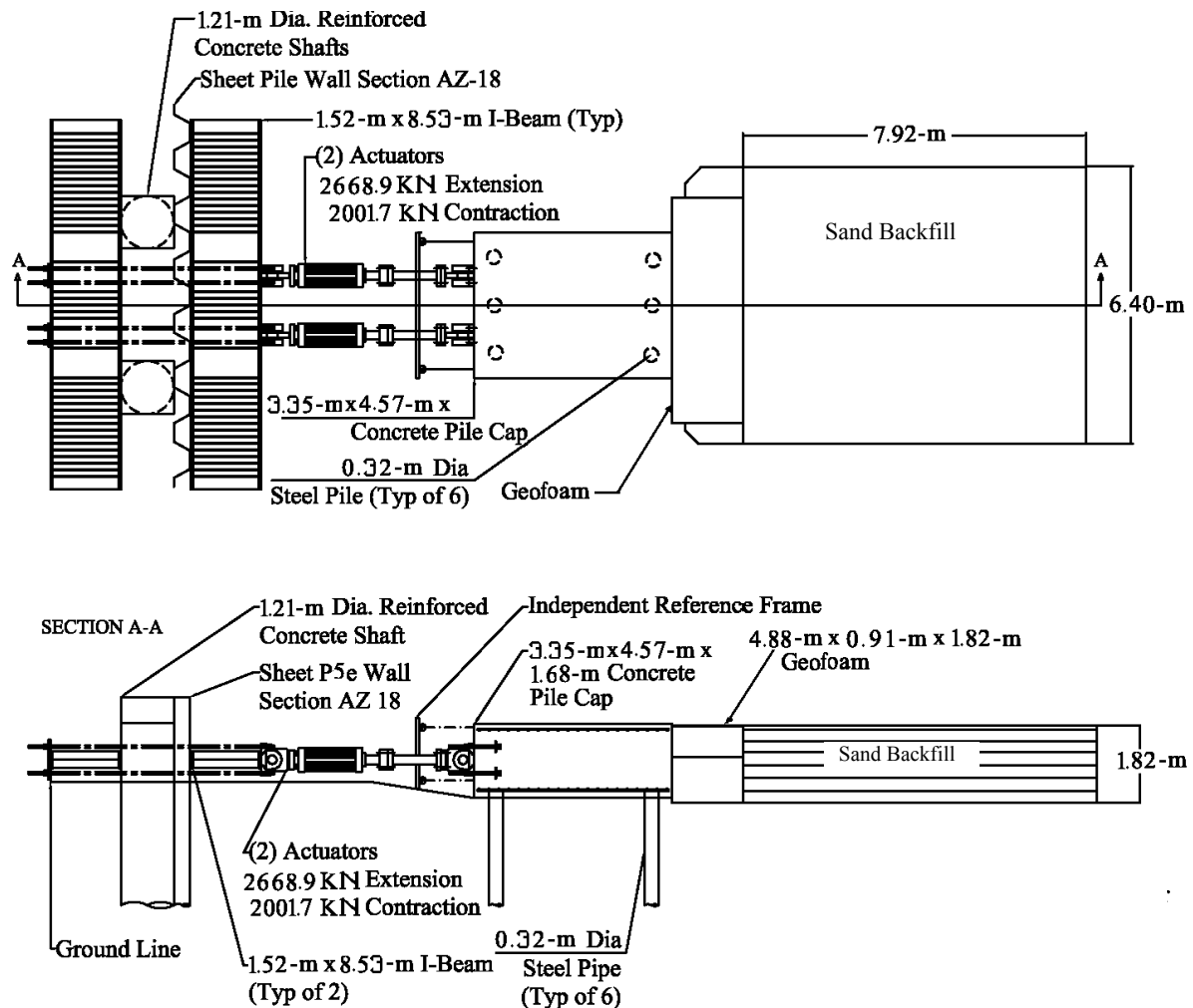


Figure 1. Plan and profile views of the test set-up showing test pile cap, geofoam inclusion, and backfill soil along with the loading system.

LOAD TEST RESULTS

The passive resistance provided by the backfill soil was determined by measuring the total load versus deflection curve and subtracting the “baseline” resistance provided by the pile cap without backfill in place. The load was applied incrementally to produce deflection increments of approximately 6 mm (0.25 in). Marsh et al (2013) reported the passive force vs. deflection curve for the test without a geofoam inclusion previously.

The measured passive force versus deflection curves obtained with and without an inclusion are presented in Figure 2. The peak passive force without an inclusion is approximately 2133 kN (480 kips) and occurs at a pile cap deflection of 5.7 cm (2.24 in) which is about 3.4% of the cap height. This is in good agreement with previously large-scale passive force tests in which the peak developed with displacements equal to 3 to 5% of the wall height

(Cole and Rollins, 2006). In contrast, the passive force vs. displacement curve with the inclusion does not reach a distinct peak but tends to increase very gradually with displacement. Therefore, at the maximum pile cap deflection of 9.5 cm (3.75 in), the cap was unloaded, shims (plywood sheets) were placed in the gap between the pile cap and the geofoam blocks, then the cap was again loaded to extend the passive force deflection curve to approximately 15 cm (6 in). At a displacement equal to 3.4% of the cap height, the passive force with the inclusion is only about 570 kN (128 kips) which represents a reduction in resistance of 73%. Even at a displacement equal to about 9% of the cap height, the passive force of 800 kN (180 kips) is still about 63% lower than the peak resistance without the inclusion. Clearly, the inclusion significantly reduced passive force.

At the conclusion of the testing, the geofoam blocks were excavated. Figure 3 provides a photograph of the bottom geofoam block on the right side of the cap in the direction of loading. The geofoam is permanently indented by the loading imposed by the pile cap. In addition, shear planes formed along the edge of the pile cap where the geofoam was unable to accommodate the large change in deformation.

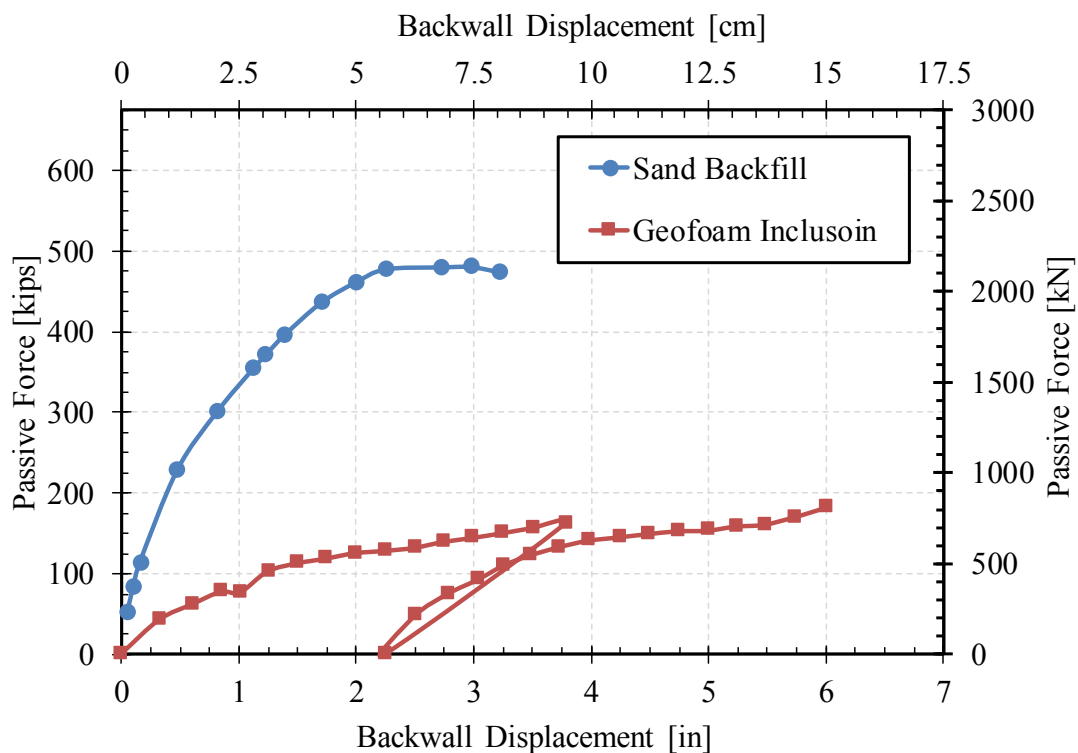


Figure 2. Plan and profile views of the test set-up showing test pile cap, geofoam inclusion, and backfill soil along with the loading system.

The displacement of the backfill with respect to distance from the pile cap face is plotted at five pile cap deflection levels for the test with the geofoam inclusion and the test with sand only in Figures 4 and 5, respectively. In the case of the test with the geofoam inclusion, results are only shown for the first cycle of load to provide a simpler comparison with the test with sand alone. The results indicate that most of the compression of the geofoam occurs in the first 0.15 m (0.5 ft) of the geofoam block behind the pile cap with strains as high as 20% with strains less than 1.0% in the rest of the geofoam. Backfill displacement of the sand behind the geofoam

typically decreases quite linearly until the pile cap displacement reaches 7.5 (3 in), at which point considerable strain (up to 9%) is developed in the zone from 1.5 to 2.1 m (5 to 7 ft). Backfill displacement decreases to less than 0.5 cm (0.3 in) at a distance of 5.2 m (17 ft). In contrast, in the sand only test, the compression in the 0.6 m (2 ft) behind the pile cap is also substantial but strain does not exceed 6%, while strain is less than 1% behind this zone. Backfill displacement at a distance of 5.2 m (17 ft) is more than twice as high as that with the geofoam.



Figure 3. Photograph of the compressed geofoam along with shear plane that developed at the edge of the pile cap.

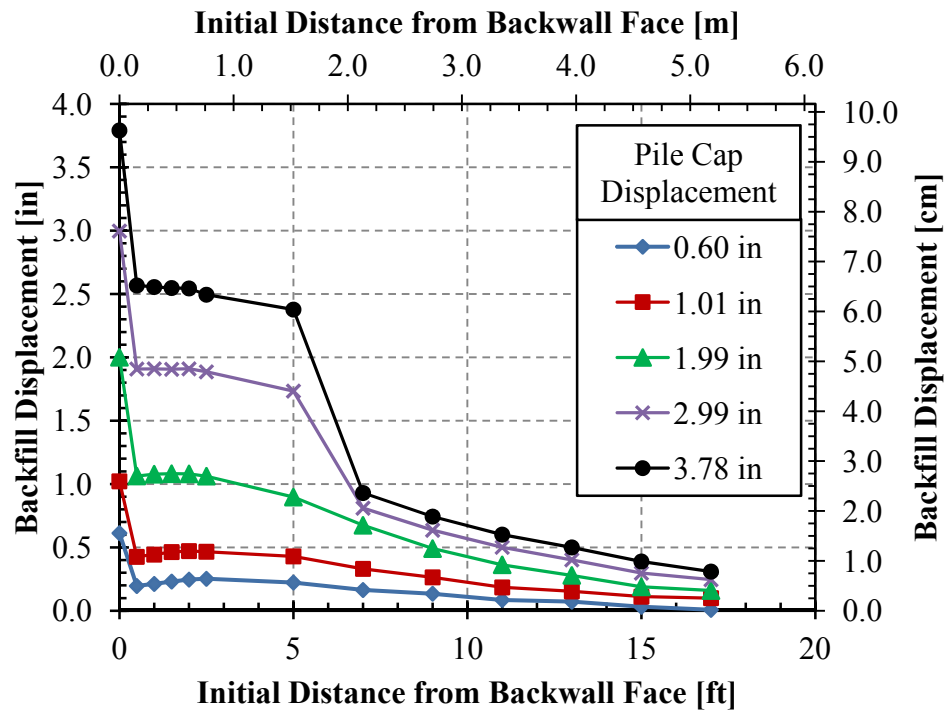


Figure 4. Backfill displacement versus distance from the pile cap at selected cap displacements for 1st loading of the geofoam inclusion test.

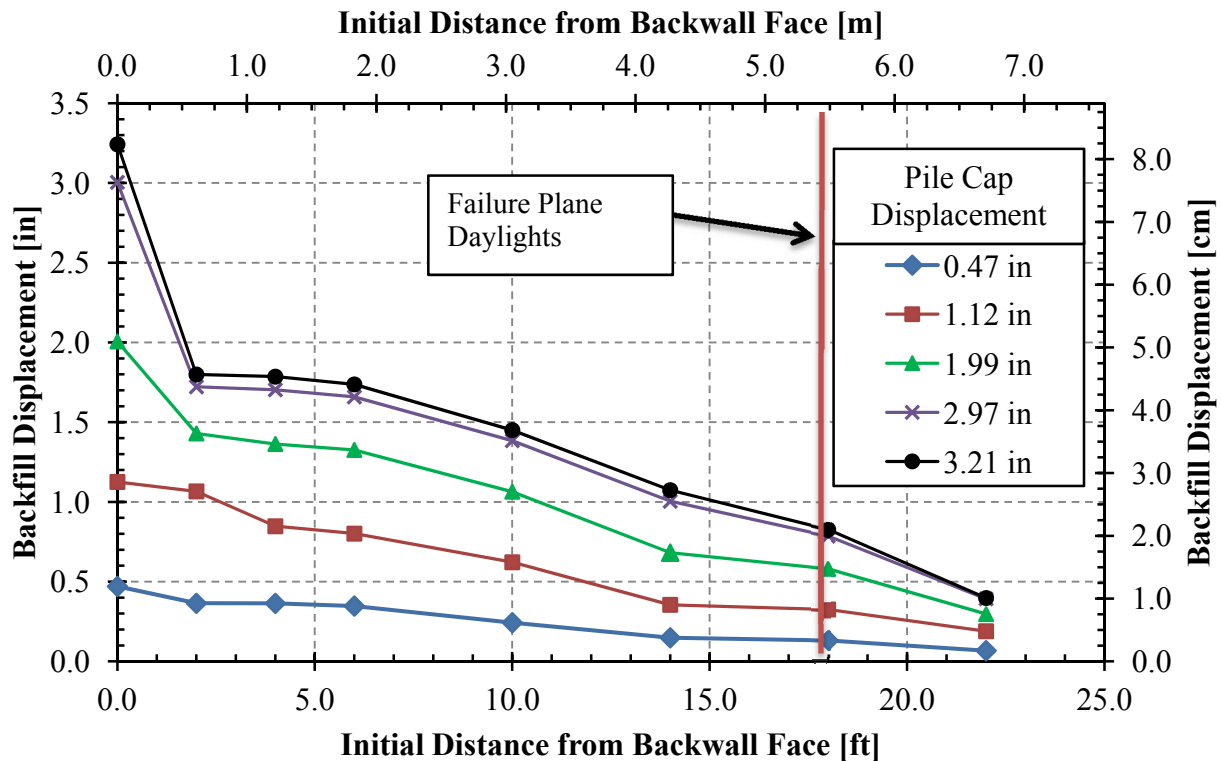


Figure 5. Backfill displacement versus distance from the pile cap at selected cap displacements for test without inclusion (sand backfill only).

Heave measurements and crack patterns for the sand backfill indicate that the failure plane extends to a distance of about 5.5 m (18 ft) behind the pile cap. In contrast, heave patterns for the backfill with geofoam indicate that the failure plane would daylight at about 3.3 m (10 ft) behind the pile cap. Columns of red sand were installed in the backfill behind the cap for both tests and the offset in columns indicates a log-spiral shape of the failure surface for the sand only backfill, but a linear “Rankine” type failure surface for the geofoam. Because the top block of geofoam was only 0.6 m (2 ft) thick, intermediate failure planes clearly developed behind these shallow blocks. This also likely explains why there was a significant decrease in the backfill displacement behind this intermediate failure wedge.

Analysis of Test Results

The ultimate passive force can be computed using a variety of methods including: Rankine, Coulomb, and Log-Spiral. The Rankine method assumes no interface or wall friction between the pile cap and backfill while the Coulomb and Log-Spiral methods consider wall friction. Both the Rankine method and the Coulomb method assume a linear failure surface while the log-spiral approach assumes a log-spiral zone immediately behind the pile cap which transitions to a triangular Rankine failure wedge near the ground surface. The ultimate passive force has been computed using all three of these methods for the backfill with geofoam inclusion and for the backfill with sand only. Table 1 summarizes the predicted and measured passive force values from the sand test while Table 2 shows the predicted and measured passive force value for the

geofoam inclusion test. In computing the ultimate passive force, the moist unit weight (γ) was taken as 18.4 kN/m^3 (117 lbs/ft^3), the sand friction angle (ϕ) was assumed to be 38.5° , and wall friction (δ) was assumed to be 0.70 for the Log-Spiral and Coulomb methods, and 0° for the Rankine method. The effective width of the failure wedge transverse to the direction of loading was 18.5 ft for the sand backfill using a 3D width correction factor proposed by Brinch-Hansen (1966). For the geofoam inclusion test, the effective width of the shear zone was also assumed to be 18.5 ft based on the observed shear crack patterns, but the wall height was taken as 6 ft to match the height of the geofoam block wall. All other parameters were the same as for the sand backfill test.

Table 1. Calculated and measured passive forces for sand backfill test.

Method	Passive Force Per width	Total Passive Force	Total Passive Force
	kN/m (kips/ft)	kN (kips)	Percent Error
Log Spiral	32.7 (24.1)	2105 (474)	-1.50%
Coulomb	48.6 (35.9)	3138 (706)	47%
Rankine	13.2 (9.7)	849 (191)	-60%
Sand Test	33.1 (24.4)	2138 (481)	N/A

Table 2. Calculated and measured passive forces for geofoam inclusion test.

Method	Passive Force Per width	Total Passive Force	Total Passive Force
	kN/m (kips/ft)	kN (kips)	Percent Error
Log Spiral	32.7 (24.1)	2105 (474)	154%
Coulomb	48.6 (35.9)	3138 (706)	278%
Rankine	13.2 (9.7)	849 (191)	2.4%
Geofoam Inclusion Test	12.9 (9.5)	831 (187)	N/A

As shown in Table 1, the Log Spiral method, which is commonly considered to be the most theoretically sound method, provides the most accurate estimate of the measured passive force for the sand backfill tests. However, the Coulomb method significantly overestimated passive force while the Rankine theory significantly underestimated the passive force that was measured. However, as shown in Table 2, the Rankine theory was the most successful at explaining the results obtained from the geofoam test while the Log-spiral and Coulomb methods greatly over predicted passive resistance. One potential explanation for the success of the Rankine theory in predicting the geofoam inclusion test results is the reduction in interface friction between the geofoam and the backfill wall or the soil backfill and the geofoam. Based on the failure surface geometry and the reduced passive force, it appears that the presence of the geofoam inclusion reduces the effective interface friction to a value close to zero which is the value assumed by the Rankine earth pressure theory.

CONCLUSION

Based on the field test results and the computer analyses, the following conclusions can be drawn:

1. Geofoam inclusions appear to be very effective at reducing the ultimate passive force which develops at abutments with sand backfills. In this case, the geofoam inclusion reduced the passive force by about 70% relative to the backfill composed only of sand.
2. Although the failure mechanism for a sand backfill typically involves a log-spiral failure surface, the governing failure mechanism for a sand backfill with a geofoam inclusion appears to be a linear shear failure similar to that described by the Rankine earth pressure theory.
3. The log-spiral method was able to predict the peak passive resistance for the sand backfill with an error of less than 10% assuming a friction angle of 38.5° with wall friction equal to 70% of the friction angle, while the Rankine method significantly underestimated resistance. In contrast, the Rankine method predicted the peak passive resistance for the backfill with the geofoam inclusion within 10%, assuming a wall friction of zero, while the log-spiral method significantly overestimated resistance.
4. The reduction in passive force produced by the geofoam inclusion appears to result from a reduction of the effective interface friction to about zero rather than excessive compression of the geofoam.
5. In computing the peak passive force for a sand backfill with a geofoam inclusion, the wall friction should be assumed to be zero and the Rankine method should be used.

ACKNOWLEDGEMENTS

Support for this research was provided by FHWA pooled fund study TPF-5(264), which was supported by Departments of Transportation from the states of California, Minnesota, Montana, New York, Oregon, Utah and Wisconsin along with FHWA. Utah served as the lead agency, with David Stevens as the project manager. Atlas EPS donated the geofoam blocks used in the study. This support is gratefully acknowledged; however, the opinions, conclusions and recommendations in this paper do not necessarily represent those of the sponsoring organizations.

REFERENCES

- ASCE (American Society of Civil Engineers). (2014) *Minimum Design Loads for Buildings and Other Structures*, Standard ASCE/SEI 7-10. Third printing. ASCE, Reston, VA.
- Bathurst, R. J., and Zarnani, S. (2013). "Earthquake Load Attenuation Using EPS Geofoam Buffers in Rigid Wall Applications." *J. Indian Geotechnical Society*, 43(4), 283-291.
- Bathurst, R. J., Zarnani, S., and Gaskin, A. (2007). "Shaking table testing of geofoam seismic buffers." *Soil Dynamics and Earthquake Engineering*, 27(4), 324-332.
- Brinch-Hansen, J. (1966). "Resistance of a Rectangular Anchor Slab." *Bulletin No. 21*, Danish Geotechnical Institute, Copenhagen, 12-13.
- Cole, R. T., and Rollins, K. M. (2006). "Passive Earth Pressure Mobilization during Cyclic Loading." *J. of Geotechnical and Geoenvironmental Engineering*, 132(9), 10.

- EPS Geofoam (2012). "Type EPS19 TechData." <<http://www.geofoam.com/technical/>>. (6/25/2015, 2015).
- Ertugurl, O., and Trandafir, A. (2012). "Reduction of Lateral Earth Forces on Yielding Flexible Retaining Walls by EPS Geofoam Inclusions." GeoCongress 2012, 2068-2077
- Ertugrul, O. L., and Trandafir, A. C. (2011). "Reduction of lateral earth forces acting on rigid nonyielding retaining walls by EPS geofoam inclusions." *J. Materials in Civil Engineering*, 23(12), 1711-1718.
- Horvath, J. S. (1997). "The compressible inclusion function of EPS geofoam." *Geotextiles and Geomembranes*, 15(1), 77-120.
- Marsh, A., Rollins, K.M., Franke, B., Palmer, K., and Smith, J. (2013) "Behavior of Zero and Thirty Degree Skewed Abutments." *J. Transportation Research*, Transportation Research Board, Washington, DC. Vol. 2363 (Soil Mechanics 2013), p. 12-20

Observation of the Progressive Failure Mechanism of Reinforced Foundation Soil Using the Digital Image Correlation Technique

Mazhar I. Arshad, Ph.D.¹; Monica Prezzi, Ph.D., P.E., M.ASCE²; and
Rodrigo Salgado, Ph.D., P.E., M.ASCE³

¹NUST College of Civil Engineering, Risalpur, Pakistan (Formerly Purdue University). E-mail: mazhar.i.arshad@gmail.com

²Lyles School of Civil Engineering, Purdue Univ., 550 Stadium Mall Dr., West Lafayette, IN 47907. E-mail: mprezzi@purdue.edu

³Lyles School of Civil Engineering, Purdue Univ., 550 Stadium Mall Dr., West Lafayette, IN 47907. E-mail: salgado@purdue.edu

Abstract

Geosynthetic materials have been widely used in reinforcing the weak soil underneath the shallow foundations in the recent years. Many previous static loading studies have shown that the bearing capacity of the soil with a shallow foundation on the surface is greatly increased when the soil is reinforced by a layer of geosynthetic material. The present study visualizes the deformation field and failure mechanism in geosynthetic-reinforced soil underlying shallow foundations using digital image correlation (DIC) technique. A small-scale calibration chamber was built to model a plane-strain condition for a strip footing system. A series of indentation tests were conducted using a rigid model strip footing on unreinforced soil and with soil reinforced with geonet and woven fabric geotextile. The effect of number of reinforcement layers on the deformation field within the bearing soil has been studied. The results highlighted the suitability of DIC technique to visualize the deformation in laboratory-scale experiments and clearly illustrated the effect of reinforcement on progressive failure mechanism of model footing.

INTRODUCTION

The indentation process of granular soil has wide application and particularly for geotechnical engineering. It has been employed theoretically in past to study the failure mechanism and predict the limit load of shallow footings. The earliest classical slip line solution for the bearing capacity problem was based on the Prandtl's analysis of punch indentation (Prandtl 1920). In order to visualize the deformation mechanism during this process various image analysis techniques have been successfully employed (White et al. 2003; Michalowski and Shi 2003; Sadek et al. 2003). Recently Tejas et al. (2009) has obtained the displacement field during the flat punch indentation of unreinforced soil. The results match with classical bearing capacity failure mechanism as given by method of characteristics (Martin 2004) and finite element analysis (Loukidis 2006).

In soft soil different types of reinforcement material and techniques have been developed to increase its load carrying capacity and minimizing the deformation. The design methods for footings on reinforced soil are based upon mostly limit equilibrium analysis assuming associated failure mechanism. Widely it is assumed that failure mechanism in reinforced soil retains the similar characteristics as proposed by Terzaghi (1996). However, in reality the type, number and

the orientation of reinforcement layers significantly alter the collapse mechanism of a footing. Binquet and Lee (1975) concluded that the use of multiple reinforcement layers increases the collapse load of strip footing on sand up to 2 to 4 times. Mostly the focus of studies in past remained on the increase of collapse load and deformation minimization with soil reinforcement. A few studies have investigated the failure mechanism of footing on reinforced soil. Yamamoto et al. (2001) used aluminum rods to model the soil and discussed the progressive failure of reinforced soil with multiple layers of paper and plastic reinforcement. Haung et al. (1990) investigated the failure pattern of footing on reinforced sand and observed the effects of reinforcement length on deformation patterns. Recently Michalowski et al. (2003) studied the influence of reinforcement layer depth on deformation pattern of strip footing using weak horizontal reinforcement. All of earliest studies concluded that the slip mechanism of reinforced soil using geosynthetics reinforcement remains similar to unreinforced soil. However, it depends upon the depth, length and number of reinforcement layers used for reinforcing purpose and their layout.

The objective of this study is primarily to investigate the characteristic displacement field during the progressive failure of indentation process of reinforced soil. Different reinforcement types and numbers of layers have been studied. Images recorded during the indentation process are analyzed using digital image correlation (DIC). Collapse loads are also reported to indicate the effect of reinforcement.

EXPERIMENTAL ARRANGEMENT

Test set up. Figure 1 shows the schematic arrangement of the test set up. The soil specimen was prepared in plexiglass transparent container. The thickness of plexiglass was kept at 25 mm to avoid the lateral deflection during indentation process. The size of container is 400 mm x 200 mm x 200 mm. A flat punch indenter of two different widths of 32 mm and 20 mm were used. Sand paper of grading 60 was glued on bottom of indenter to have rough interface surface. The indenter mounted on vertical jacking system through inline load cell was moved downward. The load was measured during indentation process. Vishay system 5000 was used to record the data from load cell at scan rate of 2 Hz. Images were recorded using frame grabber during the process using high resolution (2544x1944 pixels) CMOS camera with frame rate of 2Hz. The triggering of camera was synchronized with data logging system.

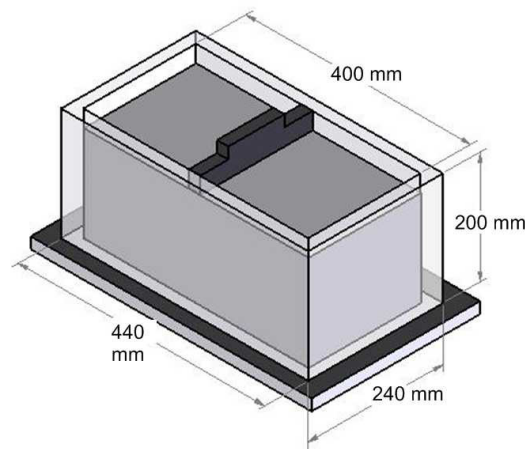


Figure 1. Schematic of experimental set up for indentation. The top of indenter is pushed downward with velocity of 1 mm/sec.

Reinforcement. Two types of reinforcement were used: a woven fabric and a miniature geonet. The size and layout of reinforcing layer is shown in Figure 2. In case of woven fabric and geonet, in addition to single reinforcing layer, experiments were also conducted with double reinforcing layers with interlayer spacing of $0.8B$.

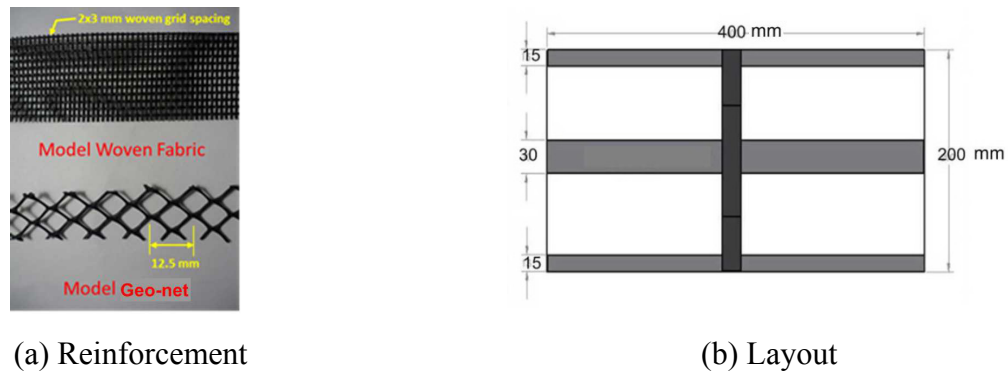


Figure 2. Model reinforcement used in experiments.

Materials used. Coarse grain silica sand designated as Q-2 ROK was used. The color of silica sand was mainly white and was not ideally suitable for image template matching. Therefore, to enhance the texture contrast and create optimum random speckle patterns, 20% by weight the sand was colored grey, oven dried and then mix with clean sand. This composition was arrived through various trials. The mechanical properties of made up soil used are given in table 1.

Table 1. Properties of soil.

Mean particle size (D_{50})	0.78mm
Maximum void ratio (e_{\max})	0.97
Minimum void ratio (e_{\min})	0.54
Specific Gravity (G_s)	2.65
Particle shape	Angular
Relative Density	20-30%

Sample preparation. Only the loose sand samples were prepared to simulate the weak soil. The horizontal sand bedding layers were created by air pulverization through a funnel. The drop height was maintained such that to achieve consistent density. The strip of geotextile reinforcement and geogrid were wish in placed at required depth of $0.8B$. For the double layers of reinforcement tests an additional layer of geotextile and geogrid was also placed at $1.8B$ depth from the top surface. To achieve horizontal surface, sand layer of 20mm thick cap was provided above the reinforcing layer. The soil above the reinforcing layer was compacted and levelled off.

Test Program. A series of six tests involving two test sets for each testing condition were performed. The tests were conducted only with loose soil densities ranging from 25-30%. Two tests were performed with unreinforced sand with 32 mm and 20mm wide indenter, for comparison of deformation patterns with reinforced soil. The tests with geotextile and geonet were conducted with depths at $0.8B$ and $1.5B$ from top surface for single and doubled layered samples. The indentation speed was kept constant in all tests through a actuator with velocity of 25 mm/min.

IMAGE ANALYSIS TECHNIQUE

Image acquisition. An image sequence during the indentation process was captured, using PCI express frame grabbers. The frame rate was kept at 2 fps. Thus the increment of velocity was constant 0.2 mm in all tests. The 256 grey colour, 8 bits images were recorded using 5 Mega pixels (2544 x 1944) monochrome CMOS camera. The cool illumination was provided using compact fluorescent lamp (CFL) in order to minimize image noise due to heating of camera sensor.

Digital image correlation. DIC is a non-contact optical method, widely used in experimental mechanics to obtain full field displacement and strain fields. The displacement field during the indentation process was measured through template matching using the DIC technique. A brief overview of technique is given here. Additional details can be found at Sutton et al. (2009).

In DIC two pair of images considered at different time increment. The first image in undeformed state is taken as reference image and second image after deformation is called as deformed image. The reference image is superposed with virtual measurement grid. The displacement is calculated on each intersection of virtual grid using image correlation. For correlation, an interrogation window which is subset of reference image is defined centered at each intersection of virtual grid. The size of this interrogation window depends upon the image contrast, displacement gradient and computation time. The interrogation window can overlap with each other depending upon the virtual grid spacing. Each interrogation window (subset) in reference image is matched in deformed image using predefined correlation criteria. The match can be searched in entire deformed image domain, but to decrease the computation cost the search radius, r (greater than expected displacement vector) is defined to limit the matching process within subdomain of deformed image by defining search window. For brief illustration we will use sum of squared difference correlation criteria. Let us consider a subset of size of length L is selected in reference image. The light intensity grey level distribution of reference image is defined by discrete function $f(x, y)$. After displacement of (u, v) the deformed image light intensity grey value function interpolated as $g(x, y)$. To find the best match than the least square sum of squared correlation criteria $C(x, y)$ is minimized for each candidate displacement vector. For the actual displacement vector (u, v) the correlation coefficient $C(x, y)$ will be minimum. The correlation process is shown graphically in figure3.

$$C(x, y, u, v) = \sum_{i,j=-L/2}^{L/2} W_{i,j} [f(x + i, y + j) - (x + i + u, y + i + v)]^2 \quad (1)$$

where $W(i, j)$ is weight function to approximate the sub pixel intensity value using high order spline function. In this study correlated solutions DIC software VIC 2D was used to perform the correlation.

Camera calibration. The displacement field obtained from DIC technique is in image pixel coordinates. To convert this image coordinates into real world coordinates camera calibration is performed using the principal of photogrammetry. The calibration target was imaged in the testing chamber and images were recorded. Thereafter the scale of image to world coordinates was determined. In these experiments 1 pixel represented 0.15 mm. The precision of DIC as reported by Sutton et al [12] is typically 0.01 pixels. In this way the accuracy of measurement is equal to 1.5 μm .

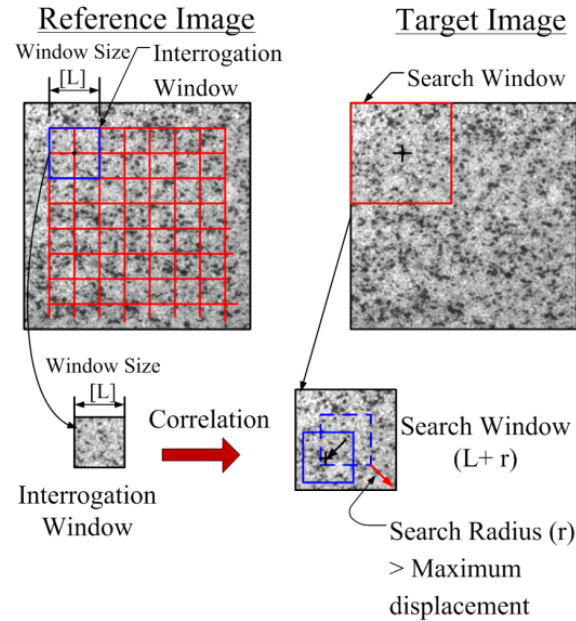


Figure 3. Digital image correlation process.

Strain Formulation. Since focus of this study is to investigate the failure process of strip footing, therefore finite strain formulation was adopted. The displacement field obtained from DIC is approximated using quadratic shape function considering 7x7 pixel neighbourhood in least square fashion. The coefficients are obtained to fit the local surface. Then the local gradient of displacement ($\frac{\partial u}{\partial x}, \frac{\partial u}{\partial y}, \frac{\partial v}{\partial x}, \frac{\partial v}{\partial y}$) are calculated at the centre of neighbourhood. The Lagrange strains are obtained as follows.

$$E_{xx} = \frac{\partial u}{\partial x} + \frac{1}{2} \left[\left(\frac{\partial u}{\partial x} \right)^2 + \left(\frac{\partial u}{\partial y} \right)^2 \right] \quad (2)$$

$$E_{yy} = \frac{\partial v}{\partial y} + \frac{1}{2} \left[\left(\frac{\partial v}{\partial x} \right)^2 + \left(\frac{\partial v}{\partial y} \right)^2 \right] \quad (3)$$

$$E_{xy} = \frac{1}{2} \left(\frac{\partial u}{\partial x} + \frac{\partial v}{\partial y} \right) + \frac{1}{2} \left[\left(\frac{\partial u}{\partial x} \frac{\partial u}{\partial y} \right) + \left(\frac{\partial v}{\partial x} \frac{\partial v}{\partial y} \right) \right] \quad (4)$$

The volumetric strain can be obtained for plane-strain formulation as:

$$E_{vol} = e_{xx} + e_{yy} \quad (5)$$

DISPLACEMENT FIELD PATTERNS

The deformation fields for selected tests are presented in color contours. The contours of total vertical and horizontal displacement field along with total shear strain and volumetric strain field are also presented. Deformation fields corresponding to 0.1B to 1B vertical displacement and post failure stages are reported. Load displacements curves are also presented as indicator for collapse load. Since the indenter was tight fit in testing chamber, thus the friction between Plexiglas walls influenced the collapse load. Therefore the collapse load may be slightly over predicted.

Load displacement curves. Figure 4 shows the load-displacement curves of all tests with and without geotextile reinforcements. It is quite evident from the load-displacements curves that the limit load of footing with reinforcement increases significantly about 3-5 times than that of the unreinforced tests. The use of double layer increases the collapse load to 1.6 times than that of single layer reinforcement of each type. The difference between two types of reinforcements is not significant however tests with woven fabric shows slight greater limit load. Similarly, the collapse load of 32 mm wide footing is observed to be about twice than the 20 mm wide footing in unreinforced soils.

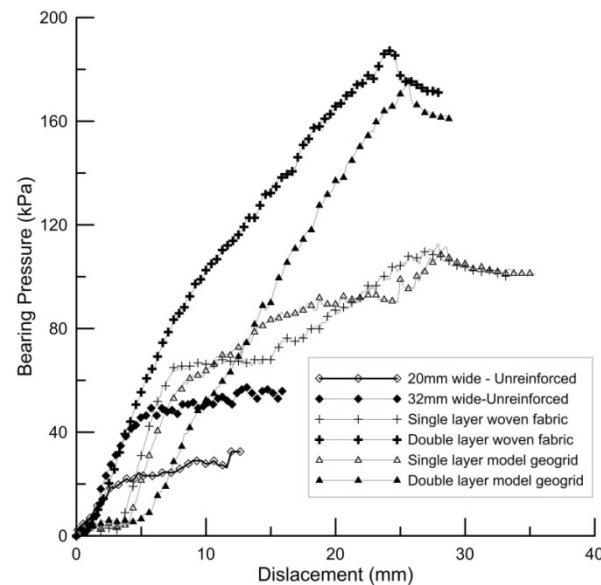


Figure4. Load-displacement curves of all tests.

Displacement field of un-reinforced soil. Figure 5 shows the displacement field for 20mm wide footing. The boundary effects was observed from sidewalls in case of 32 mm wide footing therefore only the 20 mm wide indenter was used in subsequent tests. The displacement field represents the symmetric process along the centreline of footing and clearly matches with Prandtl slip line solution. The vertical compression nose cone is observed under the footing, followed by log spiral slip line. The narrow width shear band extended towards the surface, while deep punching shear zone observed extending from corner of footing. An upward heave corresponding to 5% B was observed in both cases and it extended till 5B on both sides at failure. The ratio of maximum horizontal to vertical displacement is 35%. The vertical deformation along the centerline of footing extends till 7B and thereafter it becomes negligible.

Displacement field of reinforced soil. The results for single and double layer reinforcement with geotextile woven fabric are reported here only owing to the length of paper. However, it was observed that the woven fabric geotextile reinforcement have slightly pronounced effect on failure mechanism.

Single layer reinforcement at 0.8 B depth. Figure 6 shows the evolution of normalized horizontal (U/B) and vertical displacements (V/B) of reinforced soil with woven fabric, corresponding to the 5%, 10%, 25%, 50% and 100% B of strip footing displacements. The displacement field indicates that at small footing displacement up to 5%B, the displacement field is unaltered by the reinforcing layer and follows the indentation process slip pattern, similar to

the unreinforced soil. However, at greater footing penetration a clear discontinuity in displacement fields is observed owing to the pull-out mechanism of the reinforcement layer. This discontinuity is observed more in horizontal displacement field than the vertical displacement field. At large footing displacements, the slip is aligned with reinforcing layer and inward movement of soil is observed. However, below the reinforcing layer, the displacement field resembles the unreinforced soil and follows log-spiral slip mechanism.

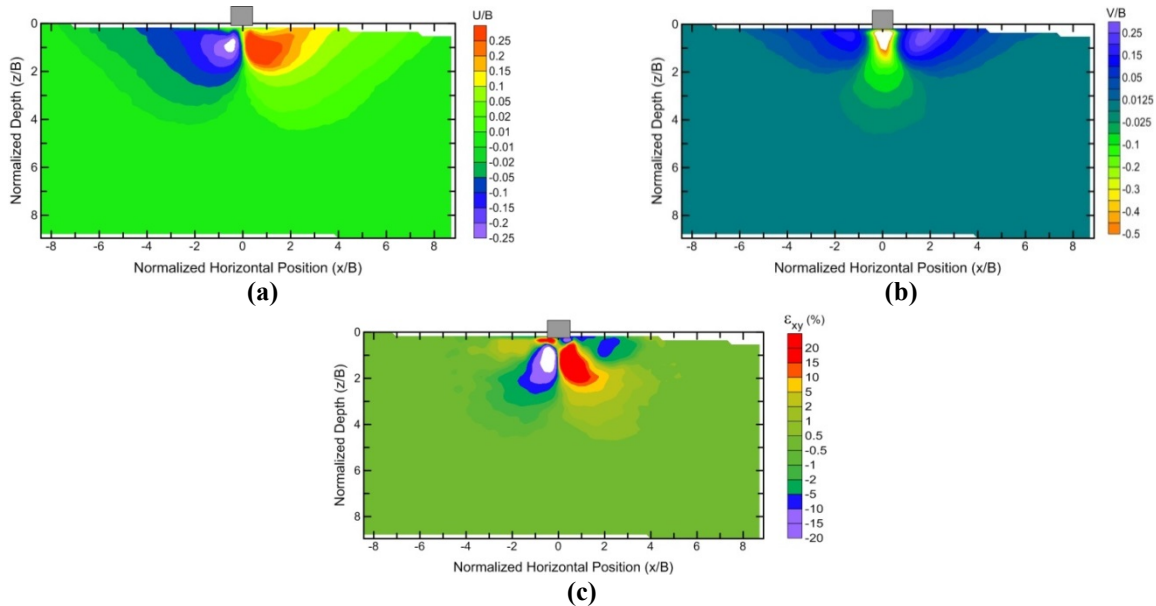


Figure 5. Normalized displacement field corresponding to 1 B footing displacement in unreinforced soil (a) horizontal displacement (b) vertical displacement, and (c) shear strain contours.

Figure 7 shows the evolution of shear strain (ϵ_{xy}) for woven fabric geotextile reinforced soil. Comparatively intense strain localization is observed along the reinforcement in woven fabric reinforced soil test as compared to model geogrid reinforced test. At smaller footing displacement the shear strain mobilizes above the reinforcing layer, is similar to unreinforced soil, however as footing is displaced more, the shear band starts forming along the length of reinforcement layer, until the pull-out capacity of reinforcement is mobilized and eventually thick intense shearing banding is observed. Below the reinforcing layer, radial pattern shear strain is observed similar to unreinforced soil.

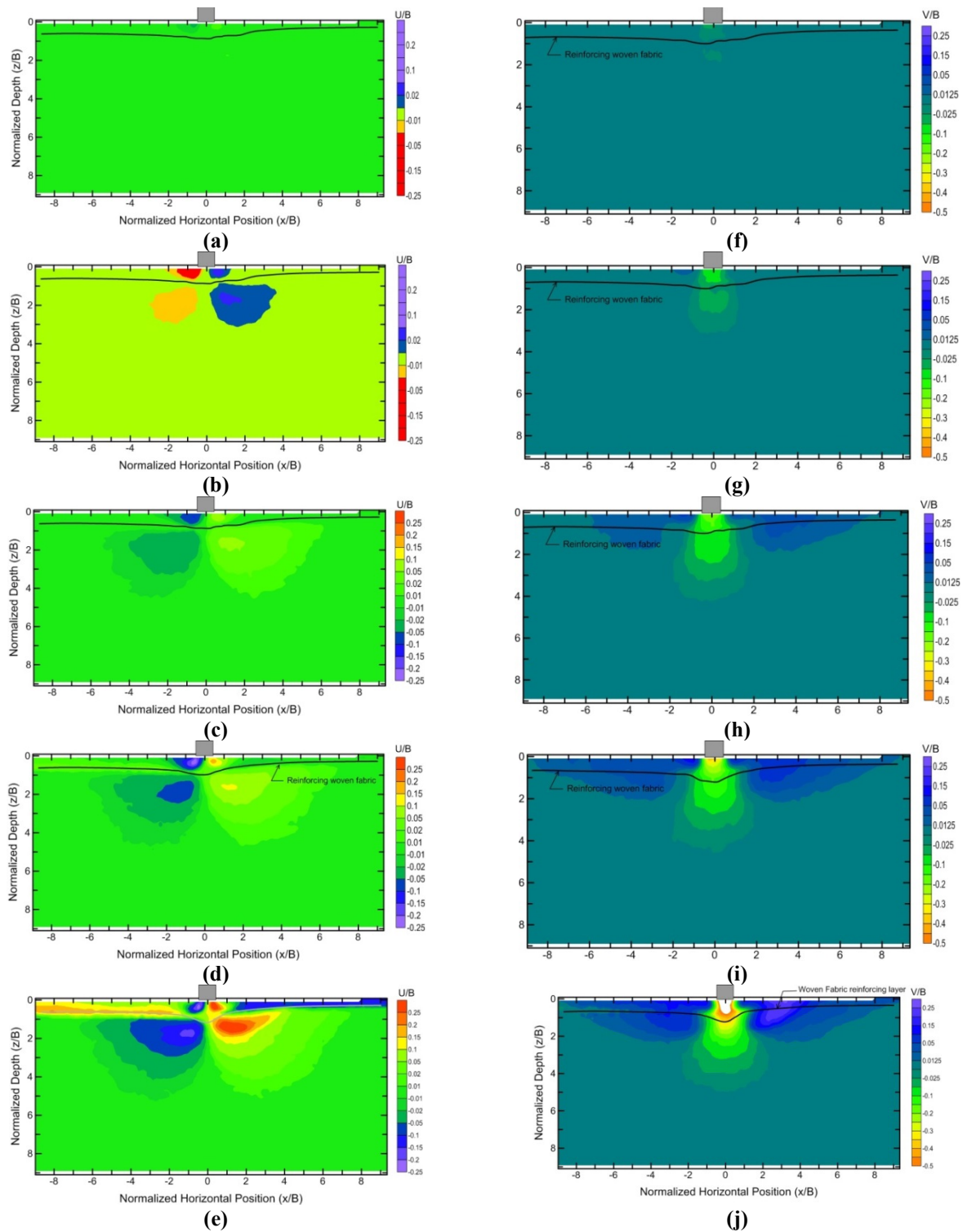


Figure 6. (Color) 20 mm wide footing displacement field corresponding to 0.05B, 0.1 B, 0.25B, 0.5B and 1B footing displacement in reinforced soil with single layered woven fabric geotextile.

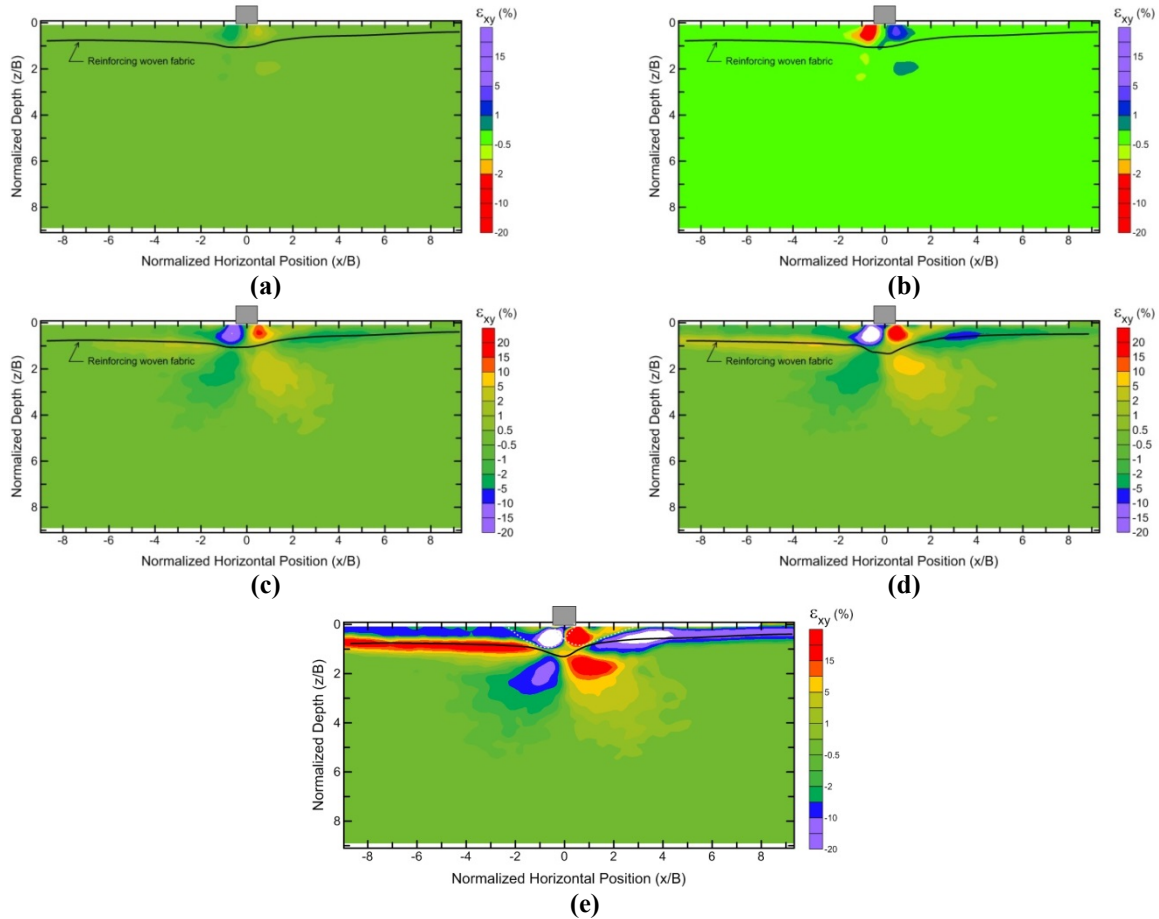


Figure7. (Color) Shearing strain evolution corresponds to 0.05B, 0.1 B, 0.25B, 0.5B and 1B footing displacement in reinforced soil with single layered of woven fabric.

Double layers reinforcement at 0.8 B and 1.8B depths. Figure 8 shows the normalized horizontal (U/B), vertical displacements (V/B) and shear strain (E_{xy}) plots of reinforced soil with two layers of woven fabric, corresponding to 1B footing displacement representative of limit condition. The displacement field indicates that, the displacement pattern is similar to that of the unreinforced soil. However, below the reinforcing layer a clear discontinuity in displacement fields is observed owing to the pull-out mechanism of the reinforcement layers. This discontinuity is observed more in horizontal displacement field than the vertical displacement field similar to singly layered reinforced soil. The slip is aligned with reinforcing layer and inward movement of soil is pronounced. However, below the reinforcing layer, the displacement field resembles the unreinforced soil and follows log-spiral slip mechanism. A complex failure mechanism is observed involving two distinctive shear banding along the reinforcement layer coupled with Prandtl type slip pattern.

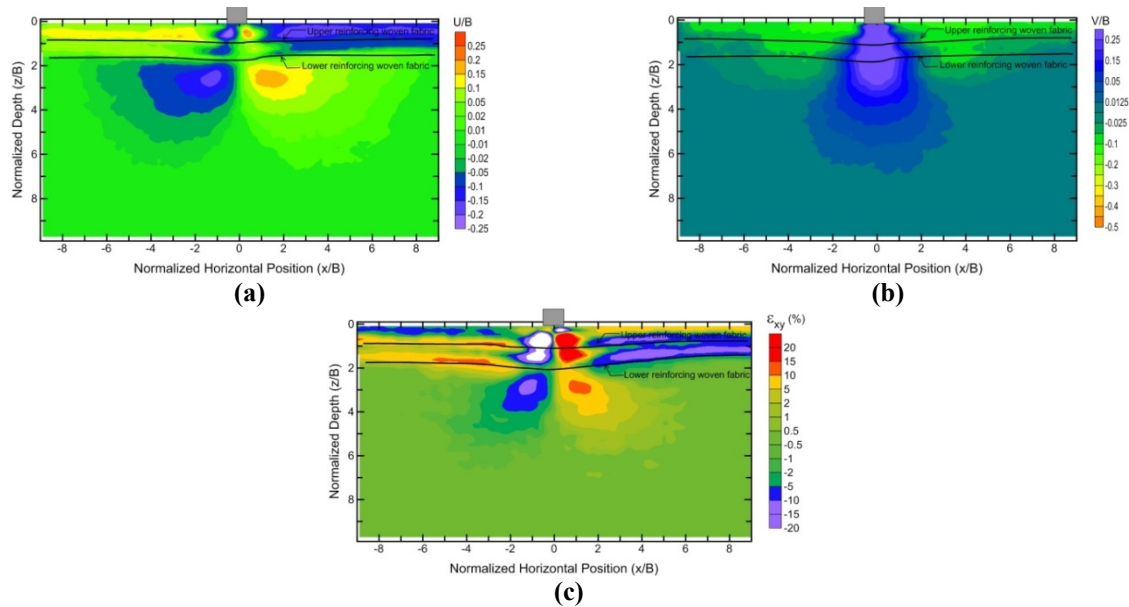


Figure 8. Normalized displacement field corresponding to 1 B footing displacement in doubly reinforcement layers of woven fabric (a) horizontal displacement (b) vertical displacement, and (c) shear strain contours.

CONCLUSION

The deformation and failure mechanism of strip footing has been studied using the digital image correlation technique. The effect of reinforcement and number of reinforcing layers on displacement field has been evaluated by simple micro mechanical modelling approach. The conclusions drawn from study are summarized as under:

1. The characteristics of displacement field for strip footing are altered significantly by the presence of reinforcing layer especially in case of doubly reinforced soil.
2. The existing limit equilibrium solutions will have limitation in predicting the bearing capacity of reinforced soil.
3. The current study will be great help in developing the limit equilibrium solution for bearing capacity of reinforced soil and is being considered in future work.
4. From the displacement pattern, the effect of reinforcement on bearing capacity slip pattern can be simplified by superposition the two different failure mechanisms; the pullout mechanism of geotextile reinforcement at the given embedment depth and the traditional limit bearing capacity slip mechanism of unreinforced soil, below the reinforcing layer.

REFERENCES

- Binquet J. and Lee, K.L. (1975a). Bearing capacity tests on reinforced earth slabs, *Jl. of Geotech Engg Div. ASCE*, 101(GT12), 1241-1251.
- Haug, C.C. and Tatsuka, F. (1990). Bearing capacity of horizontal reinforced sandy ground, *Jl of Geotextile & Geomembranes*, 9(I)51-82.
- Loukidis, D. (2006). Advanced Constitutive Modeling of Sands and Applications to Foundation Engineering, PhD Thesis, Purdue University, USA.

- Martin, C.M. (2004). Analysis of Bearing Capacity of Soil, ABC Software.
- Michalowski, R.L. and Shi, L. (2003). Deformation Patterns of Reinforced Foundation Sand at Failure, J of Geotechnical & Geoenvironmental Eng, ASCE ,129(6)439-449.
- Prandtl, L. (1920). Uber die Harte Plasticsher Korper, Nachr. Kgl.Ges.Wiss. Gottington, Math, phys. K.I.
- Terzaghi,K. (1966) Theoritical Soil Mechanics., Wiley, New York. USA.
- Tejas, G.M., Gananamanickam, E.P, Saldana, C. and Chandersekar, S. (2009). Proceedings of 6th Intl Conference on Micromechanics of Granular Media , 263-266.
- White D.J., Take W. A. and Bolton, M.D. (2003). Geotechnique , 53(7),619-631
- White D.J., Randolph, M. and Thomson, B. (2005). JI of Physical Modelling in Geotechnics , 3,01-12.
- Sadek, S., Iskander, M.G. and Liu, J. (2003). JI of Computing in Civil Eng,ASCE, 17(2),88-96
- Salgado,R. The engineering of foundations, McGrawHill, USA.
- Sutton, M.A., Orteu, J.J. and Schreier, H. W.,(2009). Image correlation for shape, motion and deformation measurements, Springer, New York, USA.
- Yamamoto, K. and Kusuda, K. (2001). Failure mechanisms & bearing capacities of reinforced foundations, J of Geotextile & Geomembranes, 19(20021)127-162.

NOTATIONS

B	width of footing	U	Horizontal displacement in mm
D	depth of footing	V	Vertical displacement in mm
z	depth	E_{xx}	Horizontal Lagrange Strain
x	Horizontal position	E_{yy}	Vertical Lagrange strain
y	Vertical position	E_{xy}	Shear strain Lagrange
u	Horizontal displacement in pixels	E_{vol}	Volumetric strain
v	Vertical displacement in pixels	kPa	Kilopascals.

Numerical Modelling, Design, and Construction of a Geotextile-Reinforced Soil-Metal Buried Structure (GRS) under Deep Fills in Challenging Soil Conditions

Meckkey El-Sharnouby, Ph.D., P.Eng.¹; Dave Worsley, A.Sc.T.²; Phil Carroll, P.Eng.³; and Calvin D. VanBuskirk, P.Eng., P.Geo⁴

¹Atlantic Industries Limited, 395 Waydom Dr., ON, Canada N0B 1E0. E-mail: melsharnouby@ail.ca

²Atlantic Industries Limited, 395 Waydom Dr., ON, Canada N0B 1E0. E-mail: dworsley@ail.ca

³Atlantic Industries Limited, 395 Waydom Dr., ON, Canada N0B 1E0. E-mail: pcarroll@ail.ca

⁴Terratech Consulting Limited, P.O. Box 201, Salmon Arm, BC. E-mail: calvinvb@shaw.ca

Abstract

This paper presents a case history of design and construction of a geotextile reinforced soil-metal (GRS) 2040 mm diameter structural plate culvert under a 42 m high embankment at a mine in South America. The geotechnical data indicated that the underlying SAPROLITE and laterite soils were very soft with predicted consolidation settlement under the conduit and embankment of up to 3m. Due to the complexity of the problem, two-dimensional non-linear finite element analysis was employed to analyze the soil-structure and soil-geotextile interaction. Results showed that the composite system considerably improved the performance of the culvert under the considered loading conditions. The structure was constructed in 2015 to 2016 and it is reported that the structure is performing satisfactory. The composite GRS-culvert system provided a viable solution for challenging site conditions.

INTRODUCTION

Traditional buried metal structure systems comprise of corrugated metal structures surrounded by an engineered backfill envelope, commonly a well graded granular material. Depending on the corrugation profile, corrugated metal structures are classified as shallow, deep corrugated, or deeper corrugated (CAN/CSA-S6-14). Shallow corrugated plate structures first came into commercial use in the 1930s. Early structural capacity tests were conducted to quantify compressive strength of conduits and bolted plate seam strengths. For most of the 20th century, empirical design methods were used, such as AISI (1993) method, a working stress method and AASHTO (2014), an LFRD method. These methods focused on keeping the conduit in ring compression by having minimum height of cover limits and putting limits on conduit flexibility for the purposes of handling and backfilling. Various design methods were developed in the 1960s to allow shallow corrugated structures to be used in long span structures and/or under deep covers (Abdel-Sayed et al. 1993). Only in the last two or three decades, have rigorous design methods been used for design of shallow corrugated plate. This allowed researchers to develop design code equations, and practitioners to analyze applications that are more complex, such as, conduits under deep cover, induced positive arching, potential for significant settlement, and pull-apart along the barrel direction – similar to the application being discussed in this paper.

A geotextile-reinforced soil (GRS) metal culvert is a buried metal arch with backfill reinforced with geotextile for part or all of the backfill height, as shown in Figure 1. In 2002, Terratech Consulting Limited began investigating the benefit of incorporating geotextile-reinforced soil (GRS), which involves tightly spaced geotextile layers placed in the compacted backfill zone around the corrugated metal arch. This work included: removing the conventional footings; and incorporating deadman anchors to connect the metal arch to the GRS. Construction of the first GRS Arch was complete in 2005, and to date nearly hundreds of these structures have been constructed in Canada with spans ranging from 1.2 to 14 m. Four notable benefits of the GRS design are: (1) Removal of large rigid footing components for open bottom structures; (2) ability to use less than optimum backfill materials; (3) effective elimination of piping potential (soil loss) due to the encapsulation of the backfill within geotextile; (4) overall increase in strength and stiffness of the fill surrounding the metal arch.

This paper presents a case history of design, construction and monitoring of a geotextile-reinforced soil (GRS) 2040 mm diameter structural plate culvert approximately 204 m long and under a 42 m high embankment. This embankment, which fills an existing incised ravine, would eventually serve as road crossing for mine haul trucks. The site is located at a gold ore and processing plant located in northeastern Suriname near the border with French Guiana in South America, as shown in Figure 2.

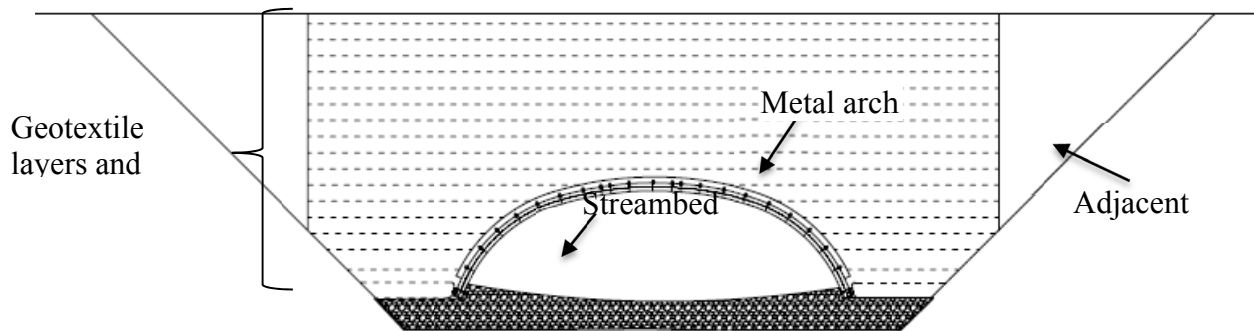


Figure 1. Typical schematic of GRS metal arch system.

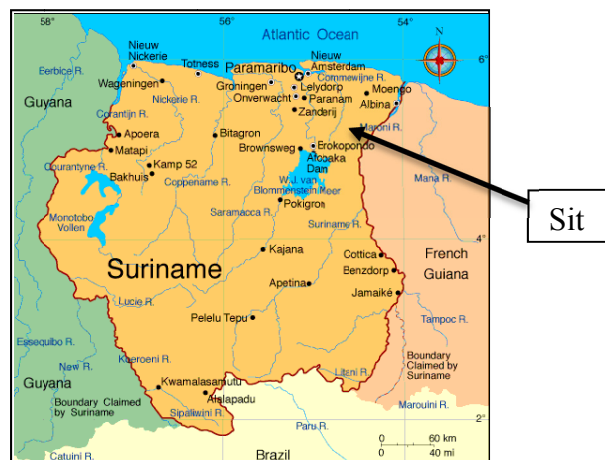


Figure 2. Site location.

SITE CONDITIONS

A geotechnical investigation revealed that subsurface conditions consisted of deep layers of saprolite/laterite overlaying sap rock and bedrock, extending up to 100m below the ground surface. Field samples showed the saprolite had 0%-30% sand and 100%-70% clay and silt, average plastic limit of 41% and liquid limit of 52%. The saprolite plots below the A-line on the plasticity chart, and was classified as silt (ML) according to USCS. The effective friction angle and cohesion from triaxial testing was 29.2 degrees and 12.9 kPa, respectively. The estimated consolidation settlement under the mid-section of the proposed pipe and embankment was up to 3 m.

PROPERTIES OF STRUCTURE AND GEOTEXTILE

The structure is a round structural plate culvert with an inside diameter of 2040 mm and corrugation profile of 200 mm x 55 mm, as shown in Figure 3, and is known commercially as MP200. The culvert thickness varied from 5 mm to 8 mm along the 204 m culvert length, and had a yield strength of 355 MPa. Section properties of the structure are provided in Table 1.

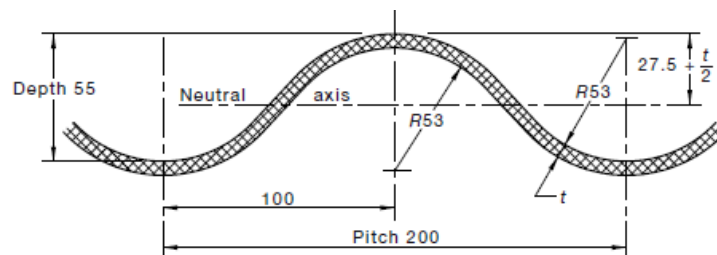


Figure 3. Corrugation profile, after AS/NZS 2041.6-2010.

Table 1. Section properties of culvert at mid-section (after AS/NZS 2041.6-2010).

Specified thickness (mm)	Area of section (mm ² /mm)	Elastic section modulus (mm ³ /mm)	Moment of inertia (mm ⁴ /mm)	Plastic section modulus (mm ³ /mm)
8	9.49	116.86	3681	169.15

DESIGN

Key design considerations of this structure included, settlement of up to 3m in the foundation soils, backfill height of up to 42 m, differential settlement along the conduit, and unconventional backfill material (saprolite) at both ends of the pipe. To satisfy all design requirements with acceptable safety margins, a geotextile-reinforced soil metal conduit (GRS conduit) system was adopted for this crossing.

Preliminary analysis showed that the geotextile does not contribute to the load sharing mechanism until the conduit wall has yielded. It was found that the geotextile need to be strained sufficiently to contribute to the load sharing mechanism. An effective solution was to place a layer of uncompacted backfill above the backfill, as shown in Figures 4 and 5. This encouraged positive arching and allowed the geotextile to be “activated” and contribute to the load sharing mechanism. Additionally, to reduce the potential of differential settlement of the backfill on both

sides of conduit, geotextile layers were placed below the culvert. The mechanical properties of the geotextile used are shown in Table 2.

Backfill along most of the culvert consisted of poorly graded sand with gravel and silt mixtures, classified as SP-SM (ASTM D2487-11, 2011). The effective friction angle from triaxial testing was 42.6 degrees. It had a maximum dry density of 2182 kg/m³ with moisture content of 7.3%. SAPROLITE from nearby stockpile was used as backfill on along 10m of the pipe on either side of inlet and outlet, and in the area beyond the backfill zone. It had a maximum dry density of 1616 kg/m³ with optimum moisture of 17.8%.

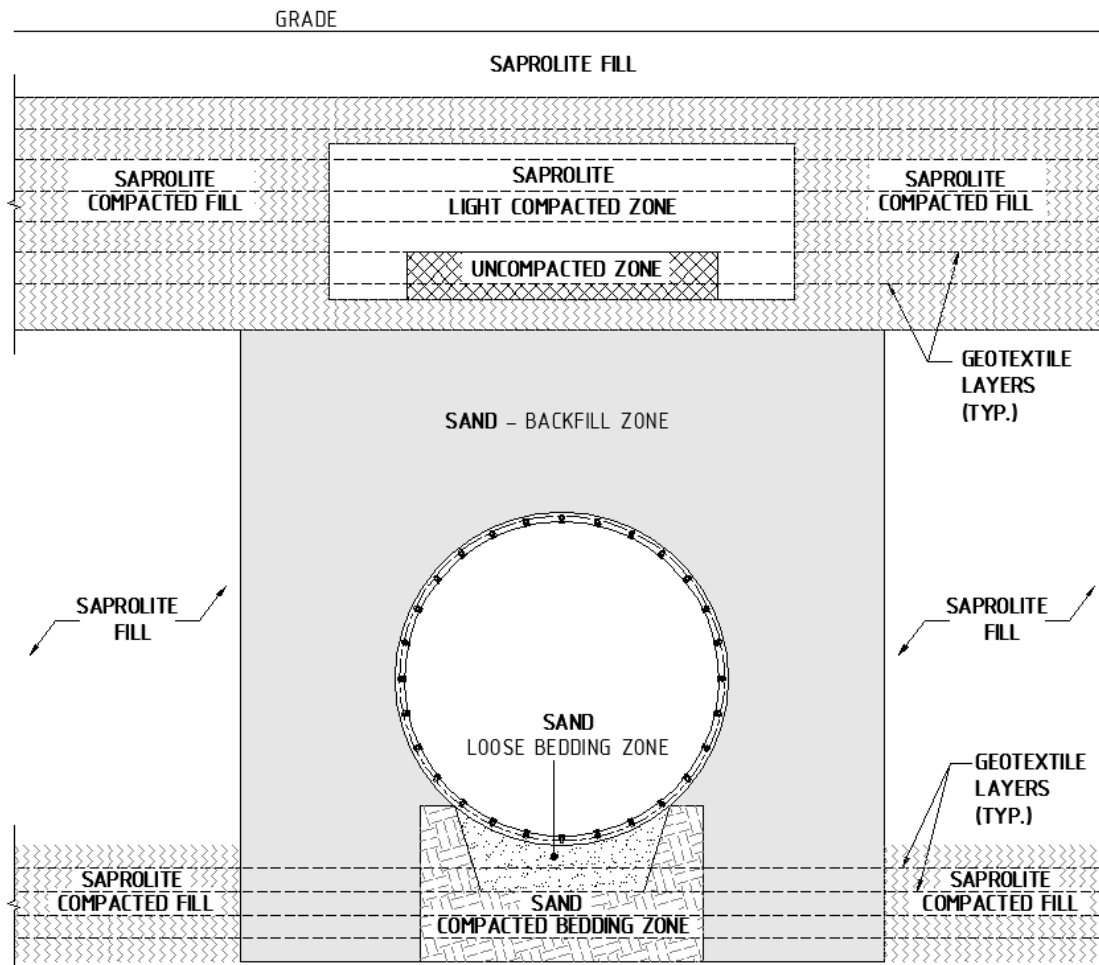


Figure 4. Cross section view with backfill zones at mid-section of culvert.

Table 2. Mechanical properties of geotextile.

Geotextile location	Tensile strength	Long term design strength
Above culvert	300.4 kN/m	148.9 kN/m
Below culvert	38.5 kN/m	8.0 kN/m

AASHTO (2014) LRFD method. AASHTO (2014) is widely used as design code for structural plate design. AASHTO (2014) requires that conduits be investigated at the strength limit for seam strength, buckling strength and wall area, and flexibility checks for the purpose of handling

and backfilling. In lieu of flexibility checks, the CAN/CSA-S6-14 requires that a flexural check during construction be done. As can be seen, these code design requirements imply that explicit flexural checks are not required. In addition, these codes do not provide consideration for high settlement that could result in additional, post-construction, compression stresses and the possibility of flexural loads. Furthermore, the codes do not provide guidance on soil stiffness values for unconventional backfill conditions.

Numerical analysis. Due to the complexity of the problem, two-dimensional non-linear finite element analysis was employed to analyze the soil-structure-geotextile interaction. The hardening soil model was used for backfill and side fill soils. The parameters were estimated based on triaxial testing of the sand and SAPROLITE, as shown in Table 3.

The conduit was modelled using 2D plate elements that in principle allow three degrees of freedom at each node, axial and vertical deformation, and rotation. The interface between the conduit and the surrounding soil was defined through interface elements that were assigned properties relative to the surrounding soil. The backfill was allowed to separate and re-attach to the conduit throughout the analysis. Multiple analyses were conducted to determine possible bounds of the problem including consideration of the anticipated 3 m settlement of the in-situ soil. A typical mesh defining the various model components is shown in Figure 5.

Table 3. Parameters of backfill and side fill soils.

Material name	Classification	Unit weight, kN/m^3	Friction angle, degrees	Cohesion, kPa	Reference stiffness, MPa	Stiffness exponent
Sand with gravel and silt mixtures	SP-SM	21.4	42.6	0	22.5	0.9
Saprolite	ML	19	29.2	12.9	6	1.0

Figures 6 through 11 show the finite element analysis results for the conventional culvert and for the GRS culvert. Figure 6 shows that the conventional culvert is experiencing negative arching, however, Figure 7 shows the GRS culvert has positive arching, i.e. load above culvert is being distributed to adjacent soils. Figures 8 and 9 shows that the GRS-culvert system resulted in 32% reduction in bending moment. Similarly, Figures 10 and 11 show the GRS culvert experienced 12% less in thrust.

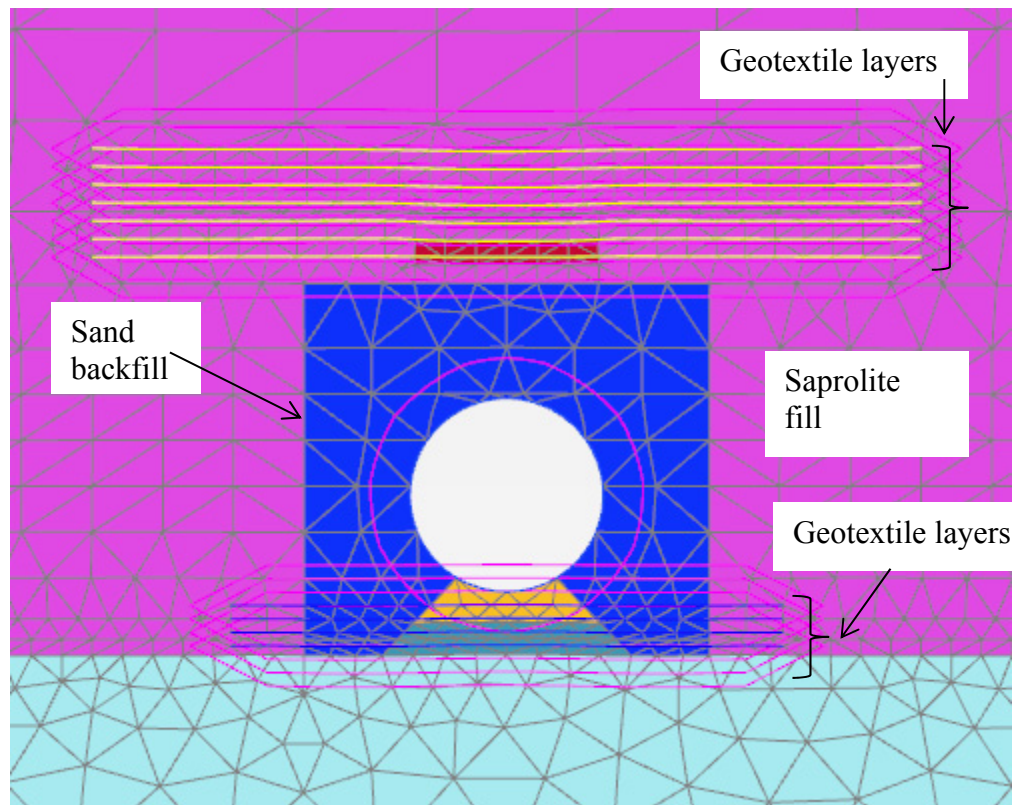


Figure 5. Typical finite element mesh-GRS-culvert.

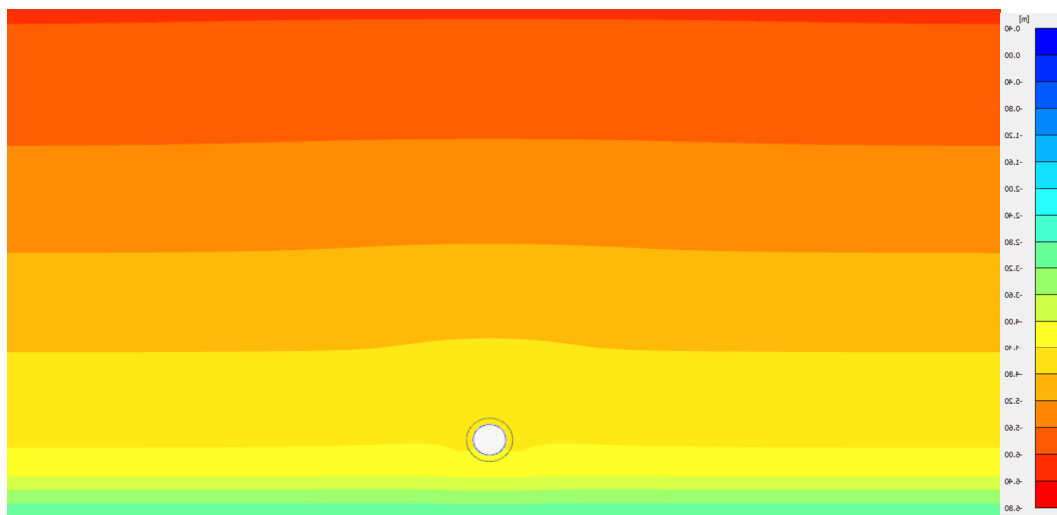


Figure 6. Conventional culvert - deformation contours under 42 m backfill height .

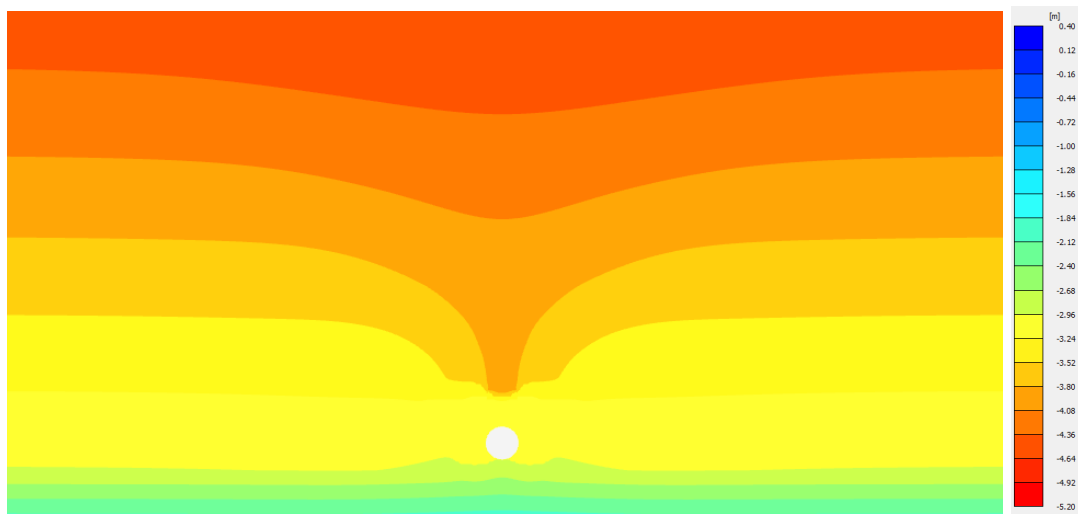


Figure 7. GRS Culvert - Deformation contours under 42 m backfill height.

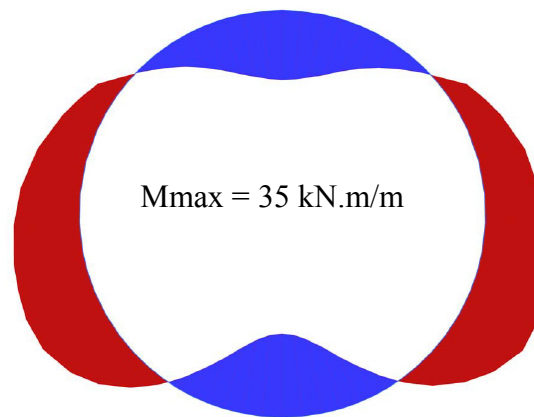


Figure 8. Conventional Culvert - Bending moment diagram under 42 m backfill.

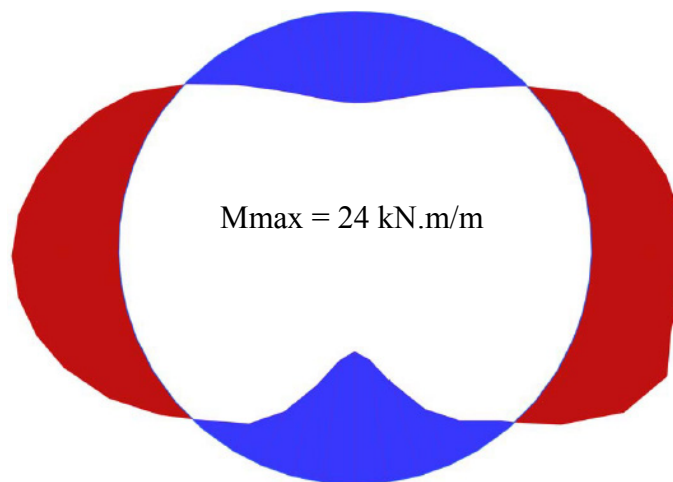


Figure 9. GRS Culvert - Bending moment diagram under 42 m backfill height.

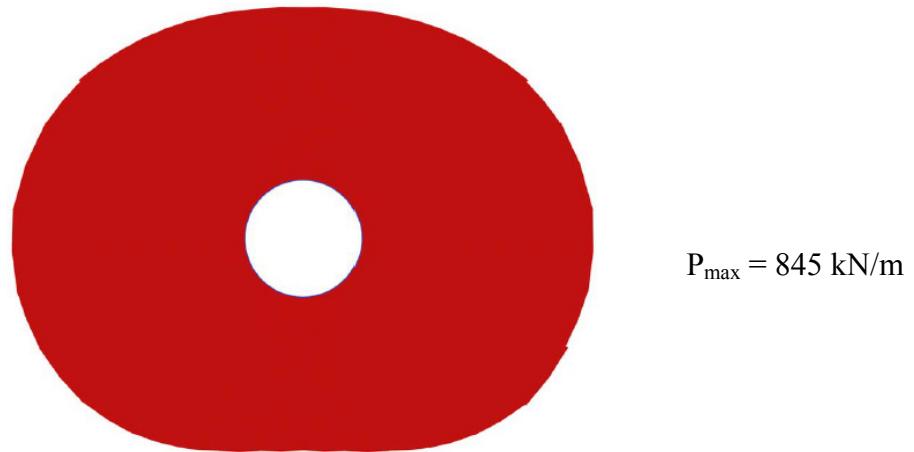


Figure 10. Conventional Culvert - Thrust diagram under 42 m backfill height.

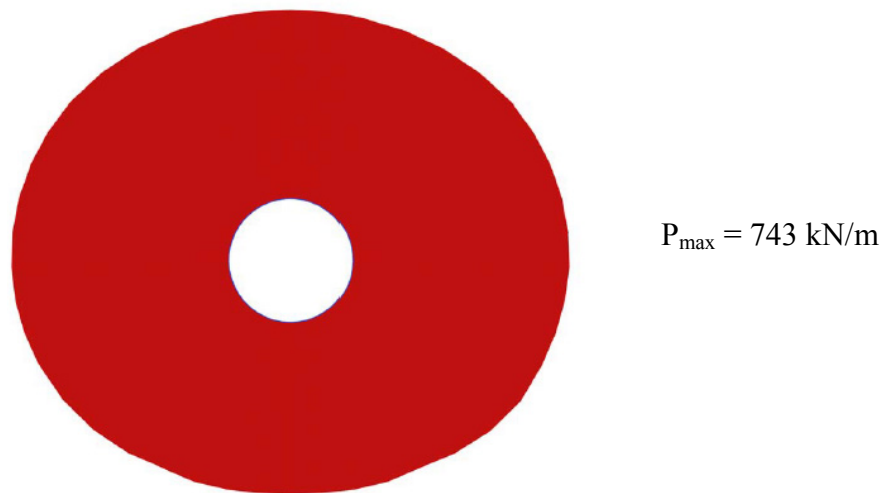


Figure 11. GRS Culvert - Thrust diagram under 42 m backfill height.

Table 4 shows that the conventional culvert satisfies all AASHTO (2014) requirements. However, the FEA analysis shows that the conventional culvert has developed a plastic hinge at working loads. The results from GRS culvert FEA analysis show a reduction in the stress on the structure to 75% yield, revealing the advantage of reinforcing the backfill with “activated” geotextile layers. Both the AASHTO and CHBDC S6-14 codes require a combined axial and bending moment check for deep corrugated structures at the ultimate limit state, the value of which must be less than 1.0. Applying this same check to the conventional culvert shows it is 1.25 whereas the GRS culvert is 0.85. This shows that in this case, a combined moment/axial check, similar to that for deep-corrugated structures is necessary and should not be waived.

Table 4. Internal forces and design according to AASHTO and additional flexural criterion.

8mm thickness; 45 m backfill height; Fy = 300 MPa	AASHTO	FEA-no geotextile	FEA-GRS-culvert
Max. thrust, kN/m	810	845	745
Bending moment, kN.m/m	-	34	24
Buckling-Wall area-Seam (AASHTO 2014 section 12.7)	pass	pass	pass
Combine moment/axial at working loads	-	117% Fy> does not pass	90% Fy-pass
Combine moment/axial (CAN/CSA- 06-14 section 7.6.3.3.2)	-	1.25	0.85-pass

CONSTRUCTION AND STRUCTURE MONITORING

Construction was originally planned to be completed during the dry season, but due to project delays, construction extended into the rainy season. Special consideration was given to the saprolite fill as the rain causes the compacted moisture content to be higher than the optimum moisture content. On a few occasions, the contractors removed and recompacted saprolite layers.

As mentioned above, the saprolite was used as side fill along most of the pipe and backfill at both ends of the pipe. Figure 12 shows the saprolite as side fill. As can be seen, there were issues at some locations to maintain a near vertical slope of the saprolite. Consequently, saprolite side fill was graded flatter as can be seen in Figure 13.

To qualitatively monitor the culvert's state of stress during the backfill installation, the culvert cross-section shape was monitored at twenty stations along its length, as shown in Figure 14. Survey shots were taken by a total station at the spring line, crown and invert locations. At the time of writing this paper, survey data was only available to a cover height of 34 m.

Figure 15 shows measured and predicted change in rise at station 9 and 10. The change in rise is less than 1% of the nominal 2040 mm rise, which illustrates low stress in the conduit. Figure 15 also shows that the change in rise predicted by the FEA analysis is in relatively close agreement with field measured values.

Figure 16 shows the 2040 mm diameter culvert after it is fully backfilled and in service below the 42 m high embankment. Looking upstream from the outlet, the culvert is maintaining its cross-section upstream towards in the inlet. This indicates that the structure is performing satisfactory, as predicted by the finite element analysis.



Figure 12. View of site preparations and SAPROLITE side fill.



Figure 13. View of culvert, sand backfill and sloped saprolite.

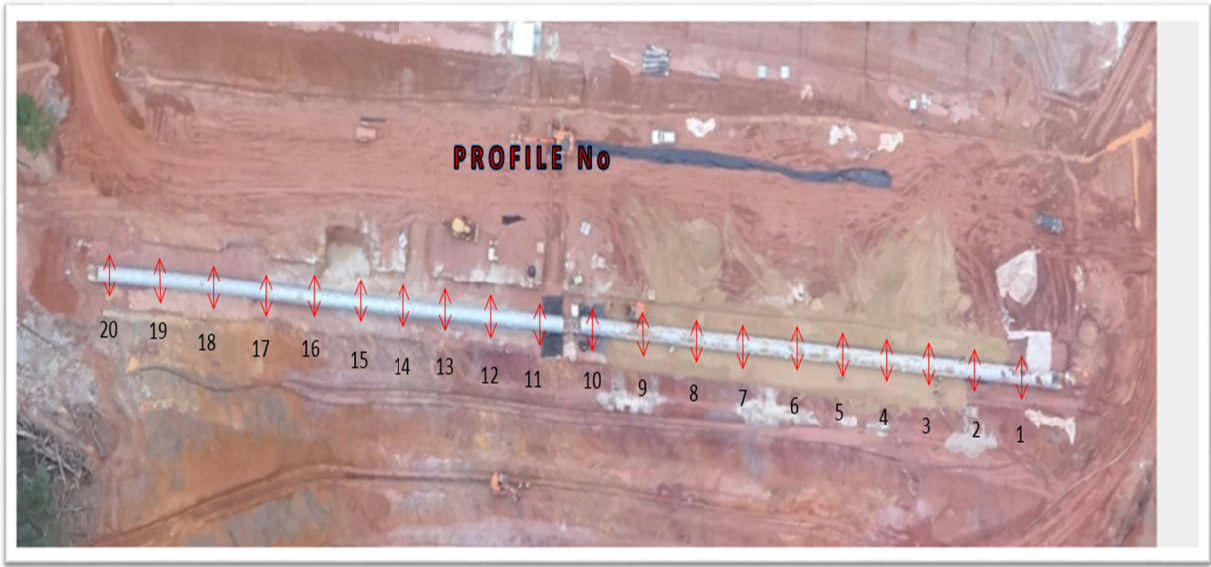


Figure 14. Photo showing locations of total stations.

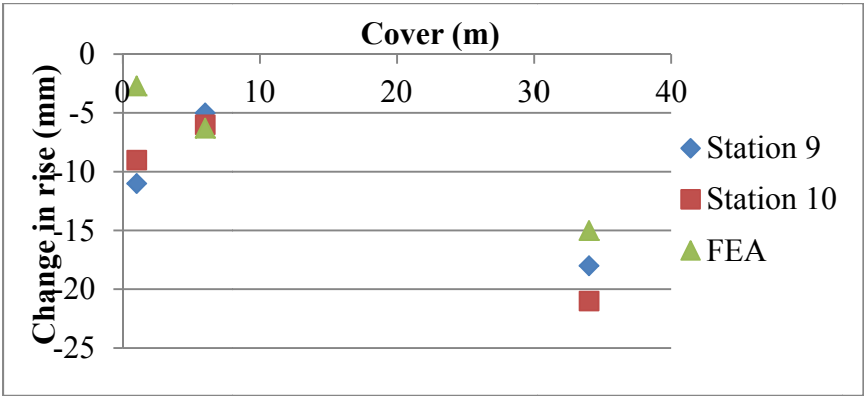


Figure 15. Measured and calculated change in rise at station 9 and 10.



Figure 16. Interior view of the in service culvert.

CONCLUSIONS

This paper presents a case history of design and construction of a geotextile reinforced soil-metal (GRS) 2040 mm diameter culvert under a 42 m high embankment. The in-situ soil conditions consisted of deep layers of saprolite and laterite which led to large predicted consolidation settlement. In addition, good quality backfill was scarce and saprolite was used to construct the embankment and for a significant portion of the backfill for the structure.

Due to complexity of the site conditions, consideration was given to plastic hinge failure mode which is not considered by AASHTO (2014). Finite element analysis showed that while the design passed by AASHTO (2014) method, plastic hinge would develop. To overcome design challenges, a composite geotextile reinforced soil-culvert system was used in this project. It is recommended that, for unconventional site conditions, structural plate should be checked for flexural capacity. For design, the combined axial and bending at ultimate limit state in AASHTO (2014) or CAN/CSA-S6-14 for deep corrugated structures can be used.

To date, the structure performance is satisfactorily. Analysis and construction show that the GRS-culvert system is a viable option in challenging site conditions.

REFERENCES

- AASHTO (Association of Highway and Transportation Officials). (2014). *AASHTO LRFD Bridge Design Specifications, Seventh Edition*. The American Association of State Highway and Transportation. Washinton, DC, USA.
- Abdel-Sayed, G., Bakht, B., and Jaeger, L. G. (1993). *Soil-steel bridges: design and construction*. McGraw-Hill Inc., New York
- AISI (1993). *Handbook of Steel Drainage and Highway Construction Products*. American Iron and Steel Institute. Washington, DC.
- ASTM D2487-11. (2011). *Standard Practice for Classification of Soils for Engineering Purposes (Unified Soil Classification System)*, ASTM International, West Conshohocken, PA, 2011, www.astm.org
- AS/NZS 2041.6:2010. (2010). *Buried Corrugated Metal Structures*. Australian/New Zealand Standard, Sydney, Australia.
- CAN/CSA-S6-14 (Canadian Highway Bridge Bridge Code) 2014. *Canadian Standard Association*. Mississauga, ON, Canada.

Protecting Buried HDPE Pipes Subjected to Ground Subsidence Using Geosynthetics

Min Zhou, Ph.D.¹; Fei Wang, Ph.D.²; and
Yan-Jun Du, Ph.D.³

¹Institute of Geotechnical Engineering, Southeast Univ., Nanjing 210096, China. E-mail: 230139499@seu.edu.cn

²Institute of Geotechnical Engineering, Southeast Univ., Nanjing 210096, China. E-mail: feiwangseu@gmail.com

³Institute of Geotechnical Engineering, Southeast Univ., Nanjing, Jiangsu, 210096, China. E-mail: duyanjun@seu.edu.cn

Abstract

High density polyethylene (HDPE) double-wall corrugated pipe is commonly used for drainage purpose. However, this type of pipe can be damaged by ground subsidence due to its relative low stiffness. In this study, physical model tests are conducted to investigate the effectiveness of geosynthetics to protect buried HDPE pipes subjected to ground subsidence. The tests are carried out in a custom-made test box with a dimension of 2 m in length, 2 m in width, and 1.5 m in height. Two model tests with the inclusion of the geotextile and the geogrid and one test without geosynthetics reinforcement are conducted. Test results demonstrate that both types of geosynthetics are effective to reinforce the HDPE pipes in the ground subsidence condition, in terms of reducing vertical displacement and circumferential strain of the pipes. The pipe protected by the geotextile performs better than that reinforced by the geogrid.

INTRODUCTION

Ground subsidence presents a challenge to the serviceability and stability of the pipelines, especially for those with low stiffness, for example, HDPE pipes. Failure of buried pipes could cause serious problems to the daily life. A road collapses and a 5 m diameter hole is formed in Hefei, China due to the buried HDPE pipe failure underneath the road which is caused by the tunneling. Twelve people were injured in this accident.

Geosynthetic reinforcement has been adopted as an effective approach to protect buried pipes from traffic loading, high thickness of soil cover and penetration of a rigid object in previous studies. Corey et al. (2014) place the geogrid layers above the steel-reinforced HDPE pipes to minimize the effect of the static loading from the soil surface on the pipes. They find that the surface settlement, pipe deflection and vertical stress at the pipe top reduced by 11%, 26% and 10% with inclusion of the geogrid reinforcement layer, respectively, compared to the unreinforced case. Bueno et al. (2005) propose a construction method called “Geovala” to reduce the vertical stresses on buried pipes by installing the geosynthetic reinforcement layers into the soil mass above the pipe. Palmeira et al. (2010) investigate the beneficial effects of different arrangements of geogrid layers around buried pipes in resisting penetrating loading, and they recommend the inverted U and wrapped-around reinforcements could be used in engineering practice. However, the investigations on the geosynthetic protection of buried pipes against the ground subsidence are very limited.

In this study, several series of model tests are conducted in a custom-made test box. Plates installed at the bottom of the box are moved downward to generate the ground subsidence. Two types of geosynthetics (i.e. geotextile and geogrid) are installed below the HDPE pipes to investigate its potential application in resisting the ground subsidence. Earth pressures, vertical displacements of the pipe, pipe strains, and settlement trough at the ground surface are measured during the downward moving of the bottom plates. The effects of the type of geosynthetic reinforcement layer on the above structural response of HDPE pipes are investigated.

TESTING INSTRUMENTATION AND MEASUREMENTS

Tested pipes and geosynthetics. Three HDPE double-wall corrugated pipes (labeled as P1, P2, and P3) with a nominal diameter of 200 mm and a length of 2 m are adopted in the model tests. The pipe stiffness is determined as 215 kPa using parallel plate loading test per ASTM D-2412-11. The woven geotextile and geogrid reinforcements are used to protect HDPE pipes from the ground subsidence. The ultimate tensile strength and tensile stiffness of the geotextile are 48 kN/m and 300 kN/m and those for the geogrid are 50 kN/m and 1700 kN/m, respectively. The geogrid has rectangular apertures of 25 mm by 33 mm.

Backfilling material. Yangtze River sand is used as the backfill material, and the uniformity coefficient and curvature coefficient of the sand are 2.86 and 0.94, respectively. Based on the Unified Soil Classification System (ASTM D2487 2011), the sand is classified as poorly graded sand (SP). The specific gravity of the sand is 2.65, and the minimum and maximum densities are 1.43 Mg/m³ and 1.74 Mg/m³, respectively.

Instrumentation. The model tests are conducted in a model box with a dimension of 2 m in width, 2 m in length, and 1.5 m in height, as shown in Figure 1. The side walls of the model box are made of 15-mm-thick polyethylene plates and reinforced by steel frames. Vaseline is placed on the wall of the model box to minimize the effect of the friction between the side wall and the backfill. The bottom of the box is built with eight movable plates, and each is 0.1 m thick, 0.25 m wide and 2 m long. The details of the model box can be found in Wang et al. (2015).

Custom-made settlement plates are used to measure the vertical displacement of the pipe and settlement of the soil surface. A square plate with side length of 50 mm and thickness of 5 mm is fixed on the both ends of a 10-mm-diameter rod, and the rod is enclosed in a PVC conduit to eliminate the soil friction. The settlement plate is made of plexiglass to minimize the effect of self-weight. Earth pressure cells in a range of 0 to 0.2 MPa are used to monitor the vertical stresses at the top of the pipe. Strain gauges in a range of 0 to 2% and an accuracy of 0.0001% are adopted in this study to measure the pipe strain during the test.

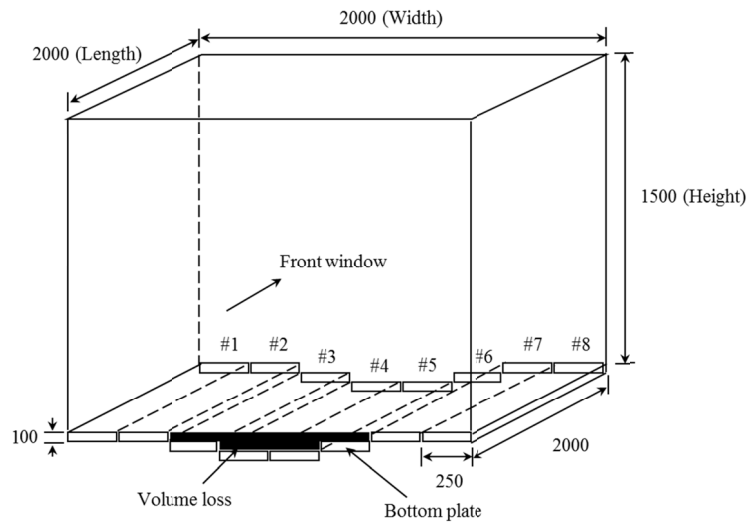


Figure 1. Schematic diagram of physical model box (unit: mm)

Model testing methodology. HDPE pipes are installed in the model box at a buried depth of 0.85 m from the backfill surface to the centerline of the pipe. Both ends of HDPE pipes are connected with the walls of the model box by custom-made fixing frames to simulate pipe joints. A geotextile layer is placed below the P1 pipe, and a geogrid layer is installed below the P2 pipe. The ends of geosynthetic reinforced layer are fixed at the wall of the model box as shown in Figure 2(a). For comparing and analyzing the influence of the geosynthetic reinforcement, the P3 pipe is not reinforced. Earth pressure cells are installed at the top of the pipe. Details of the test cases are listed in Table 1. The settlement plates are placed at the top of the pipe and the soil surface. The strain gauges are attached around the semi-circumference of the pipe and are spaced at 45° increment from the pipe top considering the bilateral symmetry relative to the vertical centerline of the pipe. Three testing profiles 1, 2 and 3 along the longitudinal direction of the pipe are instrumented, as shown in Figure 2(b). To ensure the uniformity of backfilling, the sand is backfilled using a sand pluviation device from a height of 0.7 m, and the sand density obtained is determined as 1.46 Mg/m³. A data acquisition system is connected with the earth pressure cells to record vertical stresses at a time interval of 2 seconds automatically.

The middle four bottom plates of the model box (labeled as #3, #4 #5 and #6) are lowered down step by step to simulate the land subsidence. Motion Movement pattern of the bottom plates is shown in Figure 3.

Table 1. Summary of test cases.

Case number	Pipe ID	Pipe diameter (mm)	Cumferential bending stiffness EI (kN·m ² /m)	Type of geosynthetic
1	P1	200	0.034	Geotextile
2	P2	200	0.034	Geogrid
3	P3	200	0.034	Non-reinforcement

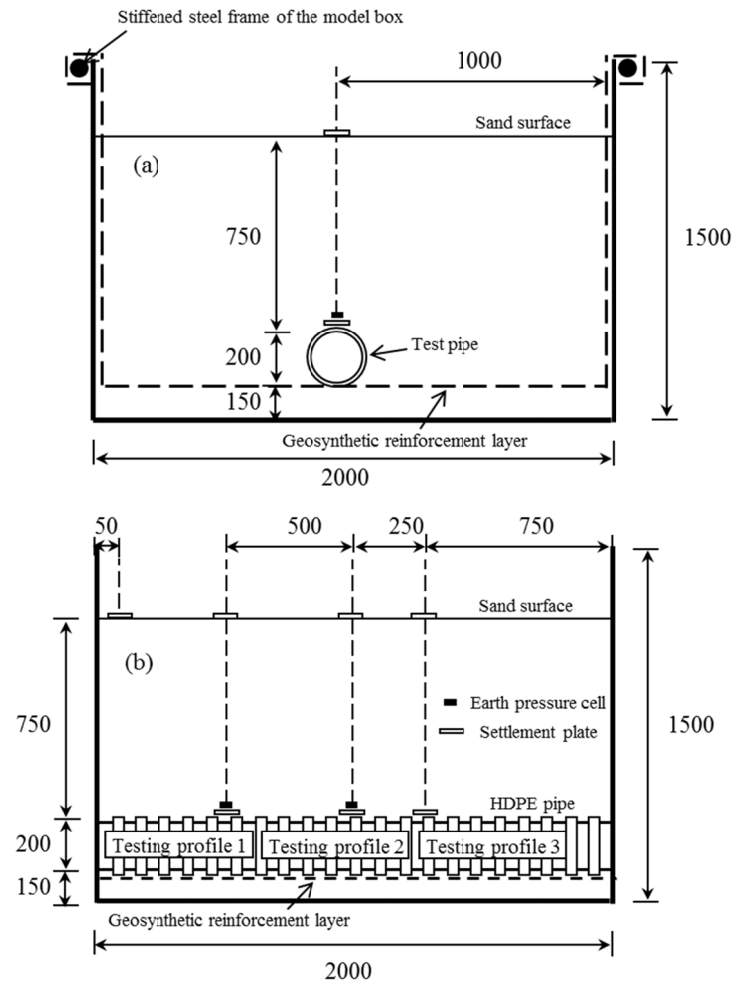


Figure 2. Schematic diagram of testing instrumentation: (a) cross-sectional view and (b) side view (unit: mm).

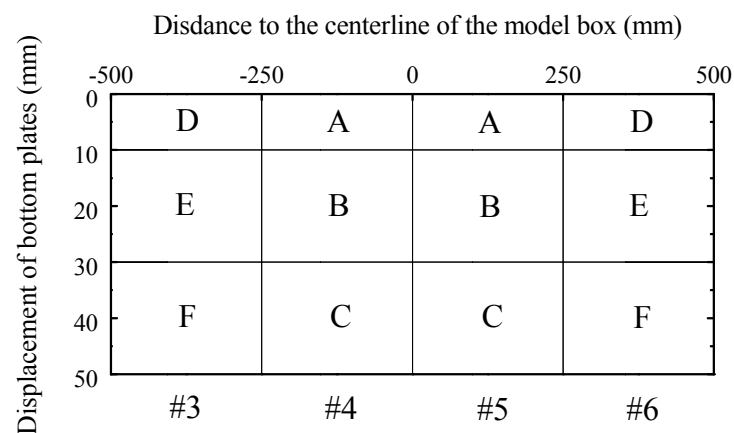


Figure 3. Motion pattern of the bottom plates of the model box (letters A to F represent the lowering sequence of bottom plates).

TEST RESULTS

Vertical displacement of tested pipes. Figure 4 shows the variation of the vertical displacement of HDPE pipes during the lowering of the bottom plates of the model box. It can be seen that during the model tests, the vertical displacements of the P3 pipe measured at the testing profiles 1, 2 and 3 are larger than those of the P1 and P2 pipes. For example, when the bottom plates #4 and #5 are lowered down to 50 mm for the third time (represented as C in Figure 4(a)), the vertical displacement of the P3 pipe at the testing profile 1 (i.e. 7.38 mm) are 12.3 and 10.5 times those of the P1 and P2 pipes (i.e. 0.6 mm and 0.7 mm), respectively. It is indicated that both geotextile and geogrid reinforcement layer are effective to reduce the vertical displacement of the HDPE pipe induced by ground subsidence.

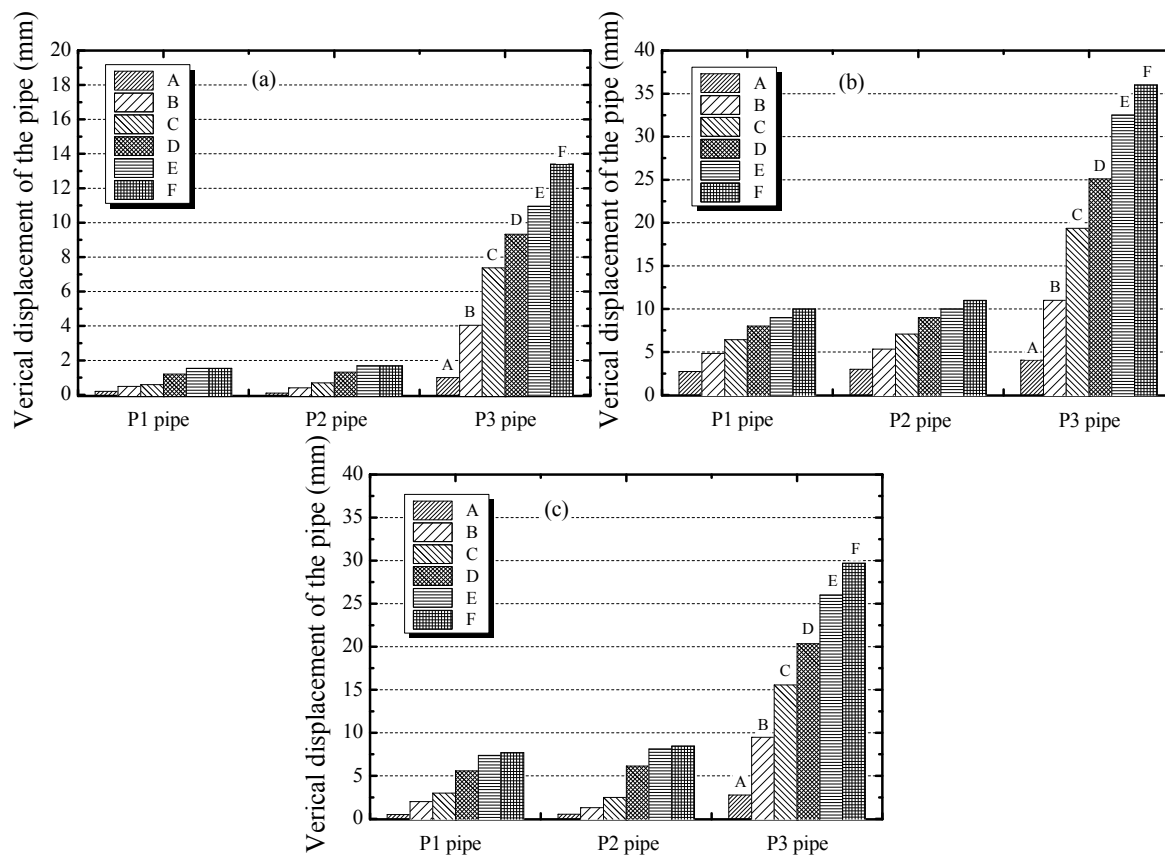


Figure 4. Variation in the vertical displacement of the pipes: (a) testing profile 1; (b) testing profile 2; (c) testing profile 3.

Earth pressure. Figure 5 shows that the earth pressures at the top of P1, P2 and P3 pipes are smaller than the geostatic stress of the backfill when the backfilling is completed, indicating the positive soil arching is triggered at the top of the pipe. When the bottom plates #4 and #5 are lowered for the first, second and third time, the earth pressures at the top of P1, P2 and P3 pipes for testing profile 1 increase by 50% to 520%, while those for testing profile 2 increase by 17% to 53%. When the bottom plates #3 and #6 are lowered for the fourth, fifth and sixth time, the earth pressures at the top of P1, P2 and P3 pipes for testing profile 1 increase by 3% to 8%, while those for testing profile 2 increase by 10% to 21%. The possible reason is that the existence of

the HDPE pipe restrains the soil settlement above the pipe. The positive soil arching triggered at the top of P1 pipe for testing profiles 1 and 2 is gradually counteracted by lowering the bottom plates #4 and #5 for the first, second and third time. As a consequence, negative soil arching is triggered with lowering of the bottom plates #3 and #6 for the fourth, fifth and sixth time. For P2 and P3 pipes, the negative soil arching is triggered at the top of the testing profile 1 and 2 from the beginning of lowering of the bottom plates during the entire test process.

The earth pressures measured at the testing profiles 1 and 2 of the P1 pipe are 6% to 45% smaller than those of the P3 pipe, indicating that the geotextile layer placed below the P1 pipe significantly reduces the negative soil arching. It is found that the earth pressures measured at the testing profiles 1 and 2 of the P2 pipe differ only 4% to 7% from those at the top of the P3 pipe. It is indicated that the negative soil arching triggered above the pipe reinforced by the geogrid layer is at the same level as that above the unreinforced pipe.

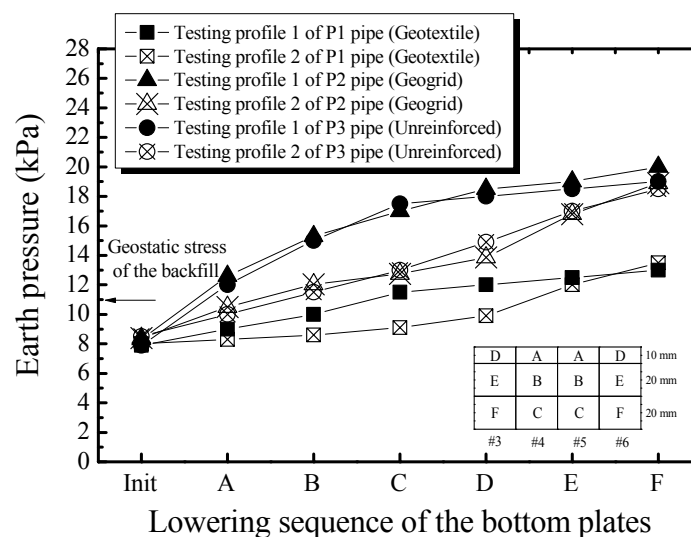


Figure 5. Variation in earth pressures (“Init” represents completion of backfilling).

Settlement trough at fill surface. Figure 6 shows the variation in the settlement trough at the fill surface above the P1, P2, and P3 pipes when the the bottom plates #4 and #5 are lowered down to 50 mm. It is seen that the vertical displacements of the fill surface measured above the P3 pipe are larger than those above the P1 pipe and P2 pipe. The lowest values of the fill surface settlement are obtained above the P1 pipe. It is illustrated that the geotextile layer placed below the pipe is most effective in terms of reducing the fill surface settlement.

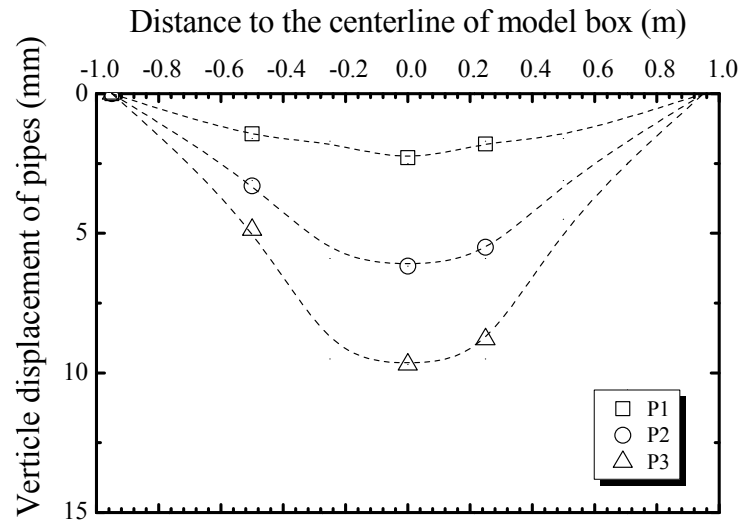


Figure 6. Variation in the settlement trough at the fill surface.

Pipe strain. Figure 7 shows that the variation in the circumferential strain of the P1, P2, and P3 pipes measured around the testing profile 2 when the bottom plates #4 and #5 are lowered down to 50 mm. It is seen that the circumferential strains of the P2 are smaller than those of the P3 pipe, and the lowest values are measured around the P1 pipe. For example, the circumferential valley strains of the P1 and P2 pipes measured at the angle of 135° from the pipe crown (i.e., -381 and -1138) are 79% and 40% smaller than that of the P3 pipe (i.e., -1891), respectively.

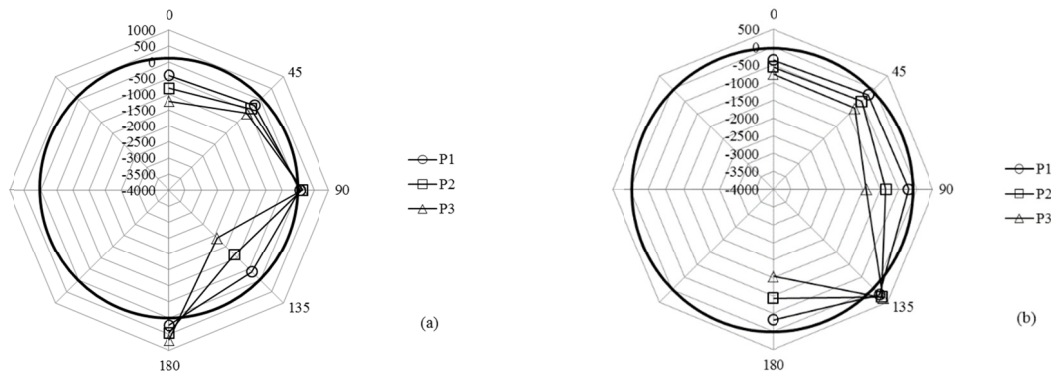


Figure 7. Variation in the circumferential strain of the pipes: (a) at valley; (b) at crest (in microstrain).

Dhar and Moore (2002) employ the crest (exterior) and valley (interior) strain to quantify bending moment of the profiled-wall pipe. In this study, because the diameter of the HDPE pipe used in the model tests is only 200 mm, the strain gauge is difficult to be attached at the interior of the pipe valley. Considering the small thickness (i.e., 2 mm) and low stiffness of the pipe wall at the valley, the magnitude of exterior and interior strains for the valley are assumed to be the same and this assumption will be validated in the further study. Therefore, the valley (exterior) strain is used to calculate the circumferential bending moment of the pipe wall as expressed by (Dhar and Moore, 2002):

$$M = EI\kappa \quad (1)$$

where EI is the circumferential bending stiffness ($\text{kN}\cdot\text{m}^2/\text{m}$); κ is the curvature of pipe wall (m^{-1}) determined by Eq. (2).

$$\kappa = \frac{\varepsilon_c - \varepsilon_v}{d} \quad (2)$$

where ε_c and ε_v are strains measured at the crest and the valley of the pipe wall, respectively; d is the corrugation depth of the pipe (m).

Figure 8 shows the variation in the circumferential bending moment of the P1, P2, and P3 pipes around the testing profile 2 when the the bottom plates #4 and #5 are lowered down to 50 mm. It is seen that the circumferential bending moment of the P1 and P2 pipes are smaller than those of the P3 pipe, especially at the spingline, haunch and invert of the pipe, indicating that the both geotextile and geogrid reinforcement layer are effective to reduce the local circumferential bending of the pipe caused by the differential settlement. However, it is worth noting that the lowest values of bending moment are monitored around the P1 pipe. It is indicative that the geotextile layer installed below the pipe is most effective to reduce the local circumferential bending of the pipe induced by ground subsidence.

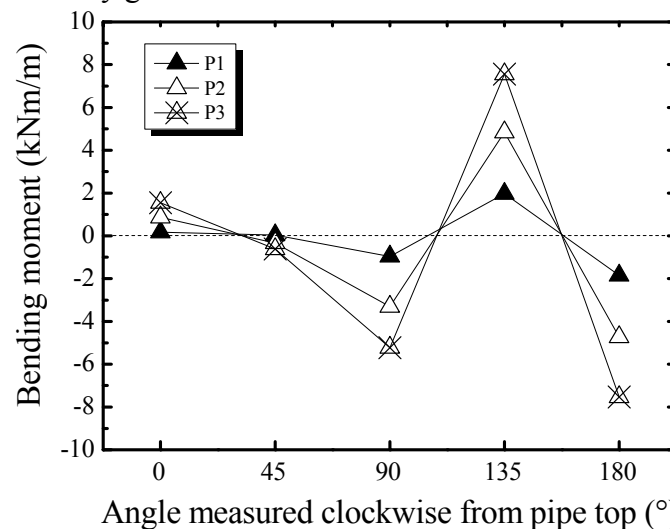


Figure 8. Variation in the circumferential bending moment of the pipes.

CONCLUSIONS

A series of the full-scale model tests are conducted to investigate the geosynthetic protection of HDPE double-wall corrugated pipes subjected to ground subsidence simulated by downward moving of bottom plates. Two HDPE pipes with nominal diameter of 200 mm reinforced by geotextile and geogrid, respectively, and a non-reinforced pipe are tested. The earth pressures, vertical displacement of the pipes, pipe strains and settlement trough of the ground surface are measured during the tests. Based on the results of this study, the following conclusions can be drawn:

1. The geotextile reinforcement layer placed below the pipe more effectively reduces the negative soil arching triggered at the pipe top, compared to the geogrid layer.
2. Both the geotextile and geogrid reinforcement layer are effective to reduce the vertical displacement of the HDPE pipe caused by the ground subsidence.

3. Both the geotextile and geogrid reinforcement layer are beneficial for relieving the local circumferential bending of the pipe. However, the pipe protected by the geotextile performs better than that reinforced by the geogrid.

ACKNOWLEDGEMENTS

The authors are grateful for the financial support of the National Natural Science Foundation of China (Grant No. 51108078, 51278100 and 41472258), Natural Science Foundation of Jiangsu Province (Grant No. BK20131294 and BK2012022), the Fundamental Research Funds for the Central Universities, Colleges and Universities in Jiangsu Province Plans to Graduate Research and Innovation (Grant No. KYLX_0144) and the Scientific Research Foundation of Graduate School of Southeast University (Grant No. YBJJ1632).

REFERENCES

- ASTM (American Society for Testing Material). (2011) *Standard test method for determination of external loading characteristics of plastic pipe by parallel-plate loading*, Standard ASTM-D2412-11. Annual Book of ASTM Standards, ASTM International, West Conshohocken, Pa.
- ASTM (American Society for Testing Material). (2011) *Standard practice for classification of soils for engineering purpose*, Standard ASTM-D2487-11 (2011). Annual Book of ASTM Standards, ASTM International, West Conshohocken, Pa.
- Bueno, B. S., Viana, P. M. F., & Zornberg, J. G. (2005). "A novel construction method for buried pipes using geosynthetics." *Proc., Geosynthetics research and development in Process*. ASCE.
- Corey, R., Han, J., Khatri, D. K., and Parsons, R. L. (2014). "Laboratory study on geosynthetic protection of buried steel-reinforced HDPE pipes from static loading." *Journal of Geotechnical and Geoenvironmental Engineering*, (140)6, 04014019-1-10.
- Dhar, A. S. & Moore, I. D. (2002). "Corrugated high density polyethylene pipe: Laboratory evaluation of two-dimensional analyses for limit states design." *Transportation Research Record: Journal of the Transportation Research Board*, (1814), 157–163.
- Palmeira, E. M., & Andrade, H. K. P. A. (2010). "Protection of buried pipes against accidental damage using geosynthetics." *Geosynthetics International*, 17(4), 228-241.
- Wang, F., Du, Y. J., & Yang, X. M. (2015). "Physical modeling on ground responses to tunneling in sand considering the existence of HDPE pipes." *ASTM Geotech. Test. J.*, 38(1), 85-97.

Numerical Study of the Effect of Pile Driving on the Position of a Neutral Plane

Arindam Dey, Ph.D.¹; and Michael C. Koch²

¹Assistant Professor, Geotechnical Engineering Division, Dept. of Civil Engineering, Indian Institute of Technology Guwahati, Assam 781039, India. E-mail: arindamdey@iitkgp.ac.in

²Rock Mechanics Laboratory, Dept. of Civil Engineering, Univ. of Hong Kong, Hong Kong. E-mail: michaelkoch044@gmail.com

Abstract

The position of the neutral plane is required to be implicitly known for the accurate determination of the magnitude and profile of negative skin friction. In contrary to the conventional analysis of bored piles, this study reports the effect of pile installation procedure on the final position of the neutral plane. Two types of initial conditions are considered, one where the pile driving is simulated (actual) and the other where the pile is considered in place (in situ). Finite element analysis exhibited that the neutral plane is at a greater depth in the ‘actual’ case relative to the ‘in situ’ case. Contours of effective stress near the pile tip implied higher soil stiffness near the pile base in the driven pile (actual) simulation, resulting in a lesser settlement and is postulated as the reason for the lowering of the neutral plane in the latter (in situ) case.

INTRODUCTION

Negative skin friction (NSF) is one of the most common problems encountered in piling engineering, and generally occurs when a pile is installed through a layer of soft consolidating clay. Such consolidation may occur due to placement of a fill or construction of a building. As the consolidation progresses, the adjacent surrounding soil settles to a larger extent relative to the pile and induces a “drag load” towards the direction of gravity. This downward drag load on the pile is termed as NSF.

One of the first experimental studies to understand NSF on a field scale was carried out by Fellenius (1972). Observations were made over a period of 43 months on two piles driven through 40m of soft clay. After 5 months, an increase of 40 tons in the axial load was reported. Fellenius (1984) highlighted the importance of ‘drag down’ on the settlement caused due to NSF. Indraratna et al. (1992) have confirmed the existence of the neutral plane (plane conforming to the zero shear stress at a particular depth of the pile) and shown the possibility of using pullout tests for evaluation of NSF. A few centrifuge studies by Leung *et al.* (2004) have helped to understand the effect of the actual condition of pile loading on the development of drag load.

A major portion of the research that exists about NSF is, however, numerical in nature. The effect of different parameters on NSF, such as pile-group effect (Lee et al. 2001), interface friction coefficient (Jeong et al. 2004), and interface model behaviour (Cao et al. 2014) have been studied. However, all of these studies have used the hypothetical assumption of “wish the pile in place” (final position of pile modelled without actually considering the actual process of pile installation). The stress changes due to the pile installation procedure aren’t accounted for in the conventional numerical simulations. This assumption is true to some extent for bored piles, but may not be valid in the case of driven piles. For Finite Element simulation of pile driving has been carried out for drained cases (Tolooiyan and Gavin 2011; Ekanayke et al. 2013) as well as undrained cases (Yi et al. 2012). The driving procedure is expected to displace the soil radially, thereby altering the stress field around the pile. Hence, starting a simulation by generating initial stresses when the pile is already in place in the soil for such cases is questionable.

The main focus of the present study is to initially simulate the driving process of a pile and subsequently consider the development of NSF. It is based on a field case history carried out by Indraratna et al. (1992) where piles were driven into soft Bangkok clay. The analysis is divided into two parts as shown in Figure 1. In the first part, the actual pile driving is executed, and in the second part, the conventional (wished in place) Finite Element modelling technique is simulated. The fill load is applied and NSF is generated by permitting consolidation. Comparisons are made between the results of the two modelling procedures and the differences are highlighted. The emphasis is to attempt and determine the parameters responsible for the observed changes and provide a plausible explanation for the same.

PROBLEM STATEMENT

The benchmark problem comprises driving an uncoated and a bitumen-coated pile into Bangkok soft clay followed by the placement of a 2 m fill to induce NSF (Indraratna et al. 1992). Prior to placing of the embankment, excess pore pressures generated due to pile driving were measured at regular intervals. The details of the benchmark problem are given as follows:

Site Characteristics. The test site was located 10 km east of Bangkok city. The subsoil comprises a thick deposit of marine clay underlying a stiff pre-consolidated layer of weathered clay. The consolidation of the soft clay is the main reason for the development of NSF and is characterised by high natural water content (up to 95%) with a plastic limit and liquid limit of 25-40% and 70-100%, respectively. The soft clay layer was underlain by stiff clay which was further underlain by a sandy stratum. Standard penetration tests (SPT) and pressuremeter tests were conducted at the site. Undisturbed samples were obtained for laboratory testing. Dutch cone (DC) and field vane shear tests were performed in the field to obtain the undrained shear strength (s_u). The lab samples were subjected to direct shear and K_0 consolidated undrained triaxial tests. Based on the initial stress conditions at the test site (prior to pile installation), the overlying clay deposits were described as normally consolidated or lightly overconsolidated materials. The

distribution of vertical and horizontal effective stress confirmed K_0 values in the range 0.60-0.75, which are the characteristics of the Bangkok subsoils.

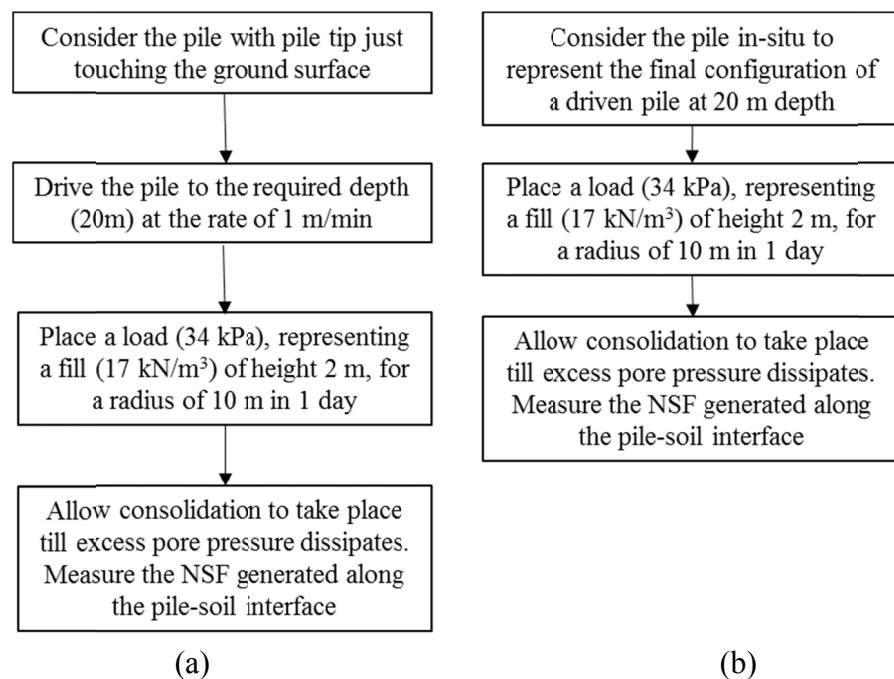


Figure 1. Problem definition for (a) actual (pile driving) case and (b) conventional in-place case (pile is considered in situ).

Pile Driving Procedure in the Field. The two hollow test piles were of the prestressed, precast, and spun concrete type, of which the outside and the inside diameters were 0.4 and 0.25 m, respectively. One was uncoated, while the other was coated with bitumen up to a depth of 25 m. Each instrumented test pile was divided into six segments, five of which were 4 m in length, with the remaining upper section being 6 m long. Load cells were placed at the pile tip as well as at the connection joints of the segments. The variations of pore pressure on the surface of the pile were determined with a closed hydraulic piezometer installed at each load cell, except at the pile tip. They were installed 0.5 and 1 m away from the centre of the pile. Both the piles were driven with the aid of jacking at the rate of 1 m/min. Initially, the first two pile segments were connected to form a unit 8-m-long. This unit was driven till a depth of 8 m and left for eight to nine days. A pullout test was then conducted. Immediately after the pullout test, the next 4 m segment was connected to make the unit 12-m-long and driving was carried out to a depth of 12 m. The pile was again left for eight to nine days and once again the pullout test was conducted. This procedure was continued to a depth of 20 m. The pile was then driven to a final depth of 25 m with a pile length of 2 m above the ground surface. An embankment 24 m x 14 m with a side slope of 2H:1V was subsequently constructed 2 m above the test area. This embankment provided the excess load for negative skin friction. Regular monitoring was performed and the observations were then taken for the subsequent nine months.

FINITE ELEMENT MODELING

The simulation of pile penetration into a soft soil is a large strain contact problem which involves many intricacies. Due to large displacements, it is essential to consider geometric nonlinearity (Bathe 1996). A material law capable of modelling the hardening and softening behaviour of soils is also necessary to accurately model this problem. The Modified Cam Clay model (Schofield and Wroth 1968) is one such constitutive model that can efficiently represent the non-linear response of soil (material nonlinearity). The Updated Lagrangian Formulation (Bathe 1996) was used in the Finite Element package ABAQUS for modelling the pile driving process.

Determination of Initial Void Ratio for Constitutive Model Parameters. The initial void ratio (e_{init}) is an extremely important component of any analysis. In the present analysis, since e_{init} was not directly given, based on the known critical state parameters, the same was back-analyzed from the field undrained shear strength data from Dutch Cone (DC) and Field Vane (FV) tests. The average e_{init} for each layer is shown in Table 1.

Material Properties. The parameters essential for modeling are summarized in Table 2. To completely define the yield surface for the critical state plasticity model, it is essential to calculate the pre-consolidation pressure p'_c . It was determined from the OCR data available from the field study at the mid depth of every layer and entered. The thin tube at the left boundary is rigid. The properties of the impermeable pile are as follows: Young's Modulus $E = 30 \times 10^6$ kN/m², Diameter $D = 0.4$ m, Poisson's ratio $\nu' = 0.33$, and Unit weight $\gamma = 15$ kN/m³.

Geometry Characteristics. An axisymmetric 2D model was used to simulate the penetration of a 20 m long pile. The basic geometry consisted of a rectangular domain. A depth of 40 m (double the length of the pile) was selected for the domain while its radius was kept at 30 m (Figure 2). The field embankment was represented by an equivalent load of radius 10 m. The 30 m radius of the domain was found to have negligible effect on the stresses generated beneath the equivalent embankment.

Placement of a Narrow Tube at Left Edge. An innovative solution has been used in the present pile driving problems, where a narrow rigid tube (~ 1 mm) is placed at the axis of symmetry (Yi et al. 2012). The interaction between the rigid tube and the soil was kept frictionless. A similar rigid, frictionless tube of 1 mm radius was considered in the FE analysis. The placement of this tube had no impact on the generation of initial stresses, permitted the radial flow of the soil away from symmetry axis and prevented the penetration of soil to the left of the axis of symmetry. The tip of the pile is also shifted 1 mm to the right as shown in Figure 2.

Table 1. Determination of e_{init} .

Layer	Depth (m)	s_u (t/m ²)	e_{cs}	λ	M	e_{init}	Average e_{init}
Weathered Clay	1.000	2.357	1.667	0.182	1.050	1.394	1.316
	2.000	5.557	1.667	0.182	1.050	1.238	
	4.000	0.902	3.052	0.514	0.970	2.733	
Soft Clay 1	6.000	0.975	3.052	0.514	0.970	2.693	2.667
	8.000	1.227	3.052	0.514	0.970	2.575	
	10.000	1.434	2.085	0.323	0.980	1.738	
Soft Clay 2	12.000	2.085	2.085	0.323	0.980	1.617	1.588
	14.000	2.180	2.085	0.323	0.980	1.603	
	16.000	2.898	2.085	0.323	0.980	1.511	
	18.000	3.282	2.085	0.323	0.980	1.471	
	20.000	2.867	1.199	0.116	0.900	0.984	
Medium Stiff Clay	22.000	3.718	1.199	0.116	0.900	0.954	0.969
	24.000	4.702	1.199	0.116	0.900	0.927	
Stiff Clay + Sand	26.000	25.268	1.199	0.116	0.900	0.732	0.829

Discretization. The Surface to Surface scheme (Wriggers 2006) was used for discretization of the continuum for contact in the model such that the pile surface was considered the master surface and the soil surface was considered the slave surface. The contact constraint was fulfilled using the penalty approach. To avoid excess penetrations of the slave node into the master surface a penalty parameter of $\epsilon = 10^4$ kN/m³ was chosen for the pile-soil interaction from a depth of 0-10 m and $\epsilon = 2 \times 10^4$ kN/m³ from a depth of 10 m to 20 m below the ground surface. The pile was driven at a rate of 1 m/min, simulated by large deformation of meshes.

Boundary Conditions. Standard boundary conditions were applied to the model except at the axis of symmetry. The motion of the rigid tube is referenced to the reference point (Figure 2) placed at its centre of gravity. Total fixities were applied to the rigid tube, prohibiting both lateral and vertical deformations. The vertical boundary on the right hand side was radially constrained while total fixities were applied at the bottom boundary. The water table was located 2 m below the ground surface. The soil above the water table was assumed to be fully saturated through capillary rise and the total pore pressure boundary condition of $u=19.62$ kPa was imposed on the top surface. This is because the top surface is free and no excess pore pressures would develop at this surface.

Table 2. Soil properties for the FE model.

Layer	Top (m)	Bottom (m)	Depth	γ_d (kN/m ³)	G_s	ν'	M	κ	λ	e_{cs}	$e_{initial}$	Φ_{cr}
Weathered Clay 1	0	2	2	11.65	2.75	0.33	1.05	0.05	0.18	1.67	1.32	26.54
Weathered Clay 2	2	4	2	11.65	2.75	0.33	1.05	0.05	0.18	1.67	1.32	26.54
Soft Clay 1	4	10	6	7.22	2.70	0.33	0.97	0.08	0.51	3.05	2.67	24.68
Soft Clay 2	10	20	10	10.23	2.70	0.33	0.98	0.06	0.32	2.09	1.59	24.91
Medium Stiff Clay	20	24	4	13.45	2.70	0.33	0.90	0.03	0.12	1.20	0.97	23.04
Stiff Clay + Sand 1	24	30	6	14.48	2.70	0.33	0.90	0.03	0.12	1.20	0.83	23.04
Stiff Clay + Sand 2	30	40	10	14.02	2.70	0.33	-	-	-	-	0.89	-

Layer	Top (m)	Bottom (m)	Depth	ϕ'	pc'	E (kPa)	Ko	OCR	k (m/day)
Weathered Clay 1	0	2	2	-	22.20	-	0.716	3	0.000676
Weathered Clay 2	2	4	2	-	55.31	-	0.716	3	0.000676
Soft Clay 1	4	10	6	-	35.58	-	0.620	1.2	0.000055
Soft Clay 2	10	20	10	-	59.41	-	0.661	1.2	0.000026
Medium Stiff Clay	20	24	4	-	103.23	-	0.666	1.4	0.000037
Stiff Clay + Sand 1	24	30	6	-	140.90	-	0.685	1.5	0.000037
Stiff Clay + Sand 2	30	40	10	30	189.65	27440	0.685	1.5	0.000037

Mesh Characteristics and Convergence. Simulation of pile driving in FEM is a large deformation process that involves severe distortion of elements. A triangle may reduce to a straight line and a quadrilateral may reduce to a triangle. Such radical alteration of the element geometry could lead to the formation of a negative Jacobian which ultimately results in the evaluation of a negative stiffness of the element which leads to convergence problems arise and the analysis will be terminated. As the Arbitrary Lagrange Eulerian algorithm was not used in the current study, and severe distortion is all but expected during the pile driving process, an ideal starting point would be to use elements with a healthy aspect ratio (ratio of length to width). To achieve this, the seeding of the mesh in the soil domain was done in such a way that the elements near the pile had an aspect ratio of 1. Lower distortions, stresses and pore pressures were expected in regions located further from the pile. As these regions were of lower interest and contributed less to the total solution, the mesh was constructed with such a bias that a lower density of mesh existed in these regions. All attempts were made to generate a structured mesh resulting in a mesh comprising of predominantly rectangular elements. Since the pile was very stiff and linear elastic in nature, much larger elements were selected for the pile and discretized. Four different cases were selected based on element sizes for the elements at the left end where contact was anticipated. A bias was laid such that the element size increased and mesh density decreased away from the pile. Based on the convergence study and the obtained accuracy of results, very fine mesh [size of the elements just beneath the pile is 0.1 m, which is half the radius of the pile] was chosen for the present study.

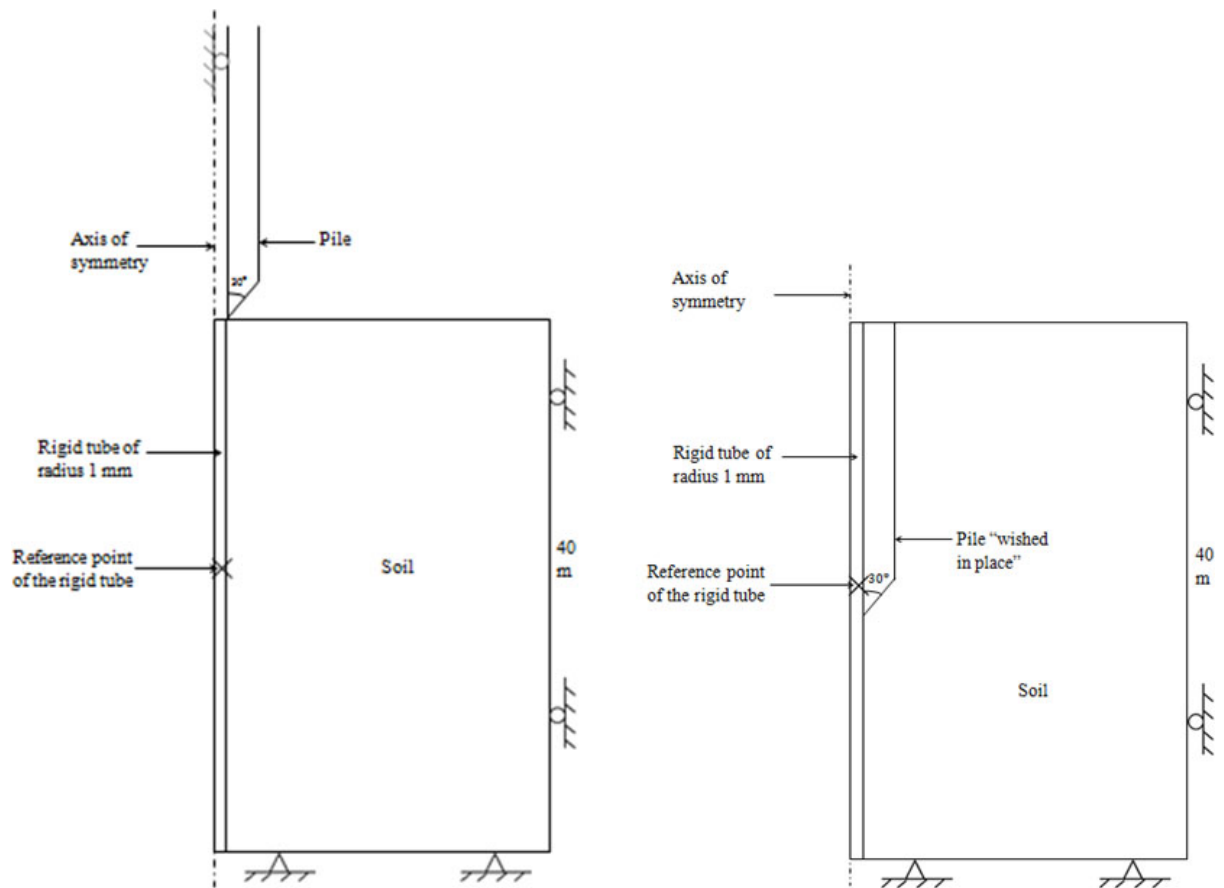


Figure 2. Scaled diagram showing position of the rigid tube and pile in the axisymmetric model for (a) pile driving case, and (b) pile wished in place.

RESULTS AND DISCUSSIONS

Validation of the FE Model. The benchmark problem of pile driving (Indraratna et al. 1992), as described earlier, has been modeled using the Finite Element Analysis (FEA). The current simulation was limited by the amount of interface friction that could be applied. An ideal means to validate the current model was to use the pore pressure dissipation data from the case study where a pile was driven after being coated with bitumen. The interface friction was negligible and was simulated by assuming a frictionless contact between soil and pile in this study. The excess pore pressures near the tip of the pile cone were plotted at depths of 8 m and 16 m as shown in Figure 3. As the position of the pile tip never coincided with any soil node, the pore pressures reported are the average of the pore pressures of the node above (due to small penalty stiffness) and below the pile tip. The excess pore pressure generated at the pile-soil interface is dependent on the soil properties as well as the penetration rate. Validation of the model is established by the close agreement of excess pore pressure (obtained from the experiment and simulation) observed at the pile-soil interface.

Analysis for Development of NSF. The model was validated for a frictionless case. However, in order to generate NSF, some interfacial friction had to be considered. The friction coefficient (μ) between the soil and pile ranged between 0.32 and 0.42 for different layers. Initial trials considering these values failed to converge due to large distortion of the elements even in the presence of automatic stabilization. Hence, a small fictional value of friction coefficient, $\mu = 0.1$ was considered for the entire length of the pile. This assumption does not conform to the field condition but was selected as a means to check the effect of pile installation on negative skin friction. In any case, it is sure that these values would yield a NSF value that would form a lower bound to what one could expect in the field. The aim was to compare the NSF developed in two cases, one where the pile was actually driven prior to fill loading and the other where the pile was considered “wished in place” before the application of fill load (Figure 2).

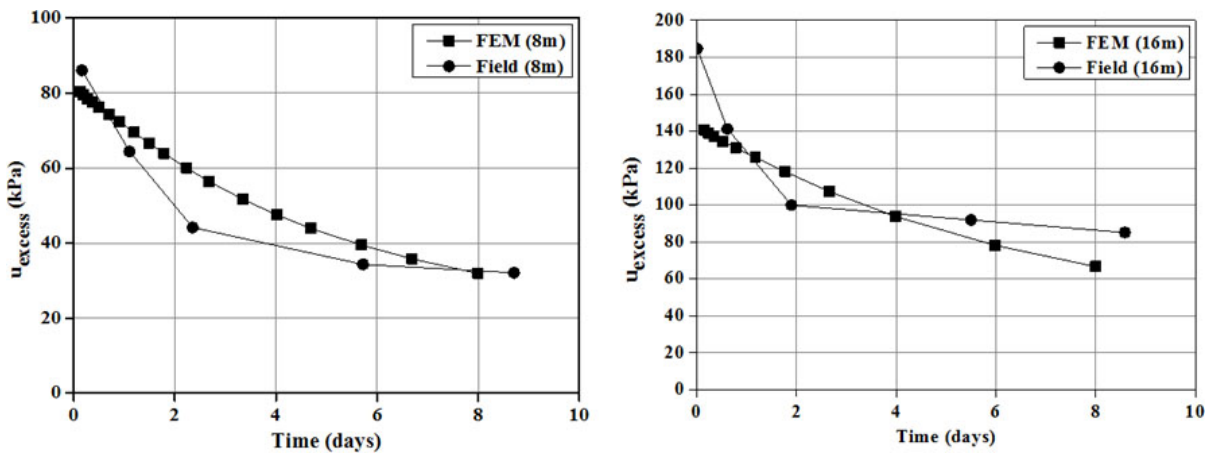


Figure 3. Comparison of excess pore pressure dissipation data between field and FEM at depths 8 m and 16 m.

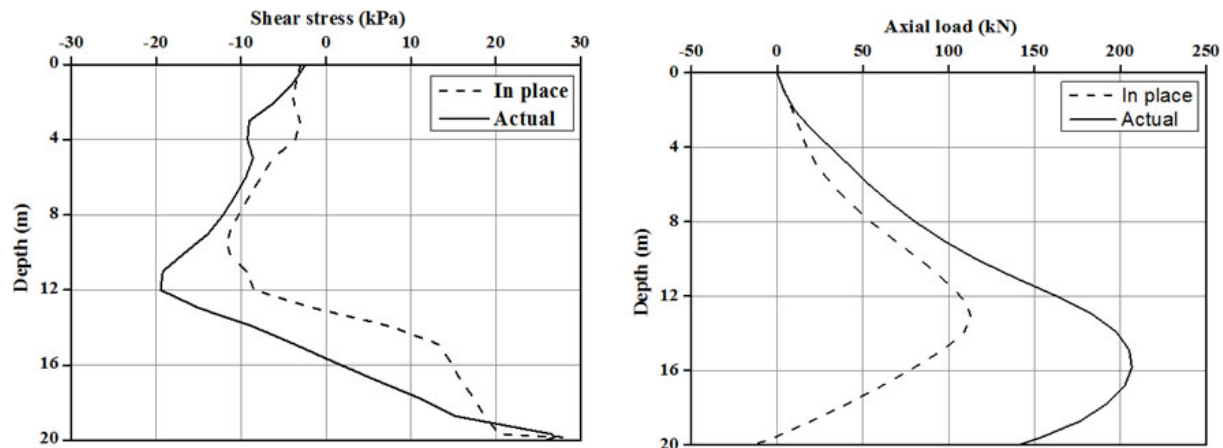


Figure 4. (a) Shear stresses due to negative skin friction, and (b) Axial load variation at different depths along the pile.

Development of Shear Stress. Once consolidation occurred, the soil settled generating negative shear stresses on the pile. Figure 4a shows the NSF generated in the two cases: *actual* representing the pile driving case and *in place* representing the “wished in place” case. For a similar set of initial conditions, the pile driving case shows a higher shear stress, almost throughout the length of the pile. The maximum value of negative shear stress in the *actual* case is almost double the magnitude of that observed in the *in place* case. Another point to be noted is the deeper location of the neutral axis for the actual case (marked by point of zero shear). The shear stresses for the two cases were integrated over the pile area to give the increment in axial load due to NSF as shown in Figure 4b. The maximum axial load in the *in place* case was around 100 kN which was almost half that seen for the *actual* case.

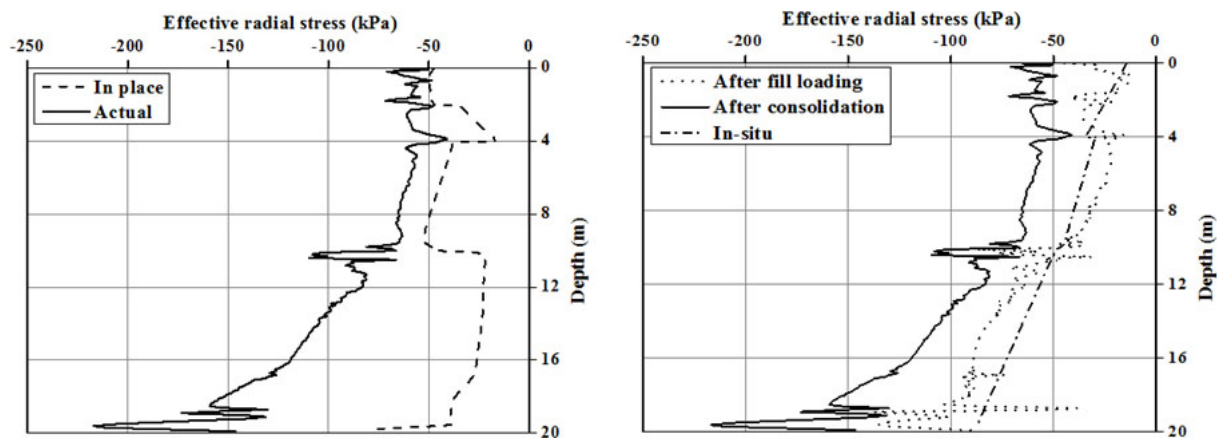


Figure 5. (a) Comparison of radial stress at the end of consolidation for the two cases (b) Comparison of effective radial stress for the *actual* case at various stages during simulation.

Effective Horizontal Stress. The effective horizontal stresses at the pile-soil interface were compared as shown in Figure 5a. The final effective radial stresses (after consolidation) in the axisymmetric model for the driven case were higher than those seen for the in place case. The negative sign is to indicate that the stresses were compressive in nature. A closer study of the radial stress data for the driven case showed that there was not much change due to the act of pile driving itself. A majority of the radial stress changes occurred post application of fill load, indicating the role of radial consolidation in increasing the effective radial stress, as shown in Figure 5b. The larger radial stresses near the pile maybe a reason for the higher NSF for the driven case.

Neutral Plane. Figure 4(a) showed that the neutral plane in the actual driven case at approximately 16m depth (i.e., about 3 m below the corresponding neutral plane of the in situ case). A general consensus is that the stiffer the material at the pile base, deeper is the location of the neutral plane (Lee and Ng 2004). Hence, it was expected that the pile driving procedure would lead to an increase in long term stiffness of the soil beneath the pile as compared to the *in place* case. The difference in the mean stress (p') beneath the pile for the two cases was seen as an effective means to gauge the corresponding difference in their stiffness. The development of

mean stress with time of an element just beneath the pile was compared as shown in Figure 6(a). The mean stress for the in-place case remained fairly constant during the consolidation process. However, a clear increase of about 50% was observed for the case when the pile was driven. The effort required for pile driving lead to an increase in the total mean stress around the pile base and as the excess pore pressures dissipated this led to an increase in the effective mean stress of the soil. Due to the higher stiffness of the soil, it is expected that the settlements at the bottom of the pile would be lower for the actual driven case. The settlements at a node at the centre of the base were plotted against time for the consolidation step as shown in Figure 6(b). The settlements in the in situ case were of the order of 7 mm while the settlements for the actual driven case were negligible. Due to the higher settlement of the pile in the *in place* case, the neutral plane occurs at a shallow depth as compared to the *actual* driven case.

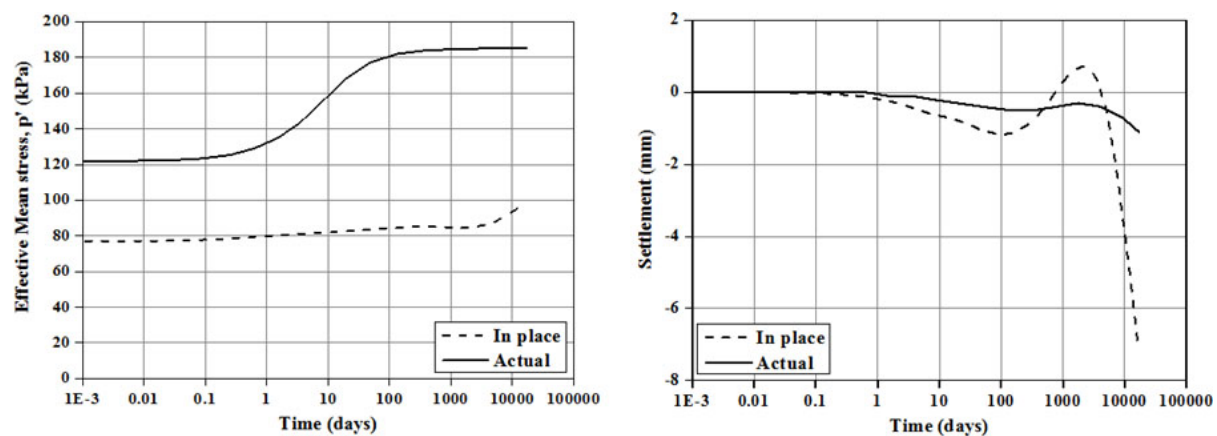


Figure 6. (a) Comparison of effective mean stress developed beneath the pile for the two cases (b) Comparison of settlements of a node at the pile base for the two cases.

CONCLUSIONS

Two analyses were carried out, one where the pile was considered in situ and the other with the actual driving, to model the resultant changes in the soil fabric. The results clearly show that pile driving had a significant effect on the magnitude of NSF. Significant radial pore pressure gradients existed through the length of the pile in the driven case. Post consolidation, the NSF observed for the driven case was higher than that observed in the in situ case. The position of the neutral plane was also observed to be deeper when driving was considered. One reason for this observation is the higher stiffness at the pile base when the driving procedure is accounted for. Comparisons of settlement of the pile base showed that the pile settled more for the *in place* case. This further reinforced the fact that the higher stiffness at the pile base produced such a combination of shear stresses around the pile that the neutral plane occurred at a greater depth (thus indicating higher zone of NSF) for the driven case as compared to the in situ case.

REFERENCES

- Bathe, K. J. (1996). *Finite Element Procedures*. PHI Learning Private Limited, India.
- Cao, W., Chen, Y. and Wolfe, W. E. (2014). "New load transfer hyperbolic model for pile-soil interface and negative skin friction on single piles embedded in soft soils." *International Journal of Geomechanics*, 14 (1), 92-100.
- Ekanayke, S. D., Liyanapathirana, D. S. and Leo, C. J. (2013). "Influence zone around a close ended pile during vibratory driving." *Soil Dynamics and Earthquake Engineering*, 53, 26-36.
- Fellenius, B. H. (1972). "Down-drag on piles in clay due to Negative Skin Friction." *Canadian Geotechnical Journal*, 9 (4), 323-337.
- Fellenius, B. H. (1984). "Negative skin friction and settlement of piles." *Second International Seminar, Pile Foundations*, Singapore, 1-12.
- Indraratna, B., Balasubramaniam, A. S., Phamvan, P. and Wong Y.K. (1992). "Development of negative skin friction on driven piles in soft Bangkok clay." *Canadian Geotechnical Journal*, 29 (3), 393-404.
- Jeong, S., Lee, J. and Lee, C. J. (2004). "Slip effect at the pile-soil interface on dragload." *Computers and Geotechnics*, 31(2), 115-126.
- Lee, C. J., and Ng, W. W. (2004). "Development of downdrag on piles and pile groups in consolidating soil." *Journal of Geotechnical and Geoenvironmental Engineering*, 130 (9), 905-914.
- Leung, C. F., Liao, B. K., Chow, Y. K., Shen, R. F. and Kog, Y. C. (2004). "Behavior of pile subject to negative skin friction and axial load." *Soils and Foundations*, 44(6), 17-26.
- Schofield, A., and Wroth, C. P. (1968). *Critical State Soil Mechanics*. McGraw-Hill, London.
- Tolooiyan, A. and Gavin, K. (2011). "Modelling the Cone Penetration Test in sand using Cavity Expansion and Arbitrary Lagrangian Eulerian Finite Element Methods." *Computers and Geotechnics*, 38 (4), 482-490.
- Wriggers, P. (2006). "Computational Contact Mechanics." Springer, The Netherlands.
- Yi, J. T., Goh, S. H., Lee, F. H. and Randolph, M. F. (2012). "A numerical study of cone penetration in fine grained soils allowing for consolidation effects." *Geotechnique*, 62 (8), 707-719.

Numerical Simulation of the Lateral Loading Capacity of a Bucket Foundation

Xu Yang¹; Xuefei Wang²; and Xiangwu Zeng, M.ASCE³

¹Research Assistant, Dept. of Civil Engineering, Case Western Reserve Univ., Cleveland, OH 44106. E-mail: xyy214@case.edu

²Research Assistant, Dept. of Civil Engineering, Case Western Reserve Univ., Cleveland, OH 44106. E-mail: xxw165@case.edu

³Frank H Neff Professor and Chair, Dept. of Civil Engineering, Case Western Reserve Univ., Cleveland, OH 44106. E-mail: xxz16@case.edu

Abstract

Bucket foundation has been used extensively in offshore facilities to resist combined lateral and moment loading. The lateral loading capacity and interaction between the soil and foundation is of great interest to geotechnical engineers. In this paper, finite element models of a bucket foundation with two aspect ratios (L/D , where L is the skirt length and D is the foundation diameter) of 0.5, 1.33, were created using the ABAQUS program. Centrifuge model tests were also conducted on the two models. The load-displacement curves of the numerical analysis and test results had good agreement, which verified the reliability of the finite element analysis method for this type of problem. In addition, several 3D numerical models of aspect ratio varied from 0.2 to 2.0 were built to evaluate the effect of the aspect ratio on the lateral loading capacity. The development and distribution of stress and plastic strain were used to study the failure mechanism of bucket foundation for different L/D ratios. The influence of the position of the lateral load applied was analyzed. Sensitivity analysis for the parameters of material properties such as the internal friction angle, the Young's Modulus, and the friction coefficient between the bucket and soil were performed using non-linear analysis with the Mohr-Coulomb soil model.

INTRODUCTION

Bucket foundations were used increasingly for offshore structures in recent years. Compared with pile foundations and gravity foundations, which have been widely used in offshore wind farms in recent years, the bucket foundation can be installed by suction, leading to a lower construction cost and shorter construction period. After installation in the seabed, the bucket foundation can advantageously utilize the soil inside the bucket to resist loading.

The structures in offshore engineering are usually subjected to a vertical loading with lateral loading. The loading is transferred to the foundations as a combined loading of vertical, lateral loading and moment. According to an analysis of a 3.5 MW wind turbine installed offshore in the UK, the effect of vertical load is relatively small compared with the lateral load and overturning moment (Byrne and Houlsby 2003). Therefore, this paper focuses on the performance of bucket foundations under lateral loading and moment.

Model tests and numerical simulations have been used to study the performance of bucket foundations. Ei-Gharbawy (1998) conducted several laboratory tests to study the pullout capacity of suction bucket foundations under vertical and inclined loading. Wang (2015) performed a group of centrifuge tests to evaluate the seismic behavior of bucket foundations in

sand. Liu (2014) built a series of three-dimensional numerical models to study the failure mode of wide-shallow bucket foundations in normally consolidated silty sand.

In the present study, various three-dimensional finite element (FE) models were established to study the lateral bearing capacity of bucket foundations and the interaction between the foundation and the soil. The stress and strain in the surrounding soil of the bucket were analyzed to investigate the mechanism of the resistance to lateral loading. Different aspect ratios (L/D) varying from 0.2 to 2.0 were employed to explore the influence of aspect ratios on the bearing capacity. Finally, sensitivity analysis of the parameters of Mohr-Coulomb model was performed based on a series of models with different material properties.

NUMERICAL MODELLING

Foundation Models, Geometry and Meshes. Two models of bucket foundation with aspect ratios 0.5 and 1.33 were made and tested under lateral loading on the centrifuge at Case Western Reserve University (Figure 1). The corresponding prototype sizes are shown in Table 1. The numerical model was built in the prototype scale. A short cylinder was fixed on the lid of the bucket to simulate part of the tower of the wind turbine. The soil was simulated as a solid cylinder with a diameter of 50 m (10D) and a height of 10 m (4L) to avoid the boundary effect. A bucket shaped pit was pre-cut in the soil and the bucket was placed in the pit before applying the load. The contact behavior of the interface between skirt and soil was simulated by normal “hard” contact model in ABAQUS (Hibbitt and Sorensen 2011). When skirt and soil were in contact, normal pressure and tangential frictional resistance, governed by Coulomb’s friction, occurred and transferred between interfaces. Separation of the skirt and soil was allowed during the analysis. Once separated in geometry, the contact stress disappeared. This paper focuses on the stress and strain of the soil, so the bucket foundation as well as the short tower were modeled as a rigid body, with loads and displacements related to a single load reference point on the top of the short tower.

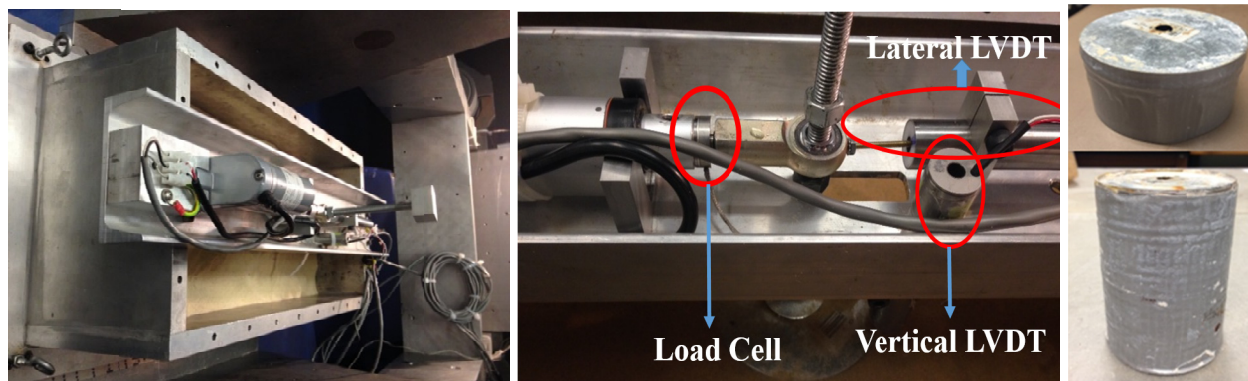


Figure 1. Apparatus and bucket models.

Typical FE meshes are shown in Figure 2. Three-dimensional 8-node linear brick elements with reduced integration were used (C3D8R) for the model. Relatively fine meshes were used in the soil near the skirt and below the toe of the bucket to obtain the local distribution

of the stress and strain, while coarser mesh sizes were applied away from the bucket considering the computational efficiency.

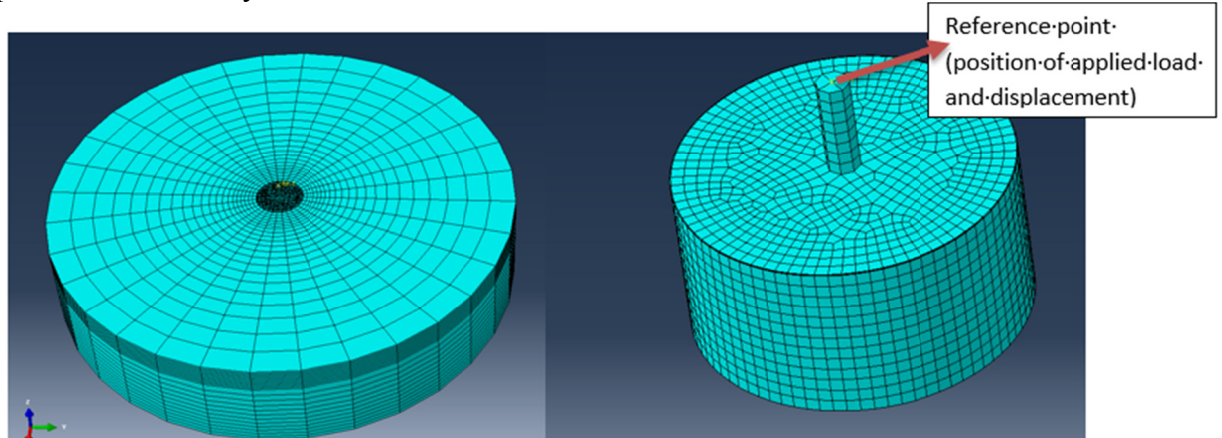


Figure 2. A typical mesh for bucket foundations.

Table 1. Prototype sizes.

Bucket foundation number	Skirt length, L (m)	Diameter, D (m)	Aspect ratio	Thickness (m)	Load point from the lid (m)
1	2.5	5	0.5	0.0125	1.5
2	5	3.75	1.33	0.0125	1.5

Foundation and Soil Properties. The bucket foundation material was steel with Young's modulus (E_s) of 200 GPa and Possion's ratio (μ) of 0.30. The sand profile in the centrifuge test was constructed with dry Toyoura sand. Direct shear tests were conducted to determine the internal friction angle of the soil (Figure.3). For sand, the direct shear test displays a higher angle of internal friction than that obtained from the simple shear test and triaxial test in general(WU et al. 2006). Therefore, a internal friction angle of 25° was chosen. The dry unit weight was measured as 14 kN/m^3 , from which the relative density of the soil can be calculated as about 30%. The soil can be stated as loose sand. The soil in the FE model was simulated as a linear elastic-perfectly plastic model, governed by the Mohr–Coulomb criterion, with Young's modulus (E_s) of 10MPa(Kezdi 1974), Possion's ratio (μ) of 0.30 ,an internal friction angle (ϕ) of 25° and a dilation angle of 5° (Vermeer 1998). The friction coefficient between the foundation and the soil was assumed as 0.1.

Loading path. Displacement-controlled analysis method was used. In the first step, gravity was applied to the soil as body force, and stress balance was adopted to avoid displacement under gravity. Then the lateral displacement was applied linearly to a reference point. The reference point was in the same position of the loading point in the centrifuge model tests, which was 1.5 m above the lid.

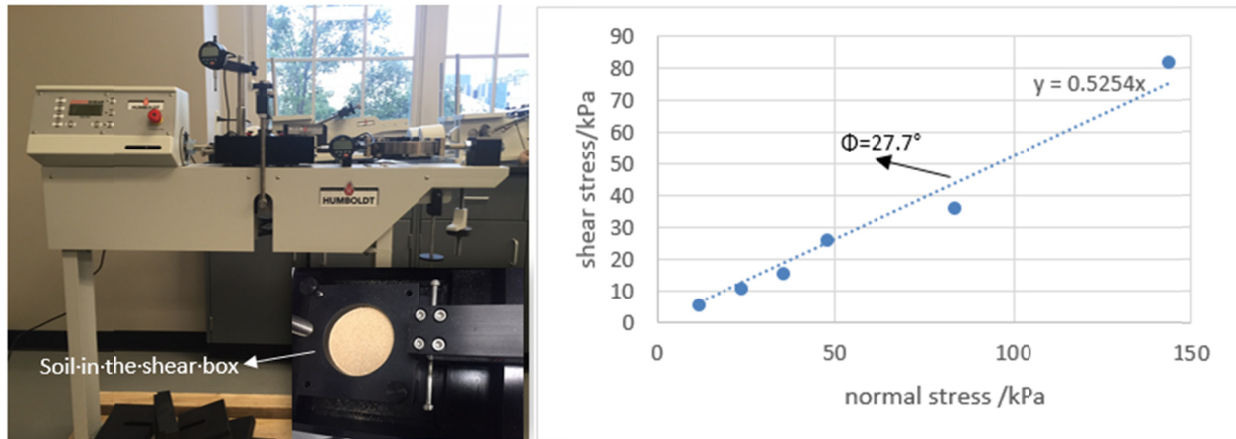


Figure 3. Direct shear tests and results.

RESULTS AND DISCUSSIONS

Load-Displacement Curves and Comparisons with the Tests. The load-displacement curves of the numerical model agree well with the results of the centrifuge test, as shown in Figure 4 and Figure 5. This means that the FE simulation is reliable and the parameters of the materials are appropriate.

Typical contact pressure distributions are shown in Figure 6 ($D=5$ m bucket is selected as an example). The stress contour indicates that the mechanism of pressure distribution is similar to the mode displayed in Figure 7 (Liu 2014). The lid and soil separate when the lateral displacement increase, therefore P_t and P_v do not exist. Obviously, most of the resistance is provided from the soil pressure between the front skirt of the bucket and the neighboring soil.

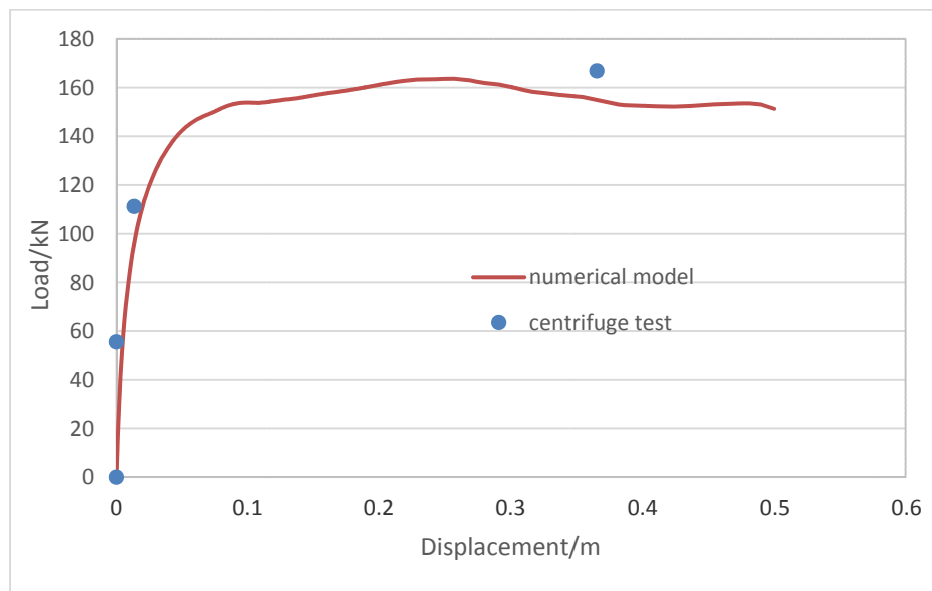


Figure 4. Load-displacement curves of both numerical results and centrifuge tests ($D=5$ m, $L/D=0.5$).

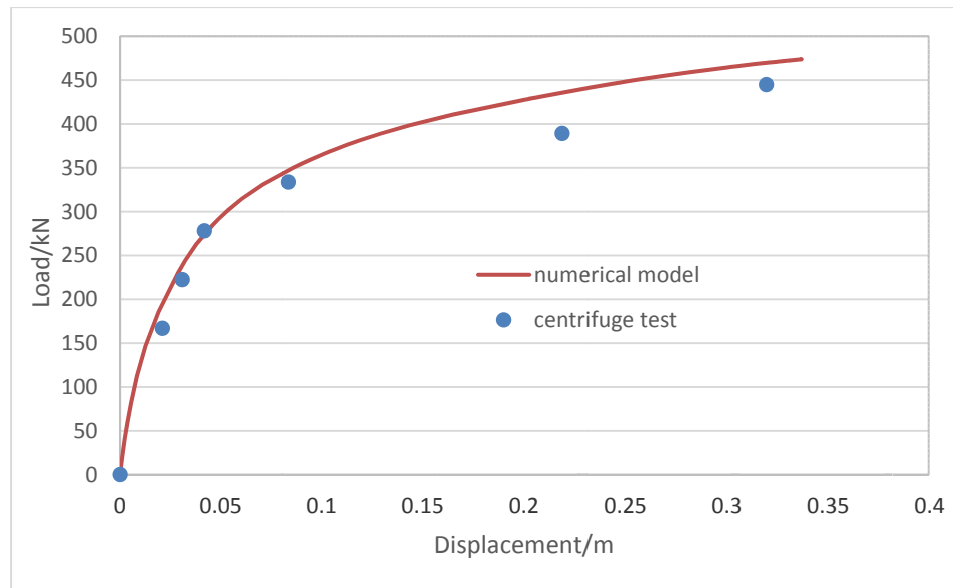


Figure 5. Load-displacement curves of both numerical results and centrifuge tests ($D=3.75$ m, $L/D=1.33$).

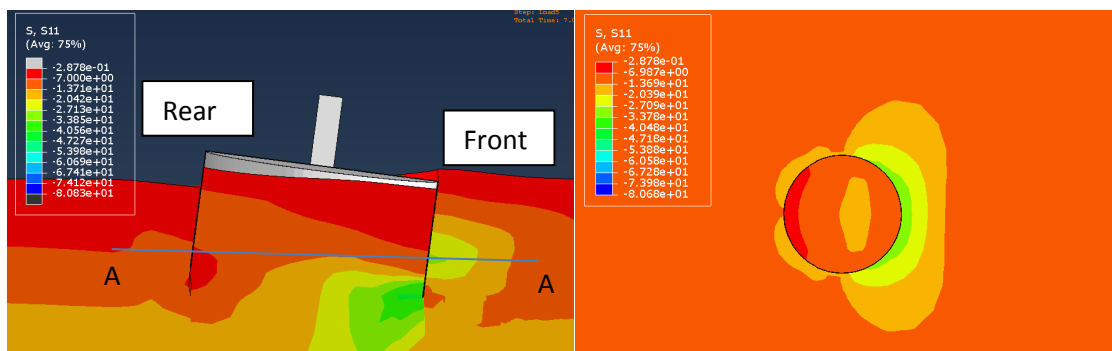


Figure 6. Contact pressure distribution (a) along the side of bucket ($D=5$ m, $L/D=0.5$) along the circumference of bucket, cross section from cut A-A.

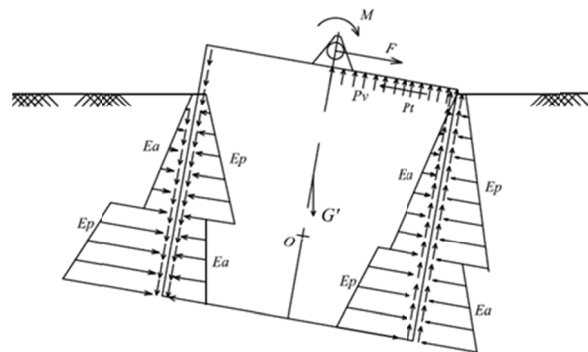


Figure 7. The mechanism of pressure distribution (Ea and Ep correspond to active pressure and passive pressure; Pt and Pv represent friction resistance and pressure of the lid respectively; and G' is the gravity of the bucket).

Figure 8 shows the process of the development of the stress. It can be seen that the passive pressure is much larger than the active pressure in the same depth and contributes to most of the lateral resistance. The maximum stress appears at the toe of the front skirt. When $d < 30$ cm, with the increase of the lateral displacement, the passive pressure increases. After that, with the rotation of the foundation, the rear skirt uplifts and a crack appears and expands between the lid and the soil, leading to a reduction in the contact area of the bucket and the soil, which consequently results in a decline in the contact pressure of the rear skirt and the soil. This decrease also appears in the load-displacement curve in which the curve goes down a little after 30 cm.

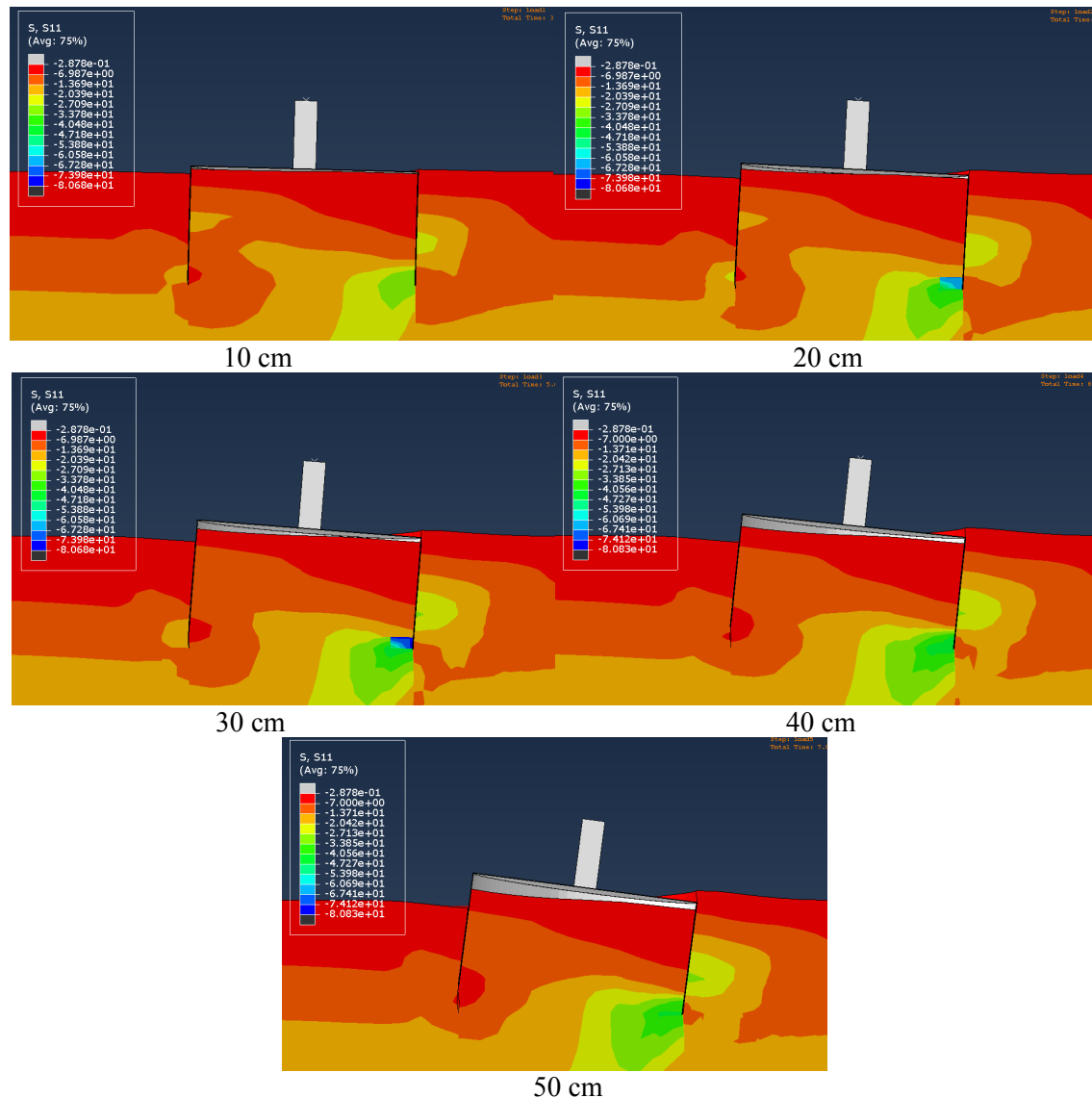


Figure 8. The development process of the stress.

LATERAL BEARING CAPACITY UNDER DIFFERENT ASPECT RATIOS

From the results of lateral bearing capacity for two bucket models with aspect ratio of 0.5 and 1.33, it was obvious that the aspect largely affects the bearing capacity of the bucket foundation,

which was also reported by previous studies (Zhan and Liu 2010). A series of numerical models were created with the same diameter of 5m, and the aspect ratio varied from 0.2 to 2.0 to study the relationship between the lateral bearing capacity and the aspect ratio.

Figure 9 and Figure 10 show the lateral load–displacement curves and the variations of the lateral bearing capacity of the bucket foundations on different aspect ratios. The lateral bearing capacity increases and accelerates obviously with the L/D ratio. When normalized by the side area of the bucket, the increasing rate is almost linear and decelerates slightly when the aspect ratio increases. This can be explained by the utilization ratio of the internal soil. A higher aspect ratio will have a better performance in bearing capacity. However, it may cause installation problems in some soil conditions (Lian et al. 2014; Yang et al. 2014). The geometry of the bucket foundation should be designed with all the aspects in consideration.

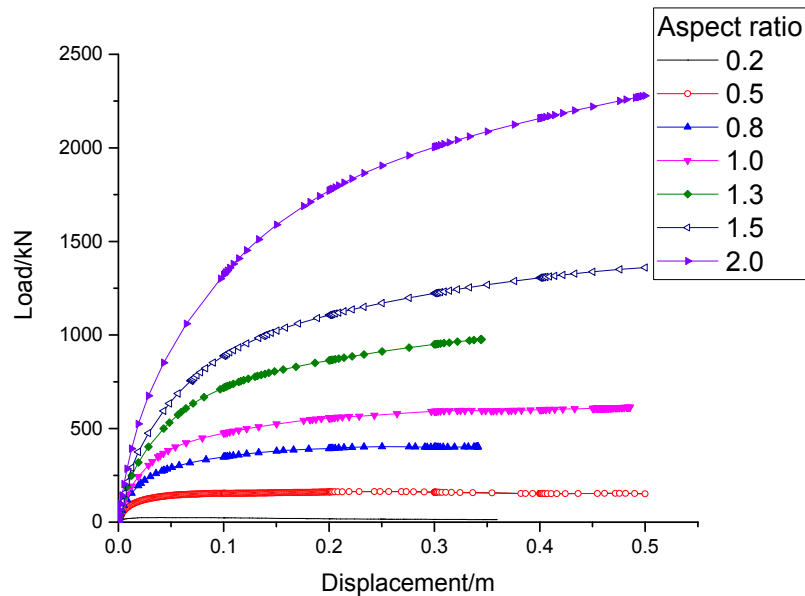


Figure 9. Load vs. Displacement under different aspect ratios.

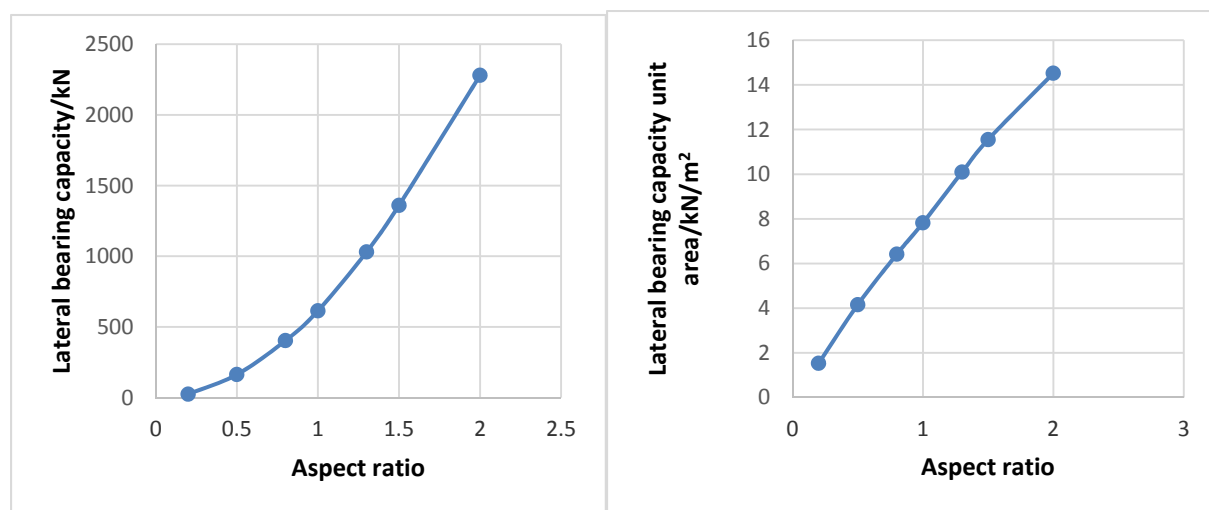


Figure 10. Bearing capacity vs. aspect ratio under different aspect ratios (left: the total bearing capacity; right: the normalized bearing capacity by area).

SENSITIVITY ANALYSIS

The selection of material properties are of great significance for numerical simulation. Some parameters such as the internal friction angle can be measured from tests while others cannot or can be hardly measured such as the dilation angle. For this reason, a group of models, with material properties varies in a range, was built to investigate the sensitivity of the parameters of Mohr-Coulomb model. The results are shown in the figures below, followed by the influences of Young's modulus, dilation angle and internal friction angle.

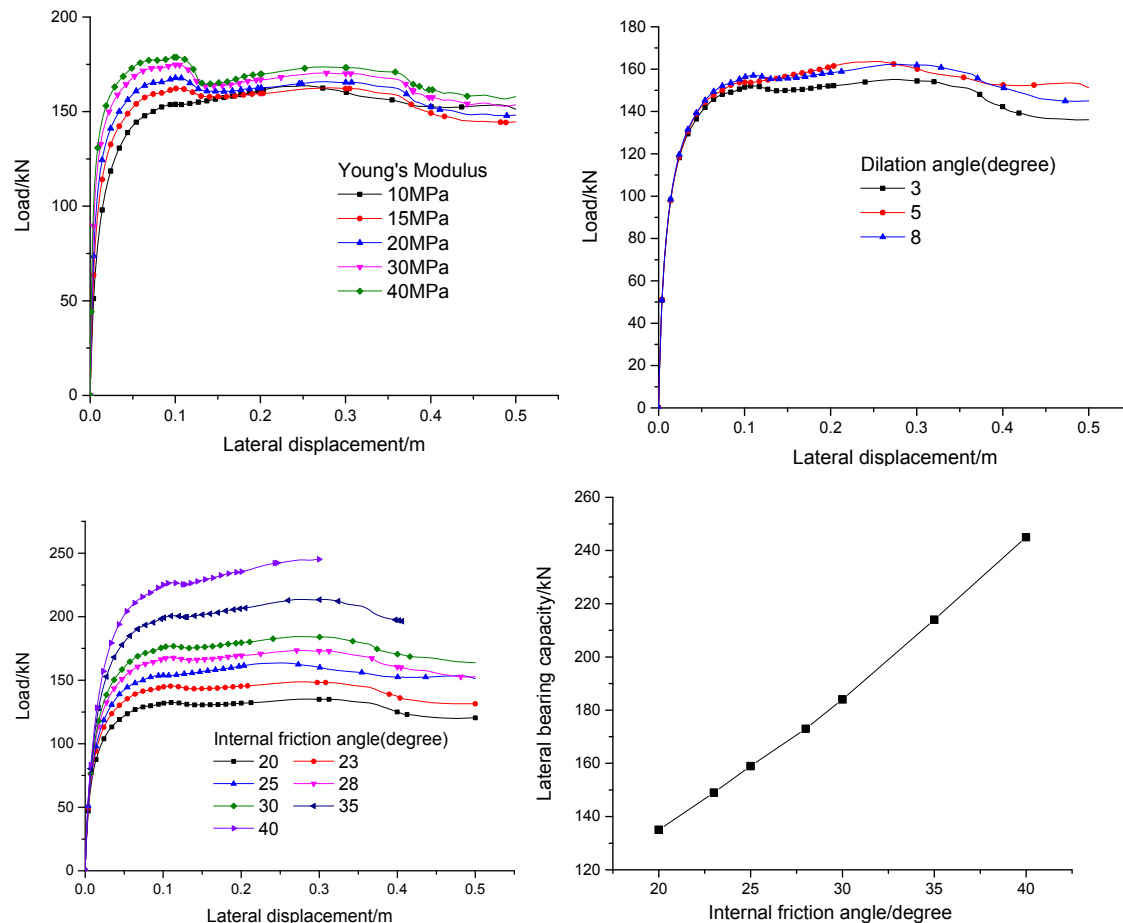


Figure 11. The load-displacement curve with various material parameters.

Young's modulus will influence the yield point of the curve but has a low impact on the ultimate bearing capacity, because the soil always has large deformation and enters a fully developed plastic status. There is no big difference on the bearing capacity of different dilation angles. The bearing capacity increase almost linearly with the increase of the internal friction.

The impacts of interaction property between the skirt and soil were discussed by varying the friction coefficients from 0.05 to 0.4, shown in Figure 12. The lateral bearing capacity increases with the increase of the friction coefficient between the skirt and soil and the trend decelerates when the friction coefficient raises.

The position of the lateral force acting on the tower also plays an important role in the lateral bearing capacity. Control models were built with different action points of the lateral load,

which are 0.0 m, 0.5 m and 1.5 m above the lid. Figure 13 depicts that the lateral bearing capacity will decrease and the trend decelerates when the action point of the lateral load elevates.

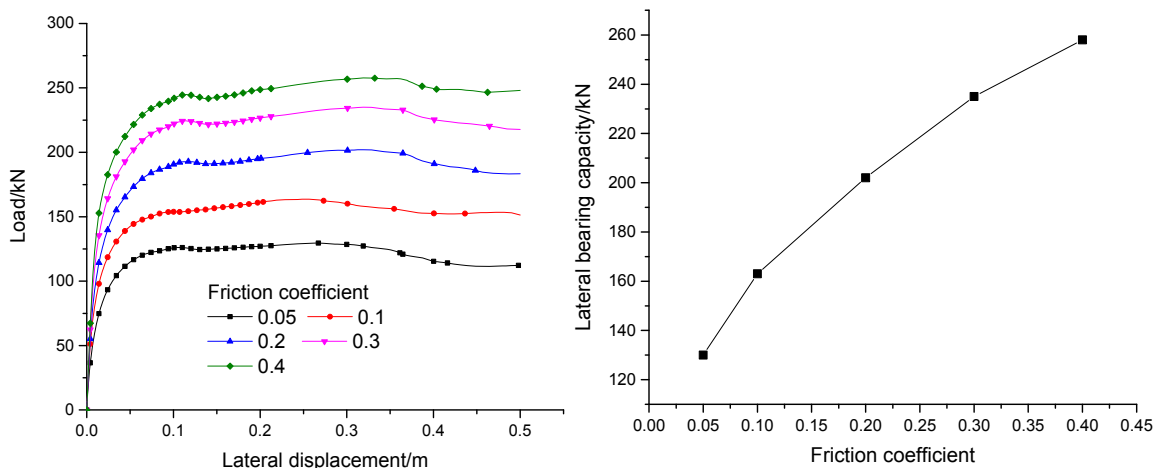


Figure 12. The load-displacement curve with various contact coefficients

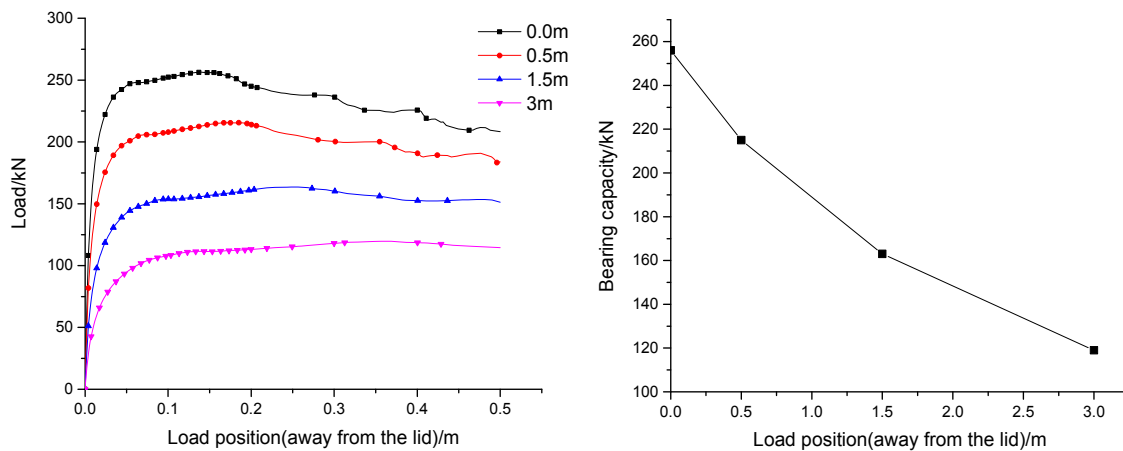


Figure 13. The load-displacement curve with various load position

CONCLUSIONS

This paper presents the numerical simulation of bucket foundations in sand. The following conclusions were reached based on the results of the three-dimensional numerical analysis.

- (1) The load-displacement curves from FE analysis match well with the results of centrifuge tests. This demonstrates that the numerical simulation using FE analysis is reliable and can be a good compensation to model tests and field trials.
- (2) The interaction between the bucket and the surrounding soil are illustrated. The soil pressure between the front skirt of the bucket and the corresponding soil contribute a large amount of the resistance. Most of the interior soil was utilized under the later loading.

- (3) The lateral bearing capacity increases and accelerates obviously with the L/D ratio. It can be concluded from the sensitivity analysis that the internal friction angle and the friction coefficient strongly affect the bearing capacity, while the Young's Modulus and the Dilation angle have little influence on it.

REFERENCES

- Byrne, B. W. and Houlsby, G. T. (2003). "Foundations for offshore wind turbines." *Philosophical Transactions of the Royal Society of London A: Mathematical, Physical and Engineering Sciences*, 361(1813), 2909-2930.
- Ei-Gharbawy, S. L. (1998). "The Pullout Capacity of Suction Caisson Foundations." PhD Thesis, University of Texas at Austin.
- Hibbitt, K., Sorensen. (2011). ABAQUS: Theory Manual. Karlsson & Sorensen.
- Kezdi, A. (1974). *Handbook of Soil Mechanics*. Elsevier, Amsterdam.
- Lian, J., Chen, F., and Wang, H. (2014). "Laboratory tests on soil-skirt interaction and penetration resistance of suction caissons during installation in sand." *Ocean Engineering*, 84, 1-13.
- Liu, M., Yang, M., and Wang, H. (2014). "Bearing behavior of wide-shallow bucket foundation for offshore wind turbines in drained silty sand." *Ocean Engineering*, 82, 169-179.
- Liu, M. (2014). "Bearing capacity and optimization design of composite bucket foundation for offshore wind turbine." PhD Thesis, Tianjin University.
- Vermeer, P A. Non-associated plasticity for soils, concrete and rock[M]//Physics of dry granular media. Springer Netherlands, 1998: 163-196.
- Wang, X., Zeng, X., Yu, H., and Wang, H. (2015). "Centrifuge Modeling of Offshore Wind Turbine with Bucket Foundation under Earthquake Loading." In IFCEE 2015.
- WU, M, FU, X, XIA, T, et al. Comparison between Unconsolidated Undrained Simple and Direct Shear Tests on Compacted Soil[J]. *Chinese Journal of Rock Mechanics and Engineering*, 2006: S2.
- Yang, X., Chen, F., Lian, J. and Wang, H. (2014). "Numerical analysis and test verification of penetration resistance for bucket foundation installation considering effect of soil squeezing." *Rock and Soil Mechanics*, 35(12), 3585-359.
- Zhan, Y. G., and Liu, F. C. (2010). "Numerical analysis of bearing capacity of suction bucket foundation for offshore wind turbines." *Electronic Journal of Geotechnical Engineering*, 15, 633-644.

Three-Dimensional Finite Element Modeling for Spudcan Penetration into a Clayey Seabed

Volkan Emren¹; Nejan Huvaj²; and Kagan Tuncay³

¹Research Assistant, Dept. Civil Engineering, Ankara Yıldırım Beyazıt Univ., 06000, Ankara, Turkey; Ph.D. student, Civil Engineering Department, Middle East Technical Univ., 06800 Ankara, Turkey. E-mail: vemren@ybu.edu.tr

²Assistant Professor, Dept. of Civil Engineering, Middle East Technical Univ., 06800 Ankara, Turkey. E-mail: nejan@metu.edu.tr

³Professor, Dept. Civil Engineering, Middle East Technical Univ., 06800 Ankara, Turkey. E-mail: tuncay@metu.edu.tr

Abstract

In this study the penetration of spudcan foundation for “jack-up rig” type offshore oil platform into a uniform clayey seabed is investigated with three-dimensional finite element modeling (Abaqus 6.14) using Coupled Eulerian Lagrangian method that can handle large deformation problems. One of the goals of this study is to compare the penetration-bearing resistance behavior of spudcan obtained by numerical study with the method suggested in InSafeJIP design guideline. For the spudcan geometry and soil properties used in this study, based on the three dimensional finite element analyses, the required penetration depth for a target bearing capacity of spudcan is less than that required by analytical method in InSafeJIP guideline. The second goal of the study is to explore the effects of some geometrical and soil variables on spudcan bearing resistance-penetration behavior. The variables in this study are spudcan diameter (7.5 to 15 m), the surface roughness of spudcan (roughness coefficient of 0 to 1.0) and undrained shear strength of clay (20 to 80 kPa). Understanding the relations between the factors and penetration behavior may help in future studies on enhanced and economical design of spudcans.

INTRODUCTION

Jack-up platforms are one of the most common types of structures that are used for offshore oil and natural gas production. A platform typically has three or four legs (steel truss-structure or pipe-section), each connected to a steel or concrete foundation called “spudcan” (Figure 1a). Spudcan diameters can be up to 25 m and they tend to have a polygonal shape (Figure 1b), which can be idealized as a cone shape. A spudcan is lowered down onto the mudline and penetrated into the seabed with penetration rates in the range of 0.01 to 1.7 m/s (Maersk Interceptor n.d.; Tho et al. 2012).

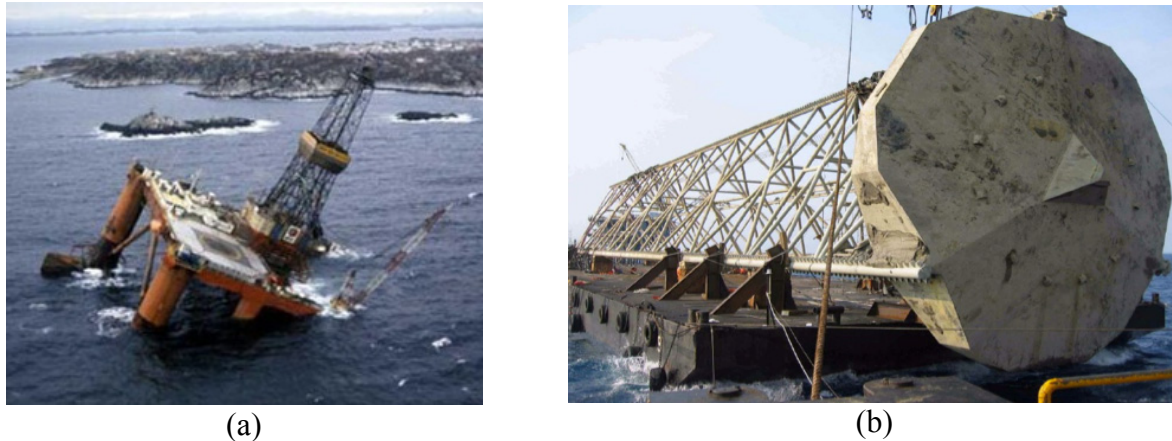


Figure 1. (a) An offshore oil rig failure (<http://www.dierk-raabe.com/dramatic-material-failure/oil-drilling-platforms/>), (b) a truss leg connected to a spudcan (Energy and Minerals Institute, n.d.).

Studies in the literature regarding spudcan penetration and their service life behavior have been carried out by various researchers as partly discussed in next section and further discussion can be found in Emren (2015). Because of the complexity of the interaction between the spudcan and the seabed during penetration, the problem involves a considerable number of variables. Some of these variables include spudcan diameter, cone angle, roughness of spudcan surface and strength properties of soil. Although there exists some analytical methods for design (SNAME (2008), InSafeJIP (Osborne et al. 2011), etc.), they may underestimate or overestimate the spudcan bearing capacity due to simplifications involved in the guidelines. Therefore, the results based on such simplistic guidelines can sometimes be on the unsafe side (e.g. can result in disasters) or they could be on the very safe side resulting in uneconomical designs (e.g. requiring too much penetration for developing sufficient bearing capacity). Investigation of the aforementioned factors and understanding their effects can provide safer and economical design of spudcans. The fundamental objective of this study is to investigate the factors that affect the penetration of spudcan type offshore foundations into cohesive seabed by carrying out three-dimensional (3D) finite element (FE) simulations, and to compare the results with the widely used InSafeJIP (Osborne et al. 2011) guideline.

BACKGROUND

In the recent literature 3D FE Coupled Eulerian Lagrangian (CEL) method is becoming more and more popular for modelling geotechnical problems with large deformations, such as penetration of spudcan into seabed (e.g. Hossain & Randolph 2009, Qiu & Henke 2011, Yu et al. 2012), Tho et al. 2012, Elkadi et al. 2014, and Zhang et al. 2014). This is because the CEL method can handle large deformation problems in a computationally efficient way.

Hossain & Randolph (2009) combine centrifuge model testing, and large deformation FE analysis to study spudcan penetration behavior into single clay layer. By presenting some dimensionless charts and bearing capacity factors from their analyses, they found that the methods presented in SNAME (2008) design guideline overestimates the required penetration depth of spudcan. Qiu & Henke (2011) used the CEL method via Abaqus software for modeling

spudcan penetration into uniform clay and uniform sand seabeds. They compared the results of the 3D numerical model with the centrifuge data and showed their consistency. Yu et al. (2012) carried out a large deformation FE study for the embedment resistance of spudcan on layered soils, which consist of loose sand overlying clay soils. Their conclusion is that SNAME (2008) significantly underestimates the reaction forces developing on the spudcan surface, hence overestimates the required penetration depth. Tho et al. (2012) used a CEL technique in order to simulate the penetration of a spudcan foundation into seabed that consists of different types of soil strata. In their study, model applicability was validated with the published experimental data presented in different studies. Elkadi et al. (2014) investigated the extreme impact forces in case of a touchdown of the spudcan into seabed with the help of the CEL method implemented in Abaqus software. They compared the numerical results with the measured data obtained in a centrifuge test and showed their similarity.

Widely used simplified analytical method presented in InSafeJIP (Osborne et al. 2011) is used in this study to compare with 3D FE method results.

METHODS

Spudcan penetration into seabed is a large-strain type geotechnical problem, where common FE methodology with small strain assumption cannot be used (except with some approximations, e.g. press and replace technique by Engin et al. (2015)). In order to model this large deformation problem, CEL method available in Abaqus Explicit software was adopted and 3D FE method analyses are conducted. Since there are no documented well-instrumented real life spudcan penetration case study in the public literature, the analytical methods depicted in InSafeJIP were used to compare with the numerical results.

The CEL method contains Lagrangian elements and an Eulerian material. An Eulerian material should contact with Lagrangian elements through Eulerian–Lagrangian contacts (general contact in Abaqus 6.14). Although, traditional Lagrangian elements distort excessively and the analyses lose its accuracy, high damage analyses, liquid sloshing, or any penetration problem can be solved easily and effectively by Eulerian analysis.

In this study, the cone-shaped spudcan was modeled as a rigid material. Generating traditional Lagrangian meshes and defining a reference point on the spudcan is required, so that any mechanical boundary condition including velocity can be defined on the reference point. Soil, on the other hand, was defined as an Eulerian material that can deform freely inside the corresponding meshes. In a Lagrangian analysis, as the material deforms, the finite elements also deform because the nodes of the elements are fixed within the material. On the other hand, nodes are fixed within space in an Eulerian analysis. Material flows inside the elements that do not deform. Thus, these kinds of elements do not need to be 100% full of material every time. Therefore, an Eulerian boundary does not correspond to an element boundary and an Eulerian mesh typically extends beyond the material boundaries. If an Eulerian material moves out of the Eulerian mesh, it disappears from the simulation. Therefore, it is important to describe predefined void meshes in which there is no Eulerian material to simulate material movement (Figure 2a).

Symmetrically half of the geometry of the problem is defined in the FE model to save time. The size of the FE model geometry is selected based on preliminary FE analyses so that the stresses and deformations in the penetration area are not affected by the closeness of the

boundaries. The model size was selected to keep a ratio of the width of the model to spudcan diameter value of 5. Therefore, for an FE model to study a spudcan with 10 m diameter, the model width is 50 m (Figure 2b). The depth and height of the model was selected as 25 m and 45 m, respectively. The upper 10 m is defined as void zone.

Boundary condition at the very bottom of the model was selected so that the movement is prevented against all directions. For the sides of the geometry, boundary fixities were provided such that translation in the directions which are normal to the surfaces are fixed, and movement in other directions which are tangential to the surfaces are allowed (Figure 2a). Eight-noded 3D Eulerian elements with reduced integration for Eulerian analysis (called EC3D8R in Abaqus) are used to discretize the soil. Different size finite elements are tried until a suitable FE mesh density is chosen for sufficient accuracy with optimum run time (approximate size of the elements was 0.7 m and total number of elements were 107328).

The penetration velocity of the spudcan is selected as 15 cm/s based on the reported velocity ranges in the literature (0.01 to 1.7 m/s (Maersk Interceptor n.d., Tho et al. 2012) and on the preliminary simulations in 3D FE models. The value is selected such that the analyses did not consume excessive amount of time (run time was about 8 hours for 10 cm/s and 1 hour for 45 cm/s penetration velocity). Further details of the FE model can be found in Emren (2015).

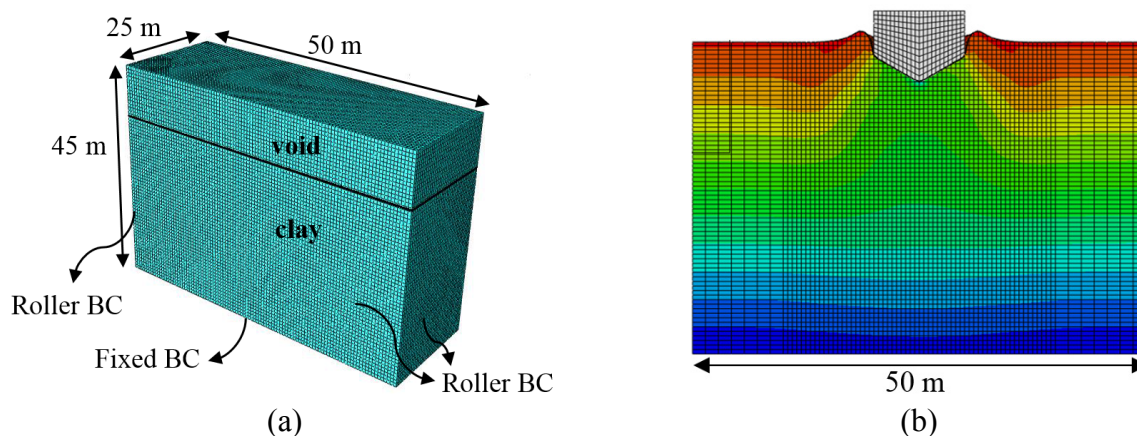


Figure 2. (a) Geometry of the FE model, (b) Front view of the model with spudcan

Spudcans having diameters in the range of 7.5 to 15 m was penetrated into cohesive layers with different undrained shear strength (20 to 80 kPa) and the bearing capacities for different depths were recorded. Those values are then compared with the bearing capacity calculations based on InSafeJIP analytical method.

The analytical method in InSafeJIP to obtain spudcan load-penetration prediction is based on fundamental bearing capacity theory for shallow foundations in geotechnical engineering. Bearing capacity is calculated as the multiplication of the plan area of the foundation and the bearing pressure, that is a function of soil strength, soil weight and foundation depth. The penetration depth “ z ” in the InSafeJIP guideline is defined as the distance between the tip of the spudcan and the mudline. Although z is the penetration depth, bearing capacity calculations require the use of “ h ” in Figure 3, as the penetration depth, which can be defined as the lowest depth of the largest plan area of the spudcan. Undrained bearing capacity factors for conical footings on clay are used in calculations (Martin & Houlsby 2003). The bearing capacity factor is modified as recommended in InSafeJIP by some factors related with soil properties, spudcan

diameter, equivalent cone diameter, cone angle and normalized penetration depth. Bearing capacity calculations are conducted for different penetration depths: (i) partial penetration case ($z \leq y_m$ condition), and (ii) full penetration cases ($z \geq y_m$) with and without backfill soil flowing onto spudcan.

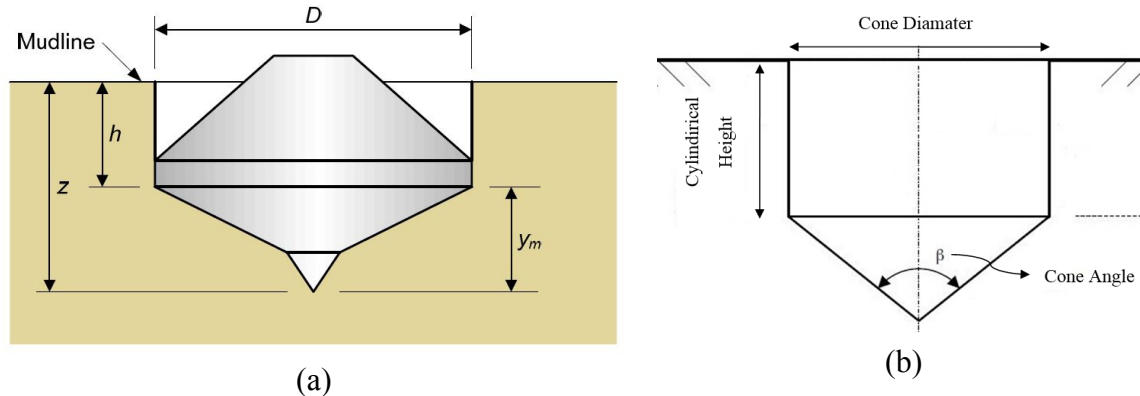


Figure 3. (a) Penetration depth z and h definition in InSafeJIP, (b) cylindrical height definition in FE model.

PARAMETRIC STUDY

In order to conduct a systematic parametric study, a certain property is changed within a preset range while all other model parameters are kept constant (Table 1). Although more comprehensive constitutive models are available in the software, elastic-perfectly plastic Mohr-Coulomb failure criterion was adopted in all the analyses since it is a simple model that is sufficient for the purposes of this study. Also, there are more input parameters needed for other constitutive models and their values are relatively more difficult to estimate without a site-specific laboratory and field tests.

Table 1. Typical values that are kept constant when the others are varied.

Parameter		Value	Unit
General	Failure Criterion	Mohr - Coulomb	-
	Drainage Type	Undrained	-
	Unit Weight	19.6	kN/m ³
Strength Parameters	Ratio of Deformation Modulus / Undrained Shear Strength	500	-
	Poisson's Ratio	0.45	-
	Internal Friction Angle	0	degree
	Undrained Shear Strength	40	kPa
	Dilatancy Angle	0	degree
Spudcan Properties	Diameter	10	m
	Cone Angle	120	degree
	Surface Roughness Coefficient	0.5	-
	Cylindrical Height	5	m

RESULTS

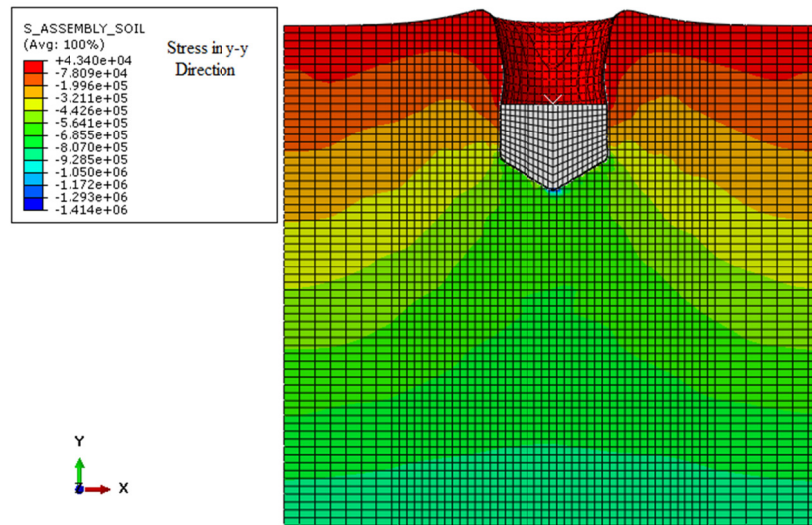
The numerical results are compared with the InSafeJIP results and parametric FE analyses are conducted for three different parameters:

- the size (diameter) of the spudcan,
- the undrained shear strength of the seabed soil
- the surface roughness of the spudcan

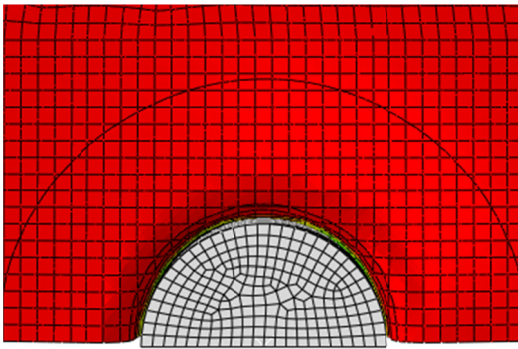
Figure 4 shows a typical vertical stress contour as the spudcan penetrates into seabed. The detailed results of all analyses can be found in Emren (2015). In Figure 4b top view of the spudcan can be seen, and in Figure 4c as the spudcan penetrates further and further into the soil, soil backfill flows onto spudcan. Penetration depth is one the main factors that affects the magnitude of the reaction forces developing on the spudcan as seen by Figure 5a. For clayey strata, as the cone penetrates deeper into the soil, vertical forces increase. This increase is sharper until the cone fully penetrates into soil, in other words, maximum cone diameter meets the mudline. After it reaches the mudline, and penetrates into the soil with constant diameter, the trend of the increase in the vertical reaction forces slows down. At the depth for which maximum diameter of cone is in contact with the ground, and at the critical cavity depth, there are sudden changes in the trend of the graphs. In Figure 5a, one can see these three changes in the trend of the graph based on InSafeJIP method. It is stated in InSafeJIP (Osborne et al., 2011) that these sudden changes occur more smoothly in practice.

Figure 5a shows the comparison of the bearing capacity values for 0.5 surface roughness of the spudcan in FE analyses and in InSafeJIP method. Up to the penetration depth of spudcan, both the guideline and FE methods give similar results. On the other hand, after that depth, InSafeJIP results start to underestimate the bearing capacity. In 3D FEM, the required penetration depth for a target bearing capacity of spudcan is less than that required by analytical method in InSafeJIP guideline.

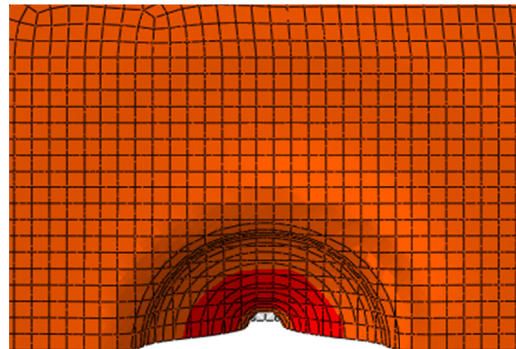
Figure 5b compares the effect of surface roughness on penetration behavior of spudcan in FE analyses. Surface roughness coefficient is one of the properties that governs the reaction forces on the spudcan (as it increases an increase in the bearing capacity is expected). This coefficient is affected by undrained shear strength of the soil, as well as the geometry and the material of the spudcan. Figure 5b shows that for fully smooth case ($\alpha = 0$), penetration resistance is smaller than the other two cases ($\alpha = 0.5$ and 1.0). Although, there is a slight difference between other two cases, they are very close to each other therefore the surface roughness is not playing a significant role in the penetration resistance. InSafeJIP (Osborne et al., 2011) suggested the use of $\alpha = 0.5$ for clayey soils unless there is information that enables the determination of it. Therefore, this may show that assumption of InSafeJIP about the roughness coefficient selection $\alpha = 0.5$ for clayey layers (unless there is no information provided) can be applicable.



(a)



(b)



(c)

Figure 4. (a) Vertical stress contours (b) top view of spudcan, as the spudcan penetrates into the seabed (c) top view after full penetration of the spudcan showing soil backflow onto spudcan.

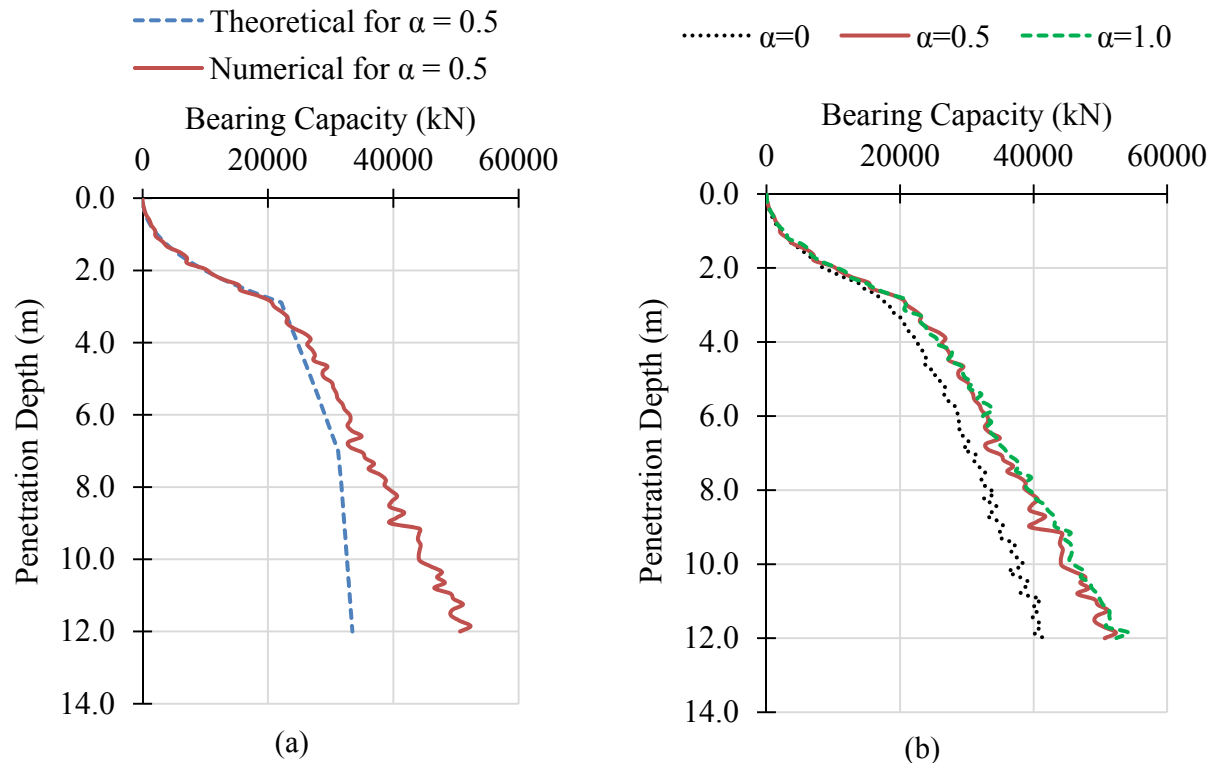


Figure 5. (a) Comparison of the FE model (numerical) and InSafeJIP (theoretical) results for $\alpha = 0.5$, (b) Comparison of different surface roughness values in FE model.

The effect of the changes in spudcan diameter and undrained shear strength on penetration resistance are demonstrated in Figure 6. It is inevitable that, the diameter of the spudcan will affect the bearing capacity significantly, as in the case of footing size effect for bearing capacity of the foundations of buildings. In this study, this effect, and its change with depth, is quantified by using four common spudcan diameters (ranging from 7.5 to 15 m) found in the literature (Figure 6a). The rest of the simulation parameters are kept constant at their given values in Table 1. For a constant cone angle (120 degrees), and constant spudcan cylindrical height (5 m), the change in the diameter results in an increase in the height of the cone, which means that when the cone of the foundation is fully penetrated into the soil, bearing capacity becomes larger than bearing capacity of smaller diameters.

The undrained shear strength can stay constant with depth or increase with depth in offshore clayey seabed (Emren 2015). In this study, constant undrained shear strength with depth is assumed. As the undrained shear strength of the clay increases, the bearing capacity increases, as expected. Figure 6b presents the change in bearing capacity with respect to embedment depth for different undrained shear strength. For a 4 times increase in c_u value, approximately 2 times increase in bearing capacity is calculated for a given depth of penetration (for c_u in the range of 20 and 80 kPa). For very soft clays, it may not be possible to reach to a desired target load unless diameter or other factors are changed as well. For softer clay, as compared to stiffer clays, critical cavity depth is shallower than the stiffer clays.

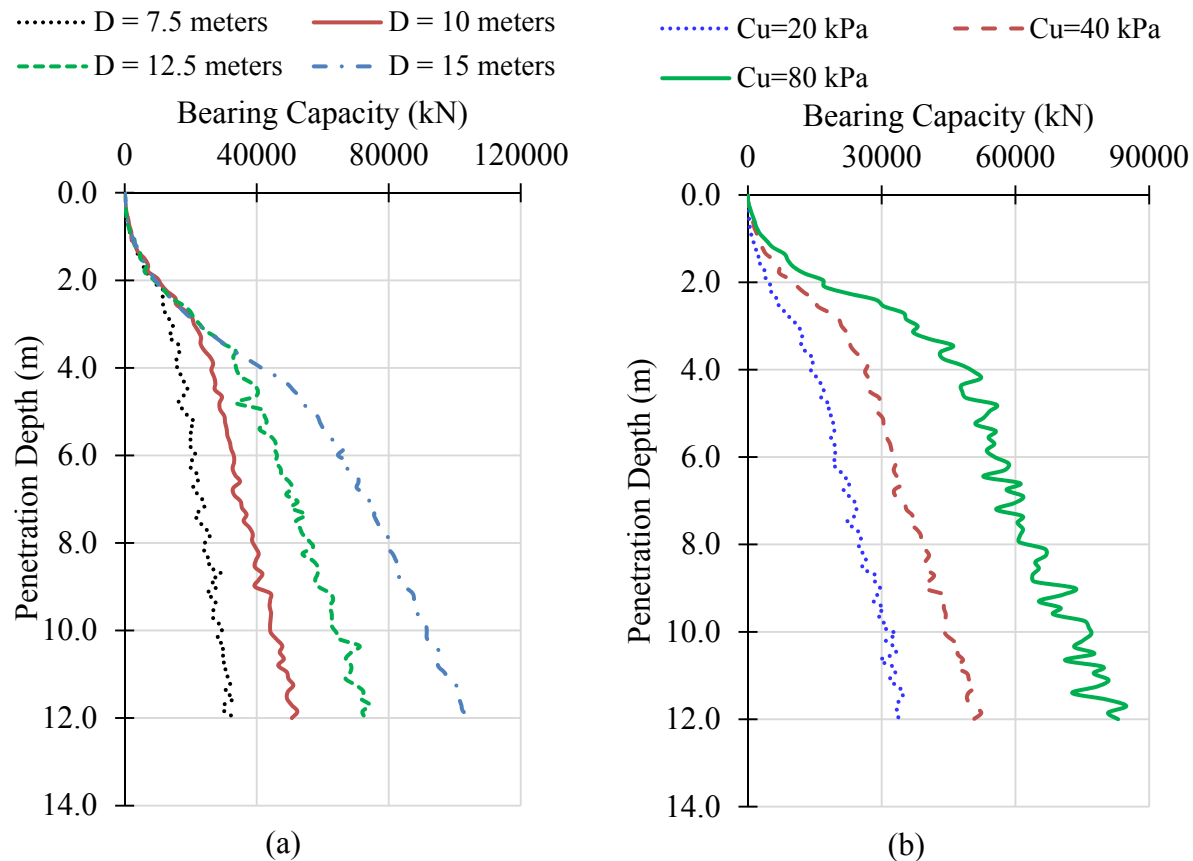


Figure 6. Bearing Capacity (kN) vs penetration depth (m) (a) for different cone diameters, (b) for Different c_u .

CONCLUSIONS

In this work, the penetration of a foundation (spudcan) for “jack-up rig”-type offshore oil platform into a uniform clayey seabed is studied with three-dimensional FE modeling using CEL method. The results of a FE analyses are compared with the InSafeJIP design guideline method. A systematic parametric study is conducted for three different parameters, and it shows their effects on the bearing capacity-penetration behavior of a spudcan. The results of this study is only valid for the spudcan geometry and soil properties used in this study. They should not be generalized. Investigation of the aforementioned factors and their effects can be beneficial for safe and economical design of spudcans. It should not be forgotten that, the key element with utmost importance is to have extensive and correct information and interpretation about the subsoil profile and their material properties.

REFERENCES

- Elkadi, A. S. K., Lottumand, H. van, & Luger, H. J. (2014). A 3D coupled Eulerian-Lagrangian analysis of the dynamic interaction of jack-up legs with the seabed. *Numerical Methods in Geotechnical Engineering*, 1255–1259.

- Emren, V. (2015), “Three Dimensional Finite Element Modeling For The Spudcan Penetration Into Clayey Seabed”, M.S. Thesis, METU Civil Engineering Department, July 2015
- Engin, H. K., Brinkgreve, R. B. J., & van Tol, F. (2015). Simplified numerical modelling of pile penetration – the press-replace technique. *International Journal for Numerical and Analytical Methods in Geomechanics*.
- Hossain, M. S., & Randolph, M. F. (2009). New Mechanism-Based Design Approach for Spudcan Foundations on Single Layer Clay. *Journal of Geotechnical and Geoenvironmental Engineering*, 135(9), 1264–1274.
- Maersk Interceptor. (n.d.). Retrieved from <http://www.maerskdrilling.com/en/drilling-rigs/jack-ups/maersk-interceptor>
- Martin, C. M., & Houlsby, G. T. (2003). Undrained bearing capacity factors for conical footings on clay. *Géotechnique*, 53(5), 513–520. <http://doi.org/10.1680/geot.2003.53.5.513>
- Osborne, J. J., Teh, K. L., Houlsby, G. T., Cassidy, M. J., Bienen, B., & Leung, C. F. (2011). “*InsafeJIP*” Improved Guidelines for the Prediction of Geotechnical Performance of Spudcan Foundations During Installation and Removal of Jack-Up Units. Surrey.
- SNAME. (2008). *Guidelines for Site Specific Assessment of Mobile Jack-Up Units*. Jersey City.
- Qiu, G., & Henke, S. (2011). Controlled installation of spudcan foundations on loose sand overlying weak clay. *Marine Structures*, 24(4), 528–550.
- Tho, K. K., Leung, C. F., Chow, Y. K., & Swaddiwudhipong, S. (2012). Eulerian Finite-Element Technique for Analysis of Jack-Up Spudcan Penetration. *International Journal of Geomechanics*, 12(1), 64–73.
- Yu, L., Hu, Y., Liu, J., Randolph, M. F., & Kong, X. (2012). Numerical study of spudcan penetration in loose sand overlying clay. *Computers and Geotechnics*, 46, 1–12.
- Zhang, Y., Wang, D., Cassidy, M. J., & Bienen, B. (2014). Effect of Installation on the Bearing Capacity of a Spudcan under Combined Loading in Soft Clay. *Journal of Geotechnical and Geoenvironmental Engineering*, (2013), 1–12.

Offshore Anchor Penetration in Sands—Granular Simulations

Nan Zhang, S.M.ASCE¹; and T. Matthew Evans, A.M.ASCE²

¹Research Assistant, School of Civil and Construction Engineering, Oregon State Univ., Corvallis, OR.

²Associate Professor, School of Civil and Construction Engineering, Oregon State Univ., Corvallis, OR. E-mail: matt.evans@oregonstate.edu

Abstract

Torpedo anchors are a viable approach for mooring marine hydrokinetic (MHK) energy devices to the seafloor. These anchors will serve to maintain station and to provide the reaction force for the MHK device. The ability of the anchor to perform these duties is a strong function of its penetration depth during installation. This is a large-strain problem not amenable to typical continuum numerical approaches. In the current work, we propose that the discrete element method (DEM) is a more appropriate tool to investigate the shallow penetration of torpedo anchors in sands. The effects of anchor mass, impact velocity, and anchor geometry are considered in the DEM simulations. The relative maximum penetration depths under these factors are quantified and presented in the paper. Comparisons are also made between DEM simulations and the empirical equation developed by Young (1967). Granular material response at the microscale during penetration are used to provide insight into system response.

INTRODUCTION

Offshore dynamically penetrated anchors (DPA), also called "torpedo" anchors or "rocket" anchors, are used for mooring deep water offshore facilities. They are constructed by a cone-tipped cylindrical steel pipe sections filled with concrete or scrap chain and have a pad eye at the top. DPA are penetrated into the seabed by the kinetic energy acquired during the free fall through the water. A mooring line is typically connected to the top of the anchor. The design of DPAs includes the estimation of embedment depth and holding capacities for both long-term and short term. Existing design methods are based on results from both experimental tests and numerical simulations. Physical experiments, including full-scale in situ testing and small-scale centrifuge models, have been performed by many researchers (e.g., True 1975; Freeman et al. 1988; Boguslavskii et al. 1996; Lieng et al. 1999, 2000; Ehlers et al. 2004; Audibert et al. 2006; Shahin and Jaksa 2006; Raie and Tassoulas 2009; O'Loughlin et al. 2013; Hossain et al. 2015). Most of these tests were performed in cohesive soils. The influence of impact velocity on embedment depth is the primary performance metric considered in these studies. The influence of anchor shape and anchor weight on penetration depth are often considered.

Relatively fewer experimental tests have been performed on anchor penetration in sandy soils. Only one instance was found in the literature of field tests on seafloor with sandy soils and cohesive soils on the Brazilian coast (Medeiros et al. 2002). Penetration depths in clay were found to be larger than in sandy soils for the same impact velocities. Projectile penetration tests on granular soils were performed mostly in military areas with very high impact velocities (≥ 300 m/s) (e.g. Pyrz et al. 1969; True 1975; Fragaszy et al. 1989; Taylor et al. 1991; Van Vooren et al. 2013). However, some other researchers focused on projectile penetration tests on granular soils with low

impact velocities (e.g. Young 1967; Wang 1969; Wang 1971). Factors such as projectile nose shape, projectile weight, gravity, and projectile body shape were considered. In practice, torpedo anchor self-weights ranging from 200 kN to 1000 kN, diameters ranging from 0.75 m to 1.2 m, and aspect ratios around 10 are reported in the literature (e.g. Medeiros et al. 2002; Ehlers et al. 2004). Impact velocities generally range from 10 to 25 m/s.

Numerical analyses of offshore anchor behavior have been performed by O'Beirne et al. (2015) to compare finite element method (FEM) results with field tests and investigate the soil response of different load inclinations during pullout. Raie and Tassoulas (2009) used computational fluid dynamics (CFD) to simulate soil behaviors under anchor penetration by approximating the soil as a fluid. Numerical analyses on cone penetration tests (similar to the mechanics of DPA) in crushable sands have also been performed (e.g., Ciantia et al. 2016), but analyses to investigate microscale soil performance in the vicinity of anchor penetration have not been reported previously. Considering seabed soil properties, 95% of seabed sediments off the Oregon coast are granular sands (Balster and Parsons 1966). In the current work, therefore, DEM is applicable to investigate the microscale response of DPAs in sandy soils.

The discrete element method (DEM) allows for the simulation of soils as a collection of individual particles and is increasingly being applied to a wide array of problems that involve granular materials in contact with geostuctures (e.g., Kress and Evans 2010; Evans and Kress 2011). DEM models predict emergent behavior in particulate assemblies based on simulation of independent particle behaviors. DEM has been previously used to study shear bands in sand, including free-field shearing (Jacobsen et al. 2007; Evans and Frost 2010; Zhao and Evans 2011; Frost et al. 2012) and also granular-continuum interface shearing (Dove et al. 2006; Kress and Evans 2010; Evans and Kress 2011; Zhang and Evans 2016). Overall, simulated material response from DEM simulations have been shown to be consistent with results from physical experiments for a variety of loading conditions (Zhao and Evans 2009; Evans and Frost 2010).

Anchor installation is the first step for deploying an offshore anchor system. In the case of DPAs for marine hydrokinetic (MHK) energy generators (e.g. wave energy converters (WEC) and tide energy converters (TEC)), anchors serve to keep devices on station and as the reaction force necessary for energy generation. The holding capacity of the anchors must bear the tensile force from ocean waves transmitted by mooring lines. The soil-anchor interface shear force as well as the anchor weight play major roles on the anchor holding capacity. Typically, the deeper the embedment, the higher the holding capacity. Apart from the properties of the seabed soils, the anchor properties (e.g., anchor weight) are combined to determine the holding capacity and allowable reaction force for a given anchor design. Much of the previous work on DPA has focused on FEM analyses, CFD analyses, or limit equilibrium solutions and are only applicable to clay sediments (Lieng et al. 2000; Raie and Tassoulas 2009; O'Loughlin et al. 2013; O'Beirne et al. 2015). However, both of these approaches neglect much of the fundamental physics occurring at the anchor-soil interface or do not consider DPAs embedded in sandy soils. This work uses DEM simulations to evaluate the response of DPA penetration into sandy soils.

DEM SIMULATIONS

Prior installation of dynamically penetrated anchors and projectile penetration tests have focused on factors like the impact velocities, nose and shaft shapes, and anchor or projectile weights and their influences on the penetration depths. The simulations below focus on similar effects on the penetration depths in a small scale and explore the microscale responses during penetration.

The geometry of the DEM model of the DPA installation is shown in Figure 1. The assembly consists of a collection of polydisperse spheres intended to simulate sandy soil specimen and larger particle bonded stick-like clump to simulate a DPA. The dimensions of the granular assembly are defined as functions of median particle size d_{50} . Figure 1 shows one penetration state when the DPA has already penetrated into the granular assembly. Mass scaling (e.g., Belheine et al. 2009; Evans and Valdes 2011) is employed to decrease simulation time; as such, the mean particle diameter is $d_{50} = 0.5$ m and other model dimensions are scaled accordingly. Specifically, model width (W), length (L), and height (H) can be expressed in terms of d_{50} as $W/d_{50} = 40$, $L/d_{50} = 40$, and $H/d_{50} = 60$, respectively. The diameter of the DPA is $D = 0.1L = 4d_{50}$. Material and model parameters are shown in Table 1.

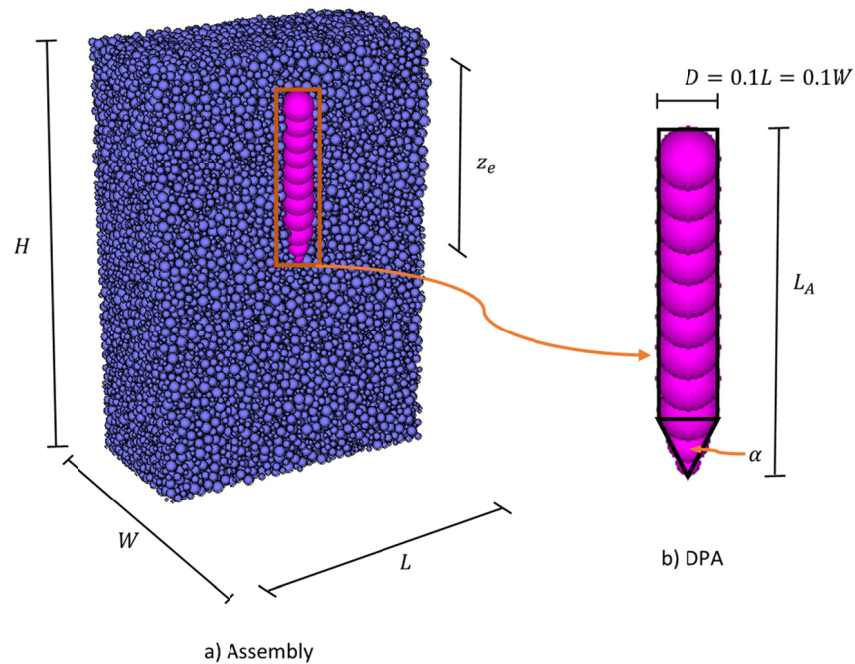


Figure 1. DEM model for DPA penetration.

A scaled gravity value is assigned for the simulation to balance the resultant gravitational force results from mass scaling. The specimen is consolidated in the assigned gravity to equilibrium by cycling the granular assembly to a state where the average unbalanced force in the assembly is less than 1% of the average contact force. This as-consolidated void ratio can be adjusted by varying the particles' and walls' friction coefficients during consolidation, with a higher friction value resulting in a looser specimen. Note that $\mu_c \in [0, \mu]$ where μ_c is the friction coefficient used during consolidation and μ is the actual particle friction coefficient. After consolidation, particle friction can be adjusted to assess the effects of particle friction on pullout resistance. Once the specimen is consolidated and equilibrated, the DPA is generated with anchor tip right above the specimen and released by assigning a negative vertical constant velocity to simulate the impact velocity in practice. Particle motion in the assembly is damped to dissipate excess energy; however, the damping ratio of the clump (i.e., the DPA) is set to be zero to model free fall. Penetration is considered complete when the anchor vertical velocity is very small relative to the impact velocity and close to the mean particle velocity. This velocity is defined as

the ending velocity. The interface shearing force is obtained by measuring the out-of-balance force on the clump. The simulations discussed herein consist of approximately 84,000 particles; one simulation requires roughly five days to complete on an Intel Xeon E5-2660v3 processor on Windows Server 2012.

Table 1. Material and model properties (baseline).

	Parameters	Value
Particles	Maximum diameter, d_{max} [m]	0.75
	Minimum diameter, d_{min} [m]	0.25
	Normal stiffness, k_n [N/m]	1×10^8
	Shear stiffness, k_s [N/m]	8×10^7
	Friction coefficient, μ []	0.31
	Density, ρ_s [kg/m ³]	2650
Model	Height, H [d_{50}]	60
	Width, W [d_{50}]	40
	Length, L [d_{50}]	40
	Initial porosity []	0.426
DPA	Normal stiffness, k_{sn} [N/m]	1×10^8
	Shear stiffness, k_{ss} [N/m]	8×10^7
	Density, ρ_a [kg/m ³]	1×10^5
	Diameter, D [d_{50}]	4

PARAMETRIC ANALYSIS

Twenty-three simulations were performed to investigate the influence of impact velocity, anchor shape, and anchor weight on penetration depth. The first set focuses on impact velocities, which range from 5 m/s to 25 m/s. The second set focuses on the anchor shapes by changing the number of particles in the anchor shaft from 1 to 8, and the last set focuses on anchor weight by changing the anchor particle density from 0.1 to $1.0\rho_a$, where ρ_a is the baseline anchor particle density. Other parameters are kept constant when focusing each of the above three sets. Relative penetration depths for different impact velocities are investigated, where the relative penetration depth is defined as the tip penetration over the anchor length as z_e/L_a (where z_e is anchor tip penetration depth, L_a is anchor length).

In practice, the anchor density is designed to be much larger than the soil density. For the simulations, the anchor particle density is set to be larger than the particle density of granular assembly, see Table 1. At the given volume, the anchor weight can be altered by modifying the anchor particle densities. Anchor shape (specifically, aspect ratio) in the simulations can be described by changing the number of particles in the anchor shaft.

Comparison will be made between DEM models and the empirical equation developed by Young (1967) through dozens of experimental tests. For impact velocities less than 60 m/s:

$$P_m = 0.53SN \frac{W^{\frac{1}{2}}}{A} \ln(2 \times 10^{-5} V_0^2 + 1) \quad (1)$$

where P_m is the penetration depth, W is the weight, A is the area, V_0 is the impact velocity, and S and N are both constants related to the soil properties. According to Young (1967), N is nose performance coefficient which is equal to 0.45 and S is a soil constant equal to 5 for a sandy soil.

RESULTS AND DISCUSSION

Figure 2 shows the anchor velocities along with penetration depth normalized by the diameter of the anchor under different impact velocities. It is clear that higher impact velocities result in higher velocities at the same normalized penetration depth (z_e/D). The velocity of real soil particles in a static state is zero. However, the velocity of particles in DEM simulations are never identically zero due to numerical vibrations in the system. Thus, the velocity of the anchor penetrated into the granular assembly will not be zero even at the equilibrium state. For the simulations, an ending velocity at which the simulation will be terminated should be specified. The ending velocity for all the simulations reported herein was set as 1 m/s. The maximum penetration depths are the anchor tip penetration depths when the vertical anchor velocity equals the ending velocity. The anchor with the highest velocity has the largest kinetic energy. It will take longer to release its kinetic energy. The penetration depth will be larger as a result.

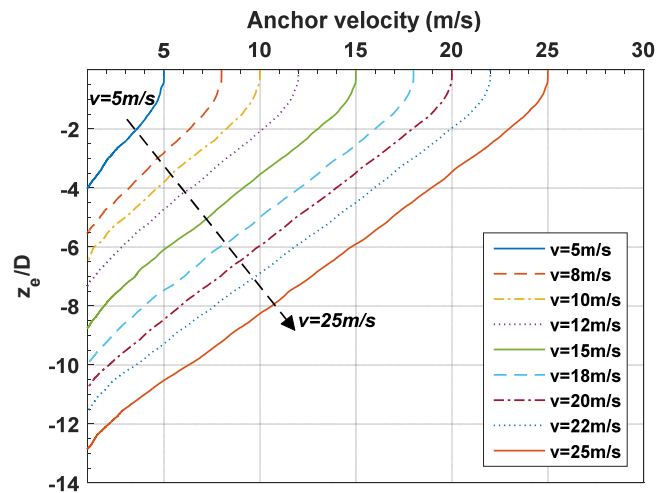


Figure 2. Anchor velocity profile during penetration under different impact velocities.

Maximum penetration depths under different impact velocities are shown in Figure 3(a) below. The maximum penetration depths are normalized by the anchor length L_a as the relative penetration depth. Results can be found that the higher the impact velocity, the higher the maximum penetration depth. The negative symbol in Figure 3 means the direction relative to the surface. The maximum tip penetration depths at higher impact velocities ($v = 22$ m/s and 25 m/s) are more than twice the length of the anchor. However, the value for lower impact velocities are near the length of the anchor.

Another factor that affects penetration is anchor weight. The anchor weight can be calculated from multiplying anchor density by anchor volume. Figure 3(b) shows the maximum relative penetration depth as a function of normalized anchor weight. Normalized anchor weight is defined as the ratio of anchor weight to the anchor weight at baseline. The impact velocity is set as 20 m/s. Simulation results show that the higher the anchor weight, the larger the maximum relative penetration depth. Maximum penetration depth increases approximately linearly with anchor weight.

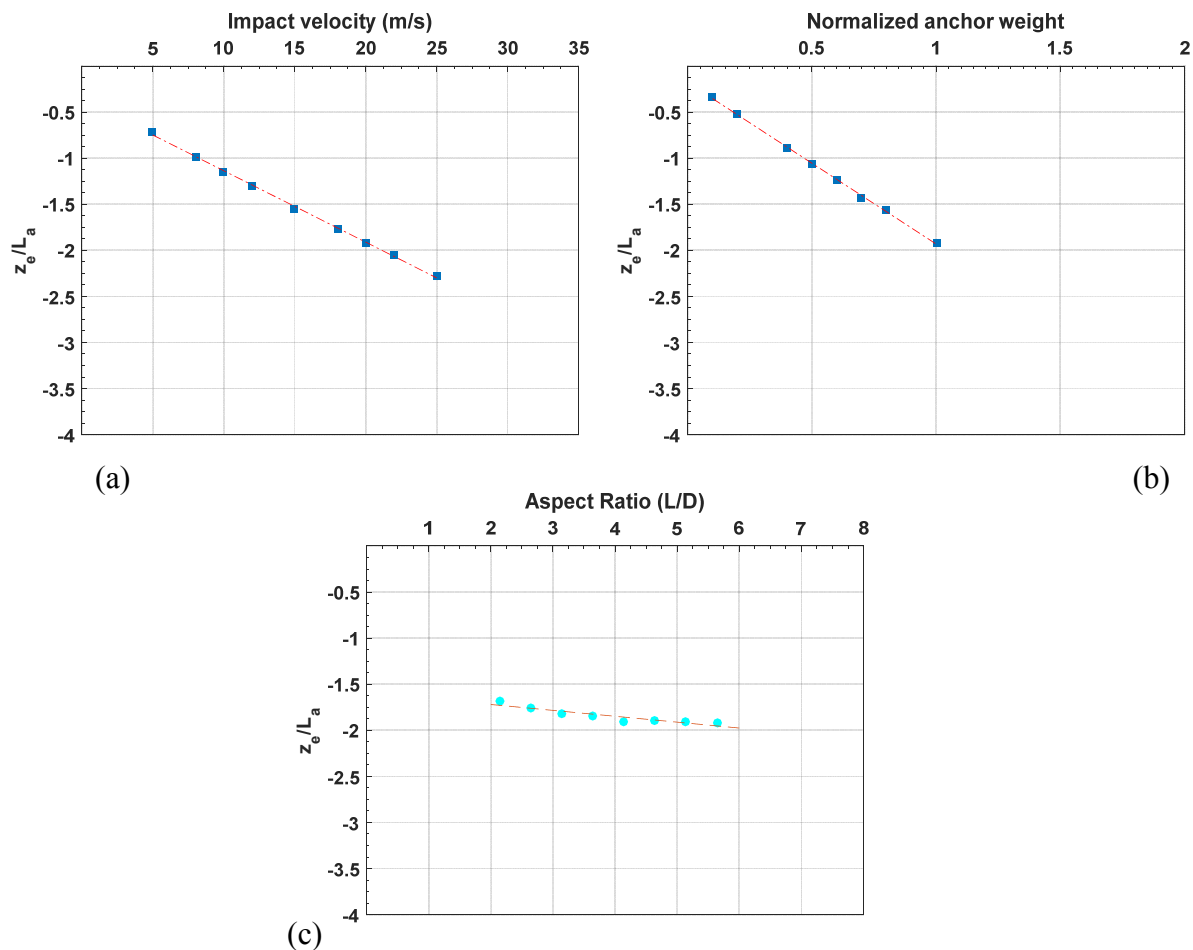


Figure 3. Maximum relative penetration depth under a) different impact velocities, b) under different normalized anchor weights, and c) under different anchor aspect ratios.

Anchor shape (aspect ratio) ranges from 2.14 to 5.64 in the simulations. Figure 3(c) shows the maximum relative penetration depth for different anchor aspect ratios. The maximum relative penetration depths vary over a narrow range (i.e. from 0.7 to 2.0). These results support the idea that anchor shape has less significance than anchor impact velocity and anchor weight.

Figure 4 shows one penetration state of the granular assembly. The left figure shows the particle impact responses and the right figure shows the particle velocity vectors at this state. Particles at the surface are disturbed the most. The particles are jumping up to flow away from the assembly and then will return to the assembly under gravity, see the left side of Figure 4. Particles around the anchor tip are also highly disturbed, as shown in the right side of Figure 4.

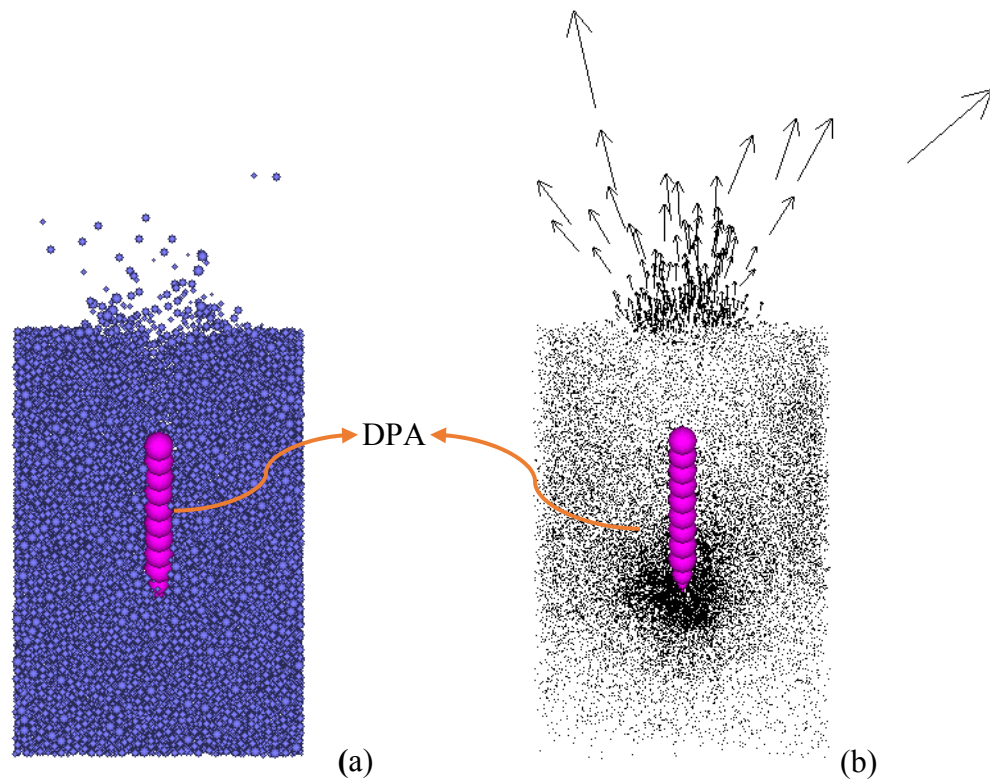


Figure 4. Velocity vectors of particles during penetration

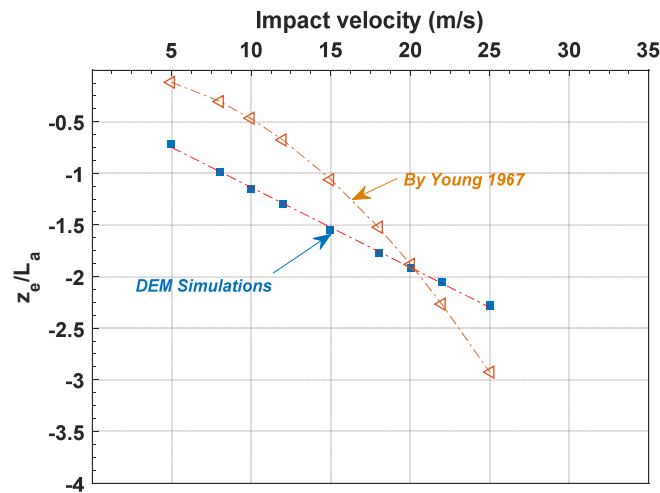


Figure 5. Comparison between DEM simulation and empirical equation developed by Young (1967).

Figure 5 shows the maximum relative penetration depth comparisons between DEM simulations and the results obtained from Equation 1. Comparing to Young (1967), DEM simulations give a linear relationship while the empirical equation gives a nonlinear one. The penetration depths are aggressive and conservative at lower and higher impact velocities, respectively, compared to the Young (1967) empirical equation.

Contact number, which is the number of points that particles touch with each other among the granular assembly, is a basic measure of the statistical state of a granular material at the particle-scale. Typically, the larger the number of contacts between a granular assembly and an interface (e.g., anchor), the more stable the fabric will be. The lower the contact numbers, the higher the disturbance the granular assembly will be. Thus, the number of contacts is directly related to the forces transmitted from interface (anchor surface) to the granular assembly. Figure 6 shows the contact numbers during penetration under different impact velocities, different aspect ratios and different density, respectively. Contact numbers are normalized by the initial contact numbers (the value before penetration). The maximum percentage of contact number loss under all the three conditions are around 23%. Penetrations result in the contact losses with a large percentage, even at the end of penetration, ~15%. Contact losses make the granular assembly less stable. Penetration depths and contact numbers influence the holding capacity of DPA: deeper penetrations result in larger lateral earth pressure and higher contact numbers.

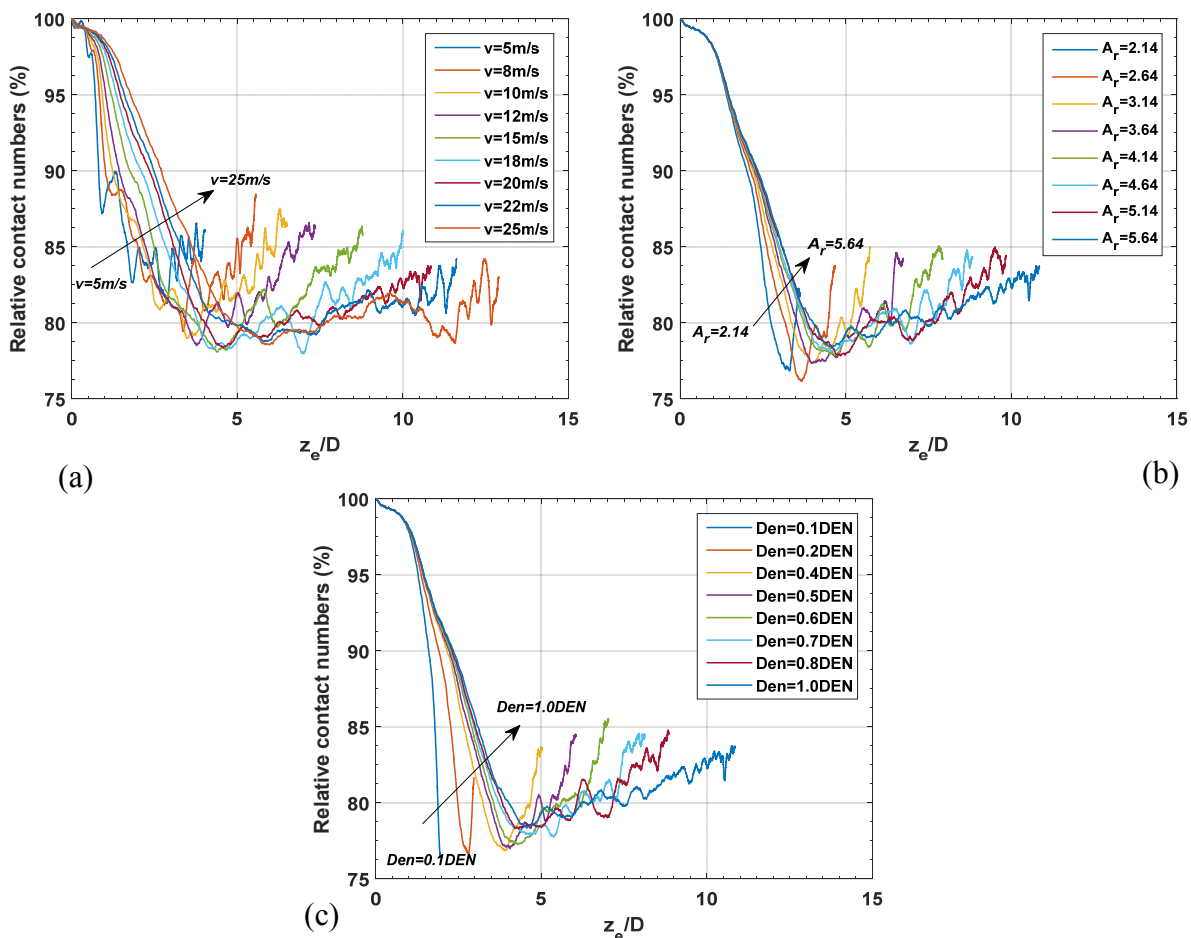


Figure 6. Contact numbers along with normalized penetration.

CONCLUSIONS

DEM simulations were performed to investigate the influences of anchor penetration velocity, anchor shape, and anchor weight on penetration behavior. Anchor velocity profiles for different

impact velocities were generated and maximum penetration depths under three different conditions are presented. The primary findings from this preliminary research are as follows:

- 1.) Under the same anchor weight and anchor shapes, the higher the anchor impact velocity, the higher the maximum penetration depth. The maximum relative penetration depth is around twice the anchor length.
- 2.) Maximum relative penetration depth increases linearly with the increase of impact velocity and anchor weight. The anchor aspect ratio has less significance on the penetration depth than impact velocity and anchor weight.
- 3.) DEM simulation results are aggressive and conservative at low and high impact velocities compared to empirical prediction.
- 4.) The penetration disturbs the particles at the soil surface and around the anchor tip. Particle contact loss is generally no more than 23%. The residual losses are around 15% compared to initial.

ACKNOWLEDGMENTS

This material is based upon work supported by the Department of Energy under Award Number DE-FG36-08GO18179. This report was prepared as an account of work sponsored by an agency of the United States Government. Neither the United States Government nor any agency thereof, nor any of their employees, makes any warranty, expressed or implied, or assumes any legal liability or responsibility for the accuracy, completeness, or usefulness of any information, apparatus, product, or process disclosed, or represents that its use would not infringe privately owned rights. The views and opinions of the authors expressed herein do not necessarily state or reflect those of the United States Government or any agency thereof.

REFERENCES

- Audibert, J.M., Movant, M.N., Jeong-Yun, W., and Gilbert, R.B. (2006). Torpedo piles: laboratory and field research. In *The Sixteenth International Offshore and Polar Engineering Conference*. International Society of Offshore and Polar Engineers.
- Balster, C. A., and Parsons, R. B. (1966). *A soil-geomorphic study in the Oregon Coast Range*. Corvallis, OR: Agricultural Experiment Station, Oregon State University.
- Belheine N., Plassiard J.P., Donze F.V., Darve F. and Seridi A. (2009). Numerical simulation of drained triaxial test using 3D discrete element modeling. *Computers and Geotechnics*, 36(1-2), 320-331.
- Boguslavskii, Y., Drabkin, S., and Salman, A. (1996). Analysis of vertical projectile penetration in granular soils. *Journal of Physics D: Applied Physics*, 29(3), 905.
- Ciantia, M. O., Arroyo, M., Butlanska, J., and Gens, A. (2016). DEM modelling of cone penetration tests in a double-porosity crushable granular material. *Computers and Geotechnics*, 73, 109-127.
- Dove, J. E., Bents, D. D., Wang, J., and Gao, B. (2006). Particle-scale surface interactions of non-dilative interface systems. *Geotextiles and Geomembranes*, 24(3), 156-168.
- Ehlers, C.J., Young, A.G., and Chen, J.H. (2004). Technology assessment of deepwater anchors. In *Offshore technology conference*. Offshore Technology Conference.

- Evans, T.M., and J.D. Frost. (2010). "Multiscale Investigation of Shear Bands in Sand: Physical and Numerical Experiments," *International Journal for Numerical and Analytical Methods in Geomechanics*, 34(15), pp. 1634-1650.
- Evans, T.M. and J.G. Kress. (2011). "Discrete simulations of particulate-structure interactions," ASCE GeoFrontiers 2011, *Geotechnical Special Publication No. 211: Advances in Geotechnical Engineering*, Dallas, TX, pp. 4252-4262.
- Fragaszy, R.J., and Taylor, T.A. (1989). Centrifuge Modeling of Projectile Penetration in Granular Soils (NO. ESL-TR-88-76). Dept. of Civil and Environmental Engineering, Washington State University, Pullman.
- Freeman, T. J., Murray, C. N., and Schuttenhelm, R. T. E. (1988). The Tyro 86 penetrator experiments at Great Meteor East. In *Oceanology'88: Proceedings of an international conference*. Society of Underwater Technology.
- Frost, J.D., T.M. Evans, Y. Lu, and X. Zhao. (2012). Selected observations from 3-D experimental and numerical studies of shear banding in biaxial shear tests. ASCE Geo-Congress 2012, *Geotechnical Special Publication No. 225: State of the Art and Practice in Geotechnical Engineering*, Oakland, CA, pp. 1116-1125.
- Hossain, M. S., O'Loughlin, C. D., and Kim, Y. (2015). Dynamic installation and monotonic pullout of a torpedo anchor in calcareous silt. *Géotechnique*, 65(2), 77-90.
- Jacobson, D.E., J.R. Valdes, and T.M. Evans. (2007). A numerical view into direct shear specimen size effects. *ASTM Geotechnical Testing Journal*, 30(6), pp. 512-516.
- Kausel, E. (2010). Early history of soil-structure interaction. *Soil Dynamics and Earthquake Engineering*, 30(9), 822-832.
- Kress, J.G. and T.M. Evans. (2010). Analysis of pile behavior in granular soils using DEM. *Proceedings of the 35th Annual Deep Foundations Institute Annual Conference*, Hollywood, CA, October 12-15.
- Lieng, J. T., Hove, F., and Tjelta, T. I. (1999). Deep Penetrating Anchor: Subseabed deepwater anchor concept for floaters and other installations. In *The Ninth International Offshore and Polar Engineering Conference*. International Society of Offshore and Polar Engineers.
- Lieng, J.T., Kavli, A., and Tjelta, T.I. (2000). Deep penetrating anchor: further development, optimization and capacity clarification. Presented at the *10th International Offshore and Polar Engineering Conference*, International Society of Offshore and Polar Engineers.
- Medeiros Jr, C. J. (2002). Low cost anchor system for flexible risers in deep waters. In *Offshore Technology Conference*. Offshore Technology Conference.
- O'Beirne, C., O'Loughlin, C.D., Wang, D., and Gaudin, C. (2015). Capacity of dynamically installed anchors as assessed through field testing and three-dimensional large-deformation finite element analyses. *Canadian Geotechnical Journal*, 52(5), 548-562.
- O'Loughlin, C., Richardson, M.D., Randolph, M.F., and Gaudin, C. (2013). Penetration of dynamically installed anchors in clay. *Géotechnique*, 63(11), 909-919.
- Pyrz, A.P. (1969). Gravity Effects on Low Velocity Penetration of a Projectile into a Cohesionless Medium (No. GSF/MC/69-6). MS Thesis, Air Force Institute of Technology, Wright-Patterson AFB, OH.
- Raie, M.S., and Tassoulas, J.L. (2009). Installation of torpedo anchors: numerical modeling. *Journal of Geotechnical and Geoenvironmental Engineering*, 135(12), 1805-1813.

- Shahin, M. A., and Jaksa, M. B. (2006). Pullout capacity of small ground anchors by direct cone penetration test methods and neural networks. *Canadian Geotechnical Journal*, 43(6), 626-637.
- Taylor, T., Frigaszy, R.J. and Ho, C.L. (1991). Projectile penetration in granular soils. *Journal of Geotechnical Engineering*, 117(4), 658-672.
- True, D.G. (1975). Penetration of projectiles into seafloor soils (No. CEL-TR-822). Civil Engineering LAB (NAVY) Port Hueneme CA.
- Van Vooren, A., Borg, J., Sandusky, H., and Felts, J. (2013). Sand Penetration: A Near Nose Investigation of a Sand Penetration Event. *Procedia Engineering*, 58, 601-607.
- Wang, W.L. (1969). Experimental study of projectile penetration in Ottawa sand at low velocities. *Journal of Spacecraft and Rockets*, 6(4), 497-498.
- Wang, W.L. (1971). Low velocity projectile penetration. *Journal of the Soil Mechanics and Foundations Division*, 97(12), 1635-1655.
- Young, C.W. (1967). The Development of Empirical Equations for Predicting Depth of an Earth-Penetrating Projectile. Rep. SC-DR-67-60, Sandia. Laboratories, May.
- Zhang, N. and Evans, T.M. (2016). "Towards the Anchoring of Marine Hydrokinetic Energy Devices: Three-Dimensional Discrete Element Method Simulations of Interface Shear." *Geo-Chicago 2016*: pp. 503-512. doi: 10.1061/9780784480137.048
- Zhao, X. and T.M. Evans. (2009). "Discrete Simulations of Laboratory Loading Conditions," *International Journal of Geomechanics*, 9(4), pp. 169-178.
- Zhao, X. and T.M. Evans. (2011). "Numerical Analysis of Critical State Behaviors of Granular Soils Under Different Loading Conditions," *Granular Matter*, 13(6), pp. 751-764.

Drop Weight Dynamic Load Testing for Construction Monitoring and Quality Control of Offshore Drilled Foundations

Seth O. Robertson¹ and Samuel G. Paikowsky, Sc.D.²

¹Doctoral Candidate, Dept. of Civil and Environmental Engineering, Geotechnical Research Laboratory, Univ. of Massachusetts Lowell, 1 University Ave., Lowell, MA 01854; GeoDynamica, Inc., 170 Morton St., Newton, MA 02459. E-mail: Seth@GeoDynamica.com

²Professor, Dept. of Civil and Environmental Engineering, Geotechnical Research Laboratory, Univ. of Massachusetts Lowell, 1 University Ave., Lowell, MA 01854; GeoDynamica, Inc., 170 Morton St., Newton, MA 02459. E-mail: Sam@GeoDynamica.com; Samuel_Paikowsky@uml.edu

Abstract

High strain drop weight dynamic load testing is an effective tool when evaluating the construction quality and axial capacity of offshore drilled deep foundations. This is a result of the complexity and cost of the alternative conventional static load tests. Drop weight systems can be designed for project specific needs, providing sufficient energy to mobilize the required resistance while permitting ease in transporting the device. Test shafts/piles can be instrumented and analyzed using the same dynamic testing techniques used for driven pile foundations. A case study is presented where drop weight dynamic load tests were utilized for offshore drilled shaft foundations. The project includes the design, construction, and quality control for a cement unloading pier at the Tema port in Ghana, Africa. The foundations are unique, consisting of 0.8m outer diameter steel pipes embedded in 1.0m rock-socketed drilled shafts. Three dynamic load tests to failure and six load verification tests were performed offshore. The load verification tests were carried out due to construction difficulties and/or complex subsurface conditions. The piles' integrity and mobilized resistances were assessed using the signal matching analysis software CAPWAP. The underlying assumptions in the one-dimensional wave equation formulation on which CAPWAP is based are violated in these complex cases. Finite element analyses were therefore performed using the PLAXIS 2D software in order to examine the validity of the one-dimensional wave equation application under such conditions. This paper briefly describes the project, the associated difficulties, the unique foundations, example load tests and their analyses, as well as some initial processing in examining the validity of the one-dimensional wave equation analyses under the tested conditions.

INTRODUCTION

Due to the way drilled deep foundations are constructed, their structural integrity and geotechnical capacity can be highly variable. Drop weight systems are used to dynamically test the capacity and integrity of drilled deep foundations (e.g. drilled shafts and caissons). These tests are especially important for high capacity piles (design load over 10.0MN) for which static load tests are either very expensive or physically difficult to conduct, in particular for offshore foundations. The drop weight devices can be designed for project specific conditions and can be

applied to in-place constructed foundations ranging from high capacity drilled shafts to low capacity micropiles e.g. Hajduk et al. 2005, Paikowsky et al. 2006, and Paikowsky 2013. Overall, the advantages of the tests include high mobility, short testing time, low cost relative to static load tests (allowing multiple tests at a single site), and integrity/construction quality evaluation concurrent with capacity determination (Paikowsky et al. 2006).

A typical drop weight system consists of four components: a frame and/or a guide for the drop weight (ram), the ram, a trip mechanism to release the ram, and a striker plate with or without a cushion. The testing entails the impact of a mass with the pile top. As such, large variation of device possibilities exists ranging from an undesirable non-guided drop of a mass by a crane to a well-designed guided system of varying ram weight and stroke, including a driving system (capblock, striking plate, cushion) at the pile's top. Review of drop weight systems which were assembled locally (and at times are site specific) are presented by Paikowsky et al. (2004).

Conventional numerical methods used for dynamic analysis of driven foundations are implemented for pre-test modelling and post-test interpretations. Strain transducers and accelerometers mounted near the pile top record the acceleration and strain caused by the passing stress-wave utilizing available PDAs (Pile Driving Analyzers). The force and velocity at the gauges' location and associated calculated values (e.g. energy) are then computed. The computer software GRL Wave Equation Analysis Program (WEAP) and the signal matching software Case Pile Wave Analysis Program (CAPWAP) by Pile Dynamics, Inc. are often used for pre-test evaluation and post-test interpretation of these field measurements, respectively. These software programs are based on the numerical solution of the one-dimensional wave equation (1-D WE). The CAPWAP signal matching technique has been shown to provide very accurate predictions for uniform driven and drilled foundations' axial capacity (Paikowsky et al. 2004; Paikowsky et al. 2006).

The 1-D WE is developed under the assumption of an elastic wave travelling in a slender uniform body (e.g. Timoshenko and Goodier 1951). The use of these methods for irregularly shaped and/or non-uniform piles where the underlying assumptions are violated is questionable. Paikowsky and Chernauskas (2008) demonstrated the limitation of the 1-D WE solution when applied, for example, to plugged pipe piles and proposed an alternative solution considering the complex wave propagation in such case. Finite element (FE) models have been implemented in this study to assess the validity of the 1-D WE analysis when applied to the dynamic measurements of deep foundations under non-uniform cross-sections.

CASE STUDY: TEMA PORT PIER, GHANA, AFRICA

Overview. Drop weight dynamic load tests were used for the design, construction, and quality control of a Perpendicular Bulk Unloading (PBU) pier in Tema Port, Ghana, Africa. The pier is supported by complex, non-uniform drilled foundations. The dynamic load tests were carried out offshore and the shafts' integrity and mobilized resistances were assessed using the signal matching analysis software CAPWAP.

The Tema Port PBU was a design/build project by Amandi Corp. of Switzerland. GeoDynamica, Inc. of Newton, MA provided the foundations' design, drop weight design, testing, and construction monitoring. The construction was completed in May 2016 and is comprised of a 50x455m structure supported on drilled shafts. The pier was constructed in two phases; Phase I modules of 20 bents and Phase II modules of 50 bents. Most pier bents are supported by seven (7) drilled shafts, resulting in 142 and 350 foundations along Phase I and II modules, respectively. Figure 1 displays an aerial photograph of the completed pier construction.

Foundation Design. Reliability Based Design (RBD) was adopted for the foundation design, primarily adhering to the AASHTO LRFD (American Association of State Highway and Transportation Officials Load and Resistance Factor Design) utilizing the NCHRP Report 507 (Paikowsky et al. 2004). The selected foundation scheme for both construction phases consists of drilled shafts 1.0m in diameter with the load from the pier to the shaft carried by an embedded 81.3cm outer diameter (OD) steel pipe (wall thickness, w.t. = 15.5mm). The axial factored design load ranges from 4,726 to 8,863kN and are consistent along each of the pier rows. The drilled foundations along Phase I construction modules were designed with a 2.0m depth rock socket in competent rock ($RQD > 50\%$) to adequately resist the 8,863kN maximum design load transferred from the super structure via the steel pipe elements. Figure 2 displays the general drilled shaft design scheme with respect to a typical subsurface profile along Phase I. Due to the residual Gneiss subsurface conditions, large site variability exists with significant variation in the depth to competent rock. As a result, the project required a location specific subsurface drilling and foundation design along the Phase II construction modules.

Subsurface Conditions. The subsurface investigation included 464 rock core borings. Ten (10) borings included Standard Penetration Tests (SPT) and were carried out at locations where better assessment of the upper residual soils was necessary. The subsurface generally consists of residual soils overlying Gneiss rock of varying degree of decomposition across the site. The quality of the rock overall decreases with depth as the distance from the shoreline increases. Visual and quantitative examination of the rock coring samples, based on Rock Quality Designation (RQD) values, led to subcategorization of the Gneiss into three (3) major layers: Completely Weathered Rock (CWR) with $RQD < 30\%$, Moderately Weathered Rock (MWR) with $30\% \leq RQD < 50\%$, and Slightly Weathered Rock (SWR) $RQD \geq 50\%$.

The mean sea-level elevation is located at 0.0m NLD (National Level Datum). The seabed is typically between -8.0 to -10.0m NLD. The maximum drilled shaft tip elevation for design purposes was restricted to -30.0m NLD due to limitations in the drilling equipment and barges for the given water depths.

Dynamic Load Testing. A drop weight device was designed by GeoDynamica, Inc. The machining of the elements was performed in the Netherlands and the assembly on site.



Figure 1. Tema Port PBU Pier aerial photograph of the completed pier construction (photograph courtesy of Amandi Corp.).

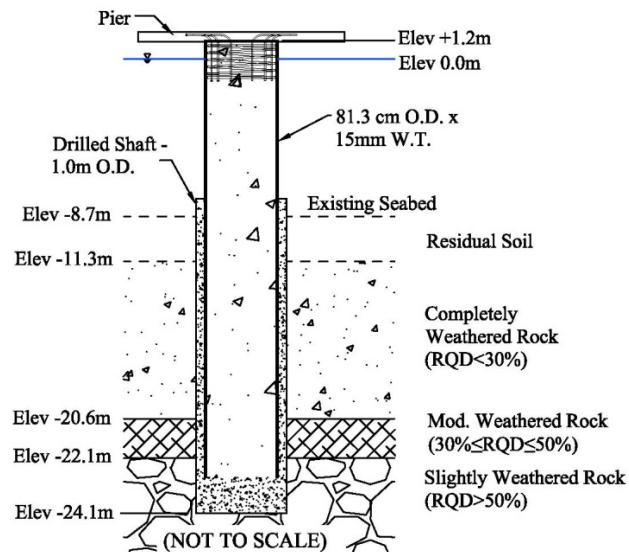


Figure 2. General drilled shaft design scheme in reference to a typical Phase I subsurface profile (GeoDynamica, Inc. 2013).

Drop weight dynamic load tests were integrated in the design process in order to address (i) nominal axial capacity and mobilized resistances along the variable subsurface conditions and (ii) the load transfer mechanisms of the complex, non-conventional non-uniform foundations. The Tema Port PBU Pier dynamic load test program included load tests to failure on three (3) sacrificial piles and non-destructive load verification (i.e. proof) tests on six (6) production piles. A proof test is carried out to mobilize or exceed the design load (e.g. 1.25 times the design load) without damaging the pile or achieving bearing capacity. Figure 3 displays a photograph of the mounted drop weight device during a drop weight test.



Figure 3. Photographs of the mounted drop weight device for offshore dynamic load tests (GeoDynamica, Inc. 2015b).

The complete details of the testing program and the extensive results are beyond the scope of the present paper. Only the results of a verification load test on Pile C-47 are provided as an example. Pile C-47 was selected for the load testing program due to problematic subsurface conditions and high loading demands along the pier row C (i.e. factored $DL = 8,863\text{kN}$). The pile was constructed within a predominantly completely weathered rock with $RQD = 0\%$ and negligible rock core recoveries. The dynamic tests were carried out prior to the completed pile construction, whereas the steel tube was filled with concrete to the seabed level only. A pre-test analysis examined the test plan for the ram weight, stroke, resistance and stress combination. A total of seven (7) impacts (blows) were applied and four (4) signal matching analyses were carried out using one of the recorded impacts. The different analyses refer to the various possibilities of modeling the pile geometry and the pile-subsurface interaction, for example:

- a. Accurately depicting the reported change in cross sections along the pile, including the steel pipe embedded in concrete (81.3cm OD) and the drilled shaft section (1.0m OD) where full compatibility between the steel and concrete was assumed.
- b. Variations of wave speed propagation, examining the steel wave speed that was relevant to the point of measurement versus a weighted wave speed considering the elastic properties of all the sections along the pile.

All analyses resulted with capacities varying in a relatively narrow range between 9,155kN to 9,436kN. Figure 4 presents the signal matching results of the analyses considering a changed cross section with a resulting capacity of 9,155kN. The designated mobilized resistance in C-47 was 9,250kN, which is 1.04 times the 8,863kN factored design load. The test validated the ability of C-47 to carry the designated loads. As the loading during the proof test did not arrive to the lower part of the foundation, the anticipated failure load (based on other piles tested to failure and load distribution) was evaluated to be significantly higher than the factored design load, comfortably accommodating a resistance factor of 0.65. The test demonstrated that the construction within a predominantly completely weathered rock with negligible recovery is capable of mobilizing sufficient resistance to stand by the load demand.

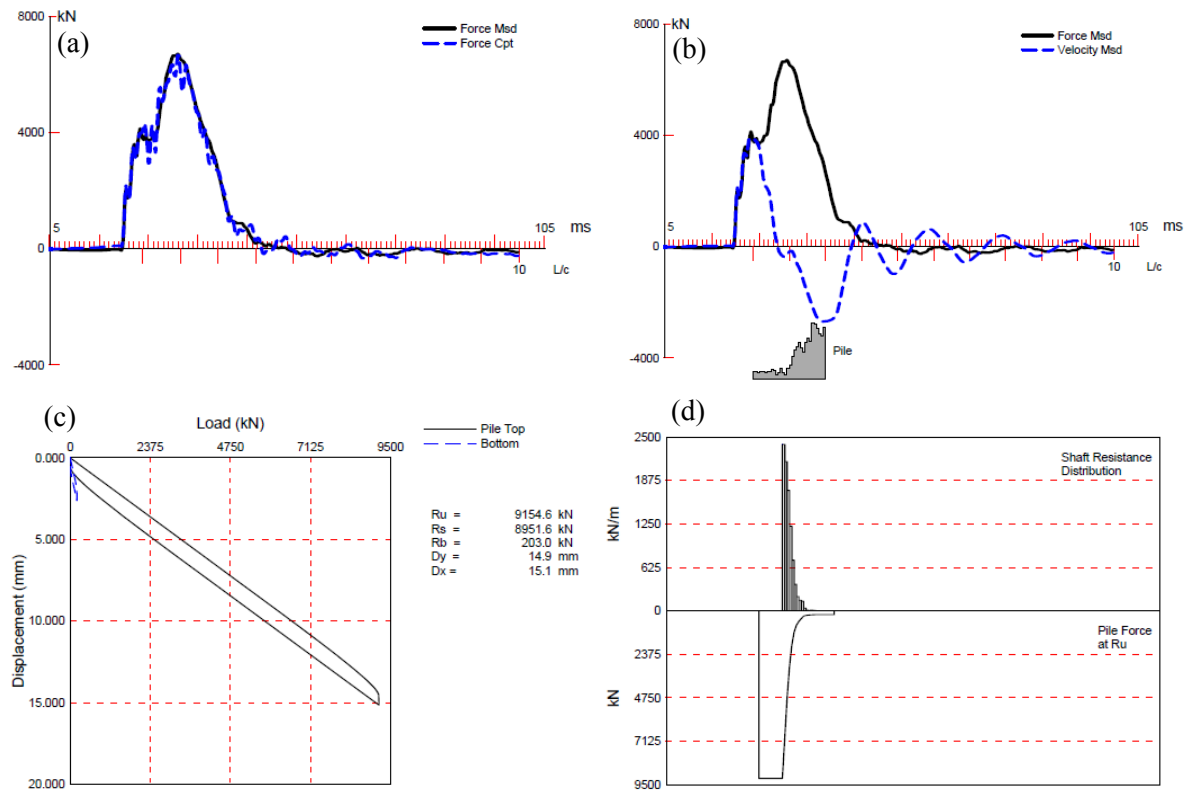


Figure 4. Signal matching analyses results for verification load test C-47, displaying (a) measured versus computed forces, (b) measured force and velocity with impedance variation along the foundation, (c) computed static load versus displacement, and (d) shaft and total resistance distribution (GeoDynamica, Inc. 2015a).

Summary and Findings. Overall, a very successful load test program was carried out, consisting of drop weight dynamic load tests performed at nine locations along the Tema Port PBU pier Phase I and II construction modules. In general, the following conclusions were made (though not all evidence could have been provided in this paper):

1. All foundation elements tested to failure stood by the geotechnical required capacity and their factored resistances exceeded the maximum factored design load for the Tema Port project. When a single marginal case was detected in the initial stage of the project it was traced to a construction defect that was corrected.
2. The foundation elements tested for load verification, while subjected to limited loading beyond design but below failure, proved the resistance exceedance of the maximum factored design load.
3. The accuracy of the resistance distribution in signal matching analyses is typically lower than the accuracy of the total resistance. The load verification test results provided

capacity in agreement with geotechnical analysis and confirmed that a large resistance is being mobilized in the upper foundation area along the residual soils and fractured rock.

4. The signal matching analyses provided insight into the mechanism of load transfer between the steel tube and surrounding concrete and soil/rock. The calculated pile impedance (i.e. EA/c) with depth suggests there is full movement of the steel pipe in contact with concrete in the upper pile segments. With increased impact energy, the load is transferred to the lower pile segments. An increase in the calculated pile impedance toward lower pile segments suggests structural compatibility between the steel, the surrounding concrete, and the rock in the socket.

ASSESSMENT OF THE 1-D WE APPLICATION TO NON-UNIFORM FOUNDATIONS

Overview. Finite element analyses were utilized to assess the validity of the 1-D WE application to the analysis of complex, non-uniform drilled foundations. In the first stage of the evaluation, simplified dynamic analyses were performed using the PLAXIS geotechnical finite element analysis software and GRL WEAP. Axisymmetric models were developed simulating a shaft with non-uniform diameter and material variation along its axis as used at the Tema Port PBU pier. These simulations served as controlled examinations of dynamic analysis of non-uniform piles. A composite pile model was then evaluated in the second stage, replicating the 81.3cm OD steel tube filled with concrete used in the project.

Approach. The soil static and dynamic response, pile model (uniform versus non-uniform), and the location of the stress-wave measurement were carefully considered. Two (2) 81.3cm OD drilled shaft models were evaluated: (1) A 100m long free-pile (i.e. no soil resistance) and (2) 31.0m long shafts embedded in a simplified two-layer system. The uniform shaft parameters replicated the previously described steel pipe embedded in concrete foundation. The foundation's cross-section was modelled in PLAXIS as a uniform section and a non-uniform section in which the steel and the concrete were modelled separately.

The static soil resistances along the shaft and tip were first evaluated in PLAXIS and subsequently exported to GRL WEAP having consistent soil resistance in both models. The ultimate static soil capacity was 8,500kN, which was defined at a pile top settlement equal to 5% of the base diameter (approximately 40mm) using the FHWA recommended failure criterion for drilled shafts (O'Neill and Reese 1999, investigated for its reliability by Paikowsky et al. 2004).

Where applicable, default skin and toe quakes of 2.54 and 13.3mm, respectively, were adopted in the WEAP. These values matched well with the local load-displacement behavior computed in PLAXIS. The soil damping along the shaft and tip were 0.33 and 0.49s/m, respectively. The stress-wave force and velocity were evaluated by the WEAP using a hammer model developed by GeoDynamica, Inc. to simulate the Tema Port drop weight device. The calculated velocity-time signatures were assessed under a 175cm stroke and 5000kN mobilized resistance at approximately 1.5m below the pile top (i.e. replicating the "gauge location"). These velocities were then applied as input in PLAXIS and the resulting calculated forces at the same

location were compared to the measured values. The selected stroke and resistance were evaluated such that the 1-D WE yielded approximately 5mm pile top permanent displacement.

Triangular, 15-noded volumetric elements were used in PLAXIS. The linear elastic and Mohr-Coulomb material models were used for the pile and soil elements, respectively. Interface elements were included at the shaft/soil boundary. Elastic restraints were imposed in the horizontal directions and a viscous boundary condition was used along the axis of symmetry. An additional viscous boundary was applied at the base of the free-pile model to prevent any spurious reflections from the pile's tip. The Rayleigh damping model was utilized in PLAXIS with 15% and 50% damping along the shaft and tip, respectively, over frequencies ranging from 50 to 100Hz. Table 1 summarizes the soil and pile strength and deformation parameters.

Table 1. Summary of Drilled Shaft and Soil Properties used in the WEAP and FE Analyses.

Material Model		Depth (m)		Total Unit Weight, γ_t (kN/m ³)	Elastic Modulus, E (MPa)	Area, A (cm ²)	Poisson's Ratio, ν	Friction Angle, ϕ' (°)	Cohesion, c' (kPa)	Stress-Wave Velocity, c (m/s)
		Start	End							
Water		0	8.5	10.0	N/A	N/A	N/A	N/A	N/A	N/A
Soil (Along Shaft)		8.5	28.5	19.5	40	N/A	0.30	40	10	N/A
Soil (Below Tip)		28.5+		22.0	500	N/A	0.20	55	100	N/A
Uniform Shaft		N/A		29.1	51,810	5189	0.10	N/A	N/A	4227
Non-Uniform	Concrete	N/A		24.6	40,000	4800	0.10	N/A	N/A	3994
	Steel	N/A		77.0	200,000	388	0.27	N/A	N/A	5041

Results and Discussion of Numerical Analyses. The results from the 1-D WE and FE comparative numerical analyses are presented in Figure 5. Figures 5a and 5b present the comparison of the free-pile and embedded shaft calculated forces by the 1-D WE and FE simulations, respectively. The distribution of stresses in the steel and concrete are displayed in Figure 5c for the non-uniform embedded shaft model simulation.

The free-pile computed forces were identical for the FE and WEAP, with an exact proportion between the force and velocity equal to the pile impedance. This behavior is consistent with the uniform, free elastic bar wave propagation theory. In addition, the uniform and non-uniform cross-sectional models yielded the same total computed force at the pile top. It can thus be concluded for this simplistic case there is full compatibility of strain between the various cross-sectional materials and the pile behaves as a single mass as assumed in the 1-D WE.

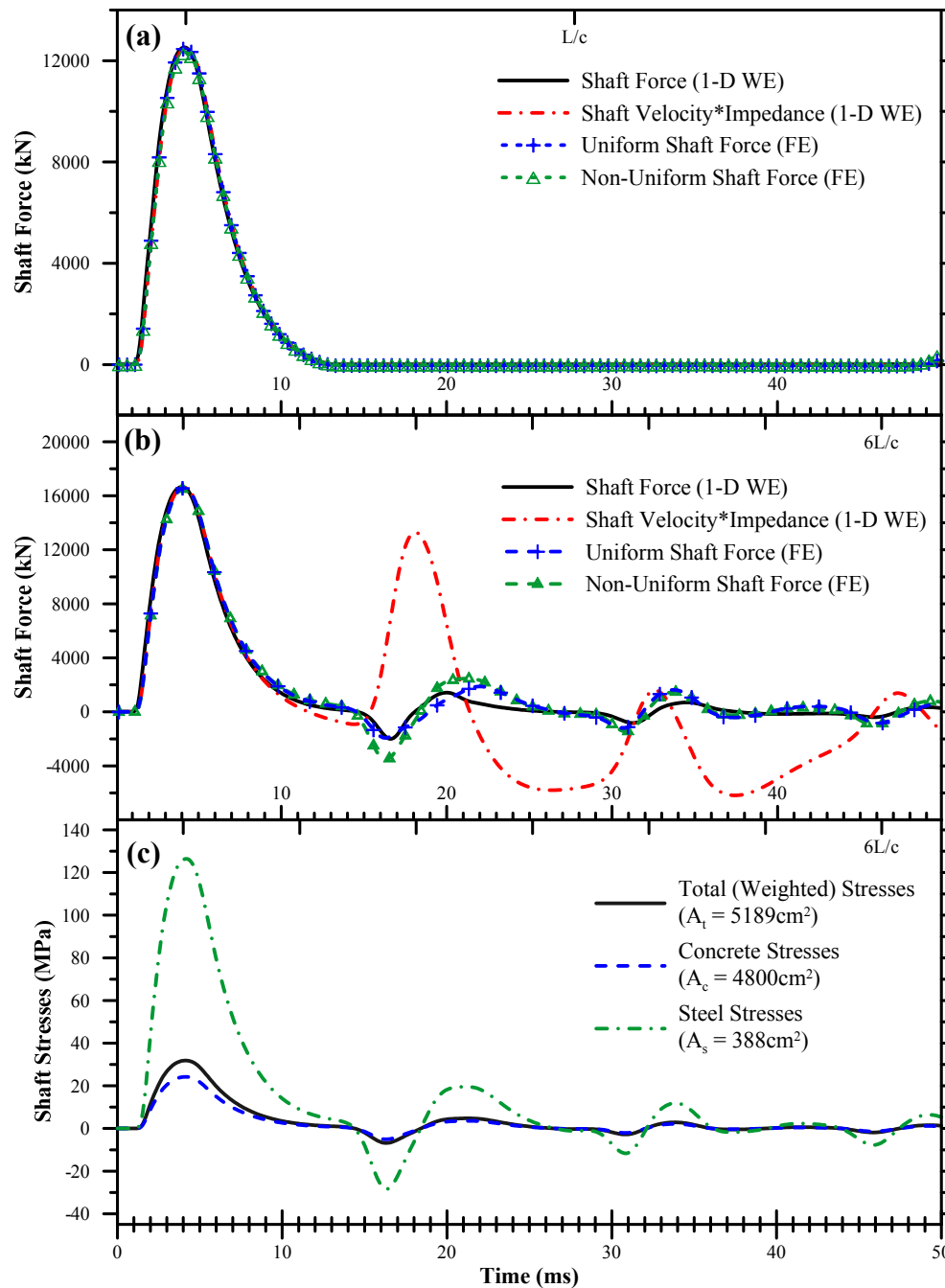


Figure 5. Comparison of calculated forces based on dynamic numerical analyses for (a) the free-pile model and (b) embedded shaft model, and (c) stress variation in the steel and concrete sections of the embedded shaft model.

The WEAP and FE models were within close agreement for the embedded pile numerical analyses. Similar to the free-pile analyses, the computed forces were identical along the free segment (prior to stress-wave reflections reaching the pile top). Minor variation in the computed forces was observed beyond L/c , although a larger difference was evident for the non-uniform cross-section model. Despite the complexity of the model and differences in the computational

approaches, the results are very promising for extension of the FE method to real-world complex, non-uniform drilled foundations as an examination of the 1D WE analysis.

SUMMARY AND CONCLUSIONS

A successful drop weight dynamic load testing program was carried out offshore on complex, non-uniform drilled foundations for the design, load verification, and quality control of the Tema Port PBU pier in Ghana, Africa. Load verification tests performed for one foundation was discussed. The dynamic tests proved that the foundation's axial capacity exceeded the required load demand despite difficult subsurface conditions and uncertainty in the geotechnical analyses during the design phase.

Numerical analyses were performed to assess the validity of applying the 1-D WE for the analysis of non-uniform drilled foundations. The simplified comparison using GRL WEAP (1-D WE) and PLAXIS (FE) included a free and a soil embedded pile model. The computed dynamic responses of the free-pile simulation were identical between the FE and 1-D WE suggesting the FE method of simulating the wave propagation is in compliance with widely accepted theory. The results of the embedded pile model were within close agreement, with minor variation in the computed dynamic responses observed beyond time L/c . The numerical evaluation, while promising, is the initial stage in assessing the broader validity of applying the 1-D WE for analysis of complex, non-uniform drilled foundations.

ACKNOWLEDGEMENTS

The project was executed for the Amandi Holding Limited Corporation in contract with the Ghana Ports and Harbours Authority for the Tema Port PBU pier. The authors appreciate the cooperation and support of Mr. Rafi Edry the President of Amandi, the Project Manager Mr. Ehud Deri, and the CEO/Chief Engineer Mr. David Ben Ayun.

REFERENCES

- Case Pile Wave Analysis Program (CAPWAP) 2006. Pile Dynamics, Inc., Cleveland, Ohio.
- GeoDynamica, Inc. 2013. "Final Design Report: Construction of Perpendicular Bulk Unloading (PBU) for the Ghana Ports and Harbours Authority", Final Design Report prepared for Amandi Holding Limited, April 2013.
- GeoDynamica, Inc. 2015a, "Dynamic Pile Proof Load Testing C-41, C-47, F-37 Results and Analyses", Report submitted to Amandi Holding Limited, April 2015, GeoDynamica, Inc., Newton, MA.
- GeoDynamica, Inc. 2015b, "Dynamic Pile Proof Load Testing E-52, E-53, C-54 Results and Analyses", Report submitted to Amandi Holding Limited, June 2015, GeoDynamica, Inc., Newton, MA.
- GRL Wave Equation Analysis Program 2010. Pile Dynamics, Inc., Cleveland, Ohio.
- Hajduk, E. L., Wright, W. B., Snow, W. L., Adams, J. C. 2005. "A Drop Weight Hammer for Dynamically Testing Micropiles in Charleston, SC", Geo3 Construction Quality Assurance/Quality Control Technical Conference, Irving, Texas, November 2005.

- O'Neill, M. W. and Reese, L. C. 1999. Drilled Shafts: Construction Procedures and Design Methods, ADSC-TL-4, FHWA-IF-99-025, FHWA, Washington, D.C.
- Paikowsky, S.G. 2013. "Dynamic Load Testing of Drilled Deep Foundations", Keynote lecture in the Swiss Geotech. Ann. Meeting, Freiburg, Switzerland, May 2013.
- Paikowsky, S. G. with contributions by Birgission G., McVay M., Nguyen T., Kuo C., Baecher G., Ayyub B., Stenerson K., O'Mally K., Chernauskas L., and O'Neill M. 2004. "NCHRP Report 507 Load and Resistance Factor Design (LRFD) for Deep Foundations", Nat. Coop. Hwy Rsrch. Progr. report for Project NCHRP 24-17, TRB, Washington, DC, pp. 134, 2004.
- Paikowsky, S.G., with contributions by Brown, D.A., Shi, L., Operstein, L., Mullins, G.A., Li, Z., Griffin, E., Liang, C., Gorczyca, J. and Mustone, T. 2006. "Innovative Load Testing Systems", Final Report submitted for project NCHRP 21-08, Transportation Research Board, Washington, DC, March 2006.
- Paikowsky S.G and Chernauskas L.R. 2008. "Dynamic Analysis of Open-Ended Pipe Piles", invited Keynote Lecture in the *8th Int. Conf. on the App. of Stress Wave Theory to Piles*, Lisbon, Portugal, September 8-10, 2008. IOS press, J.A. Santos ed. pp. 59-76.
- PLAXIS 2D 2010. Plaxis BH, Delft, The Netherlands.
- Timoshenko, S. and Goodier, J. N. 1951. Theory of Elasticity. Second Edition, McGraw-Hill Book Company, USA.

Experimental Investigation of the Horizontal Resistance of Group Suction Piles with Different Pile Spacing

Juhyung Lee, Ph.D.¹; and Jinung Do²

¹Geotechnical Engineering Research Institute, Korea Institute of Civil Engineering and Building Technology, 283 Goyangdae-Ro, Ilsanseo-Gu, Goyang-Si, Gyeonggi-Do 411-712, Korea. E-mail: leejh73@kict.re.kr

²Dept. of Civil, Construction and Environmental Engineering, North Carolina State Univ., 208 Mann Hall, Campus Box 7908, Raleigh, NC 27695-7908. E-mail: jdo@ncsu.edu

Abstract

In this study, a new type of suction pile foundation for floating structures, namely group suction piles, was proposed to improve the shortcomings of conventional single suction piles. Small-scale model tests were performed to estimate the horizontal behavior of single suction piles and group suction piles with different pile spacing (2, 3 and 4 times the pile diameter) under various loading conditions in terms of loading locations and inclinations. The horizontal behavior of group suction piles with different pile spacing was analyzed for various loading locations and load inclinations based on the model tests. For the given group pile configurations (a group pile having 9 component piles with a pile formation of 3×3), the horizontal resistance increased with increasing pile spacing. The maximum ultimate horizontal resistances were found at the loading locations of 50% of the embedded depth. Unlikely in the single suction pile case, the significantly maintained residual resistances were found for group suction piles. The residual resistances of group suction piles were at least higher than 40% of the corresponding ultimate horizontal resistances.

INTRODUCTION

An offshore floating structure is generally built at a relatively deep sea level (over 20 m), and because of the limits of required equipment and cost efficiency, the foundation is typically designed with a combined system that incorporates an anchor and mooring system instead of driven pile or drilled shaft. Currently, several types of anchors and foundations are used at deep sea levels, and among them, a drag anchor or suction pile are more commonly used because of their greater constructability and cost efficiency. Of the two, the suction pile is more popular than the drag anchor, given the latter's uncertainty in estimating bearing capacity and construction efficiency (Colliat et al. 1996).

The suction piles have many advantages over other types of anchors, such as (a) precise positioning in deep water, (b) ease of removal and relocation, (c) less dependency on heavy installation equipment, and (d) large diameter that can develop considerable resistance against significant lateral and torsional loads generated by the environmental loads and loads transferred from the superstructure. However, the potential for reinstallation of the suction piles has always been an issue for engineers. Successful installation of offshore foundations is more difficult over onshore foundations due to limited available operative time under harsh environmental conditions, such as wind, wave, and tide. Moreover, expensive offshore equipment, such as jack-up barges or offshore cranes, is required and the cost required for installation could be significant

because of slow equipment operation from their limited available operative time (Van Russel and Schontag 1997).

Recently, many studies on suction pile implementation have gotten underway in an effort to reduce the costs of suction pile installation. These studies have focused on the development of supplementary equipment improving installation efficiency by implementing percussion systems or water jets to increase the penetration capacity of the suction piles (Allersma et al. 2001; Bang et al. 2005). However, such approaches have proved not to be an ultimate solution due to the additional costs of their implementation and limitations in particular soil conditions. Thus it is necessary to develop another type of suction pile, which promises ease of installation and an improved and stable bearing capacity.

In this study, a new type of suction pile foundation for floating structures, namely group suction piles, was proposed to improve the shortcomings of conventional single suction piles. Small-scale model tests were performed to estimate the horizontal behavior of group suction piles. The horizontal behavior of single suction piles and group suction piles with different spacing (2, 3 and 4 times the pile diameter) was analyzed with varying loading locations and load inclinations.

GROUP SUCTION PILES

In this study, group suction piles are proposed as a foundation of floating structures. Group suction piles are similar in form to a general group of piles, and the structure is combined in the form of a top cap and several single suction piles as shown in Figure 1a.

This group of suction piles is a favorable structure in supporting massive loads, and is expected to show an improvement in terms of horizontal bearing capacity because the top cap can restrain rotation in horizontal loading by strongly combining the individual suction piles.

The group suction piles also have diverse advantages, especially in installation. When the individual suction piles penetrate the ground, it is possible to adjust the degree of horizontality by controlling each of them, and the top cap can serve as a guide to allow vertical installation in inclined ground. In practice, the greatest advantage is that group suction piles can modularize in construction. In other words, individual suction piles can be manufactured at the factory or on shore, and the number of suction piles can be rearranged at the construction site. Therefore, since the piles can be installed flexibly in different terrain or hydraulic conditions, construction time can be reduced significantly than other offshore foundations even including single suction pile.

The group suction piles can be used to combine single suction piles, a large diameter single suction pile can be replaced by several single suction piles. Other researchers have tried to discover the potential of group suction piles (Jee et al. 2013; Kim et al. 2014). Kim et al. (2014) studied the behavior of hybrid foundations in sand under vertical and horizontal loading of the centrifuge. In the case of vertical loading on the hybrid suction foundation with a circular mat, when displacement was induced by 20% of the diameter, the bearing capacity was 1.81 times larger than in the single suction foundation. And in the case of horizontal loading with the same conditions as above, when displacement was induced by 9% of the diameter, it was found that the bearing capacity was 1.95 times larger than those of the single suction foundation. Kim et al. concluded that, before and after contact with the ground via the mat, the behavior was significantly different from that of the single suction foundation.

At present, a research group with the Ministry of Trade, Industry and Energy in South Korea has a project underway to develop and expand the market of offshore plants from 2012

(Jee et al. 2013). This group aims to develop techniques for the installation of offshore plants at sea depths greater than 3,000 m. The focus of the group includes foundation techniques, stable lowering, dynamic positioning, and umbilical, riser, and flowline installation. Based on these techniques, a suction hybrid foundation combined mat and blade has been under review to resist external forces effectively under various loads (Figure 1b).

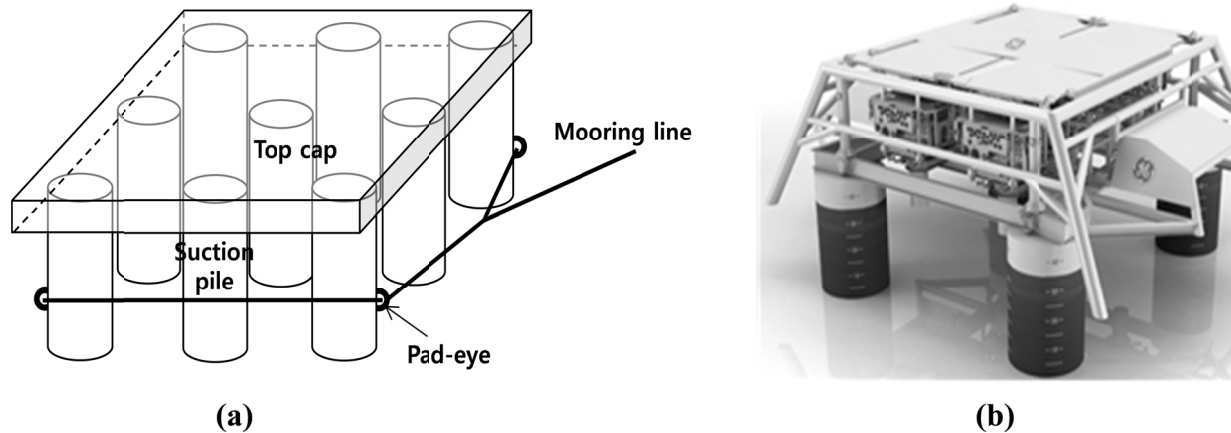


Figure 1. (a) Group suction piles and (b) suction hybrid foundation (Jee et al. 2013).

EXPERIMENTAL SETUP

Soil chamber. The soil chamber used in this study was a rectangular steel chamber. It was designed and manufactured at the Korea Institute of Civil Engineering and Building Technology using 17-22 mm thick stiff steel plates. The chamber consisted of several main parts as follows: (a) a test box, (b) a vibrating compaction system for making a specific density, (c) a load actuator for applying horizontal loading, (d) a wire and pulley system for connecting the load actuator and model pile, and (e) a load and displacement measuring system (Figure 2).

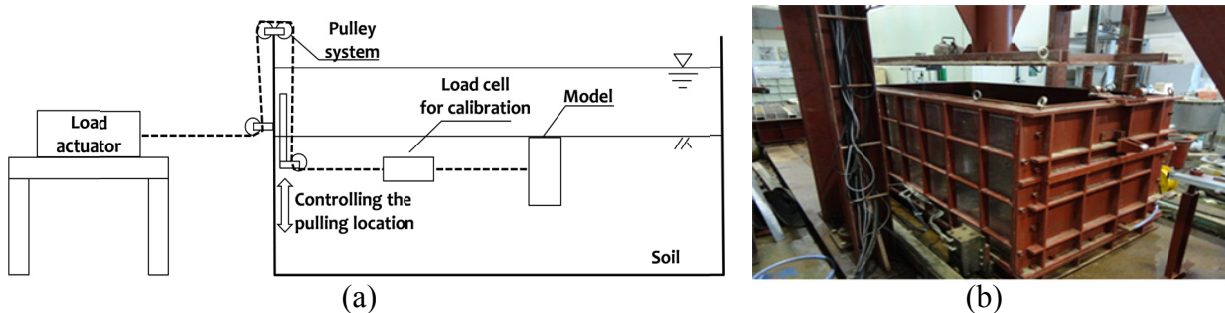


Figure 2. Scheme of testing system (a) and soil chamber (b).

Based on the boundary effect and the size of group suction piles used in this study, the size of the soil chamber was determined to be 1.0 m × 2.0 m × 1.5 m (width × length × height), and made from steel to support the corresponding weight of used soil and water and the upper confining load. The type of soil used was Jumunjin standard sand and the material properties are shown in Table 1.

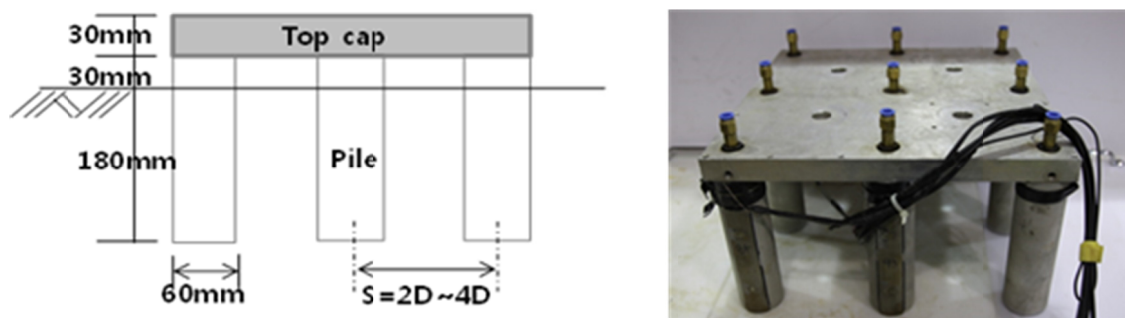
Table 1. Engineering properties of Jumunjin standard sand.

G_s	C_u	C_c	e_{max}	e_{min}	USCS
2.62	1.43	0.9	0.929	0.620	SP

Soil preparation. In general, when using a soil chamber, the raining method is widely used. The raining method uses the falling energy of sand particles when preparing the soil conditions in model tests. This method is usually useful in dry conditions, but in the case of submerged conditions like in this study, it is not suitable for preparing the ground, because the sand that is used must always be dried off after finishing the test.

Accordingly in this study, a new method was contrived other than the raining method, to establish the target relative density of the model test. A steel plate (upper plate) was installed on the vertical loading actuator so as to confine the surface of the sand, while high-compacting power generated by the vibrating compactor (550 Wh, 120 Hz) caused compaction of the soil. Hence, after saturating and disturbing the sand within the soil chamber, upper confinement was applied at the surface of the soil, and compaction could be achieved through operation of the vibrator. This is a new method of model test that achieves the target density of the soil in terms of using the principle of liquefaction (Ishihara and Yoshimine 1992; Lade and Yamamuro 1997), so that the user can control the relative density by the height of the soil.

Model group suction piles. In this study, group suction piles have been newly proposed as a foundation of huge floating offshore structures. Model group suction piles is made by connecting a pile cap and single model piles (Figure 3).

**Figure 3. Model group suction piles.**

By locating a single suction pile beneath the pile cap with 2D, 3D and 4D spacing respectively, the group model pile was set up. The group suction piles and the pile caps were processed using the same materials. The group suction pile penetrates the soil with the help of a suction pump. The group suction pile is installed at the soil chamber as shown in Figure 4. At this time, a pre-embedded wire in the soil is drawn slowly to a target loading location, by the actuator.

Additionally, to compensate for the different interfacial characteristics between field and laboratory, the relative roughness R_n (R_a/D_{50} ; R_a : average surface roughness; D_{50} : mean particle size of sand) was used (Porcino et al. 2003; Lehane et al. 1993). The R_n in this study (R_n : 0.211; R_a : 12 μm , D_{50} : 0.57 mm) is to reproduce the target prototype's properties (i.e., actual offshore foundation) (R_n : 0.229; R_a : 8 μm , D_{50} : 0.35 mm).

Test program. The test conditions of a series of group suction pile model tests are summarized in Table 2. Different center-to-center pile spacing (2D, 3D, and 4D), loading locations (0%, 25%,

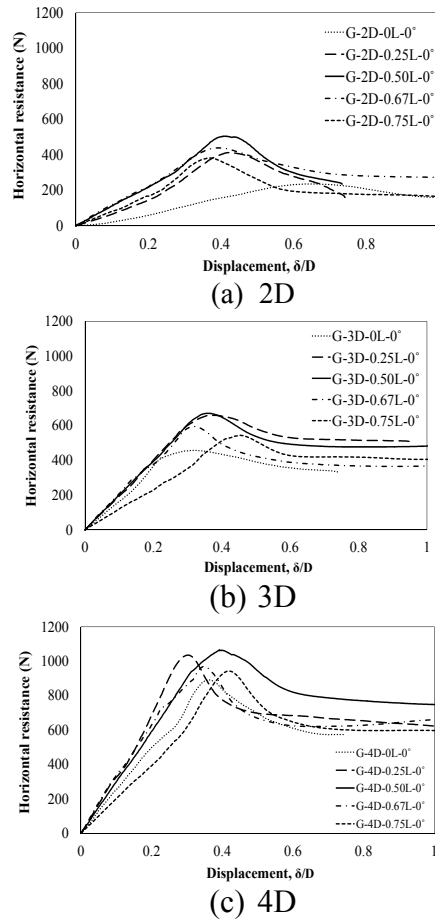


Figure 5. Horizontal resistance of normalized displacement on different spacing with no inclination.

Figure 6 is a summary of ultimate horizontal resistance (i.e., peak resistance) and residual horizontal resistance (i.e., critical resistance) at different loading locations. As seen in Figure 5 and Figure 7a, the maximum ultimate horizontal capacities were found at the loading locations of 50% D_f (i.e., $z/L=0.5$). Theoretically, the maximum horizontal resistance should be appeared at $z/L=0.67$, which is the centroid of the weight (i.e., $2/3L$). However, due to the effect of the top cap, it is concluded that the centroid of the group suction pile has been moved to the upper location (i.e., $z/L=0.5$). Also, the residual resistances (i.e., constant resistance at large displacement) of group suction piles were higher than 40% of the corresponding ultimate horizontal capacities (i.e., R_{res}/R_{ult}) (Figure 7b). However, the residual horizontal resistance is increased with pile spacing (i.e., $2D < 3D < 4D$ for R_{res}). Therefore, it indicates that the group suction pile is more stable with larger pile spacing.

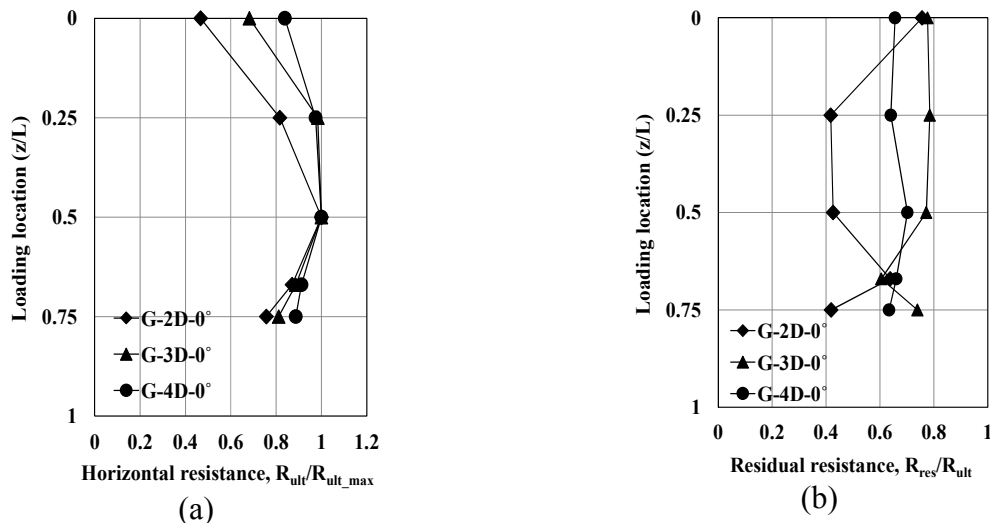


Figure 6. Summary of ultimate and residual horizontal resistance with different loading locations: (a) maximum horizontal resistance over ultimate horizontal resistance and (b) residual horizontal resistance over ultimate horizontal resistance.

Effect of load inclination. Figure 7 compares ultimate horizontal capacities of group suction piles by varying the loading location with different loading inclinations and pile spacing (*i.e.*, inclined resistance). Figure 8a presents the ultimate capacity ratios of inclined loads to horizontal loading conditions for different pile spacing and loading locations. As can be seen in Figure 7a, the reduction rate from ultimate capacity corresponding to horizontal loading conditions, to that with inclined loads, was more pronounced for the group suction piles with a pile spacing of 4D than for 3D. For the loading locations of 0% and 75% of D_f , the load inclination effect on ultimate horizontal capacity was less significant. From Figure 8a, the ultimate capacity reduction for inclined loading conditions was approximately 10-30% less than those for horizontal loading conditions.

Figure 7b represents the load inclination effect on the residual resistance of group suction piles with pile spacing of 3D and 4D. Figure 7a shows the comparison of ultimate capacity ratios of inclined loading to horizontal loading conditions, to examine the load inclination effect on residual resistance for each loading location. The load inclination effect on the residual resistance of group suction piles was least pronounced at the loading location of 25% D_f for pile spacing of 3D and at the loading location of 50% D_f for pile spacing of 4D. For group suction piles with pile spacing of 3D and 4D, the residual resistances under inclined loading conditions were 30-50% less than those under horizontal loading conditions.

In summary, based on these experimental results, an inclined load (load inclination of 20°) increases the instability of group suction piles in terms of both ultimate and residual resistances. Therefore, special care is required to assess ultimate and residual resistance of both single and group suction piles.

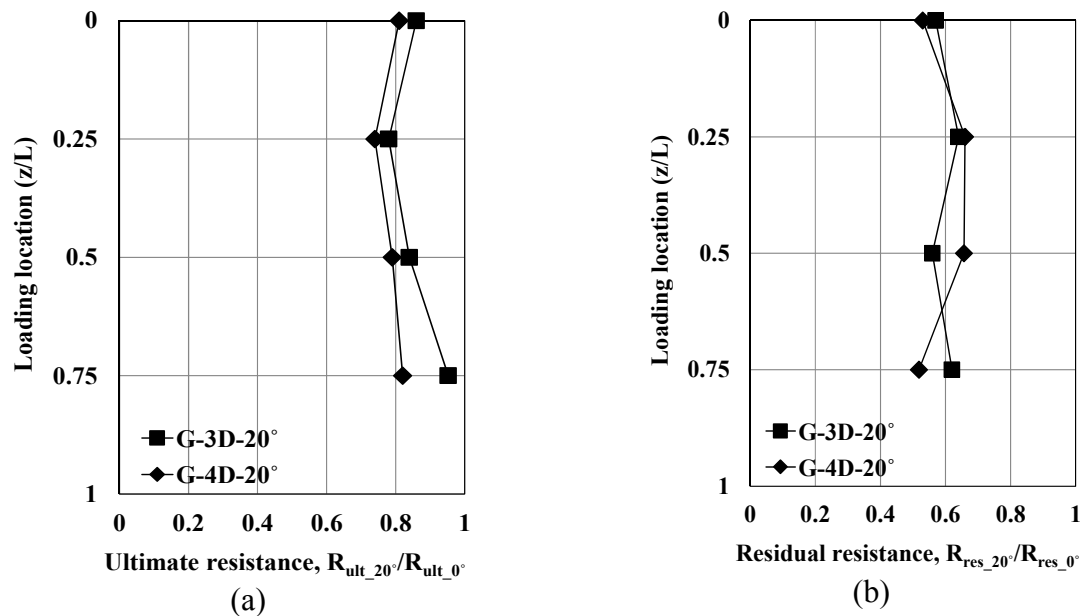


Figure 7. Comparison of inclined resistance with different loading locations (3D and 4D). (a) Maximum inclined resistance over ultimate inclined resistance, and (b) residual inclined resistance over ultimate inclined resistance.

Effect of pile spacing. Figure 8 represents the horizontal behavior of group suction piles with different pile spacing. Regardless of the loading location, group suction piles with a higher pile spacing exhibit higher ultimate capacity, initial stiffness, and residual resistance. For example, all results of strain-stress relationship of 4D spacing (i.e., solid line) are higher than those of 3D spacing (i.e., dash line), and 2D spacing (i.e., dotted line), which means the resistance and stiffness. When group suction piles are exposed to a high horizontal load, similarly to ordinary group piles, there exists a group effect due to the overlapping failure regions. The overlapping failure regions by component piles increase with decreasing pile spacing; therefore, its ultimate horizontal capacity decreases.

In the case of group suction piles, the component suction pile has a large diameter; therefore, an increase in pile spacing requires a more significant pile cap as well as high capacity equipment that can handle the group suction piles. Practical limitations exist in the use of longer pile spacing. As a result, a suction group pile's dimensions should be determined with serious consideration of both the group effect and economic efficiency.

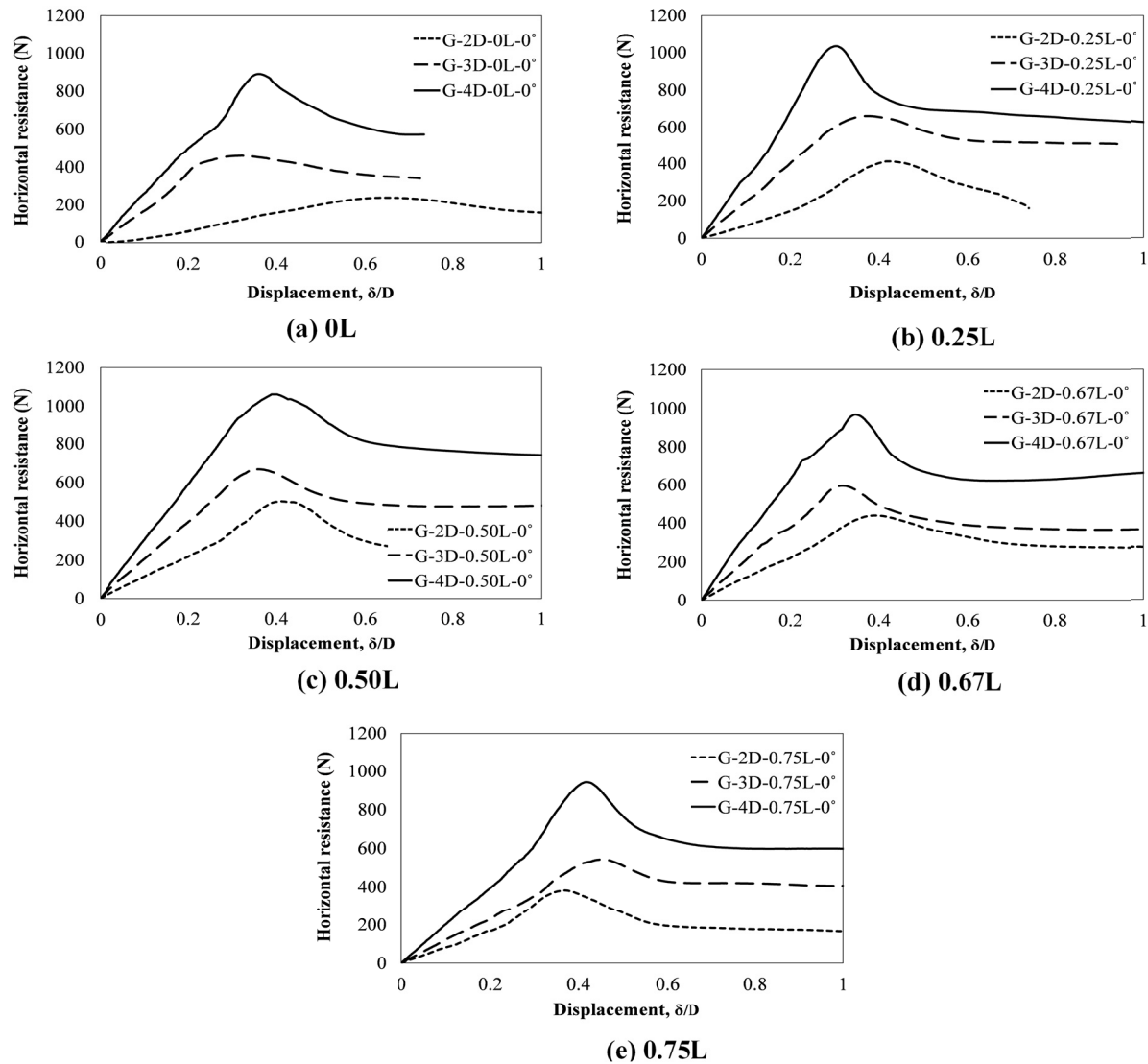


Figure 8. Horizontal behavior of group suction piles with different pile spacing.

CONCLUSIONS

The horizontal behavior of group suction piles with different pile spacing was analyzed for various loading locations and load inclinations from the model tests. Based on the findings of this study, the following main conclusions are drawn:

1. For the given group pile configurations (a group pile having 9 component piles with a pile formation of 3×3), horizontal resistance increases with increasing pile spacing. The maximum ultimate horizontal resistances were found at the loading locations of 50% of the embedded depth.
2. The significantly maintained residual resistances were found for group suction piles. The residual resistances of group suction piles were at least higher than 40% of the corresponding ultimate horizontal resistances. The ultimate and residual horizontal resistances were lower for inclined loading conditions (20 degrees) than for no inclined loading conditions.

3. Overall, such horizontal behavior of group suction piles can reduce the uncertainties of ultimate horizontal and residual resistances resulting from unexpected soil conditions and spatial variation of soil parameters.

ACKNOWLEDGMENTS

The research presented in this paper was conducted with funding from the project entitled “Horizontal excavation for life-saving and stabilization technology” at Korea Institute of Civil Engineering and Building Technology. The authors acknowledge the financial support from the institution.

REFERENCES

- Colliat, J. L., Boisand, P., Gramet, J. C., Sparrevik, P. (1996). “Design and installation of suction anchor piles at a soft clay site in the Gulf of Guinea,” *Proceedings of the annual Offshore Technology Conference*, Houston, Texas, pp.8150.
- Allersma, H. G. B., Kierstein, A. A., Maes, D. (2001). “Centrifuge modeling on suction piles under cyclic and long term vertical loading,” *Proceedings of the 10th International Offshore and Polar Engineering Conference*, Seattle, USA, May 28-June 2.
- Bang, S., Cho, Y., Kwag, D. J. (2005). “Design and installation of suction piles for breakwater foundation.” *OCEANS, 2005. Proceedings of MTS/IEEE*, Vol. 1, pp.1-6.
- Kim, J. H., Kim, S., Kim, D. S., Youn, J. U., Kim, D. J., Jee, S. H. (2014). “Centrifuge model test on load capacity of hybrid suction foundation for vertical and horizontal loading,” *KGS Spring National Conference*, pp.423-430.
- Jee, S. H., Yoon, J. U., Kim, D. J., Choi, J. Y. (2013). “Development of technique for installation of deep sea offshore plant,” *Korea Geo-environmental Society*, Vol. 14, No. 3, pp.2-9.
- Ishihara, K., Yoshimine, M. (1992). “Evaluation of settlements in sand deposits following liquefaction during earthquake,” *Soils and Foundations*, Vol. 32, No. 1, pp.29-44.
- Lade, P. V., Yamamuro, J. A. (1997). “Effects of nonplastic fines on static liquefaction of sands,” *Canadian Geotechnical Journal*, Vol. 24, No. 6, pp.918-928.
- Porcino, D., Fioravante, V., Chionna, V. N., Pedrono, S. (2003). “Interface behavior of sands from constant normal stiffness direct shear tests,” *Geotechnical Testing Journal*, Vol. 26, No. 3, pp.74-86.
- Lehane, B. M., Jardine, R. J., Bond, A. J., Frank, R. (1993). “Mechanisms of shaft friction in sand from instrumented pile tests,” *Journal of Geotechnical Engineering*, Vol. 119, No. 1, pp.19-35.
- Van Bussel, G. J. W., Schontag, C. (1997). “Operation and maintenance aspects of large offshore windfarms,” *EWEC-CONFERENCE*, pp. 272-275.

Parametric Study for Understanding the Behavior of Integral Abutment Bridges

Karrthik Kirupakaran, Ph.D., P.E.¹; and Kanthasamy K. Muraleetharan, Ph.D., P.E., G.E.²

¹Project Engineer, NTH Consultants, Ltd., 8001 Sweet Valley Dr., Suite 15, Valley View, OH 44125. E-mail: kkirupakaran@nthconsultants.com

²Professor, School of Civil Engineering and Environmental Science, Univ. of Oklahoma, 202 W. Boyd St., Room 334, Norman, OK 73019. E-mail: muralee@ou.edu

Abstract

Integral abutment bridges (IABs) are being used widely across U.S. due to the elimination of joints and the superior long-term performance of these bridges. However, the performance of IABs is dependent on the soil-structure interactions that are not well understood. This paper describes an effort to understand the complex soil-structure interactions occurring in IABs through a parametric study conducted to extend the results of a field instrumentation study on an IAB in Oklahoma to other IABs with different design variables. Abutment pile type, size and orientation, bridge length, girder depth, soil type, pre-drilled holes around abutment piles, and bridge skew angle were the variables considered in the study. Validated simulation tools GROUP and TeraDysac were used for the numerical simulations. According to the simulation results, in order to accommodate thermal movement in IABs and to reduce bending moments in abutment piles, a smaller H-pile section should be placed in weak axis bending and in pre-drilled holes with low stiffness material, especially at shallow depths. Abutment piles for IABs should be checked for capacities under combined axial force and bending moments. Longer spans with larger girders will increase the axial load on the abutment piles, and therefore long-span IABs should be designed with caution. For IABs with larger skew angles, abutment piles should be oriented in weak axis bending along the transverse direction. Biaxial bending of abutment piles in skewed IABs increases stresses in the concrete superstructure, thus the structural components for IABs with larger skew angles have to be designed carefully to accommodate the thermally-induced deformations.

INTRODUCTION

Integral Abutment Bridges (IABs) are jointless bridges, and their use has been increasing in recent years (Huang et al. 2004). An IAB provides many advantages during construction and maintenance of a bridge (Huang et al. 2004). The main advantage of an IAB is the elimination of roadway expansion joints. Thermal contraction and expansion in an IAB is accommodated by the movement of the abutments. The abutments are typically supported on steel H-piles (HP) that are oriented in weak axis bending in the longitudinal direction to better allow for abutment movements. Simpler joints between approach slabs and pavements accommodate the relative movements between the bridge and the pavement. Soil-structure interactions at the abutments occurring during thermal loading of a bridge are complex, especially in skewed and long span IABs. Because of the uncertainties in understanding these interactions, many Departments of

Only limited parametric studies of IABs are available in the literature. The main objective of the present study was to extend the insights gained from the field performance of an IAB in Oklahoma to general IABs, and to propose design guidelines for IABs with longer lengths and larger skew angles. Validated computer simulation tools GROUP (ENSOFIT 2010) and TeraDysac (Muraleetharan et al. 2003) were used to understand the long-term behavior of IABs. The base case was taken as the numerical models developed for the Oklahoma IAB in the computer programs GROUP and TeraDysac. Thermally-induced deformations of the abutments and the resultant bending moments in the abutment piles were studied in an effort to understand the performance of IABs with various configurations.

A three-span bridge carrying the northbound lanes of I-44 near Lawton, Oklahoma was used as the basis for the parametric study. This is a 64.0-m long IAB with a 10° skew (Figure 1). Skew of the IAB was not considered in the base case of parametric study. The structure includes a concrete deck supported on four girders. Each abutment wall is supported on seven HP 10x42 steel piles, and the central piers are supported on two 1.5-m diameter drilled shafts per pier. Abutment piles are embedded 0.6 m into the bottom of the abutment wall. Abutment piles are oriented in weak axis bending along the longitudinal bridge direction to offer the least resistance during thermal movements of the bridge. The soil profile at the bridge site is also shown in Figure 1. This IAB was extensively instrumented to provide data on the various movements, pile strains and earth pressures. More than three years of data and comparison to the numerical models developed for validation are presented elsewhere. Fully coupled finite element computer code, TeraDysac, was used to study long-term behavior of this IAB. The entire bridge structure was modeled in TeraDysac, incorporating the non-uniform thermal gradient that occurs in the superstructure. Detailed description of modeling and results are presented in Kirupakaran and Muraleetharan (2014). Furthermore, the computer program GROUP was also used to study the behavior of this IAB. In GROUP, the entire abutment structure comprised of seven abutment piles was considered in 3-D and subjected to axial and lateral loading. Also, the skew of IAB can be considered in GROUP analysis. Detailed description of GROUP modeling and validation of results are presented in Kirupakaran et al. (2015).



PARAMETRIC ANALYSIS, RESULTS, AND DISCUSSION

Abutment pile type, size and orientation, bridge length, girder depth, soil type, pre-drilled holes around the abutment piles, and bridge skew angle are the variables considered in the parametric study to simulate various conditions of IABs. The variables are selected based on the literature review and the behavior of the Oklahoma IAB.

Abutment Pile Type, Size, and Orientation. In the literature, a range of discussions have been presented regarding the type of abutment piles used in IABs. Steel H-piles are frequently used in the design of IABs, however, cast-in-place (CIP), prestressed and pipe piles had also been used by various agencies. H-piles have been used in a wide range of bridge spans and soil conditions with two types of pile orientations: weak axis bending and strong axis bending. CIP piles utilize driven steel pipes which are later filled with concrete, and steel reinforcement is placed in the top section of the piles. Prestressed concrete and pipe piles are sometimes used for short span IABs.

In this parametric study, the behavior of HP 10x42 steel piles, HP 12x53 steel piles and 0.305-m diameter CIP piles are investigated for seasonal temperature variations (95°F). HP 10x42 piles were oriented in both weak axis bending and strong axis bending, however, HP 12x53 piles were oriented only in weak axis bending. Furthermore, the behavior of CIP piles with a 0.305-m diameter was also investigated and compared to that of H-piles. A 64.0-m long, three-span straight IAB (Bridge A) was considered in this study. The number of abutment piles and pile spacing were constant (seven piles per abutment with spacing of 2.134 m). Variables considered in this parametric study are summarized in Table 1. The number of piles under the abutments was selected based on the vertical load-carrying capacity of the abutment piles. The axial load due to the superstructure was considered in calculating the number of piles required for the abutments. The computed GROUP pile bending moment with different pile types and sizes are shown in Figure 2. According to Figure 2, the largest bending moment occurred when CIP piles were used. From the computed results, CIP piles may be used only in short IABs subjected to smaller bridge movements. Except for CIP piles, HP 10x42 piles oriented in strong axis bending caused larger bending moments in the abutment piles than the other pile configurations considered in the modeling. The computed bending moment for HP 12x53 piles oriented in weak axis bending were larger than the bending moments for HP 10x42 piles oriented in weak axis bending.

The orientation of H-piles with reference to the bridge longitudinal axis affected the thermally-induced deformation in the abutment piles since the stiffness of the H-piles varies according to the bending axis. The orientation in weak axis bending helped to reduce the bending moments that occur in the abutment piles. The orientation in weak axis bending will also help to reduce the thermally-induced concrete stresses in the superstructure. The length of the bridge and the type of soil surrounding the abutment piles also play an important role in the behavior of abutment piles. According to this parametric study, steel H-piles are most suitable to support abutments in IABs. The inherent flexibility of steel H-piles allows them to endure constant flexure induced by the cyclic thermal strains of the superstructure. Using a smaller H-pile section sufficient to carry vertical loads and orienting H-piles in weak axis bending will ensure the effective performance of IABs for temperature changes.

Bridge Length and Girder Depth. In practice, the length of an IAB is often limited. Girder depth and bridge length are often related, and in general, deeper girders are used for longer bridges. For multi-span bridges, to reach the same bridge length, the bridges can be constructed of more short-span shallow girders or fewer long-span deep girders. Numerous span combinations exist for the considered bridge length and depth ranges. In this study, three combinations illustrated as Bridge A, Bridge B and Bridge C were investigated. Bridge A and Bridge B had the same girder depths (Type III Pre-stressed Concrete Beam, PCB) and different bridge lengths. Bridge B (128.0 m, 6 spans) was twice as long as Bridge A (64.0 m, 3 spans). Bridge B (6 spans) and Bridge C (3 spans) had the same total bridge length (128.0 m) and different girder depths. Bridge C had Type IV PCB girders, which was deeper than that of Type III PCB girders used in Bridge B. To reach the same total length, six spans of girders were required in Bridge B and three spans in Bridge C. Bridges considered in this parametric study were straight IABs with the abutment piles oriented in weak axis bending. Different types of bridge configurations considered in this parametric study are summarized in Table 2. Except for the varied parameters described above, other bridge parameters and soil conditions were kept constant.

Table 1. Sectional properties for different types of abutment piles

Description	Pile Type	Bending Axis	Young's Modulus (GPa)	Moment of Inertia (m ⁴)	Cross-Sectional Area (m ²)
Case 1	HP 10x42	Weak	200	2.980×10^{-5}	0.008
Case 2	HP 10x42	Strong	200	8.741×10^{-5}	0.008
Case 3	HP 12x53	Weak	200	5.286×10^{-5}	0.010
Case 4	0.305-m CIP	-	31.3	2.50×10^{-3}	0.0845

The computed GROUP pile bending moment for different bridge and superstructure configurations are shown in Figure 3. According to Figure 3, the bending moment occurring in the abutment piles depends on the total bridge length. For the same bridge length, the computed bending moments are similar. The expansion and contraction of the superstructure were closely related to the total bridge length. The expansion and contraction of Bridge A was approximately half of that of Bridge B. From the analyses, with the increase of total bridge length from 64.0 m to 128.0 m; the expansion and contraction of the superstructure and the bending moment in abutment piles increased correspondingly. There is not much variation in the bending moment for Bridge B and Bridge C, however, using longer spans with larger girders (i.e., Bridge C) will increase the axial load on the abutment piles. Furthermore, larger thermal gradients will exist across the depth of superstructure when longer span girders are used for the bridge. Greater thermal gradients will increase the concrete stresses within the superstructure due to the larger depth of girders. Therefore long-span IABs should be designed with caution, ensuring that thermally-induced abutment pile bending moments and concrete stresses are limited within the allowable ranges.

Type of Soil Surrounding Abutment Piles. Since the abutment piles were rigidly connected to the bridge superstructure, the type of soil surrounding the abutment piles has a direct effect on

abutment pile behavior and an indirect effect on the behavior of superstructure. The following soil types were investigated in the parametric study: loose sand, dense sand, soft clay, stiff clay and very stiff clay. A 64.0-m long, three-span straight IAB (Bridge A) was considered in this parametric study. Abutment piles (seven HP 10x42 piles) were oriented in weak axis bending. Types and properties of soils surrounding the abutment piles are listed in Table 3 (Reese et al. 1976). Computed GROUP pile bending moments for different types of soils are presented in Figure 4.

Table 2. Different types of bridge configurations

Description	Bridge A	Bridge B	Bridge C
Bridge Length (m)	64.0	128.0	128.0
Number of Spans	3	6	3
Girder Type	Type III PCB	Type III PCB	Type IV PCB
Girder Length (m)	18.29	18.29	36.58
Abutment Pile Type	HP 10x42	HP 10x42	HP 10x42
Number of Piles	7	7	12
Pile Spacing (m)	2.134	2.134	1.189

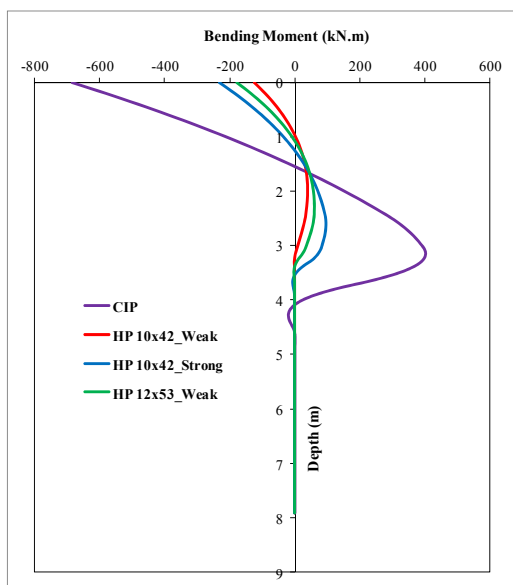


Figure 2. Variation in bending moment for different abutment piles

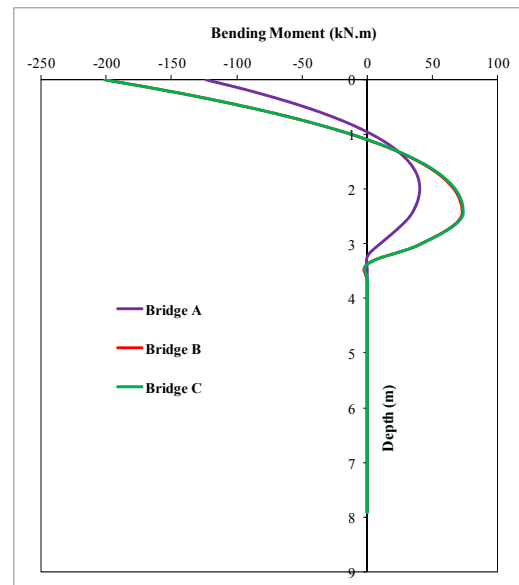
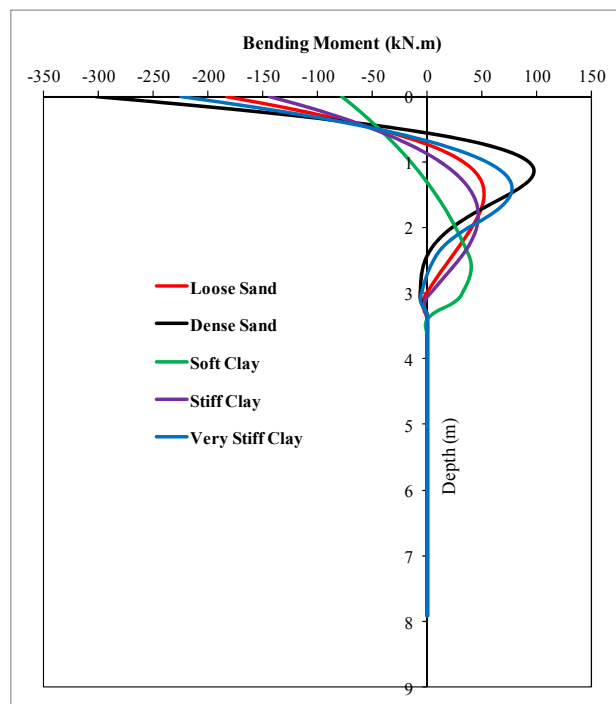


Figure 3. Variation in bending moment for different bridges

Soil surrounding the pile had a significant effect on the behavior of the abutment piles. According to Figure 4, dense sand and very stiff clay layers surrounding the piles created the largest bending moments in the piles. The stiffness of soil directly affects the abutment pile behavior. When the stiffness of soil is increased, flanges of the pile cross-section near the pile head will partially yield and the plastic hinges may occur for longer IABs and larger temperature variations. Pre-drilled holes should be used to improve the behavior of the abutment piles when a stiffer soil layer is located surrounding the piles at shallow depth.

Table 3. Properties of different types of soils

Soil Layer	Unit Weight (kN/m ³)	Soil Lateral Stiffness, k (kN/m ³)	Undrained Cohesion, c (kN/m ²)	Internal Friction Angle (o)	Strain Factor, ϵ_{50}
Loose sand	15.63	6 790	-	30	-
Dense sand	20.72	61 000	-	40	-
Soft clay	17.1	8 140	20	-	0.02
Stiff clay	20.5	136 00	90	-	0.007
Very stiff clay	22.1	271 000	240	-	0.004

**Figure 4. Variation in pile bending moments for different types of soils surrounding piles**

Pre-Drilled Holes around Abutment Piles. In IABs, yielding of abutment piles may occur due to the thermally-induced deformation of the abutments. To satisfy the safety and durability requirements, the development of plastic hinges should be avoided. The following conditions may favor the yielding of abutment piles: (i) stiff soil conditions (ii) long bridge spans (iii) large environmental temperature changes and (iv) large coefficient of thermal expansion of construction materials. To construct IABs in such conditions, pre-drilled holes may be needed. It should be pointed out that low initial construction and maintenance costs are the two important advantages of IABs. When pre-drilled holes are used, extra cost due to pre-drilling would be added, however, the enhanced in-service performance of IABs will reduce the future maintenance and repair costs. From the literature, pre-drilled holes filled with a loose material have been shown to improve the performance of abutment piles that are subjected to lateral loading. Size, depth, and backfill material of the pre-drilled hole affect the ductility of the abutment piles subjected to lateral loading.

In this parametric study, the effect of pre-drilled holes on abutment pile behavior was investigated. Pre-drilled holes were modeled for the case of stiff clay soil condition. Pre-drilled holes with two different diameters (Hole A – diameter 0.914 m, Hole B – diameter 2.134 m) and two different lengths (Hole B – length 2.134 m, Hole C – length 3.353 m) were investigated in the study. The length of Hole A is 2.134 m and the diameter of Hole C is 2.134 m. In practice, pre-drilled holes are often filled with a loose material such as bentonite slurry, and in this study, loose sand fill was assumed. A 64.0 m long, three-span straight IAB (Bridge A) was considered in this parametric study. Abutment piles (seven HP 10x42 piles) were oriented in weak axis bending. Different types of pre-drilled hole configurations considered in this parametric study are summarized in Table 4. Note that although 0.914-m and 2.134-m diameter holes may not be used in practice, they are considered here to study the relative behavior. Using smaller diameter holes in TeraDysac will be computationally time consuming. The finite element model developed in TeraDysac was used for this parametric study. The computer program GROUP considers infinitely long soil layers around the piles, and therefore a hole cannot be modeled in GROUP. The finite element models developed in TeraDysac are presented in Figures 5 and 6, showing a Type A hole (smaller diameter) and Type B hole (larger diameter), respectively.

Table 4. Different types of pre-drilled hole configurations

Description	Hole A	Hole B	Hole C
Hole Length (m)	2.134	2.134	3.353
Hole Diameter (m)	0.914	2.134	2.134

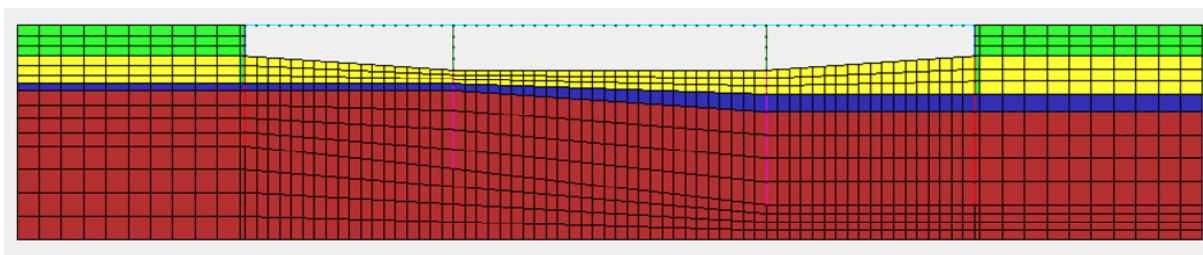


Figure 5. Finite element model for Hole A

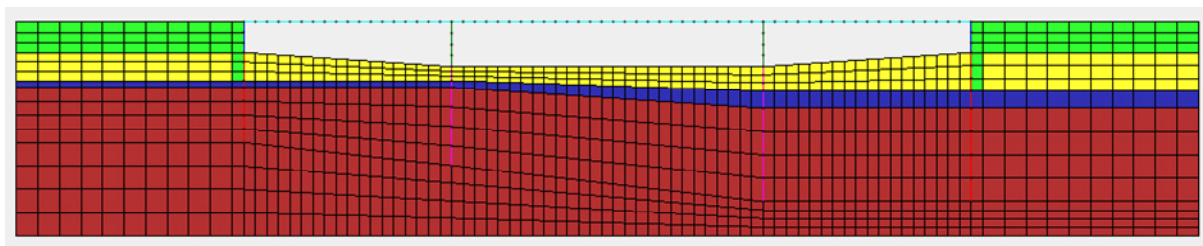


Figure 6. Finite element model for Hole B

Computed TeraDysac abutment deformations for pre-drilled holes having different diameters are presented in Figure 7. Computed TeraDysac pile bending moments in abutment piles for different pre-drilled hole configurations are shown in Figure 8. According to Figure 7, there was not much difference in the abutment deformations when the diameter of pre-drilled hole is increased for Hole B. However, as illustrated in Figure 8, the bending moment in the abutment piles decreased when the pre-drilled hole diameter is increased for Hole B. The computed bending moments show, for stiff clay, the bending moment of piles were reduced due

to the presence of the larger diameter pre-drilled hole. Negligible difference of abutment pile bending moments was observed when the depth of pre-drilled holes was increased from 2.134 m to 3.353 m (Holes B and C). When the abutment deformation becomes larger due to the thermal loading, the depth of the pre-drilled hole will also play a role in the bending moment of piles. For long-span IABs, bending moments in the abutment piles due to temperature changes may become larger, and accommodating pre-drilled holes will help to reduce the yielding of the abutment piles.

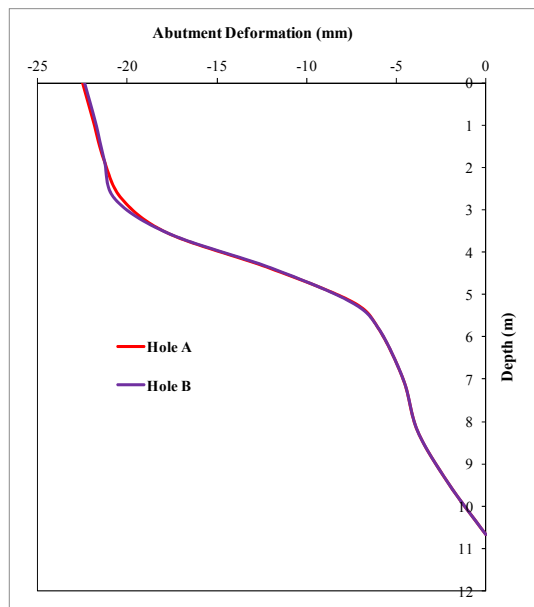


Figure 7. Abutment deformation

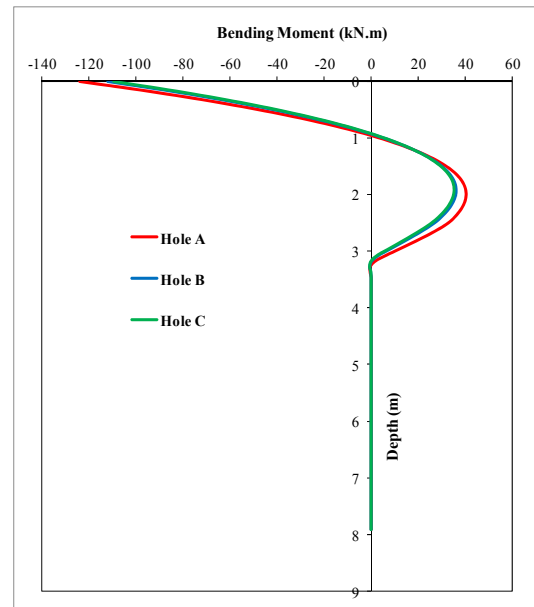


Figure 8. Variation in bending moment

Bridge Skew Angle. In practice, skewed bridges are sometimes unavoidable due to the terrain at the bridge site or road alignment. Behavior of skewed IABs is much more complicated than straight IABs due to the complexity of the soil-structure interactions. Soil pressure variation behind the abutment backwall is affected by the skew of bridge as the thermal loading of the superstructure is not symmetric in skewed IABs. Changes in soil pressure will also affect the behavior of the abutment piles in skewed IABs. Very few articles have been published in the literature regarding the behavior of the skewed IABs. The behavior of skewed IABs is not fully understood and design agencies are reluctant to build IABs with larger skew angle. Different from straight IABs, in addition to the normal pressure acting against the surface of the abutments, the friction between the abutment and backfill material becomes very important. In this study, a 64.0-m long three-span IAB with three different skew angles (10° , 20° , 30°) was investigated. Abutment piles (seven HP 10x42 piles) were oriented in weak axis bending. The computer program GROUP was used for this parametric study. The variations of pile bending moment in the longitudinal and transverse directions for different skew angles are shown in Figures 9 and 10, respectively.

According to Figures 9 and 10, there was an increase in the bending moment in the longitudinal and transverse directions when the skew angle of the bridge is increased. It may be explained that for the skewed bridge, the total force due to the backfill soil pressure was smaller than that of the straight IABs. In the skewed IAB, the reduction in the backfill soil pressure

increased the amount of abutment pile bending and thus, larger bending moments were observed. Biaxial bending of abutment piles takes place in the skewed IABs as the thermal loading of the superstructure is not symmetric in skewed IABs.

The biaxial bending of the abutment piles in skewed IABs increases the stresses in the concrete superstructure, especially for long-span IABs and larger temperature changes. When the bridge skew angle becomes larger, the bending moment in the transverse direction becomes larger than the bending moment in the longitudinal direction. With skewed IABs, the soil passive pressure developed in response to thermal movement has a component in the transverse direction as well. Within certain limits of the skew angle, the transverse component of passive pressure and soil friction will resist the bridge movements, however, for larger skew angles, this resistance is insufficient and significant bending moments in transverse direction are generated. Therefore, in such cases, abutment piles should be oriented in weak axis bending along the transverse direction of the bridge in order to accommodate the larger bending moments in the transverse direction. Furthermore, the structural components for the IABs with larger skew angles have to be designed carefully to accommodate the thermally-induced deformations in the superstructure and avoid distresses within the superstructure.

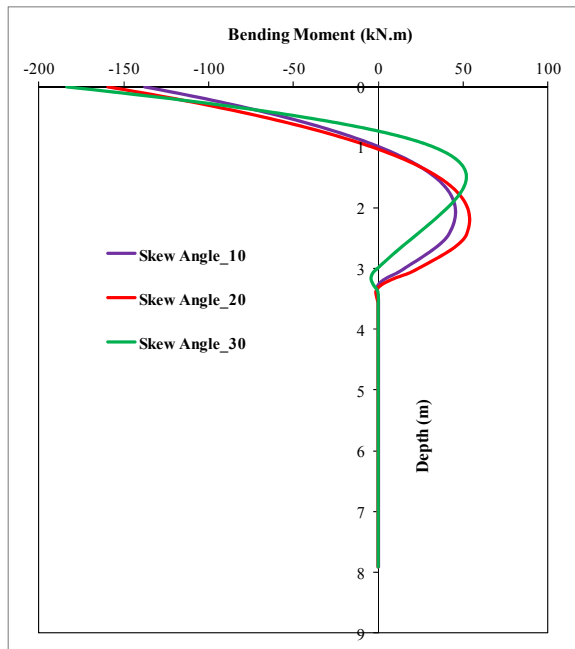


Figure 9. Bending moment variation in longitudinal direction

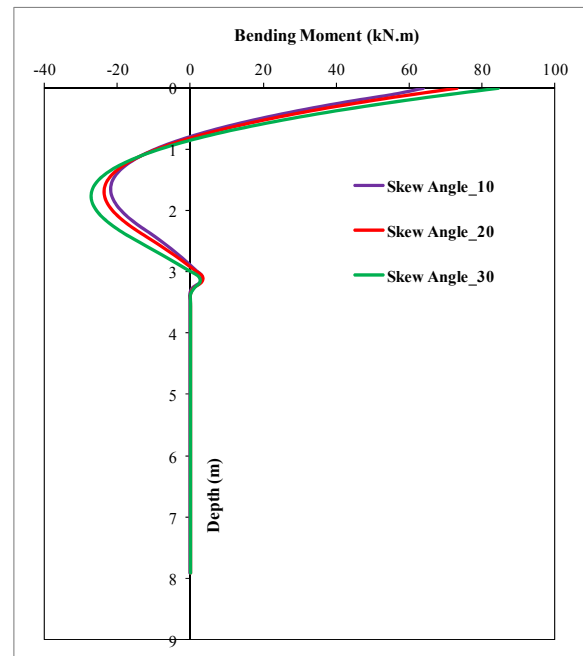


Figure 10. Bending moment variation in transverse direction

CONCLUSIONS

According to the simulation results of this study, in order to accommodate thermal movement in IABs and to reduce bending moments in abutment piles, a smaller H-pile section should be placed in weak axis bending and in pre-drilled holes with low stiffness material, especially at shallow depths. Abutment piles for IABs should be checked for capacities under combined axial force and bending moments. Longer spans with larger girders will increase the axial load on the

abutment piles, and therefore long-span IABs should be designed with caution. Using a compressible material with soil reinforcement will reduce the passive pressures and settlement of soil behind the abutments. For IABs with larger skew angles, abutment piles should be oriented in weak axis bending along the transverse direction. Biaxial bending of abutment piles in skewed IABs increases stresses in the concrete superstructure, thus the structural components for IABs with larger skew angles have to be designed carefully to accommodate the thermally-induced deformations.

ACKNOWLEDGEMENTS

This research was supported by the Oklahoma Transportation Center (OkTC Project No. OTCREOS7.1-37) and this support is acknowledged. The assistance provided by the Oklahoma Department of Transportation is also gratefully acknowledged.

REFERENCES

- ENSOFT, Inc (2010). *Computer program GROUP 8.0 for Windows*, Austin, TX.
- Huang, J., French, C.E., and Shield, C.K. (2004). "Behavior of Concrete Integral Abutment Bridges." *Report No. 2004-43*, Minnesota Department of Transportation, St. Paul, Minnesota.
- K. Kirupakaran, K. K. Muraleetharan, and G. A. Miller. (2015). "Soil-Structure Interactions in a Skewed Integral Abutment Bridge." *IFCEE 2015: International Foundations Congress and Equipment Exposition*, San Antonio, Texas, 309-318.
- Kirupakaran, K., and Muraleetharan, K.K. (2014). "Numerical Modeling of an Integral Abutment Bridge in Oklahoma." *Proceedings of the Istanbul Bridge Conference 2014*, Istanbul, Turkey.
- Krier, D. (2009). "Modeling of Integral Abutment Bridges Considering Soil-Structure Interaction Effects." *Ph.D. Dissertation*, School of Civil Engineering and Environmental Science, University of Oklahoma, Norman, Oklahoma.
- Muraleetharan, K.K., Ravichandran, N., and Taylor, L.M. (2003). "TeraDysac: TeraScale Dynamic Soil Analysis Code." *Computer Code*, School of Civil Engineering and Environmental Science, University of Oklahoma, Norman, Oklahoma.
- Reese, L.C., Touma, F.T., and O'Neill, M.W (1976). "Behavior of Driven Piers under Axial Loading." *Journal of the Geotechnical Engineering Division*, Proceedings of the American Society of Civil Engineers, 102(GT5): 493-510.

Applications of the Continuous Wavelet Transform Method in Crosshole Sonic Logging Tests

Farnyuh Menq, Ph.D.¹; Shin Tower Wang, Ph.D., P.E.²; and William Isenhower, Ph.D., P.E., M.ASCE³

¹Dept. of Civil, Architectural and Environmental Engineering, Univ. of Texas at Austin, 301 E. Dean Keeton St., Austin, TX 78712. E-mail: fymenq@utexas.edu

²Ensoft Inc./Lydon C. Reese & Associates (LCR&A), 3003 West Howard Ln., Austin, TX 78728. E-mail: stw@ensoftinc.com

³Ensoft Inc./Lydon C. Reese & Associates (LCR&A), 3003 West Howard Ln., Austin, TX 78728. E-mail: wmi@ensoftinc.com

Abstract

Crosshole Sonic Logging tests are commonly used to determine the integrity of drilled shafts. However, selections of signal arrival times can be subjective. Different persons may pick different arrival times from the same record. The lack of consistency can be a source of disputes. This paper proposes use of the integrated continuous wavelet transform (ICWT) method, which applies continuous wavelet transform to interpret direct arrival measurements. The key feature of the method is transferring a nonlinear sinusoidal-like signal to a linear phase angle plot. Peaks in the recorded signal are shown as 0-degree phase. By selecting the time point of 0 degrees with an amplitude above the noise level, the arrival time of the first peak can be uniquely identified. This method removes subjectivity between operators. The ICWT method can also be used for other tests that measure travel time intervals (i.e. pulse echo and seismic CPT tests).

INTRODUCTION

Crosshole Sonic Logging (CSL) is a common test method for determining the integrity of drilled shafts (ASTM 6760-14). In preparation of the tests, steel or PVC access tubes are tied to the rebar cage and installed in the drilled shaft. Access tubes are filled with water for transmitting ultrasound waves. A photograph of a typical test setup is shown in Figure 1. An ultrasound emitter (source) and a receiver are lowered to the bottom of the access tubes. As the operator pulls both the source and the receiver up to the top of the drilled shaft, ultrasound waves are transmitted from the source through the concrete and to the receiver at preset depth intervals. Travel time and energy are determined from the time signals recorded by the receiver. These values are used in evaluating the qualities of the concrete between the source and the receiver. The CSL method can also be used for integrity tests of diaphragm walls, concrete dams, and other similar structures.

One of the challenges of the CSL method is that determining the travel time can be subjective. For cases where CSL are used in only identifying voids, the accuracy of travel time measurement may not be as critical. However, for cases where CSL is utilized for quality control of concrete strength, precise measurements of travel time are important. Because of noises caused by electrical interferences and/or harmonic distortions, different persons may pick a different point from the same time record. The lack of consistency can be a source of dispute between parties.

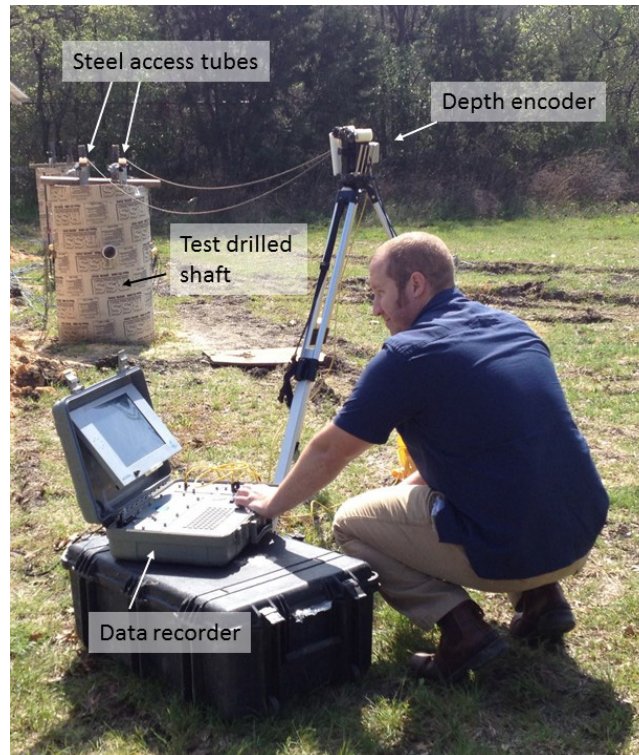


Figure 1. Photograph of a crosshole sonic logging test

To overcome this problem, this study proposes a novel method, called Integrated Continuous Wavelet Transform (ICWT) method, which applies Continuous Wavelet Transform (CWT) for direct arrival measurements. The key feature of the method is transforming a nonlinear, sinusoidal-like signal to a linear, phase angle plot. Peaks in the recorded signal are shown as a phase angle of 0 degrees, and troughs are shown as phase angles of ± 180 -degrees. By selecting the time point of a phase angle of 0 degrees with an amplitude above the noise level, the arrival time of the first peak can be easily and uniquely identified. Use of this method removes possible subjectivity by the operator in determining travel times of the CSL tests. The ICWT method and two example applications of the method to CSL tests are described in this paper.

CONTINUOUS WAVELET TRANSFORM (CWT)

A wavelet is a small, local, wave-like function. In mathematics, a continuous wavelet transform (CWT) is used to divide a time signal into wavelets of various scales along the time axis. The outputs of the CWT are named as wavelet coefficients. Generally, scales are expressed in Fourier frequency and the wavelet coefficients are shown in 3-D time-frequency plots (Addison, 2002). To illustrate the benefits of CWT in determining arrival time, a synthetic time record was created by adding high frequency noises to a clean 40 kHz sine-wave signal. The original 40 kHz sine-wave signal is shown in Figure 2(a), the high frequency noise signals of 80 and 200 kHz are shown in Figure 2(b), and the combined time record is shown in Figure 2(c). It should be noted that the 200 kHz signal has a constant amplitude throughout. However, amplitudes of both the 40, and the 80 kHz signals, vary with time. As shown in Figure 2(a), travel time can be measured by determining the difference between the source signal (a downward pulse) and the first arrival

pulse (an upward pulse). As shown in the figure, the difference is 0.0001 second (0.1 ms). However, as shown in Figure 2(c), with added noises, the exact locations of the source signal and the first arrival pulse are both difficult to identify.

CWT provides a mathematical way of separating the original signal from added noise. The same synthetic time record with added noises is shown in Figure 3(a). The CWT outputs of amplitude and phase time frequency plots are shown in Figures 3(b) and 3(c). As CWT is computed in time scale, it is common to use period scales (period = 1/frequency) in the frequency axis. As shown in Figure 3(b), the CWT amplitude time vs. frequency plot presents the synthetic time record in both time and frequency axes. With the added frequency axis, energy at frequencies of 40, 80, and 200 kHz can be separated. It is easy to see that the amplitude of 200 kHz signal appear to be constant throughout the entire length of the record. For 40 kHz signal, amplitude increases around 0.1 ms. It peaks at 0.3 ms then decreases again afterward. For 80 kHz signal, amplitude increases at 0.1 ms. It peaks at about 0.23 ms, decreases to zero at 3.5 ms, and increases again after 3.5 ms. It should be noted that variations of the 80 kHz signal are difficult to observe in Figure 3(a). This figure illustrates a great benefit of CWT, as it can separate frequency contents of a time signal along the time axis.

In the CWT phase time vs. frequency plot shown in Figure 3(c), 0 degrees is plotted in light yellow, +180 degrees is plotted in dark blue, and -180 degrees is plotted in red. By comparing Figure 3(a) and Figure 3(c), one will find that peaks in the time record are shown with phase angles of 0 degrees on the CWT phase plot, and troughs are shown with phase angles of ± 180 degrees. The cycles of the 40, 80, and 200 kHz signals can be clearly observed in Figure 3(c). In each cycle, phase angle varies from -180 to +180 degrees. As there is no 40 and 80 kHz energy between 0.02 and 0.1 ms, the phase angle in these region appears to be irregular. Similarly, phase angle around 80 kHz range also shows an irregular pattern near 0.35 ms where the amplitude of the 80 kHz signal drops down to zero.

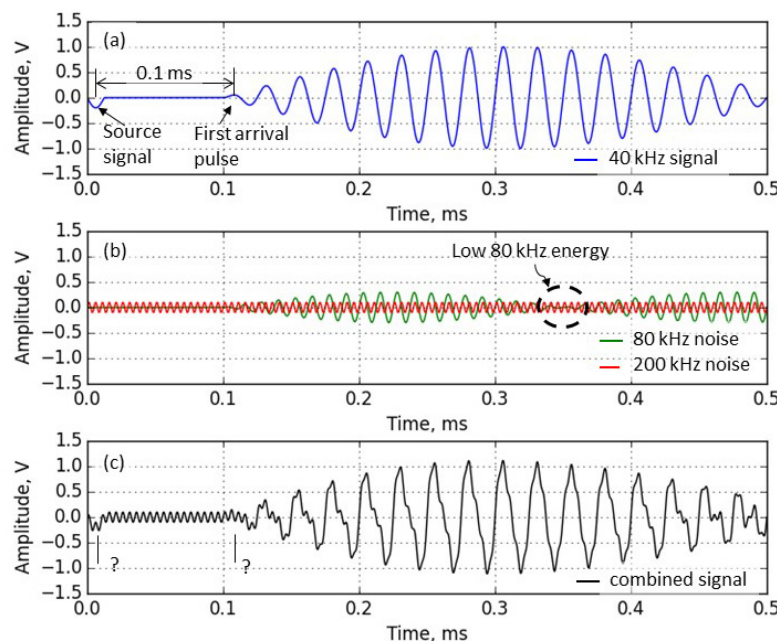


Figure 2. A synthetic time record

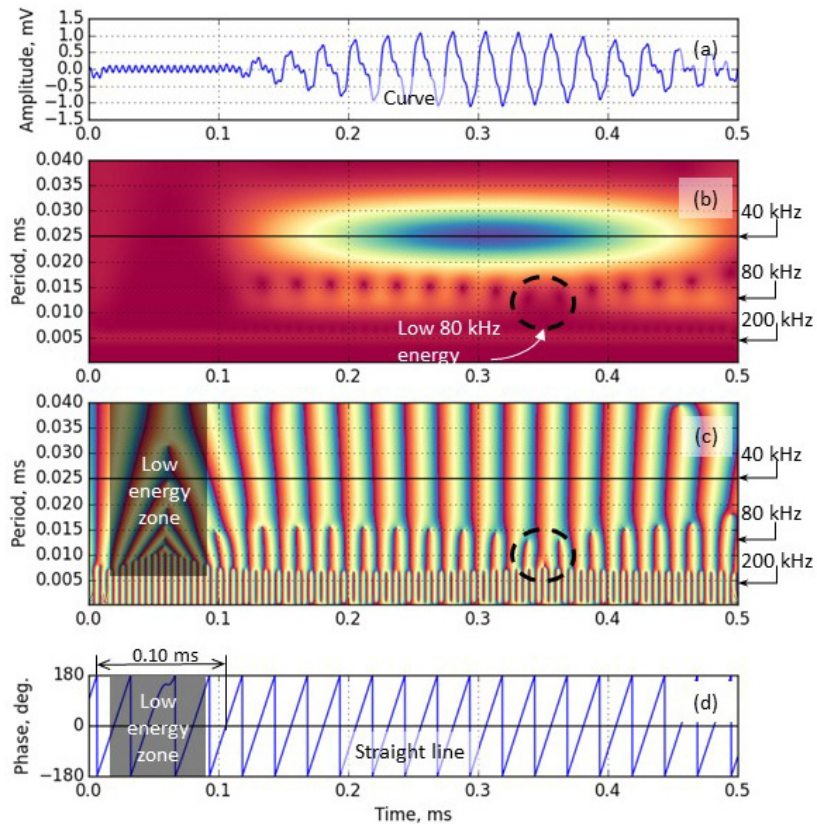


Figure 3. Continuous Wavelet Transform of the synthetic time record

The cross section of the CWT phase time-frequency plot at 40 kHz is shown in Figure 3(d). As the source signal is a negative pulse, the exact time of the source signal are determined by selecting the time point where phase angle drops from +180 to -180 degrees. On the other hand, the first arrival signal is a positive pulse, the time point of zero-degree phase angle is selected. The time difference between these two points is 0.10 ms. This is a unique benefit of using a complex wavelet. Instead of selecting arrival time from a sinusoidal curve shown in Figure 3(a), one can determine arrival time from the phase angle plot shown in Figure 3(d). Since the crosshole source signals are sinusoidal curves, they can be expressed with a sinusoidal function as $\sin(\omega t)$, where ω is the angular frequency and t is time. This is a nonlinear function of time. On the other hand, phase angle, expressed as ωt , is a linear function of time. Generally speaking, it is a much simpler task to select a time point of a particular amplitude from a straight line (a linear function) than from a nonlinear sinusoidal curve.

In this synthetic signal, energy is only presence in three discrete frequencies. A carefully designed low-pass filter can remove the 80 and 200 kHz signals. However, in other cases, where energy presence continuously in a range of frequencies, applying a digital filter can create ringing artifacts to a transient signals. In addition, low-pass filters cannot generate amplitude or phase time frequency plots.

CROSSHOLE SONIC LOGGING

In Crosshole Sonic Logging tests, an electrical pulse is used to drive the source emitter at its resonant frequency. The resonant frequency (test frequency) of the emitter is generally between 30 and 100 kHz (ASTM 6760-14). Energy of frequencies other than the test frequency are considered to be noise. As illustrated in Figure 3(d), by plotting wavelet coefficients only at the test frequency, we can remove/filter energy from the other frequencies (e.g. 80 and 200 kHz). In addition, the phase output of the CWT converts the time signal from a nonlinear sinusoidal curve to a linear phase angle line. The proposed ICWT method utilizes these two features of CWT to determine the travel time of CSL tests. To illustrate the benefits of the proposed method, two examples from CSL test results are discussed below. The first example shows a drilled shaft with a simulated soil intrusion zone. The second example shows a drilled shaft with debonded access tubes.

Example drilled shaft with a simulated soil intrusion zone. For research purposes, three test shafts were constructed at Ensoft Inc. in Austin, Texas. One of these shafts, named “west shaft”, was constructed with steel access tubes for CSL Testing. A photograph of the west shaft during CSL test is shown in Figure 1. Within this shaft, a controlled soil intrusion zone was created using a plywood box filled with sand. The size of the box was $76 \times 178 \times 457$ mm ($3 \times 7 \times 18$ inches). The top of the box was placed at 3.05 m (10-ft) from the top of shaft. A photograph of the wooden box tied on the rebar cage is shown in Figure 4. The west shaft is 0.61 m (2-ft) in diameter with a total length of 6.25 m (20.5 ft), of which, 0.914 m (3-ft) is above the ground surface. Eight US #8 bars are used as longitudinal reinforcement, placed evenly around the shaft circumference. US #4 circular hoops are used as transverse reinforcement. Soil conditions at the shaft location consist of 1.83 m (6 ft) of stiff clay underlain by a lightly weathered limestone formation.

Conventionally, time signals are plotted in a variable-area waterfall plot as shown in Figure 5. Area of the time signal is filled with black ink if the amplitude of the signal is greater than 0, but is left blank if the amplitude of the signal is less than 0. Since only two colors are used, energy of each time record cannot be identified in the variable-area waterfall plot. As shown in Figure 5, a separate relative energy plot is required to show the relative amplitude of each time signal (ASTM D6760-14). The location of the embedded wooden box can be identified in the figure at depths between 3.05 and 3.51 m (10 and 11.5 ft). The CWT amplitude time vs. depth plot at the test frequency of 42 kHz is shown in Figure 6. The recorded time signals are overlaid on top of the CWT amplitude time vs. depth plot. As shown in the figure, the location of the embedded wooden box can be clearly identified at a region with lower CWT amplitude. Information from the CWT amplitude time vs. depth plot is much easier to interpret than that from the variable-area waterfall plot shown in Figure 5.

The CWT phase-time versus depth plot from the “west shaft” is shown in Figure 7. The recorded time signals are overlaid on top of the CWT phase-time versus depth plot. Two black lines shown in Figure 6 and Figure 7 mark the locations of source signal and the first arrival pulse at various depth. The travel time is the time difference between these two lines. The two black lines are selected using the “smart trace” function developed at Ensoft Inc. As signals are triggered with a controlled pulse, locations of the source signals are constant, hence, a vertical line. In practice, only the first arrival pulse is needed for determining the travel time. The “smart trace” function implements the Integrated Continuous Wavelet Transform (ICWT) method in

selecting locations of source signal and the first arrival pulse. As shown in Figure 7, the source signal trace follows the blue and red boundary line tracing a downward pulse (± 180 -degree phase angle). The first arrival pulse trace follows a light yellow color line tracing an upward pulse (0-degree phase angle) at the first upward pulse that is above the noise level. Energy distributions, shown in the amplitude plot, are integrated in the process of determining which cycle of the upward phases to be selected.

The travel time selected based on visual selections of two different operators next to the automatic “smart trace” selection using the ICWT method is shown in Figure 8. Results from all three selections are close to each other. However, as shown in the figure, due to the complexity of the recorded time signals, different operators may pick a different point from the same curve. In contrast, the automatic “smart trace” selection, using the ICWT method, results at the same point on the time record independent from the subjective judgement of the operator.



Figure 4. A photograph of the wooden box tied on the rebar cage

It should be pointed out that in some areas the visual selections are close to each other but a bit far from the ICWT selections. This is because of the presence of high frequency noise. If we focused on Zone “A” in Figure 5, we will find the second and the third “black strips” are about the same width. This means that they are signals of a similar period (frequency). However, the widths of the first black strip vary with depth and are generally shorter. This means that it is from a signal of a higher frequency. In other words, the first cycle is contaminated by higher frequency noise. The amplitude of the first cycle in the CSL signal is generally small and can be close to noise level. As illustrated in Figure 2(c), it is difficult to identify the initial arrival time of a noisy signal. On the other hand, ICWT method removes/filters energy from other frequencies by plotting wavelet coefficients only at the test frequency. As shown in Zone “A” in Figure 7, the width of the first three cycles starting from the first arrival pulse are about the same. In other words, they are signals of the same frequency. As a result, selections from ICWT method are more accurate than those from visual selections.

Example drilled shaft with debonded access tubes. The second example is a drilled shaft tested by Ensoft Inc. in 2011. This drilled shaft is 20.1 m (66 ft) long, with a diameter of 1.676 m (5.5 ft). A side by side comparison of a variable- area waterfall plot with relative energy curve (Figure 9a) and a CWT amplitude time vs. depth plot (Figure 9b) from the drilled shaft is shown in Figure 9. Because of their large number, the time signals are not overlaid on the CWT

amplitude time vs. depth plot. As shown in the figure, location of arrival time is near the boundary between yellow and blue color. The relative energy of the time signals can be observed from the intensity of the blue color. Both travel time and relative energy can be easily observed in the CWT amplitude time vs. depth plot which makes it much easier in identifying the areas of debonded access tubes.

The CWT phase time vs. depth plot is shown in Figure 10. The first arrival pulse follows a light yellow color line tracing an upward pulse. In the debonded access tube area, locations of the first arrival pulse show a wide variation between 0.2 and 0.4 ms. Similar to Figure 7, focusing on Zone “B” in Figure 9, we will find the first “black strip” varies with depth and is narrower than the second and third “strips.” On the other hand, as shown in Figure 10, the widths of the first three cycles starting from the first arrival pulse are about the same in areas of sound concrete. With the built-in filter function, selections from ICWT method can better reject high frequency noise and provide accurate and unique first arrival time selections.

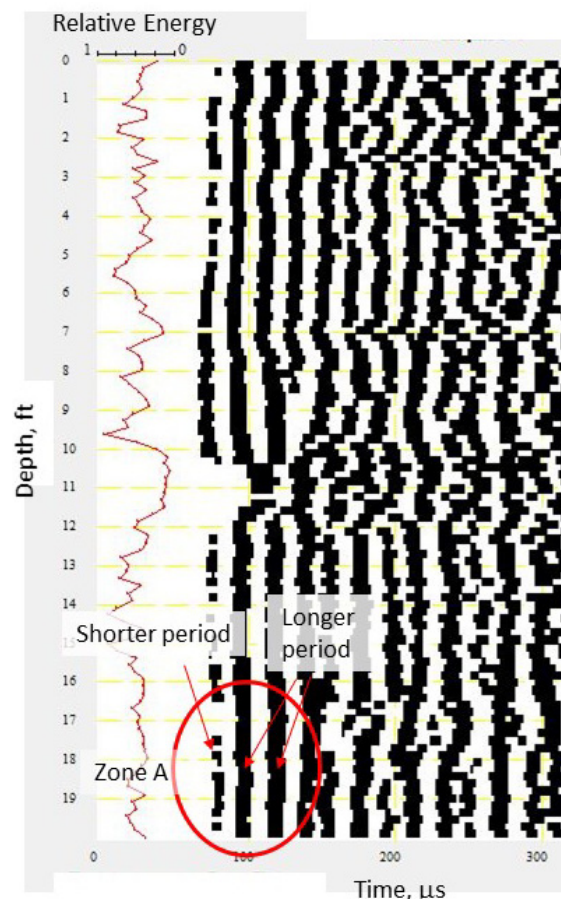


Figure 5. Conventional representation of CSL test results

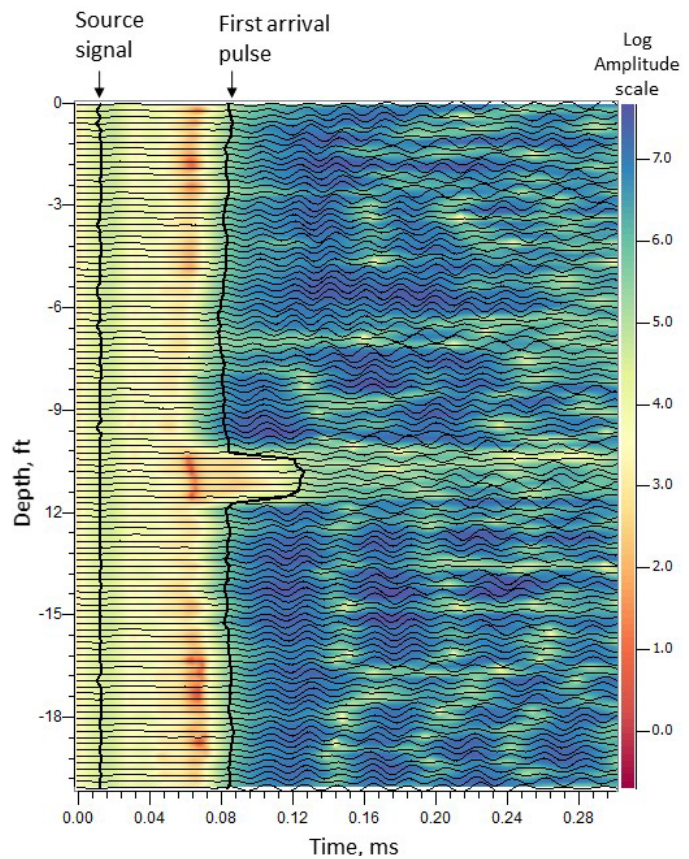


Figure 6. CWT amplitude time vs. depth plot with scaled time records

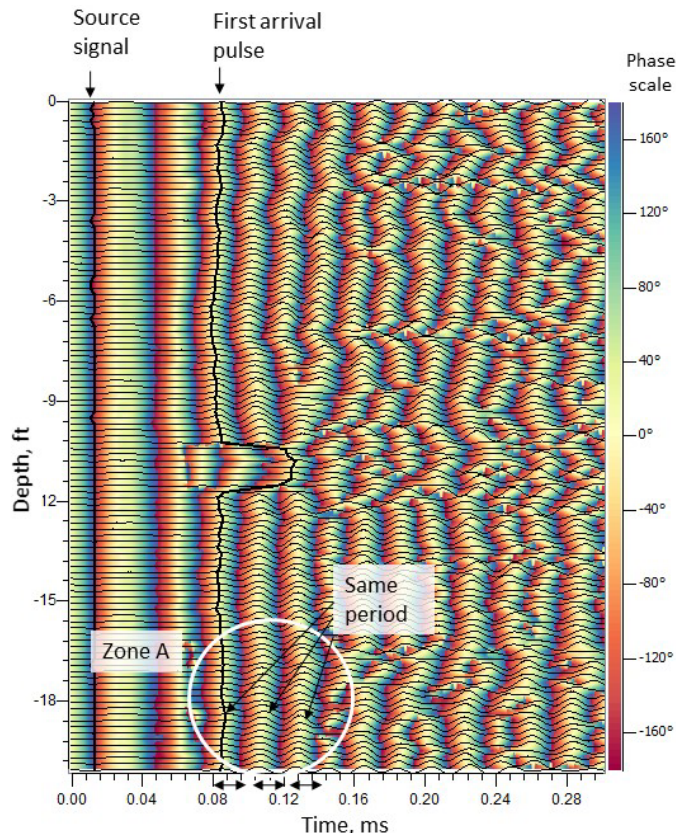


Figure 7. CWT phase time vs. depth plot with traces of time records for West Shaft

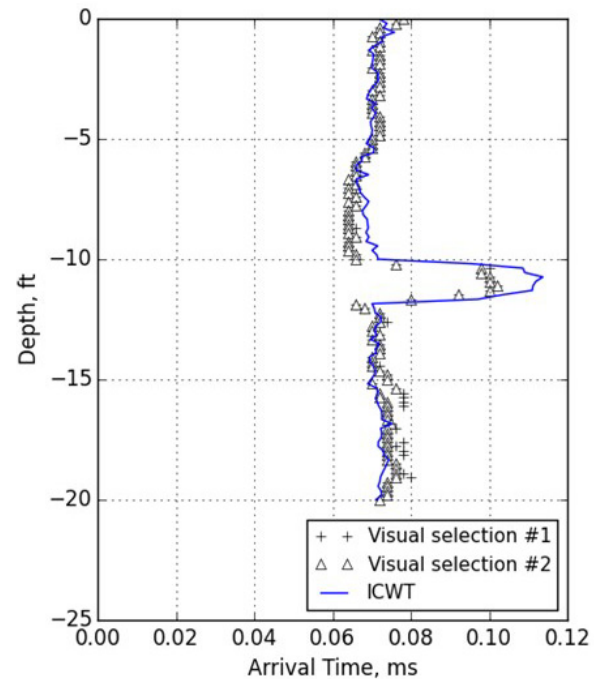


Figure 8. Comparison of selected travel times between 2 visual selections and an automatic selection from ICWT

CONCLUSIONS

This paper describes the Integrated Continuous Wavelet Transform method (ICWT). This method utilizes both the amplitude and phase outputs from Continuous Wavelet Transform (CWT) to determine signal arrival times in Crosshole Sonic Logging (CSL) tests. The phase output of the CWT converts the time signal from a nonlinear sinusoidal curve to a linear phase angle line. This conversion makes it easy to select a time point, whether at a peak or at a trough of a time signal. The built-in filter function removes high frequency noise and makes arrival time selections more consistent than those obtained from traditional visual examinations. It should be noted that although ICWT provides a simple and consistent way of selecting the arrival time, it is not intended as the sole means of pile acceptance or rejection. Incorrectly calculated arrival times are possible and that the accuracy of the method depends on selection of the test frequency and the noise level.

In practice, a careful review of the arrival time, CWT amplitude plots, and other related information from a qualified engineer is warranted. Although not shown in this article, the ICWT method can also be used in other tests that measure travel time intervals, including pulse echo tests, parallel seismic tests, downhole tests, and others.

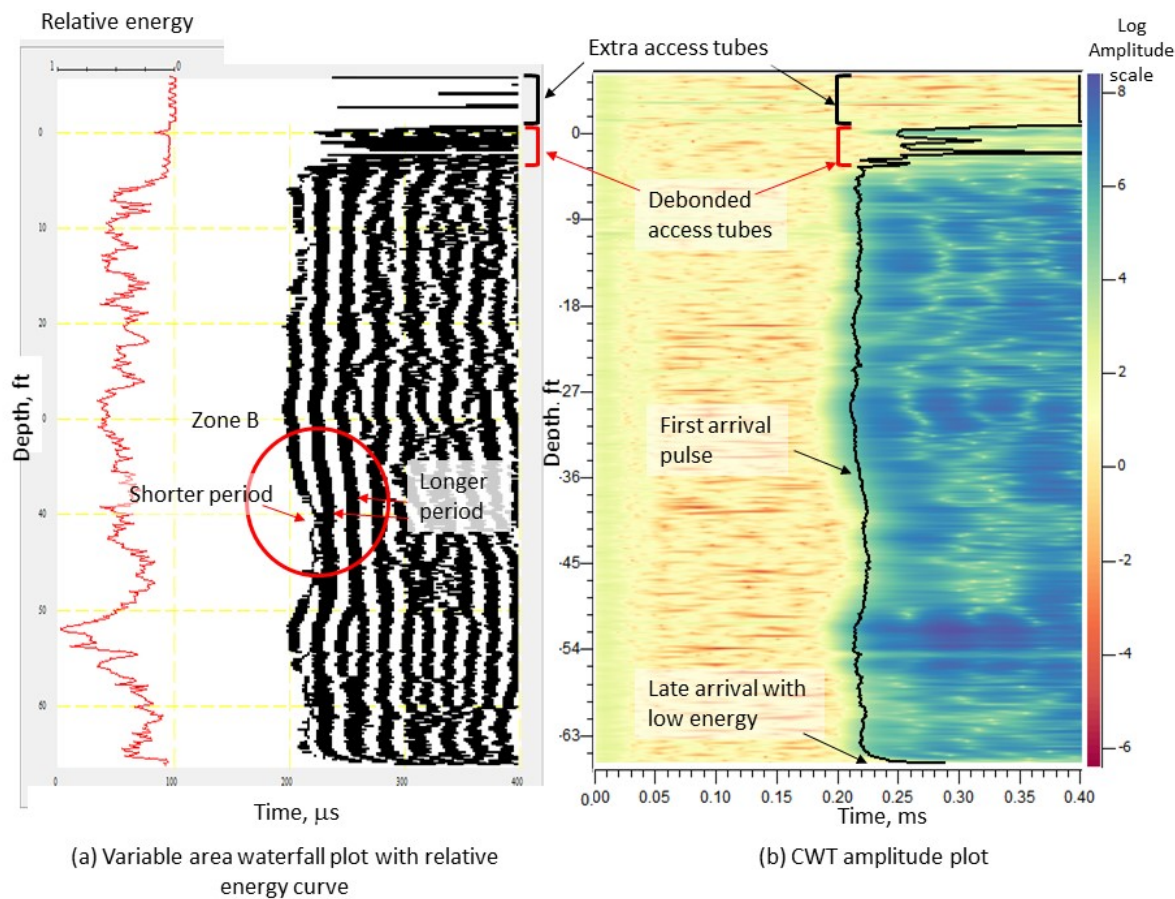


Figure 9. Comparison of (a) conventional representation of CSL test results and (b) the CWT amplitude time vs. depth plot

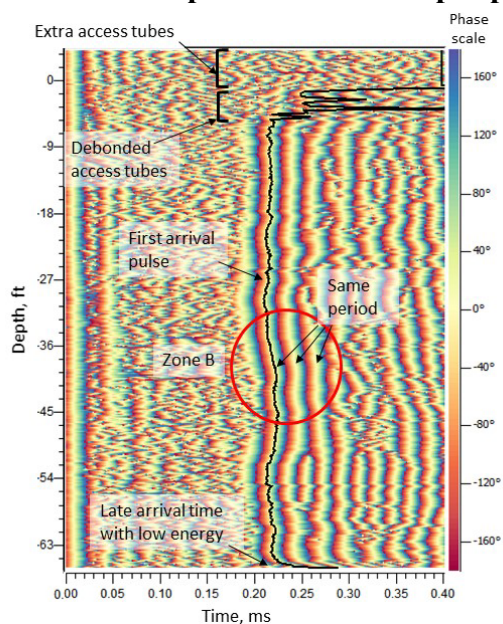


Figure 10. CWT phase time vs. depth for test shaft with debonded access tubes

REFERENCES

- Addison, P.S. (2002). *The Illustrated Wavelet Transform Handbook: Introductory Theory and Applications in Science, Engineering, Medicine and Finance*, CRC Press, 353 p.
- ASTM International (2014). ASTM D6760-14, Standard Test Method for Integrity Testing of Concrete Deep Foundations by Ultrasonic Crosshole Testing, ASTM International, West Conshohocken, PA, 2014.

A Robust Method for a Lateral Loading Analysis of Large Diameter Piles

Bret N. Lingwall, Ph.D., P.E., M.ASCE¹; Byron Foster²; Omololu Ogunseye³; and James Gingery, Ph.D., P.E., M.ASCE⁴

¹Dept. of Civil and Environmental Engineering, South Dakota School of Mines and Technology, 501 East St. Joseph St., Rapid City, SD. E-mail: bret.lingwall@sdsmt.edu

²Kleinfelder, Inc., 849 West Levoy Dr. Suite #200, Taylorsville, UT 84123. E-mail: bfoster@kleinfelder.com

³Dept. of Civil and Environmental Engineering, South Dakota School of Mines and Technology, 501 East St. Joseph St., Rapid City, SD.

⁴Kleinfelder, Inc., 550 W C St #1200, San Diego, CA 92101. E-mail: jgingery@kleinfelder.com

Abstract

One of the principle shortcomings with lateral analysis of large diameter pile foundations is the reliance on beams on elastic foundation. Within numerical modeling, the fundamental nature of the interactions of steel to concrete, steel to soil, and concrete to soil are often difficult to constrain in non-linearity. Modeling with a simplified cracked modulus for the pile does not capture the path from linearity to non-linearity. The progressive occurrence of concrete cracking with yielding rebar and steel casing, with concrete crushing results in pile non-linearly under bending. Furthermore, the interaction of the structural materials and soil beyond Winkler relationships is desirable so that soil can flow around the foundation and assessment of stress changes in the field to affect adjacent facilities. For large displacement problems the ability of the shaft to rotate, bend, shear, twist, and “oval” under complex lateral loads is important. A numerical methodology that addresses these shortcomings was developed. This paper briefly presents the method along with comparison with conventional methods.

INTRODUCTION

Large diameter deep foundations of diameter greater than 3 feet may be auger piles, cast in steel shell piles, drilled shafts, bored precast piles, etc. For convenience in this paper, we refer to large diameter deep foundations as Large Diameter Shafts (LDS). The interaction between concrete and steel is fundamental to the non-linear behavior of LDS for problems of large lateral displacements. The conventional approach to modeling LDS under lateral displacements is via a beam on elastic foundation (BEF) approach such as P-Y methods or strain wedge methods (Ashour et al. 2009). The soil-structure interaction in BEF approaches is a local phenomenon, whereas large displacement problems may have soil-structure interaction over large areas. The use of an empirically derived P-Y curve with a non-linear structural model was demonstrated to be appropriate for small displacement problems (Reese and Wang 1994). Similarly, strain wedge methods utilizing passive earth pressure wedges have been demonstrated to be appropriate for those problems (Ashour et al. 2001). However, for large displacement problems, the pile may influence soil behavior as much as the soil influences the pile behavior, a more interactive relationship between soil and structure. For these types of problems, the pile structural model must have non-linearity with the ability to rotate, bend, shear, compress (or “oval”) and otherwise undergo three-dimensional movements from complex lateral loading. Use of finite element analysis has been employed on many occasions to solve this problem (Lombardi et al.

2010; Elgamal 2010), most often for smaller diameter piles. We propose a new method for capturing the complex non-linear soil structure interaction of large displacement loading of LDS using finite difference techniques where concrete and steel are modeled explicitly in three dimensions.

Typical loading of a LDS from inertial loads of a superstructure are often limited in the imposed displacements of a portion of a LDS or the head. Typical full-scale lateral load tests on both slender piles and LDS are often limited less than 6 inches of pile head displacement. Large displacement loading of LDS can come from many sources. Land sliding is one such example, where displacements up to several meters can occur that results in non-linear behavior of the LDS (Ong et al., 2015). Lateral spreading loads is another potentially large displacement problem. In conventional BEF modeling of landslides and lateral spreads, a displacement profile is imposed upon the pile and resultant moments are determined. This method assumes that free-field landslide or spreading displacements are identical to those imposed on the LDS, with no influence of the LDS on the soil displacements. Another example of a large displacement problem is surface fault rupture displacing several meters (Bray et al. 1994). For a LDS within a fault zone, the potential displacements may be at the top of the LDS, the base of the LDS, or at intermediary locations along the length of the LDS (Loli et al. 2009).

The amount of soil displacement in landslides, lateral spreads, and surface fault rupture will depend on the size and rigidity of the LDS. The amount of resulting non-linear behavior of the LDS will depend on the amount and distribution of the soil displacements. Simulation of these large displacement problems requires analytical techniques that couple the effects of soil on LDS and LDS on soil. Just as mat foundations influence surface fault ruptures (Oettle and Bray 2013), it is logical that LDS will also influence fault rupture.

BEF methods have been updated and refined, but issues remain. Dodds and Martin (2007) provide a summary of these limitations. We developed the proposed method of this paper in part to overcome limitations. Dodds and Martin (2007) note diameter affects rotational moment stiffness as a principle limitation of BEF methods, and that the assumption that soil response is independent of LDS diameter is incorrect. LDS may undergo rigid body rotation due to rotational moment stiffness unlike long, slender piles. Dodds and Martin (2007) and Ashour et al. (2001) discuss pile non-linearity and the importance of non-linear structural models. In summary of these authors, if LDS maximum moment are sufficient to mobilize non-linear structural behavior, appreciable reductions in resistance to pile movement occur. One additional limitation is the assumption that the LDS cannot undergo torsional rotations or torsional stresses from unbalanced superstructure or soil displacement loads. These limitations aside, the non-linear BEF structural models do incorporate important non-linear behavior, and serve as a convenient and practical analysis method for researchers and practitioners. The limitations enter when applying these non-linear BEF models to problems of large displacement without modification. To address these limitations, use of advanced techniques has been widely proposed.

There are several ways to model laterally loaded LDS using numerical modeling techniques. One approach is to treat the soil as a continuum and to model the foundation using non-dimensional structural elements such as beam or “pile” elements). However, representation of the interaction between a rupturing fault plane or other large displacement problem and a non-linear LDS using non-dimensional pile elements may not fully capture the complexities of the soil-structure interaction. Additionally, the element stiffness matrix in this method must be modified for non-linearity. It is possible to capture some of this non-linear behavior as

progressive deformation and cracking occurs within the pile by varying Young's Modulus, Moment of Inertia, and Polar Moment of Inertia (J) for torsional loading, or by allowing yield to occur at the nodal points by specifying plastic moment capacities to each node. An alternative way to model the LDS via continuum elements with an elastic constitutive model and material properties as demonstrated by Kim and Jeong (2011), which requires the analyst to use a composite elastic modulus for the concrete and steel of the LDS. This approach does not capture the non-linear nature of the complex concrete and steel interaction within a LDS. One may also model the LDS using continuum elements with an elasto-plastic model such as the Mohr-Coulomb. The advantage is more closely captured plastic deformations. The disadvantage of the Mohr-Coulomb model is that it is elastic-perfectly plastic, so the "cracked" zones in the concrete will exhibit constant strength and stiffness after the concrete has yielded unless modified to incorporate brittle behavior. Tassios and Vintzeleou (1987) suggest tracking the state of stress within each individual zone and modifying the friction angle of the concrete to be compliant with changes in stress level. This is computationally intensive and would only be possible for small models with relatively low zone density. This also does not solve the lack of steel reinforcing in the concrete continuum, which provides much of the post-crack tensile capacity of the LDS.

A 2-node pile or beam structural element is a non-dimensional element that does not occupy any physical space in a 3D model and therefore does not reflect the diameter effect on pile behavior. To compensate for the lack of physical volume of beam elements, Wu (2006) uses four beam elements spaced at the equivalent boundaries of the shaft to take into account the effect of pile diameter on pile response via "outlining". The use of multiple node pile elements to represent a LDS volume makes it possible to account for the diameter effect on response. A structural section represented by multiple pile elements has geometric properties (bending moment of inertia and section area) that are evenly distributed across the section. This approach is useful for conventional analysis of laterally loaded LDS where displacements are small and effect of the pile movement is inconsequential to the surrounding soil mass. However, the overall non-linear behavior of these lines of beam elements still may not represent the complete behavior of a displacing large diameter shaft, the effects on the soil mass, or the torsional/twisting response of LDS to large displacement problems. Two alternative approaches that may compensate for most the limitations: Khosravifar et al. (2014) and McGann et al. (2012). Both use a very complex 3D approach using a combination of structural beam-column elements at the center of the LDS linked to soil contact elements lining the annulus of the LDS. The formulation of the linkages and soil contact elements differ between these two methods. Both methods rely on the linkage to a single beam element at the center of the LDS. However, these methods are very complex and have not been widely adopted in numerical modeling codes. These methods also critically lack the physical mass of the LDS, imparting stress into the soil mass beneath and around the LDS.

PROPOSED METHOD

Our proposed method uses numerical code FLAC3D (Itasca 2013) with explicit representation of pile components using continuum elements for concrete, one-dimensional ("cable") elements for rebar, and shell ("liner") elements for steel casing. Dodds and Martin (2007) provide practical guidance on mesh densities appropriate for FLAC3D, which we have followed. This proposed method overcomes all shortcomings of other methods noted by Dodds and Martin. The continuum elements use the Mohr-Coulomb constitutive linear elastic-perfectly plastic model

with stiffness and strength properties of concrete, while rebar is modeled using cable elements with steel properties. For steel reinforcing, we embed structural cable elements in the concrete with the same physical locations, geometry and properties of reinforcing steel. We represent interaction between concrete and steel by a bonded interface that restricts displacement prior to rupture of the interface with subsequent slippage. This approach results in a nearly rigid bond. The assumption of a nearly rigid bond is not strictly correct, as rebar will slip and pull out of the concrete as deformation increases. Stress redistribution occurs as concrete cracks, and stress transfers from the concrete to the rebar and back again through the bond. This is a complex phenomenon, very difficult and time consuming to validate within a model. A more realistic rebar-concrete interface that exhibits some lesser degree of strength and stiffness may influence the results. Future research to confirm the degree of influence. In our approach we allow large-strain, post-failure sliding of the tensile elements and continuum elements. We set the bond strength between concrete and steel reinforcing derived from pullout test data from similar reinforcing bars in concrete.

We model the mechanical stress-strain behavior of steel using a linear elastic-plastic relationship as shown, with no strain hardening. This allows the rebar to yield and deform plastically with increasing foundation displacement. As steel reinforcement within concrete is inherently a tensile phenomenon, the use of one-dimensional elements with no bending stiffness is reasonable. The tensile elements may be longitudinal, transverse, or placed in spiral/hoops as confining steel. A number of these elements placed in series form finely discretized bars and hoops/spirals with many nodes. The steel reinforcing tensile elements provide confinement to the concrete which is modeled as stress dependent such that confinement via steel increases concrete strength in a manner similar in results to that proposed by Mander et al. (1988) though with different approach.

We model steel shells using three node eighteen degree of freedom “liner” shell elements with steel properties for the casing around the perimeter of the concrete continuum for the concrete infill. Each of the three nodes has 6 degrees of freedom in translation and rotation in three dimensions. We place FLAC’s built-in structural “liner” shell elements around concrete at the perimeter of the cased LDS. “Liner” elements are desirable for the shell as they have interfaces on both sides of the elements that can interact with soil on the outside and concrete on the inside. The steel-to-concrete interaction is critical for modeling of a concrete-filled steel tube such as a cased LDS.

Liner element nodes have three connectivity links connecting the structural nodes to the surrounding zones and to each other. The constitutive relationship assigned to the link controls the interaction between the structural elements and the surrounding zones. One link is on the “outside” of the liner element connecting to soil, and an “inside” link connecting to the concrete within the casing. The link on the “outside” is a typical soil to structure interface with sliding and separation allowed using the interface properties of steel to soil. The linkage on the “inside” of the liner element is a steel to concrete interface with sliding and separation allowed using the properties of steel to concrete as developed for concrete filled steel tubes, with adhesion and friction between the concrete and steel (Han et al. 2006; Zhang et al. 2012). The third linkage in liner elements connects the elastic liner elements together at each node. In FLAC3D, yielding is not permitted within liner elements, but is permitted between elements in linkages. We use this third linkage to produce yield in the steel casing, by yielding linkages. We idealize steel casing as a set of hoops placed around the pile, with links assigned between each row of hoops. The link connectivity is required in the pile axial direction for simulation of bending-induced tensile or

compression yield of the casing. An assumption of 1D strain allows calculation of the stiffness (k), and yield strength of the connectivity links from steel properties and the area of the elements. We replace the inter-node linkages between structural nodes to simulate elastic-perfectly plastic behavior in the liner elements by allowing yield to occur within the links between the hoops. The other connectivity links between element and continuum (and associated degrees of freedom at each node) are preserved unaltered. By increasing the number of elements and decreasing their size around the LDS, we simulate a numerically robust yield condition for a steel tube with or without concrete inside or soil outside. We derived the stiffness of the linkage spring between Liner Shell elements from the relationship presented by Fish and Belytschko (2007) for shell element stiffness with the same stiffness as the triangular elements they link. The stiffness relationship by Fish and Belytschko (2007) is a constant strain plane-stress relationship specifically developed for triangular shell elements.

We model the concrete for simulations of LDS constitutively using an elasto-plastic relationship with Mohr-Coulomb failure criteria (friction angle and cohesion) estimated from typical concrete compressive strength. Tensile strength and Young's Modulus of concrete is estimated from the compressive strength or specific testing on the concrete material in question. Once concrete compressive and tensile strengths are determined, we estimate the friction angle and cohesion strength parameters using Mohr circles (Chen, 2007). We capture the effects of concrete confinement in a frictional term (ϕ_c) for stress dependent concrete strength. The concrete has a stress independent component to its strength (c_c) and a stress dependent component ϕ_c . Further research will evaluate the effects of confining stress on concrete modeled using internal frictional terms such as ϕ_c . Though the use of a term such as ϕ_c is coincidental to soil friction angle, the symbol ϕ_c represents the shear stress dependency of a material to normal stress levels and does not necessarily represent the friction between soil particles in shear. Brittle behavior of concrete in tension and compression is included in the model, as noted by Mander et al. (1988), as critical to the non-linear behavior of reinforced concrete. This brittle behavior uses a conventional tensile cut-off, where at the tensile strength of the material, brittle failure occurs and the material has zero strength. Strains levels for the brittle behavior vary for different concretes with typical values reported by Mander et al. (1988). In the case where a concrete continuum zone has "cracked" under brittle tensile criteria, we reduce the tensile strength of the entire zone is instantaneously to zero.

We establish deflection and bending moment profiles indirectly by using diametric strain profiles measured within diametric pairs of compression and tensile longitudinal rebar. We use the curvature profile in conjunction with a moment-curvature diagram from a conventional non-linear section analysis to estimate the bending moment in pile simulation. Once the bending moments are established, we calculate the shear force by differentiating the bending moment diagram. The major assumption of the curvature calculation is that plane sections remain plane, and that the strain profile across the section is linear.

With a continuum model for concrete with compressive strength and ability to brittle fracture, and steel cable elements for rebar, and liner shell elements for steel casing, we couple the composite behavior of the two materials for both cased and uncased LDS with and without reinforcing steel. To verify that this coupling produced reasonable results for reinforced concrete, we performed a series of calibration exercises. These calibration simulations included simply supported reinforced concrete beams, cantilever beam push-over tests, short captive column shear tests, laterally loaded embedded pile comparisons with BEF methods, and a concrete-filled steel tube (CFST) simply supported beam test, as described in the following sections.

VALIDATION WITH STRUCTURAL ELEMENT TESTS

Validation of the approach began with comparison of simulation results to data observed from structural experiments. The first validation exercises we performed were simply supported beam tests. Simply supported reinforced concrete beam tests in the engineering literature provide a suitable baseline for validation. These simulations were critical to the development of the method but are not presented here for brevity, but will be reported in other publications at later date. These simulations demonstrated that the moment-curvature relationship used for a specific composite structural member from fiber analysis is critical to comparison of results between methods, but is not critical to the model's performance. Since the 3D model is, in many respects, forming a fiber analysis of sorts, with initial cracking of concrete, initial yield of first rebar, etc. captured directly, we only use moment curvature relationships to convert the measured curvature in the element and strains on individual tensile elements to an internal bending moment.

Our second stage of the validation was to compare simulation results with measurements of column and simply supported concrete filled steel tube experiments (CFST) such as Han et al. (2006). Concrete filled steel tubes are an excellent analogy to steel casing around LDS. We performed several other CFST models, but only the Han et al. (2006) comparisons are presented in this brief paper. Figure 1 shows our calculated cracking pattern in the concrete material at maximum moment. In Figure 1, zones that have exceeded the tensile capacity of the concrete have cracked along the extreme fiber of the CFST. This cracking pattern is in good agreement with the observed cracking reported by Han et al. (2006).

Both simply supported reinforced concrete and CFST structural models are failures via bending. We also simulated an alternative load path, shear of a column for validation purposes. So called "captive short columns" in concrete walls under earthquake loading are an observed example of failure via shear loading. Guevara and Garcia (2005) show an example of such situations and the distresses to reinforced concrete from this shear loading. Due to space constraints, these simulation results are not presented here. Captive column simulations showed the importance of confining steel to the analysis model. Thus, simulations of bending and shear demonstrated the critical importance of inclusion of individual tensile elements for both longitudinal and transverse steel in beams and columns.

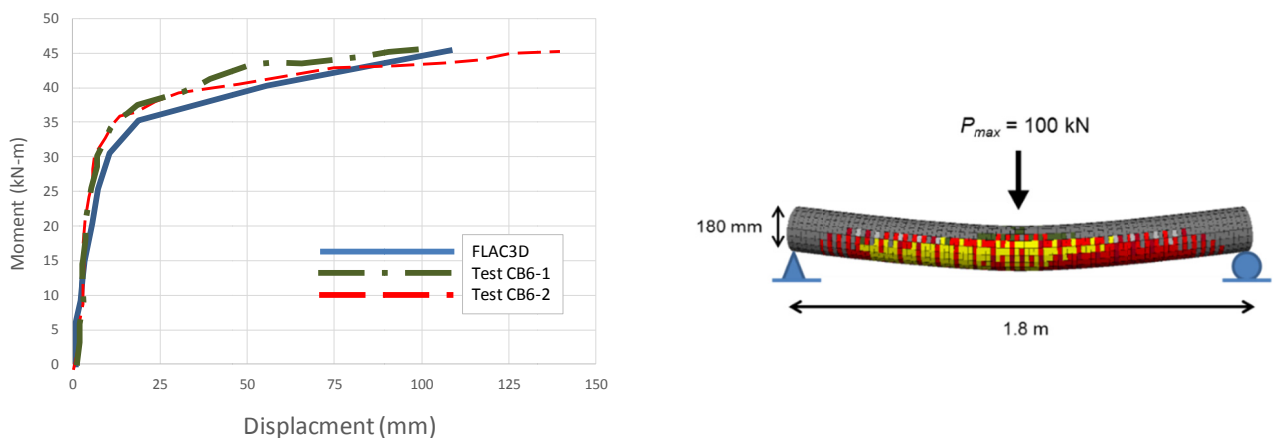


Figure 1. Comparison between Han et al. (2006) Data and Numerical Simulations.

COMPARISON WITH BEF APPROACHES

Validation with structural beam and column experiments gave confidence in the capability of the method for simulating non-linear behavior in the structural portion of the soil-structure interaction problem. The coupled response of a soil-structure system, the interaction, between the rigid and compliant elements in the ground also required validation. A simple fixed-base pushover analysis of an LDS with no soil was chosen for the validation. We compared pushover analysis results against theoretical analytical solutions, and the results of commercially available P-Y and strain wedge software. The geometry of the pushover analysis for the uncased LDS included longitudinal and spiral reinforcement. The loading at the top of the LDS is purely horizontal in a free head condition. We based the moment-curvature for conversion of FLAC3D curvature data into moments on theoretical non-linear section analysis, calculated to be identical to the moment-curvature used by both the P-Y and strain wedge software packages. An identical LDS simulation was also performed but with a steel casing around the LDS and no reinforcement. Reinforcement of the 10-ft diameter 100-ft length LDS was #18 and #4, 60-ksi bars for the uncased model, and casing was 1 inch thick for the cased model. We present a small sample of results here. We attempted several different geometries and reinforcing details with similar results, as long as confining steel hoops were included. The results of the our models again proved to be sensitive to the effects of confining steel, a reasonable result considering that the concrete is modeled with stress dependency. The results are similar between all three methods up to 9 inches of pile head deflection. At deflections higher than 9 inches, the results diverge, with the strain wedge method showing the softest response and FLAC3D showing the stiffest response. The reasons for this divergence at increasing pile head deflection come from two main sources. 1) For cased LDS, the moment-curvature relationships between methods were different. We developed Fig. 2 with the same relationship for LPile and FLAC3D, but the strain wedge Model internally calculated different moment-curvature. 2) At these loads, the conventional software packages had reached maximum stable solutions.

The results of the uncased pushover test showed very good agreement between methods. The cased pushover test also showed good agreement up to 9 inches of pile head displacement, which is still promising. The final phase of validation of the proposed method was comparisons to laterally loaded LDS models from P-Y and strain wedge methods, including soil resistance. A set of cased and uncased laterally loaded models with 9 and 10 ft diameters of length between 72 and 134 ft were developed. The soil around the shafts was modeled as sand with $\phi' = 32^\circ$ and unit weight of 125 pcf. No cohesion was used for this analysis, although the method is capable of including cohesion in the soil model. We developed spring properties for all three methods for a medium dense sand with stress normalized Standard Penetration Test blow counts of 15 at 60% energy. We show a small sample of results of this final phase of validation in Figure 2. The FLAC3D result are in generally good agreement with the P-Y and strain wedge results. Further work is needed to compare the proposed method using FLAC3D to a suite of full-scale laterally loaded LDS load tests and case histories including case histories with landslides or surface fault rupture causing the distress to the LDS.

CONCLUSION

We propose a method for analysis of lateral loads on LDS imparted from large soil displacement problems such as lateral spreading, landslides, tunnel collapse, and surface fault rupture. We

implemented the method using FLAC3D with individual structural elements to simulate reinforcing bars, liner elements for steel casings, and brittle elastic-plastic continuum elements with tension cut-off for concrete. We have validated against beam and CFST structural experiments and captive column shear tests. We validated the method with simple pushover analysis as well as a BEF laterally loaded LDS in sand. This method must still be validated to full-scale laterally loaded LDS tests. Results compare well between the proposed methods, structural experiments, and non-linear analyses from conventional approaches. Further work is required to document the proposed method's robustness in additional loading conditions and geometries, and to compare to full-scale LDS case histories and load tests.

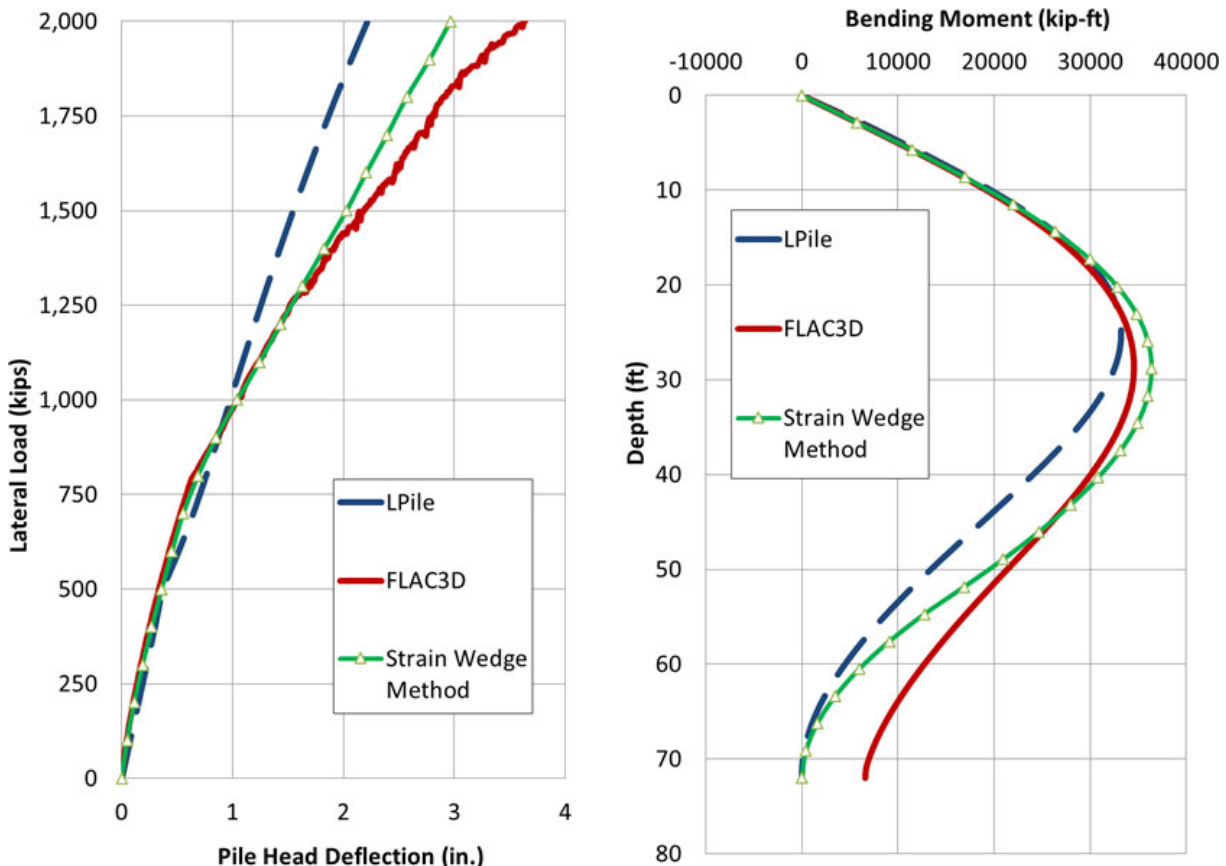


Figure 2. Cased laterally loaded pile simulation results

ACKNOWLEDGMENTS

The author wish to thank Professor J. Bray of the University of California at Berkeley for his guidance on this project for problems of surface fault rupture affects to bridge foundations.

REFERENCES

- Ashour, M., Norris, G., and Shamsabadi, A. (2001). "Effect of the non-linear behavior of pile material on the response of laterally loaded piles." *4th International Conferences on Recent Advances in Geotechnical Earthquake Engineering and Soil Dynamics*. San Diego, CA.

- Bray J.D., Seed, R. B., Cluff, L. S., and Seed, H.B. (1994). "Earthquake fault rupture propagation through soil." *J. Geotech. and Geoenviron. Eng.*, 120(3), 543-561.
- Chen, W.F. (2007). *Plasticity in Reinforced Concrete*, McGraw-Hill, New York, NY.
- Dodds, A.M., and Martin, G.R. (2007). "Modeling pile behavior in large pile groups under lateral loading." *Technical Report MCEER-07-0004*, Buffalo, NY.
- Elgamal, A. (2010). "Calibrated 3D computational modeling of Soil-Structure systems and liquefaction scenarios." *5th International Conferences on Recent Advances in Geotechnical Earthquake Engineering and Soil Dynamics*. San Diego, CA.
- Ensoft (2013), LPILE v. 2013.7.03, Ensoft Inc., Austin, TX.
- Fish, J., and Belytschko, T. (2007). *A First Course in Finite Elements*. Wiley and Sons, Chichester, West Sussex, England.
- Guevara, L.T., and Garcia, L.E. (2005). "The captive- and short-column effects," *Earthquake Spectra*, 21(1), 141-160.
- Han, L.H., Lu, H., Yao, G.H., Liao, F.Y. (2006). "Further study on the flexural behavior of concrete-filled steel tubes." *Journal of Construction Steel Research*, 62(1), 554 – 565.
- Kim, Y. and Jeong, S. (2011). "Analysis of soil resistance on laterally loaded piles based on 3D Soil-Pile interaction." *Computers and Geotechnics* 38, 248-257.
- Khosravifar, A., Boulanger, R.W., and Kunnath, S.K. (2014). "Effects of liquefaction on inelastic demands on extended pile shafts." *Earthquake Spectra*, 30(4), pp. 1479-1773.
- Loli, M., Bransby, M. F., Anastasopoulos, I., and Gazetas, G. (2009). "Interaction of caisson foundations with a seismically rupturing normal fault: centrifuge testing versus numerical simulation." *Geotechnique*, 62, No. 1, 29-34.
- Lombardi, D., Durante, M.G., Dash, S.R., and Bhattacharya, S. (2010). "Fixity of piles in liquefiable soils." *5th International Conferences on Recent Advances in Geotechnical Earthquake Engineering and Soil Dynamics*. San Diego, CA. Paper 5.39a.
- Mander, J.B., Priestley, M.J.N., and Park, R. (1988). "Theoretical stress-strain model for confined concrete." *Journal of Structural Engineering*, 114(8), pp. 1804-1826.
- McCann, C.R., Arduino, P., and Mackenzie-Helnwien, P. (2012). "Development of simplified analysis procedure for piles in laterally spreading layered soils." *Pacific Earthquake Engineering Research Center*, December 2012.
- Oettle, N.K., and Bray, J.D., (2013). "Geotechnical mitigation strategies for earthquake surface fault rupture." *J. Geotech. and Geoenviron. Eng.*, 139(11), 1864-1874.
- Ong, D.E.L., Leung, Y.K., Chow, Y.K., and Ng, T.G. (2015). "Severe damage of a pile group due to slope failure." *J. Geotech. and Geoenviron. Eng.*, 141(5).
- Reese, L.C., and Wang S.T. (1994). "Analysis of piles under lateral loading with nonlinear flexural rigidity." *U.S. FHWA Int. Conf. On Design and Construction of Deep Foundation*, FHWA, Washington, D.C.
- Tassios, T. P. and Vintzeleou, E. N. (1987). "Concrete-to-concrete friction." *Journal of Structural Engineering*, 113(4), 832-849.
- Wu, G. (2006). "VERSAT-P3D dynamic 3D finite element analysis of single piles and pile groups." *Wutech Geotechnical International*, B.C., Canada.
- Zhang, J., Denavit, M.D., Hajjar, J.F., and Lu, X. (2012). "Bond behavior of concrete filled steel tubes." *Engineering Journal*, Fourth Quarter, 2012.

Development of Empirical Models to Estimate the Increase in Pile Resistance (Set-Up) with Time

Md. Nafiul Haque, Ph.D., A.M.ASCE¹; and Murad Y. Abu-Farsakh, Ph.D., P.E., M.ASCE²

¹Louisiana Transportation Research Center, Louisiana State Univ., 4101 Gourrier Ave., Baton Rouge, LA 70808. E-mail: cefars@lsu.edu

²Louisiana Transportation Research Center, Louisiana State Univ., 4101 Gourrier Ave., Baton Rouge, LA 70808.

Abstract

This paper presents the analyses of twelve prestressed concrete (PSC) instrumented test piles that were driven in different locations of Louisiana to develop analytical models to estimate the increase in pile resistance (soil set-up) with time. The twelve test piles were driven mainly in cohesive soils. Detailed soil characterizations including laboratory and in-situ tests were conducted to determine the different soil properties. The test piles were instrumented with vibrating wire strain gauges, piezometers and pressure cells. Several static load tests (SLT) and dynamic load tests (DLT) were conducted on each test pile at different times after end of driving (EOD) to quantify the magnitude and rate of set-up. Measurements of load tests confirmed that pile resistance increases almost linearly with the logarithm of time elapsed after EOD. Case pile wave analysis program (CAPWAP[®]) were performed on the restrikes data and were used along with the load distribution plots from the SLTs to evaluate the increase of shaft resistance of individual soil layers along the piles. The logarithmic set-up parameter “A” for unit shaft resistance was calculated for 70 individual clayey soil layers, and the database set of A was correlated with different soil properties. Nonlinear multivariable regression analyses were performed between A and different soil properties, and three different empirical models are proposed to predict the soil set-up parameter “A” as a function of soil properties.

INTRODUCTION

It is well known that the axial resistance of piles usually increases with time after driving in cohesive soils. Many researchers (e.g., Likins et al. 1989, Bullock et al. 2005, Paikowsky et al. 2005, Lim and Lehane, 2014) have studied this increase in resistance, known as “set-up.” Several empirical, analytical and numerical techniques have been proposed over the past few decades to predict the magnitude and rate of soil set-up with time. It has been well recognized that the magnitude of set-up is dependent upon the pile size, pile length, pile material, soil type and soil strength (Preim et al. 1989; Ng et al. 2013)

Soil set-up phenomenon is mainly attributed to three main mechanisms: (1) Dissipation of excess porewater pressure (PWP) (consolidation), (2) Thixotropic effect, and (3) Aging effect. During pile driving, the surrounding soil is displaced predominantly radially along the shaft and vertically and radially beneath the toe, thus generating a significant amount of excess PWP. In addition, the soil within the vicinity of pile face loses its strength due to an increase in excess PWP, disturbance of the soil structure and the soil remolding (Bullock et al. 2005, Lim and Lehane, 2014). As the excess PWP starts to dissipate, the effective stress of the disturbed soil starts to increase, and consequently set-up primarily occurs due to the increase in shear strength and the increase in lateral stresses against the pile (Preim et al. 1989; Ng et al. 2013; Chen et al. 2014). Thixotropic effect (or regaining of soil strength of disturbed soil with time) also plays a

significant role at the early stage of set-up. Any set-up occurs after the completion of excess PWP dissipation is mainly due to “aging” effect (i.e., time-dependent change in soil properties at a constant effective stress) (Schmertmann, 1991). Several empirical models (e.g., Guang-Yu, 1988; Skov and Denver, 1988; Ng et al. 2013, Lim and Lehane, 2014) have been proposed to estimate the soil set-up resistance with time. Of these models, the relationship developed by Skov and Denver (1988) is considered the most popular relationship due to its simplicity. They postulated that the pile resistance increases with the logarithm of time as follows:

$$\frac{R_t}{R_{t_0}} = A \log_{10} \frac{t}{t_0} + 1 \quad \dots (1)$$

where: R_t = total pile resistance at time, t ; R_{t_0} = total pile resistance at reference time, t_0 ; t = time elapsed since end of initial pile driving; t_0 = initial reference time, a reference time before which there is no predictable R_{t_0} increase as a function of elapsed time (i.e., R_{t_0} increase is non-linear with respect to elapsed time); A = set-up parameter (log-linear). The “ A ” parameter can be assumed, back-calculated from field data, or gleaned from empirical relationships available in the literature. However, most of the available models in literature (e.g., Skov and Denver, 1988) did not consider the soil properties in their formulations and that the total resistance (R_t) was mostly used instead of the shaft resistance (R_s). However, very few researchers (e.g., Guang-Yu, 1988; Ng et al. 2013; Karlsrud et al. 2014; Haque et al. 2016) incorporated the soil properties in their set-up models.

OBJECTIVE

The objective of this study is to develop analytical models to estimate the set-up parameter “ A ” for individual soil layers from soil properties. The “ A ” parameters of individual soil layers were back-calculated using the unit shaft resistance (f_s) rather than the total pile resistance (R_t) as proposed by Skov and Denver (1988) model. The soil properties of individual soil layers for each test pile location [i.e., undrained shear strength (S_u), Atterberg limits, sensitivity (S_r) and vertical coefficient of consolidation (c_v)] were obtained from the laboratory tests and/or interpreted from the piezocone penetration tests (PCPT) and piezocone dissipation tests. The back-calculated set-up parameters “ A ” were correlated with selected soil properties and nonlinear analytical models were developed to estimate the shaft resistance set-up for individual soil layers along the pile length.

TEST SITE AND SUBSURFACE GEOETCHNICAL CONDITION

Test Location and Test Piles (TP). Five different sites were selected in Louisiana to perform the soil set-up study: Bayou Zourie, Bayou Lacassine, Bayou Teche, Bayou Bouef and LA-1. Detailed description of the Bayou Zourie, Bayou Lacassine and LA-1 project sites can be found in Chen et al. (2014), Haque et al. (2014), and Haque et al. (2016), respectively. This set-up study was performed only on 12 square PSC instrumented test piles driven in cohesive-dominated subsurface soil conditions. The objective of this study is to develop analytical models that can predict soil set-up for individual soil layers along the pile length. To meet this criterion, the test piles were instrumented with strain gauges to calculate the increase in shaft resistance of individual soil layers at different times after EOD. A combination of piezometers and pressure

cells were also installed in selected test piles to measure the total and porewater pressure and hence the effective lateral stresses on pile face.

Geotechnical Subsurface Characterization. Both laboratory and in-situ tests were conducted at each test pile location to evaluate the different soil properties. 7.6-cm Shelby tube samples were retrieved from boreholes drilled at different depths for comprehensive laboratory testing. Water content, unit weight, Atterberg limits, one-dimensional consolidation tests and unconsolidated undrained (UU) triaxial tests were performed on selected soil samples to characterize the subsurface soil conditions. The in-situ testing program included both piezocone penetration and dissipation tests and standard penetration test (SPT). One-dimensional consolidation tests were also performed to calculate the coefficient of consolidation (c_v) of soil in the absence of PCPT dissipation tests. Table 1 presents the subsurface soil properties of the test piles locations.

Table 1: Summary of the soil properties and set-up parameter “A”

Pile ID	Testing Period (Days)	Nos and Types of Soil Layers		Ranges of Soil Properties				Ranges of set-up parameter “A”		Set-Up Ratio	
		Clayey	Sandy	S_u (kPa)	PI (%)	OCR	S_t	Clayey Soil Layer	Sandy Soil Layer	R_i/R_{to}	R_s/R_{so}
LA-1-TP-2	7	7	1	7-35	4-25	0.4-0.7		0.35-0.53	0.15	4.9	7.5
LA-1-TP-3	13	6	3	38-49	16-37	0.4-0.8		0.31-0.43	0.07-0.13	2.4	3.4
LA-1-TP-4a	6	8	3	8-45	46-77	0.3-0.6		0.38-0.51	0.13-0.24	5.0	9.9
LA-1-TP-4b	6	11	3	8-78	26-77	0.2-0.6		0.22-0.47	0.13-0.24	2.3	2.9
LA-1-TP-5a	6	4	2	23-44	20-50	0.5-1.3		0.24-0.33	0.23-0.24	4.2	5.2
LA-1-TP-5b	6	6	2	23-51	20-50	0.5-1.3		0.20-0.28	0.15	2.0	2.4
BL-TP-1	217	6	1	72-123	4-25	1.0-2.5	4-6	0.13-0.26	0.10	2.1	2.3
BL-TP-2	23	6	1	85-145	16-37	1.3-3.0	2-5	0.16-0.27	0.08	1.7	2.0
BL-TP-3	181	6	1	79-124	17-35	1.2-1.9	3-6	0.14-0.26	0.05	1.6	1.9
BB-TP-1	28	4	2	51-59	16-35	0.4-2.9	3-5	0.29-0.48	0.05	2.0	3.3
BZ-TP-1	76	3	2	116-	37-75	2.0-3.0	2-4	0.15-0.29	0.17-0.26	1.5	1.8
BT-TP-1	32	3	3	10-20	36-52	0.5-0.7		0.28-0.40	0.02-0.09	1.2	1.2
Total Soil Layers = 94		70	24	Average “A” parameter				0.31	0.15		

LOAD TESTING PROGRAM

The load testing program was designed to measure the increase in pile resistance with time (or soil set-up). Table 1 summarizes the testing period, set-up ratio (resistance during a load test / initial driving resistance), and the back-calculated set-up factor “A” for the individual soil layers along the 12 instrumented test piles. The dynamic measurements were acquired with Pile Driving Analyzer[®] (PDA) during initial driving and subsequent restrike events to evaluate the increase in pile resistances with time. In addition, the CAPWAP[®] was used to evaluate the shaft resistance of individual soil layers. The set per blow and level of energy delivered to the pile or shaft top, are important parameters that should be considered to determine whether the ultimate resistance has been mobilized. Researches (e.g., Rausche et al. 2008) have shown that a permanent set of less than 2.5 mm (a blow count of 400 blows/m or 120 blows/ft.) may not mobilize the ultimate pile resistances. The permanent sets for all the test piles were higher than the 2.5 mm in this study. It is most likely that full pile resistances had been mobilized for all test piles.

SLTs were performed after 6 to 217 days from EOD to evaluate the increase in soil resistance with time in each test pile as compared to DLT restrikes. The nominal pile resistance from the static load tests was determined based on the modified Davisson interpolation method (1972). Figure 1 presents the result of a SLT that was conducted on Test Pile LA-1-TP-2.

Embedded strain gauges were used to calculate R_s , R_{toe} and R_t during each SLT, and to estimate the distribution of R_s along the pile length. The axial load transfer can be determined from the strain measurements, the cross-sectional area and the Young's modulus of the pile (Fellenius et al. 1989). The modulus of concrete was back-calculated for each load test using the strain data measured by the "sister bar" strain gauges, which were installed at ground level. A constant modulus of concrete was used for strain gauge data analysis in each load test. Figure 1b depicts an example of the load distribution plot obtained during the SLT on LA-1-TP-2.

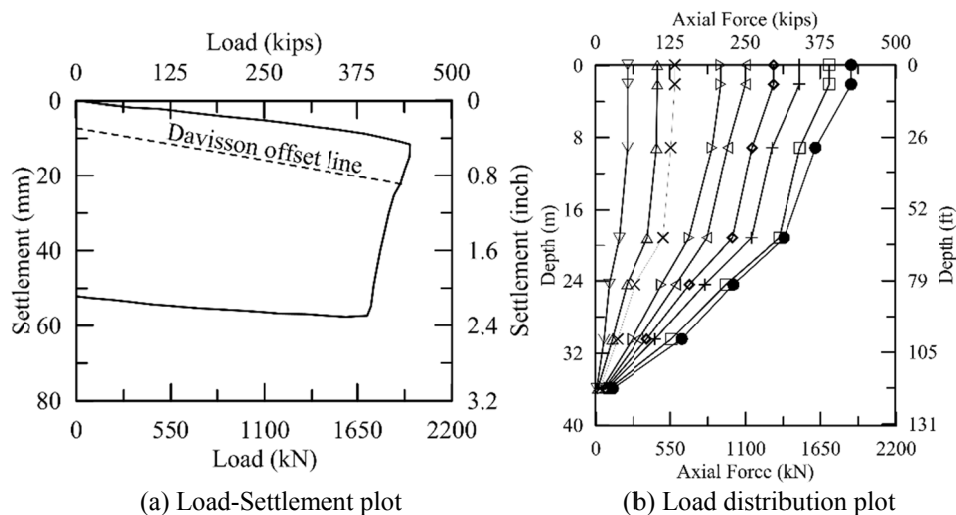


Figure 1: Results of static load test.

RESULTS

Set-Up in Terms of Total (R_t) and Shaft (R_s) Resistance. The total pile resistances estimated from the DLTs and SLTs are analyzed to study the set-up behavior for all test piles. All the test piles exhibited a significant amount of set-up as shown in Table 1. The shaft resistance set-up for all test piles is presented in Figure 2. Figure 2 shows that the test piles of the LA-1 site exhibited a higher amount and rate of shaft set-up compared to the test piles of other sites. The presence of very soft soil at the project location (i.e., near Gulf of Mexico) as compared to the other test pile locations contributed to this behavior. The figure demonstrates that the shaft resistances are best fitted to linear logarithmic of time with high coefficients of correlation (R^2). As seen in Table 2 and Figure 2, the soil set-up was mainly due to increase in R_s . The R_{toe} was almost constant over time for all the test piles.

Set-Up of Individual Soil Layers. Most of the available set-up models in literature consider either the total pile resistance set-up or the total shaft resistance set-up. As a result, the soil properties of subsurface soil layers were not incorporated into those models, which results in difficult implementation of set-up models on different soil conditions. In this study, the unit shaft resistance (f_s) (shaft resistance / contact area) was used to analyze the set-up behavior for individual soil layers along the pile length (Equation 2). The set-up behavior for individual soil layers were calculated with the aid of vibrating wire strain gauge measurements during the SLTs, and from CAPWAP[®] analyses during the DLTs.

$$\frac{f_s}{f_{s0}} = 1 + A \log \frac{t}{t_0} \quad (2)$$

Examples of analyses of set-up for individual soil layers are presented in Tables 2 for the TP-1 of Bayou Lacassine. The published literature (e.g., Paikowsky et al. 2005; Ng et al., 2013) documents that set-up is mainly dominant in clayey soil layers, and that small amounts of set-up were observed in sandy soil layers. Similarly, the sandy soil layers in this study also exhibited smaller amounts of set-up due to quick dissipation of excess PWP after EOD. Table 2 shows that the clayey soil layers exhibited an average shaft resistance increase of 100% to 230%, while sandy soil layers exhibited an average shaft resistance increase of 70% during the testing period.

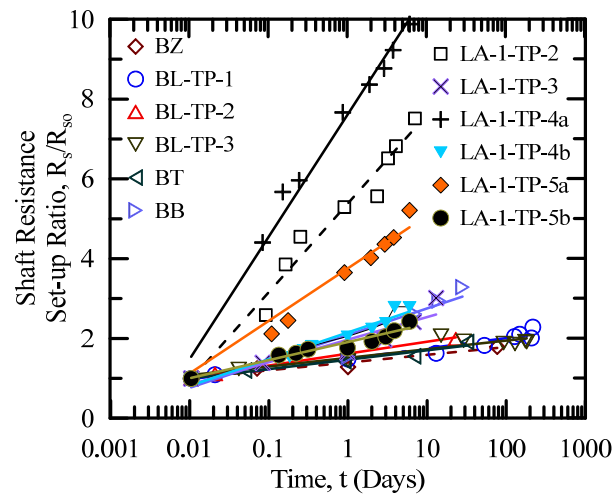


Figure 2. Shaft resistance set-up for all test piles.

Table 2: Example of set-up for some soil layers. The 5th layer was deleted for space.

Events	Time (Days)	2 nd Layer		3 rd Layer		4 th Layer*		6 th Layer		7 th Layer		8 th layer	
		Res. kN	Set-up Ratio	Res. kN	Set-up Ratio	Res. kN	Set-up Ratio	Res. kN	Set-up Ratio	Res. kN	Set-up Ratio	Res. kN	Set-up Ratio
EOD	-	152	1.0	89	1.0	151	1.0	125	1.0	107	1.0	85	1.0
1 st DLT		173	1.1	95	1.1	172	1.1	136	1.1	123	1.1	91	1.1
2 nd DLT	1	306	2.0	166	1.9	185	1.2	179	1.4	150	1.4	115	1.3
1 st SLT	13	371	2.4	196	2.2	193	1.3	187	1.5	161	1.5	116	1.4
2 nd SLT	53	462	3.0	218	2.4	197	1.3	228	1.8	168	1.6	139	1.6
3 rd SLT	127	480	3.2	254	2.8	231	1.5	232	1.9	193	1.8	142	1.7
4 th SLT	148	491	3.2	261	2.9	242	1.6	236	1.9	205	1.9	143	1.7
5 th SLT	208	485	3.2	240	2.7	218	1.4	236	1.9	208	1.9	147	1.7
3 rd DLT	217	498	3.3	280	3.1	257	1.7	250	2.0	219	2.0	168	2.0
"A" parameter		0.26		0.12		0.10		0.15		0.14		0.13	

*Sandy soil layer

Correlations between Soil Properties and Set-Up Parameter "A". The set-up rate in this study as measured by the set-up rate "A" parameter is calculated using the unit shaft resistance for each soil layer along the pile length. A total of 94 soil layers from 12 PSC test piles driven in five different project sites were included in the analyses. Clayey soil behavior was dominant in 70 clayey soil layers and the remaining 24 soil layers exhibited sandy soil behavior. The average value of the "A" parameter for clayey and sandy soil layers was 0.31 and 0.15, respectively. The effects of soil properties on the "A" parameter were investigated here to develop correlations

between the “A” parameter and different soil properties. The soil properties that have significant influence on the “A” parameter were identified as S_u , PI, c_h or c_v , and S_t .

Effects of Undrained Shear Strength (S_u). The S_u in this study was correlated with the “A” parameter for the individual clayey soil layers. S_u was experimentally measured for 70 clayey soil layers, and ranges from 7 kPa to 157 kPa. The clayey soil layers of the LA-1 project with the lowest S_u values generally exhibited higher rate and magnitude of set-up compared to the clayey soil layers of the other sites. The correlation between S_u and the “A” parameter is presented in Figure 3a. A review of the figure clearly demonstrates that there is an inverse-power relationship between the “A” parameter and S_u .

Effects of Plasticity Index (PI). Atterberg limit tests were performed on all 70 clayey soil layers. PI values range from 4% to 77%. The correlation between the PI and the “A” parameter is presented in Figure 3b. A review of the figure shows that a linear proportional relationship exists between the PI and the “A” parameter, with a relatively high coefficient of correlation ($R^2 = 0.73$) for the relationship.

Effects of Coefficient of Consolidation (c_v). The coefficient of consolidation (c_v or c_h) is believed to be one of the most important factors that influences the set-up behavior of clayey soils. In-situ piezocone dissipation tests were performed, and the c_h values were calculated using the Teh and Houlsby (1991) interpretation method. Laboratory consolidation tests were also performed on soil samples collected at LA-1 and Bayou Teche pile sites. The correlation between c_v and the “A” parameter for this study is depicted in Figure 3c, a review of which shows that there exists an inverse linear proportional relationship between the “A” parameter and $\log c_v$.

Effects of Sensitivity (S_t). Due to the thixotropic properties of the soil, the subsequent remolding and reconsolidation of the disturbed soil at the soil-pile interface zone will also be associated with long-term increase in soil strength, depending on the S_t value of the soil. The correlation between S_t and the “A” parameter is presented in Figure 3d, a review of which shows that there exists a linear proportional relationship between the S_t and the “A” parameter, similar to the PI-“A” relationship.

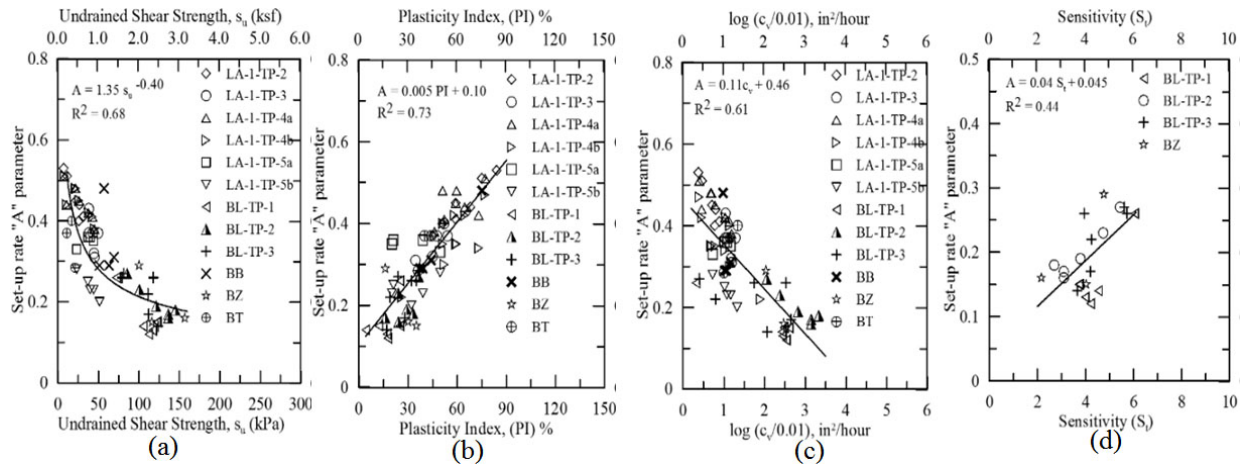


Figure 3: Correlation of set-up parameter “A” with different soil

Development of Empirical Models for the “A” Parameter

Non-linear multivariable regression analyses were conducted to develop empirical models to estimate the “A” parameter from soil properties. Three different empirical models were developed for the “A” parameter using three different levels of soil properties for use in design based on available soil properties. The procedure to develop the three different empirical models is similar, with the only difference being incorporating different soil properties. Two soil parameters (S_u and PI) that are usually available on typical soil borelogs are used to develop a simple empirical model for the “A” parameter in the Level 1 empirical model. Three soil parameters (S_u , PI , and c_v) are incorporated in the Level 2 empirical model. The c_h (or c_v) parameter is usually not available on typical soil borelogs; however, it is believed to be the most important parameter that can incorporate the effect of consolidation on a set-up model. The Level 3 empirical model is complex to implement, but the effect of S_t is incorporated in this level. The correlation results between the “A” parameter and the selected soil properties (Figure 3) such as S_u , PI , S_t , c_v were used to develop the empirical models. All possible regressions procedures were examined to select the best subset of predictor. R-Square, adjusted R-Square, sum of square error (SSE), and mean square error (MSE) were used as criteria to assess best predictors. Once preliminary models were selected, detail statistical analyses such as significance of the model as whole (F test) and significance of the partial multiple regression coefficient (t test) were carried out. The following three analytical models were selected among all models after examining all the statistical analyses.

$$\text{Level-1: } A = f(S_u, PI) = \frac{0.79 \left(\frac{PI}{100} \right) + 0.49}{\left(\frac{S_u}{1 \text{ tsf}} \right)^{2.03} + 2.27} \quad \dots (3)$$

$$\text{Level-2: } A = f(S_u, PI, c_v) = \frac{1.12 \left(\frac{PI}{100} \right) + 0.69}{\left[\left(\frac{S_u}{1 \text{ tsf}} \right)^{1.44} \right] \left[\log \left(\frac{c_v \text{ in}^2}{0.01 \text{ hour}} \right) \right]^{0.54} + 3.19} \quad \dots (4)$$

$$\text{Level-3: } A = f(S_u, PI, c_v, S_t) = \frac{0.44 \left(\frac{PI}{100} \right) (S_t) + 2.20}{\left[\left(\frac{S_u}{1 \text{ tsf}} \right)^{1.94} \right] \left[\log \left(\frac{c_v \text{ in}^2}{0.01 \text{ hour}} \right) \right]^{1.06} + 10.65} \quad \dots (5)$$

Figures 4a, 4b, and 4c present the comparison of measured versus predicted “A” parameter of the 70 individual clayey soil layers. The models that were developed to predict the “A”

parameter from soil properties for the three different levels (Equations 3 thru 5) need to be incorporated into Equation 2 to predict the unit shaft resistance set-up, f_s , as follows:

$$\frac{f_s}{f_{s0}} = 1 + \frac{0.79 \left(\frac{PI}{100} \right) + 0.49}{\left(\frac{S_u}{1 \text{ tsf}} \right)^{2.03} + 2.27} \log \frac{t}{t_0} \quad \dots (6)$$

$$\frac{f_s}{f_{s0}} = 1 + \frac{1.12 \left(\frac{PI}{100} \right) + 0.69}{\left[\left(\frac{S_u}{1 \text{ tsf}} \right)^{1.44} \right] * \left[\log \left(\frac{c_v}{0.01 \frac{\text{in}^2}{\text{hour}}} \right) \right]^{0.54} + 3.19} \log \frac{t}{t_0} \quad \dots (7)$$

$$\frac{f_s}{f_{s0}} = 1 + \frac{0.44 \left(\frac{PI}{100} \right) (S_t) + 2.20}{\left[\left(\frac{S_u}{1 \text{ tsf}} \right)^{1.94} \right] * \left[\log \left(\frac{c_v}{0.01 \frac{\text{in}^2}{\text{hour}}} \right) \right]^{1.06} + 10.65} \log \frac{t}{t_0} \quad \dots (8)$$

where, $t_0 = 1$ day and f_{s0} = unit shaft resistance at 1-day restrike for individual soil layer.

Equations 6, 7, and 8 can be implemented to estimate the increase of f_s with time for individual clayey soil layers at any time after EOD. The f_s can then be multiplied by the contact area to calculate the shaft resistance, R_{si} , of that layer. In the absence of sandy soil layers, the shaft resistances of all clayey soil layers along the pile length can be added to evaluate the total shaft resistance, R_s , of the pile. A constant value of $A = 0.15$ (*average value of the “A” parameter of all sandy soil layers in this study*) is proposed to estimate the f_s value for the sandy soil layers and hence to calculate the shaft resistances of the sandy soil layers. Since no set-up was observed for the toe resistance, R_{toe} , in this study, nor reported in the literature (e.g., Ng et al. 2013), no set-up is considered in calculating R_{toe} to estimate the total pile resistance, $R_t = R_s + R_{toe}$.

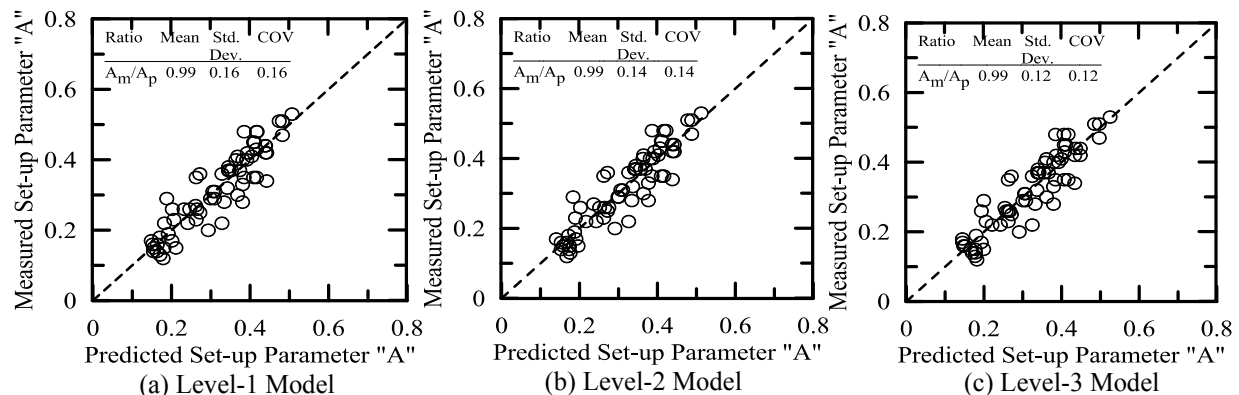


Figure 4: Comparison of measured versus predicted “A” parameter for development of models.

Model Verification. Other available soil set-up data from 18 test piles were analyzed here to verify the developed empirical set-up models in Equations 6, 7, and 8. The three developed models were used to predict the “A” parameters for the individual soil layers of the 18 test piles, followed by calculating the R_t values using the methodology described earlier. Figure 5 presents a comparison between the measured and predicted “A” parameter for the three empirical models. Figure 5 shows good agreement between measured and predicted values.

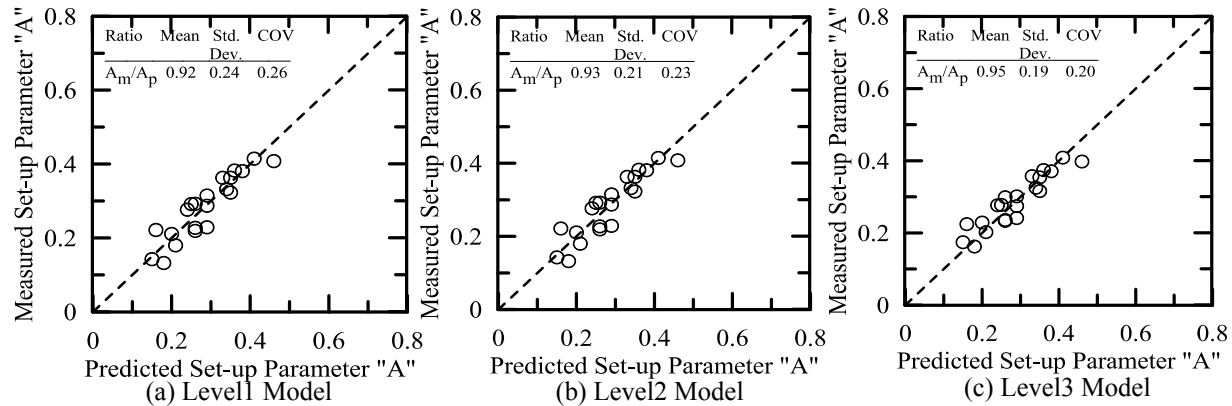


Figure 5: Comparison of measured versus predicted “A” parameter for verification of models.

SUMMARY AND CONCLUSIONS

A soil set-up study was conducted on 12 instrumented test piles from five different projects in Louisiana, driven mainly in cohesive soils containing interlayers of sand and silt. Laboratory and in-situ soil testing were conducted at the test pile locations to characterize the subsurface soil profile. Based on the results of this study, the following conclusions can be drawn:

1. The load test results of this study showed that set-up is predominantly a shaft resistance phenomenon that follows a linear logarithmic time rate after EOD. No set-up was observed in toe resistance. Hence, total resistance set-up was the same as shaft resistance set-up behavior and followed a linear logarithmic time rate after EOD.
2. The CAPWAP[®] analyses from DLTs and the load-distribution plots from SLTs were used to calculate the shaft resistance for individual soil layers along the piles. Almost all the clayey soil layers exhibited significantly more set-up than sandy soil layers.
3. The set-up rate parameter “A” was back-calculated for individual soil layers. A total of 94 pile segments were considered in this study; clayey soil behavior was dominant in 70 soil layers. The corresponding average values of the “A” parameter for clayey and sandy soil layers were 0.31 and 0.15, respectively.
4. The “A” parameter exhibited good correlations with different soil properties. The undrained shear strength (S_u), plasticity index (PI), coefficient of consolidation (c_v or c_h), and sensitivity (S_t) have shown significant influence on the “A” parameter. The “A” parameter decreases with increasing S_u and c_v , and increases with increasing PI and S_t .
5. Three different models were developed to estimate the “A” parameter and the increase of unit shaft resistance (f_s) with time for the clayey soil layers. The models incorporate different soil properties in three different complexity levels with similar implementation procedures. Comparison between measured and predicted “A” parameter and “ f_s ” values are in good agreement.
6. The recommended period to implement the developed models from this study is up-to 4 months from EOD as the rate of set-up became slower after that period.

ACKNOWLEDGEMENTS

This research is funded by the Louisiana Transportation Research Center (LTRC Project No. 11-2GT) and LADOTD (State Project No. 736-99-1732).

REFERENCES

- Bullock, P. J., Schmertmann, J. H., McVay, M. C. & Townsend, F. C. (2005). Side shear setup. I: Test piles driven in Florida. *J. Geotech. Geoenviron. Engng*, Vol. 131(3), pp. 292–300.
- Chen, Q., Haque, Md. N., Abu-Farsakh, M., and Fernandez, B. A. (2014). Field investigation of pile setup in mixed soil. *Geotechnical Testing Journal*, Vol. 37(2), pp. 268-281.
- Davisson, M. T. (1972). High capacity piles. *Proceedings of the Soil Mechanics Lecture Series on Innovations in Foundation Construction*, ASCE, Reston, VA, pp. 81-112.
- Fellenius, B. H., Riker, R. E., O'Brien, A. J., and Tracy, G. R. (1989). Dynamic and static testing in soil exhibiting set-up. *Journal of Geotech. Eng.*, Vol. 115(7), pp. 984-1001.
- Guang-Yu, Z. (1988). Wave equation application for piles in soft ground. *Proc. 3rd Intl. Conf. on the Application of Stress-Wave Theory to Piles*, Ottawa, pp. 831-836, Canada.
- Haque, Md. N., Abu-Farsakh, M., Chen, Q., and Zhang, Z. (2014). Case study on instrumenting and testing full-scale test piles for evaluating set-up phenomenon. *Journal of Transport Research Record* 2462, pp. 37-47.
- Haque, Md. N., Abu-Farsakh, M., and Tsai, C. (2016). Field investigation to evaluate the effects of pile installation sequence on pile set-up behavior for instrumented test piles. *Geotechnical Testing Journal*, Vol. 39(5), DOI: 10.1520/GTJ20140259, pp. 1-17.
- Haque, Md. N., Abu-Farsakh, M. Y., Zhang, Z., and Okeil, A. (2016). Developing a model to estimate pile set-up for individual soil layers on the basis of PCPT data. *Journal of Transport Research Board* 2579, DOI. 10.3141/2579-03, pp. 17-31.
- Karlsrud, K. (2014). Ultimate shaft friction and load displacement response of axially loaded piles in clay based on instrumented pile tests. *J. Geotech. Geoenviron. Engng*, Vol. 140(2), pp. 481 – 495.
- Likins, G. E., Hussein, M. H., and Rausche, F. (1988). Design and testing of pile foundations. *Proceedings to the third international conference on the application of stress-wave theory to piles*: Ottawa, Canada; pp. 644-658.
- Lim, J. K. and Lehane, B. M. (2014). Characterisation of the effects of time on the shaft friction of displacement piles in sand. *Geotechnique*, Vol. 64 (6), pp. 476-485.
- Ng, K. W., Suleiman, T. M., and Sritharan, S. (2013). Pile setup in cohesive soil. II: Analytical quantifications and design recommendations. *J. Geotech. Geo. Engng*, Vol. 139 (2), pp. 210-222.
- Paikowsky, S. G., Hajduk, E. L., and Hart, L. J. (2005). Comparison between model and full scale time dependent pile capacity gain in the Boston area. *ASCE Geotechnical Special Publication 132 Advances in Deep Foundations*, pp. 1-16.
- Preim, M. J., March, R., and Hussein, M. H. (1989). Bearing capacity of piles in soils with time dependent characteristics. *Proceedings of the international conference on piling and deep foundations*: London, England; pp. 363-370.

- Rausche, F., Likins, G., and Hussein, M. H. (2008). Analysis of post-installation dynamic load test data for capacity evaluation of deep foundations. *Proc. From Research In Practice in Geotechnical Engineering (Geo-Congress 2008)*, GSP No. 180, Louisiana, pp. 312-330.
- Schmertmann, J. H. (1991). The mechanical aging of soils. *J. Geotech. Engng*, Vol. 117 (9), pp. 1288-1330.
- Skov, R. & Denver, H. (1988). Time-dependence of bearing capacity of piles. *In Proceedings of the 3rd international conference on the application of stress-wave theory to piles* (ed. B. G. Fellenius), pp. 879–888. Vancouver, Canada: BiTech Publishers.

Robust Geotechnical Design of Piled-Raft Foundations for Tall Onshore Wind Turbines

Shweta Shrestha¹; Nadarajah Ravichandran, Ph.D.²; and Parishad Rahbari³

¹Graduate Student, Glenn Dept. of Civil Engineering, Clemson Univ., 123 Lowry Hall, Clemson, SC 29634. E-mail: shwetast@clermson.edu

²Associate Professor, Glenn Dept. of Civil Engineering, Clemson Univ., 202 Lowry Hall, Clemson, SC 29634. E-mail: nrvavic@clermson.edu

³Graduate Student, Glenn Dept. of Civil Engineering, Clemson Univ., 123 Lowry Hall, Clemson, SC 29634. E-mail: prahbar@clermson.edu

Abstract

A robust geotechnical design optimization procedure for piled-raft foundation to support a 130 m tall wind turbine on clayey soil is presented in this study. The initial geotechnical design indicated that the differential settlement of the piled-raft system controls the final design. A parametric study was conducted by varying the wind speed and undrained cohesion to establish a relationship between the design variables (number and length of pile and radius of raft) and random variables (wind speed and undrained cohesion). Finally, a robust design optimization was conducted considering the material cost and the robustness as the objectives. The standard deviation of the response which is the differential settlement of the foundation system was considered as the measure of robustness of the design. The optimization yielded a set of acceptable designs and presented as a Pareto front which can be used to select the best design using the knee point concept.

INTRODUCTION

Wind is one of the fastest growing renewable energy sources in the world. It provides clean, environmentally friendly, and sustainable energy and will not deplete over time like fossil fuels. Global Wind Report 2015 (GWEC, 2015) reported that by the end of 2015, the global cumulative installed wind capacity increased by more than 17 % from the preceding year. However, it accounts for only 3.3 % of the total electricity generation. By the end of 2015, the United States added 4000 new wind turbines contributing 8,598 MW of energy, a 13 % increase in the total installed capacity from the end of 2014 (GWEC, 2015). Although a significant number of wind turbines were installed in the United States during the last year, it only contributed to 4.7 % of the total electricity generation. Hence, it is vital to increase the energy production from the sustainable source such as wind, in order to meet the energy demand of growing population.

One of the cost effective solutions to increase the contribution of wind energy to the global energy production is to increase the height of the tower where higher and steadier wind speed can be accessed. Since the wind energy is directly proportional to the cubic power of wind speed, a taller tower can produce more power. Lewin (2010) stated that an increase in turbine elevation from 80 m to 100 m would result in 4.6% higher wind speed which would increase the power production by 14%. Likewise, an increase in tower height from 80 m to 120 m would

result in 8.5% higher wind speed, increasing the power production by 28%. These findings are useful for making decision on the number of turbines and their heights to produce a certain amount of wind energy. Since a wind farm project has higher initial construction cost and lower operation cost, it is logical and cost-effective to increase the wind energy production by building taller towers rather than increasing the number of turbines.

Although building taller towers increases the wind energy production, it poses a significant challenge to the geotechnical engineer in selecting suitable foundation type, performing geotechnical design, and selecting economical design that meets the design requirements. The increase in the tower height increases not only the vertical load but also the lateral load and bending moment that must be resisted by the foundation. The larger loads make the geotechnical design complicated and also results in bigger foundation especially in weak soils. Since a significant percentage of total cost goes into the construction of foundation, it is necessary to develop new procedures to aid the engineers to select suitable foundation type and design variables. Among the many foundation types commonly used in practice, the piled-raft foundation is considered as the effective foundation for supporting tall wind turbines. The geotechnical design of the piled-raft foundation is complicated, especially when it is subjected to large lateral load and bending moment and supported by weak soil. The complexity further increases due to the existence of a large number of acceptable designs with various combinations of raft radius, number of piles, and length of pile. Incorporation of uncertainties in the loading (wind speed) and soil properties can pose additional challenge in selecting the design that not only satisfies the design requirements but also is independent of the variations in soil properties and design loads. In such situations, a robust design optimization technique can be used to select the best design with suitable raft size and number of piles for the given performance requirement and cost limitation.

In this study, the geotechnical design procedure of a piled-raft foundation is presented for a sample 130 m tall hybrid wind turbine tower subjected to a mean wind speed of 125 mph at a potential wind farm site in Charleston, SC. A parametric study was also carried out to examine the effect of the variation in random variables such as wind speed and soil properties (undrained cohesion in this study) on the design outcome. Finally, a robust design optimization was performed considering the material cost and the standard deviation of differential settlement as objectives. The design optimization result is presented graphically in the form of a Pareto front which can be used to select best design for a given performance requirement and cost limitation.

ASSESSMENT OF DESIGN PARAMETERS

Design load calculation. The design load consists of dead load and wind load. The dead load was calculated as the sum of weight of tower and other components of wind turbine, such as nacelle and rotor. The wind turbine tower considered in this study is a hybrid hollow cylindrical tapering tower with the lower 93 m made of concrete and the upper 37 m made of steel. The base and the top diameters of the towers are 12.0 m and 4.0 m, respectively. Corresponding unit weights of the concrete and steel were used to calculate the dead load of the tower. The appropriate weights of nacelle and rotor for the given height of the tower were obtained from Malhotra (2011). The final dead weight was calculated to be 51.71 MN. The wind load was calculated considering the mean survival wind speed of 125 mph following the procedure described in ASCE 7-10 (2010). Since most of the wind turbines have the survival wind speed within 112 mph to 134 mph (Wagner and Mathur 2013) and its range lies in between 89 mph and

161 mph, the mean survival wind speed of 125 mph was considered to be appropriate for this study. The lateral load and bending moment acting at the base of the tower were obtained by considering the wind load along the tower height and drag force acting on the nacelle. The total lateral load and bending moment were calculated to be 2.26 MN and 144.89 MNm, respectively.

Soil properties. The necessary geotechnical parameters of soil required for the design of the piled-raft foundation were obtained from a geotechnical report from North Charleston, SC (WPC, 2010). It is worth noting that this geotechnical report was produced for the construction of one of the world's largest turbine testing facilities in Charleston, SC. The summary of the soil profile and geotechnical parameters are given in Table 1. The undrained cohesion (c_u) provided in Table 1 is the average value for each layer, determined using the variation of c_u with depth of 9 CPT soundings, provided in the report by WPC (2010). The obtained c_u value of the third layer (i.e. Cooper Marl) was found to be significantly lower compared to the value reported (140 to 280 kPa) in previous studies for similar soil (Camp, 2004). Still, the average value obtained from the CPT soundings was used in this study. Since the c_u of the second and the third layer are approximately the same, the average value of the second and third layer was assigned for both layers. At this site, the ground water table was located at 1.52 m below the ground surface.

Table 1. Generalized soil properties

Layer	Depth (m)	Soil type	Unit weight (kN/m ³)	c_u (kPa)	ϕ' (°)	E (kPa)	Poisson's ratio
1	0 - 1.22	Medium dense sand	17.28	0	34	6.00×10^4	0.4
2	1.22 - 9.15	Soft to firm clay	16.50	85.23	0	3.74×10^4	0.5
3	Below 9.15	Cooper Marl	19.64	85.32	0	3.00×10^4	0.5

GEOTECHNICAL DESIGN OF PILED-RAFT FOUNDATION

The basic idea behind the use of hybrid foundation such as piled-raft is quite straightforward, i.e. to increase bearing capacity of the foundation with the use of raft and to decrease total and differential settlements with the use of deep foundation. However, the quantification of the percentage of total load carried by the raft and the piles is the most challenging task in the design of piled-raft foundation. This is mainly due to lack of understanding of complex soil-raft-pile interaction and the mobilized strength along the interface at a given settlement value. Thus, a reliable design guideline is not yet available, especially for the foundation subjected to the combined bending moment, lateral load, and vertical loads.

In this study, a preliminary geotechnical design of the piled-raft foundation was performed following the procedure outlined by Hemsley (2000) in which the procedure proposed by Poulos and Davis (1980) and Randolph (1994) are incorporated. The factors considered in the preliminary design are the ultimate vertical load, bending moment and lateral load capacities, the total and differential settlements, and the rotation of the tower. The size of raft and the size and number of piles required to satisfy the design requirements were determined in the preliminary design stage. A minimum factor of safety of 2 (Hemsley, 2000) was considered to be safe for the vertical load, lateral load, and bending moment capacity checks and the vertical misalignment of

the tower within 3 mm/m was considered to be safe against the rotation of the tower (Grunberg and Gohlmann, 2013).

Vertical capacity. The vertical capacity of the piled-raft foundation was calculated as the lesser of: (i) the sum of ultimate capacities of the raft and all the piles and (ii) the ultimate capacity of a block containing piles, raft, soil and the portion of the raft outside the periphery of the pile group. The bearing capacity of the pile was calculated using α method and the raft was calculated using the general bearing capacity equation. The calculated vertical load capacity of the piled-raft was compared with the total vertical design load. The final design was controlled by the individual failure (i.e. either raft or pile group fails). The final factor of safety for vertical load capacity was determined to be 3.39, which meets the design requirement.

Moment capacity. The ultimate moment capacity of the piled-raft foundation was estimated as the lesser of: (i) the ultimate moment capacity of the raft and all the piles and (ii) the ultimate moment capacity of a block. The ultimate moment capacity of the raft, the pile group, and the block were determined using the method presented in Hemsley (2000). It was observed that the design was controlled by individual failure and the final factor of safety for moment capacity was determined to be 3.42, which meets the design requirement.

Lateral capacity. The lateral pile capacity of a single pile was determined using the solutions by Broms' (1964) for cohesive soil outlined in Gudmundsdottir (1981). Although this method is used for the analysis of a single pile, it was used to compute the lateral capacity of every pile in the piled-raft foundation system assuming all of them behave in a similar manner. The ultimate lateral load capacity and the lateral deflection of a single pile were calculated using the horizontal coefficient of subgrade reaction. The calculated lateral load capacity of the piled-raft foundation was compared with the design lateral load. The factor of safety was found to be 11.98 and the lateral deflection was 8.92 mm.

Vertical load - settlement behavior. The vertical load-settlement behavior of the piled-raft foundation was estimated by using the approach proposed by Poulos (2001) in conjunction with the method of estimating load sharing between the raft and the piles presented in Randolph (1994). The load sharing between the raft and the piles can be estimated on the basis of stiffness of the raft, piles, and the piled-raft. The stiffness of the piled-raft, K_{pr} was estimated using Equation 1 given below proposed by Randolph (1994).

$$K_{pr} = X K_p; \quad X = \frac{1 + (1 - 2\alpha_{rp}) K_r / K_p}{1 - \alpha_{rp}^2 (K_r / K_p)} \quad (1)$$

where K_r is the stiffness of raft, K_p is the stiffness of pile group, and α_{rp} is the raft-pile interaction factor. The raft-pile interaction factor was assumed to be 0.8 because as the number of pile in the group increases, the interaction factor increases and trends toward a constant value of 0.8 as reported by Randolph (1994). Among the various methods to estimate the raft stiffness, the method outlined by Randolph (1994) was used. The stiffness of the pile group was estimated using the method proposed by Poulos (2001), where the target stiffness of the piled-raft was first determined by dividing the total vertical load by the assumed allowable settlement and then Equation 1 was solved to determine the stiffness of the pile group. The stiffness of piled-raft will remain operative until the pile capacity is fully mobilized at load P_A . Finally, the load-settlement

relationships established in Equation 2 were used to obtain the vertical load-settlement (P vs. S) curve for the piled-raft foundation which is presented in Figure 1.

$$\text{For } P \leq P_A; S = \frac{P}{K_{pr}} \quad \text{For } P > P_A; S = \frac{P_A}{K_{pr}} + \frac{P - P_A}{K_r} \quad (2)$$

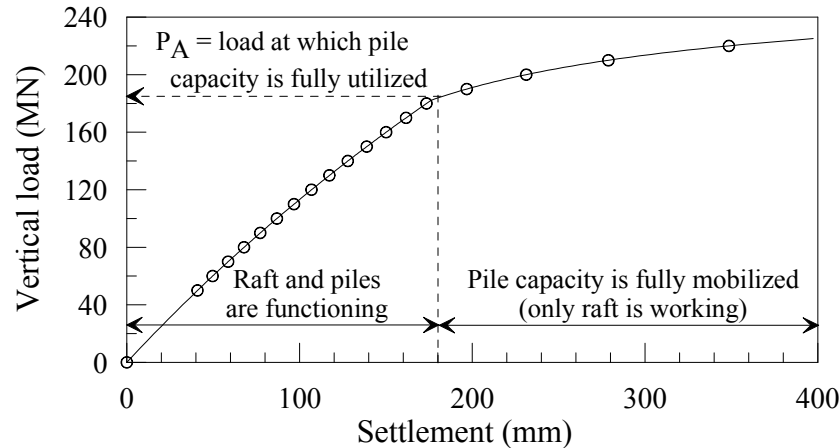


Figure 1. Calculated vertical load-settlement curve for the piled-raft foundation

It was found that under the vertical design load of 51.71 MN, the piled-raft foundation settles vertically by 42.41 mm. It can be inferred from Figure 1 that the vertical design load doesn't exceed the load at which pile capacity is fully utilized (P_A) which means that both raft and piles are functioning to support the design load.

Differential settlement and rotation. The calculation of differential settlement of the piled-raft foundation subjected to moment is complicated and there is no accurate procedure available in the literature. In this paper a new technique is proposed to calculate the differential settlement of the piled-raft foundation. In this method, the percentage of total bending moment carried by the raft and the pile group is adjusted until the differential settlement of individual components (i.e., raft and pile group) are equal. The resulting equal differential settlement is considered as the differential settlement of the piled-raft foundation. The principle behind it is that the raft and the pile group are coupled, therefore it can be anticipated that they will rotate simultaneously as a block when the bending moment is applied. The vertical shortening and extension of piles due to the lateral deflection is assumed to be negligible in this study. The calculation of differential settlements of each component of piled-raft foundation (i.e. raft and pile group) are discussed below.

Differential settlement of raft. To determine the differential settlement of raft, first its rotation (θ) due to wind load was calculated using Equation 3 given below by Grunberg and Gohlmann (2013).

$$\theta = \frac{M_{found}}{c_s I_{found}}; c_s = \frac{E_s}{f' \sqrt{A_{found}}} \quad (3)$$

where M_{found} is the fixed-end moment at the soil-structure interface (percentage of moment shared by raft resulting in equal differential settlement as of piles in this study), c_s is the foundation modulus, I_{found} is the second moment of inertia for area of foundation, E_s is the

modulus of elasticity of soil, f' is the shape factor for overturning (0.25), and A_{found} is the area of the foundation. Then the simple trigonometric relationship was used to determine the differential settlement of the raft with the known value of θ .

Differential settlement of piles. The differential settlement of the pile group was estimated on the basis of individual pile settlement profile due to the resultant vertical load using Fellenius (1999) method. The resultant vertical loads acting on each pile were calculated as the sum or difference of the vertical load due to dead load and the vertical load induced due to bending moment. Then the settlement profile of the piles in 2-dimensional elevation was estimated by a straight line. This procedure was repeated by adjusting the bending moment shared by the raft and piles until their settlement profile matched. Finally, the differential settlement of the piled-raft system was found to be 44.30 mm which gives the rotation of 0.17° . This amount of rotation will induce horizontal displacement of 383.7 mm at the top of the tower, which is within the acceptable limit.

The final design resulted in a raft of radius 7.5 m and thickness 1.2 m at a depth of 1.5 m supported by 40 pre-stressed concrete piles of width 0.457 m and length 24.2 m arranged equally in the circumference of 5.3 m and 6.7 m. The final design is shown in Figure 2.

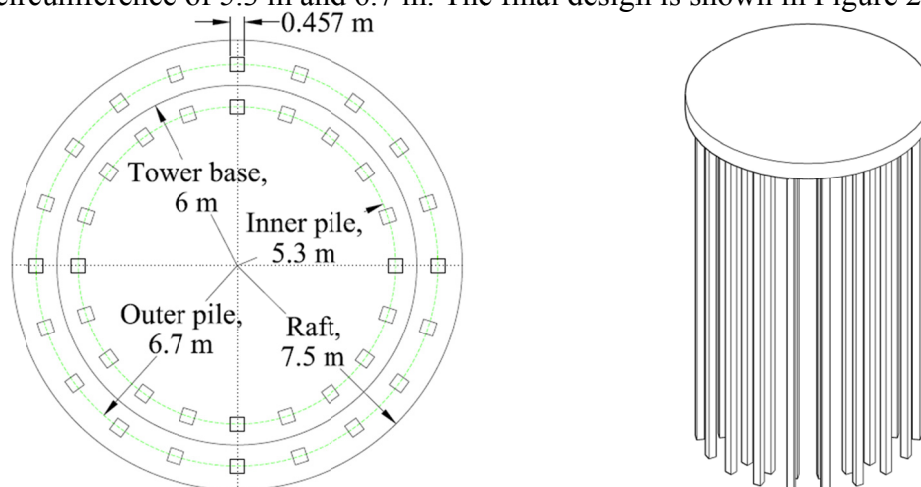


Figure 2. Plan view and 3-D view of designed piled-raft foundation

PARAMETRIC STUDY

To account for the effect of variations in loading and soil properties on the design results, a parametric study was conducted considering possible variations in wind speed and undrained cohesion of the soil. For each case of parametric study, only one design parameter (number of piles- N_p , length of pile- L_p , or radius of raft- R_r) was changed at a time to meet all the design requirements. The detail of the parametric study and the results are presented below.

Variation in wind speed. The wind speed (V) was varied between the range of survival wind speed, between 89 mph and 161 mph with a mean (μ_w) of 125 mph and a standard deviation (σ_w) of 18 mph. The designs were performed for 5 wind speeds (89, 107, 125, 143, and 161 mph) which represent $\mu \pm 2\sigma$ range following the procedure presented in the previous section. The undrained cohesion was kept constant at its mean value for this parametric study. The change in N_p , L_p and R_r to meet the design requirements are shown in Figure 3. The results show that N_p , L_p , and R_r increase with increasing wind speed. From Figure 3 (c) it appears that the radius of raft for the lower 3 wind speeds is the same. This is because it is the minimum requirement based on the base diameter of the tower.

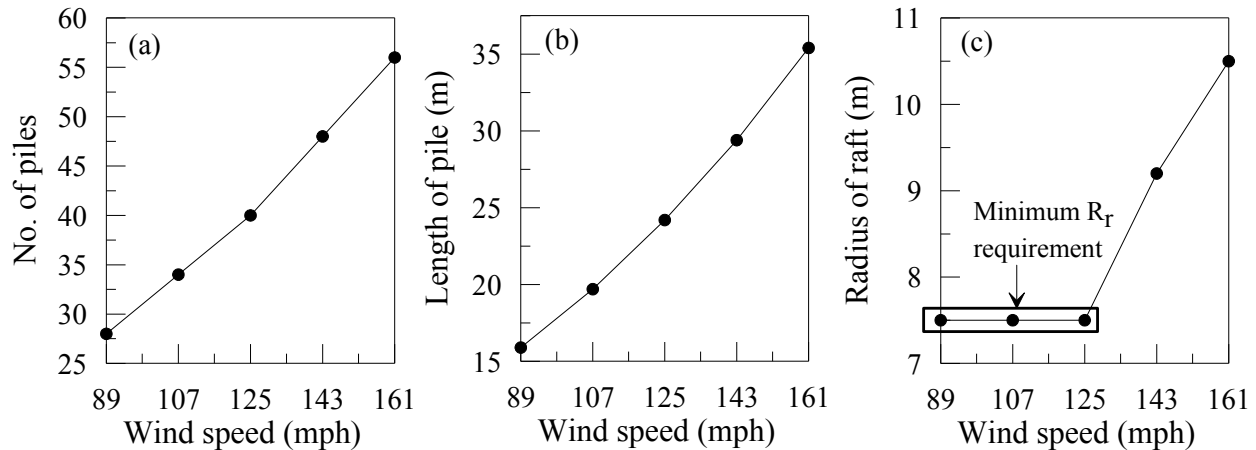


Figure 3. Effect of variation in wind speed on (a) number of piles, (b) length of pile and (c) radius of raft

Variation in undrained cohesion. Considering medium site variability, a covariance (COV) of 25 % was assumed for the determination of variation in undrained cohesion. With the COV of 25 % and mean c_u (μ_{cu}) of 85.3 kPa, the standard deviation for undrained cohesion (σ_{cu}) was determined to be 21.3 kPa, hence c_u was varied between 42.7 kPa to 127.9 kPa. The wind speed was kept constant at its mean value while varying c_u . The results shown graphically in Figure 4 indicate that N_p , L_p , and R_r decrease with increasing c_u . For the lowest c_u , piles were arranged in three circumferences in order to meet all the design requirements without facing group effect. In Figure 4 (c), it can be seen that R_r remains the same even with an increase in c_u because it is the minimum requirement of R_r based on the base diameter of the tower.

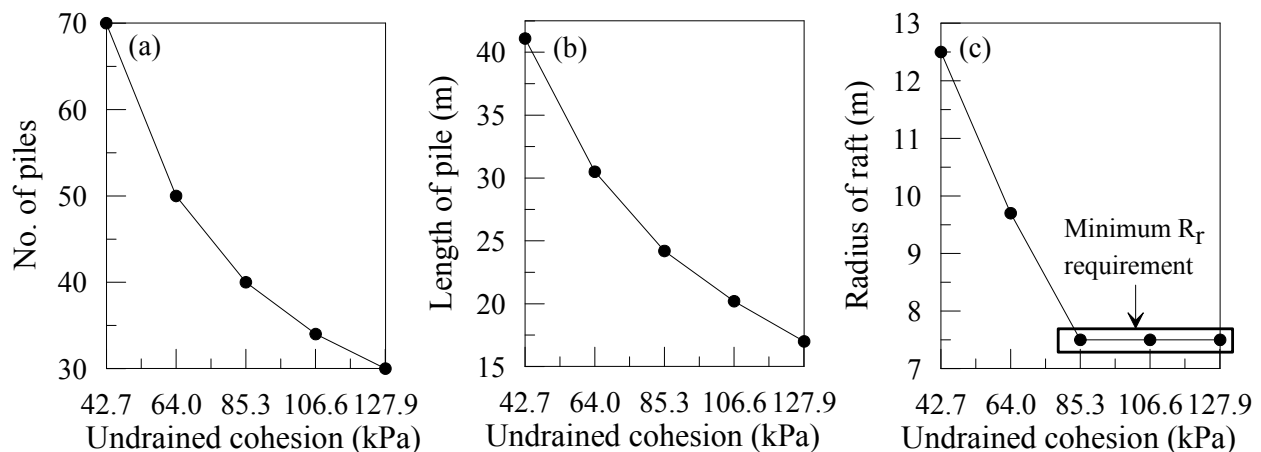


Figure 4. Effect of variation in undrained cohesion on (a) number of piles, (b) length of pile and (c) radius of raft

ROBUST DESIGN OPTIMIZATION

The design optimization of the piled-raft foundation was performed considering V and c_u as uncertain parameters (known as random variables) and differential settlement (S_{diff}) as the response of concern. A bi-objective optimization was performed using Genetic Algorithm to reduce the effect of uncertainties on the response and to capture a set of designs in terms of cost

efficiency and insensitivity of the design to the uncertain parameters. To achieve these, two objectives, the material cost of the piled-raft foundation and the standard deviation of differential settlement were computed and minimized through an optimization procedure. The cost of foundation was calculated based on the unit material cost of the raft (\$188.35/m³) and the pre-stressed concrete pile (\$160.72/m) obtained from RSMeans (2013). The standard deviation of the differential settlement was computed by coupling Monte Carlo simulation with optimization procedure. For this purpose, several design sets (L_p , N_p , and R_r) were selected and the corresponding differential settlements were determined for a range of values for the selected random variables. Then, a regression analysis was performed on the differential settlement analysis results to establish a simplified relationship between the response (S_{diff}) and the input variables (V , c_u , L_p , N_p , and R_r) which is presented in Equation 4.

$$S_{diff} = \exp(26.37 + 3.65 \ln(V) - 2.35 \ln(c_u) - 3.33 \ln(L_p) - 3.98 \ln(N_p) - 2.11 \ln(R_r)) \quad (4)$$

For each design set, 10,000 simulations were performed to compute the standard deviation of differential settlement. The preferred designs resulting from the optimization are demonstrated graphically in Figure 5. This is known as the Pareto front in robust design optimization. All the designs in the Pareto front are considered equally optimum. A clear trade-off relationship between the material cost of the foundation and the standard deviation of response can be inferred from the resulted Pareto front. In other words, decreasing the material cost of the foundation may result in designs of higher vulnerability and response variability against uncertainties. It can be observed in Figure 5 that when the standard deviation of differential settlement increases from 5.1 mm to 6.1 mm, the material cost of the foundation decreases from about \$361,000 to \$351,000.

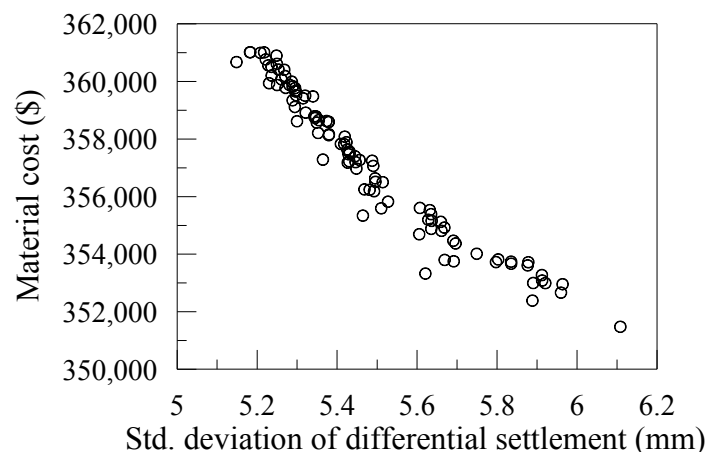


Figure 5. Pareto front optimized to both material cost and standard deviation

The resulted Pareto front can be judged by designers and the best design can be selected based on engineering preferences and available resources such as specific budget. Generally, when comparing Pareto front concept to a conventional design, it should be noted that the least costly design is the most sensitive design and is usually considered as the final design in conventional practices where the uncertainties are not involved. Nevertheless, the most preferred design (i.e. balancing both objectives) can be obtained from Pareto front using knee point concept.

CONCLUSION

A robust design optimization procedure for a piled-raft foundation to support tall wind turbine on a clayey soil is presented in this paper. Based on the deterministic geotechnical design result, it was found that the differential settlement and corresponding rotation controls the final design. The results of the parametric study showed that the design requirements can be met by either increasing the number of piles, length of pile, or radius of raft when the wind speed increases. Opposite was true to the undrained cohesion which is the other random variable. The design optimization resulted in the Pareto front which showed a clear trade-off relationship between the material cost of the foundation and the standard deviation of response (differential settlement). Such a relationship is useful to select the best design for the given performance requirement using the knee point concept.

REFERENCES

- ASCE (American Society of Civil Engineers). (2010). *Minimum Design Loads for Buildings and Other Structures*, Standard ASCE/SEI 7-10, ASCE, Reston, VA, USA, ISBN 978-0-7844-1085-1.
- Broms, B. B. (1964). "Lateral Resistance of Piles in Cohesive Soils." *Journal of the Soil Mechanics and Foundation Division*, Proceedings of the American Society of Civil Engineers, 90(SM2), 27-63.
- Camp, W.M. (2004). "Site Characterization and Subsurface Condition for the Cooper River Bridge." *GeoTrans Conference*, Geo-Institute, Los Angeles, CA, 1, 347-360.
- Fellenius, B.H. (1999). "Basics of foundation design." 2nd edition, BiTech Publishers, Richmond, British Columbia.
- GWEC (Global Wind Energy Council). (2015). "Global Wind Report 2015."
- Grunbeg, J. and Gohlmann, J. (2013). "Concrete Structures for Wind Turbines." *Wilhelm Ernst & Sohn*, Berlin, Germany, ISBN 978-3-433-03041-7.
- Gudmundsdottir, B. (1981). "Laterally loaded piles." M.S. thesis, University of Alberta, Edmonton, Alberta, Canada.
- Hemsley, J.A. (2000). "Design applications of raft foundations." *Thomas Telford Ltd.*, Heron Quay, London, ISBN 0727727656.
- Lewin, T.J. (2010). "An investigation of design alternatives for 328-ft (100-m) tall wind turbine towers." Master's Thesis, Iowa State University, Ames, IA, USA.
- Malhotra, S (2011). "Selection, Design and Construction of Offshore Wind Turbine Foundations, Wind Turbines." Dr. Ibrahim Al-Bahadly (Ed.), *InTech*, ISBN 978-953-307-221-0.
- Poulos, H.G. and Davis, E.H. (1980). "Pile foundation analysis and design." *John Wiley*, New York, USA.
- Poulos, H.G. (2001). "Piled raft foundation: design and applications." *Geotechnique*, 51(2), 95-113.
- Randolph, M.F. (1994). "Design methods for pile groups and piled rafts." *State-of-the-Arts Report, 13th International Conference on Soil Mechanics and Foundation Engineering*, New Delhi, India, 5, 61-82.
- RSMeans Building Construction Cost Data 2013, *Construction Publishers & Consultants*, Norwell, MA, ISBN 978-1-936335-56-5.
- Wagner, H.J. and Mathur, J. (2013). "Introduction to Wind Energy Systems: Basics, Technology and Operation, 2nd Edition." *Springer*, Verlag Berlin Heidelberg, ISBN 9783642329753.

WPC, A Terracon Company (2010). "Geotechnical Engineering Report: Clemson Wind Turbine Testing Facility North Charleston, South Carolina." WPC Project No. EN105060.

Drivability and Performance of Steel H-Piles in Schist Saprolite

Lei Gu, P.E.¹; Sarah E. McInnes, P.E.²; and Ara G. Mouradian, P.E.³

¹Geotechnical Project Engineer, Gannett Fleming, Inc., 1010 Adams Ave., Audubon, PA 19403. E-mail: lgu@gfnet.com

²District Geotechnical Engineer, Pennsylvania Dept. of Transportation, Engineering District 6-0, 7000 Geerdes Boulevard, King of Prussia, PA 19406. E-mail: smcinnnes@pa.gov

³Vice President/Chief Geotechnical Engineer, Gannett Fleming, Inc., 1010 Adams Ave., Audubon, PA 19403. E-mail: amouradian@gfnet.com

Abstract

Although driven steel H-piles are often an economical alternate for bridge foundations, prediction of pile drivability and length in very dense saprolite remains a great challenge pertaining to design and construction practices. A study to evaluate the performance of steel H-piles driven into thick saprolite layers was conducted for several bridge projects in Southeastern Pennsylvania. These saprolite layers of the Wissahickon Schist Formation are completely weathered but retain the fabric and structure of the parent bedrock. A database of numerous test piles from selected projects was established to provide a quantitative understanding of pile geotechnical resistances, pile lengths and a qualitative prediction of the driving conditions. All piles were driven to absolute refusal which is a function of the hammer type, efficiency, and driving procedure. High strain dynamic tests were performed on all piles at the end of initial driving. The results of restrike testing on selected piles were used to evaluate set-up effects on piles in these intermediate geomaterials. Geotechnical resistances from case pile wave analysis program (CAPWAP) were compared against static analysis values to quantify the pile performance. In addition, statistical attributes of the pile database were summarized for pile embedment into saprolite, hammer efficiency, and maximum driving stresses, etc. The paper presents the results of the pile drivability study, identifies the influence of saprolite thickness on pile geotechnical resistances and lengths, and provides recommendations for future projects with similar design challenges.

INTRODUCTION

The Pennsylvania Turnpike Commission (PTC) has planned to rehabilitate portions of the Pennsylvania Turnpike (I-276) between the Philadelphia Interchange and the Delaware River Bridge. The overall project includes a free-flowing interchange between I-95 and I-276, tolling modifications, bridge reconstruction, and widening of the two interstates. As part of the I-95/I-276 Interchange Project, a Pile Testing Program (Gannett Fleming, Inc. 2011) was performed to provide a better understanding of pile drivability and evaluate the geotechnical resistance of driven steel H-piles. The Pile Testing Program consisted of six, Grade 50, H-piles driven at three different locations. The piles were three HP12x74 sections and three HP14x89 sections. All piles were driven to Pennsylvania Department of Transportation (PennDOT) Case 2 Absolute Refusal, defined as 20 blows per inch in soft or decomposed rock, or dense or hard soil strata

(PennDOT 2016). The piles were furnished with normal duty tip reinforcement for hard driving conditions.

The project site is underlain by the Pennsauken Formation, Bridgeton Formation, and Trenton Gravel. The Pennsauken Formation, Bridgeton Formation, and Trenton Gravel have thicknesses of up to 30 feet. These formations are underlain by the Wissahickon Formation, consisting of highly micaceous, coarsely crystalline rock. Typically, the Wissahickon Formation is composed of schist and mica schist. The schists are quartz and feldspar rich. Above bedrock, is a very dense, silty sand, saprolitic strata of varying thickness. The saprolite layer is completely weathered but retains fabric and structure of the parent bedrock. During the subsurface investigations, SPT N-values greater than 50 and spoon refusals (automatic hammer) were observed in this stratum.

This saprolite stratum, with a variable thickness of up to 38 feet, could affect the estimated pile tip elevations. The Pile Testing Program was intended to:

1. Evaluate the pile drivability into a thick saprolite layer to Case 2 Absolute Refusal.
2. Determine the nominal axial geotechnical resistance of the piles, including skin friction and tip resistances, and determine if the geotechnical or structural resistance controls the design.
3. Identify if varying saprolite thickness will influence the nominal geotechnical resistance of the piles.

PILE INSTALLATION

All piles were installed using an ICE I-19v2 single acting diesel hammer, which was equipped with a 4,015 lb ram capable of delivering 43,225 ft-lbs of energy at the rated stroke of 10.8 feet and 48,742 ft-lbs of energy at the maximum stroke of 12.1 feet. The stroke height generally varied from 7 to 11.3 feet during driving.

Each pile was monitored with Pile Driving Analyzer (PDA) equipment at the end of initial driving (EOID) and at the beginning of restrike (BOR). The PDA provided continuous, real time data, including Case Method pile capacity, energy per hammer blow, compressive and tensile stresses within the pile, stroke height, and blows per minute during driving. Continuous monitoring and verification of the stroke height were needed to verify the theoretical energy required to advance the pile. The Case Method pile resistances were obtained during driving for each hammer blow. A Case Pile Wave Analysis Program (CAPWAP) analysis was also performed with both EOID and BOR data for each test pile.

TEST RESULTS AND DISCUSSIONS

Pile Resistances. All six test piles penetrated into the saprolite stratum. Piles at Test Locations 1 and 2 could not be driven to the estimated top of rock elevation and were terminated at absolute refusal (20 blows per inch) in saprolite. Piles at Test Location 3 (TP-3 and TP-3B) penetrated slightly into bedrock according to the adjacent boring. Table 1 shows saprolite penetration, unit resistance and corresponding blow counts at BOR for steel H-piles.

A resistance factor of 0.65 was used to determine factored geotechnical resistance from PDA data for each test pile (PennDOT 2012). All test piles achieved factored geotechnical resistance greater than the structural resistance indicating the geotechnical resistance does not control the pile design. Since the factored geotechnical resistances exceeded the factored structural

resistances for each of the piles tested, pile design should be determined by the factored structural resistance for the structures.

Table 1. Saprolite penetration and unit resistance

Location	Pile Type	Pile Penetration Layers	Embedment (ft)	Unit Resistance (Restrike) (ksf)	BOR Blow Counts
TP-1	12x74 TP-1	Saprolite ₁	5.5	1.5	15/0.75 in.
	14x89 TP-1B	Saprolite ₂	6.2	2.3	
		Saprolite ₁	5.5	2.2	18/in.
		Saprolite ₂	4.1	3.0	
TP-2	12x74 TP-2	Saprolite ₁	18.0	2.7	10/0.25in.
	14x89 TP-2A	Saprolite ₂	4.0	4.6	
		Saprolite ₁	18.0	3.2	9/0.03in.
		Saprolite ₂	3.5	3.6	
TP-3	12x74 TP-3	Saprolite ₁	15.0	3.3	10/0.03in.
	14x89 TP-3B	Saprolite ₂	4.0	3.4	
		Saprolite ₁	15.0	2.2	12/0.375in.
		Saprolite ₂	2.0	2.8	

Notes: 1. Saprolite₁ is defined as N-values > 40 blows for 12 inches. Saprolite₂ is defined as N-values > 50 blows for 6 inches or less

Saprolite Embedment. At TP-1, the saprolite embedment was the least, resulting in a higher end bearing component. The skin friction component was 10% and 23% at EOID increasing to 18% and 30% at BOR for the H-piles. At TP-2, the saprolite embedment was the most, resulting in skin friction component of 43% and 47% at EOID increasing to 50% and 54% for restrike. At TP-3, the saprolite embedment was between TP-1 and TP-2. The skin friction component was 35% and 43% at EOID increasing to 43% and 49% at BOR for the H-piles. Generally, skin friction increases with time after initial driving, as shown in Figure 1. Furthermore, the increase in skin friction varies directly with the stratum's density. As evidenced in each pile, a similar increase in unit skin friction coincides with the pile penetrating dense to very dense residual and/or saprolite strata.

It appears that for the contractor's selected hammer, the H-piles were able to penetrate through the Saprolite₁ layer (SPT N-values of > 40 blows for 12 inches), but were only able to penetrate 3.5 to 6 feet into the denser material, Saprolite₂ layer (SPT N-values of > 50 blows for 6 inches or less). TP-3 was essentially founded on rock while piles at TP-1 and TP-2 were terminated in saprolite. Estimated pile tip elevations can be raised in areas with a thick Saprolite₂ layer since it is unlikely that all piles will penetrate to top of rock. This will affect the

prices of furnished pile lengths and splices anticipated by the contractor. Alternately, savings will be realized in construction with pile deduct lengths.

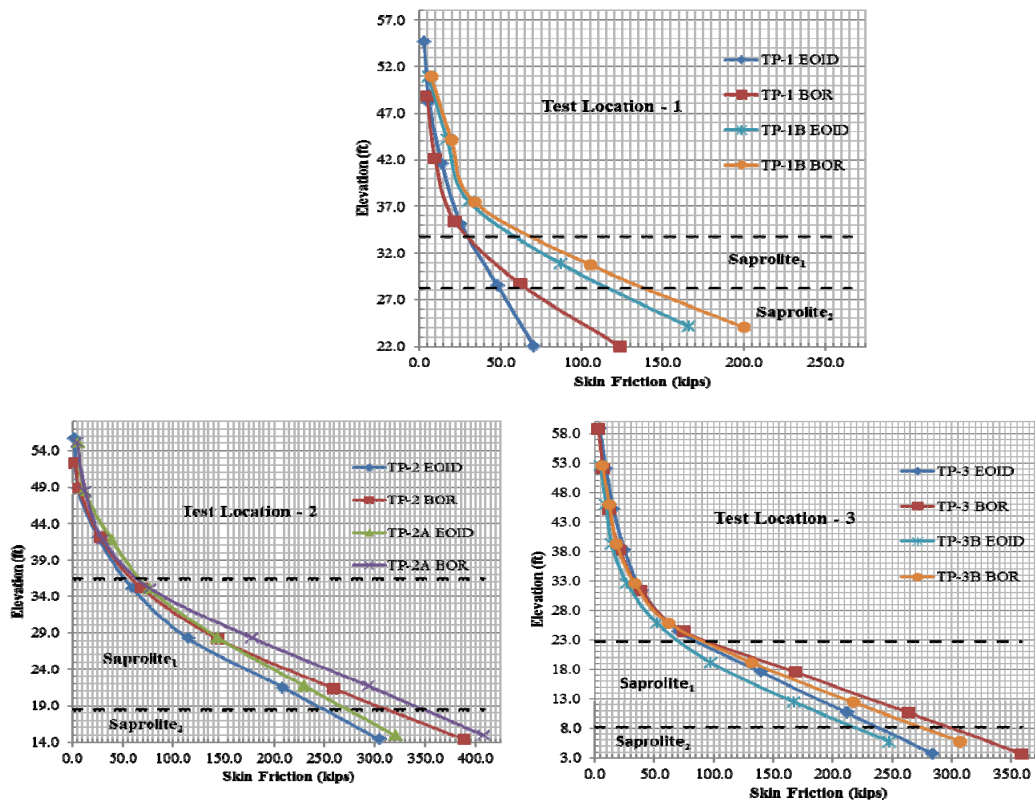


Figure 1. Skin friction at EOID and BOR.

Static Analysis. Gannett Fleming utilized the computer program DRIVEN (Mathias and Cribbs 1998), developed by FHWA, to determine the preliminary static geotechnical resistance of the various pile sizes for the actual test program pile driving depths. The DRIVEN software utilizes the Nordlund (1963) Method for determining axial resistance of piles in cohesionless soils. The Nordlund Method is a semi-empirical method developed from a database of 41 pile load tests carried to failure on 8 different projects. Both DRIVEN and CAPWAP H-pile resistance computations consider a box perimeter for skin friction and a box area for end bearing. The box perimeter and end bearing assume the H-pile section will get “plugged” by the soil being penetrated. In addition, the steel driving shoe welded to the tip of H-piles will increase the cross section area of the pile tip. Table 2 compares nominal pile resistances and skin friction contribution for DRIVEN calculations and CAPWAP analyses from PDA monitoring.

DRIVEN computations underpredicted the nominal geotechnical axial resistances for the HP12x74 pile at TP-1 and overpredicted nominal axial resistances for the HP14x89 piles at locations TP-2 and TP-3. DRIVEN computations were similar to the CAPWAP values for the HP14x89 pile at TP-1, the 12x74 piles at TP-2 and TP-3. The end bearing component of the DRIVEN calculations was generally lower for TP-1 and generally higher for TP-2 and TP-3 when compared to CAPWAP values. The Nordlund method limits the effective stress to approximately 3,130 psf for end bearing computations. The limiting value for end bearing was encountered for piles at TP-2 and TP-3 due to the deeper tip elevations resulting in higher

effective overburden stress values. Due to its limitation as a semi-empirical method, the DRIVEN calculations are not as accurate as site-specific PDA computations and should only be used for a preliminary estimate of pile resistance prior to static load test or PDA testing data.

Table 2. DRIVEN and CAPWAP geotechnical resistance comparison.

Location	Pile Type	Analysis	Nominal Geotechnical Resistance (kips)	Nominal	Nominal	Percent Skin Friction
				Skin Friction (kips)	End Bearing (kips)	
TP-1	12x74	DRIVEN	529	157	372	30%
		CAPWAP EOID	690	70	620	10%
		CAPWAP BOR	670	123	547	18%
	14x89	DRIVEN	662	174	488	26%
		CAPWAP EOID	727	166	560	23%
		CAPWAP BOR	670	200	470	30%
TP-2	12x74	DRIVEN	678	248	430	37%
		CAPWAP EOID	650	304	346	47%
		CAPWAP BOR	720	388	332	54%
	14x89	DRIVEN	900	311	589	35%
		CAPWAP EOID	745	320	425	43%
		CAPWAP BOR	815	409	407	50%
TP-3	12x74	DRIVEN	737	307	430	42%
		CAPWAP EOID	660	284	376	43%
		CAPWAP BOR	730	359	371	49%
	14x89	DRIVEN	953	364	589	38%
		CAPWAP EOID	700	247	453	35%
		CAPWAP BOR	721	307	414	43%

Pile Hammer Energy. The geotechnical resistances were achieved using an open-ended diesel hammer with a rated potential energy of 43,225 ft-lbs. The energy transfer efficiency ranged from 50 to 75%, which is high for single acting diesel hammers. This is partially due to the hammer operating at a maximum stroke of 11.0 to 11.3 feet, which is higher than the rated energy stroke of 10.8 feet.

ADDITIONAL CASE STUDY

Two additional case studies of on-going H-pile projects in Southeast Pennsylvania were selected to further evaluate the drivability of these piles into varying thicknesses of saprolite. The database of test piles in schist saprolite was established to provide a better understanding of pile lengths and geotechnical resistances for H-piles in these intermediate geomaterials.

Case Study No.2 (I-95/I-276 Test Piles during Construction). A section (D10) of the I-95/I-276 Interchange Project is currently under construction. A viaduct structure (Structure No. S-29446) is proposed to carry the future I-95 northbound traffic over Ramp D, the improved I-276, Durham Road, and New Rodgers Road. The structure will consist of one partial height abutment, one full height abutment, and thirteen piers. The site is located generally southwest of the Pile Test Program sites. A minimum of two HP14x89 test piles were driven at each substructure. Both ICE I-19v2 and ICE I-30v2 single-acting diesel hammers were used to install the piles. For both hammers, the maximum driving stress at absolute refusal is below the design specified yield strength and the ultimate resistance is adequate based on a resistance factor of 0.65. High strain dynamics tests using a PDA were performed on all piles at end of initial driving.

Both DRIVEN and CAPWAP H-pile resistances on twenty-two test piles were computed based on the available soil/rock information and pile driving data. CAPWAP analysis was performed using EOID data. The comparison results are shown in Figure 2. Similar to the Pile Testing Program cases prior to construction, Nordlund method yielded inconsistent geotechnical pile resistances. At the same time, it is noted that for piles penetrating deeper into saprolite layer, DRIVEN computations generally overpredicted nominal axial resistances for the HP14x89 piles.

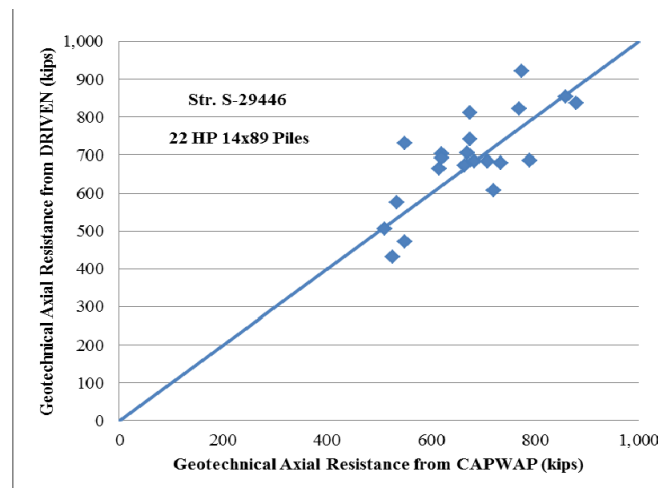


Figure 2. Geotechnical resistance comparison for twenty-two HP14x89 piles.

With two different hammers, the H-piles were able to penetrate through the Saprolite₁ layer for most cases. It is also true, however, that the piles could only penetrate 5.7 feet on average into the Saprolite₂ layer. Frequency diagram of the pile penetration depth in Saprolite₂ is shown in Figure 3. These observations are in agreement with the Pile Testing Program cases. The piles were not able to reach top of rock in areas with a thick dense saprolite layer even with a larger ICE I-30v2 hammer.

Case Study No.3 (I-95 Section GIR Pier 19N to Pier 25N). As part of the I-95 Section GIR rehabilitation, approximately three miles of limited access freeway between Race Street and Ann Street in the City of Philadelphia is proposed for reconstruction. The existing dual steel bridge structure is approximately 3400 feet in length and has 49 spans in each direction. The proposed

viaduct substructure will be supported on HP14x102 steel piles driven to PennDOT Case 2 absolute refusal. The project site is also underlain by the Trenton Gravel Formation. At the site, the Wissahickon Formation of the Pre-Cambrian Age lies beneath the Trenton Gravel Formation. The Wissahickon Formation is described in *Engineering Characteristics of the Rocks of Pennsylvania* (Geyer and Wilshusen 1982) as an oligoclase-mica schist that is coarsely crystalline.

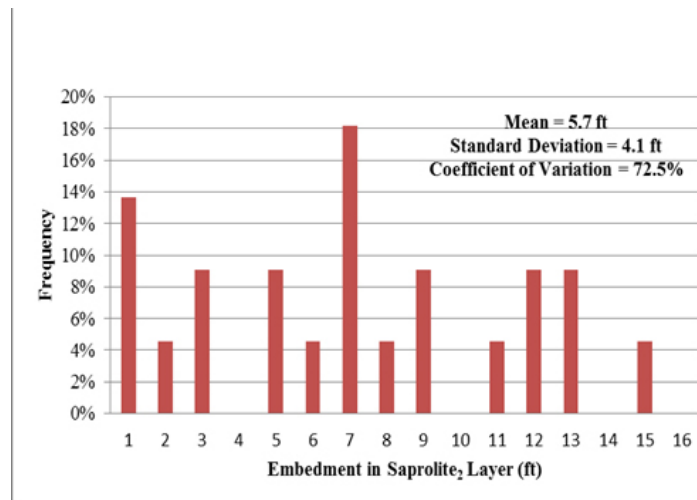


Figure 3. Frequency diagram of pile embedment in Saprolite₂ for twenty-two HP14x89 piles (I-95/I-276 project)

Both ICE I-30v2 and ICE I-36v2 single-acting diesel hammers were used to install the piles for the project. Dynamics tests using a PDA were performed on thirty-two piles from Pier 19N to Pier 25N. The nominal axial resistances from CAPWAP analysis ranged from 714 to 1402 kips for these piles. The pile hammer energy transfer efficiency ranged from 30 to 63% with an average of 43%. The hammers provided consistent efficiency, i.e., a very low coefficient of variation (COV), below 20%. At the same time, with the larger pile hammer (ICE I-36v2), maximum driving stresses of 50 ksi was observed in one pile. The average driving stress was 34.7 ksi, with a coefficient of variation less than 15%.

By using the larger hammer, the H-piles were able to penetrate deeper into the Saprolite₂ layer in some cases, as shown in Figure 4. It is also noted however that the piles could still only penetrate 5.2 feet on average into the Saprolite₂ layer. It is, therefore, essential to make more accurate estimate on driven pile length in very dense saprolite.

CONCLUSIONS

A test pile program was conducted due to the challenge of predicting H-pile drivability and length in very dense schist saprolite. Two additional case studies were performed to further investigate pile performance. Steel H-piles are all driven to Case 2 Absolute Refusal in three case studies. Absolute Refusal is a relative specification, given that it is a function of the hammer type, efficiency, and driving procedure. The hammer potential or rated energy will vary depending on the contractor's selected hammer type, efficiency, etc. A WEAP analysis should be performed prior to test pile driving to confirm the suitability of the contractor selected pile

hammer. The piles could be driven deeper with a larger pile hammer, however, high driving stresses above 50 ksi could be observed.

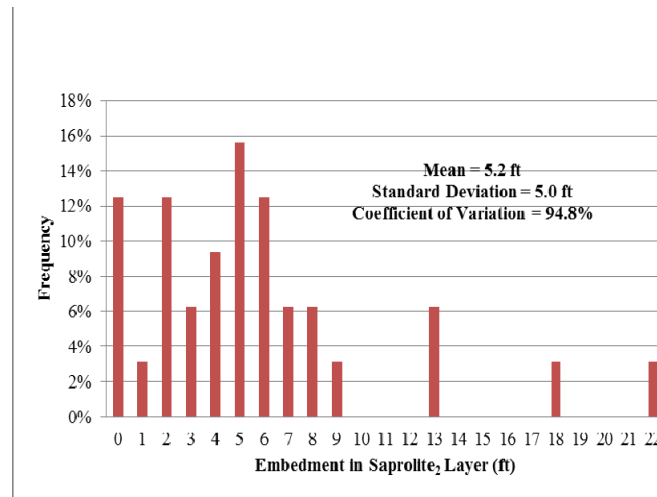


Figure 4. Frequency diagram of pile embedment in Saprolite₂ for thirty-two HP14x102 piles (I-95 GIR project)

Static analysis method provided by DRIVEN is not as accurate as site specific PDA computations and should only be used for a preliminary estimate of pile axial resistance prior to static load test or PDA testing data.

Results from both test pile programs indicate that piles generally penetrate less than 10 feet into the very dense saprolite. Based on this information, estimated pile lengths could be reduced which will result in a large amount of cost savings during construction. In the final design and construction documents, the specification of hammer types and selection of specific hammer models will be vital to the H-pile geotechnical performance. Although a contractor will select a hammer to drive the most number of piles in the shortest duration, the Engineer and inspector must verify that a sufficient energy will be delivered to the piles.

ACKNOWLEDGEMENTS

The authors would like to thank the following offices for their involvement in this study: PennDOT District 6-0 and Gannett Fleming Valley Forge, Pennsylvania.

REFERENCES

- Gannett Fleming, Inc. for Pennsylvania Turnpike Commission (2011), *Pile Testing Program Summary Report*, Valley Forge, Pennsylvania.
- Geyer, A.R. and Wilshusen, J.P. (1982), *Engineering Characteristics of the Rocks of Pennsylvania*, Pennsylvania Geological Survey, 4th Series.
- Mathias D. and Cribbs, M. (1998), "DRIVEN 1.0: A Microsoft Windows based program for determining ultimate static pile capacity." Federal Highway Administration, Washington, D.C.

- Nordlund, R.L. (1963), "Bearing capacity of piles in cohesionless soils." *Journal of Soil Mechanics and Foundation Engineering*, Soil Mechanics and Foundation Division, ASCE, Vol. 89, SM 3: 1-36.
- Pennsylvania Department of Transportation (2012), *Design Manual, Part 4*, Publication 15M, Harrisburg, Pennsylvania.
- Pennsylvania Department of Transportation (2016), *Specifications*, Publication 408, Harrisburg, Pennsylvania.

Elastic Analysis of Differential Settlements for Steel Storage Tank Foundations

Suranga Gunerathne¹; Hoyoung Seo, Ph.D., P.E., M.ASCE²; William Lawson, P.E., Ph.D., M.ASCE³; and Priyantha Jayawickrama, Ph.D., M.ASCE⁴

¹Ph.D. Student, Dept. of Civil, Environmental, and Construction Engineering, Texas Tech Univ., 911 Boston Ave., Lubbock, TX 79409. E-mail: suranga.gunerathne@ttu.edu

²Assistant Professor, Dept. of Civil, Environmental, and Construction Engineering, Texas Tech Univ., 911 Boston Ave., Lubbock, TX 79409. E-mail: hoyoung.seo@ttu.edu

³Associate Professor, Dept. of Civil, Environmental and Construction Engineering, Texas Tech Univ., 911 Boston Ave., Lubbock, TX 79409. E-mail: william.d.lawson@ttu.edu

⁴Associate Professor, Dept. of Civil, Environmental and Construction Engineering, Texas Tech Univ., 911 Boston Ave., Lubbock, TX 79409. E-mail: priyantha.jayawickrama@ttu.edu

Abstract

Estimation of differential settlements for large steel storage tanks is a very important design consideration; however, there is a lack of readily available analysis tools which can be used to accurately and conveniently compute tank differential settlements under various bottom plate dimensions and soil stiffnesses. This paper presents a continuum-based, elastic analysis model for a uniformly loaded, circular tank foundation resting on soil. The analysis captures the three-dimensional nature of the soil-structure interactions and produces settlement profiles of the tank foundation and the surrounding soil. The soil is assumed to behave as a linear-elastic material in a semi-infinite half space, and the foundation is modeled as a circular plate with a finite thickness. The governing differential equations are derived based on energy principles and calculus of variations. Input parameters for the analysis model are the plate diameter, plate thickness and elastic constants of the soil and plate. Model validation includes comparing results from this study with those from the literature and from finite element analyses, and these comparisons show good agreement. Parametric studies are then carried out to investigate the effects of plate diameter, plate thickness, and soil stiffness on differential settlement between the center and the edge of the circular plate. Based on the results from the parametric studies, design charts for use in preliminary design of circular tank foundations are proposed to estimate the differential settlement for given soil properties and plate geometry.

INTRODUCTION

Large steel tanks are widely used in many industries to store liquid. These tanks are sufficiently flexible structures to transmit the load from the liquid and self-weight to a foundation. Foundation settlements of the steel tanks are classified into three types: uniform settlement, planar tilt, and differential settlement. The differential settlement can be further subdivided into dish-shaped settlement and localized depressions (Marr et al. 1982). Excessive uniform settlement and planar tilt may cause operational problems related to serviceability but no threat to structural integrity of a tank. On the other hand, an excessive differential settlement is very damaging to the structure and often leads to ultimate limit states such as rupture of the bottom plate or rupture of the shell-bottom plate connection (Marr et al. 1982; D'orazio and Duncan 1987). When assessing tolerable deflections of superstructures, an angular distortion α is usually

preferred over the differential settlement Δw because the same differential settlement causes different degrees of distortion for different span lengths (Salgado 2008). In the case of a circular tank foundation, the span length can be taken as the radius r_p of the tank bottom plate when the differential settlement Δw is defined as the difference in settlements between the center and the edge of the bottom plate ($\alpha = \Delta w/r_p$). The tolerable angular distortion values proposed in literature and in tank design guidelines range from 0.020 to 0.050, which correspond to 1/50 to 1/20, respectively (Langeveld 1974; Rosenberg and Journeaux 1982; Marr et al. 1982; D'orazio and Duncan 1987; API 2001). Although estimation of differential settlement of flexible foundations is a very important design consideration, there is a lack of readily available analysis tools that can be used to compute the differential settlement under various plate dimensions and soil stiffnesses. This paper presents a continuum-based, elastic analysis model for a uniformly loaded, circular tank foundation resting on a soil. The analysis effectively captures the three-dimensional nature of the soil-structure interactions and produces settlement profiles of the tank foundation and the surrounding soil. This paper first presents the mathematical formulation and the derivation of the equations using variational principles. The method of analysis is then described, and the results from this study are compared with those from the literature and the FEA. Finally, design charts that can be used to estimate the differential settlement between the center and the edge of the circular plate for preliminary design are presented based on results from parametric studies.

METHOD OF ANALYSIS

Problem Definition. The analysis considers a circular plate of diameter $B (=2r_p)$ and thickness t_p resting on a semi-infinite, homogenous soil deposit (Fig. 1). The homogeneous soil deposit is assumed to be linear elastic and isotropic with elastic properties described by Young's modulus E_s and Poisson's ratio ν_s . The circular plate is assumed to behave as a linear elastic material with a Young's modulus E_p and a Poisson's ratio ν_p . The soil layer extends infinitely in the horizontal and downward vertical directions. Since this problem is axisymmetric, a cylindrical (r - θ - z) coordinate system is used to define soil-plate system. The z -axis passes through the center of the plate, and the positive z direction points downward. A uniformly-distributed load q acts on the circular plate and represents the weight of tank itself and liquid in the tank.

The vertical displacement of soil u_z at any point in the soil medium is assumed to be a product of separable variables (Vallabhan and Das 1991; Seo et al. 2009; Salgado et al. 2013) and is given by

$$u_z(r, z) = w(r)\phi(z) \quad (1)$$

where $u_z(r, z)$ = vertical soil displacement at any point (r, z) within the soil mass; $w(r)$ = function that represents the vertical soil displacement profile at ground surface; $\phi(z)$ = dimensionless function that describes the decay of the vertical soil displacement with increasing depth. The $\phi(z)$ function is assumed to be equal to one at the soil-plate interface [$\phi(0) = 1$], and this condition ensures proper soil-plate contact [*i.e.*, $u_z(r, 0) = w(r)$]. Furthermore, the $\phi(z)$ function must vanish at infinite depth [$\phi(\infty) = 0$] below the ground surface because there should not be any vertical displacement at such depth. Horizontal and tangential soil displacements (u_r and u_θ) due to the vertical load are typically much smaller compared to the vertical soil displacement u_z , so they are neglected in the analysis.

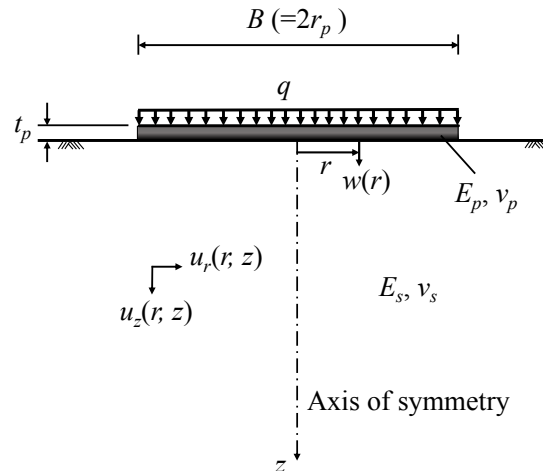


Figure 1. Uniformly loaded circular plate on elastic soil

Governing Differential Equation. In this analysis, the principle of minimum potential energy is used to obtain the equilibrium of the system. The principle of minimum potential energy states that a conservative system attains its equilibrium formation when its total potential energy is at a minimum. The total potential energy Π of the soil-plate system, including both internal and external potential energies, is given by

$$\begin{aligned} \Pi = & \frac{D}{2} \int_0^{2\pi} \int_0^{r_p} \left[(\nabla^2 w)^2 - \frac{2(1-\nu_p)}{r} \frac{dw}{dr} \frac{d^2 w}{dr^2} \right] r dr d\theta + \\ & + \frac{E_s}{2(1+\nu_s)(1-2\nu_s)} \int_0^\infty \int_0^{2\pi} \int_0^\infty \left[(1-\nu_s) \left(\frac{d\phi}{dz} \right)^2 w^2 + \frac{(1-2\nu_s)}{2} \left(\frac{dw}{dr} \right)^2 \phi^2 \right] r dr d\theta dz \\ & - \int_0^{2\pi} \int_0^{r_p} q w r dr d\theta \end{aligned} \quad (2)$$

where ∇^2 is a Laplace operator and $D (= E_p t_p^3 / [12(1-\nu_p^2)])$ is a flexural rigidity of foundation.

In Eq. (2), the first integral term that contains D and ν_p represents elastic strain energy stored in the plate due to bending. The second integral term that contains E_s and ν_s corresponds to the elastic strain energy of isotropic elastic soil continuum. Finally, the third integral term that contains q represents potential energy due to external load on the soil-plate system. As seen in Eq. (2), the total potential energy of the soil-plate system is expressed in terms of the elastic constants and the functions w , ϕ , and their derivatives. Governing differential equations of the functions $w(r)$ and $\phi(z)$ are obtained by applying the principle of minimum potential energy (*i.e.*, $\delta\Pi = 0$) to Eq. (2) and using variational calculus.

For the function $w(r)$, two sub-domains are considered: within the plate diameter ($0 \leq r \leq r_p$) and outside the plate ($r_p \leq r < \infty$). The governing differential equation for the function w within the plate ($0 \leq r \leq r_p$), representing the vertical deflection of the plate itself, is given as

$$D\nabla^4 w - 2t\nabla^2 w + kw = q \quad (3)$$

where the parameters k and t appearing in Eq. (3) are defined as follows:

$$k = \frac{E_s(1-\nu_s)}{(1+\nu_s)(1-2\nu_s)} \int_0^\infty \left(\frac{d\phi}{dz} \right)^2 dz \quad (4)$$

$$2t = \frac{E_s}{2(1+\nu_s)} \int_0^\infty \phi^2 dz \quad (5)$$

The parameter k has a unit of force/length³ and represents the compressive resistance of the soil, which is conceptually the same as a modulus of subgrade reaction. On the other hand, the parameter t has a unit of force/length and accounts for the shearing resistance of the soil.

The differential equation for the function w outside the plate ($r_p \leq r < \infty$), representing the vertical displacement of the soil at ground surface, is given as

$$-2t\nabla^2 w + kw = 0 \quad (6)$$

with boundary conditions of $w = w(r_p)$ at $r = r_p$ [$w(r_p)$ is a deflection of the plate at $r = r_p$, and this boundary condition represents displacement continuity at $r = r_p$] and $w = 0$ at $r = \infty$. Eq. (6) is a form of the modified Bessel differential equation, and its solution using the boundary conditions is given by

$$w(r) = w(r_p) \frac{K_0(\beta r)}{K_0(\beta r_p)} \quad (7)$$

where

$$\beta = \sqrt{\frac{k}{2t}} \quad (8)$$

and K_0 = modified Bessel functions of the second kind of zero order.

The governing differential equation for soil displacement decay function $\phi(z)$ is given as

$$\frac{d^2\phi}{dz^2} - \gamma^2\phi = 0 \quad (9)$$

where

$$\gamma = \sqrt{\frac{(1-2\nu_s)}{2(1+\nu_s)} \frac{\int_0^\infty \left(\frac{dw}{dr} \right)^2 r dr}{\int_0^\infty w^2 r dr}} \quad (10)$$

The parameter γ has a unit of per length and determines the rate at which the vertical soil displacement diminishes in the vertical direction (Vlasov and Leont'ev 1966).

By solving Eq. (9) with boundary conditions of $\phi(0) = 1$ and $\phi(\infty) = 0$, the decay function is obtained as

$$\phi(z) = e^{-\gamma z} \quad (11)$$

Substituting Eq. (11) into Eqs. (4) and (5), the parameters k and $2t$ are rewritten as follows:

$$k = \frac{E_s(1-\nu_s)}{(1+\nu_s)(1-2\nu_s)} \left(\frac{\gamma}{2} \right) \quad (12)$$

$$2t = \frac{E_s}{2(1+\nu_s)} \left(\frac{1}{2\gamma} \right) \quad (13)$$

Iterative Solution Scheme. In order to solve Eqs. (3) and (6) to obtain the vertical displacement w , the soil resistance parameters k and t must be known. The k and t parameters are functions of the parameter γ [refer to Eqs. (12) and (13)], which in turn depends on w . Due to this interdependence of the soil and plate differential equations, an iterative solution scheme is required. First, an initial value of $\gamma (= \gamma_{\text{old}})$ is assumed and the values of k and t [see Eqs. (12) and (13)] are then obtained. With the k and t parameters known, Eqs. (3) and (6) can be solved and the displacement function w is obtained. Then, a new value of $\gamma (= \gamma_{\text{new}})$ is calculated using the computed displacement function w and its derivative dw/dr [see Eq. (10)] and γ_{new} is compared against the assumed initial value. If the differences are greater than the prescribed tolerance (a value of 10^{-5} was used in this study), iterations are continued with the calculated value of γ taken as the new guess ($\gamma_{\text{old}} = \gamma_{\text{new}}$) until the differences between γ_{old} and γ_{new} from two successive iterations fall below the prescribed tolerance.

ANALYSIS RESULTS

Analysis Validation. In order to validate the analysis method, results from this study were compared against those from FEA and the elastic solutions available in the literature: 1) Ahlvin and Ulery (1962) for flexible foundation and 2) Gerrard and Harrison (1970) for rigid foundation. The validation considered two cases with steel plate diameters B of 1 and 10 meters subjected to a uniformly distributed load q of 60 kPa. For these two cases, parameters are assumed as $E_p = 200$ GPa, $\nu_p = 0.3$, $t_p = 150$ mm, $E_s = 20$ MPa, and $\nu_s = 0.2$.

Fig. 2 shows the vertical displacement profile at the ground surface obtained from this study, from FEA, and from the elastic solutions. The elastic solution by Gerrard and Harrison (1970) is for a perfectly rigid plate and therefore always yields the uniform settlement directly beneath the plate, regardless of plate diameter. Similarly, the analytical solution for a perfectly flexible foundation obtained by Ahlvin and Ulery (1962) always produces non-uniform settlement. However, intuitively, a plate should become more flexible as the plate diameter increases with all other conditions being the same. Both the analysis method and FEA correctly show this behavior; the smaller plate with $B = 1$ m [Fig. 2(a)] behaves more like a rigid foundation whereas the larger plate with $B = 10$ m [Fig. 2(b)] shows a behavior similar to a flexible foundation under the same soil conditions. Further, the results from this study show that the vertical soil displacement diminishes faster in the horizontal direction than those from FEA. From the comparisons shown in Fig. 2, it can be seen that the analysis method proposed in this paper captures plate-soil interactions reasonably and that there is close agreement between the results from the analysis and those from FEA and from analytical solutions.

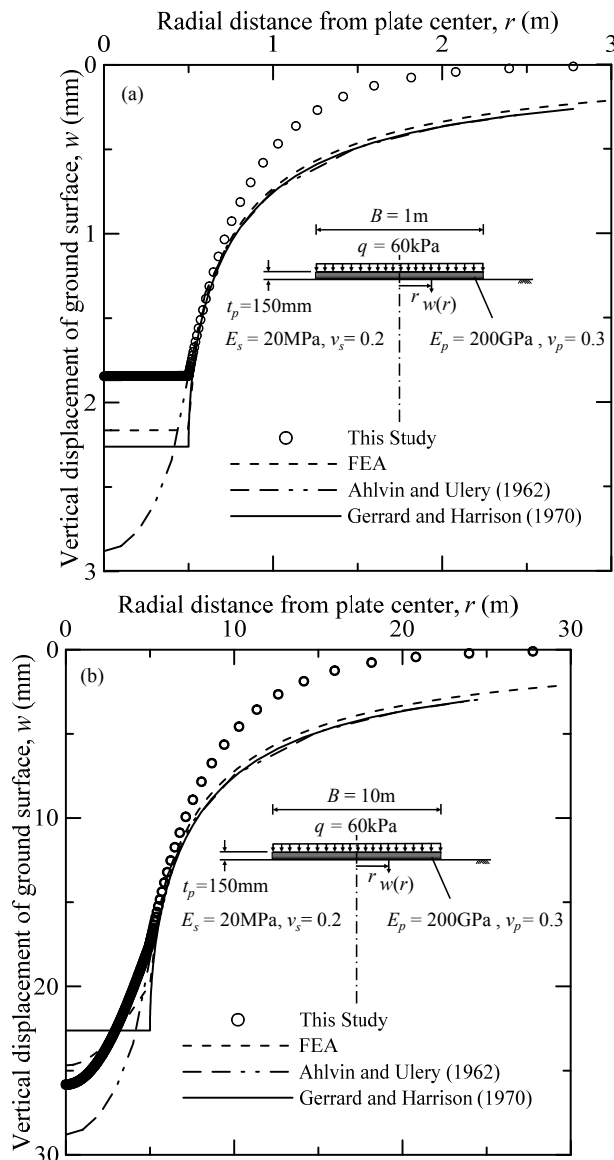


Figure 2. Comparison of vertical displacements obtained from this study with those from elastic solutions available in literature for (a) for $B = 1 \text{ m}$; (b) for $B = 10 \text{ m}$

Parametric Study. Using the analysis method developed in this study, a parametric study was performed to investigate the effects of plate diameter, plate thickness, and soil stiffness on the flexibility of a plate subjected to a uniform pressure. In all subsequent analyses, values of q , E_p , ν_p , and ν_s are assumed to be 24 kPa, 200 GPa, 0.3, and 0.2, respectively.

The parametric study investigated the effect of the steel plate diameter on the flexibility of a plate by varying B from 2 m to 50 m while keeping $t_p (= 150 \text{ mm})$, $E_p (= 200 \text{ GPa})$, and $\nu_p (= 0.3)$ the same. Two soil conditions were considered. Dense or stiff soils were represented with $E_p/E_s = 1,000$ (i.e., $E_s = 200 \text{ MPa}$), and loose or soft soils were represented with $E_p/E_s = 10,000$ (i.e., $E_s = 20 \text{ MPa}$).

Fig. 3 presents a plate edge-to-center settlement ratio, $w(r)/w(0)$, versus normalized radial distance, r/r_p , for various plate diameters with $E_p/E_s = 1,000$ and $10,000$. For both soil conditions, a plate becomes more flexible when B increases. For the same plate diameter, a plate shows more flexible behavior when the founding soil is stiffer. For example, the edge-to-center settlement ratio $[w(r_p)/w(0)]$ of the 2-m-diameter plate (represented with thick solid lines) is about 0.91 [see Fig. 3(a)] and 0.99 [see Fig. 3(b)] for $E_p/E_s = 1,000$ and $10,000$, respectively (note that this does not mean that the differential settlement, $w(0) - w(r_p)$, will be also larger for a plate on stiffer soils). When the plate diameter becomes large enough, however, the effect of soil stiffness on the flexibility of the plate becomes minimal and the edge-to-center settlement ratios converge to about 0.6 regardless of soil conditions.

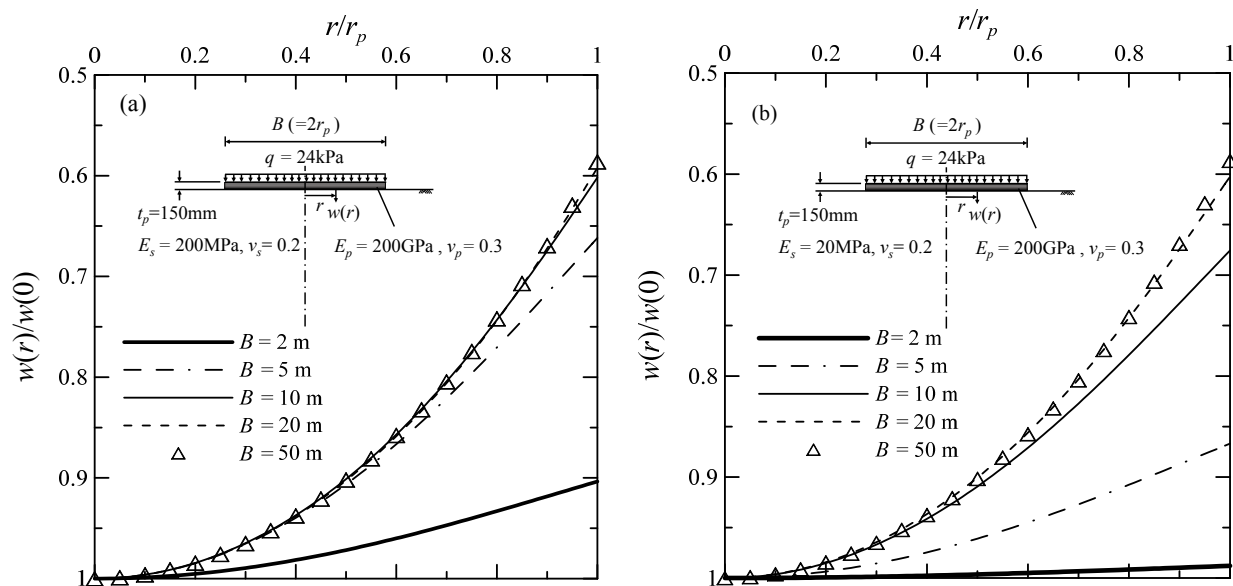


Figure 3. Edge-to-center settlement ratio versus normalized radial distance for various plate diameters with (a) $E_p/E_s = 1,000$ and (b) $E_p/E_s = 10,000$

In addition to the plate diameter, the effect of plate thickness t_p on the flexibility of a plate was investigated by changing t_p from 5 mm to 150 mm while keeping $E_p (= 200 \text{ GPa})$ and $\nu_p (= 0.3)$ constant. Further, the effect of soil stiffness on the flexibility of a plate was investigated by varying E_p/E_s from 100 to 100,000 while keeping $t_p (= 150 \text{ mm})$, $E_p (= 200 \text{ GPa})$, and $\nu_p (= 0.3)$ constant. $E_p/E_s = 100$ (*i.e.*, $E_s = 2,000 \text{ MPa}$) represents extremely stiff ground such as intermediate geomaterials or soft rocks, whereas $E_p/E_s = 100,000$ (*i.e.*, $E_s = 2 \text{ MPa}$) represents very weak soils such as very soft clays. Results from these parametric studies were used to develop design charts presented in subsequent sections.

Design Charts. In this section, design charts for use in *preliminary design* of the circular storage tank are presented. First chart is showing normalized plate modulus from which a settlement at the center of the plate can be computed when q , E_p , E_s , B , and t_p are known (Poisson's ratios of

the steel plate and the soil are assumed to be 0.3 and 0.2, respectively). Then a second chart from which the edge settlement can be obtained is presented.

In order to present results from the parametric study more effectively, a normalized plate modulus k_p is defined as follows:

$$k_p = \frac{qB^2}{w(0)E_pt_p} \quad (14)$$

where q = applied uniformly distributed load; $w(0)$ = settlement at the plate center; E_p = Young's modulus of plate; B = plate diameter; and t_p = plate thickness.

Fig. 4(a) presents the values of normalized plate modulus k_p versus relative stiffness of plate to soil E_p/E_s for a wide range of plate diameter-to-thickness ratios B/t_p . When a loading condition, plate dimension, and soil stiffness are known, the normalized plate modulus k_p is obtained from Fig. 4(a) and the center settlement is then computed from Eq. (14).

Fig. 4(b) shows the edge-to-center settlement ratio $[w(r_p)/w(0)]$ versus E_p/E_s for various values of B/t_p . For the same value of B/t_p , edge-to-center settlement ratio $w(r_p)/w(0)$ increases with increasing E_p/E_s , indicating that a plate behaves in a more rigid manner when soil stiffness decreases [note that the value of $w(r_p)/w(0) = 1$ means that the vertical displacement is uniform underneath the plate, representing a rigid plate]. For the same soil condition, a plate becomes more flexible when B/t_p increases. However, when the plate diameter is extremely large compared to its thickness or the plate thickness is extremely thin compared to its diameter ($B/t_p = 1,000$ and $10,000$), a plate always behaves in a flexible way (the edge-to-center settlement ratio converges to a value of about 0.6 regardless of soil stiffness). On the other hand, for a plate with $B/t_p = 5$, representing very small tank diameter or very thick plate thickness, the edge-to-center settlement ratio remains constant at value of one for most ranges of E_p/E_s until the soil becomes very stiff (E_p/E_s becomes smaller than 1,000).

In order to compute differential settlement of a circular tank, the center settlement $w(0)$ is first obtained from Fig. 4(a) and Eq. (14) and the edge settlement $w(r_p)$ is obtained using the corresponding edge-to-center settlement ratio provided in Fig. 4(b). The differential settlement is then computed as the difference between $w(0)$ and $w(r_p)$. It should be noted that a larger value of $w(r_p)/w(0)$ does not necessarily mean a larger differential settlement. When a steel tank sits on intermediate geomaterials or soft rocks, the edge-to-settlement ratio can be large but the differential settlement is negligible because the magnitude of the settlement itself is very small.

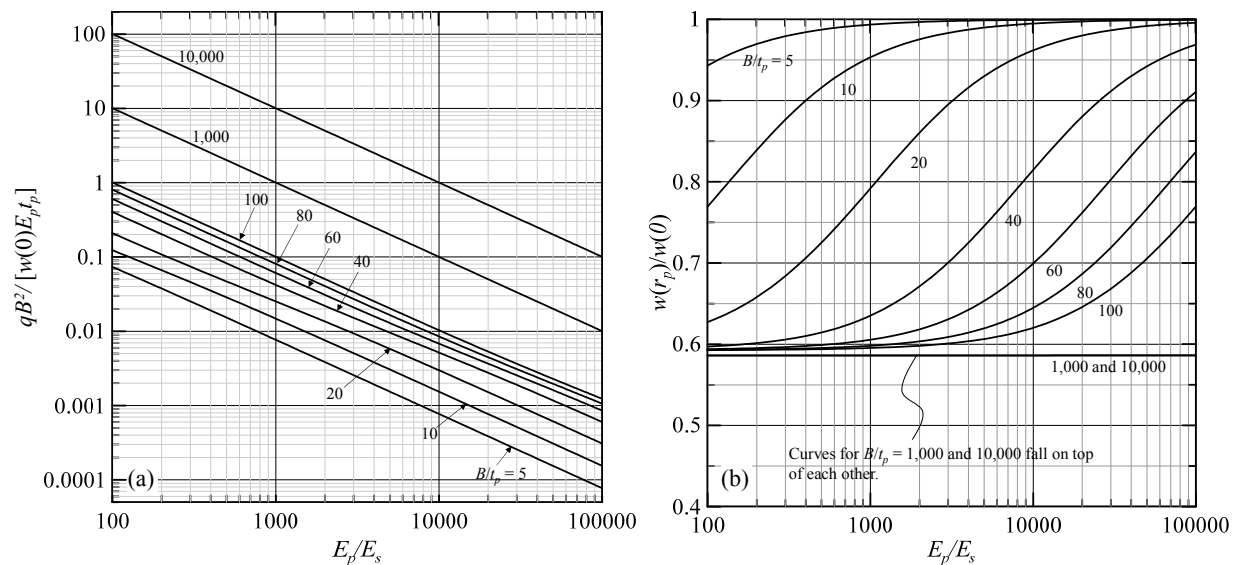


Figure 4. (a) Normalized plate modulus $[k_p = qB^2/(w(0)E_pt_p)]$ and (b) edge-to-center settlement ratio $[w(r_p)/w(0)]$ versus relative stiffness of plate to soil (E_p/E_s) for various values of plate diameter-to-thickness ratio (B/t_p).

Although the present analysis method is based on rigorous mathematical principles, nonlinearity of soil behavior and the horizontal displacement of soil have not been considered in the analysis. Therefore, Figs. 4(a) and 4(b) are not applicable under high loading conditions where large degradation of soil modulus and plastic deformations of soils are expected. Furthermore, because the present analysis assumes linear elasticity, permanent volume change of soil is not considered in the analysis. Therefore, long-term consolidation settlement in clayey soil may increase total foundation settlement and change the differential settlement of the plate. Design charts presented in Figs. 4(a) and 4(b) are intended to be used in *preliminary design* of circular tank foundations when a quick estimation of the differential settlement for given soil properties and plate geometry under small load is needed.

SUMMARY AND CONCLUSIONS

A continuum-based, elastic analysis for a uniformly-loaded, circular tank foundation on homogenous soil was presented in this study. The soil was assumed to behave as a linear-elastic material and the foundation was modeled as a circular plate with finite thickness. The governing differential equations were derived using the principle of minimum potential energy and calculus of variations. The analysis captures the three-dimensional nature of the plate-soil interactions and produces settlement profiles of the tank foundation and the surrounding soil.

The results of the analyses presented in this paper for various plate dimensions and soil stiffnesses compare well with those of FEA, but with less computational effort. Parametric studies show the plate edge-to-center settlement ratio increases (indicating more flexible behavior) when the plate diameter increases, the plate thickness decreases, and the founding soil becomes stiffer. However, when the plate diameter becomes large enough or the thickness becomes very thin, the edge-to-center settlement ratio converges to about 0.6 regardless of soil conditions. In order to facilitate the use of the analysis, design charts providing the normalized

plate modulus and the edge-to-center settlement ratio were developed. Using these charts, the settlements at the plate center and at the edge under small loads can be obtained for various values of plate dimensions and soil stiffnesses for use in preliminary design.

REFERENCES

- Ahlvin, R. G., and Ulery, H. R. (1962). "Tabulated Values for Determining the Complete Pattern of Stresses, Strains and Deflections beneath a Uniform Load on a Homogeneous Half Space." Highway Research Board Bulletin, Issue 342, pp 1-13
- American Petroleum Institute (API). (2001). API Standard 653: Tank inspection and, repair, alteration and reconstruction. 3rd edition
- D'orazio, T. B., and Duncan, J. M. (1987). "Differential settlements in steel tanks." *Journal of Geotechnical Engineering*, 113(9), 967-983.
- Gerrard, C. M. and Harrison, W. J., (1970). "Stresses and displacements in a loaded orthorhombic halfspace." C.S.I.R.O. Aust. Div. App. Geomech. Tech., Paper No. 9, pp. 312-335
- Langeveld, J. M. (1974). "The design of large steel storage tanks for crude oil and natural gas." *Proceedings of the Annual Meeting of the International Institute of Welding*, 35-95
- Marr, A. W., Ramos, J. A., and Lambe, W. T. (1982). "Criteria for settlement of tanks." *Journal of the Geotechnical Engineering Division, ASCE*, 108(8), 1017-1039.
- Salgado, R., Seo, H., and Prezzi, M. (2013). "Variational Elastic Solution for Axially Loaded Piles in Multilayered Soil." *International Journal for Numerical and Analytical Methods in Geomechanics*, Vol. 37, No. 4, pp. 423-440
- Salgado, R. (2008). *The engineering of foundations*. McGraw Hill, New York.
- Seo, H., Basu, D., Prezzi, M., and Salgado, R. (2009). "Load-settlement response of rectangular and circular piles in multilayer soil." *Journal of Geotechnical and Geoenvironmental Engineering*, 135(3), 420-430.
- Vallabhan, C. V., and Das, Y. C. (1991). "Analysis of circular tank foundation." *Journal of Engineering Mechanics*, 117(4), 789-797.
- Vlasov, V.Z., and Leont'ev, N. N. (1966). "Beams, plates and shells on elastic foundations." NTIS Accession No. N67-14238, Israel Program for Scientific Translations, Jerusalem, Israel.

Sustainable Slope Protection and Cut-Off Wall Installation in Densely Populated Areas by the Press-In Piling Method

Takefumi Takuma, A.M.ASCE¹; and Shigeru Kambe²

¹Giken America Corporation, 5770 Hoffner Ave., Suite 101, Orlando, FL 32822. E-mail: ttakuma@gikenamerica.com

²Giken America Corporation, 5770 Hoffner Ave., Suite 101, Orlando, FL 32822. E-mail: skambe@gikenamerica.com

Abstract

The press-in pile driving method utilizes hydraulic force to push piles into the ground by holding onto previously driven piles. The hydraulic force is provided by a sound-attenuated power pack. It generates very low noise and almost no vibration. It is also suited for physically constrained projects and for projects with limited access. Some urban projects require pile driving in low head room or with very small clearance from existing structures. In other cases, pile driving may have to be conducted without an access road to the piling location. This paper will discuss the solutions for those otherwise very difficult levee embankment upgrade and earth retaining projects with pressed-in sheet pile and pipe pile walls.

PRINCIPLE OF THE PRESS-IN PILE DRIVING METHOD

The Press-in Pile Driving Method typically presses the piles by clamping onto a few previously installed piles. The piling equipment of this type works on top of previously installed piles and can therefore move forward without the aid of a service crane (See Figure 1). This method does not use vibrating or percussive force to drive piles and therefore it may be regarded as an environmentally friendly piling method. Its advantages over other piling methods are as follows.

1. Generates very low noise (70dB at 2m or 6.6 feet from the source) and is practically vibration free (2.0mm/s peak particle velocity at 2.5m or 8.2 feet from the source) per White et al. (2002).
2. The equipment is relatively small and its clamping points are much lower than those by other piling methods. The lower clamping points enable the equipment to work in physically tight working conditions, both horizontally and vertically.
3. With attachments, it can deal with hard soil conditions very effectively.
4. It can achieve much more accurate pile installation thanks to a combination of better control of the piles and lower clamping points compared to other piling equipment.

As can be seen on the steps 4 and 5 in Figure 1, the equipment can lift itself up by holding onto the halfway driven pile, release the clamps, and move itself forward without the aid of a crane. It can also go through corners using dummy piles without a crane. The same system can extract piles by reversing the sequence.

Attachments are developed to drive piles in hard soil conditions. The high pressure water jet attachment can effectively press piles into dense sand and silt layers while a continuous flight auger attachment can drive piles into stiff clay, gravels, cobbles, boulders, and soft rock. These attachments work simultaneously with pile driving, minimizing settlement of the surrounding ground without having to bring in a large drill machine for pre-boring (Bergeron 2010).

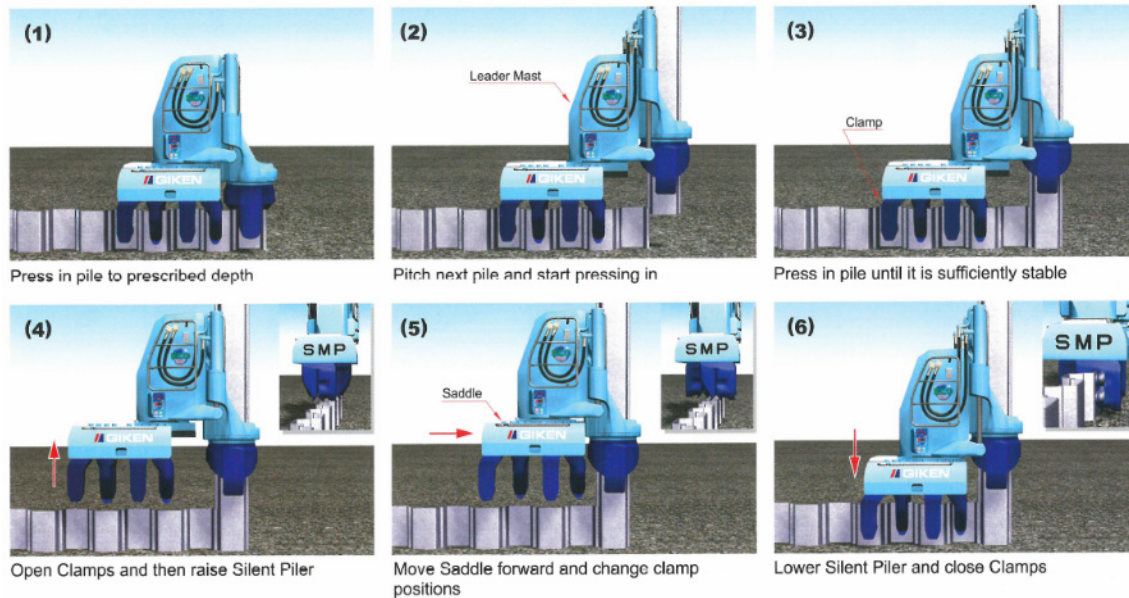


Figure 1. Sequence of the Press-in Piling Operation

The Press-in Principle can be applied to various types of piles such as pipe piles as well as U and Z-shaped sheet piles of various sizes. Sheet pile sizes commonly used by the press-in pile drivers in the U.S. include PZ35 (575mm wide), AZ19-700 (700mm wide), and PZC26 (708mm wide). 500mm (20 inch) wide and 40m (131 foot) long U-shaped sheet piles have been driven with this method.

Some of the Press-in pile drivers are specifically developed to drive piles under very low overhead clearance or right against adjacent structures. With the aid of a Clamp Crane which clamps onto and moves on previously driven piles along with Pile Runner or a pile transporter which also travels on driven piles between the Clamp Crane and a faraway material supply point, the piling operation can be done without an access road (see Figure 2).

With the Press-in Principle as a basis, the Gyro Press Method uses press-in force with simultaneous and continuous rotation to drive pipe piles. Thanks to a cutting shoe welded at the toe of each pile, a pipe pile can be installed not only in hard soil but also in reinforced concrete structures without removing them. See Figure 3 as to how the Gyro Press Method works. Pipe piles with a diameter of 800mm (31.5 inches) and length of 59.5m (195 feet) have been successfully driven with this method.

GARDERE CANAL IMPROVEMENTS PHASE II - NEW ORLEANS, LOUISIANA

The Gardere Canal is located in the New Orleans suburb of Harvey in Jefferson Parish on the west bank of the Mississippi River with the majority of the City of New Orleans on the other side. This SELA-06 Gardere Canal Phase 2 project was part of a multi-year Southeast Louisiana Urban Flood Control Project (abbreviated as SELA) by the U.S. Army Corps of Engineers and local agencies to enhance the flood control ability in New Orleans and its surrounding areas. Figure 4 shows the typical levee conditions prior to the construction.

Figure 5 shows the site's soil conditions; mostly soft clay except a silty fine sand layer between 5.5m (18 feet) and 7.0m (24 feet) below the GL. Figure 6 shows a typical cross section of the levees both before and after construction.

Approximately 4,000 pairs of PZ35 sheet piles were pressed in to form a wider and concrete lined channel. The Press-in Piling Method was specified to minimize the noise and vibration levels of the sheet pile installation work since the levees ran through the densely populated residential and commercial areas.

Two units of pile drivers were used to drive sheet piles to facilitate the progress of the project. A caterpillar-mounted service crane on one side of the levee hoisted the sheet piles to both machines as shown in Figure 7. The construction noise and vibration were successfully mitigated and the sheet piles were installed at high accuracy as shown in Figure 8. Since its completion, there have been an increased number of projects with the Press-in piling specified in this region due partly to the success of this project.

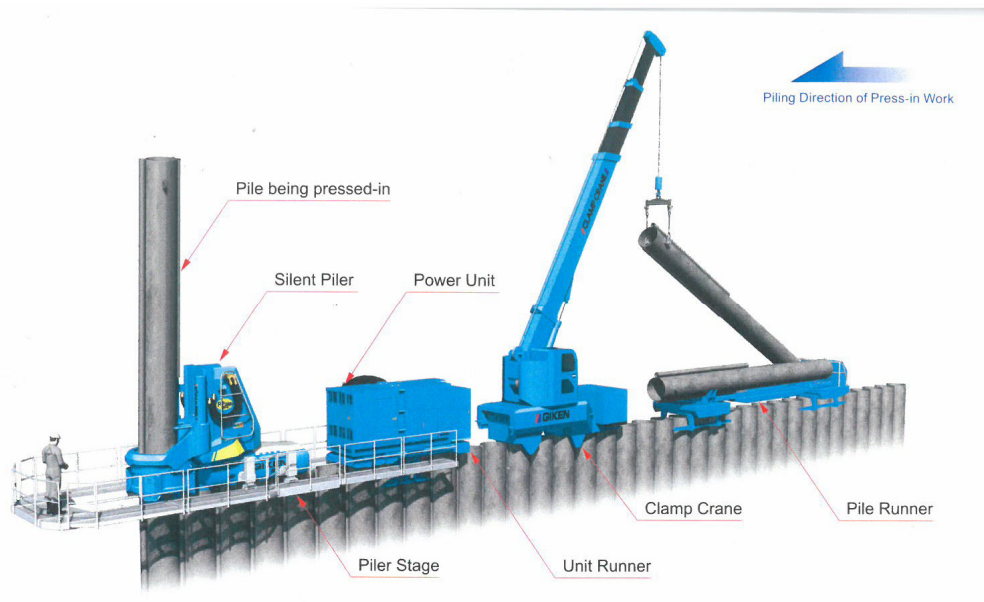


Figure 2. Press-in Piling Operation Without Access Road

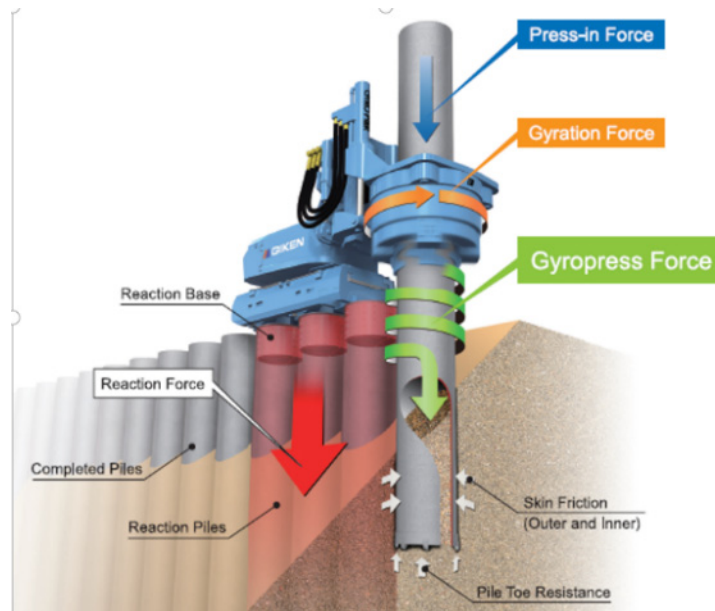


Figure 3. Gyro Press Method



Figure 4. Gardere Canal Levees before Construction

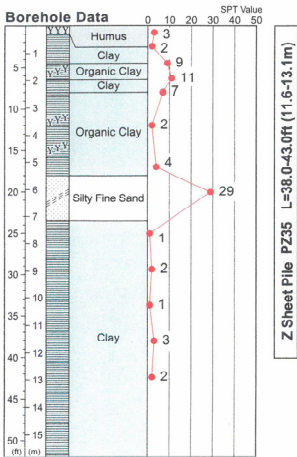


Figure 5. Soil Conditions

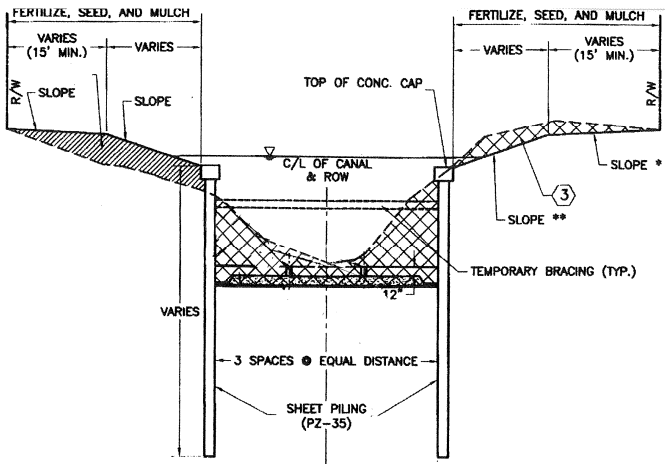


Figure 6. Typical Cross Section



Figure 7. Press-in Pile Drivers and Service Crane



Figure 8. Alignment of Pressed-in Sheet Piles

SANDALWOOD CANAL IMPROVEMENTS JACKSONVILLE, FLORIDA

The Sandalwood Canal In-channel Improvements Project (Hodges Blvd. from Beach Blvd. to Atlantic Blvd., Project No. P-80-01) was to repair the flood-damaged earthen levees as well as to increase the drainage capacity of an existing canal by widening/deepening with sheet piles pressed into the levees running through a densely populated area of Jacksonville, Florida. See Figure 9 for a typical cross section of the canal.

In order to minimize the noise/vibration and also to reduce in-stream exposure of pile driving equipment during construction, two units of Press-in pile drivers were used. The work was done during the dry season of winter. Since the widths of the levee shoulders were relatively narrow (approximately 3 m or 10 feet) for a truck crane to maneuver through, a 10 ton capacity Clamp Crane was used for hoisting sheet piles to the pile drivers. The soil conditions were primarily sandy with the SPT values between 10 and 45 as shown in Figure 10.

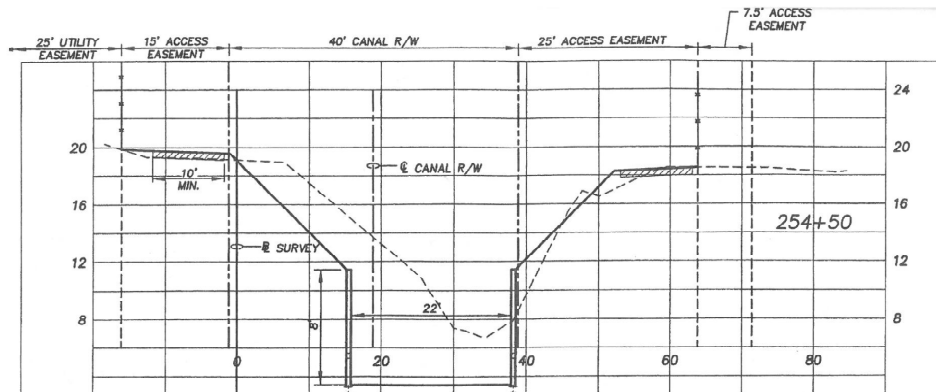


Figure 9. Typical Section

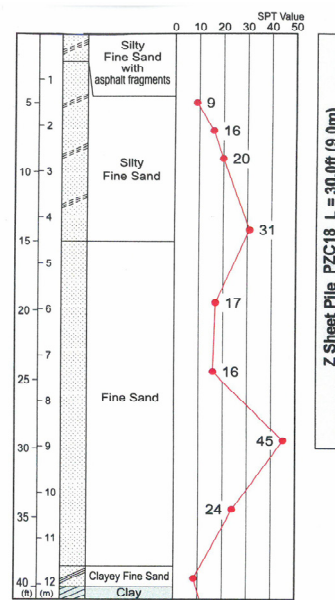


Figure 10. Soil Conditions.

The noise and vibration during the sheet pile driving were limited by the specifications in the following manner; *“The hydraulic press-in equipment shall not produce more than 70dB of noise, at a distance of 25 feet from the equipment, while in operation. It shall not produce any measurable vibration at the ground surface, at a distance of 25 feet from the equipment, while in operation.”*

Figure 11 shows two Press-in pile drivers with a Clamp Crane working on top of already installed sheet piles. Approximately 950 pairs of 7.0 m (23 foot) to 9.0 m (30 foot) long PZC18 sheet piles were driven without causing damage to the nearby homes. Figure 12 shows the completed sheet pile walls with a weir.

MYOSHOJI RIVER RESTORATION PROJECT-TOKYO, JAPAN

The Myoshoji River is one of Kanda River’s tributaries located approximately 15 km (9 miles) northwest of downtown Tokyo, Japan. Although only 9.7 km (5.9 miles) long with its watershed

being relatively small, the river runs through densely populated residential and commercial areas of the city. Very heavy rainfall (263mm, i.e., 10.3 inches) on one September evening in 2005 flooded more than 3,300 units of buildings in the area. This project was to widen the river to increase the drainage capacity and to reduce the flood risk by installing 634 ϕ 1,000 mm (39.4 inch) pipe piles into the existing concrete retaining walls. The pile depth varied from 11 to 22 m (36 to 72 feet). A Gyro Press pile driver was utilized to drive the pipe piles into the concrete retaining walls without removing them. Each pile had a cutting shoe at its toe to facilitate the driving operations (Takuma et al. 2013). Since the roads on both sides of the river were quite narrow for site access and had to be kept open for the local traffic almost all the time, a combination of a Gyro Press pile driver, a Clamp Crane, and a Pile Runner was used. The tube pile sections were delivered to the project's material handling point with a flat bed truck and transferred to the Pile Runner, which subsequently transported them on the rail placed on the top of the driven piles to the Clamp Crane's pick-up point without blocking the road traffic.



Figure 11. Clamp Crane Pitching Sheet Piles to Press-in Pile Drivers



Figure 12. Driven Sheet Piles

Figure 13 shows the project’s typical cross section and Figure 14 shows the site’s hard soil conditions containing dense sand, sandy gravel, and consolidated silt layers with SPT values higher than 50 at and below 12.5 meters (41 feet) from the ground. Figure 15 shows the Gyro Press pile driver at work directly installing a pile into an existing concrete abutment of one of the bridges.

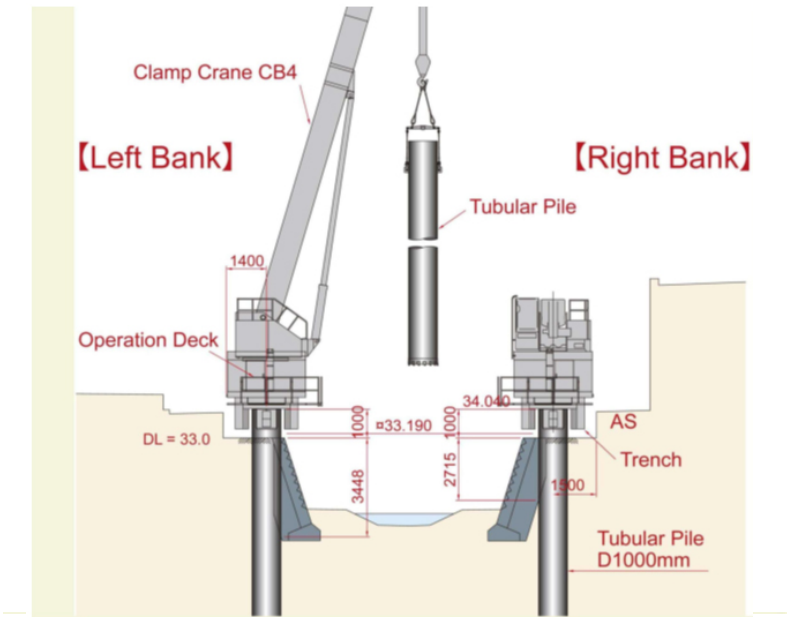


Figure 13. Section of Myoshoji River Restoration Project

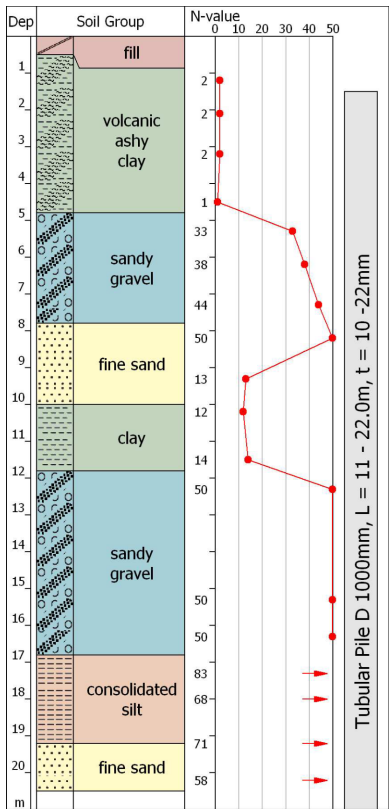


Figure 14. Geotechnical Conditions of Myoshoji River Restoration Project



Figure 15. Gyro Press Piling Directly into Concrete Bridge Abutment

CONCLUSIONS

The Press-in Pile Driving Method is highly suited for piling projects in urban areas due to its low noise and low vibration advantages over other piling methods. It can effectively deal with projects with limited access as well as those with difficult soil conditions. With these environmentally friendly features, this method reduces construction-induced damage to nearby structures and disturbance to densely populated areas surrounding levee upgrades and earth retaining projects.

ACKNOWLEDGEMENT

The authors appreciate the assistance provided by Hiroyuki Nishimura of Japan Press-in Association and Ian Vaz of Giken America Corp.

REFERENCES

- Bergeron, A. (2010), "Banging and Shaking Get Beat by 98 Tons of Quiet Persuasion", *Engineering News Record*, March 22, 201, McGrawHill, New York, Page 14
- Takuma, T., Nishimura H. and Kambe, S. (2013), "Low Noise and Low Vibration Tube Pile Installation by the Press-in Piling Method", *Proceedings of 2013 Annual Conference of Deep Foundations Institute*, Hawthorne, NJ
- White, D., Finlay, T., Bolton, M. and Bearss, G. (2002), "Press-in Piling: Ground Vibration and Noise During Piling Installation", *Proceedings of the International Deep Foundation Congress*, ASCE Special Publication 116, Reston, VA

Load-Carrying Capacity of Slab-on-Grade Foundations Supporting Rack Post Loads

Xiaochao Tang, Ph.D., A.M.ASCE¹; and Mohamad N. Jilati, Ph.D.²

¹Dept. of Civil Engineering, Widener Univ., 349B Kirkbride Hall, One University Place, Chester, PA 19013. E-mail: xtang@widener.edu

²Dept. of Civil Engineering, Widener Univ., 349C Kirkbride Hall, One University Place, Chester, PA 19013. E-mail: mnjlilati@widener.edu

Abstract

Industrial slabs-on-grade are commonly used for warehouse facilities such as storage, retail, and distribution centers. Typical industrial floor slabs are essentially unreinforced concrete usually poured directly onto compacted subgrade. A limited number of studies have shown that the current common practice of design may be overly conservative and yields an excessively high slab thickness, which leads to a high cost of the floor slab. This study aims to experimentally investigate and verify a newly emerged design method that typically results in a smaller slab thickness and significant cost savings. Laboratory-scale slabs-on-grade were built inside a concrete-lined testing box using local soils and aggregates. A total of four 6 ft by 6 ft concrete slabs representing three different concrete mix designs and two slab thicknesses were tested under static loads that simulate storage rack post loads. Based on the limited number of tests, a preliminary finding was that the traditional design method seems to be overly conservative while the newer method may be too liberal.

INTRODUCTION

The current common practice of constructing an industrial warehouses floor slab involves pouring concrete directly onto compacted subgrade. These floor slabs, often referred to as Slab-On-Grade (SOG), are generally subjected to concentrated loads up to about 20 kips as a result of racking columns with baseplates. The floor slabs are designed to prevent punching failure along with onset cracking due to moments which is theoretically the most likely failure mode. Punching failure almost never occurs in the field and it is recognized that micro-cracks are always a distinct possibility due to shrinkage.

Design charts from Ringo and Anderson (1996) are currently commonly used by the industry to design slabs on grade, which often results in a slab thickness ranging from 6 in to 10 in. A previous study has revealed that the typical industrial slab thickness of 6 in to 10 in may be overly conservative (Shentu et al., 1997). Based on test results and numerical modeling, a simplified analytical method was also developed by Shentu et al. (1997):

$$d = [(F_s P_a) / (1.72[(k_s R_1 / E_c) 10^4 + 3.60] f_t' \beta)]^{0.5} \quad \text{Equation (1)}$$

where:

d = slab thickness in inches

F_s = factor of safety, taken here as 3.0

P_a = allowable load carrying capacity of the slab on grade in pounds.

k_s = modulus of subgrade reaction in pci

R_1 = one half the width or diameter of the column baseplate in inches

E_c = modulus of elasticity of concrete, taken here as 4,000,000 psi.

f_c = tensile strength in flexure of concrete in psi.

β = load reduction factor

The target modulus of subgrade reaction, k_s , was 175 pci or higher to mimic the local condition in the field. The soil layer and the aggregate layer were compacted at optimal water contents in this study. Static plate load tests using a hydraulic jack and a reaction frame were conducted in accordance with ASTM D 1196 standard to measure the in-place modulus of subgrade reaction. Modulus of elasticity of the concrete was estimated based on the 28-day strength using the common empirical relation $E_c = 57,000 \sqrt{f_c}$.

The slab radius of relative stiffness, b , is calculated to remove the boundary condition influence on the slab strength using the following equation:

$$b = [E_c d^3 / (12(1 - \mu^2) k_s)]^{0.25} \quad \text{Equation (2)}$$

where: μ is Poisson's ration and taken as 0.15.

In the past, concentrated loads for SOG were calculated using the linear elastic theory. This is acceptable if the loads are relatively small. To discover the ultimate load-carrying capacity of a SOG the elastoplastic characteristics of concrete must be considered. SOG may carry significant additional load after onset cracking of concrete, which is not considered in traditional methods. The additional load carrying capacity after cracking allows for shallower thicknesses in design (Azzi and Laird, 2008).

The objective of this study is twofold: 1) to experimentally investigate and examine the newer Shentu method for designing slabs-on-grade; 2) to make comparisons with the current common design method and identify necessary modifications to the current method. It is recognized that the load-carrying capacity of slab-on-grade foundation is a function of a number of factors including concrete strength, slab thickness, stiffness of soil subgrade, interface and interaction between the concrete slab and subgrade. Furthermore, it is known that there is a number of different failure modes of a slab-on-grade such as punching shear failure, flexural bending failure, failure due to negative moment, and cracking due to shrinkage and curl. This study was limited to selecting and testing two concrete mixtures and two slab thicknesses for each of the mixtures.

STATIC LOAD TEST

The laboratory testing was carried out at the Charles L. Bartholomew Civil Engineering Laboratory at Widener University. The test sections were constructed in a deep, concrete-lined box as shown in Figure 1-a. Dimensions of the box are 6.5 ft (length) \times 6.5 ft (width) \times 5.5 ft (depth). From the bottom to the top, each test section consists of a 36-in subgrade soil layer, an 8-in aggregate leveling course layer, and a concrete slab of 3 in or 4 in thick, depending on the

test section. The subgrade soil was acquired from a local construction site located in central Pennsylvania and classified as sandy lean clay with gravel (SC). The aggregate leveling course was constructed using densely-graded aggregates classified as 2A by the Pennsylvania Department of Transportation (PennDOT, 2010). Two kinds of concrete mix designs were utilized to cast four slabs with thicknesses of 3 in and 4 in for each of the mix designs. One mix design represents the local industrial common mix used for slab-on-grade foundations while the other concrete mix includes fiber reinforcements. The 28-day compressive strength of the aforementioned two concrete mix was 4241 psi and 4031 psi, respectively. It should be pointed out that slab radius of relative stiffness based on concrete modulus, subgrade stiffness, and slab thickness indicated that smaller concrete slabs could be used without influencing the boundary conditions.

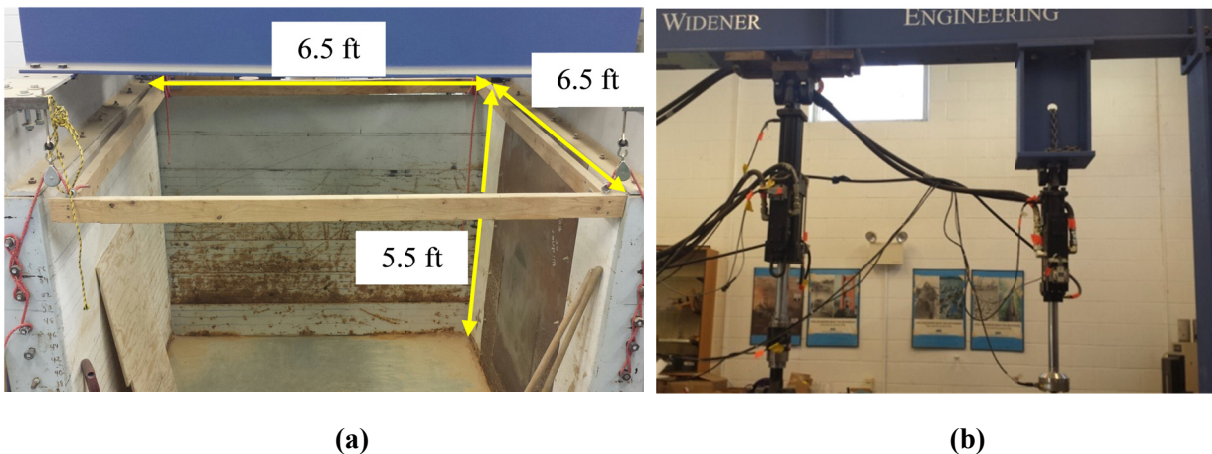


Figure 1. Laboratory facilities used in this study: (a) testing box; (b) hydraulic actuators.

The construction of the test section was started by preparing the subgrade soil at the target moisture content. A waterproof membrane was placed at the bottom and sides of the subgrade to minimize the loss of moisture and change of subgrade condition. The subgrade was constructed in several 6-in lifts in order to achieve adequate compaction. A vibratory plate compactor was used to compact the soil. Sand cone tests were performed for each lift after compaction to check the degree of compaction and moisture content. The base aggregate was compacted in several lifts and at its optimum moisture content. The degree of compaction was 100% of the maximum dry density in accordance with the PennDOT specification (PennDOT 2010). The same compacted soil subgrade and leveling base course was used for all sets of the tests. Due to the constraint of time, instead of pouring the concrete directly onto the subgrade for each of the slabs, the concrete slabs were precast and installed on top of the aggregate leveling layer. Compared to cast-in-place concrete slabs in field, it is expected that the precast slabs would have a reduced friction with the underlying leveling layer and thus a slightly reduced load-carrying capacity.

An electro-hydraulic servo actuator with a loading capacity of 35 kip was positioned above and along the central line of the concrete box and was used to apply monotonic pseudo-static loads onto the test sections (Figure 1-b). The contact area between the actuator and the slab was a 3 in \times 3 in steel plate applied directly in the center of each slab. The loading was displacement-controlled at a rate of 0.17 in per minute. All of the concrete slabs were allowed to cure for at least 28 days and were loaded until failure.

RESULTS AND ANALYSIS

Due to unreliable measurements, measurements from two of the four test sections were unable to be used in this study. Figure 2 shows the load-displacement measurements from the static load test for the 3-in-thick slab and the 4-in-thick slab. The maximum load for the 3-in slab is 7.2 kips while the 4-in slab failed at 9.5 kips. Since the 4-in slab used a concrete mix design with plastic fiber reinforcement, the load-displacement relation exhibited a slightly more ductile behavior at the initial stage of the loading.

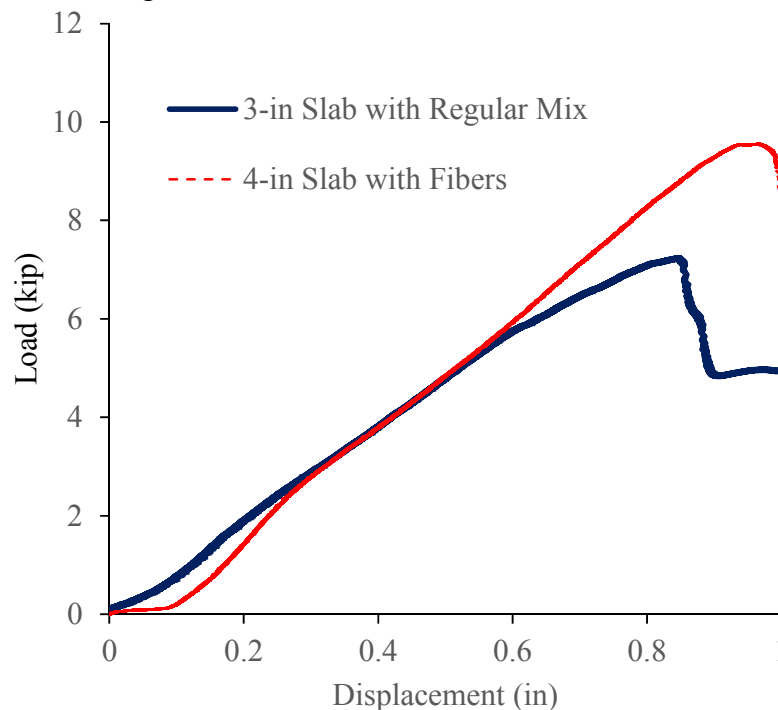


Figure 2. Load-displacement results for different slabs.

Both the more conventional design method/charts from Ringo and Anderson (1996) and the newer method based on Shentu (1997) were used to calculate and predict respective load-carrying capacity of the test sections in this study. While the measured ultimate load of the 3-in slab was 7.2 kips, the traditional method and Shentu method yield a load-carrying capacity of 4.2 kips and 34 kips, respectively. This indicates that the Shentu method may significantly overestimated the load-carrying capacity while the traditional method may produce a conservative prediction of the load-carrying capacity. For the 4-in fiber slab section, the measured ultimate load was 9.5 kips and the traditional and Shentu method yield a load-carrying capacity of 6.9 kips and 62 kips, respectively.

SUMMARY AND CONCLUSIONS

A total of four scaled slabs with two different mixture designs and two slab thickness for each mix design were built and tested. The slabs were placed on top of the soil and aggregate in the geotechnical testing box and loaded to failure. Measurements for two of the slab sections were not usable and not included in this study.

Upon comparing the experimental ultimate loads and the ultimate loads estimated from the traditional method and Shentu method, it was found that two separate tests on different slab depths and mix designs resulted in the same general trend between the experimental ultimate loads and the design equation or chart. It was observed that under the particular loading conditions of this study, the experimental load-carrying capacities were closer with that estimated by the traditional method than that from the Shentu method. In comparing the experimentally measured and predicted loading capacities, it appears that the traditional method may be overly conservative while the method based on Shentu's study (1997) may be too liberal. Additionally, in the traditional design method, a factor of safety of three is applied to the traditional method which for the 3-in slab was 1.4 kips well below the experimental ultimate load of 7.2 kips. Likewise, the 4-in fiber slab traditional allowable load was 2.3 kips compared to the experimental 9.5 kips.

It should be noted that, due to a limited number of tests, cautions should be exercised in interpreting the results. More tests on different slab thickness and soil subgrade reaction moduli should be conducted to verify conclusions and findings from this study.

ACKNOWLEDGEMENTS

The authors wish to thank Andrew Brown, Nick Gentile, Robert Getz, James Siglin, Gregg Smith, and Stephen Yarosh for conducting experimental work. Assistance with the experiments from Mr. Karl Nelson and Mr. Andy Nodolski are acknowledged. Financial support from Conewago Enterprises is gratefully acknowledged.

REFERENCES

- Azzi, V. D. and Laird, R. H. (2008). "Load Carrying Capacity – Concrete Slabs on Grade with Concentrated Loads." *Structure Magazine*. pp. 18-21.
- Pennsylvania Department of Transportation (PennDOT). (2010). *Publication No. 242, Pavement Policy Manual*, Pennsylvania Department of Transportation, Bureau of Maintenance and Operations, Harrisburg, PA.
- Ringo, B. C. and Anderson R. B. (1996). *Designing Floor Slabs on Grade: Step-by-Step Procedures, Sample Solutions, and Commentary*. Aberdeen Group, Addison, IL.
- Shentu, L., Jiang, D., and Hsu, C. (1997). "Load-Carrying Capacity for Concrete Slabs on Grade." *Journal of Structural Engineering*, Vol. 123 (1), pp. 95-103.

A Semi-Analytical Solution for the Analysis of Axially Loaded Pile Groups in Layered Elastic Soil

Faraz S. Tehrani, Ph.D.¹; Rodrigo Salgado, Ph.D., P.E., F.ASCE²; and Monica Prezzi, Ph.D., M.ASCE³

¹Dept. of Geotechnical Engineering, Deltares, Rotterdamseweg 185, 2629 HD Delft, The Netherlands. E-mail: faraz.tehrani@deltares.nl

²Lyles School of Civil Engineering, Purdue Univ., 550 Stadium Mall Dr., West Lafayette, IN 47906. E-mail: salgado@purdue.edu

³Lyles School of Civil Engineering, Purdue Univ., 550 Stadium Mall Dr., West Lafayette, IN 47906. E-mail: mprezzi@purdue.edu

Abstract

A semi-analytical solution is presented in this paper for analysis of axially loaded pile groups embedded in multilayered elastic soil profiles. The proposed method links the soil displacement around a pile group to the axial displacement of the piles in the group through displacement decay functions assigned to the piles. The product of the axial displacement of each pile and its associated decay function is then summed up for all piles in the group. Principle of virtual work and calculus of variations are used to derive the governing differential equations that describe the response of the soil and piles. The governing differential equations that predict the response of the piles are solved analytically using the method of eigenvalues and eigenvectors, whereas the differential equations that describe the soil decay functions are solved numerically using the finite-difference method. The method produces displacement fields that are very close to those produced by the finite element method but with less computational effort.

INTRODUCTION

Piles are designed such that they are able to sustain vertical loads from the superstructure without bearing capacity failure or excessive settlement that would lead to structural damage and serviceability problems. The design of piled foundations, in general, is controlled by settlement since it is very likely that by the time limit bearing capacity is reached, serviceability will have already been compromised. Pile groups are very common in foundation design because a single pile does not often have enough capacity to sustain a structural load individually.

There has been considerable research on the response of vertically loaded piles, which shows the importance of the problem. Several computational approaches have been developed to analyze vertically loaded single piles and pile groups. These approaches can be classified into seven different categories: (1) subgrade reaction method (e.g., Kraft et al. 1981; Armaleh and Desai 1988), (2) boundary element method (e.g., Poulos 1968; Poulos 1979; Butterfield and Banerjee 1971a; Butterfield and Banerjee 1971b), (3) finite element method (e.g., Ottaviani 1975; Pressley and Poulos 1986; Trochanis et al. 1991), (4) simplified analytical methods (e.g., Randolph and Wroth 1979; Mylonakis and Gazetas 1998; Guo and Randolph 1999; Lee and Xiao 2001), (5) hybrid methods (e.g., O'Neill et al. 1977; Chow 1986a), (6) infinite and finite layer methods (e.g., Cheung et al. 1988; Zhang and Small 2000), and (7) variational calculus-

based methods (e.g., Shen et al. 1997; Lee and Xiao 1999; Seo and Prezzi 2007; Seo et al. 2008; Basu et al. 2008; Seo et al. 2009; Seo et al. 2011; Salgado et al. 2013; Tehrani et al. 2015).

This paper presents a semi-analytical solution for analysis of vertically-loaded pile groups in multi-layered, elastic soil. The main goal of the analysis is to relate the total displacement of the piles to the loads applied on them and provide estimates of the displacement of the soil surrounding the piles. The analysis assumes that the vertical displacement at any point in the soil is a function of the displacements of each of the piles in the group. The principle of virtual work and calculus of variations are used to formulate the problem. The analysis is applicable to both single piles (by simply making the number of piles equal to 1) and pile groups.

METHODOLOGY

In a pile group problem, displacement of each of the piles in the group influences the displacement of the piles and the surrounding soil. The displacement field $\{u(x, y, z)\}$ for the entire soil-pile system can be expressed in a Cartesian coordinate system as a summation of n_p unknown functions, where n_p is the number of piles in the group, as follows:

$$u_z = \sum_{i=1}^{n_p} w_i(z) f_i(x, y) \text{ \& } u_x = u_y = 0 \quad (1)$$

where $w_i(z)$ is the vertical displacement of pile i , and $f_i(x, y)$ is a decay function for pile i that accounts for the decrease in soil displacement with increasing distance from pile i . Each of the n_p decay functions varies from 1 at the location of pile i to zero both at the locations of all the other piles and at an infinite distance from the pile group.

Differentiation of (1) produces the infinitesimal strain field (with the conventional geomechanics sign):

$$\varepsilon_{kl} = -\frac{1}{2}(u_{k,l} + u_{l,k}) \quad (2)$$

The elastic stress-strain relations follow:

$$\sigma_{kl} = 2G_s \varepsilon_{kl} + (K_s - 2/3G_s) \varepsilon_{mm} \delta_{kl} \quad (3)$$

where G_s and K_s are the shear and bulk moduli of an elastic soil.

The virtual strain energy density function is expressed as:

$$\sigma_{kl} \delta \varepsilon_{kl} = \sigma_{zz} \delta \varepsilon_{zz} + 2\sigma_{xz} \delta \varepsilon_{xz} + 2\sigma_{yz} \delta \varepsilon_{yz} \quad (4)$$

The balance of internal and external virtual works follows:

$$W_{int} - W_{ext} = \sum_{i=1}^{n_p} E_{pi} A_{pi} \int_{z=0}^{z=L_p} \left(\frac{dw_i(z)}{dz} \right) \delta \left(\frac{dw_i(z)}{dz} \right) dz + \int_{\Omega_{soil}} \sigma_{kl} \varepsilon_{kl} d\Omega_{soil} - \sum_{i=1}^{n_p} Q_i \delta w_i(z) \Big|_{z=0} = 0 \quad (5)$$

where E_{pi} is the Young's modulus of pile i material, A_{pi} is the cross-sectional area of pile i , and Q_i is the axial load applied on pile i .

Equation (5) can be fully expanded, after stress and strain substitutions. After expansion, each of the terms in equation (5) has a first variation of some variables, which can be condensed as:

$$\sum_{i=1}^{n_p} \{ \Lambda_i(z) \delta w_i + \Theta_i(x, y) \delta f_i \} = 0 \quad (6)$$

Equation (6) is satisfied only if the functions $w_i(z)$ and $f_i(x, y)$ are known or the coefficients $\Lambda_i(z)$ and $\Theta_i(x, y)$ are equal to zero. This requirement leads to the governing differential equations and boundary conditions for the vertically loaded pile group problem. These differential equations, which are known as Euler-Lagrange equations, result in the functions $w_i(z)$ and $f_i(x, y)$ that balance the internal and external virtual energy of the pile-soil system. It is assumed that the elastic properties of every soil layer are independent of depth within that layer. Therefore, the Euler-Lagrange equation for the i^{th} pile and k^{th} layer is derived as:

$$-E_{pi} A_{pi} \frac{d^2 w_{i,k}(z)}{dz^2} + \sum_{j=1}^{n_p} \left\{ -t_{ij}^{z,k} \frac{d^2 w_{j,k}(z)}{dz^2} + k_{ij}^{z,k} w_{j,k}(z) \right\} = 0 \quad (7)$$

for $z \leq L_p$, and

$$\sum_{j=1}^{n_p} \left\{ -t_{ij}^{z,k} \frac{d^2 w_{j,k}(z)}{dz^2} + k_{ij}^{z,k} w_{j,k}(z) \right\} = 0 \quad (8)$$

for $z > L_p$.

where

$$t_{ij}^{z,k}(z) = \iint_{xy} (K_{s,k}(z) + 4/3 G_{s,k}(z)) f_j(x, y) f_i(x, y) dx dy \quad (9)$$

$$k_{ij}^{z,k}(z) = \iint_{xy} \left[G_{s,k}(z) \frac{\partial f_j(x, y)}{\partial x} \frac{\partial f_i(x, y)}{\partial x} + G_{s,k}(z) \frac{\partial f_j(x, y)}{\partial y} \frac{\partial f_i(x, y)}{\partial y} \right] dx dy \quad (10)$$

The boundary conditions for the i^{th} pile are also derived from equation (5). At $z = 0$:

$$\left\{ \begin{array}{l} w_{i,1}(z) = w_{i0} \\ or \\ -E_{pi} A_{pi} \frac{dw_{i,1}(z)}{dz} - \sum_{j=1}^{n_p} t_{ij}^{z,1} \frac{dw_{j,1}(z)}{dz} = Q_i \end{array} \right. \quad (11)$$

At $z = H_k < L_p$:

$$\left\{ \begin{array}{l} w_{i,k} = w_{i,k+1} \\ E_i A_i \frac{dw_{i,k}(z)}{dz} + \sum_{j=1}^{n_p} t_{ij}^{z,k} \frac{dw_{j,k}(z)}{dz} = E_i A_i \frac{dw_{i,k+1}(z)}{dz} + \sum_{j=1}^{n_p} t_{ij}^{z,k+1} \frac{dw_{j,k+1}(z)}{dz} \end{array} \right. \quad (12)$$

At $z = H_k = L_p$:

$$\left\{ \begin{array}{l} w_{i,k} = w_{i,k+1} \\ E_i A_i \frac{dw_{i,k}(z)}{dz} + \sum_{j=1}^{n_p} t_{ij}^{z,k} \frac{dw_{j,k}(z)}{dz} = \sum_{j=1}^{n_p} t_{ij}^{z,k+1} \frac{dw_{j,k+1}(z)}{dz} \end{array} \right. \quad (13)$$

At $z = H_k > L_p$ and $k < n_{total}$:

$$\begin{cases} w_{i,k} = w_{i,k+1} \\ \sum_{j=1}^{n_p} t_{ij}^{z,k} \frac{dw_{j,k}(z)}{dz} = \sum_{j=1}^{n_p} t_{ij}^{z,k+1} \frac{dw_{j,k+1}(z)}{dz} \end{cases} \quad (14)$$

Finally, at infinite depth, $z = H_{n_{total}} \rightarrow \infty$ and $w_{i,k} = 0$.

Equations (7) and (8) represent systems of second-order ODEs for the layers above and below the pile base, respectively. The eigenvalue method is used to solve the coupled ordinary differential equations for the pile displacement.

The Euler-Lagrange equation for the decay function associated with pile i is derived by collecting the terms containing $\delta f_i(x, y)$ in equation (5). It follows:

$$\sum_{j=1}^{n_p} \left\{ -t_{ij}^{xy} \frac{\partial^2 f_j(x, y)}{\partial x^2} - t_{ij}^{xy} \frac{\partial^2 f_j(x, y)}{\partial y^2} + k_{ij}^{xy} f_j(x, y) \right\} = 0 \quad (15)$$

where

$$t_{ij}^{xy} = \int_{z=0}^{\infty} G_s(z) w_j(z) w_i(z) dz = \sum_{k=1}^{n_{total}} \int_{H_{k-1}}^{H_k} G_{s,k}(z) w_{j,k}(z) w_{i,k}(z) dz \quad (16)$$

$$\begin{aligned} k_{ij}^{xy} &= \int_{z=0}^{\infty} (K_s(z) + 4/3 G_s(z)) \frac{dw_j(z)}{dz} \frac{dw_i(z)}{dz} dz \\ &= \sum_{k=1}^{n_{total}} \int_{H_{k-1}}^{H_k} (K_{s,k}(z) + 4/3 G_{s,k}(z)) \frac{dw_{j,k}(z)}{dz} \frac{dw_{i,k}(z)}{dz} dz \end{aligned} \quad (17)$$

with boundary conditions:

$$f_i(x, y) = \begin{cases} 1 & \text{within cross section of pile } i \\ 0 & \text{within cross section of other piles} \end{cases} \quad (18)$$

Additionally, at the boundaries of the soil domain (i.e. $x \rightarrow \pm\infty$ or $y \rightarrow \pm\infty$), the decay function reaches zero.

Rewriting of equation (15) as:

$$\begin{aligned} & -t_{ii}^{xy} \frac{\partial^2 f_i(x, y)}{\partial x^2} - t_{ii}^{xy} \frac{\partial^2 f_i(x, y)}{\partial y^2} + k_{ii}^{xy} f_i(x, y) \\ & + \sum_{j=1, j \neq i}^{n_p} \left\{ -t_{ij}^{xy} \frac{\partial^2 f_j(x, y)}{\partial x^2} - t_{ij}^{xy} \frac{\partial^2 f_j(x, y)}{\partial y^2} + k_{ij}^{xy} f_j(x, y) \right\} = 0 \end{aligned} \quad (19)$$

shows that the fourth term on the left side of equation (19) includes the effect of the other piles in the group on the contribution of pile i to the soil displacement field (as represented by f_i). This coupling was found to be superfluous with respect to the accuracy of the results of the analysis since the most important coupling between the piles in the group is captured by equations (7) and (8). Additionally, because the values of the coefficients of equation (19) are within a narrow range for all the piles, consideration of that term can produce an ill-conditioned coefficient

matrix for large groups. A simplifying assumption that eliminates this shortcoming and reduces computation time is to simply neglect the fourth term of the left side of equation (19). This simplification leads to:

$$-t_{ii}^{xy} \frac{\partial^2 f_i(x, y)}{\partial x^2} - t_{ii}^{xy} \frac{\partial^2 f_i(x, y)}{\partial y^2} + k_{ii}^{xy} f_i(x, y) = 0 \quad (20)$$

A 2D central-difference finite difference formulation is used to solve Eq.(20).

The final solution is obtained iteratively. At first iteration, coefficients \bar{t} and \bar{k} appearing in the pile differential equations are guessed. Based in the piles boundary conditions, pile displacement profiles are obtained by solution of the system of differential equations for the piles. This makes it possible to compute the quantities t^{xy} and k^{xy} , which appear in the differential equations for the decay functions, which allows new estimates of the decay functions to be determined. Then the new values of \bar{t} and \bar{k} are then calculated and the iterations continue until the solution converges.

Neglecting lateral displacement of soil due to vertical displacement of piles results in relatively stiff pile response. Therefore, adjustment of the properties of the elastic soil are necessary to compensate for the relatively stiff pile response as suggested by Basu et al. (2008). It was found that setting the soil Poisson's ratio $\nu_s = 0$ and modifying the shear modulus G_s as:

$$G_s^* = 0.65 G_s (1 + 1.25 \nu_s^2) \quad (21)$$

produces more accurate results. With the modified Poisson's ratio and shear modulus, the bulk modulus is reduced to $K_s = 2/3 G_s^*$. These substitutions for G_{si} and K_{si} with G_{si}^* and K_{si}^* were done in the equations derived for the proposed semi-analytical method before results were obtained for the modified analysis. The analysis performed using the modified soil properties is denoted by SAM* throughout this paper.

ANALYSIS AND RESULTS

The accuracy of the proposed method is verified by analyzing a 3×3 group of circular piles installed in a layered soil profile. Figure. 1 shows the properties of the soil and piles. The center-to-center pile spacing s is taken as $3B_p$. A vertical displacement of 10 mm was applied to the head of each pile (which implies a rigid cap over the piles). The soil domain is 100 m ($=200B_p$) long, 100 m ($=200B_p$) wide, and 40 m deep.

Results of the analyses are presented in Figure. 2. The figures show the vertical displacement profiles of the soil at the ground surface as well as the vertical displacement profiles of each pile obtained both from the analyses with and without modified soil properties and from the finite element method (FEM) performed using ABAQUS CAE (Abaqus 6.12.2). The FEM analyses relied on 20-noded brick elements, with domains identical to those of the SAM analyses. It is shown in Figure. 2 that there is good agreement between the results from the analyses using the modified soil elastic properties and those from the finite element method. A summary of the computational effort in the pile group analysis using FEM and SAM is presented in Table 1.

Analyses (SAM*) were also carried out with modified soil properties for a single pile and symmetric pile groups (1×2 and 2×2) consisting of 0.5-m-diameter circular piles with $E_p = 30$ GPa embedded in a uniform soil profile with $E_s = 15$ MPa and $\nu_s = 0.5$ ($G_s = 5000$ MPa and $E_p/G_s = 6000$). The center-to-center spacing between adjacent piles is taken as $2.5B_p$, while the pile length was varied from 5 to $50B_p$. Results of the analyses for the single pile (1×1 pile group)

were compared with those from FEM and Butterfield and Banerjee (1971a) (see Figure. 3a). For the pile groups (1×2 and 2×2 pile groups), the results of the analyses were compared with those from FEM, Butterfield and Banerjee (1971a) and Guo and Randolph (1999) (see Figure. 3b). The results of the analyses are shown in terms of the axial load (Q_t) acting on the head of the piles normalized with respect to the product of the pile head settlement (w_t), the soil shear modulus (G_s) and the pile diameter (B_p) versus the length-to-pile diameter ratio. From the comparisons shown in Figure. 3, it can be seen that there is close agreement between the results of the analyses proposed in this paper and those of Butterfield and Banerjee (1971a) and Guo and Randolph (1999).

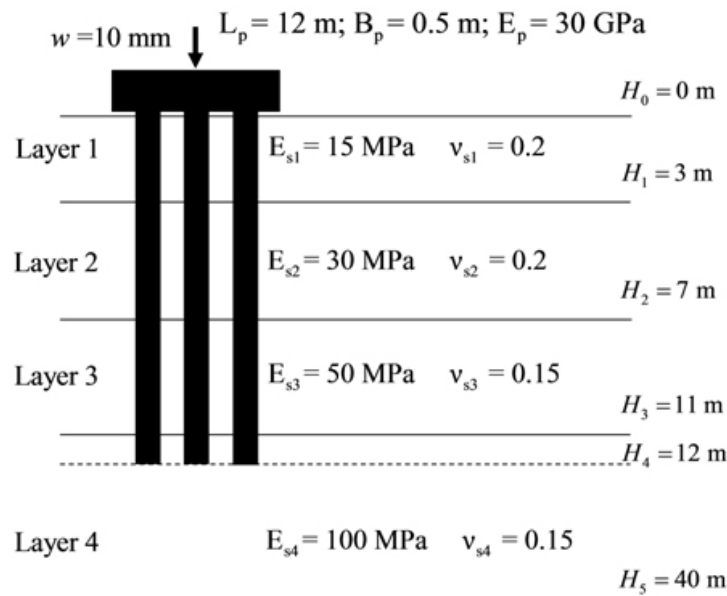


Figure. 1. Soil profile used in the verification analysis.

SUMMARY AND CONCLUSIONS

This paper presented a method for the analysis of vertically loaded single piles and pile groups embedded in multi-layered elastic soil. The solution relied on a displacement field that is a summation of the product of the vertical displacement of every pile in the pile group and their associated decay functions. The principle of virtual work and calculus of variations were used to derive the governing equations that predict the response of vertically loaded piles and the surrounding soil. One of the major advantages of this analysis is its potential for incorporation of any constitutive model, since it does not rely on the superposition principle. Another advantage of the proposed method is that it can be used for any pile group configuration and pile geometry. The results of the analyses proposed in this paper compares well with finite element predictions with less computational effort.

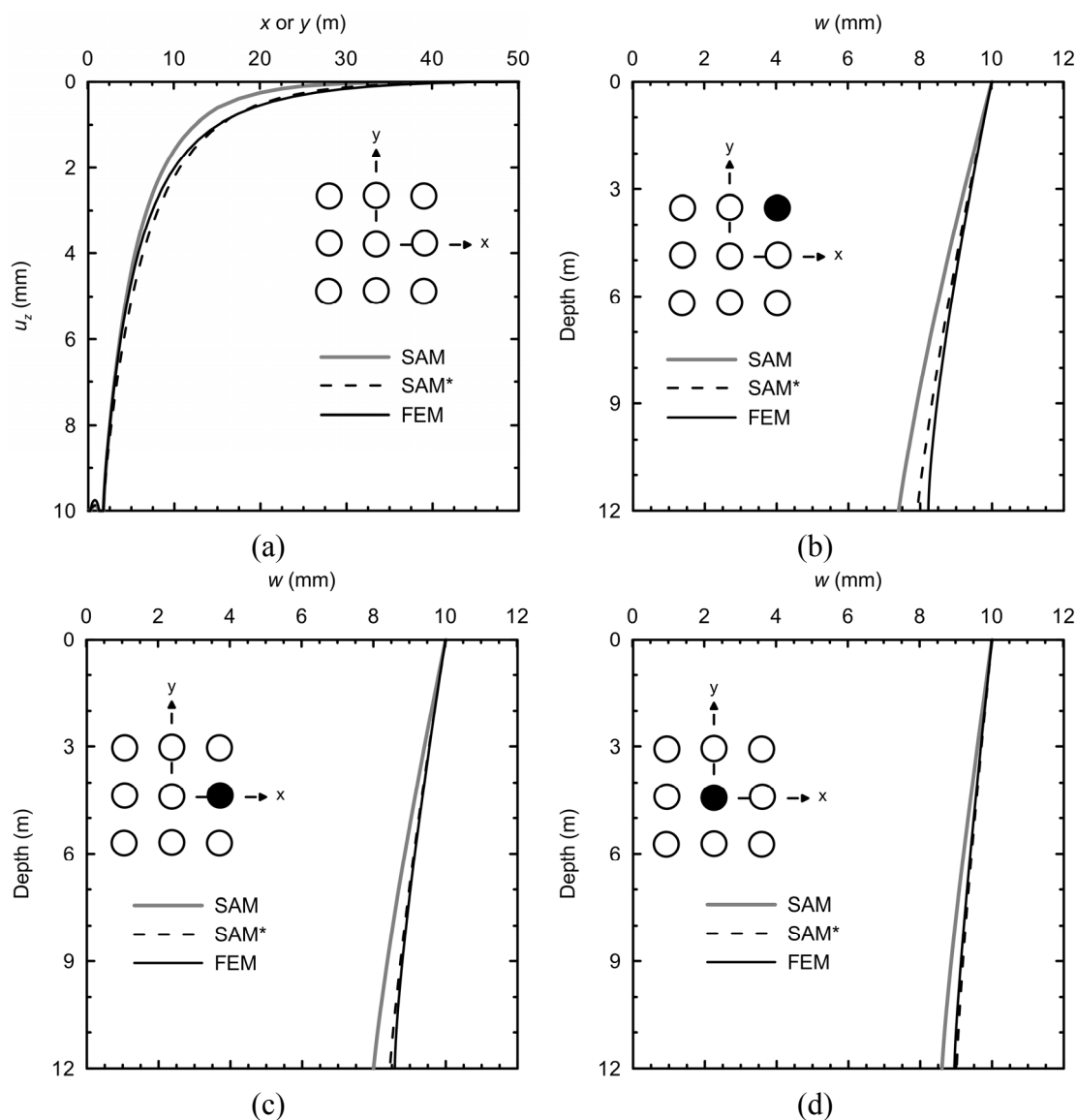


Figure 2. Soil and pile displacement profiles due to 10 mm pile head settlement of a 3×3 pile group: (a) vertical displacement at the ground surface and (b) vertical displacement of the corner piles, (c) vertical displacement of the edge piles, and (d) vertical displacement of the center pile (from Tehrani et al. 2016).

Table 1. Computational effort for each pile group analysis.

Case	FEM		SAM and SAM*		
	Number of Elements	Total CPU Time (sec)	Number of Surface Nodes	Number of Iterations	Total CPU Time (sec)
3×3 Pile Group	375999	1724.2	32761	7	445.3

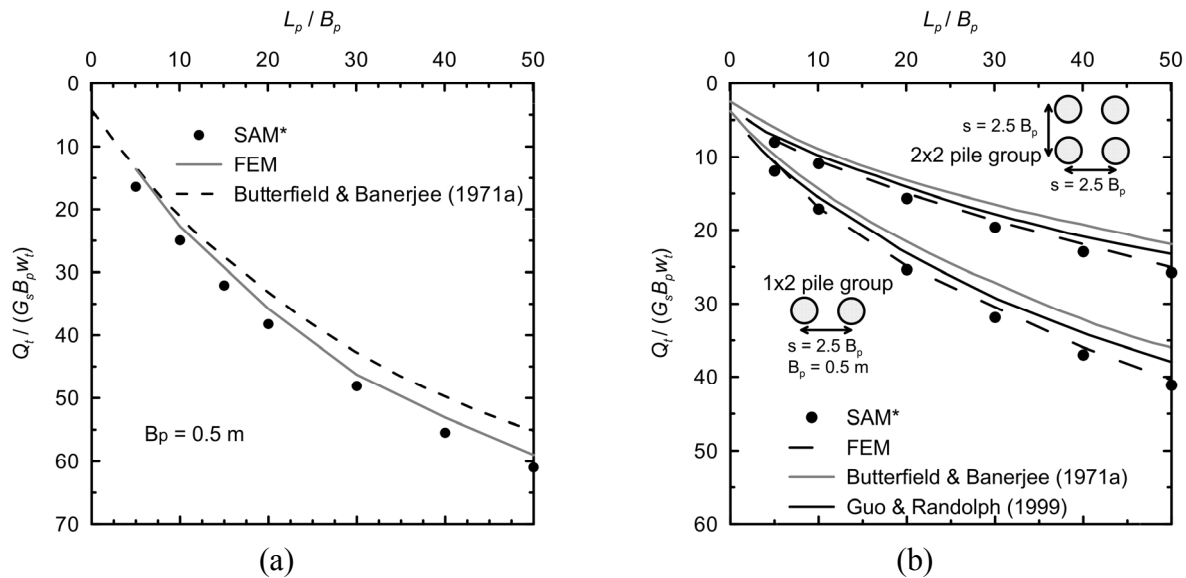


Figure 3. Comparison of pile head stiffness for: (a) a single pile and (b) 1×2 and 2×2 pile groups embedded in a soil with $E_p/G_s = 6000$ and $\nu_s = 0.5$ (modified after Tehrani et al. 2016).

ACKNOWLEDGEMENT

This material is based upon work supported by the National Science Foundation under Grant No. 0969949. The authors are very grateful for this support.

REFERENCES

- Abaqus 6.12.2 [Computer software]. SIMULIA, Johnston, RI.
- Armaleh, S., and Desai, C. S. (1988). "Load-deformation response of axially loaded piles." *Journal of Geotechnical Engineering*, 113(12), 1483–1500.
- Basu, D., Prezzi, M., Salgado, R., and Chakraborty, T. (2008). "Settlement analysis of piles with rectangular cross sections in multi-layered soils." *Computers and Geotechnics*, 35(4), 563–575.
- Butterfield, R., and Banerjee, P. K. (1971a). "The elastic analysis of compressible piles and pile groups." *Geotechnique*, 21(1), 43–60.
- Butterfield, R., and Banerjee, P. K. (1971b). "The problem of pile group-pile cap interaction." *Geotechnique*, 21(2), 135–142.
- Cheung, Y. K., Guo, D. J., and Tham, L. G. (1988). "Analysis of pile group by infinite layer method." *Géotechnique*, 38(3), 415–431.
- Chow, Y. K. (1986). "Analysis of vertically loaded pile groups." *International Journal of Numerical and Analytical Methods in Geomechanics*, 10(1), 59–72.
- Guo, W. D., and Randolph, M. F. (1999). "An efficient approach for settlement prediction of pile groups." *Geotechnique*, 49(2), 161–179.
- Kraft, L. M., Ray, R. P., and T., K. (1981). "Theoretical t-z curves." *Journal of Geotechnical Engineering*, 107(11), 1543–1561.
- Lee, K. M., and Xiao, Z. R. (1999). "A new analytical model for settlement analysis of a single pile in multi-layered soil." *Soils and Foundations*, 39(5), 131–143.

- Lee, K. M., and Xiao, Z. R. (2001). "A simplified nonlinear approach for pile group settlement analysis in multilayered soils." *Canadian Geotechnical Journal*, 38(5), 1063–1080.
- Mylonakis, G., and Gazetas, G. (1998). "Settlement and additional internal forces of grouped piles in layered soil." *Géotechnique*, 48(1), 55–72.
- O'Neill, M. W., Ghazzaly, O. I., and Ha, H. B. (1977). "Analysis of three-dimensional pile groups with non-linear soil response and pile-soil-pile interaction." 9th Offshore Technology Conference, Houston, Texas, 245–256.
- Ottaviani, M. (1975). "Three-dimensional finite element analysis of vertically loaded pile groups." *Geotechnique*, 25, 159–174.
- Poulos, H. G. (1968). "Analysis of the settlement of pile groups." *Geotechnique*, 18, 449–471.
- Poulos, H. G. (1979). "Group factors for pile-deflection estimation." *Journal of Geotechnical Engineering*, 105(12), 1489–1509.
- Pressley, J. S., and Poulos, H. G. (1986). "Finite element analysis of mechanisms of pile group behavior." *International Journal for Numerical and Analytical Methods in Geomechanics*, 10(2), 213–221.
- Randolph, M. F., and Wroth, C. P. (1979). "An analysis of the vertical deformation of pile groups." *Géotechnique*, Thomas Telford, 29(4), 423–439.
- Salgado, R., Seo, H., and Prezzi, M. (2013). "Variational elastic solution for axially loaded piles in multilayered soil." *International Journal for Numerical and Analytical Methods in Geomechanics*, 37, 423–440.
- Seo, H., Basu, D., Prezzi, M., and Salgado, R. (2009). "Load-Settlement Response of Rectangular and Circular Piles in Multilayered Soil." *Journal of Geotechnical and Geoenvironmental Engineering*, American Society of Civil Engineers, 135(3), 420–430.
- Seo, H., and Prezzi, M. (2007). "Analytical solutions for a vertically loaded pile in multilayered soil." *Geomechanics and Geoengineering: An International Journal*, 2(1), 51–60.
- Seo, H., Prezzi, M., and Salgado, R. (2008). "Settlement analysis of axially loaded piles." 6th International Conference on Case Histories in Geotechnical Engineering, Arlington, VA, August 2008.
- Seo, H., Prezzi, M., and Salgado, R. (2011). "Elastic analysis for axially loaded piles in multilayered soil." 13th International Conference of the International Association for Computer Methods and Advances in Geomechanics (IACMAG), Melbourne, Australia, May 2011, 984–990.
- Shen, W. Y., Chow, Y. K., and Yong, K. Y. (1997). "A variational approach for vertical deformation analysis of pile group." *International Journal for Numerical and Analytical Methods in Geomechanics*, 21(11), 741–752.
- Tehrani, F. S., Salgado, R., & Prezzi, M. (2015). Analysis of Axial Loading of Pile Groups in Multilayered Elastic Soil. *International Journal of Geomechanics*, 16(2), 04015063.
- Trochanis, A. M., Bielak, J., and Christiano, P. (1991). "Three-dimensional nonlinear study of piles." *Journal of Geotechnical Engineering*, American Society of Civil Engineers, 117(3), 429–447.
- Zhang, H., and Small, J. C. (2000). "Analysis of capped pile groups subjected to horizontal and vertical loads." *Computers and Geotechnics*, 26(1), 1–21.

Laboratory Study of the Effect of Pile Surface Roughness on the Response of Soil and Non-Displacement Piles

Faraz S. Tehrani¹; Fei Han²; Rodrigo Salgado³; and Monica Prezzi⁴

¹Researcher/Consultant, Deltares, Delft, The Netherlands.

²Ph.D. Student, Lyles School of Civil Engineering, Purdue Univ.

³Charles Pankow Professor of Civil Engineering, Lyles School of Civil Engineering, Purdue Univ.

⁴Professor of Civil Engineering, Lyles School of Civil Engineering, Purdue Univ.

Abstract

This paper presents the results of axial load tests performed on instrumented model piles with different surface roughnesses. The model piles were pre-installed in a large-scale, half-circular chamber with a viewing window in its flat-side wall. Uniform silica sand samples in dense and medium dense states were prepared using dry pluviation. Digital image correlation technique (DIC) was used to study the effects of pile surface roughness and soil density on the response of the soil during loading of the model piles. Test results show that the extent of the zone next to the pile that is affected by loading of the pile increases as the pile surface roughness and soil density increase. The development of a shear band next to the pile shaft was also studied by carefully analyzing images taken with a digital microscope during loading of the model piles. Furthermore, the shaft resistances of the loaded piles were measured during the loading tests to investigate the effect of soil density and surface roughness on the response of the model piles.

INTRODUCTION

There are several factors that affect the unit shaft resistance of non-displacement piles installed in sand, such as the roughness of the pile-sand interface (Fioravante 2002), initial sand density and stress state (Loukidis & Salgado 2008).

A shear band is formed when a densely packed volume of sand is sheared. As shown by Uesugi et al. (1988), the formation of a shear band in sand next to an interface with another material, such as concrete or steel, depends on the interface roughness. Sand particles slide, roll and tend to move away from a rough surface (dilation), but tend to slide along a smooth surface without significant rolling and deformation. Therefore, thicker shear bands tend to form when the sliding interface is rough (Uesugi et al. 1988). The roughness of the surface of a pile is typically quantified by the normalized roughness ratio $R_n = R_t/D_{50}$, where R_t is the maximum roughness (defined as the maximum vertical distance between a peak and a trough of the surface over a length L_m equal to the mean diameter D_{50} of the sand). The thickness of a shear band t_s is generally defined in terms of the spatial variation of the displacement gradient during shearing (Uesugi & Kishida 1987; Desrues & Viggiani 2004); it has been reported to range from 5 to 30 times the mean particle diameter D_{50} (Uesugi et al. 1988).

The quantification of displacement and deformation fields in soil using algorithms such as Particle Image Velocimetry (PIV) and Digital Image Correlation (DIC) has become possible in the past years with development of more advanced digital cameras (Arshad et al. 2014; Tehrani et al. 2016). DIC compares a sequence of digital images of a body undergoing

deformation using a correlation scheme to produce the displacement and strain fields within the deformed body.

This paper presents the results of axial load tests performed on model non-displacement (pre-installed or "wished in place") piles embedded in uniform silica sand samples prepared in a large-scale DIC chamber. The effects of the pile surface roughness and sand density on the mobilization of shaft resistance in pre-installed model piles are addressed and the DIC technique is used to obtain the displacement and strain fields in the soil next to the non-displacement model piles throughout the loading process. Additionally, grain-scale observations of particle movement within and next to a shear band are used to characterize its formation next to the model pile shaft.

EQUIPMENTS AND MATERIAL

Test Equipment and Data Acquisition Systems. The pile load tests were carried out in a pile testing facility located at the Bowen Laboratory at Purdue University. Figure 1 shows the testing equipment used in this research. The test setup consists of a half-circular steel chamber with a diameter of 1680 mm and height of 1200 mm (details are shown in Arshad et al. (2014) and Tehrani et al. (2016)), a sand pluviator, a loading system, a reaction frame, and 790-mm-long solid half-circular piles made of brass with diameter $B = 31.75$ mm and embedded length = 490 mm. Digital images of the model piles and soil are taken from three observation windows in the front chamber wall.

The model pile diameter was chosen so that the ratio of the pile diameter to the D_{50} of the test sands ($B/D_{50} \approx 48.9$) remained greater than 20 to avoid scale effects at the pile tip level (Salgado 2013). A 10-kN compression load cell was embedded at the base of the pile to measure the base resistance. A 20-kN tension-compression load cell was also embedded between the loading jack and the head of the pile to measure the applied axial load. The difference between the load measured by the top and base load cells is equal to the shaft load carried by the pile during the loading test.

A half-circular, air-rubber bladder, confined between a metal plat at the bottom and a reaction plate at the top, was used to apply a 50-kPa pressure on the top surface of the soil samples (soil samples are prepared to a height of 1040 mm).

Images were recorded during the pile load tests using a digital image acquisition system consisting of three Complementary Metal-Oxide-Semiconductor (CMOS), machine-vision digital cameras with 5 Mega Pixel (MP) resolution. The cameras were equipped with low-distortion lenses of 12.5 mm fixed focal length. Images were taken at a frequency of 2 frames per second (fps). The sensors used for measuring the axial force and shaft resistance during loading of the model pile were connected to a separate data acquisition system.

Sand and Interface Properties. The test sand (Ohio Gold Frac sand) is a coarse-grained silica sand with sub-angular particles. It is classified as a poorly graded (SP) sand according to the Unified Classification System (ASTM D2487).

Table 1 summarizes the main properties of the test sand.

A number of direct shear tests were performed on glass-soil, brass-glass and pile shaft-soil interfaces. Materials with three different values of pile surface roughness were used in the tests: brass, brass covered by sand paper #120 and brass covered by sand paper #50. Table 2 provides the interface critical-state friction angles for the tested interfaces.

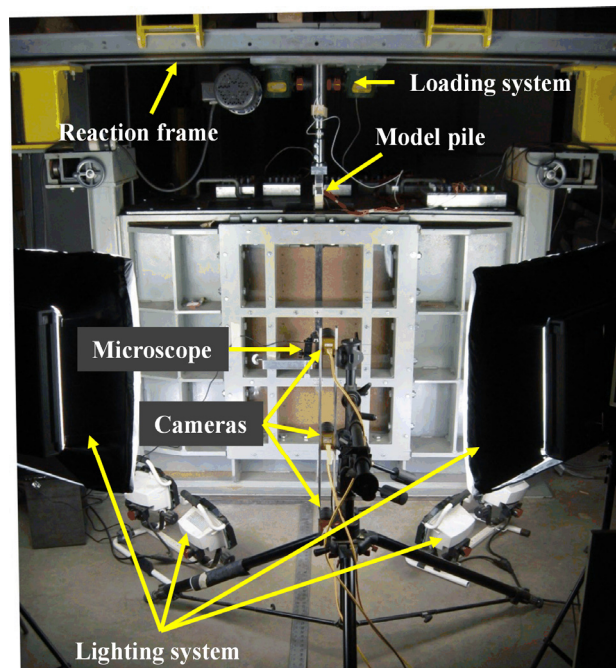


Figure 1 – Experimental facility for pile load testing (after Tehrani et al. 2016).

Table 1 – Properties of Ohio Gold Frac sand.

G_s	D_{50} (mm)	C_c	C_u	e_{max}	e_{min}	1B_r (%)	$^2\phi_c^{DS}$ (°)
2.65	0.65	0.96	1.47	0.853	0.537	2.65	36.7

¹Relative breakage, as defined by Hardin (1985), based on the results of one-dimensional compression tests performed on very dense samples ($D_R = 85\%$) with normal stresses of up to 10 MPa

²Critical-state friction angle based on direct shear tests

Table 2 – Interface critical-state friction angles from direct shear tests.

Interface	Interface friction angle δ	δ / ϕ_c^{DS}
Sand-Glass [*]	9.0°	0.25
Brass-Glass	9.3°	N.A.
Brass-Sand [*]	19.7°	0.54
#120 Sand paper-Sand [*]	28.4°	0.77
#50 Sand paper-Sand [*]	31.1°	0.85

^{*} Interface critical-state friction angle

Image Analysis

Processing of the images taken during model pile load tests were performed using the digital image correlation software VIC-2D (Correlated Solutions 2009). The subset size, which can be thought of as analogous to the representative element volume (REV) in continuum mechanics, was optimized through a parametric study and the dimensions of 25 pixels \times 25 pixels (\approx

$7D_{50} \times 7D_{50}$) was adopted throughout this study. More details about the DIC technique as used in the present work can be found in Arshad et al. (2014).

LOAD TESTS

Six pile load tests were performed in the DIC chamber in medium dense and dense sand samples subjected to a surcharge of 50 kPa. The effect of the pile surface roughness was assessed by attaching sand paper of different surface roughness to the shaft of the model piles. Table 3 provides the pile load test conditions.

The model pile was pre-installed in the calibration chamber before sample preparation. The embedment depth of the pile was 490 mm (15.4*B*). The pile was maintained inside the chamber and against the plane of symmetry (Plexiglas wall) using a series of turn-buckles placed between the pile and the opposite wall of the chamber. Medium dense and dense sand samples were prepared by air pluviation using a large pluviator placed above the DIC chamber at a fixed position (sand drop height > 500 mm). The target sample densities were achieved through addition or removal of diffuser sieves. The turn-buckles were removed gradually as the sample was prepared. For sample density and uniformity verification, nine miniature thin tube samplers with inner diameter equal to two inches were placed at three different heights within the sand sample and were later used to determine density locally. The variation in sample density was determined to be within ± 3 -5%. The surcharge was applied gradually on top of the sample by inflating the half-circular, air-rubber bladder using a laboratory air-pressure line.

Table 3 – Shaft surface roughness and sand density for the tests performed on non-displacement piles.

Test #	Surface material	Maximum surface roughness R_t (μ m)	Normalized shaft roughness $R_n = R_t/D_{50}$	Relative density D_R (%)
1	Brass	19.3	0.03	90.8
2	#120 Sand paper	169	0.26	90.1
3	#50 Sand paper	741	1.14	86.0
4	Brass	19.5	0.03	67.5
5	#120 Sand paper	169	0.26	66.4
6	#50 Sand paper	741	1.14	66.1

The model pile was loaded at a rate of ≈ 0.1 mm/s (6 mm/min) until it penetrated one pile diameter ($B=31.75$ mm) into the sand sample. Digital images were acquired simultaneously by three cameras during the loading process at a constant frame rate of 2 fps. The force at the head and base of the pile was measured throughout the tests.

RESULTS AND DISCUSSION

Soil Displacement and Strains

Radial displacement. Tests 1 and 4 with smooth pile surface did not show any significant change in the soil displacement and deformation field, therefore the associated image analysis results are not presented in this paper. Figure 2 shows the planar distribution of normalized radial displacement u/B in dense and medium dense soil samples after $1.0B$ (31.8 mm) pile head settlement for piles with non-smooth surface roughness ($R_n = 0.26$ and 1.14). In these plots, r/B is the normalized radial distance from the pile centerline ($r/B = 0.5$ at the pile shaft), and z/B is the normalized vertical distance from the sand sample surface. Since there is no significant motion in the soil beyond a radial distance of approximately $3B$ (95.3 mm) from the pile centerline, results are shown only up to that distance. For all tests, the initial embedment depth of the pile is $z_b = 15.4B$ (490 mm). Figure 2(a) to (d) show that the soil next to the medium rough ($R_n = 0.26$) and rough ($R_n = 1.14$) piles embedded in the dense sand samples undergoes greater radial displacements than the soil next to the same piles in the medium dense sand samples. In general, the radial displacement increases with increasing density and increasing pile surface roughness. It can be seen in Figure 2 that for all values of surface roughness, the radial displacement increases with depth.

Shear deformation. The spatial distribution of finite shear strain E_{rz} next to the loaded non-smooth piles is shown Figure 3. The strains are calculated from the beginning of loading to the end of $1.0B$ (31.8 mm) pile head settlement. A shear strain of 2% in these contour plots was taken as reference for what would be considered large shear strains. As shown in Figure 3, for piles with medium rough and rough interfaces, the zone with shear strain exceeding 2% in the dense sand and medium dense sand samples extends radially up to $r=1.0B$ (31.8 mm). It is observed that there is no significant difference between the extent of this zone for the rough piles embedded in the medium dense and dense sand samples.

Analysis of the Response of Soil near the Pile Shaft. A digital portable microscope was placed at the second window of the DIC chamber at $z = 9.5B$ (301.6 mm) to study the formation of the shear band next to the pile shaft. The resolution of the microscope in these cases was ≈ 0.02 mm/pixel.

A shear band can be viewed, conceptually, as separating two moving "rigid" blocks. Therefore, the shear band in these tests can be taken as the boundary between two zones with high ratio of vertical displacement. **Figure 4** shows the position of the left boundary of the shear band within the soil domain at the end of pile loading for tests including piles with rough surfaces (tests 2, 3, 5 and 6). The vertical axis z_{rel} in Figure 4 is measured relative to the vertical position of the midpoint of the observed area. In Figure 4, r_0 denotes the radius of the model pile. The thickness of the shear band is clearly greater for the roughest piles with $R_n = 1.14$ than for the piles with $R_n = 0.26$. Table 4 summarizes the maximum $t_{s,max}$ and average $t_{s,ave}$ thickness of the shear band for the tests performed.

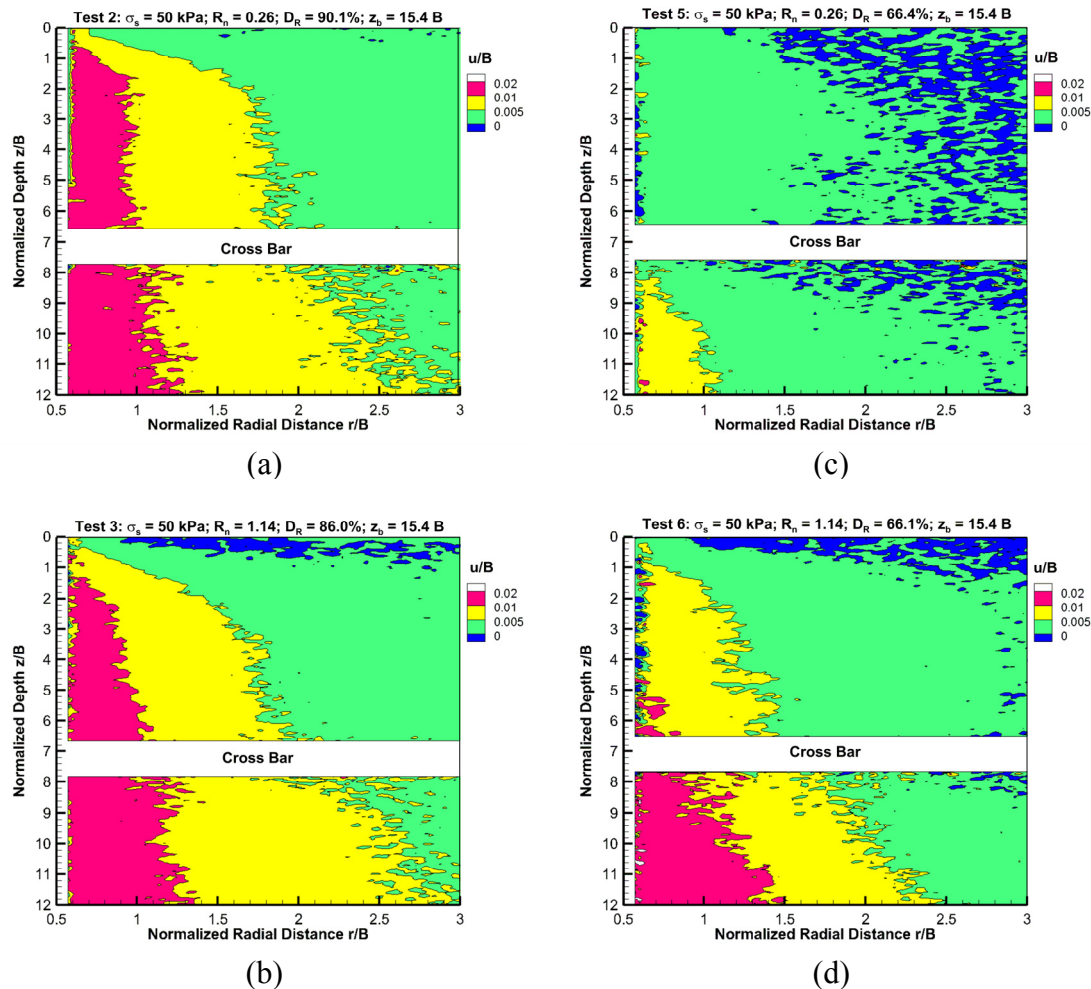


Figure 2 – Spatial distribution of normalized radial displacement u/B for: (a) Test 2 with dense sand, (b) Test 3 with dense sand, (c) Test 5 with medium dense sand and (d) Test 6 with medium dense sand (modified after Tehrani et al. 2016).

According to Table 4, the shear band thickness in the medium dense sand is slightly greater than that in the dense sand (for piles with the same surface roughness). This happens because the higher density of the sand on either side of the incipient shear band makes it less attractive for the shearing process to broaden than to continue to develop where dilation is underway. This is also observed in element testing, with shear bands gradually increasing in size for increasingly less dense sand. Although the discussion of scale effects in the shaft resistance of model piles have focused on the B/t_s ratio, this does not mean that the shaft resistance would be exclusively dependent on this ratio; it depends also on the absolute value of t_s . This means that a pile with a high value of this ratio (a typical pile in the field under realistic conditions) would not be equivalent to a smooth model pile with the same B/t_s ratio. Scale effects would not disappear because the mechanics of shaft resistance for the model pile with smooth surface, in which sliding takes place between the pile and the first line of particles next to it, with essentially no shear band formation, is different from what is observed for the real bored pile, which does have a rough surface and thus a shear band with nonzero thickness.

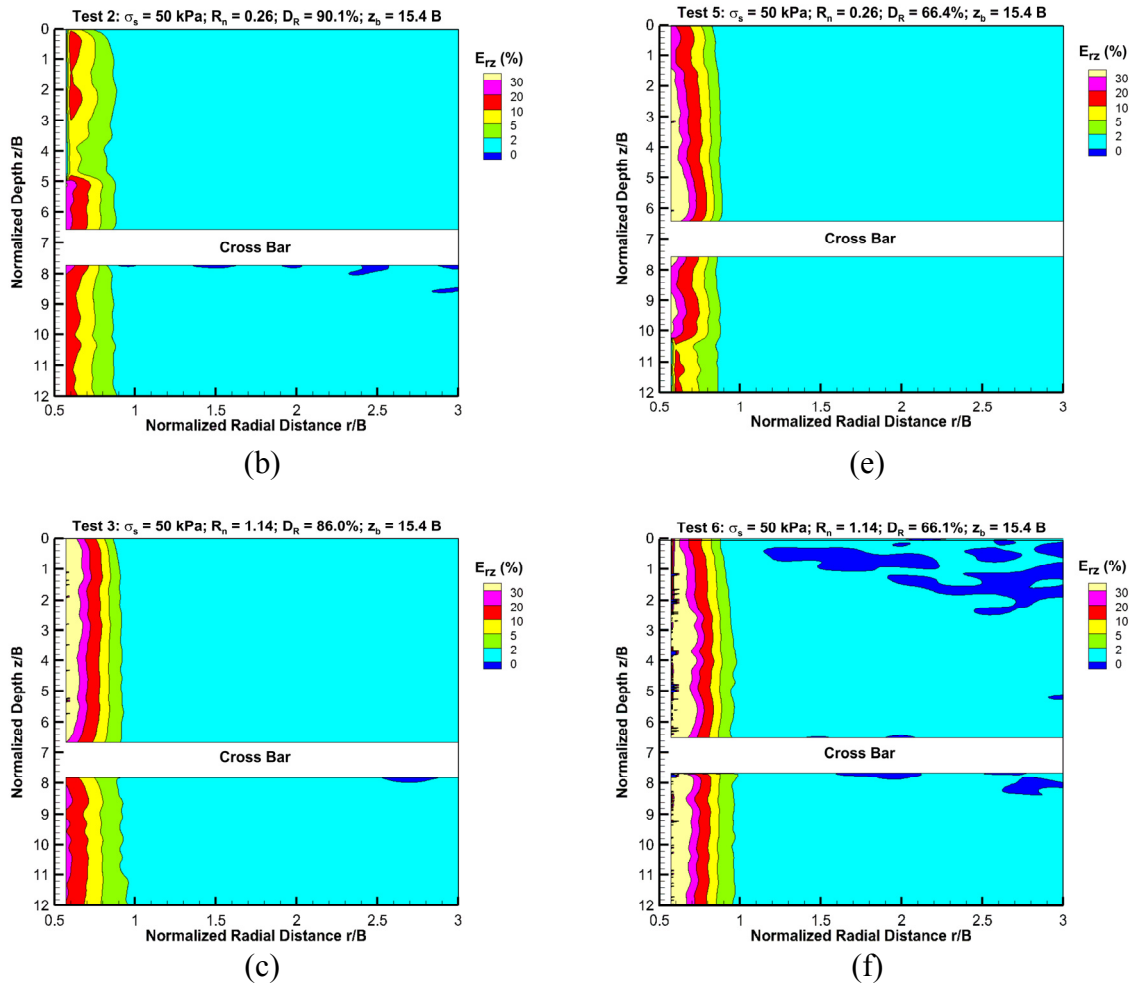


Figure 3 – Spatial distribution of shear strain E_{rz} for: (a) Test 2 with dense sand, (b) Test 3 with dense sand, (c) Test 5 with medium dense sand and (d) Test 6 with medium dense sand (modified after Tehrani et al. 2016).

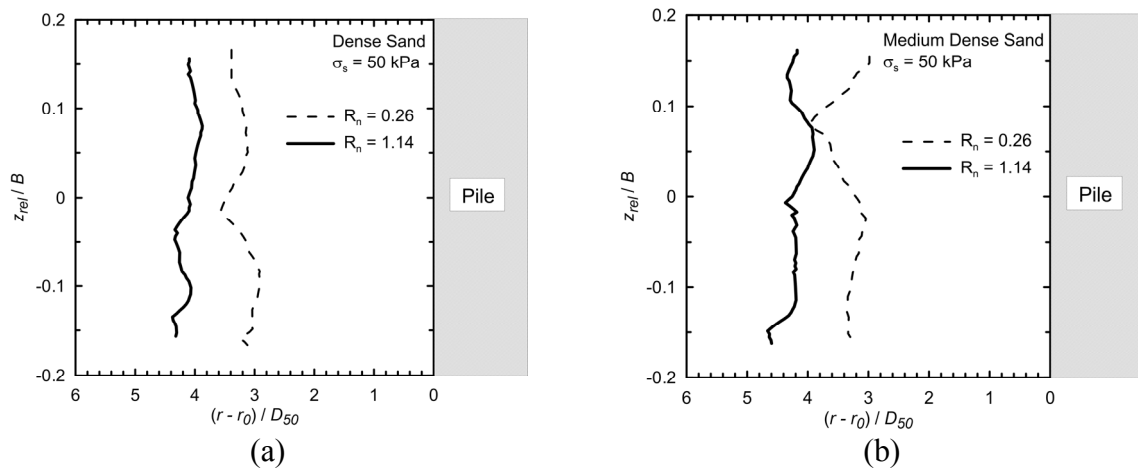


Figure 4 – Shear band boundary next to the piles for the: (a) dense sand sample and (b) medium dense sand sample (modified after Tehrani et al. 2016).

Table 4 – Dimensions of the shear band next to the tested model piles.

Test #	D_R (%)	R_n	$t_{s,max}/D_{50}$	$t_{s,ave}/D_{50}$
2	90.1	0.26	3.9	3.2
3	86.0	1.14	5.0	4.1
5	66.4	0.26	4.5	3.4
6	66.1	1.14	5.2	4.2

Figure 5 shows the average unit limit shaft resistance ($q_{sL,ave}$) at the end of pile loading for all tests.

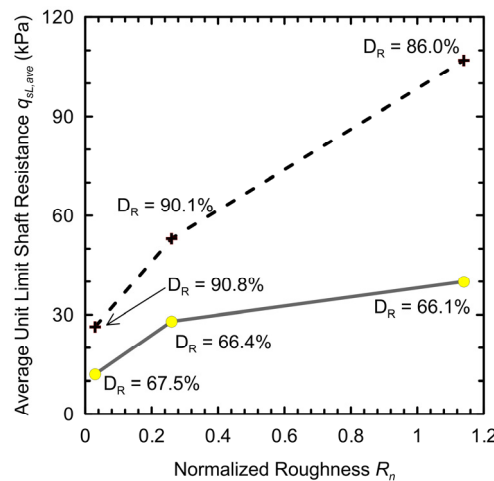


Figure 5 – Effect of surface roughness and soil density on average limit unit shaft resistance of the pre-installed model piles (modified after Tehrani et al. 2016).

The shaft resistance was calculated by subtracting the load measured at the head and base of the piles and dividing it by the surface area of the pile shaft. The unit limit shaft resistance was corrected to exclude the contribution from the pile-glass interface at critical state. Figure 5 shows that the average unit limit shaft resistance $q_{sL,ave}$ of the model piles increases with increasing interface roughness and increasing sand relative density. The effect of surface roughness on the average unit limit shaft resistance of the model piles is more pronounced for the dense than for the medium dense sand samples.

SUMMARY AND CONCLUSIONS

This paper presented the results of axial load tests performed on non-displacement model piles. The tests were performed in a half-circular calibration chamber on medium dense and dense samples of a sub-angular silica sand prepared using dry pluviation. The half-circular model piles, with normalized pile surface roughness R_n equal to 0.03 (characterizing a relatively smooth interface), 0.26 and 1.14 (characterizing a very rough interface), were pre-installed (“wished in place”). For rough piles embedded in dense and medium dense sand, the maximum shear band thickness ranged from $3.9D_{50}$ to $5.2D_{50}$, while the average shear band thickness was in the $3.2D_{50}$ to $4.2D_{50}$ range. No shear band was observed next to a smooth pile. The test results showed that surface roughness and soil density highly determines the response of pile embedded in sand. The tests show that the shaft resistance of a non-displacement pile increases as the soil density and

the roughness of the pile surface increase. For the same vertical pile head settlement, the displacements and strains in the soil near the pile increase as the surface roughness of the piles increases. An increase in the pile roughness or in the soil density led to more extensive deformation at greater distances from the pile shaft.

ACKNOWLEDGEMENTS

This material is based upon work supported by the National Science Foundation under Grant No. 0969949. The authors are very grateful for this support.

REFERENCES

- Arshad, M., Tehrani, F. S., Prezzi, M. & Salgado, R. (2014). Experimental study of cone penetration in silica sand using digital image correlation. *Geotechnique*, 64(7), pp.551–569.
- ASTM D2487-11 (2011). Standard practice for classification of soils for engineering purposes (Unified Soil Classification System). In *Annual Book of ASTM Standards*. West Conshohocken, PA.
- Correlated Solutions, 2009. Vic-2D.
- Desrues, J. & Viggiani, G. (2004). Strain localization in sand: an overview of the experimental results obtained in Grenoble using stereophotogrammetry. *International Journal for Numerical and Analytical Methods in Geomechanics*, 28(4), pp.279–321.
- Fioravante, V. (2002). On the shaft friction modelling of non-displacement piles in sand. *Soils and foundations*, 42(2), pp.23–33.
- Loukidis, D. & Salgado, R. (2008). Analysis of the shaft resistance of non-displacement piles in sand. *Geotechnique*, 58(4), pp.283–296.
- Salgado, R. (2013). The mechanics of cone penetration: Contributions from experimental and theoretical studies. In *Proceedings of Geotechnical and Geophysical Site Characterization 4, ISC4*. CRC Press (Keynote paper), pp. 131–153.
- Tehrani, F. S., Han, F., Salgado, R., Prezzi, M., Tovar, R. D., & Castro, A. G. (2016). Effect of surface roughness on the shaft resistance of non-displacement piles embedded in sand. *Geotechnique*, 66(5), pp.386–400.
- Uesugi, M. & Kishida, H. (1987). Tests of the interface between sand and steel in the simple shear apparatus. *Géotechnique*, 37(1), pp.45–52.
- Uesugi, M., Kishida, H. & Tsubakihara, Y. (1988). Behavior of sand particles in sand-steel friction. *Soils and foundations*, 28(1), pp.107–118.

The Sensitivity of Settlement Predictions for an Axially Loaded Drilled Shaft to ϵ_{50}

Kevin Stanton¹; Maryam Ostovar²; and Ramin Motamed, Ph.D., P.E., M.ASCE³

¹Ph.D. Candidate, Univ. of Nevada, Reno, Dept. of Civil and Environmental Engineering, 1664 N. Virginia St., Reno, ND 89557. E-mail: kevinstanton@nevada.unr.edu

²Masters Student, Univ. of Nevada, Reno, Dept. of Civil and Environmental Engineering, 1664 N. Virginia St., Reno, ND 89557. E-mail: mostovar@nevada.unr.edu

³Assistant Professor, Univ. of Nevada, Reno, Dept. of Civil and Environmental Engineering, 1664 N. Virginia St., Reno, ND 89557. E-mail: motamed@unr.edu

Abstract

A blind prediction of the load-settlement response of an axially loaded drilled shaft in Santa Catarina, Brazil, was carried out in June of 2015. The original results were developed using “best-estimate” soil properties within a t - z analysis framework developed by Norris (1986) and modified by Ashour et al. (1998). However, this approach relies heavily on the estimation of the axial strain at 50% of maximum deviatoric stress, termed ϵ_{50} . Thus, a thorough literature review was carried out on published ϵ_{50} values and empirical relationships. The original estimates of ϵ_{50} were also varied in this study to explore how sensitive the prediction results are in this regard. It was found the average root mean squared error between the predicted and measured results were significantly affected by changes in ϵ_{50} and that the t - z style predictions were substantially influenced by the estimates of ϵ_{50} , highlighting the need for proper and careful estimation of this important parameter.

INTRODUCTION

The computer program CGI-DFSAP (Computers and GeoEngineering Inc. 2011) was employed to carry out a class A prediction of a full scale load test on a bored pile (drilled shaft) conducted for the International Pile Prediction Event, supported by ISSMGE. This software estimates axial load-settlement behavior with a unique type of t - z analysis which is outlined in Ashour and Helal (2012) and Ashour et al. (2010). The procedure involves the implementation of a semi-empirical model for the stress-strain behavior of soils to derive load transfer curves for both side-shear and end-bearing in cohesive, cohesionless, rock and c - ϕ materials. This approach was selected because it has shown promise in recent studies (Motamed et al. 2015; Stanton et al. 2015).

MODELING IN CGI-DFSAP

The required input parameters for CGI-DFSAP vary depending on the material type in question. At a minimum, however, values for the effective unit weight (γ') and the strain at 50% of the peak deviatoric stress (ϵ_{50}) must be given. While ϵ_{50} can be determined internally by the program, the approximation is crude and therefore to minimize prediction errors, this parameter was estimated using correlations with the coefficient of uniformity and void ratio for sand (Norris 1977) and with undrained shear strength for clay (Evans and Duncan 1982). Additional

properties which required estimation for this prediction exercise included the undrained shear strength of clay and the effective friction angle of sand.

The test shaft (ET5) was modeled as a circular reinforced concrete section with a diameter of 1 m and an embedded length of 24.4 m. Based on the as built information, the reinforcing steel to concrete ratio (A_s/A_c) was computed to be 1.44% and the thickness of concrete cover was 0.18 m. Also, the shaft was modeled assuming a free head fixity condition.

INTERPRETATION OF IN-SITU SOIL DATA

Three different sources of in-situ soil data in the vicinity of the test shaft were provided as a part of the blind prediction exercise including Cone Penetration Test (CPT), shear wave velocity (V_s) and Standard Penetration Test (SPT). A spreadsheet was developed to consider as much of the available soil data simultaneously for the important step of defining the material properties entering the CGI-DFSAP model. With this tool, a multitude of empirical and theoretically based relationships were employed to estimate the required input.

Comparison of the implied soil index and strength parameters from each of the three data types reveals that the correlations from the V_s and CPT data are generally in close agreement. While the SPT data correlations matched well for friction angle, they were significantly low at depths between 10 and 20 m for cohesion and unit weight. These comparisons are shown in Figure 1. The development of the charts shown in Figure 1 is discussed in the following sub-sections.

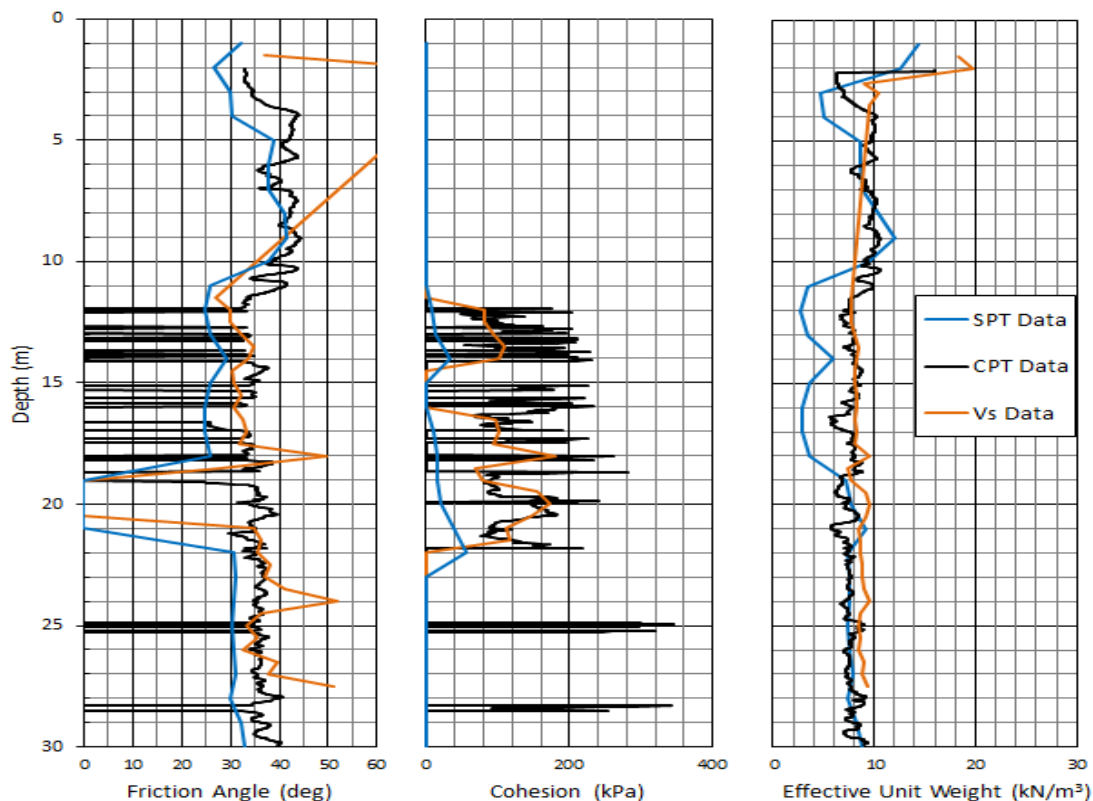


Figure 1. Comparison of soil properties estimated using CPT, SPT and V_s data

CPT Data. The CPT data from CPT-03 was first re-analyzed according the updated Robertson (2009) methodology to identify the implied soil behavior types (SBT). This procedure involves normalizing measured resistance values to correct for the effects of overburden pressure and generally provides more precise and accurate estimate of SBT than provided by the Robertson (1986) approach. A comparison of the SBT's suggested by Robertson (1986) and Robertson (2009) is shown for this site in Figure 2. It should be noted that the use of the normalized SBT led to more layers being assumed to exhibit cohesive behavior.

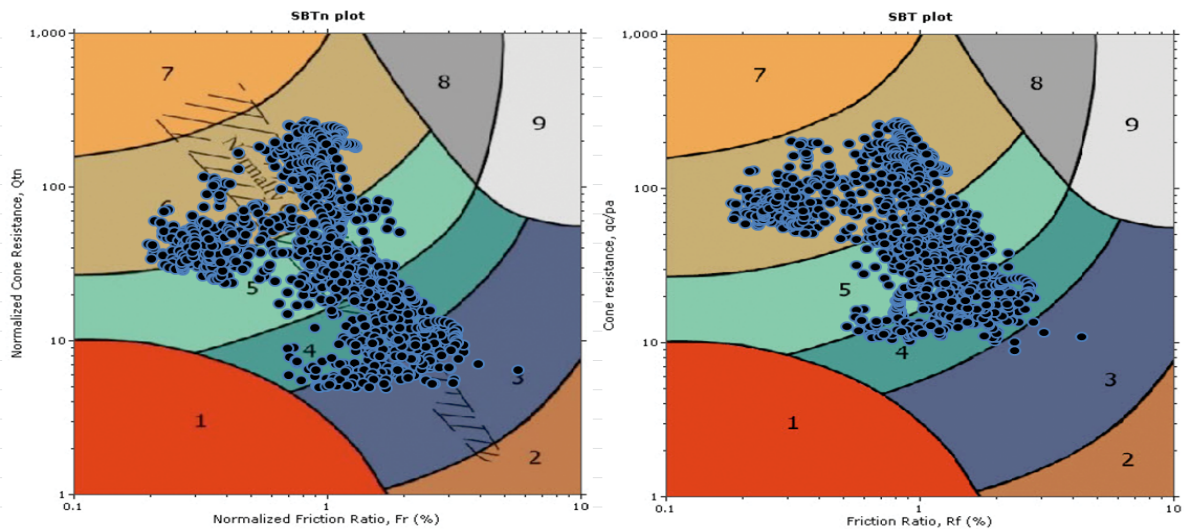


Figure 2. Comparison of soil behavior types suggested by Robertson (1986) (right) and Robertson (2009) (left) for CPT-03

Empirical correlations were employed to estimate the soil unit weight (Robertson and Cabal, 2010), undrained shear strength (Robertson, 2012), internal friction angle (Mayne, 2007), overconsolidation ratio (Robertson, 2009), and relative density (Robertson and Cabal, 2010). The determination of soil unit weight and therefore the normalized cone resistance required an iterative process which was conducted in the aforementioned spreadsheet. Also, the coefficient of uniformity of sand layers was approximated based on the visual manual classifications given in the boring logs and by inspecting the available sample images for SPT-03.

Shear Wave Velocity. The V_s data from SDMT-03 was used to estimate the previously discussed required parameters. An iterative procedure was employed to estimate unit weights and overburden pressure so that values could be converted to normalized shear wave velocity as in Mayne (2007). This allowed for the estimation of friction angle (Hatanaka and Uchida, 1996) and undrained shear strength (Dickenson, 1994). It should be noted that the determination of friction angle required that the V_s data first be converted to SPT blow counts corrected for hammer efficiency (N_{60}) using relationships given in Bellana (2009).

The SPT and CPT data was also correlated to V_s and normalized V_s (V_{s1}) to gain insight concerning which data sets were the most reliable. This was accomplished using the recommendations from Wair et al. (2012) for SPT and from Robertson (2012) for CPT. Overall, the correlations from CPT matched the measured V_s data more closely at shallow to medium depths and those from SPT matched more closely for deeper layers.

Standard Penetration Data. The SPT data was correlated to unit weight using recommendation from Bowles (1988). This enabled the estimation of friction angle (Hatanaka and Uchida, 1996) and undrained shear strength (Kulhawy and Mayne, 1990). Similar to before, the V_s and CPT data were converted to SPT blow counts corrected for hammer energy and overburden stress ($N_{1,60}$). This was achieved using guidelines given in Bellana (2009) for V_s and Lunne et al. (1997) for CPT. While the values estimated from CPT matched very closely with the measured data at all depths, the approximation of SPT from V_s was excessively high at depths less than 10 m and between 20 and 25 m. This was taken into consideration when developing the finalized soil profile.

Finalized Soil Profile. The assumed soil profile modeled in CGI-DFSAP for the blind prediction is shown in Table 1. Considering the points from the previous discussion of the material properties indicated by the CPT, SPT and V_s data, the CPT data was most heavily relied on for layer discretization, friction angles and undrained shear strength. The soil unit weights were based equally on the V_s and CPT data except for depths between 3.5 and 11.5 m for which no V_s measurements were recorded.

Table 1. Assumed soil layering and properties for blind prediction.

Base Depth (m)	Mean Normalized SBT	Assumed Soil Type	γ' (kN/m ³)	ϕ' (deg)	Su (kPa)	ε_{50} (%)
2.15	5	Silty Sand	16.02	32.9	0	1
3.8	5.14	Silty Sand	7.17	35.2	0	0.8
5.9	6	Silty Sand	9.77	42.4	0	0.55
7.05	5.68	Silty Sand	8.61	38.2	0	0.75
9.6	6	Silty Sand	9.95	42.5	0	0.6
11.55	5.64	Silty Sand	9.26	39	0	0.75
14.1	4.19	Clayey Silt	7.62	33.1	145	0.5
16	4.77	Clayey Silt	8.12	34.8	0	0.6
16.9	3.71	Silty Clay	6.53	26.2	117.8	0.6
18.69	4.88	Clayey Silt	7.99	34.2	189.7	0.5
19.85	3.17	Silty Clay	6.8	34	106	0.55
20.5	4.09	Clay	7.63	0	170	0.5
21.7	3.17	Clay	6.89	0	110.5	0.8
30	5.64	Silty Sand	7.44	35.9	170.5	0.7

Blind Prediction Results. The results of blind prediction are summarized in Figure 3 and Table 2 below. Note that w is the shaft head settlement, Q is the total axial load, z is the depth below the ground surface and N is the amount of load carried between a given depth and the base of the shaft (24.4 m depth). Also, Q_s and Q_b are the components of axial load carried in side-shear and end-bearing respectively.

SENSITIVITY ANALYSIS

In order to evaluate the sensitivity of the shaft response to ε_{50} , a thorough literature review was carried out to collect the recommended ε_{50} values in published literature for different soil types. The reviewed papers included: Kondner et al. (1963), Sullivan et al. (1979), Reese and Sullivan

(1980), Evans et al. (July 1982), Dunnivant et al.(1989), Jeong et al. (2007); Kim et al. (2009), Javadi et al. (2009), Zhang et al. (2013), McClellan (2013), Ebrahimian et al. (2015). According to the reviewed literature, a range for the ε_{50} was determined considering the soil type, depth, undrained shear strength, friction angle, and unit weight for each layer. Table 2 presents the summary of different ranges of ε_{50} based on Table 1's assumed soil profile. A summary of the predicted range for ε_{50} is presented in Table 3 which illustrates the range for the ε_{50} for each soil layer. As it can be seen in this table, the selected ε_{50} values for the blind prediction exercise are comparable to the range selected for the sensitivity study. Overall, the range of ε_{50} increases when soil type changes from clayey silt to silty sand and clay, respectively. Furthermore, the range of ε_{50} generally increases when unit weight, undrained shear strength and friction angle also increase.

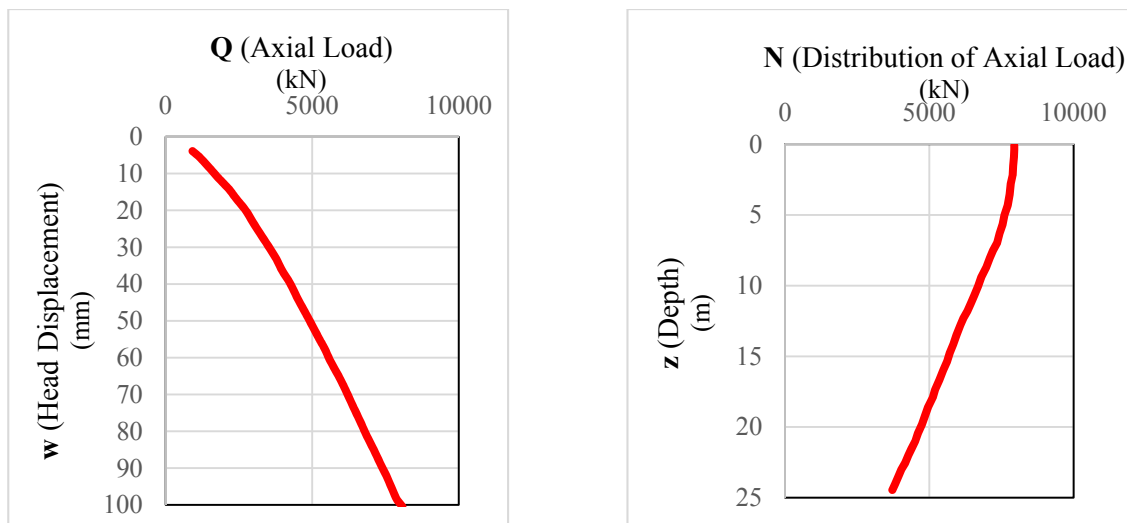


Figure 3. Predicted axial shaft head load-settlement response (left) and load distribution for a settlement equal to 10% of the shaft diameter (right)

Table 2. Predicted loads at failure ($w/D=10\%$).

Component	Load (kN)
Q (total)	7921
Q_s (side-shear)	437
Q_b (end-bearing)	3546

The sensitivity study results are summarized in Figure 4 and Figure 5. These include the axial load versus head displacement and load distributions for the lower limit of ε_{50} , the upper limit of ε_{50} , the original estimate of ε_{50} (blind prediction), and the measured field load test during the Araquari field test.

As can be seen in Figure 4, all of the measured and predicted results show an increase in load with rising the head displacement. However, the measured values are slightly underpredicted. In addition, application of the upper limit of ε_{50} produces a slight increase compared to the blind prediction while application of the lower limit of ε_{50} has the opposite effect.

For the distribution of axial load versus depth, the measured results fall between the predictions from the upper and lower limits of ε_{50} at shallow depths. However, the behaviour of the blind prediction is smaller than the measured results before 9.6 meters depth and it shows greater values at the upper depth (Figure 4). Figure 4 illustrates the distribution of axial loads as an output.

Table 3. Assumed soil layering and properties for sensitivity analysis.

Layer No.	Base Depth (m)	Assumed Soil Type	ε_{50} (%) for blind prediction	Range of ε_{50} in sensitivity analysis (%)
1	2.15	Silty Sand	1	0.3-4.7
2	3.8	Silty Sand	0.8	0.1-3.5
3	5.9	Silty Sand	0.6	0.15-3.5
4	7.05	Silty Sand	0.8	0.1-3.5
5	9.6	Silty Sand	0.6	0.15-3.5
6	11.55	Silty Sand	0.8	0.15-3.5
7	14.1	Clayey	0.5	0.4-1.5
8	16	Clayey	0.6	0.5-3.5
9	16.9	Silty Clay	0.6	0.3-1.5
10	18.69	Clayey	0.5	0.5-3.5
11	19.85	Silty Clay	0.6	0.3-1.5
12	20.5	Clay	0.5	0.5-7
13	21.7	Clay	0.8	0.5-1.5
14	30	Silty Sand	0.7	0.5-1.5

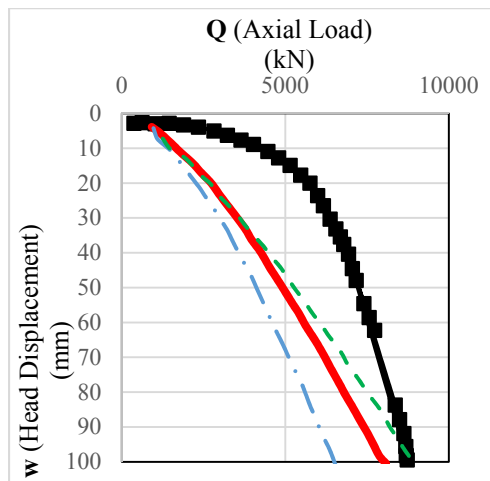


Figure 4. Comparison chart for predicted axial shaft head load-settlement response

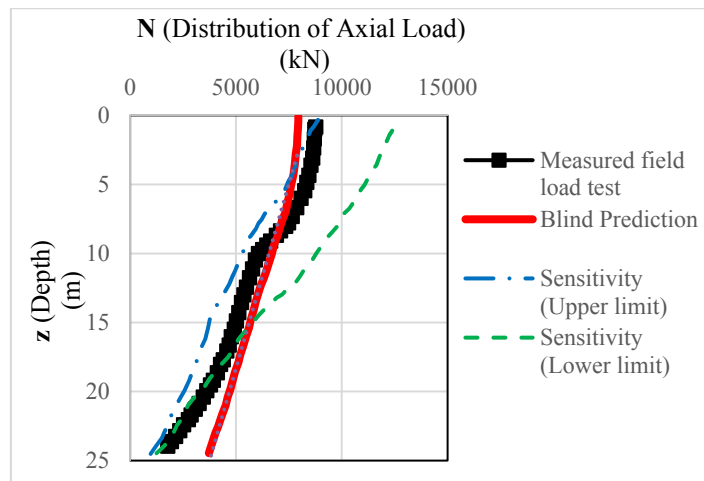


Figure 5. Comparison chart for predicted load distribution for a settlement equal to 10% of the shaft diameter

To gain further insight from the sensitivity analyses, Figure 6 and Figure 7 illustrate the root mean square error (RMSE) between the predicted and measured results. To calculate RMSE, the square root of the sum of the squared residual errors between the predicted and measured results were taken.

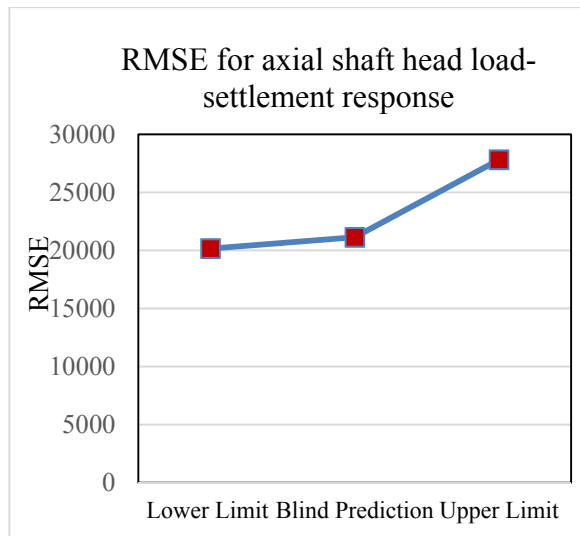


Figure 6. Average root mean square error (RMSE) between the predicted and measured results for axial shaft head load-settlement response

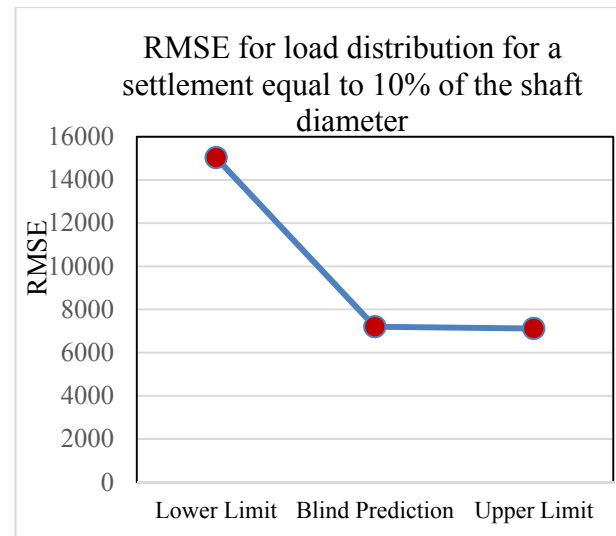


Figure 7. Average root mean square error (RMSE) between the predicted and measured results for a settlement equal to 10% of the shaft diameter

According to Figure 6, the overall error increases as ϵ_{50} increases for axial shaft head load-settlement response. Alternatively, for the load distribution, the lower limit of ϵ_{50} produces a much greater error than the blind prediction and the upper limit of ϵ_{50} (Figure 7). While this may seem counterintuitive, it may actually be reasonable for the two visualizations of the results to react in such seemingly different ways to ϵ_{50} . The nature of the load-transfer method is such that the resistance offered by one layer will affect the mobilized resistance in adjacent layers. Thus, the relationship between ϵ_{50} and the computed axial load distribution may be somewhat complex and should not necessarily follow the same pattern with regard to error as the load-settlement response.

CONCLUSION

A t - z style analysis was employed to obtain the load-settlement response and axial load distribution of a drilled shaft which is shown in Figures 4 and 5. It is observed that prediction quality of the response of the drilled shaft is significantly dependent on the assumed material parameters for the soil layers, especially within the range of estimated values for ϵ_{50} . The sensitivity study further exhibited the need for careful selection of the parameter ϵ_{50} when predicting the axial response of drilled shafts. This highlights the need for proper sampling and testing of the soils, including carrying out laboratory tests such as triaxial compression on collected samples.

REFERENCES

- Ashour, M., & Helal, A. (2012). Response of Axially Loaded Piles in Sands with and without Seismically Induced Porewater Pressures. *Int. J. of Geomechanics*, doi:10.1061/GM.1943-5622.0000273.
- Ashour, M., Norris, G. M., Elfass, S., & Al-Hamdan, A. Z. (2010). Mobilized side and tip resistances of piles in clay. *Computers and Geotechnics*, 37(7), 858-866.
- Ashour, M., Norris, G., & Pilling, P. (1998). Lateral Loading of a Pile in Layered Soil Using the Strain Wedge Model. *J. of Geotechnical and Geoenvironmental Eng.*, ASCE, 124(4), pp. 303-315.
- Bellana, N. (2009). Shear Wave Velocity as Function of SPT Penetration Resistance and Vertical Effective Stress at California Bridge Sites. *M.S. Thesis*, University of California, Los Angeles.
- Bowles, J. E. (1988). *Foundation analysis and design*. McGraw-Hill Book Company Limited, England, ISBN: 0-07-006776-7.
- Computers & GeoEngineering, Inc. (2011). CGI-DFSAP. Ret. April 7, 2015, from <http://cgi-dfsap.com/>.
- Cone Penetration Test Software. (2008, January 1). Retrieved April 12, 2015, from <http://www.novotechsoftware.com/geotechnical-software/cone-penetration-test-software/>
- Dickenson, SE (1994). *Dynamic Response of Soft and Deep Cohesive Soils during the Loma Prieta Earthquake of October 17, 1989*. PhD thesis, Dept. of Civil and Enviro. Eng., University of California, Berkeley, CA.
- Dunnavant, T.W., O'Neill, M.W. (1989). Experimental p-y Model for Submerged, Stiff Clay. *J of Geotechnical Eng.*, ELSEVIER, 115(1), pp. 95-114.
- Ebrahimian, B., Nazari, A., Yousefnia Pasha, A. (2011). Influence on Lateral Rigidity of Offshore Piles Using Proposed p-y curves. *J of Ocean Eng.*, ELSEVIER, 38, pp. 397-408.
- Evans, L.T., & Duncan, G.M. (1982). Simplified analysis of laterally loaded piles. University of California Berkeley, Rept. No. UCB/GT/82-04.
- Hatanaka, M., & Uchida, A. (1996). A simple method for the determination of Ko-value in sandy soils. *Soils and foundations*, 36(2), 93-99.
- Javadi, A.A., Rezaia, M. (2009). Intelligent Finite Element Method: an Evolutionary Approach to Constitutive Modeling. *J of Advanced Engineering Informatics*, ELSEVIER, 23, pp. 442-451.
- Jeong, S., Kim, Y., Kim, J. (2015). Evaluating ε_{50} for Lateral Load-Displacement Behavior of Piles in Clay. *J of Ocean Eng.*, ELSEVIER, 96, pp. 149-160.
- Kondner, R.L., Zelasko, J.S. (1963). A Hyperbolic Stress-Strain Formulation in Sands. *Proceeding of the Second Panamerican Conference on Soil Mechanics and Foundation Eng.*, 1, pp. 289-324.
- Kulhawy, F. H., and Mayne, P. W. (1990). "Manual on estimating soil properties for foundation design." Electric Power Research Institute, Palo Alto, Calif.
- Lunne, T., Robertson, P.K., and Powell, J.J.M. (1997). CPT in geotechnical practice. Chapman and Hall, New York, USA.
- Mayne, P.W., 2007. In-situ test calibrations for evaluating soil parameters. *Characterization & Engineering Properties of Natural Soils*, Vol. 3, Taylor & Francis Group, London: 1602-1652.

- Motamed, R., Stanton, K., Nasimifar, M., Pearson, N., and Kluzniak, B. (2015) A Methodology for Axially Loaded Drilled Shaft Performance Predictions Using DFSAP. IFCEE 2015: pp. 1791-1805. doi: 10.1061/9780784479087.163
- McClellan, Z.R. (2013). Comparison of Soil Shear Strength Parameters and p-y Curves for Laterally Loaded Piles in Granular Soil. *University of Utah*, Master Thesis UMI No. 1544611.
- Norris, G.M. (1977). The Drained Shear Strength of Uniform Quartz Sand as Related to Particle Size and Natural Variation in Shape and surface Roughness. *PhD thesis*, University of California, Berkeley.
- Norris, G. M. (1986). Theoretically Based BEF Laterally Loaded Pile Analysis. *Third Int. Conf. on Numerical Methods in Offshore Piling*, Nantes, France, pp. 361-386.
- Robertson, P. K., & Cabal, K. L. (2010, May). Estimating soil unit weight from CPT. In *2nd International Symposium on Cone Penetration Testing* (pp. 2-40).
- Robertson, P.K., Campanella, R.G., Gillespie, D., and Greig, J., (1986). Use of Piezometer Cone data. *In-Situ'86 Use of In-situ testing in Geotechnical Engineering*, GSP 6 , ASCE, Reston, VA, Specialty Publication, pp 1263-1280.
- Robertson, P. K. (2009). Interpretation of cone penetration tests-a unified approach. *Canadian Geotechnical Journal*, 46(11), 1337-1355.
- Robertson P.K. (2012). Interpretation of in-situ tests—some insights. *Proceedings, 4th International Conference on Geotechnical and Geophysical Site Characterization (ISC-4)*, R.Q. Coutinho and P.W. Mayne, eds., Pernambuco, Brazil, pp. 22.
- Stanton, K., Motamed, R., Elfass, S., & Ellison, K. (2015) An Evaluation of T-Z Analysis Methods. *Proceedings, The 40th Annual Conference on Deep Foundations*, Oakland, CA, page 27-36.
- Sullivan, W.R. (1979). Unified Method for Analysis of Laterally Loaded Piles in Clay. *J of Numerical Methods in Offshore Piling*, pp. 135-146.
- Wair, B. R., DeJong, J. T., & Shantz, T. (2012). Guidelines for Estimation of Shear Wave Velocity Profiles. *PEER Report 2012/08*.
- Zhang, L., Ahmari, S. (2013). Nonlinear Analysis of Laterally Loaded Rigid Piles in Cohesive Soil. *International Journal for Numerical and Analytical Methods in Geomechanics*, 37, pp. 201-220.

Multi-Level O-Cell Tests on Instrumented Bored Piles in the Mekong Delta

H. M. Nguyen¹; A. J. Puppala²; U. D. Patil³; L. Mosadegh⁴; and A. Banerjee⁵

¹Ph.D. Student, Dept. of Civil Eng., Univ. of Texas at Arlington, TX 76019. E-mail: haitdmu@gmail.com

²Professor, Dept. of Civil Eng., Univ. of Texas at Arlington, TX 76019. E-mail: anand@uta.edu

³Faculty Research Associate, Dept. of Civil Eng., Univ. of Texas at Arlington, TX 76019. E-mail: ujwalkumar.patil@uta.edu

⁴Ph.D. Student, Dept. of Civil Eng., Univ. of Texas at Arlington, TX 76019. E-mail: leila.mosadegh@mavs.uta.edu

⁵Ph.D. Student, Dept. of Civil Eng., Univ. of Texas at Arlington, TX 76019. E-mail: aritra.banerjee@mavs.uta.edu

Abstract

Multi-level O-cell tests were carried out on two strain-gauge instrumented bored piles at the Can Tho Bridge crossing the Hau (Bassac) River in the Vietnamese Mekong Delta. The soil profile consists of about 70 m thick soft, deltaic silty clay deposited on dense to compact sand. The test piles, 2.0 and 2.5 m in diameter, were installed into 87 and 98 m depth, respectively, by a combination of casing the upper length and using bentonite slurry to stabilize below the casing. The lower and upper O-cell assemblies in the two test piles were located 2.5 m through 3.0 m and 12 m through 15 m above the respective pile toe level, respectively. The tests were performed in four Stages and the maximum loads applied by the lower and upper O-cells were about 21 and 26 MN, respectively. The measurements indicated that the pile toe stiffness of Pile TP1 was very low. The fit of the q-z Ratio Function shows ratio exponents of 0.2 and 0.1 for Pile TP1 and TP2, respectively. The stress-movement curves at the strain gage level GL1 show no tendency toward an ultimate resistance. The evaluation of the strain-gauge data showed that the pile axial stiffness was a function of the induced strain, ranging from a stiffness of 103 through 85 GN. The average unit resistance of both pile shafts placed in dense sand layer is about 460 kPa.

INTRODUCTION

The Can Tho Bridge completed in 2008 is a cable-stayed bridge over the Hau (Bassac) River connecting the Vinh Long Province and Can Tho City in the Vietnamese Mekong Delta. It has a 6-lane carriageway measuring 23 m in width, with 4 lanes for traffic and two lanes for bicycles and motorbikes. The total length of bridge is about 2,750 m, with a 550 m long main span and the height above the river water level is 39 m. The main bridge is a seven spans stayed bridge placed on eight marine piers. The spans are 550 m for central span (repetition), 150m for next back span and 40m for each back span. The north and south Main Bridge pylon is founded on a group of 30 and 36 bored piles each of 2.5m diameter with 92 and 94 m embedment depth, respectively. The south approach structures are placed on 1.2 m through 1.5 m diameter bored piles to 60 m through 87 m embedment. The north approach structures are supported by groups of twelve 1.2 m diameter bored piles with 75 m embedment depth for the first three piers and thirty-six 0.45 m square driven precast concrete piles for the twelve remaining piers with embedment depths ranging from 33 through 39 m.

To verify that the design of the pile support is satisfactory, static loading tests were performed on two piles with 2.5 and 2.0 m diameter. The 2.5 and 2.0 m diameter test piles were constructed at the north bank and the south bank of the Hau River. The test piles were installed into 98 and 87 m depth, respectively. Both piles were strain-gage instrumented. The static loading test was performed by means of the multi-level bi-directional O-cell test (Osterberg 1989; 1998). The results of the test are presented and correlated to the site conditions.

SOIL PROFILE

The soil profile at the locations of the test piles consists of surficial layers of soft clay and silt to 11 m and 15 m depths, respectively, underlain by compact silty sand to about 55 m depth followed by dense to very dense silty sand (Figure 1). At Pile TP1, two clay zones were encountered from 93 to 99 m depth and 107 to 117 m depth in the borehole. At Pile TP2, a sand zone was encountered between 11 to 16 m depth in the borehole. Table 1 summarizes the soil parameters for the soil layers. The pore pressure distribution is hydrostatic and corresponds to a groundwater table at about 1 m depth below ground surface. Figure 1 shows the distribution of SPT N-indices close to the location of the test piles.

TABLE 1 Soil Parameters.

Items		Layer 1	Layer 2	Layer 3	Layer 4	Layer 5
Water content (W_n)	%	40	26	38	29	24
Saturated density (ρ_{sat})	kg/m ³	1,780	1,920	1,810	1,920	1,960
Void Ratio (e_0)	-	1.150	0.759	1.054	0.815	0.682
Liquid Limit (LL)	%	42	-	44	41	-
Plastic Limit (PL)	%	23	-	22	20	-
Clay Fraction	%	32	8	41	39	4
Silt Fraction	%	50	16	42	31	6
Sand Fraction	%	18	76	17	30	90
Friction Angle (ϕ)	(⁰)	6	17	8	16	23
Cohesion (c')	kPa	11	-	15	28	-
SPT Index range	bl/0.3m	2-7	16-23	2-29	23-48	> 60

PILE INSTALLATION

The two test piles, TP1 and TP2, in 2.5 m and 2.0 m diameter were constructed using reverse circulation technique with casing advanced ahead of the hole to 98 m and 87 m depth below the ground surface on July 05, 2005 and April, 17 2006, respectively. The drilling of Pile TP1 was done under polymer slurry into about 58 m depth and was later replaced by bentonite slurry upon drilling completion at 98 m depth; while for the Pile TP1, the bentonite slurry used for whole drilling depth.

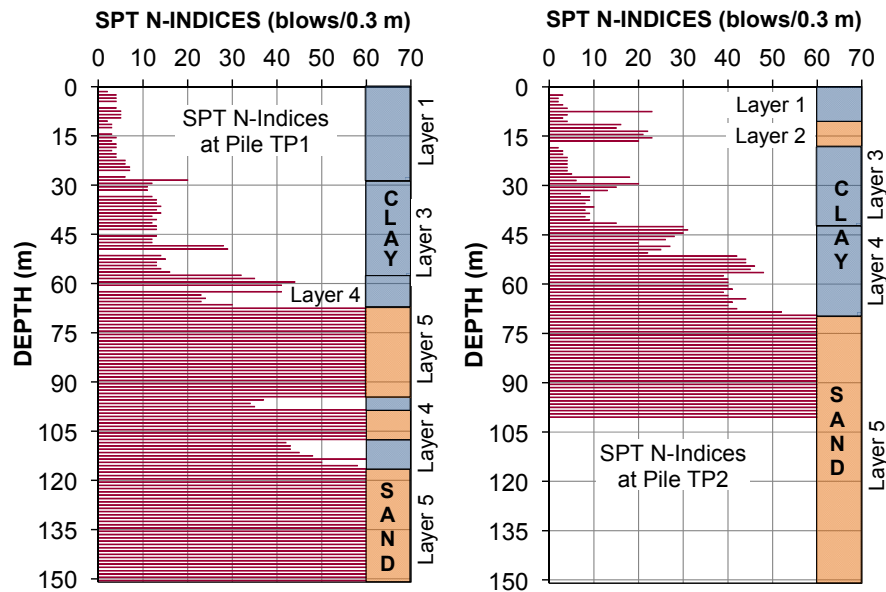


Figure 1. SPT N-Indices close to Pile TP1 and TP2

The pile TP1 was supplied with a reinforcing cage of fifty-two 35 mm bars to 18 m depth and twenty-six 35 mm bars below this depth to 98 m depth, resulting in a steel reinforcement area of 500 cm² and 250 cm² and a reinforcement ratio of 1.0 % and 0.5 % of the 4.9 m² total nominal pile cross section, respectively. The pile TP2 was supplied with a reinforcing cage of forty-four 32 mm bars, resulting in a steel reinforcement area of 350 cm² and a reinforcement ratio of 0.8 % of the 3.14 m² total nominal pile cross section. The concrete cylinder strength used in Piles TP1 and TP2 was about 34.2 MPa and 33.1 MPa after casting 16 days and 7 days, respectively.

The test piles were constructed by first inserting 2,644 mm and 2,040 mm outer diameter temporary casings, respectively, to 13 m depth. Thereafter, the shafts of pile TP1 and TP2 were drilled to 98 m and 87 m depth, respectively, using reverse circulation drilling. Before placing concrete, the shafts were cleaned and a reinforcing cage attached with the Cell assembly at 2.5 m through 12.0 m and 2.0 m through 14.0 m above the cage end were lowered into the shaft, respectively. The cell levels of Pile TP1 had three 660 mm diameter cells at each level and the cell levels of Pile TP2 had two 540 mm cells at the lower level and three 330 mm cells at the upper level.

Each test pile was instrumented with two pairs of diametrically opposed vibrating wire strain-gages at one level below the lower cells, two levels between two cell levels, and four levels above the upper cells, as shown in Figure 2. The static loading test on Pile TP1 was performed on July 20, 2005, 15 days after concreting and Pile TP2 was tested on May 03, 2006, 16 days after placing concrete. The complete test reports are available in Loadtest (2005 and 2006).

LOADING PROCEDURE

The test program on Pile TP1 and TP2 was carried out in five and four Stages, respectively. In the Stage 1, the lower cells of both piles were pressurized to assess the toe resistances and the shaft resistances below the lower cells. The loading of Pile TP1 was carried out in a cycle of ten load increments to 18.5 MN and thereafter the lower cells were unloaded in four decrements. For

the Pile TP2, the loading was performed in two cycles of ten and twelve increments to 11.6 MN and 19.2 MN, respectively. Then, the test pile was unloaded in three and five decrements, respectively.

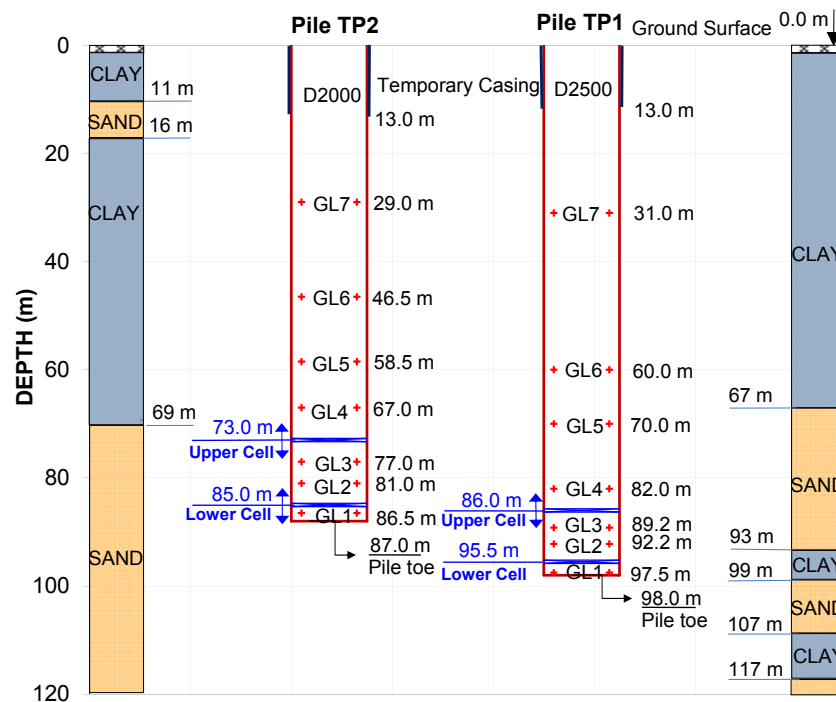


Figure 2. Details of installed instrumentation

In the Stage 2, the upper cells of both piles were pressurized to assess the shaft resistances between the two cell levels and above the upper cells. The lower cells were left free to drain during loading of the upper cells until the shaft resistances between the two cell levels were fully mobilized. Then, the lower cells were closed off and the loading was continued to evaluate the shaft resistances above the upper cells. The upper cells of Pile TP1 and TP2 were pressurized in five and three loading increments to load of 4.55 MN and 8.74 MN, respectively. At these load levels, increase in strain was observed at Strain Gauge Level 1, indicating mechanical load transfer was occurring through the lower assembly to the lower pile section below the lower cell. Therefore, the lower cells were closed off and thereafter the upper cells were pressurized in eleven and ten additional loading increments to load of 25.99 MN and 25.30 MN, respectively. The upper cells of Pile TP1 were locked off to hold the maximum loading level of 25.30 MN to carry out the test Stage 3; while, the upper cells of Pile TP2 were depressurized to zero load level in five decrements before beginning the test Stage 3.

In the Stage 3, prior to unloading, the upper cells of pile TP1 were locked while lower cells were re-pressurized to assess the lower side shear and end bearing characteristics on loads in excess of those applied in Stage 1. The lower cells were pressurized to load of 19.94 MN. Then, both the upper and lower cells were depressurized in one decrement. The lower cells of pile TP2 were pressurized in eight loading increments to load of 4.30 MN and unloaded in five decrements. This Stage was done to compare the capacity of the middle pile section against those obtained from Stages 1 and 2. The Stage 3 was conducted whilst the upper O-cell assembly was left free to drain.

In the Stage 4, the confined compression tests of the pile segments between two cell levels were performed for both piles. For the Pile TP1 after loading the Stage 3, both the cell assemblies were pressurized simultaneously to conduct a confined compression test on the middle pile section. The cells were pressurized in seven loading increments to load of 16.54 MN and then the cells were depressurized in one decrement. For the Pile TP2 after loading the Stage 3, both the lower and upper cells were pressurized simultaneously to conduct a confined compression test on the middle pile section. The cells were pressurized in eight equal loading increments to load of 11.63 MN and then the cells were depressurized in one decrement.

In the Stage 5, only the test on pile TP1 was performed. The lower cells were first repressurized to close up the upper cell expansion to allow reloading and the hydraulics was locked off before proceeding with the re-loading of the upper cell assembly. This Stage was conducted to assess the behavior of the upper side shear under applied loading in excess of those applied in Stage 2. The maximum load achieved in the upper cell assembly was about 25.79 MN and the simultaneous load recorded in the lower cells was 21.34 MN. Both the cell assemblies were depressurized in eleven decrements.

LOAD-MOVEMENT MEASUREMENTS

Figure 3 represents the load-movement curves of five loading Stages of Pile TP1. Figure 3a shows the load-movement curves measured from the loading of the Stage 1 and 3. The maximum downward and upward movement at the maximum loading of 18.48 MN in the test Stage 1 is about 67.93 mm and 4.14 mm, respectively; while, at the maximum loading of 19.94 MN in the test Stage 3, these movements are about 17.70 mm and 2.44 mm, respectively. Figure 3b displays the load-movement curves of the loading Stage 2. The maximum downward and upward movement at the maximum loading of 25.30 MN is about 107.99 mm and 7.19 mm, respectively. Figure 3c reports the load-movement curves of the loading Stage 3. At the maximum load of 16.54 MN, the maximum downward and upward movement is about 13.92 mm and 1.60 mm for lower cells, 2.41 mm and 1.25 mm for upper cells, respectively. Figure 3d plots the load-movement curves of the loading Stage 4. At the maximum load of 25.79 MN, the maximum downward and upward movement is about 114.42 mm and 4.45 mm, respectively.

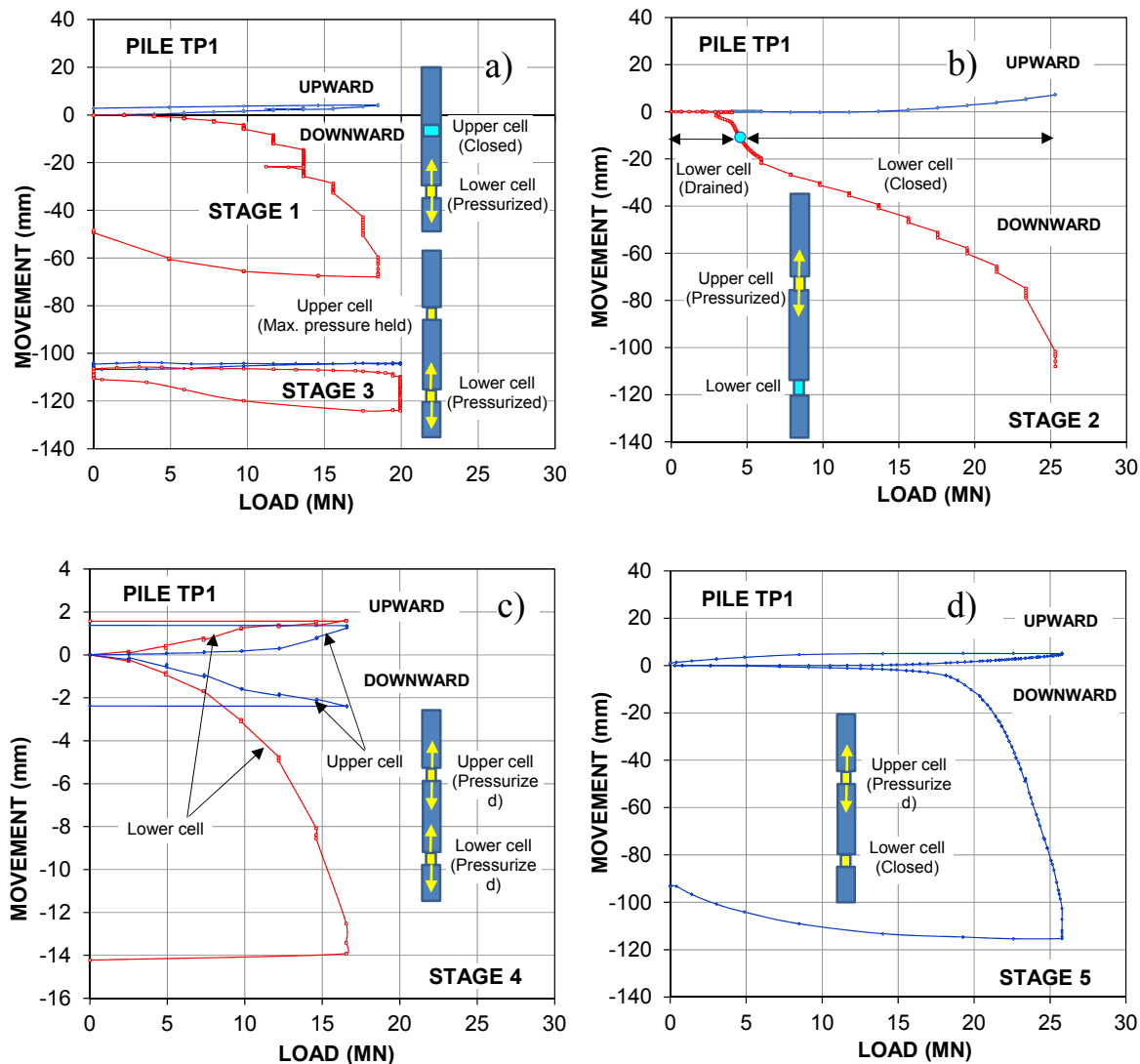


Figure 3. Load-movement curves of pile TP1 loaded from Stage 1 through 5

Figure 4 shows the load-movement curves of five loading Stages of Pile TP2. Figure 4a indicates the load-movement curves of the two loading cycles in the Stage 1. The maximum downward and upward movement at the maximum loading of 11.56 MN in cycle 1 is about 4.33 mm and 1.19 mm, respectively; while, at the maximum loading of 19.15 MN in cycle 2, these movements are about 72.16 mm and 3.82 mm, respectively. Figure 4b provides the load-movement curves of the loading Stage 2. The maximum downward and upward movement is about 82.10 mm and 31.56 mm at the maximum load of 25.99 MN, respectively. Figure 4c gives the load-movement curves of the loading Stage 3. The maximum downward and upward movement is about 0.36 mm and 27.28 mm at the maximum load of 4.30 MN, respectively. Figure 4d presents the load-movement curves of the loading Stage 4. The maximum downward and upward movement is about 11.58 mm and 30.44 mm for lower cells at the maximum load of 4.30 MN, 31.44 mm and 1.08 mm for upper cells at the maximum load of 13.92 MN, respectively.

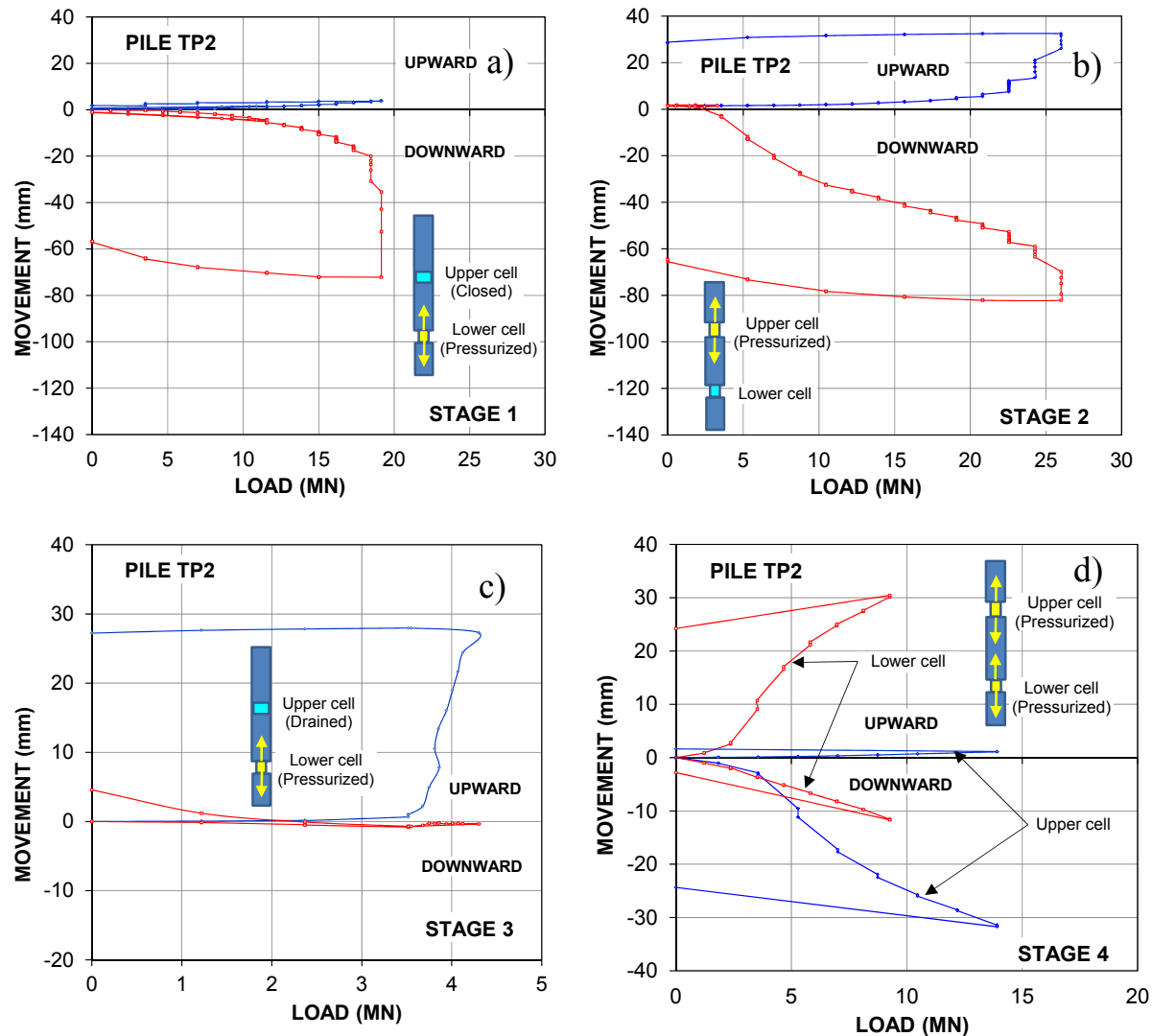


Figure 4. Load-movement curves of pile TP2 loaded from Stage 1 through 4

STRAIN GAGE MEASUREMENTS

To convert the measured strains into loads, the determination of pile material stiffness, AE , is important. From the load-strain relationship of the strain gages close to the cell assemblies, the stiffness of the test piles TP1 and TP2 estimated is about 103 GN and 85 GN, respectively. The evaluated pile Young's modulus, E , for the two piles correlated to 21 GPa and 27 GPa for the nominal pile cross section of piles.

Figure 5 contains the unit shaft resistance-movement curves of the Pile TP1 at the test Stage 1 and 2. The unit shaft resistances of the test Stage 3, 4 and 5 are not reported because the cycled loading has enormously influenced on the measured shaft resistances. In the test Stage 1, the pre-peak unit shaft resistance of lower cell-GL1 (left diagram) is about 440 kPa at movement of about 12 mm, which is greater than the pre-peak unit shaft resistance of lower cell-GL2 (right diagrams) about 3.5 times at movement of about 1 mm. It should be noted that the segment of pile from the gage level GL2 to pile toe was placed in clay layer and thus it is likely that the low

shaft resistance of the lower cell-GL2 was affected by the presence of left-behind slurry filter cake between the pile and the soil. The average unit shaft resistance of clay layer (GL1-GL2) is about 285 kPa. In the test Stage 2, the pre-peak unit shaft resistance of upper cell-GL3 (left diagram) is about 170 kPa at movement of about 5 mm, which is less than the upper cell-GL4 (right diagrams) about 2.0 times at same movement. It is noted that the pile length from GL2 to GL4 was placed in the same soil condition and this means that the shaft resistances at these depths have to be relatively equal. However, both test Stages showed that the unit shaft resistances between the two cell levels was about 170 kPa and it has become clearly that the value of this shaft resistance has not reflected the soil condition at the site. Therefore, the unit shaft resistance measured from the upper cell to GL4 (about 340 kPa) is relatively reasonable to consider for sand layer in this pile. The shaft resistances above GL4 to the pile head has been insignificantly mobilized for all test Stages.

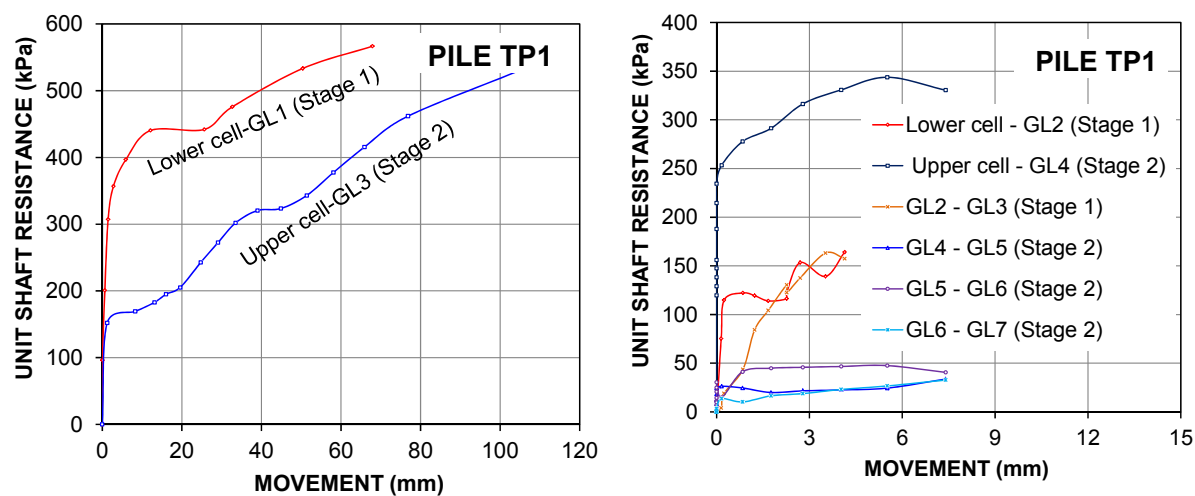


Figure 5. Unit shaft resistances versus movements of Pile TP1

Figure 6 provides the unit shaft resistance-movement curves of the Pile TP2 at the test Stage 1 and 2. The unit shaft resistances of the test Stage 3 and 4 are not displayed due to the dramatic influences of the cycled loading. The peak unit shaft resistance of lower cell-GL1 is about 583 kPa at movement of about 5 mm, which is greater than lower cell-GL2 in the right diagrams about 2.5 times at movement of about 3 mm in the test Stage 1 (The left diagram of Figure 6). As shown in Figure 2, the pile segment from pile toe to GL4 was installed in the same sand layer and therefore the low shaft resistance of the lower cell-GL2 in this pile was also affected by the presence of left-behind slurry filter cake as the Pile TP1. In the test Stage 2, the pre-peak unit shaft resistance of upper cell-GL4 (right diagram) is about 90 kPa at movement of about 1.2 mm, which is too small in comparison with the pile TP1 at this depth. It is no doubt that the shaft resistances in sand layer measured above GL2 have not reflected the actual condition of dense sand layer. For clay layer above GL4, the shaft resistances GL4-GL5, GL5-GL6 and GL6-GL7 are about 75, 50 and 25 kPa at movement of about 3 mm, respectively. The shaft resistances measured in this clay layer are useful for considering development of negative skin friction in the long-term condition.

Therefore, to consider the shaft resistance of sand layer for designing pile, it is reasonable to take average of the shaft resistances measured from the upper cells to GL4 in the Pile TP1 and from the lower cells to GL1 in the Pile TP2. In this case, the average unit shaft resistance of sand layer is about 460 kPa.

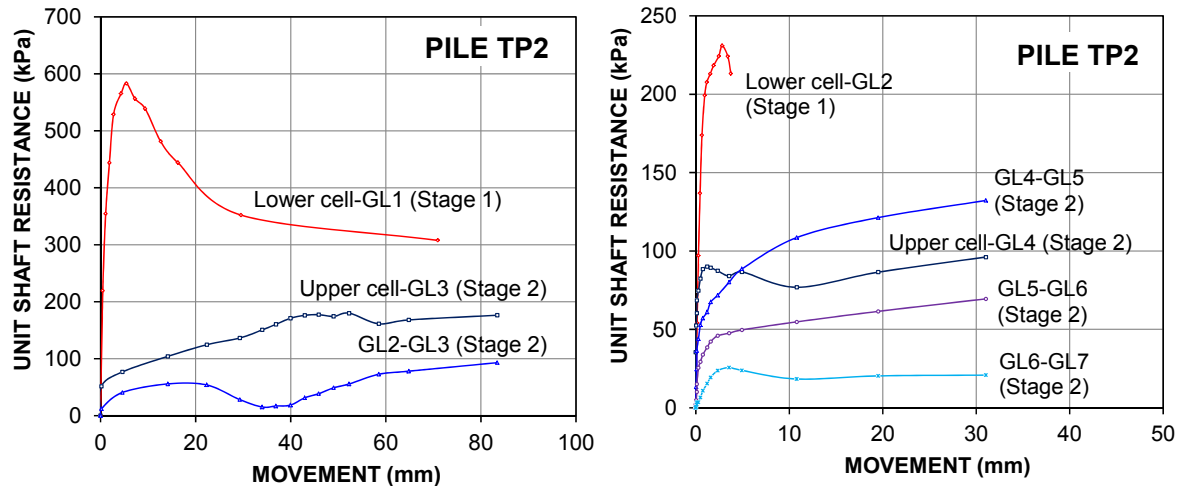


Figure 6. Unit shaft resistances versus movements of Pile TP2

PILE TOE LOAD-MOVEMENT MEASUREMENTS

For both piles, the lowest gages, GL1, was located very close to the pile toe as shown in Figure 2. Figure 7 shows the GL1-stresses vs. the telltale-measured pile toe movements. The GL1-stresses were determined as the load at Gage Level GL1 divided by the nominal area of the pile shafts below the Level GL1 and of the pile toes. As indicated in Figure 2, the toe of pile TP1 was placed on clay layer and therefore its response is significantly softer than the toe of Pile TP2. The curves display no tendency toward an ultimate resistance, confirming the fact that toe capacity does not exist (Fellenius 1999; 2016). The dashed curves show the fit of the q - z Ratio Function (Fellenius 2016) to the respective toe-curves. The fit to the TP1 and TP2 toe curves has been made for ratio exponents of 0.2 and 0.1, respectively.

CONCLUSIONS

The results of the multi-level O-cell tests on the two large-diameter bored piles in the Vietnamese Mekong Delta have been presented. The following conclusions can be drawn from these tested piles.

At the lower cell location, the maximum load is about 21.4 MN and 19.2 MN for Pile TP1 and TP2, respectively. The maximum upward movements are about 4 mm for both piles. The maximum downward movements are about 234 mm and 103 mm for Pile TP1 and TP2, respectively.

At the upper cell location, the maximum load is about 25.8 MN and 26.0 MN for Pile TP1 and TP2, respectively. The maximum upward and downward movements are about 9 mm through 33 mm and 146 mm through 82 mm for Pile TP1 and TP2, respectively.

The evaluated pile Young's modulus, E , for the two piles correlated to 21 GPa and 27 GPa for the nominal pile cross section of piles.

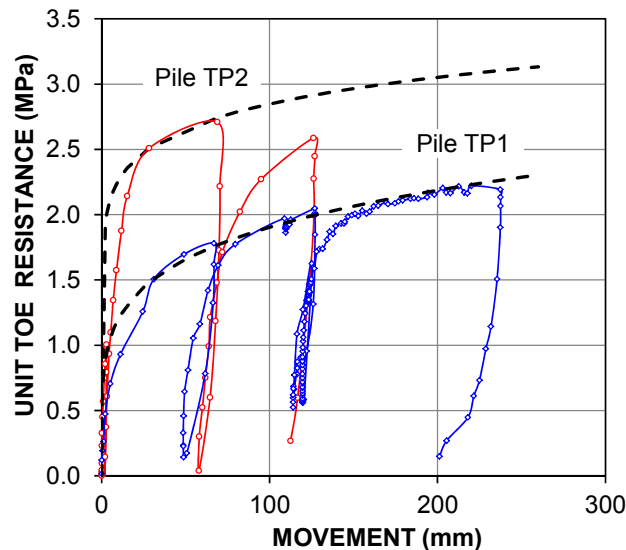


Figure 7. Stress at GL1 versus toe movements of Pile TP1 and TP2

The average unit resistance of both pile shafts placed in dense sand layer is about 460 kPa. For both piles, the unit shaft resistances measured between the two cell levels are too small, which have not reflected the soil condition at the site.

The toe stiffness of Pile TP1 was very low because it was placed in the clay layer and moreover it is likely that the construction had left soil debris at the bottom of the drilled hole.

The fit of the q - z Ratio Function shows ratio exponents of 0.2 and 0.1 for Pile TP1 and TP12, respectively. The stress-movement curves at the strain gage level GL1 show no tendency toward an ultimate resistance.

REFERENCES

- Fellenius, B.H. (1999). "Bearing capacity—A delusion?" Deep Foundation Institute, Hawthorne, NJ, Proc. of Annual Meeting, Dearborn, MI, Oct. 14-16, 1999, pp. 17.
- Fellenius, B.H. (2016). "Basics of foundation design." Revised Electronic Edition, www.Fellenius.net, pp. 453.
- Loadtest International Pte. Ltd. (2005, 2006). "Reports on Bored Pile Testing, Binh Loi Than Son Nhat, Vietnam, LTI-2257-2 and LTI-2257-3." pp. 203 and pp. 179.
- Osterberg, J.O. (1998). "The Osterberg load test method for drilled shaft and driven piles: The first ten years." 7th Int. Conf. on Piling and Deep Foundations, Deep Foundation Institute, Vienna, Austria, June 15-17, 1998, pp. 17.

Use of High-Strain Dynamic Testing to Efficiently Design and Construct Bridge Foundations in Glacial Soils

Morgan Race, Ph.D., A.M.ASCE¹; Bryan Field, P.E.²; and Matthew Glisson, P.E., M.ASCE³

¹Braun Intertec Corporation, 11529 West 79th St., Bldg 21, Lenexa, KS 66214. E-mail: mrace@braunintertec.com

²Braun Intertec Corporation, 11001 Hampshire Ave S, Minneapolis, MN 55438. E-mail: bfield@braunintertec.com

³Braun Intertec Corporation, 12727 Olive Blvd Ste 300, St. Louis, MO 63141. E-mail: mglisson@braunintertec.com

Abstract

The design of driven piles in glacial tills and outwash soils is frequently conservative in regards to pile length and foundation cost and ineffective in accurately characterizing the soil-pile interaction. Technology such as high-strain dynamic testing can be utilized to more efficiently and sustainably design and construct deep foundation systems. High-strain dynamic testing was utilized in a design-build project in the Minneapolis/St. Paul metropolitan area to characterize the properties of the soil-pile interaction and more economically construct the substructure foundations. At each substructure, initial drive and restrike tests were performed on 12 3/4-inch outside-diameter, steel, closed-ended pipe piles driven into glacial soils. The unit side resistances and unit end bearing resistances were determined from wave matching analyses using CAPWAP on restrike and/or initial drive data. The differences in the predicted and measured unit side resistance and unit end bearing resistance in glacial till and outwash soils for driven pile are discussed. For the seven structures currently completed, the actual driven pile lengths varied from 24.9 percent greater to 50.7 percent less than the expected lengths and the driven pile lengths were shortened on average by approximately 3.9 percent corresponding to an overall cost savings of approximately \$98,000.

INTRODUCTION

In glacial soils, closed-ended driven pipe piles are commonly used to maximize both side and end bearing resistances. Multiple static analysis methods (α -method, β -method, Lambda method, Meyerhof method, Eslami and Fellenius method, etc.) are available to estimate the capacity of driven piles before pile installation. During and after pile installation there are static and dynamic methods to estimate the ultimate or nominal geotechnical resistance of the piles including, but not limited to: high-strain dynamic test, force-pulse test, static load test, Engineering News Record (ENR) formula, and Gates formula. In current design reports, resistance factors are associated with the level of field control testing method anticipated, but does not account for specific soil deposits unless a regional calibration is performed. The static design methods do not specifically represent the soil-pile interaction between glacial soils which are characterized by over-consolidation due to glacier retreat and embedded gravel, cobbles, and boulders. For a large design-build project in the Minneapolis/St. Paul metropolitan area, closed-ended driven pipe piles were used as the foundation systems for eleven structures. The contractor drove the piles into primarily glacial till and outwash soils and Braun Intertec Corporation (Braun) performed

initial drive and restrike tests at each substructure unit. From the driven pile installation, the predicted total resistance and unit resistance during design were compared with the measured resistances using high-strain dynamic testing to determine the cost savings associated with the high-strain dynamic testing.

BACKGROUND

TH 610 Project. The Trunk Highway 610 Completion project (TH 610) is located in Hennepin County, Minnesota, within the city limits of Maple Grove. Minnesota Department of Transportation (MnDOT) used a two-phase, alternative procurement, project-delivery method (design-build) process to select a design-build contractor to deliver the project. After scoring the technical proposals and receiving pricing, MnDOT awarded a design-build contract to the contractor offering the best-value (in Minnesota adjusted score equals proposed price divided by technical score), which was Lunda Construction Company out of Black River Falls, Wisconsin.

The primary purpose of this new, roadway alignment is to connect existing TH 610 to Interstate 94 (I-94) and provide another major, interstate-artery mode in the Minneapolis/St. Paul metropolitan area. The project limits extend approximately 2 1/2 miles between Elm Creek Boulevard and Interstate 94 (I-94) with the proposed alignment running predominately along CSAH 81 and 101st Avenue North (Figure 1). The project generally includes the design and construction of eight (8) bridges, two (2) at-grade tunnels, an embankment load transfer platform (LTP), five (5) reinforced soil slopes (RSS), seven (7) retaining walls, and general roadway and embankment construction of mainline TH 610.

In Minnesota, the majority of the glacial sediment was deposited during the Wisconsin Age approximately 75,000 years ago (MGS 1997). The glacial till was deposited approximately 14,000 years ago. The Des Moines lobe till of the Pine City moraine, is typically an over-consolidated, low-plasticity, gray to brown cohesive soil with the potential for embedded gravel, boulders, and cobbles. Glacial outwash soils range from poorly graded sand (SP) to well graded gravel (GP) to silty sand (SM) all with the potential for embedded boulders and cobbles. According to the Minnesota Geological Society Map M-178 (2007), the soils at the TH 610 project site consist primarily of glacial till and outwash soils, labeled as Qci, Qna, and Qnh (Figure 2 and Table 1). The glacial tills in the site vicinity are characterized by sandy/loamy-clays with pebbles, cobbles, and boulders. Similarly, the glacial outwash soils are a combination of sand, gravelly sand, and sandy gravel with the potential for embedded cobbles and boulders.

Static Analysis Method. Braun used the computer program, UniPile, version 5.0, by Unissoft Geotechnical Solutions Ltd., to estimate the static nominal geotechnical resistance (R_n) of the closed-ended pipe piles for support of the bridge and retaining wall foundations. For this project, Braun used the Beta-method, an effective stress method further described in Fellenius (2007), to estimate the static geotechnical resistance for these piles based on standard penetration test (SPT) borings and cone penetration test (CPT) soundings.

The equations to calculate the unit side resistance and unit end bearing resistance in the Beta-method are as follows.

$$r_s = c' + \beta \sigma'_z \quad (\text{Fellenius 2007}) \quad (1)$$

$$r_t = N_t \sigma'_z \quad (\text{Fellenius 2007}) \quad (2)$$

Where r_s is the unit side resistance (ksf), c' is the effective cohesion (ksf), β is the beta coefficient, σ'_z is the vertical effective stress at depth z (ksf), r_t is the unit end bearing resistance (ksf), and N_t is the toe bearing capacity factors.

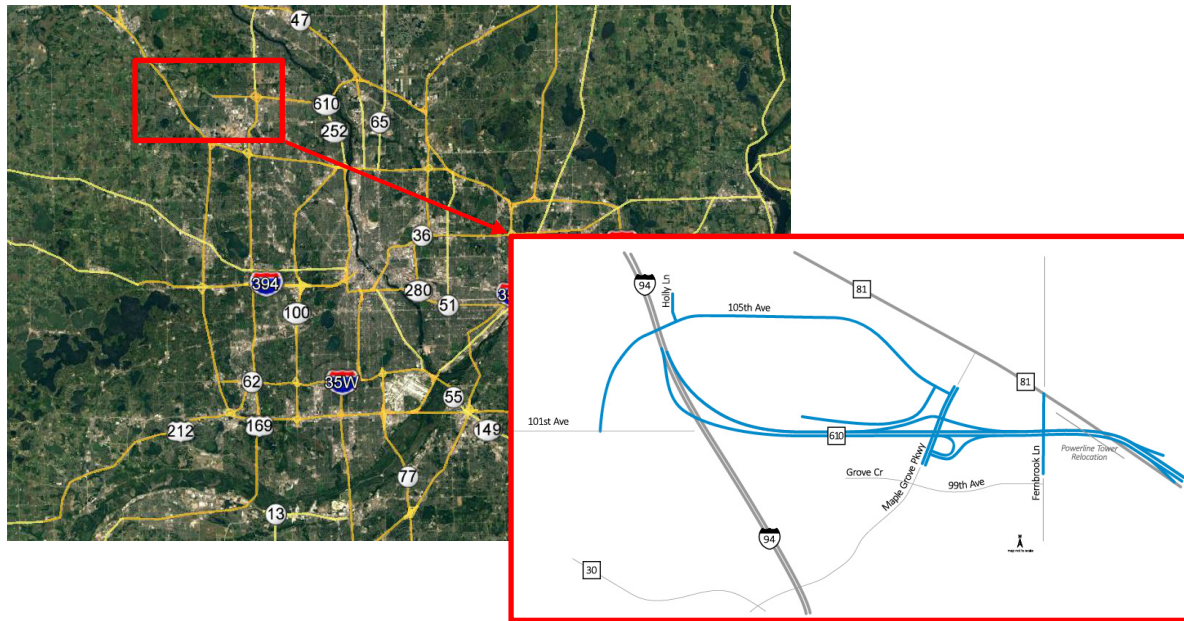


Figure 1. Minneapolis/St. Paul metropolitan area with a cutout of the TH 610 completion project site (©Google Earth 2016; MnDOT 2016).

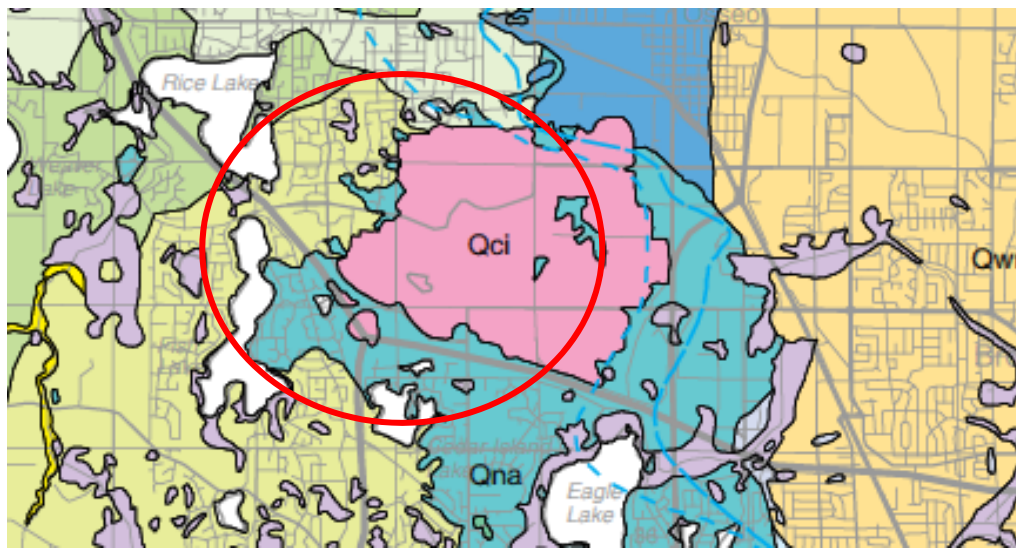


Figure 2. Surficial geology map at the TH610 Site (modified from Minnesota Geological Society Map M-178 2007).

The value β in Equation 1 for unit side resistance is determined using Bjerrum-Burland beta coefficients, which are based on soil type and effective friction angle. Similarly, Equation 2 for the unit end bearing resistance includes toe bearing capacity factors (N_t), which are also based on soil type and effective friction angle. Table 2 (modified from Table 9-6 FHWA Publication No. NHI-05-042 2006) presents typical β and N_t values used in our evaluations.

Table 1. Soil type descriptions based on Map M-178 (Minnesota Geological Society Map M-178 2007).

Soil Symbol	Soil Type	Description
Qci	Outwash	Ice-contact stratified deposit consisting of sand, gravelly sand, and cobbly gravel deposited by meltwater.
Qna	Till	Sandy till primarily consisting of loam-to-sandy loam sediment with pebbles, cobbles, and boulders.
Qnh	Till	High-relief tills primarily consisting of loam-textured sediment scattered with pebbles, cobbles, and rare boulders.

Table 2. Design parameters for glacial till (lean clay) and glacial outwash (poorly graded sand) soils (modified from FHWA 2006).

Soil Type	Consistency	Blow Count, N_{60} (bpf)	Friction Angle, ϕ (deg.)	Cohesion, c (psf)	β	N_t
Lean Clay (CL*)	Soft	2 - 4	-	250 - 500	0.15	3
	Firm	5 - 8	-	750 - 1,200	0.19	8
	Stiff	9 - 15	-	1,500 - 2,500	0.20 - 0.29	14 - 19
	Very Stiff	16 - 30	-	2,500 - 4,500	0.30 - 0.35	25 - 30
	Hard	31 - 60	-	4,500 - 9,000	0.36 - 0.40	30 - 33
	Very Hard	61+	-	10,000	0.41 - 0.50	37 - 40
Poorly Graded Sand (SP/SP-SM*)	Very Loose	0 - 4	28 - 29	-	0.15 - 0.20	15 - 20
	Loose	5 - 10	30 - 31	-	0.21 - 0.25	20 - 30
	Medium Dense	11 - 17	32 - 33	-	0.26 - 0.39	30 - 45
	Medium Dense	18 - 24	33 - 34	-	0.40 - 0.52	45 - 60
	Dense	25 - 30	35	-	0.53 - 0.59	60 - 75
	Dense	31 - 50	36 - 38	-	0.60 - 0.75	75 - 120
	Very Dense	51+	38 - 40	-	0.76 - 0.90	120 - 150

*Classification based on ASTM D2487 (2011).

High-Strain Dynamic Pile Testing. Braun performed high-strain dynamic testing using a model PAX Pile Driving Analyzer® (PDA) manufactured by Pile Dynamics, Inc. The purpose of high-strain dynamic pile testing is to measure the pile-driving stresses, hammer energy transfer, and to aid in evaluating the pile's load-carrying capacity and pile integrity. The PDA uses the software program PDA-W to control data processing and presentation during and after acquisition. The PDA-W program digitally records the analog signals from the strain transducers and piezoresistive accelerometers. PDA-W digitally integrates acceleration to determine velocity. For the steel pile, a density of 492 pounds per cubic foot (pcf), an elastic modulus of 30,000 kips per square inch (ksi) and a resulting wave speed of 16,807.9 feet per second (ft/s) was used.

To estimate the soil resistance parameters, wave-matching evaluations of the dynamic data collected in the field by the PDA using the Case Pile Wave Analysis Program (CAPWAP), version 2006-3 were performed. CAPWAP uses an iterative process to compare the computed force and velocity to the measured pile data, while modifying the soil resistance parameters until

obtaining a reasonable best fit of the soil model for the particular pile tested. The wave-matching evaluation also provides an estimated nominal pile resistance, referred to by the program as the CAPWAP capacity, at the time of testing and differentiates the estimated end bearing and skin friction components of the total pile capacity.

Bias Factors. Bias factors are more frequently used in relation to load and resistance factor design (LRFD) calibration studies. To calibrate the resistance factors for a specific site/state, the amount of uncertainty has been accounted for with a bias factor of the resistance (λ) which was defined by Abu-Farsakh et al. (2010) as the ratio of the measured resistance (R_m) and the predicted resistance (R_p) as presented in Equation 3. In relation to this project, bias factors will be utilized to determine the ratio between the measured total or unit side resistance determined from high-strain dynamic testing of pipe piles and predicted total or unit side resistance using the static analysis method in UniPile.

$$\lambda = \frac{R_m}{R_p} \quad (\text{Abu-Farsakh et al. 2010}) \quad (3)$$

RESULTS

Predicted Versus Measured Resistance. The total resistance values from the initial and restrike test data and the predicted data are presented in Figure 3. From the initial test data, the measured total resistance, excluding the predicted total resistance value at 940 kips, has an average bias of about 81 percent of the predicted total resistance (Table 3). However, there was significant “setup” in the majority of the test piles and the measured total resistance from restrike is approximately 122 percent of the predicted total resistance. Allowing the test pile to sit for one to four days and then restriking the test pile yields results similar to the predicted design geotechnical resistance of the piles.

Comparing Figure 3a and b, there are only eight test piles with measured total resistances greater than the predicted total resistance from the initial drive test data, but there are 22 test piles from the restrike test data. At many of the test pile locations, there are glacial till soils which “setup” and increase the adhesion/resistance along the side of the pile as the pile is in the ground longer. Accounting for the increase in resistance due to “setup” of the soil will maximize the capacity of each driven pile and potentially minimize the cost of the foundation system.

The unit side resistance values from the design phase of the project and from the initial and restrike tests are presented in Figure 4 and Table 3. While the average bias factor for the measured unit side resistance from the initial drive test is only 83 percent of the predicted unit side resistance, the measured unit side resistance using the restrike data is approximately 156 percent of the predicted unit side resistance. Although there was a large increase in the measured unit side resistance from the initial PDA test to the restrike PDA test, there was also a nine percent increase in the standard deviation of the bias factors for the unit side resistance. Because the sites have both glacial till and glacial outwash soils, the increase in the measured unit side resistance with increased time in the ground is not linear or even guaranteed. Theoretically, there should be significantly less increase in unit side resistance for piles that are driven into glacial outwash soils versus piles that are driven into glacial till soils. While there is no differentiation between the types of soil within this paper, the topic will be further investigated to more accurately characterize the increase in geotechnical resistance due to “setup” of glacial till and outwash soils.

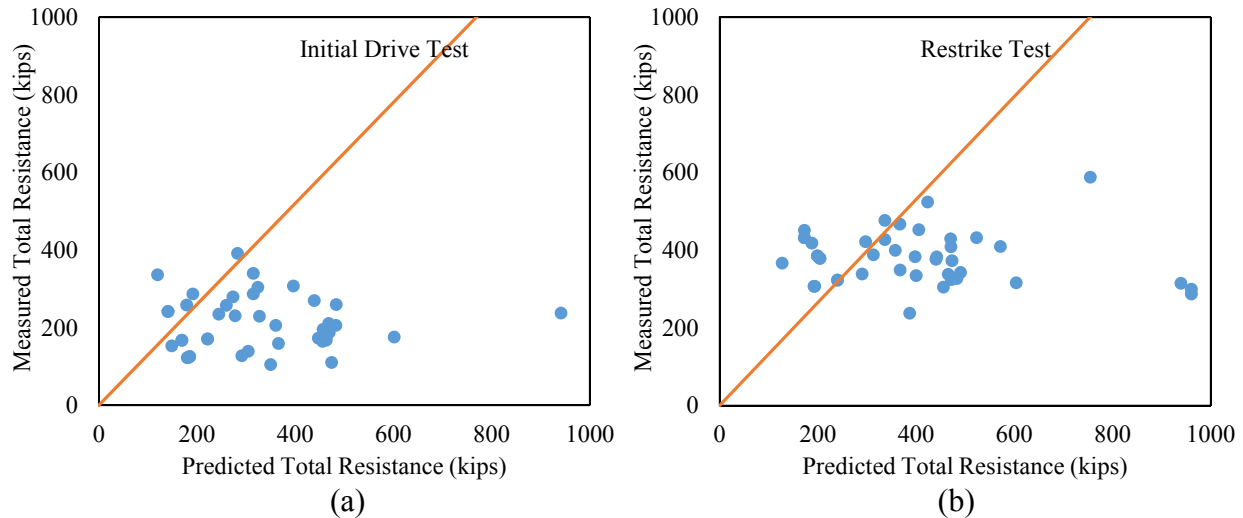


Figure 3. Predicted versus measured total resistance for driven closed-ended pipe piles in glacial till and outwash soils in the twin cities metro area using a) initial drive test data and b) restrike test data.

Table 3. Summary of the high-strain dynamic test data.

Type of Resistance	Type of Test	Number of Samples	Average Bias Factor	Standard Deviation	Coefficient of Variation
Total Resistance	Initial	41	0.81	0.50	0.62
	Restrike	43	1.22	0.64	0.52
Unit Side Resistance	Initial	324	0.83	1.72	2.07
	Restrike	363	1.56	1.87	1.20

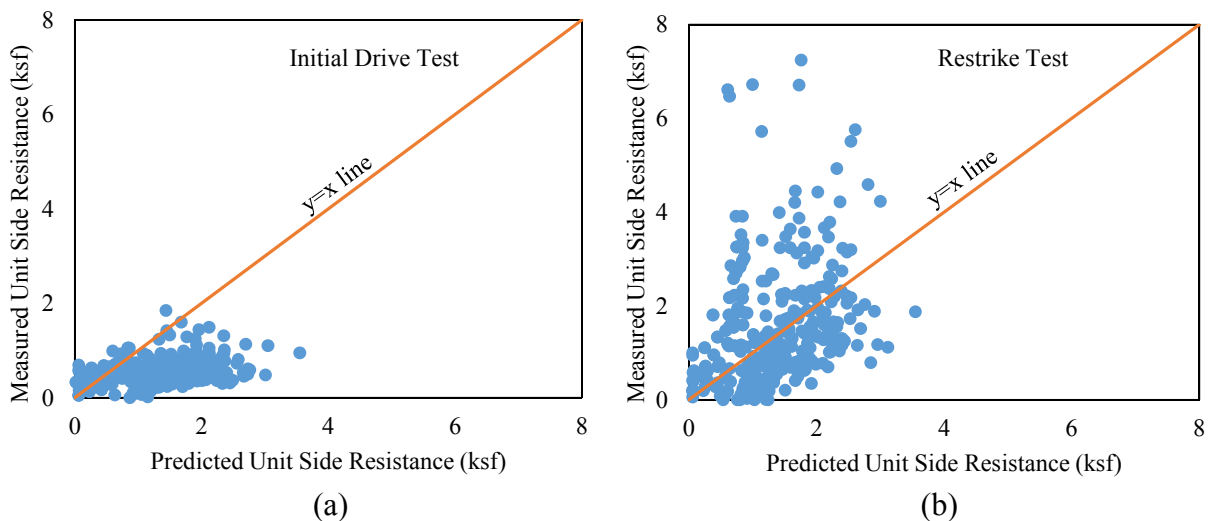


Figure 4. Predicted versus measured unit side resistance for driven closed-ended pipe piles in glacial till and outwash soils in the twin cities metro area using a) initial drive test data and b) restrike test data.

Based on the scatter of the data and the coefficient of variation of the bias factor (COV), the effective stress method, used as described in the background section, under-predicted the unit resistances (side or end bearing) of a closed-ended steel pipe pile driven into glacial soils. The difference in the predicted and measured unit resistance values using high-strain dynamic testing and the effective stress method is likely due to non-homogeneous soil stratigraphy at the site. However, the predicted total resistance is an average of 19 percent higher than the initial drive pile resistance and 22 percent lower than the restrike resistance. The COV of the bias is in the range of a medium variable site, which is a reasonable assumption for the size and soil variability at the site. Based on the average and COV of the bias factors of the total resistance, the effective stress method can be used to predict the pile resistance in glacial soils where some setup will occur (typically cohesive soils).

Cost Analysis. The average installed length of the piles for eleven, pile-supported structures in relation to the design production length are presented in Figure 5. In general, the difference in the installed and design length is within 10 feet of the design length, but the length differences for Retaining Wall (RTW) 27W15 and RTW 27W16 range between 11 and 45 feet. The weighted average percent difference in the design and installed length of piles for each structure ranges from approximately 35 percent less than anticipated to 16 percent greater than anticipated (Table 4).

Although more structures have a net installed length of pile less than the designed length, there are more piles in the structures that had an installed length greater than the design length (in particular Bridges 27W15 and 27W16). Pile were driven longer for Bridge 27W15 and portions of RTW 27W15 because construction constraints relating to active power lines and railroad tracks were more important than the cost savings relating to soil setup. Due to time constraints, not all of the piles have been driven yet and not all of the data is analyzed currently; however, using the data available there is almost a net zero with the overall installed length of pile compared to the anticipated length of pile. Excluding the data from Bridge 27W15 and RTW 27W15, the average percent difference in pile lengths is -12.0 percent.

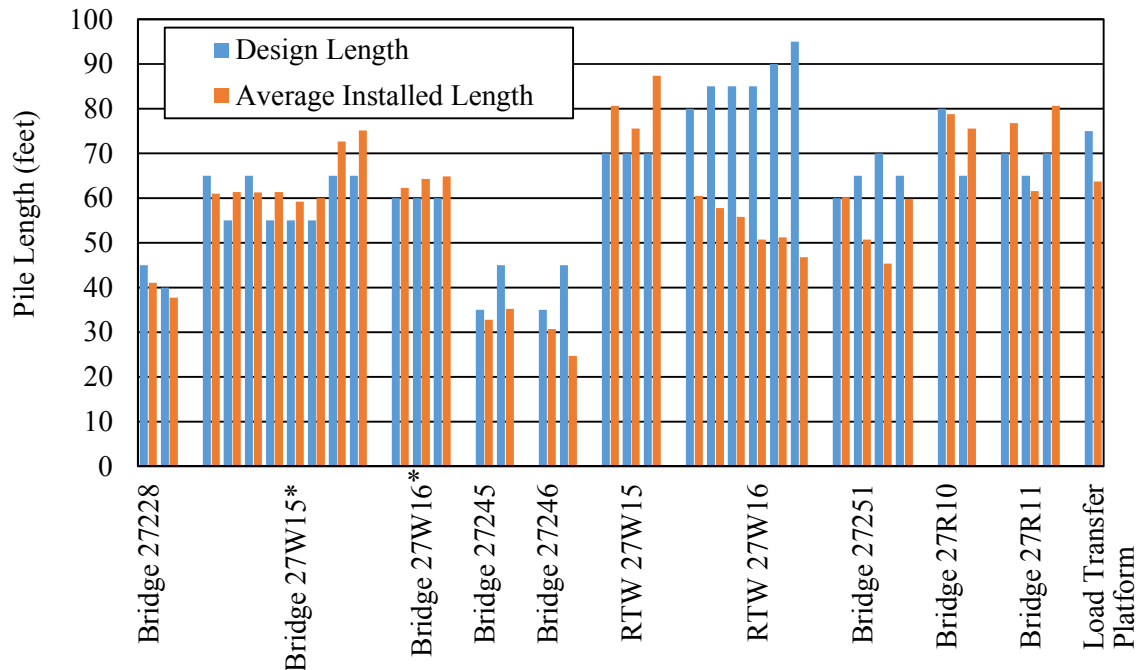


Figure 5. Length of the piles installed versus the designed length of the piles.

Table 4. Summary of the completed production piles.

Structure	Number of Piles	Weighted Average Percent Difference in Pile Lengths (%) [*]	Approximate Excess Cost (USD) ^{**}
Bridge 27228	81	-7.2	-7,500
Bridge 27W15	483	6.9	57,700
Bridge 27W16	114	6.0	12,200
Bridge 27245	71	-13.7	-12,500
Bridge 27246	67	-28.5	-24,500
RTW 27W15	37	16.2	12,600
RTW 27W16	39	-34.8	-35,300
Bridge 27251	161	-14.9	-48,800
Bridge 27R10	14	7.4	2,000
Bridge 27R11	21	6.6	3,000
Load Transfer Platform	167	-15.1	-56,600
Total	1255	-3.9⁺	-97,700

^{*}Negative percent difference correlates to an average installed length less than an average design length.

^{**}Negative cost savings correlates to cost savings.

⁺Excluding the data from Bridge 27W15 and RTW 27W15, the average percent difference in pile lengths is -12.0 percent.

The cost of each foundation system was investigated to evaluate if there were additional savings from determining a site-specific criteria using the high-strain dynamic testing besides using a higher resistance factor during the design. The cost of the pile foundation system was determined from the number of piles and the estimated pile lengths for each substructure. Using an average cost of \$30 per linear foot of driven pile, the difference in cost between the designed

foundation system and the installed foundation system is presented in Table 4. The negative cost values correspond to money saved and the positive values represent additional money spent, compared to the final design cost estimate. Primarily, the foundation systems of three structures cost more money than anticipated, Bridge 27W15, Bridge 27W16, and RTW 27W15. Even considering the longer piles driven for Bridge 27W15 and RTW 27W15, there was an overall savings of approximately \$97,700 for foundation systems of 11 structures on the TH 610 project. The cost savings presented accounts for a portion of the time savings for the pile installation during the construction but does not represent the value added to the project by shortening the overall construction schedule.

CONCLUSIONS

Based on the measured total and unit resistance values from the initial drive testing, it was determined the actual resistances were approximately 82 percent of the predicted total and unit side resistance values. After restrike testing, the actual total and unit side resistance values increased to 122 and 156 percent of the predicted resistance values, respectively. Accounting for soil setup by performing initial drive and restrike tests, and using the recommended driving criteria from high-strain dynamic testing, it was determined there were significant cost savings associated with the foundation systems for the TH 610 project.

In general, a direct correlation between the utilization of initial or restrike drive criteria and cost savings was realized for the TH 610 project. Five of the eleven structures considered had a net negative cost in relation to the anticipated design pile foundation system. However, the piles for Bridge 27W15 and RTW 27W15 were driven harder than the recommended driving criteria because there were time constraints due to active power lines and railroad tracks. Overall there was a net savings from the anticipated cost of the foundation systems of eleven structure of \$98,000 US by using driving criteria from high-strain dynamic tests.

ACKNOWLEDGEMENTS

The authors would like to acknowledge Lunda Construction Company and Minnesota Department of Transportation for their contribution in the TH 610 Completion Design-Build Project.

REFERENCES

- ASTM (American Society of Testing and Materials). (2011). "Standard Practice for Classification of Soils for Engineering Purposes (Unified Soil Classification System)." Annual Book of ASTM Standards, Designation D2487, Vol. 4.08, ASTM, West Conshohocken, PA.
- FHWA (Federal Highway Administration). (2006). Design and Construction of Driven Pile Foundations. Publication No. NHI-05-042, 968 pgs.
- Fellenius, B.H. (2015). Basics of Foundation Design. Electronic Edition: www.Fellenius.net, 432 pgs.
- Google Earth. (2015). Version 7.1.5.1557.
- Minnesota Geological Survey (MGS), University of Minnesota (Lusardi, B.A.). (1997). Minnesota at a Glance: Quaternary Glacial Geology. St. Paul, Minnesota, 4 pgs.

- Minnesota Geological Survey (MGS), University of Minnesota (Meyer, G.N.). (2007). Surficial Geology of the Twin Cities Metropolitan Area, Minnesota [Map M-178]. 1:125,000. Retrieved from <https://conservancy.umn.edu/handle/11299/58220>.
- MnDOT (Minnesota Department of Transportation). (2016). "HWY 610: Traffic Impacts." <http://www.dot.state.mn.us/metro/projects/610west/>. September 30, 2016.

Underpinning a Boston Landmark for the Ages: The First Church of Christ, Scientist (TFCCS), the Original Mother Church (TOMC), Foundation Repairs

Giuliana A. Zelada, P.E.¹; and Sean M. Homem, P.E.²

¹Senior Project Manager, Simpson Gumpertz and Heger Inc., 41 Seyon St., Suite 500, Bldg 1, Waltham, MA 02453. E-mail: gazelada@sgh.com

²Senior Staff II, Simpson Gumpertz and Heger Inc., 41 Seyon St., Suite 500, Bldg 1, Waltham, MA 02453. E-mail: smhomem@sgh.com

Abstract

Dealing with the consequences of lowered groundwater levels and consequent untreated timber pile deterioration in Boston's Back Bay is not uncommon. Urban sprawl in this area in the late 1800s and early 1900s was made possible through land reclamation, filling in the remnants of the old bay. Untreated timber piles were often used as the foundation of choice in these conditions. Unfortunately, urban construction also resulted in decreased groundwater levels as a result of underground construction, leaking utilities, and leaking basements. The Mother Church (TMC), located on The First Church of Christ, Scientist (TFCCS) campus, is a historic landmark in downtown Boston supported on hundreds of untreated timber piles, and has long been implementing a system of movement and groundwater monitoring to identify any areas at risk of timber pile deterioration. In particular, the surveys indicated that the bell tower of The Original Mother Church (TOMC) was at a high risk of having deteriorated timber piles, and test pit investigations confirmed this. To mitigate future settlements, and extend the service life of the structure, we designed and implemented a foundation underpinning and repair scheme consisting of two phases: underpinning of the main tower with steel needle beams and pre-loaded micropiles, and cut-and-post underpinning in the remaining areas of the TOMC. The design and construction of the foundation underpinning had to accommodate for highly congested and restricted access areas, maintain the integrity of the unreinforced masonry tower structure during the load transfer process, incorporate micropiles needled through the forest of timber piles below the tower, and provide for a system with minimal future settlement and a service life in the order of 500 years. The project was completed successfully and on schedule, with minimal adjustments to the contract plan. Follow up movement monitoring surveys shows no additional movement of the TOMC bell tower has occurred.

BACKGROUND

The First Church of Christ, Scientist (TFCCS), also known as The Mother Church (TMC) by Christian Scientists, is a historical landmark in the heart of the Back Bay area in Boston, Massachusetts, located within a 14.5 acre Christian Science campus. The Mother Church consists of two adjoining building structures built in separate years. The Original Mother Church (TOMC) (Photo 1) was built in 1894 and consists of a triangular-shaped granite stone and brick masonry structure featuring a 126-ft tall bell tower; the entire structure is supported on untreated spruce timber pile foundations bearing on a sand and gravel stratum encountered about

11 ft below the slab-on-grade. The Mother Church Extension (TMCX) was built in 1906 and consists of a domed steel framed structure with perimeter granite and clay brick masonry, supported on concrete pile caps on untreated timber piles similar to TOMC.

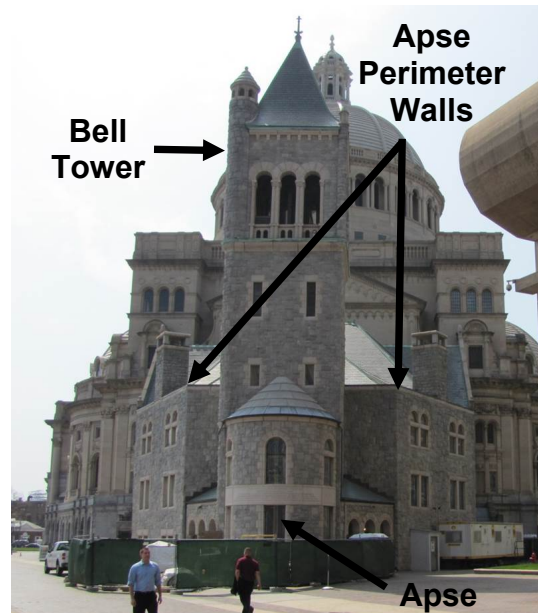


Photo 1: The Original Mother Church (TOMC)

The use of untreated timber piles as foundation support was common in the northeastern U.S. at the end of the 19th century and beginning of the 20th century, when industrialization and a desire for rapid expansion of urban areas led to the use of urban-fill to reclaim land to the sea. Early on it was recognized that untreated timber piles needed to be submerged below water to limit pile deterioration due to wood-destroying fungi and/or soft rot attack, by limiting the available oxygen to the microbes. Therefore, the installation of untreated timber piles typically required the pile cutoff to be below the lowest expected in-service groundwater level. Historically, the tops of untreated timber piles in Boston were cut at or below El. 5.0 ft (Boston City Datum, BCB).

TFCCS recognized the risk for deterioration of TMC timber pile foundations and starting in the 1960s commenced a monitoring program which included the determination of groundwater levels, movement surveys, and test pit investigations to expose the untreated timber piles and determine their condition.

By 2005 settlement data obtained from the movement monitoring level surveys indicated a relatively significant ongoing settlement trend near the apse of TOMC, with an approximate rate of settlement of about 0.08 in./yr. LVDT displacement transducer (LVDT) instruments located in TOMC bell tower also indicated about 0.14 in. of lateral movement had occurred, which together with the settlement survey data suggested a slight rotation of the bell tower. The settlement trend in TOMC correlated with data obtained from the groundwater level monitoring program, which indicated a trend of decreasing groundwater levels. Groundwater levels were as low as El. 3.6 ft at the TOMC apse, the apparent locus of the lowered groundwater levels under TMC. Based on test pit investigations performed in the TOMC apse in the 1990s and in 2002, the tops of the untreated timber piles in this area ranged from about El. 4.5 ft to El.

4.8 ft. Thus, the tops of timber piles were estimated to have been exposed by up to 0.9 to 1.2 ft above groundwater.

While test pit investigations had been performed at TOMC apse, the location of the investigations had always been the same, namely a test pit located at the “apex” of the structure. No test pit investigations had ever been performed to determine the condition of the untreated timber piles under the TOMC bell tower itself. In 2008, TFCCS authorized an investigation into the cause of settlement of the TOMC bell tower, which included excavation of a test pit in the interior of TOMC, immediately adjacent to one of the bell tower foundation walls, and installation of additional movement monitoring devices.

TOMC Bell Tower Investigation. A test pit excavation adjacent to the TOMC bell tower foundation walls was performed in 2009. A 6 to 13 in. thick stratum of loose laid brick infill underlain by an 8 to 22 in. thick, unreinforced concrete slab was encountered immediately below the 4 to 6 in. thick basement slab. The TOMC tower structure was supported on granite foundation caps that measured 3 ft wide by 2 ft deep by 4 ft long, each supported on 3 to 4 untreated timber piles. Subsurface conditions below the concrete slab consisted of about 2.0 ft of miscellaneous fill (sand and gravel with trace of silt, some brick, cobbles, and wood fragments); over organic soils consisting of dark brown organic silt and peat which extended to the bottom of the test pit at about El. 1.4 ft. At some locations, there was a 2 to 3 in. gap between the bottom of the granite foundation cap and the top of the soil surrounding the timber piles, likely caused by secondary settlement of the organic soils underlying the miscellaneous fill.

The test pit excavation exposed a total of twelve 10 to 12 in. diameter spruce timber piles. Large areas of deteriorated wood and cavities at the tops of several of the piles were visually obvious (Photo 2). Generally, all piles appeared to be in fair to poor condition above the groundwater table and good to excellent condition below groundwater. We removed three-foot long sections of select piles for further examination, sampling and testing in our laboratory. Steel posts were used to replace the cut pile sections to restore support to the tower.



Photo 2: Deteriorated Top of Timber Pile Under the TOMC Bell Tower Foundation Wall.

Laboratory testing on the extracted timber pile sections included macroscopic and microscopic observations, compressive strength testing following ASTM procedures, specific gravity, and moisture content measurements. Results indicated advanced deterioration due to biological attack (fungal attack, soft rot attack or bacterial attack) was limited to the very tops of

the piles (up to about 6 in. from the top of the piles) and the outer 1/2 in. to 3/4 in. of the pile surfaces at lower regions (both above and below groundwater). This is consistent with the fact that deterioration of untreated wood embedded in earth originates at the surface (where oxygen is most readily available), and propagates inward as the microbes continue to grow. The results were also consistent with recent research findings that have shown that both soft rot and bacterial wood attack can occur underwater, although they both typically progress much slower than decay caused by fungi and their advance is typically limited to the sapwood thickness, i.e. the outer perimeter of the timber pile. The average compressive strength of timber pile samples was 2,181 psi, roughly 93% of the published average strength for sound white spruce wood. Based on the strength test results, the remaining compressive strength of the piles supporting TOMC bell tower, even where soft rot and bacteria were present, was only starting to diminish.

Movement monitoring performed in 2009 indicated that TOMC bell tower had settled up to an additional 0.25 in. since 2005, and lateral movement had increased to 0.2 in., resulting in an 0.05° overall rotation.

REPAIR DESIGN DEVELOPMENT

Foundation Underpinning Options. The overall impact of deterioration on the timber piles supporting TOMC bell tower, in terms of strength loss, was limited to the very tops of the piles. However, the section loss and softened conditions at the tops of the piles result in load shedding to the surrounding piles that remained in contact with the granite caps, causing settlement. Continued exposure to air associated with lowered groundwater elevations would likely accelerate the rate of fungal decay in the near term. Based on the level of pile top deterioration observed in 2009, recharging this area would likely slow but not eliminate the rate of biological deterioration. If more pile tops were to lose contact with the granite caps due to deterioration, and more load was transferred to other surrounding piles, there was a potential for overloading timber piles providing actual support to the structure. Even if the compressive strength of the pile section was adequate to sustain the loads, the increase in loading would be accompanied by increased settlement. The additional load could also exceed the bearing capacity of the sand and gravel stratum on which the timber piles are founded, resulting in more settlement. Due to these risks, foundation underpinning became the preferred repair approach.

We evaluated two alternative underpinning approaches: the traditional cut and post method (Option 1), which consists of replacing the deteriorated tops of the existing timber piles with concrete-filled steel posts, and the use of micropiles (Option 2). Each of these methods was considered for underpinning both the TOMC bell tower wall foundations and the bearing wall foundations and columns supporting the apse structure surrounding the bell tower.

We originally considered performing the cut-and-post underpinning of the TOMC perimeter bearing walls from exterior pits excavated alongside the walls. However, these exterior pits would be approximately 17 ft deep requiring the installation of a robust support of excavation system, and there was limited space for the pits due to existing utilities and the presence of a jet grout curtain wall around the apse. Therefore, any cut-and-post underpinning at TOMC apse would need to be performed from interior pits. Cut-and-post underpinning would involve saw-cutting the existing slab-on-grade; removing and disposing the under-slab unreinforced concrete and brick; temporarily re-routing or supporting the numerous existing utilities as needed (including but not limited to steam, hot and chilled water, and HVAC ducts); excavating, bracing, and dewatering pits up to 7.5 ft deep to provide access to the timber piles; cutting and underpinning timber piles with new steel posts and steel shims; and encasing the

steel posts with concrete. Underpinning pit excavation required sequencing to prevent simultaneous removal of large sections of the existing slab-on-grade, which contributed to the lateral stability of the bell tower and perimeter foundations walls in the apse.

Due to the limited available headroom in the basement area and the required excavation depth at the exterior walls to allow construction of the micropile-to-wall connections, micropiles were not economically feasible for the TOMC perimeter bearing walls. Therefore, the use of micropiles for underpinning was only considered for the TOMC bell tower foundation as there was adequate headroom, albeit limited to just over 8 ft of clearance. Micropiles would be installed along both sides of each bell tower foundation wall; coring through the existing slab-on-grade and underlying concrete and brick would be required prior to installing the micropiles. The bell tower walls would be horizontally cored to install steel needle beams to be supported by micropiles at each end. In order to limit post-construction settlements of the tower, preloading was required to transfer a significant portion of the existing structural load from the existing timber piles to the new micropile foundations. Major utility and equipment relocation would also be required as several utilities were supported along the tower foundation walls. Although the micropile and needle beam underpinning option for TOMC bell tower was significantly more expensive than traditional cut-and-post underpinning, the TOMC bell tower was of heightened importance to TFCCS, as it housed a room used by the church's founder. TFCCS requested that the underpinning of the TOMC bell tower be designed for a 500-year service life. Repairs would therefore incorporate pre-loaded micropiles and a cathodic protection system. The remaining portion of the TOMC apse would incorporate the more traditional cut-and-post underpinning.

TOMC Tower Underpinning Design Considerations. The majority of the walls of the TOMC apse were underpinned using cut-and-post methods, performed prior to the micropile underpinning of the TOMC bell tower. During the cut-and-post phase, we gathered existing condition information to assist with micropile underpinning design, including the as-built locations of the existing timber piles and granite pile caps.

The tower structure projects approximately 45 ft vertically above the roof of the main TOMC structure and shares its west wall with the TOMC structure. The tower wall extends 126 ft above the plaza level slab (i.e. the apse slab at the same elevation as outside grade). The plaza level slab is connected to the North and South Tower walls as well as the entire semi-circular apse perimeter. We assumed that the main TOMC structure and the bell tower act independently from one another. This is based on field observation that the two structures are not rigidly connected but are adjacent to one another. See Figure 1 for a plan of the existing conditions.

Prior to determining a micropile layout, we used RISA3D software to model the existing tower and apse assembly and simulate the existing tower deformation and foundation loading conditions. We used this model as a baseline against which to compare the performance of the proposed underpinning system. We included the timber pile supports as springs along the base of the tower walls, provided lateral spring supports at the plaza level slab along the north, south and east walls, and provided lateral spring supports at the west wall interface.

In order to determine the proposed needle beam and micropile layout, we performed a series of model iterations to determine how the load was being distributed to the new foundation system given the presence of various discontinuities in the tower walls. The needle beam and pile assemblies were modelled as non-yielding vertical supports. Our target was to maintain a

minimum pile spacing of approximately 3 pile diameters (approximately 21 in.) and not to exceed applied axial vertical pile loads of 100 kips.

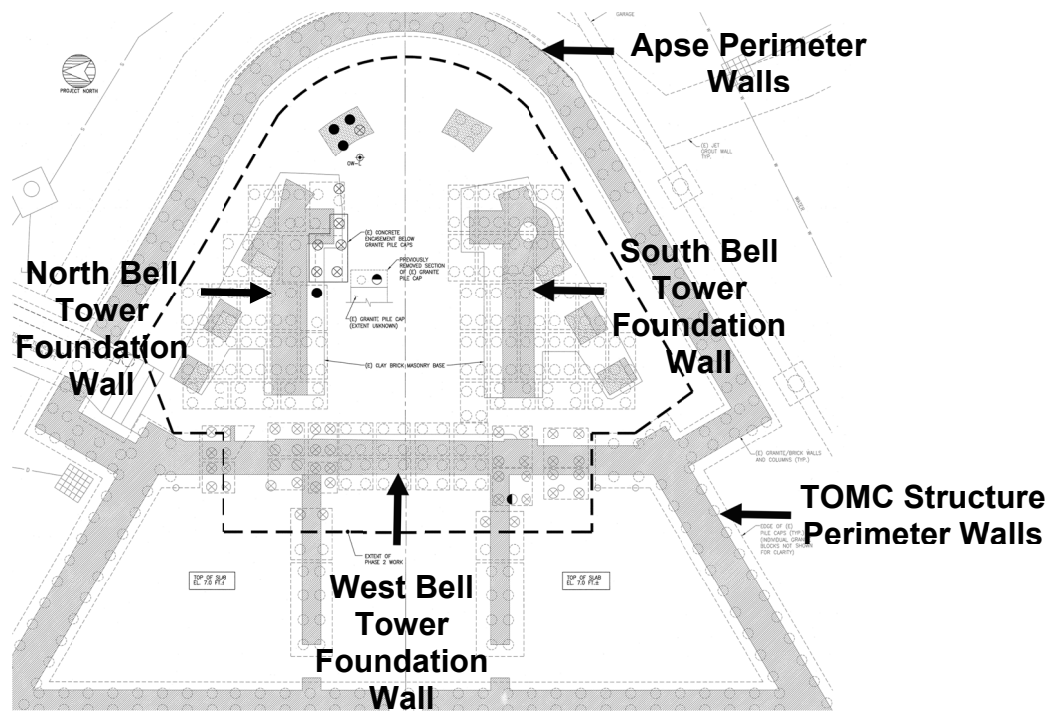


Figure 1: Existing TOMC Tower Foundation Conditions

The typical needle beam assembly consisted of a single, wide flange needle beam, ranging in size from W12 to W18, inserted through a cored opening in the existing wall and supported by one pile at each end. However, there were several atypical locations where changes to the assembly needed to be made to accommodate the existing geometry or concentration of loads. One example included supporting the corners of the east tower wall. In the basement area, there is a large opening in the east wall leading to the Apse. The majority of the load from the east wall is supported by the corner of the wall on each side of the opening and the typical needle beam assembly was not sufficient to support all of the load. At this wall we used “T-shaped” assemblies, which consisted of a needle beam through the cored wall, supported by a pile on one end and a beam connected to two piles on the more heavily loaded end (see Figure 2).

Once we developed a layout that satisfied the specific site constraints, we modeled the various needle beam assemblies by attaching the needle beams to the base of the tower wall with rigid links that transferred axial loads only. We performed multiple iterations of this model with various needle beam sizes and support conditions, which included modeling the piles as non-yielding supports or as spring supports, until we arrived at a tower deflections and rotations that did not exceed the deflections under the original design conditions.

The final design consisted of 58 micropiles and 44 needle and transfer beams supporting the tower walls and apse columns. In order to limit future settlement and distress we recommended transferring approximately 80% of the calculated dead from the existing foundation to the proposed needle beams and piles. To achieve this, we specified a sacrificial flat jack between the top of the needle beam and the top surface of the pocket in the walls, see

Figure 3 for the drawing detail. Another model mimicking the preloading sequence indicated that the preloading would not shift additional load onto the existing timber piles, but would rather relieve load.

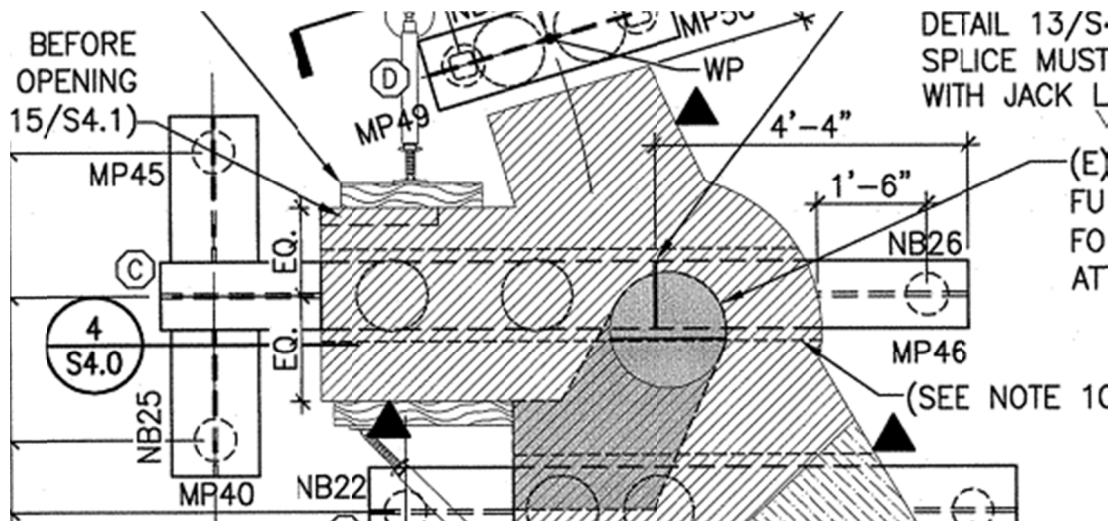


Figure 2: T-Shaped Needle Beam Assembly

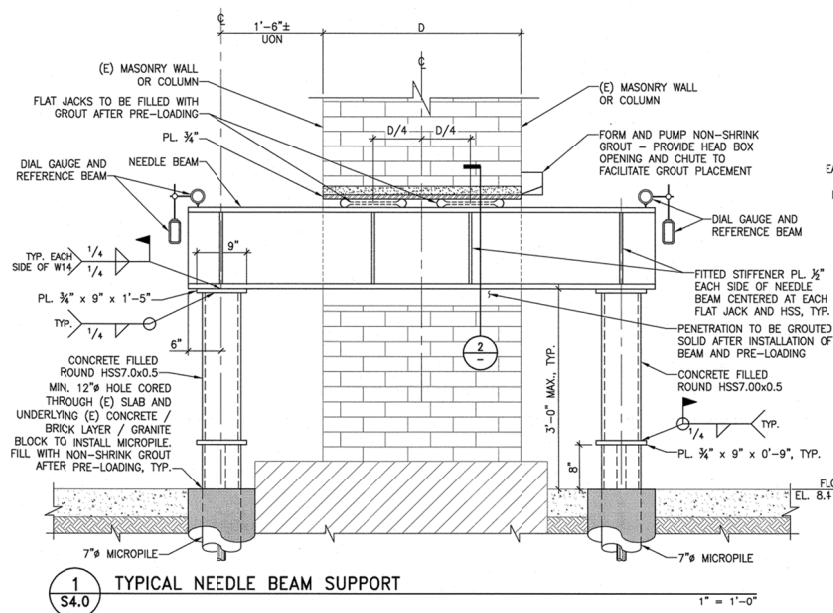


Figure 3: Typical Needle Beam Support Detail

Tower Deflections. Assuming that the tower was originally constructed with the needle beam assemblies as its primary support, we estimated the tower would deflect approximately 0.55 in. vertically under the full design loads (dead and live loads). We determined that 80% of the dead load was equivalent to roughly 65% of the full design load. Therefore, we estimated that if the needle beams and piles were pre-loaded to 80% of the dead load, they would deflect approximately 0.3 in. Under these conditions, in the event that timber pile deterioration

continued and the remaining 35% if the design load was transferred to the needle beams and piles, the post-underpinning tower deflection should not exceed about 0.25 in.

For the timber pile and needle beam models, we determined the overall angular distortion of tower and apse structures by comparing the lateral deflections at the top and bottom of each structure loaded under dead load, live load and snow load. The distortions and angular rotations are comparable in each case.

Micropile Design. The calculated maximum micropile demand was approximately 97 kips. We designed pressure-grouted micropiles with an outside diameter of 7 in., a design factor of safety of equal to 2, and an ultimate soil-grout bond capacity of 2.5 tsf in the sand and gravel stratum. We designed micropiles with a bond length of 22 ft for an allowable capacity of 100 kips (Type I) and with a bond length of 11 ft for an allowable capacity of 50 kips (Type II).

Masonry Testing. During the wall coring required for needle beam installation, the existing wall would be supported by a series of piers between the needle beam openings. Our analysis indicated that the maximum masonry wall compressive stress at the brick masonry piers (395 psi) was greater than the allowable stress typically attributed to similar masonry of this vintage (250 psi). The strength of the brick was critical in confirming that the load path was adequate during the needle beam installation. In order to verify the allowable stress for the existing tower masonry walls, we obtained masonry prism samples and performed compressive strength testing. The strength testing indicated the tower masonry had an ultimate compressive strength of 2,000 to 4,000 psi. Therefore, the allowable compressive stress ranged from approximately 450 to 900 psi and exceeded the maximum calculated compressive stress.

Service Life. The owner requested a service life of 500 years. We utilized a cathodic protection system for all of the steel installed. This required welding all of the casing together, welding the casing to the pile top plates, welding the top plates to the needle beams, and verifying that the micropile center bar fully contacted the micropile top plates. The life expectancy of the installed anodes is greater than or equal to 200 years. Therefore, to achieve the 500 year service life, the anodes will need to be replaced at least twice.

Engineer-Contractor Collaboration during the Design Phase. During the early stages of the design process, we regularly interacted with the contractor. We collaborated to identify construction related issues that could be accommodated for in the design, and we assisted the contractor to identify limitations or difficulties with their proposed construction methods. Examples of some of the collaboration efforts included:

- The design required that installation of the needle beam and pile assemblies through the tower foundation walls and the preloading be phased to limit the stress concentrations on the remaining portions of the foundation walls. The contractor requested that we allow for all of the needle beam pockets to be cored/cut at the same time to expedite the schedule. We developed simplified models to demonstrate that the wall openings needed to be sequenced as the remaining “piers” between the needle beam pockets would be inadequately sized to support the tower. Ultimately we developed an installation and preloading sequence that allowed the contractor to core/cut a certain number of non-contiguous needle beam pockets in series. Installation and preloading of the needle beam and pile assemblies in each series group would be performed at the same time. This

allowed the contractor to reduce the construction schedule without compromising the integrity of the existing structure.

- The contractor proposed achieving the preloading of the piles by installing the jacks atop each micropile and reacting against the needle beams, rather than reacting against the foundation walls. Preloading the piles directly required installation of a steel plate and bearing grout pad between the top surface of the needle beams and the bottom of the top surface of the needle beam pockets in the foundation walls. To evaluate the efficiency of the load transfer with this configuration, we developed a simplified model of the steel plate and bearing grout pad between the needle beam assembly and masonry wall. Based on the results of this model, we determined that the load would not be adequately transferred to the piles using the contractor's proposed jacking scheme, and we recommended that the contractor perform the jacking as originally specified.
- We updated the construction drawings and micropile layout based on the as-built timber pile and pile cap locations observed during cut-and-post underpinning phase of construction.
- The contractor proposed utilizing a concrete transfer beam that would support the needle beams and connect all the micropiles along each side of the foundation walls. This would allow the contractor more flexibility with the pile locations as the needle beams would not need to line up with micropiles on each side of the wall. We performed an analysis and design of a concrete transfer beam to support the needle beams. Ultimately, we did not recommend the use of a concrete transfer as it could cause an overloading of piles.
- We performed a study of the fire-resistance of the proposed structural steel elements and provided recommendations on how to achieve code-required fire rating of the steel elements.

CONSTRUCTION PHASE

Construction Considerations. Prior to pile installation, the contractor performed slab cores and excavated 2 – 3 ft below the slab at each of the pile locations to identify conflicts or obstructions. We found several locations where existing piles or granite pile caps interfered with the proposed pile location. Since we performed this work prior to construction, we modified the location of the piles and needle beams as needed. In most cases, we moved the piles away from the wall, since this is where the existing timber piles were concentrated. As the needle beam length increased, we modified sizes as needed to provide adequate strength or limit deflections.

Access to the tower base was limited with only crawl spaces and narrow doorways providing pedestrian access. The limited height dictated the equipment to be used and the casing lengths needed to be used to advance the micropiles. 3 ft long casing was used for the majority of the production piles, with 2 ft casing being used at locations with the least headroom. The drill rig had a mast height of approximately 98 in., which is among the shortest drill rig masts available for this application. Since this was an indoor application, we required that the drill power pack be located outside the building. . In order to get the pile rig into the space, the contractor hoisted the rig through a plaza level window into the bathroom adjacent to the tower, see Photo 3. The contractor shored the existing, elevated clay masonry floor with shoring posts in the crawl space below the floor to support the rig, see Photo 4. In addition to getting the equipment into the space, some of the needle beams weighed up to 1,900 lbs and could not be

carried in by the contractor. The contractor installed a crane rail, supported by the existing steel framing, to hoist and lower the equipment as needed.



Photo 3: Micropile drill rig hoisted through window into the bathroom.



Photo 4: Shoring posts installed below bathroom along path of rig travel.

The access and clearance constraints resulted in some special conditions. At the northwest corner of the tower, height constraints on each side of the west wall required that we provide an assembly that differs from the typical needle beam assembly. East of the west wall, there is an archway opening that is approximately 5 ft in height, restricting drill rig access; we therefore proposed a pile be installed on each side of this opening. West of the west tower wall there was no access to the crawl space below the elevated floor slab; we therefore required that the piles on the west side of the west tower wall be drilled from the bathroom floor above the crawl space. We proposed an “H-shaped” assembly that consists of one beam that is passed through and supports the west wall and is supported by two support beams. The two support beams are supported by two piles each (see Figure 4).

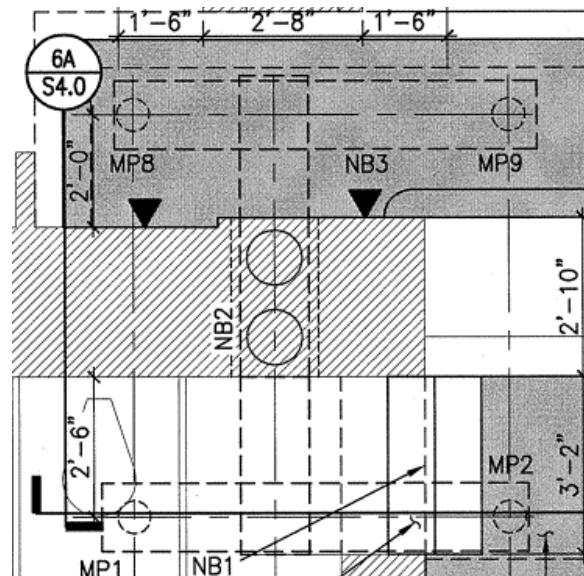


Figure 4: H-Shaped Needle Beam Assembly

Micropile Load Testing. The contractor conducted a load test on a 100 kip pile (Type I) with our oversight. The pile was instrumented with strain gauges along its length, tell tales at various elevations, and displacement gauges. Based on the load test results, we determined that the ultimate capacity of the Type I pile was approximately 180 kips. Although this was less than the ultimate calculated capacity, this ultimate pile capacity provided a factor of safety of 1.86, which we considered adequate.

Movement Monitoring during Construction. We performed movement monitoring on a weekly basis, or more frequently based on specific site conditions, to detect potential vertical and horizontal movements during repairs. The movement-monitoring program included displacement monitoring points (DMPs) located at the plaza level and on the TOMC structure at the basement level, vibrating-wire tiltmeters (tiltmeters), vibrating-wire crackmeters (crackmeters), and the LVDT, all located at the TOMC tower. Only minor settlement ($< 1/8$ -in.) occurred during construction, and provided positive real-time feedback on the design and construction approach.

CLOSING REMARKS

Since the completion of the underpinning project in 2010, annual movement monitoring surveys have indicated little to no continued movement of the structure and visual observations indicate no additional distress. A groundwater recharge system was put into operation at TOMC in 2013 to maintain the groundwater levels above the tops of the remaining timber piles.

The success of this project was in large part the result of extensive collaboration between the owner, contractor, and engineer. Due to the sensitive nature and historical importance of this structure, proper planning and coordination allowed for a flexible design that was able to accommodate modifications during construction resulting from differing site conditions.

Augered Cast-in-Place Pile Foundation Design and Construction for the MLK Bridge, New Stadium Project, Atlanta

Graham Elliott, Ph.D., P.E., M.ASCE, C.Eng., MICE¹; Natale Marini, MSCE, P.E.²; Matthew Meyer, P.E., D.GE, M.ASCE³; and W. Morgan NeSmith, P.E.⁴

¹WSP Parsons Brinckerhoff, 3340 Peachtree Rd. NE, Atlanta, GA 30326. E-mail: elliottg2@pbworld.com

²WSP Parsons Brinckerhoff; presently, HNTB, 3715 Northside Pkwy NW #600, Atlanta, GA 30327. E-mail: nmarini@hntb.com

³Langan Engineering and Environmental Services, Inc., Parkside Corporate Center, 15150 NW 79th Court, Suite 200, Miami Lakes, Miami, FL 33016. E-mail: mmeyer@langan.com

⁴Berkel & Co. Contractors, Inc., 7300 Marks Ln., Austell, GA 30168. E-mail: mnesmith@berkelapg.com

Abstract

Augered cast-in-place (ACIP) piles were installed for an elevated roadway in the City of Atlanta, as part of the infrastructure improvements for a new stadium project. The design-build project team opted to support the continuous span bridge on groups of 610 mm diameter ACIP piles, principally to avoid noise and vibration issues in the downtown environment. The ground conditions comprised a sequence of fill, Piedmont residual soil and partially weathered rock (PWR), overlying precambrian metamorphic rocks. Results of two instrumented static load tests on non-production piles demonstrate the axial loads are transferred principally in shaft resistance. Mobilized unit side resistance values of 73 kN/m² in the Piedmont residual soil and 199 kN/m² in the PWR were derived from strain gauge arrays. For production piling, confirmation of the embedment lengths and grout volumes were key quality control parameters, verified during construction with automated monitoring equipment (AME).

INTRODUCTION

This paper presents details of the use of augered cast-in-place (ACIP) piles for a new elevated roadway in the City of Atlanta. The new bridge supports MLK Jr. Drive over Mangum Street on the south side of the new stadium (Figure 1). The infrastructure was required to improve the east-west commute routes.

Although ACIP piles are a common deep foundation type for buildings in the south eastern USA (e.g. Hebner 2003; NeSmith 2003), their use as foundations for bridges is rare, despite FHWA guidance published a decade ago (Brown *et al.* 2007), seminal work on this pile type published over twenty years ago (Fleming 1995, DFI 1990) and the original patent and subsequent licenses for this pile type being granted in the United States in the late 1950's. Local practice on highway bridges is to use driven H piles and drilled shafts. ACIP piles were selected here primarily to avoid noise and vibration issues and to achieve some economy, as the pile type was also being used for the adjacent parking deck. The results of two instrumented static load tests on non-production ACIP piles at the bridge site described in this paper provide insights into mobilized unit side resistance values for ACIP piles in Piedmont residual soil and partially weathered rock (PWR).

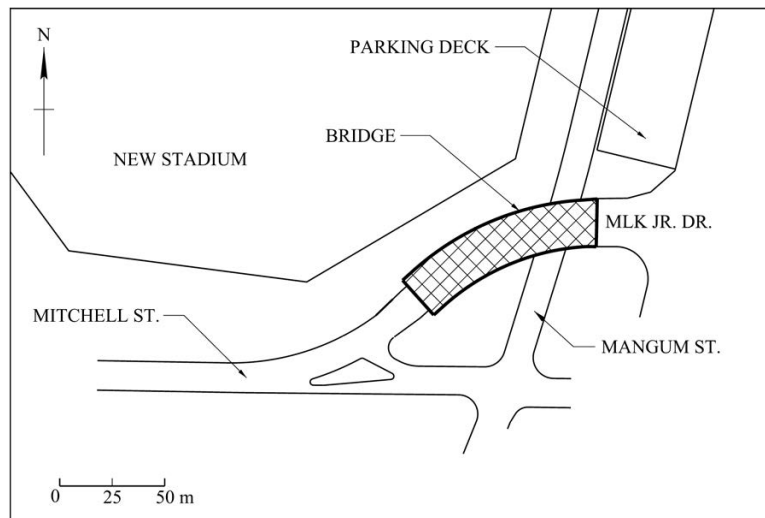


Figure 1. Location plan.

BRIDGE STRUCTURE

The curved bridge comprises seven steel girders in continuous span across three bents (Figure 2). The width of the bridge is 22.27 m (outside edge to outside edge). The total length of the bridge along the profile grade line is 94.72 m. The span from Bent 1 to Bent 2 is 46.86 m in length and the span from Bent 2 to Bent 3 is 44.38 m. From the center of the Bent 3 cap, the girders cantilever 3.48 m to join with the existing elevated roadway structure. The minimum vertical clearance over Mangum Street is 5.64 m. Bent 1 is supported on a row of seven ACIP piles joined in a bent cap on which the girders are seated, and the piles are encapsulated by a mechanically stabilized earth (MSE) wall. At Bent 2, two reinforced concrete piers are each founded on a group of nine ACIP piles in a 3 x 3 rectangular arrangement, spaced at 3 and 4 pile diameters. The two reinforced concrete piers at Bent 3 are each supported on a group of six ACIP piles, in a 3 x 2 arrangement spaced at 4 and 4.25 pile diameters. The cast in place concrete deck carries two lanes in each direction and two sidewalks. A new storm water cistern and pump house was constructed beneath the bridge. This required an excavation of about 6 m below the existing grade of Mangum Street, that was supported by a soldier pile and lagging wall with tieback anchors.

GROUND PROFILE

The ground profile is a sequence of fill, residual soil and PWR overlying Precambrian metamorphic rocks, typical of Atlanta. The residual soil consists of silty sands, sandy silts and clayey silts with mica. With increased depth the residual soils retain relict structures from the parent materials in an intermediate zone or 'saprolite', that grades into PWR. The contacts are gradational and highly variable, typical of the Piedmont Physiographic Complex (see Sowers and Richardson 1983). Eight standard penetration test (SPT) borings were drilled at the bridge site (Figure 2). A synthesis of the SPT N-values from all borings exhibited wide scatter, typical of Piedmont soils. Design of the foundations was therefore done using borings on a bent specific basis. Defining PWR as material with an N-value greater than 100 (see Sowers and Richardson 1983), the top surface of the PWR varied by about 13 m across the bridge from Bent 1 to Bent 3.

The depth to sound competent rock was highly variable. It was encountered at Bent 1, but not at Bent 2 or Bent 3 within the depth of the borings drilled at these respective locations. Hard zones in the PWR were found, that caused auger refusal and a switch to coring, but the core recoveries in these zones were zero. The SPT N-values corresponding to the depths below the top of the two test piles are presented in Figure 3, for borings in the vicinity of Bent 1 (4 borings near test pile CB-1) and at Bent 2 (2 borings near test pile CB-2). Groundwater was encountered in the residual soil at 3.9 m below the top of test pile CB-1 and at 5.2 m below the top of test pile CB-2. Figure 3a shows that at CB-1, the top of PWR was encountered at a depth of approximately 15 m below the top of test pile, with a distinctive break to higher N-values. The ground profile at CB-2 was far more variable. Although hard zones were encountered within the borings at around 13 m below the top of the pile, with SPT N-values greater than 100, the top of the PWR was not well defined and competent rock was not encountered despite the test pile being 33.5 m in length. N-values greater than 100 are plotted on Figure 3 at a value of 100 for simplicity.

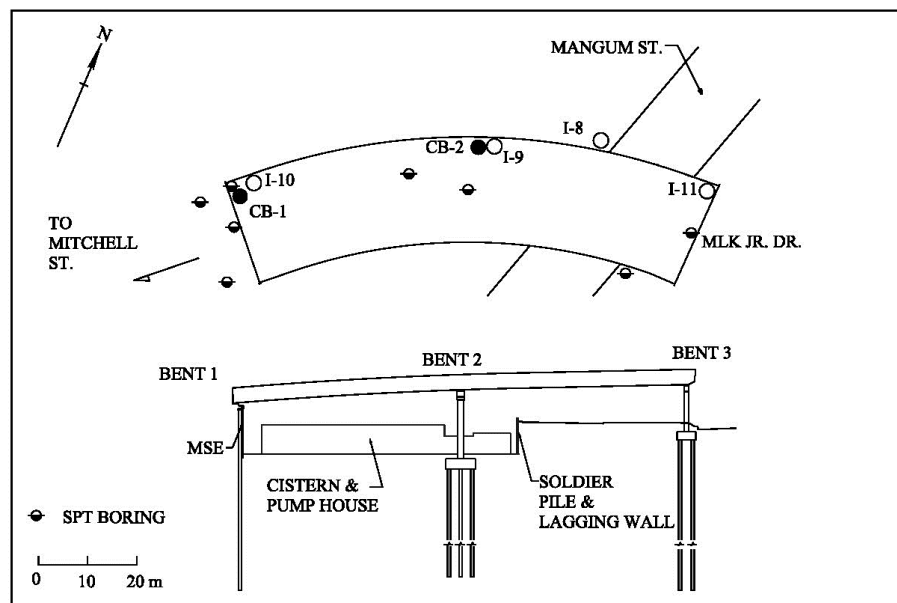


Figure 2. Bridge plan and profile, with locations of borings, test piles and indicator piles.

TEST PILE INSTALLATION

To justify use of ACIP piles for the bridge on this project, satisfactory load deflection performance had to be demonstrated on two instrumented non-production test piles. To demonstrate constructability in the variable ground profile, four non-production ‘indicator piles’ were also required (see I-8 through I-11 on Figure 2). Two installation criteria were developed. Criterion 1 was defined as installation of the pile through residual soil and PWR, with refusal on competent rock. Criterion 2 was defined as embedment of the pile in PWR only, without bearing on competent rock. All piles (including production piles) were installed with measurement of drilling parameters using Automated Monitoring Equipment (AME). The AME logs provide near continuous records of penetration rate, rotation speed, hydraulic fluid pressure on the turntable driving the auger rotation (known as KDK pressure), auger withdrawal rate, and grout

flow rate. Select output parameters from the AME records for the test piles are presented in Figures 4 and 5. Figure 4 shows that the penetration rate of the auger reduces below a depth of 15 m in test pile CB-1, which corresponds to the top of the PWR. The KDK pressure increases in the PWR. The penetration rate reduces significantly at the termination depth, indicative of refusal on competent rock (Criterion 1). In contrast, Figure 5 shows a steady KDK pressure through most of the drilling at test pile CB-2. The penetration rate declines steadily without a sharp break, consistent with refusal Criterion 2. A summary of the installation parameters for the two test piles and four indicator piles is presented in Table 1.

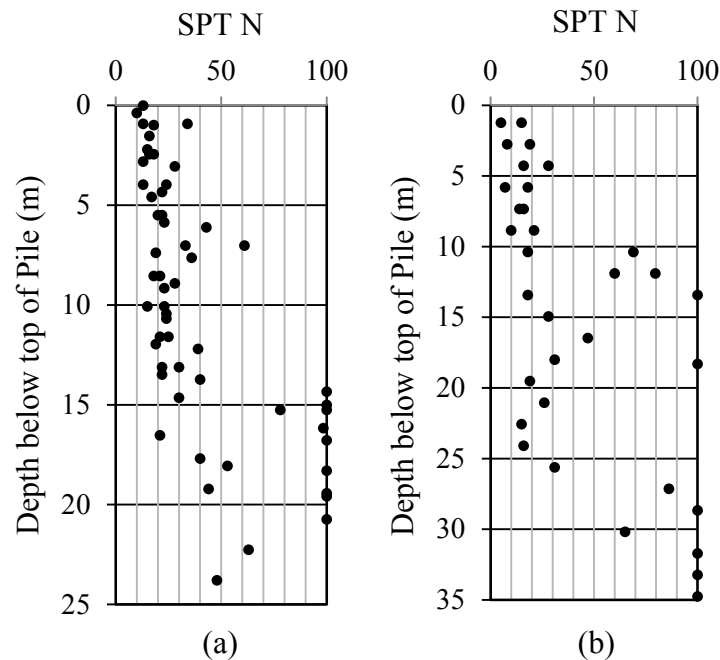


Figure 3. SPT N-value vs. depth below top of test pile: (a) CB-1 and b) CB-2.

Table 1. Summary of test pile and indicator pile construction.

Pile ID	Drilling Time (mins)	Pile Length (m)	Refusal Criterion	Grout Factor (%)	Grouting Time (mins)
CB-1	8	22.4	1	126	7
CB-2	12	33.5	2	123	10
I-8	18	45.7	2	122	15
I-9	18	45.0	2	122	12
I-10	17	33.7	1	122	11
I-11	26	45.8	2	129	13

Figures 4 and 5 also show the grout flow rates. From these data, incremental grout factors were computed for each 1.5 m depth in the piles. The grout factor is the ratio of grout volume injected to the theoretical cylinder volume of the pile. Fleming (1995) recommended that a grout factor in the order of 120 percent be achieved, and this is supported by Brown *et al.* (2007). This

overall grout factor was achieved in all the test piles and indicator piles (Table 1), although some incremental grout factors per 1.5 m depth interval were below 120 %. This prompted adjustments to the grouting procedures for the production piles. The grout used for the test piles was designed to achieve a minimum unconfined compressive strength of 45 N/mm² at 28 days and it included additives to enhance flow and reduce bleed.

STATIC LOAD TESTS

Test pile CB-1 was loaded in accordance with “Procedure A: Quick Test” per ASTM D1143 with a maximum test load of 8900 kN (Table 2 and Figure 6a). Given constraints with the adjacent soldier pile and lagging wall supporting Mangum Street, the reaction pile system at CB-2 could not achieve the desired maximum test load. Test pile CB-2 was therefore loaded to twice the design load and then held in accordance with “Procedure B: Maintained Test”. An unload and reload loop was then performed with a subsequent overload to a maximum test load of 8001 kN, in accordance with “Procedure C: Loading in Excess of Maintained Test” (Table 2 and Figure 6b). As well as verifying the axial load capacity of the tests piles, confirmation of the load transfer mechanism was achieved using arrays of sister bar strain gauges fixed to the center reinforcing bars at intervals throughout both test piles.

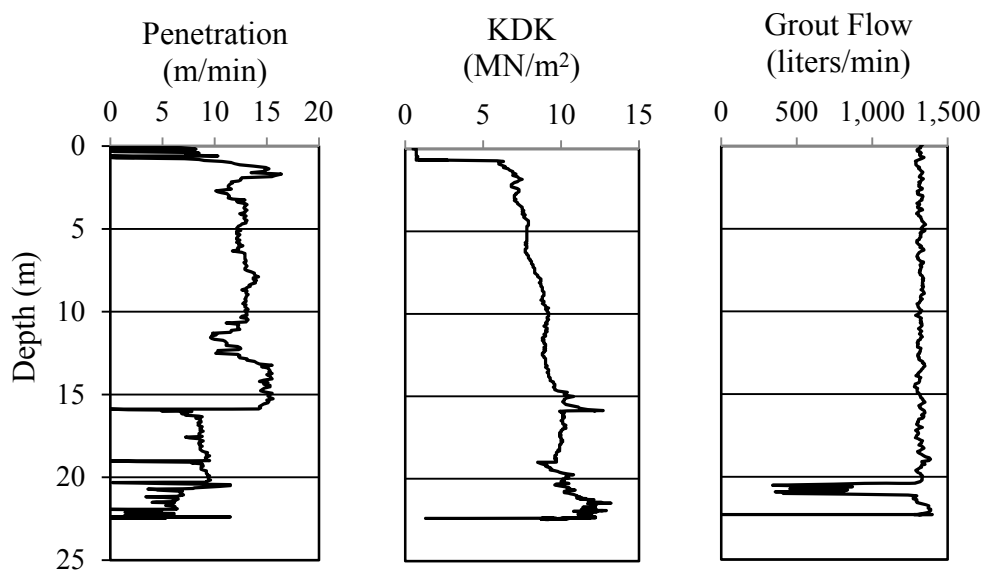


Figure 4. AME data for test pile CB-1 at Bent 1.

The Geotechnical Ultimate Limit State (GULS) of an ACIP pile is typically defined as a pile head deflection equivalent to 5 % of the pile diameter (Brown et al. 2007). For 610 mm diameter ACIP piles, the GULS is therefore defined as a pile head deflection of 30.5 mm. Table 3 and Figure 6 show neither test pile reached this condition, although CB-2 approached it with a deflection of 4.4 % of the pile diameter. At the design load (DL), both test piles exhibited satisfactory behavior with less than 6 mm of pile head deflection. Reduction of the strain gauge data is presented in Figure 7. These data demonstrate that the load is carried principally on the pile shafts in side resistance, irrespective of the refusal criterion. At the maximum test load

(Table 2) the proportion of load carried on the shafts, evaluated from the strain gauges, was 73 % and 90 % for test piles CB-1 and CB-2 respectively.

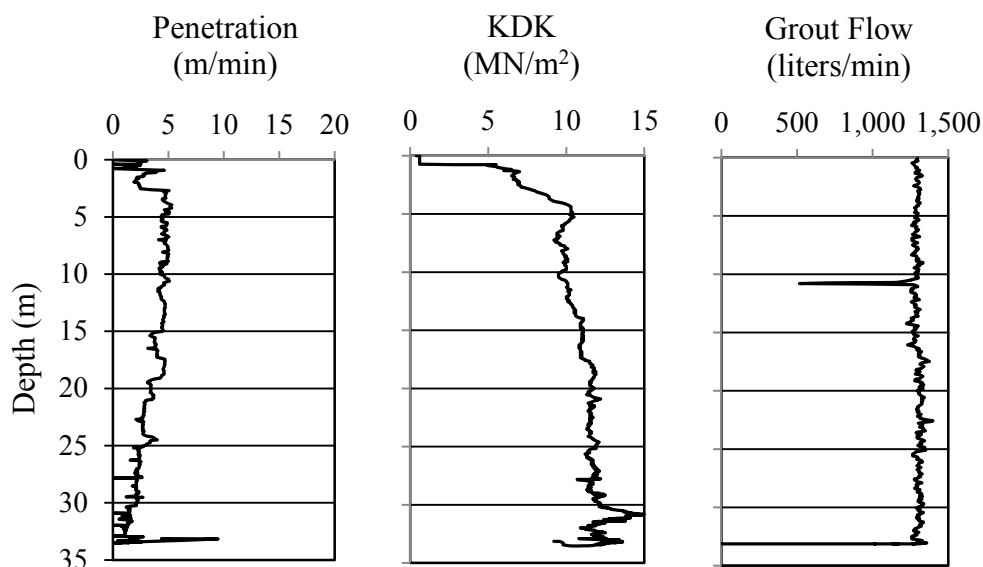


Figure 5. AME data for test pile CB-2 at Bent 2.

Table 2. Summary of pile head vertical deflection

Pile ID	Design Load (kN)	Max. Test Load (kN)	Pile Head Deflection (mm) at Load		
			DL	2DL	MTL
CB-1	3338	8900	4.5	11.9	18.2
CB-2	3338	8001	5.9	19.7	26.8

DL = design load; MTL = maximum test load.

Given that test pile CB-2 approached a pile head deflection close to 5%, the strain gauge data from this pile are instructive, because it is reasonable to conclude that the shaft side resistance was approaching fully mobilized values within the shallower subsurface materials and mobilized values at deeper depths. Strain gauges SG1 through SG3 (Table 3) are located in a depth range commensurate with the residual soil. From Figure 7b, the proportion of the maximum test load carried over this depth interval (18.3 m) was 2.55 MN. This equates to a mobilized unit side resistance of 73 kN/m². Strain gauges SG4 through SG8 (Table 3) are located in a depth range commensurate with PWR. The proportion of the maximum test load carried on the shaft over this depth interval (12.2 m) was 4.65 MN. This equates to a mobilized unit side resistance value of 199 kN/m².

The load from SG3 in pile CB-2 appears lower than it might actually be. The pile is transitioning from residual soil to PWR at this depth, with a possibility of a small change in diameter. A change in diameter will impact the magnitude of load derived from the strain gauge.

The mobilized unit side resistance values compare favorably with those found for conventional drilled shafts constructed in Piedmont soils under bentonite and polymer fluids (see Brown 2002). Mayne and Harris (1993) reported unit side resistance for a drilled shaft (test shaft

C2) constructed at the Georgia Institute of Technology campus. At failure, the unit side resistance was 66 kN/m^2 . Maximum unit side resistance values for another drilled shaft (test shaft C1) drilled at the campus did not reach failure, but a maximum unit side resistance value of 73 kN/m^2 was reported for the residual soil, and 234 kN/m^2 for the PWR which are similar to the values found for the ACIP test pile CB-2 at the bridge. Casing was not used for either of the test shafts C1 and C2. The campus site is about 1.6 miles north of the bridge.

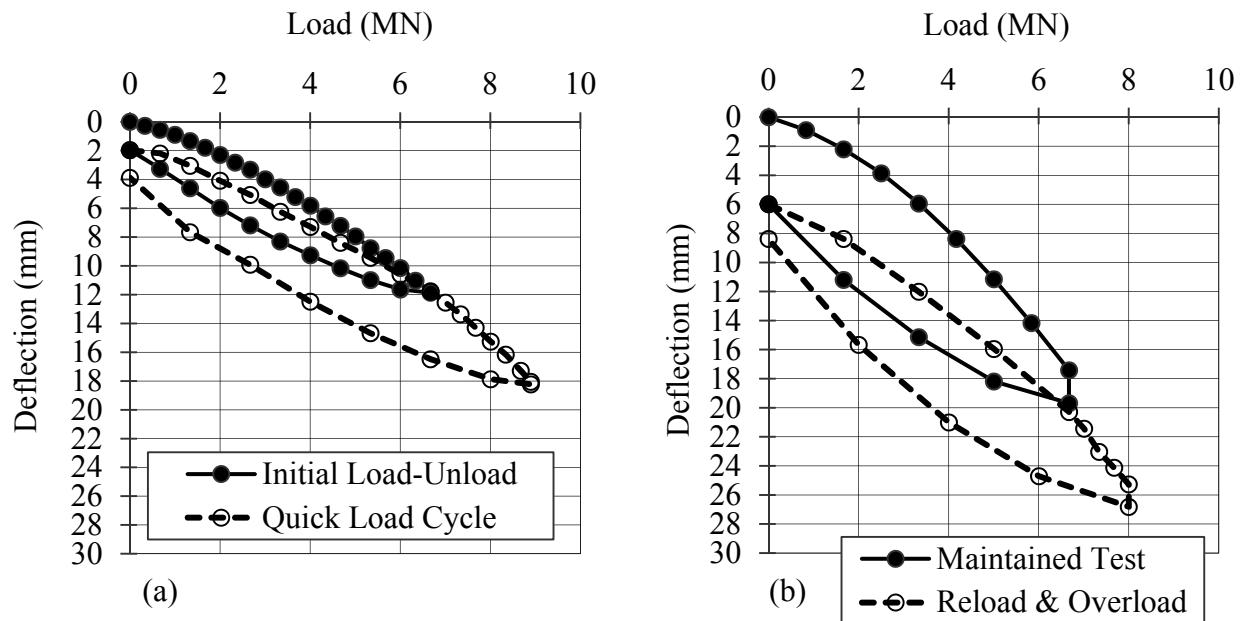


Figure 6. Load-deflection plot for compression load tests: (a) CB-1 and (b) CB-2.

Table 3. Depths of strain gauges below top of test pile.

Strain Gauge ID	CB-1	CB-2
	Depth below Top of Pile (m)	Depth below Top of Pile (m)
SG1	1.52	1.52
SG2	10.06	9.14
SG3	15.24	18.29
SG4	19.35	21.34
SG5	20.88	22.86
SG6	22.40	28.96
SG7	--	32.00
SG8	--	33.53

FOUNDATION CONSTRUCTION

The results of the test program enabled production piling to begin, that followed industry practice (DFI 2003, 2010, Brown *et al.* 2007). AME records for production piles showed auger penetration rates in the PWR of approximately 1.5 to 3 m/min. The required minimum compressive strength of the grout was 41 N/mm^2 . Reinforcement cages 10.5 m in length were lowered into the piles after grouting, and consisted of nine 25 mm diameter bars for longitudinal

reinforcement plus a 35 mm diameter center bar inserted to full depth as a quality control measure. Shear steel comprised 16 mm diameter bars. Pile cap construction required thermal controls, with hoses routed through the pile cap steel to enable circulation of cooling water during concrete hydration and curing.

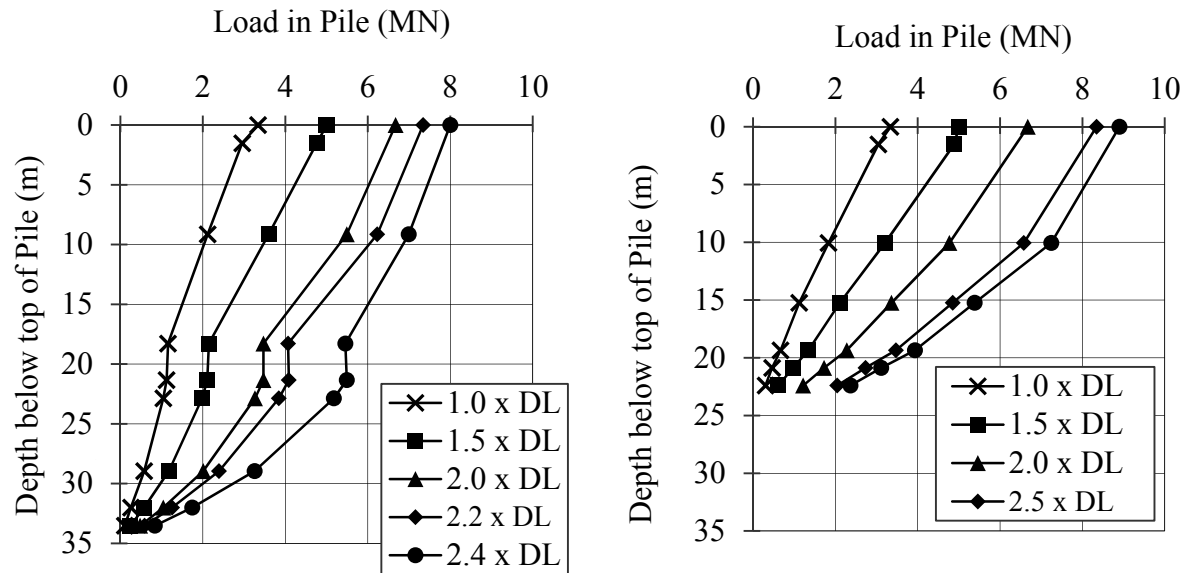


Figure 7. Load transfer from strain gauges in test piles: (a) CB-1 and (b) CB-2.

CONCLUSIONS

The data presented in this paper, together with the observations made during production piling leads to the following conclusions:

1. The ACIP piles in Piedmont residual soil and PWR are predominantly shaft controlled at the capacity and lengths tested for this project, with most of the load carried in side resistance.
2. Mobilized unit side resistance values in Piedmont residual soil and PWR were 73 kN/m^2 and 199 kN/m^2 respectively.
3. With careful application of AME during construction, coupled with static load testing, ACIP piles provide an alternative to conventional driven H-piles and drilled shafts for bridge foundations in the Piedmont geology. Where noise and vibration concerns occur in urban environments, ACIP piles offer benefits over driven piles, and their speed of construction provides advantages over drilled shafts.

ACKNOWLEDGEMENTS

Thanks are extended to Mr. B. Van Der Meer of the design build joint venture for permission to publish this paper. Mr. C. Dirton assisted with figure preparation. The structural engineering team was Mr. P. Austin, Mr. M. Fraker, P.E., Mr. D. Haxton, P.E., and Mr. S. Jarrett, P.E.

REFERENCES

- ASTM International (2013). "Standard Test Methods for Deep Foundations Under Static Axial Compressive Load." *Book of Standards Volume 04.08*, ASTM D1143/D1143M-07 (2013).
- Brown, D.A. (2002). "Effect of construction on axial capacity of drilled foundations in Piedmont Soils." *Journal of Geotechnical and Geoenvironmental Engineering*, 128(12), 967 – 973.
- Brown, D.A., Dapp, S.D., Thompson, III, W.R. and Lazarte, C.A. (2007). "Design and Construction of Continuous Flight Auger (CFA) Piles." *FHWA Geotechnical Engineering Circular, No. 8, FHWA-HIF-07-03*. U.S. Department of Transportation, Federal Highway Administration, Washington, D.C., pp.228.
- Deep Foundations Institute (1990). *Augered Cast-In-Place Pile Manual*. Deep Foundations Institute, Hawthorne, New Jersey.
- Deep Foundations Institute (2003). *Augered Cast-In-Place Pile Manual, Second Edition*. Deep Foundations Institute, Hawthorne, New Jersey.
- Deep Foundations Institute (2010). *Inspector's Guide to Augered Cast-In-Place Piles, Second Edition*. Deep Foundations Institute, Hawthorne, New Jersey.
- Fleming, W.G.K. (1995). "The understanding of continuous flight auger piling, its monitoring and control." *Proceedings of the Institution of Civil Engineers*, 113(3), 157 – 165.
- Hebner, G.C. (2003). "Local use and design of augered, cast-in-place piles in the Southern Piedmont Province." *Deep Foundation Institute Specialty Seminar - Augered, Cast-In-Place Piles Atlanta, Georgia, April 25, 2003*. 3 - 27.
- Mayne, P.W. and Harris, D.E. (1993) "Axial load displacement behavior of drilled shaft foundations in Piedmont Residuum." *FHWA Technical Report 41-30-2175*.
- NeSmith, W.M. (2003). "A History of the Use of ACIP Piles for Major Projects in Atlanta." *Deep Foundation Institute Specialty Seminar - Augered, Cast-In-Place Piles, Atlanta, Georgia, April 25, 2003*, 99 - 104.
- Sowers, G.F. and Richardson, T.L. (1983). "Residual Soil of the Piedmont and Blue Ridge." *Transportation Research Record*, No. 919. National Academy Press. Washington D.C., 10-16.

General Bearing Capacity Theory and Soil Extraction Method for the Mitigation of Differential Settlements

Rozbeh B. Moghaddam, P.E., Ph.D., M.ASCE¹; and Priyantha W. Jayawickrama, Ph.D., M.ASCE²

¹Dept. of Civil, Environmental, and Construction Engineering, Texas Tech Univ., 911 Boston Ave., Lubbock, TX 79409. E-mail: rozbeh.moghaddam@ttu.edu

²Dept. of Civil, Environmental, and Construction Engineering, Texas Tech Univ., 911 Boston Ave., Lubbock, TX 79409. E-mail: priyantha.jayawickrama@ttu.edu

Abstract

Differential settlements experienced by a number of historic monuments have been remediated using the soil-extraction method. Italy's *leaning Tower of Pisa* and the Mexico City's *Metropolitan Cathedral* are two well-known structures where the soil-extraction method was applied to address issues associated with differential settlements. This paper describes a case study for a seven-story building in Mexico City, where differential settlements generated vertical inclinations ranging from 241-mm (9.5-in) to 310-mm (12.0-in) to the north, and 70-mm (2.75-in) to 98-mm (3.9-in) to the east. For the remediation of these inclinations, the soil-extraction method was applied through rectangular cavities excavated underneath the foundation element. The general bearing capacity theory was used to determine the location and dimensions of these cavities. After finalizing the soil-extraction process, an average settlement and upward movement of 87-mm (3.5-in) and 24-mm (1.1-in) were recorded, respectively. After the completion of the soil-extraction process, all deformations were brought within tolerable limits specified by the local building code.

INTRODUCTION

This paper presents the work completed for soil-extraction method applied to a seven-story building located in Mexico City, Mexico. Furthermore, the general theory of bearing capacity and its application to the soil-extraction method is described. Finally, results from surveying and monitoring are presented and discussed.

Thick deposits of compressible clays, regional water extraction, and high seismic activity combined with pre-19th century historical monuments, have created a difficult and challenging environment for geotechnical engineers in Mexico City, (Ovando et al. 2001). From building inspections completed after the Mexico City 1985-earthquake, a significant number of buildings suffered differential settlements after the earthquake. However, a number of these structures did not surpass the serviceability criterion mandated by local codes, and continued service operations for years after.

A seven-story building lost its verticality during the Mexico City's 1985-earthquake and continued operations until 2005 when due to the regional subsidence, deformations exceeded the tolerable limit. Based on surveying and monitoring results, the building experienced differential settlements leading to vertical inclinations ranging from 241-mm (9.5-in) to 310-mm (12.0-in) to the north, and 70-mm (2.75-in) to 98-mm (3.9-in) to the east. To remediate differential settlements and further bring displacements within serviceability limits, the soil-extraction method was analyzed and implemented.

According to Ranzini (2001) most of differential settlements and the tilting of the structures built on shallow foundations, are closely related to the consolidation process of the soil layers beneath the foundation. Other factors such as shape of the structures, eccentricity in loading, groundwater extraction, and construction in the vicinity contribute to the consolidation creating settlements. Research studies and detailed analyses have been completed to create predictive models for these settlements and further minimize their impact on the serviceability of structures. Furthermore, research projects have been performed to study the remediation of differential settlements.

One method used in Mexico City during 1990s, was the soil-extraction method applied to the Metropolitan Cathedral. This method was first proposed by Fernando Terracina (1962) for stabilization of the Tower of Pisa, but for reasons outside of the scope of this paper, the process was not applied to the tilted monument. For the particular case of the Tower of Pisa, Terracina (1962) proposed the soil-extraction method based on the assumption that increasing pressure at the north end of the Tower, could relieve pressure at the south end of the Tower that suffered greater settlements. If this condition was achieved, then the tower's inclination as well as the pressures at the southern edge of the foundation will be reduced (Terracina 1962).

Mexico City's Metropolitan Cathedral. The construction of Mexico City's Metropolitan Cathedral was completed in multiple phases starting in 1573 and finishing in 1813. This heavy structure is located in downtown Mexico City and atop of Aztec's *Templo Mayor*, Figure 1. After conquering the *Aztec Empire*, Hernan Cortes and the Conquistadors started the construction of a church at the site of *Templo Mayor* using stones from a former Aztec temple to further consolidate the Spanish Power, (Santoyo et al. 2008). After additions and modifications, this initial church became the Metropolitan Cathedral and currently considered the *largest* Cathedral in the America, (Aguilera 2013). The heavy structure has suffered differential settlements mainly caused by Mexico City's subsidence and the consolidation of large compressible clays located underneath the structure.

During 1980s and 1990s, due to severe structural damage and the risk of losing a historic monument, a rehabilitation and restoration plan was presented to the Mexico City's government. During a surveying and monitoring project carried out from 1989 to 1990, the settlement rates and differential settlements were determined. After determining the final average annual settlement and the critical points throughout the Cathedral, Terracina's soil-extraction method was applied to the Mexico City's Metropolitan Cathedral starting in 1993. The process consisted of creating a series of radial 100-mm (4-in) diameter auger holes at different levels beneath the foundation system and completed from inside of vertical circular shafts installed throughout the Cathedral, Figure 2. These auger holes were eventually closed due to the clay's plastic flow, creating vertical displacements at the surface level.

Italy's Tower of Pisa. The construction of the eight-level Tower of Pisa with approximately 60-m (200-ft) in height started in 1173 with the belfry completed between 1360 and 1370. According to Salgado (2008), the foundation soil of the tower consisted of approximately 300-m (984-ft) of sediments deposited by *Arno River* and the Tyrrhenian Sea (dated back to the time when the sea on the west coast of Italy, reached the city of Pisa). Soil layers nearby the ground surface can be described as a 9-m (30-ft) thick silty-sandy soil followed by approximately 30-m (100-ft) of marine clay. Due to higher compressibility of the silt material located towards the

south of the tower, settlements were developed faster compared to the north end part of the tower, Figure 4 (a).

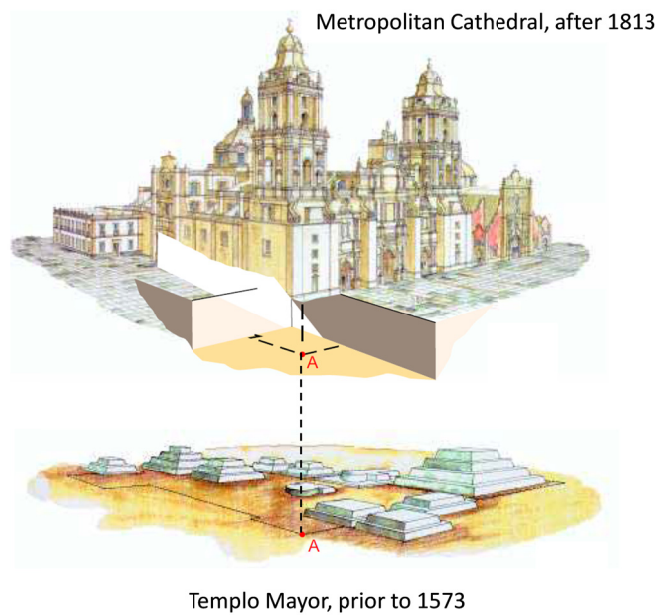


Figure 1. Mexico City's Metropolitan Cathedral atop of Aztec's Templo Mayor (Santoyo et al. 2008)

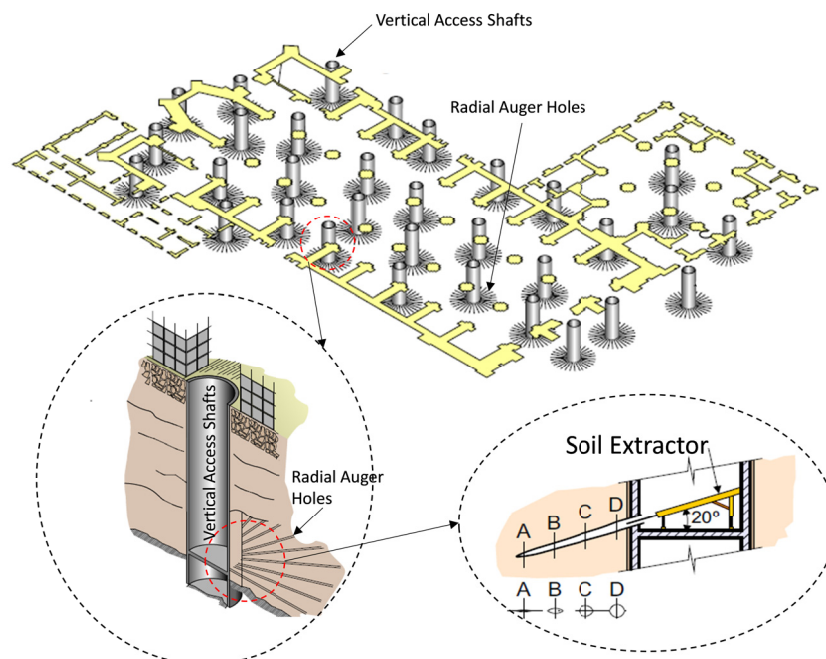


Figure 2. Soil-extraction method and details applied to Mexico City's Metropolitan Cathedral (Santoyo et al. 2008)

To prevent the tower to experience further settlements in the south and to preserve the historic monument, the soil extraction method was applied for the stabilization of the Tower of Pisa. The removal of volumes of soil from underneath of the foundation and took place at the north-end of the Tower, (Burland et al., 2002). The process consisted of drilling auger holes from the surface (Burland et al. 2009) with an inclination of 20° to 30° from the horizontal and extending to a maximum length of 22-m (73-ft), Figure 4. These dimensions located the cylindrical soil extractors at approximately 4.5-m (15-ft) below the center of the tower's foundation, Figure 3. This process did not *correct* the inclination of the tower but it did achieve the objective of the project which was the *stabilization* of the tower.

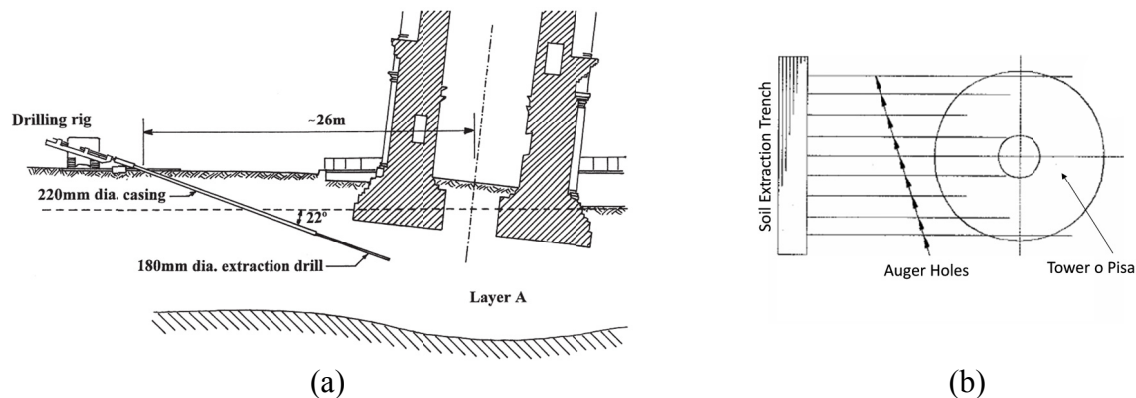


Figure 3. Soil-Extraction method applied to the Tower of Pisa (a) Section View, (Burland et al. 1998) and (b) Plan View (Terracina 1962)

CHARACTERISTICS OF THE BUILDING

The case study presented in this paper is for a seven-story building formed by reinforced concrete frames and slabs, constructed in a rectangular area of 488.0-m^2 (5253-ft^2), and supported by a reinforced concreted cell-foundation (i.e. compensated foundation). During the site reconnaissance the depth of foundation was measured at 2.23-m (7.30-ft) below the ground surface. According to structural information, the net pressure transferred to the foundation soil was approximately 60-kPa (1250-psf).

Results from surveying and monitoring prior to any work related to the rehabilitation of the structure showed that the differential settlements experienced by the building generated vertical inclinations which ranged from 241-mm (9.5-in) to 310-mm (12.0-in) to the north, and 70-mm (2.75-in) to 98-mm (3.9-in) to the east, Figure 4.

SUBSURFACE CONDITIONS

In addition to existing geotechnical information, one auger-boring (POS-1) and two test pits were completed to depths of 6.10-m (20-ft) and 2.0-m (6.6-ft), respectively. Disturbed and undisturbed samples were recovered and tested in the laboratory. According to field visual description and laboratory tests, the soil immediately beneath the foundation's bottom slab consisted of a light brown silty sand (SM) with an average water content of 25% which extended to a depth of 4.0-m (13.0-ft). Following the silty sand layer and with a thickness of 1.25-m (4.1-ft), a low to high

plasticity brown sandy silt (ML-MH) with 64% of fines, and average water content of 50% was encountered. A green to light gray sandy clay (CL) with an average water content of 70% was located between 5.25-m (17.2-ft) and the maximum depth of boring. From laboratory testing an average cohesion $c = 15$ kPa (317-psf), an angle of friction $\phi = 28^\circ$, and a unit weight of 16 kN/m^3 (102-pcf) were assigned to the material below the foundation's bottom slab.

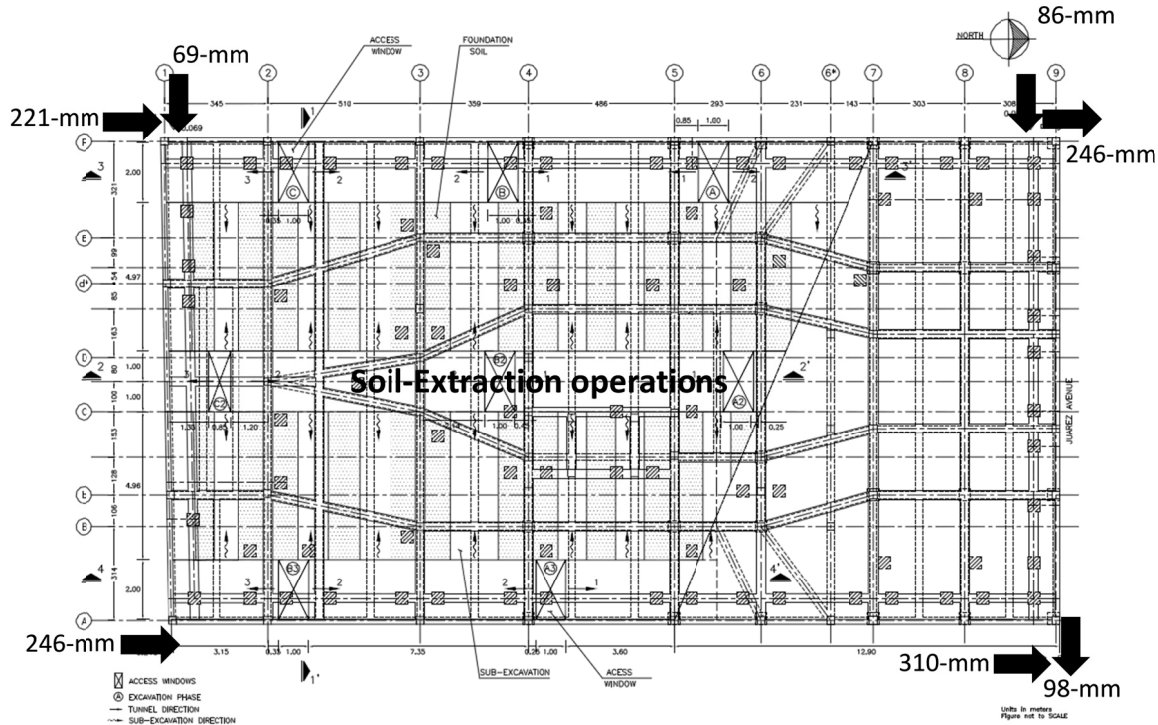


Figure 4. Vertical Inclinations recorded at each corner of the building

SOIL-EXTRACTION METHOD

Based on vertical inclinations of the building, it was determined that the soil-extraction operations will be conducted within the trapezoidal area representing approximately 2/3 of the total footprint area of the building, Figure 5. Considering that the tilting of the building was mainly towards northeast, it was reasonably assumed that increasing pressures in the south and southwest of the structure will create settlements and will reduce inclinations of the building registered at the north side of the structure. Basically, the objective of the soil-extraction operation was to create settlements in the south and southwest portion of the structure, and upward movements in the north and northeast of the building.

General Bearing Capacity Theory and soil-extraction. Terzaghi (1943) developed the ultimate capacity theory by demonstrating that for a loaded footing with width “B”, the failure surface beneath the footing is comprehended as a plastic equilibrium zone represented by the area “abcde” which was further divided into 3 main zones: Zone I. Triangular wedge under the foundation base, Zone II. Zones of radial shear intersecting the horizontal at angles $45^\circ - \phi/2$, and Zone III. Passive Rankine zones, Figure 5.

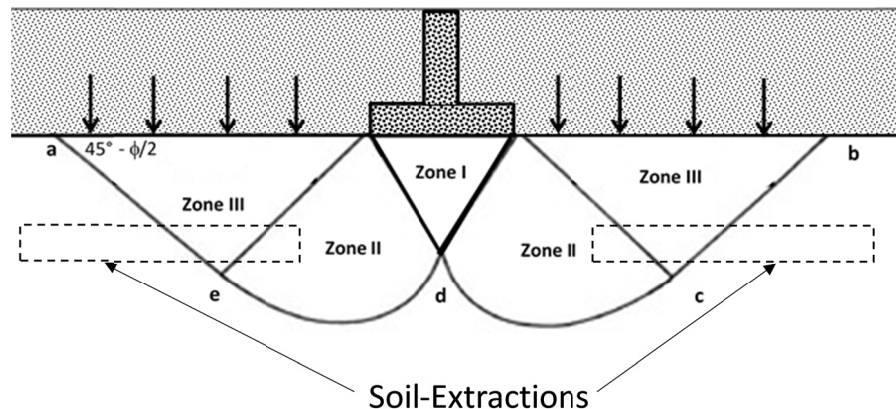


Figure 5. Schematics of Terzaghi's general bearing capacity theory.

Applying the theory of static equilibrium to the triangle wedge (Zone I), it is observed that for the Zone I to remain in equilibrium, the sum of vertical components of the resistances sourced to the shear strength parameters (c , ϕ) and the Rankine passive forces (P_{pn}), should be equal to the sum of the load applied to the foundation (P) and the weight of the soil wedge (W_w), Figure 7 (b). According to this, if any of the resistance sources is reduced to a level where the static equilibrium is no longer satisfied, then Zone I will have a downward movement creating deformations at the surface and the base of the foundation. It is reasonably assumed that by removing volumes of soil from zones II and III, Figure 6, the resultant force (P_p) shown in Figure 7, will be gradually reduced to a level where the static equilibrium is not satisfied, and Zone I will move downwards creating settlements at the surface.

The foundation of the building consisted of cell-foundation i.e., compensated foundation with top and bottom rigid slabs. The soil-extraction method was implemented beneath the bottom slab and to apply the general bearing capacity theory, it was reasonably assumed that the bottom slab consisted of a series of footings placed at a very close distance, and for each footing the Terzaghi's general bearing capacity theory would apply, Figure 8.

As previously discussed, by creating cavities (i.e. soil-extractions) within the zone of shear resistance (Zone II) and Rankine's passive resistance (Zone III), the static equilibrium for the soil wedge (Zone I) becomes unbalanced, and settlements are generated at the surface. Based on this approach, the soil-extraction method using the general bearing capacity theory was implemented for the project described in this paper.

Soil-Extraction construction procedure. Considering space limitation due to adjacent in-service buildings, the soil-extraction process was carried out from underneath the building. The process was completed in three phases: (1) Excavation of Access pits and Maneuver tunnels (2) Protection of the tunnel walls, and (3) excavation of cavities, i.e. soil-extractions.

As part of Phase (1), eight access pits were identified throughout the bottom slab and excavated to a depth of 2.0-m (6.5-ft). From each access pit, maneuver tunnels were excavated until convergence, Figure 9. Phase (1) and (2) were simultaneous activities, where the tunnel was excavated and the walls were protected. The protection system consisted of 70-mm (2.75-in) thick mortar shotcrete placed in two layers with a 6x6-6/6 wire mesh in between and reinforced with bracing systems comprising 100-mm×300-mm (4-in×12-in) wood beams placed vertically (similar to soldier piles) and braced with 100-mm (4-in) diameter struts in two levels, Figure 10.

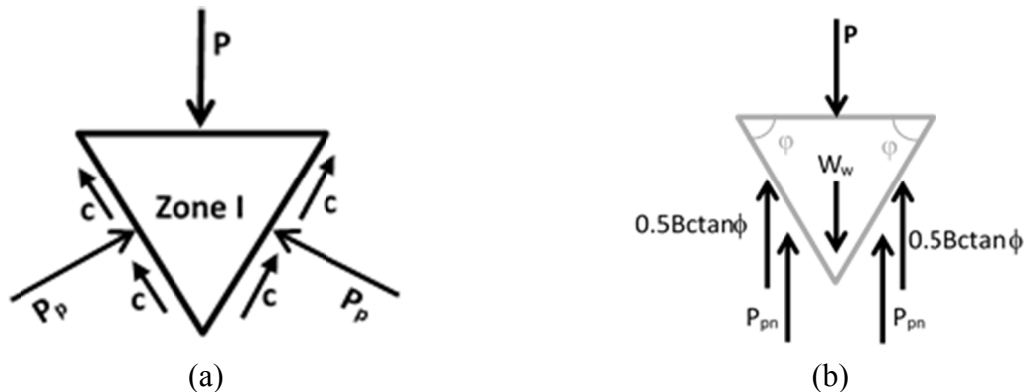


Figure 6. Free body diagram for Zone I (a) Resultant forces (b) Vertical components

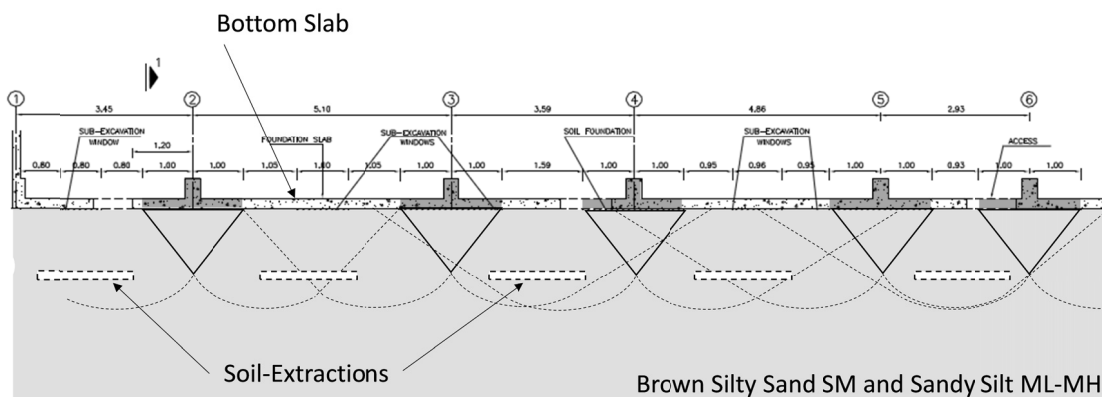


Figure 7. Bottom slab of the foundation hypothesized as a series of footings

MONITORING AND RESULTS

A total of 49 surveying points were marked and monitored during the sub-excavation process, and vertical displacements associated with the building were recorded daily. During the initial excavation process (Phase 1 and Phase 2), the building experienced an upward movement due to the soil's elastic response, Figure 11. The building presented an average upward movement of 12-mm (0.5-in) measured in a period of three months, with major concentration in the south and southwest of the structure. The upward movement gradually shifted to a settlement, after all soil-extraction cavities were completed. Maximum deflections recorded during the soil-extraction process are summarized in Table 1, and the monitoring plot corresponding to the two axes with major deflections are shown in Figure 11.

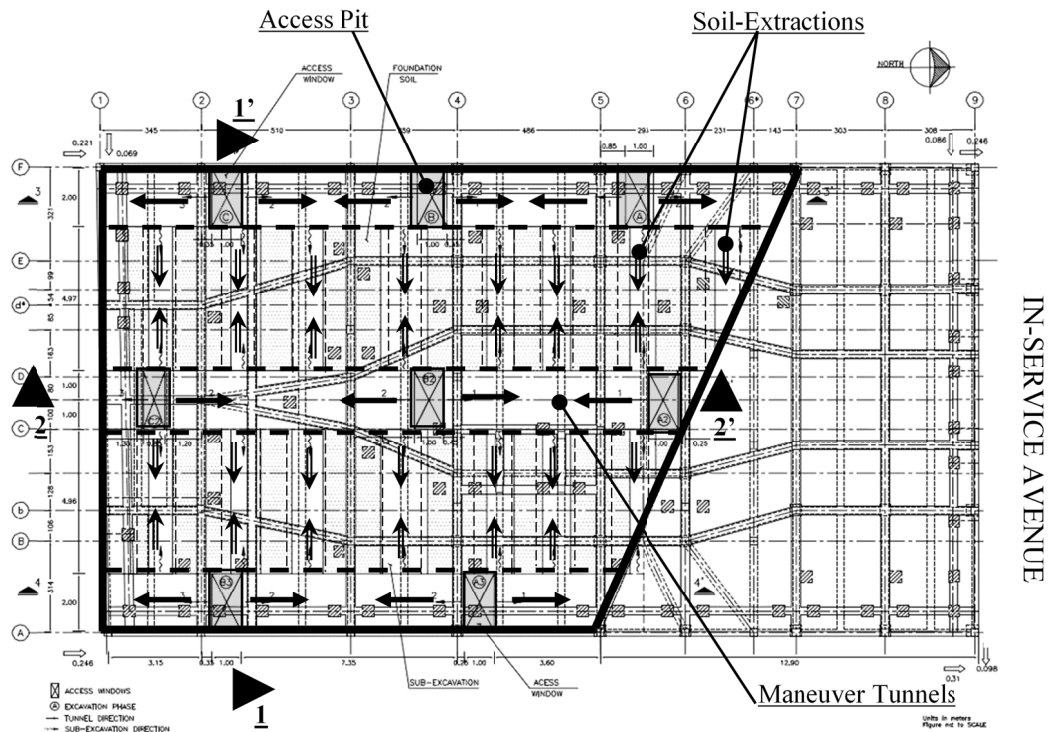


Figure 8. Access Pits, Maneuver Tunnels, and Soil-Extractions

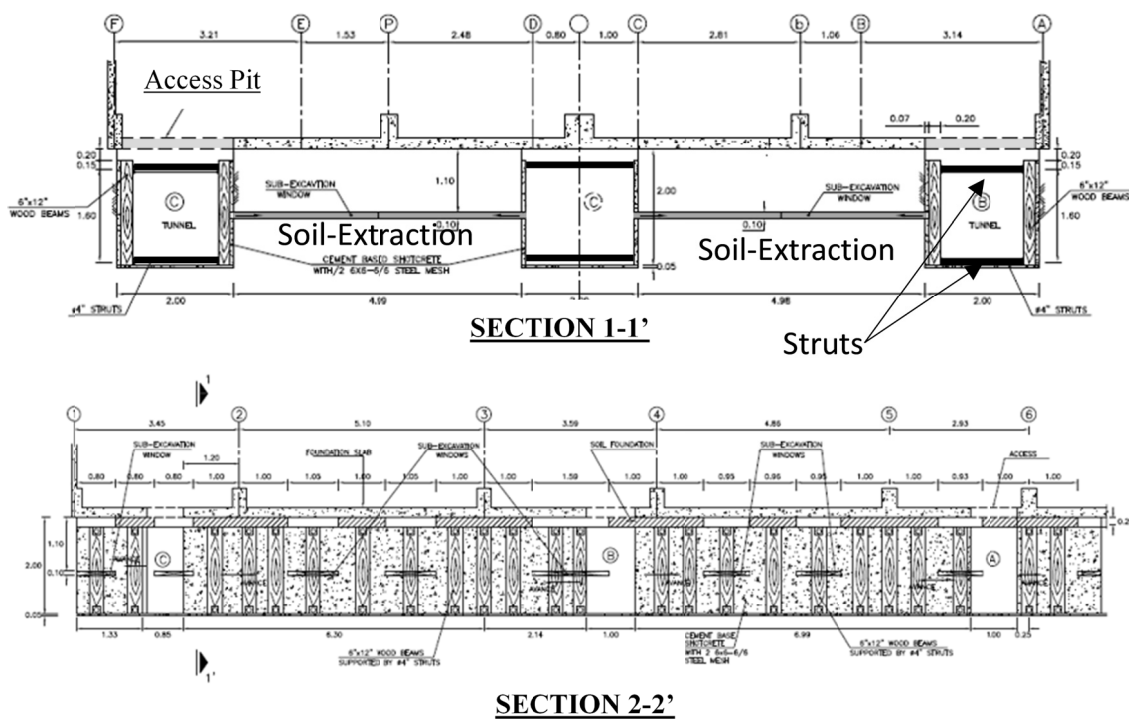
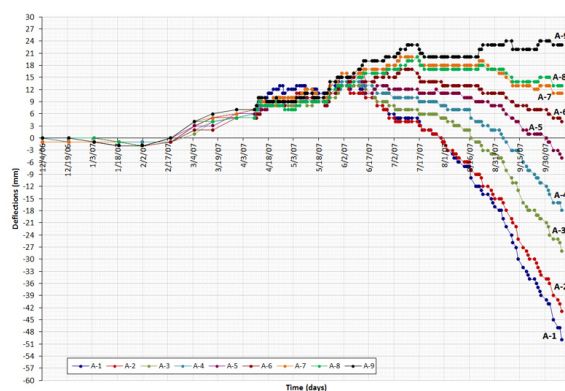


Figure 9. Section view of the soil-extraction process

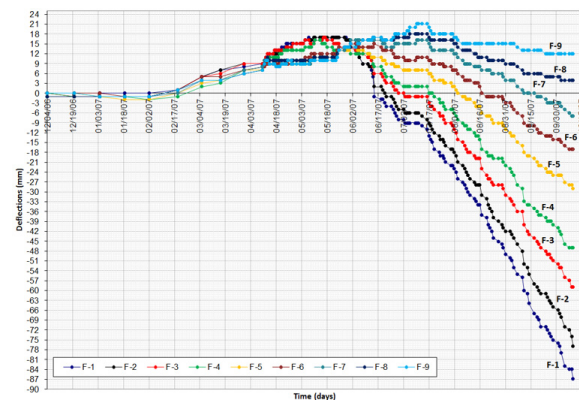
At the end of the soil-extraction process, 87.0-mm (3.5-in) settlement for point F-1 located at the southwest corner of the structure and 27.0-mm (1.10-in) upward movement for the point A-9 located at the northeast corner of the structure, were recorded. As it is noted in Table 1, all movements indicate a deflection pattern starting with major settlements in the south side of the structure (Figure 9-Points A-1 to F-1), and ending with slight upward movements in the north side (Figure 9-Points A-9 to F-9). From these movements and at the end of the process, the inclinations of the superstructure were within tolerable limits.

Table 1. Maximum Deflections recorded at each survey point

Axis	Deformations (mm)	Axis	Deformations (mm)
A-1	- 50	D-3	-46
A-9	+22	D'-6	-10
B-3	-35	d-1	-82
B-6	+1	d'-9	+17
b-1	-61	E-3	-51
b'-6	+17	E-6	-12
C'-2	-58	F-1	-87
C'-9	+18	F-9	+12



(a)



(b)

Figure 10. Monitored Settlements for (a) Axis A and (b) Axis F

SUMMARY AND CONCLUSIONS

This paper presented the case of seven-story building which lost its verticality after Mexico City's 1985 earthquake with the vertical inclinations surpassing the tolerable limits in 2005. For the rehabilitation and stabilization of this building and its associated vertical inclinations, the soil-extraction method was proposed and implemented.

Due to space limitation and adjacent structures, the soil-extraction method was not implemented using auger holes and drilling operations. Instead of generating plastic flow in the material beneath the foundation through circular auger holes, the general bearing capacity theory was used to determine the location and dimensions of the soil extraction cavities excavated in rectangular shapes. The soil-extraction process was completed in three main phases where the access pits and maneuver tunnels were excavated followed by the protection of the tunnel walls, and finally the excavation of the soil-extraction cavities.

Results from monitoring and surveying showed that at the end of the soil-extraction process, a total of 87.0-mm (3.5-in) settlement for point F-1 located at the southwest corner of the structure and 27.0-mm (1.10-in) upward movement for and point A-9 located at the northeast corner of the structure were recorded.

Soil-extraction method and its application to leaning structures requires careful monitoring and rigorous engineering analyses, prior and during the process. The soil-extraction method was successfully implemented for the project presented in this paper and at the end of the soil-extraction process, the building's deflections were brought within tolerable limits. Furthermore, this study confirms the shear zone and Rankine's passive zone, outlined in the general bearing capacity theory, can be weakened by manipulating these zones.

REFERENCES

- Aguilar J. P. (2013) "Catedral Metropolitano, Hundimiento y Rescate-Metropolitan Cathedral, subsidence and Rescue", Instituto de Ingenieria de la Universidad Autonoma de Mexico (UNAM), 1st Edition, UNAM
- Burland, J. B., Jamiolkowski, M. B., & Viggiani, C. (2009) "Leaning Tower of Pisa: Behavior after stabilization operations" *International Journal of Geoengineering Case Histories*, 1, 156-169
- Burland, J., Jamiolkowski, M., & Viggiani, C. (2002) "Preserving Pisa's treasure" *Civil Engineering*, 72(3), 42-49
- Ovando-Shelley, E., & Santoyo, E. (2001) "Underexcavation for leveling buildings in Mexico City: case of the Metropolitan Cathedral and the Sagrario Church" *Journal of architectural engineering*, 7(3), 61-70
- Ranzini, S. M. T. (2001) "Stabilisation of leaning structures: the Tower of Pisa case" *Geotechnique*, 51(7), 647-648
- Salgado, R. (2008) *The engineering of foundations* McGraw Hill, New York
- Santoyo E. and Ovando E. (2002) "Paralelismo entre las Torre de Pisa y la Catedral de Mexico-Parallelism Aspects of the Tower of Pisa and Mexico City's Cathedral", Sociedad Mexicana de Ingenieria Estructural (Mexican Society of Structural Engineering), 189 - pp. 1269-1298
- Santoyo E. and Ovando S. E. (2008) "Catedral y Sagrario de la Ciudad de Mexico-Mexico City's Cathedral and Sagrario Church" CONACULTA and TGC Geotecnia
- Terracina, F. (1962) "Foundation of the Tower of Pisa" *Geotechnique*, 12 (4), Pages 336-339

Minimization of the Cost and CO₂ Emissions for Strip Footings under Dynamic Loading Using a Big Bang-Big Crunch Algorithm

Andrew Assadollahi, Ph.D., E.I.¹

¹Assistant Professor, Dept. of Civil and Environmental Engineering, Christian Brothers Univ., 650, East Parkway South, Memphis, TN 38104. E-mail: aassadol@cbu.edu

Abstract

A procedure is developed to minimize cost and CO₂ emissions for the design of reinforced concrete strip footings subjected to dynamic loading, satisfying geotechnical limit states and using a big bang-big crunch (BB-BC) algorithm. The objectives of this research are to develop low-cost and low-CO₂ emission designs of strip footings when subjected to dynamic loading. Cost is based on materials and labor required for the construction of strip footings. The CO₂ emissions are associated with the extraction and transportation of raw materials; processing, manufacturing, and fabrication of products; and the emissions of equipment involved in the construction process. The cost and CO₂ objective functions are subjected to dynamic soil bearing and dynamic displacement limits. A design example is presented to compare low-cost and low-CO₂ emission designs. Results are presented that demonstrate the effects of different magnitudes of applied dynamic loads for strip footings founded in different types of soils.

INTRODUCTION

Low-cost designs of engineering systems have always been a concern in engineering practice. Since the annual emissions of carbon dioxide (CO₂) have grown by about 80% since 1970 and were estimated to be 77% of total anthropogenic greenhouse gas emissions in 2004 (UNIPCC 2007), the consideration of CO₂ emissions in structural reinforced concrete design has become a prudent area of research. In addition, there has been no investigation into the design of strip footings subjected to seismic loading for low-cost and low-CO₂ emissions which consider the geotechnical limit states of dynamic bearing capacity and dynamic displacement limits using evolutionary methods.

Big Bang-Big Crunch (BB-BC) has been shown to be a computationally efficient heuristic method to solve a variety of optimization problems. Erol and Eksin (2006) proposed the original BB-BC algorithm which involved exploiting the power of the mean of a population using an abstract model of the lifecycle of the universe. A set of normally distributed solutions is generated about the weighted mean of the solution space in each “Big Bang” stage. After the solutions are evaluated, a “Big Crunch” stage computes a new center for the next “Big Bang” based on the fitness of the various solutions. Over successive cycles of Big Bangs and Big Crunches, the standard deviation of the normal distribution of new solutions decreases and the search tends to become more localized in the neighborhood of the best solution. The optimization is assumed to have converged when some measure of the averaged solution and/or the best solution ceases to improve over a number of cycles.

The form of the objective function for this optimization is consistent with that presented by Camp and Assadollahi (2013). Both the cost objective function and the CO₂ emission objective function include the unit emissions associated with excavation, formwork, reinforcing steel, and concrete.

The general form of the optimization problem is given as

$$\text{Minimize: } f_{\text{cost}} = \sum_{i=1}^R C_i a_i(x_1, x_2, \dots, x_n) \quad \text{or} \quad f_{\text{CO}_2} = \sum_{i=1}^R E_i a_i(x_1, x_2, \dots, x_n) \quad (1)$$

$$\text{Subject to: } p_j(x_1, x_2, \dots, x_n) \leq 0 \quad (2)$$

where f_{cost} is the cost function and f_{CO_2} is the CO₂ emission function, C_i are the unit costs, E_i are the unit CO₂ emissions, a_i are the amount of material and construction units, x_i are the design variables, n is the number of design variables, R is the number of material and construction units, and p_j are the penalty functions.

STRIP FOOTINGS SUBJECTED TO SEISMIC ACCELERATIONS

Strip (or continuous) footings are shallow foundations in which the width-to-length ratio approaches zero and are generally reinforced. The primary load-transferring mechanism between the strip footing and the soil during a seismic event is the seismic bearing capacity. Richards et al. (1993) developed a seismic bearing capacity theory for strip footings in granular soils. Figure 1 shows a cross-section view of a strip footing with the assumed failure surface for seismic bearing capacity analysis (Richards et al., 1993). P is the applied uniform compressive load, α_{AE} is the inclination angle for active pressure conditions, and α_{PE} is the inclination angle for passive pressure conditions. The footing thickness T is taken as a constant. The two geometric design variables for the optimization are the foundation width, B , and the foundation depth of embedment, D_f . The seismic bearing capacity is computed as:

$$q_{uE} = \gamma D_f N_{qE} + 0.5 \gamma B N_{\gamma E} \quad (3)$$

The factor of safety against seismic bearing failure is given as:

$$FS = \frac{q_{uE} B}{P + W} \quad (4)$$

where W is the self-weight of the footing per unit length, given as:

$$W = \gamma T B \quad (5)$$

The settlement of a strip footing due to seismic loading is given by Richards et al. (1993) as:

$$S_{EQ} = 0.174 \frac{V^2}{A g} \left(\frac{k'_h}{A} \right)^{-4} \tan(\alpha_{AE}) \quad (6)$$

where V is the peak velocity for the design earthquake in m/sec, A is the acceleration coefficient for the design earthquake and g is the acceleration due to gravity (9.81 m/sec²) and k'_h is the critical horizontal coefficient of acceleration due to the earthquake.

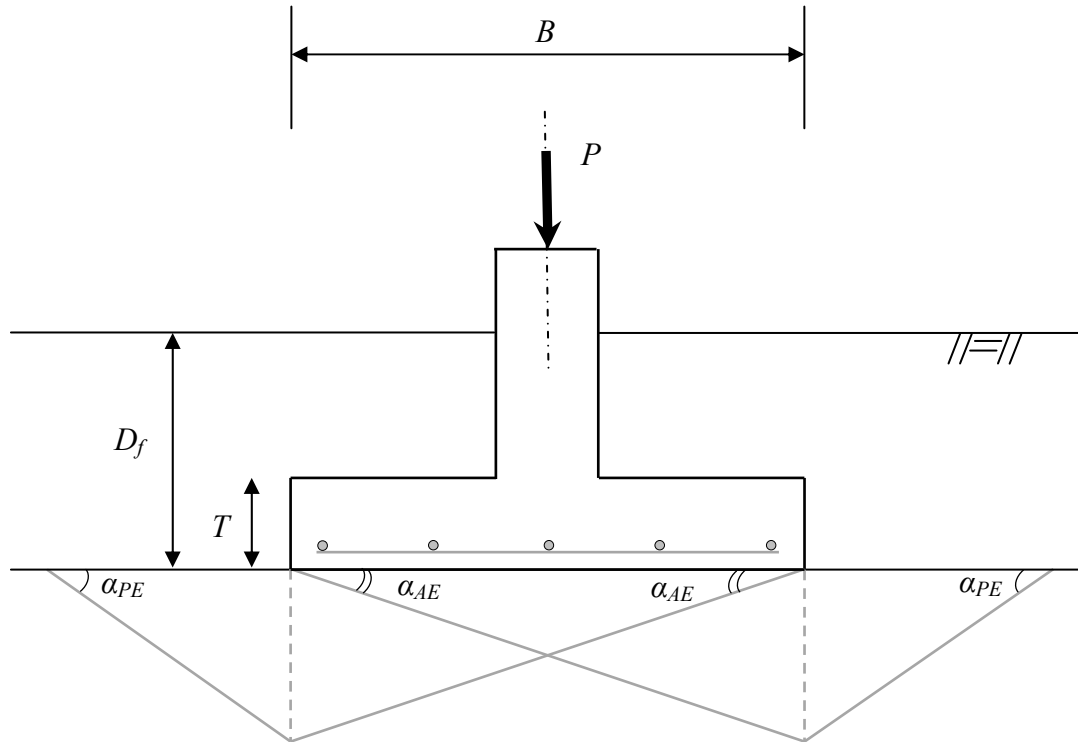


Figure 1. Strip Footing with Failure Surface for Seismic Bearing Capacity.

CONSTRAINTS

To ensure stability of the geomaterial and to provide safety and stability against geotechnical limit state failure, different design constraints are imposed. Each design constraint is posed as a penalty on the overall objective function of the design and is non-zero only when violated. The sum of the constraint penalties will be zero for feasible designs. If the factor of safety against seismic bearing capacity is less than the minimum required factor of safety, the safety factor penalty is given as:

$$p_{FS} = 1 - \frac{FS}{FS_{min}} > 0 \quad (7)$$

where FS_{min} is the minimum factor of safety against seismic bearing failure. In order to ensure the shallow foundation behaves as a strip footing as opposed to a spread footing, a length-to-width ratio of at least ten is specified. If the length is less than ten times the width, the length penalty is given as:

$$p_{length} = 1 - \frac{10B}{L} > 0 \quad (8)$$

In order for a strip footing to be considered a shallow foundation rather than a deep foundation, the depth of embedment must be less than four times the width. If the depth of embedment is greater than four times the width, the depth penalty is given as:

$$p_{depth} = 1 - \frac{D_f}{4B} > 0 \quad (9)$$

If the total vertical settlement is greater than the maximum allowable settlement, the settlement penalty is given as:

$$p_{sett} = 1 - \frac{S_{max}}{S_{EQ}} > 0 \quad (10)$$

where S_{max} is the maximum allowable settlement of the strip footing.

A total penalty function is used to enforce the penalties p_j on the objective function. The total penalty for a candidate low-cost or low-CO₂ emission design k is a function of the summation of the safety factor, settlement, and geometric constraints. The penalized objective function F_k is a product of the cost or CO₂ objective function of candidate design k and its total penalty:

$$F_k = \left(1 + \sum_{j=1}^3 p_j \right)^{\xi} f_k \quad (11)$$

where ξ is a positive penalty exponent taken as 2.0 (Camp and Assadollahi 2015). The penalty expression imposes a numerical penalty on the value of the objective function that tends to reflect the degree at which the constraints are violated by a candidate set of design variables.

BIG BANG-BIG CRUNCH OPTIMIZATION

Erol and Eksin (2006) developed the original BB-BC optimization from an abstract model of the lifespan of the universe. In the initial Big Bang stage, solution variables are uniformly randomly distributed throughout the search space. Next, during the contraction of the Big Crunch stage, a center of mass \vec{x}_{cm} is computed from the initial population using penalized objective function values as:

$$\vec{x}_{cm} = \frac{\sum_{k=1}^{NC} \frac{\vec{x}_k}{F_k}}{\sum_{k=1}^{NC} \frac{1}{F_k}} \quad (12)$$

where \vec{x}_k is the position of candidate k in an n -dimensional search space and NC is the candidate population size. For the subsequent iterations of the Big Bang stage, new candidate solution positions \vec{x}_k^{new} are normally distributed around the center of mass by:

$$\vec{x}_k^{new} = \beta_1 \vec{x}_{cm} + (1 - \beta_1) [\beta_2 \vec{x}_l + (1 - \beta_2) \vec{x}_g] + \frac{r\alpha(\vec{x}_{max} - \vec{x}_{min})}{n_{cycle}} \quad (13)$$

where β_1 and β_2 are values in the range $[0, 1]$ that weight the influence of the local best solution \vec{x}_l and the global best solution \vec{x}_g on the center of mass of new population positions, r is a random number from a standard normal distribution, α is a parameter limiting the size of the search space, \vec{x}_{max} and \vec{x}_{min} are the upper and lower limits on the values of the design variables, and n_{cycle} is the number of Big Bang iterations. If a design variable is generated outside of the prescribed range, that value is reset to the appropriate minimum/maximum values (Erol and Eksin 2006). The global best solution \vec{x}_g is limited to candidates that have no penalty applied to their objective function values.

Numerical results indicate that a population of 300 initial candidate solutions is adequate to balance computational efficiency and overall algorithm performance. A general stopping

criterion of 3,000 analyses is used. Computational results show that $\beta_1 = 0.3$ and $\beta_2 = 0.6$ routinely provide the best footing designs for this example. Using a value of $\alpha = 1$ in Equation (7) enables the initial search to sample the full range of values for each design variable.

DESIGN EXAMPLE

The objective of this design example is to investigate the cost and CO₂ emissions impact of strip footings subjected to seismic accelerations. All designs will satisfy geotechnical limit states.

The fitness function is defined as:

$$f_{cost} = C_e V_e + C_f A_f + C_r M_r + C_c V_c + C_b V_b \text{ or } f_{CO_2} = E_e V_e + E_f A_f + E_r M_r + E_c V_c + E_b V_b \quad (14)$$

where C_e is the unit cost of excavation, C_f is the unit cost of formwork, C_r is the unit cost of reinforcement, C_c is the unit cost of concrete, C_b is the unit cost of backfill, E_e is the unit emission of excavation, E_f is the unit emission of formwork, E_r is the unit emission of reinforcement, E_c is the unit emission of concrete, and E_b is the unit emission of backfill. The computations of the volume of excavation V_e , area of formwork A_f , mass of the reinforcement M_r , volume of concrete V_c , and volume of compacted backfill V_b are consistent with the methodology used by Camp and Assadollahi (2013).

Unit costs (Wang and Kulhawy 2008) and emissions (Yepes et al. 2012) values are based on the extraction and the transportation of raw materials; processing, manufacturing, and fabrication of products and machinery; and the emissions of equipment involved in the construction process and are summarized in Camp and Assadollahi (2013). Table 1 lists the specified loading, footing, and soil design parameters. The parameters are based on typical values of a dry sand, typical factors of safety, and allowable settlements of strip footings. Table 2 lists the summary of the low-cost and low-CO₂ designs developed by the BB-BC procedure based on the input parameters given in Table 1.

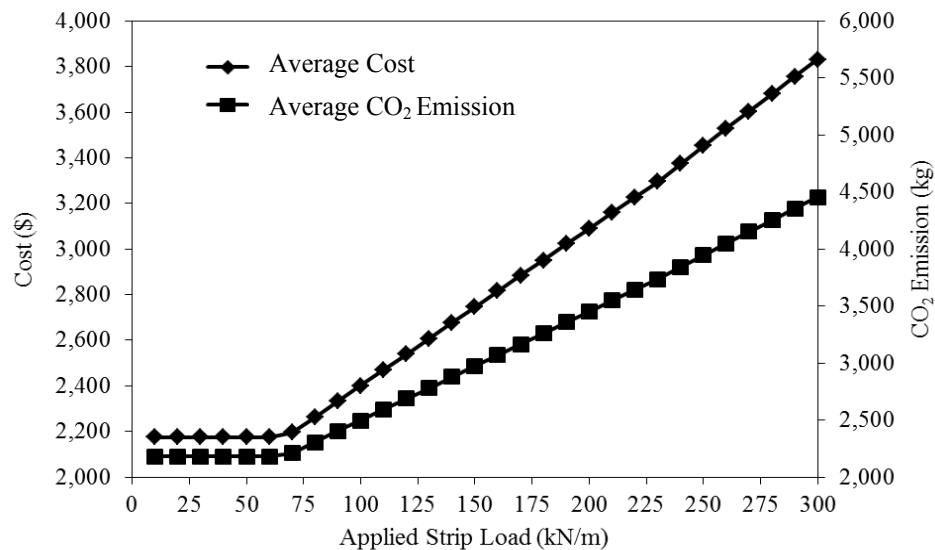
Figures 2 through 8 show a plot of average cost and average CO₂ emissions as the applied strip load, acceleration factor, earthquake velocity, critical horizontal coefficient of acceleration, factor of safety, allowable settlement, and soil unit weight vary, respectively. The purpose of these sensitivity studies is to show how average cost and average CO₂ emissions change as different input parameters are varied.

Table 1. Input Parameters

Input parameter	Unit	Symbol	Value
Internal friction angle of Soil	<i>degree</i>	ϕ'	30
Unit Weight of Soil	<i>kN/m³</i>	γ_s	18.5
Acceleration Factor	—	A	0.3
Earthquake Velocity	<i>m/s</i>	V	0.4
Critical Horizontal Acceleration Coeff.	—	k'_h	0.1
Applied Strip Load	<i>kN/m</i>	P	250
Footing Length	<i>m</i>	L	15.24
Footing Thickness	<i>m</i>	T	8.10
Minimum Footing Width	<i>m</i>	B_{min}	0.3
Minimum Embedment Depth	<i>m</i>	$D_{f,min}$	1.0
Maximum Allowable Settlement	<i>mm</i>	S_{max}	100
Safety Factor for Seismic Bearing Capacity	—	FS_{min}	3.0

Table 2. Designs Based Low Cost and Low CO₂ Emissions

Design Variables	Cost Analysis	CO ₂ Emissions Analysis
$D_f(m)$	2.37	2.37
$B(m)$	1.02	1.02
Excavation (m^3)	48.62	48.62
Concrete Formwork (m^2)	12.39	12.39
Reinforcement (kg)	175.72	175.72
Concrete (m^3)	5.92	5.92
Backfill (m^3)	42.69	42.69
Best	\$ 3,441.56	3,935.35 kg
Average	\$ 3,446.26	3,941.93 kg
Std. Dev.	\$ 5.81	7.84 kg

**Figure 2. Average Cost and Average CO₂ Emissions as a Function of Applied Strip Load.**

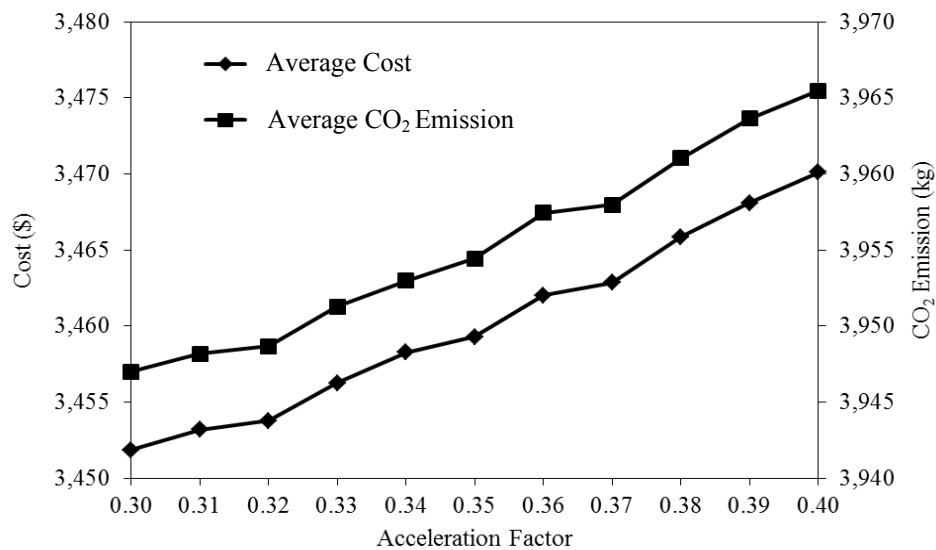


Figure 3. Average Cost and Average CO₂ Emissions as a Function of Acceleration Factor.

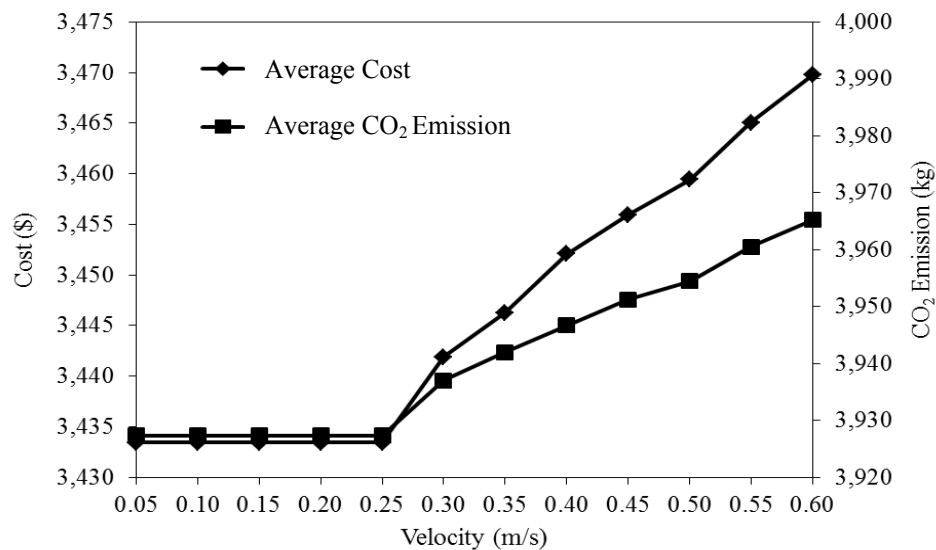


Figure 4. Average Cost and Average CO₂ Emissions as a Function of Earthquake Velocity.

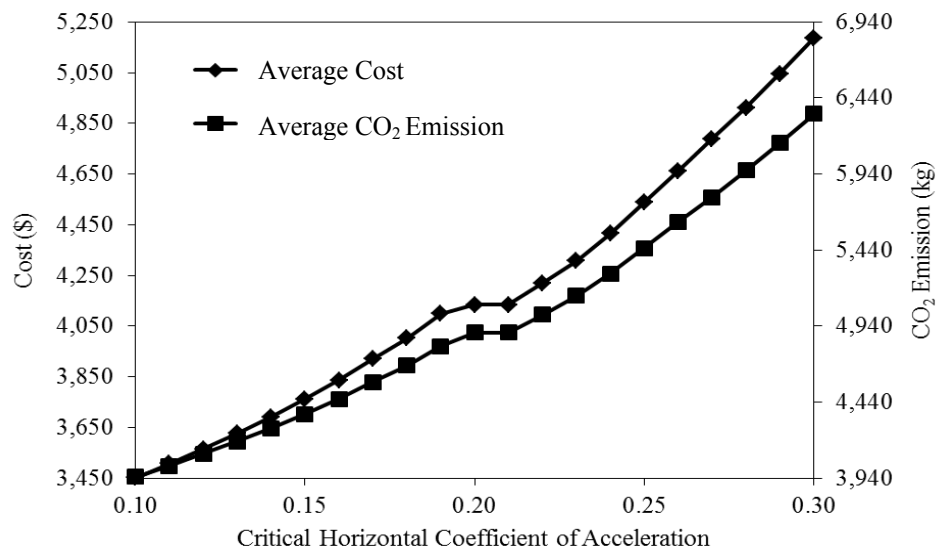


Figure 5. Average Cost and Average CO₂ Emissions as a Function of Critical Horizontal Coefficient of Acceleration.

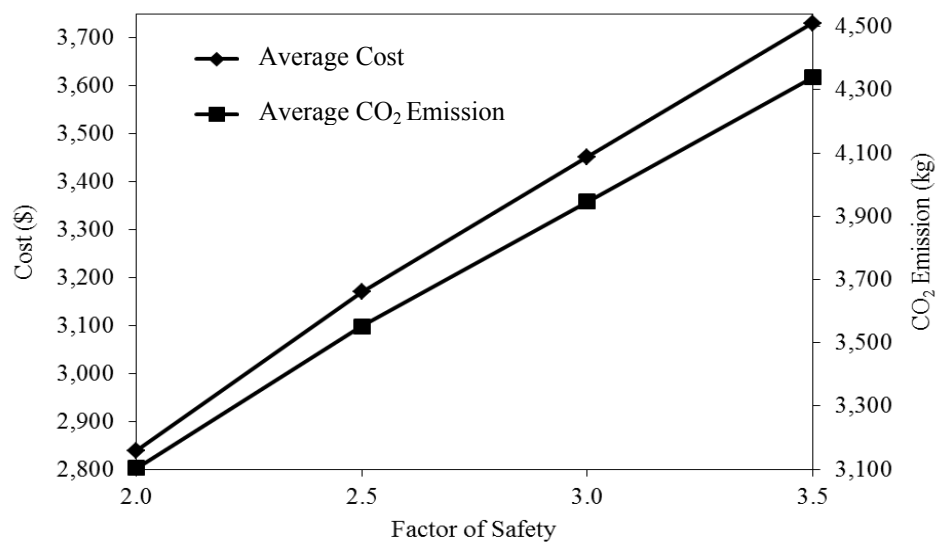


Figure 6. Average Cost and Average CO₂ Emissions as a Function of Factor of Safety.

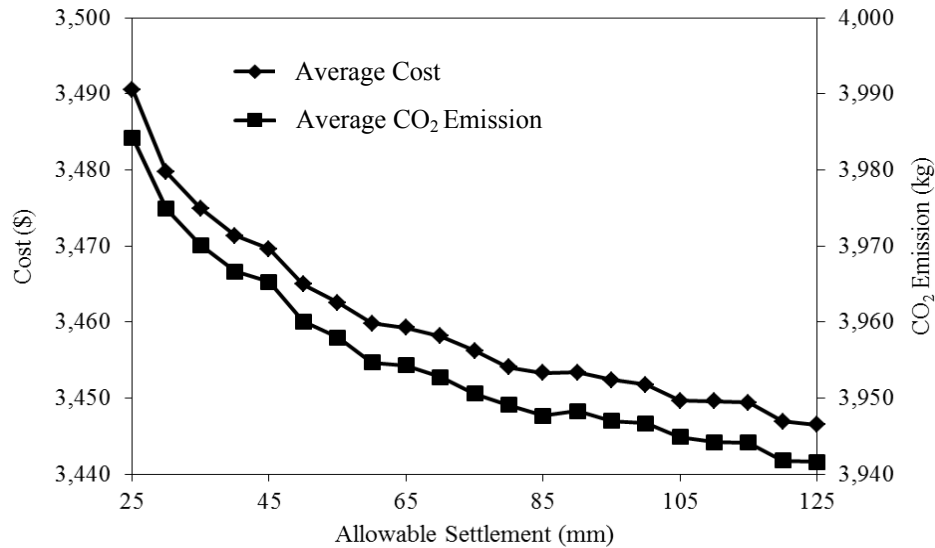


Figure 7. Average Cost and Average CO₂ Emissions as a Function of Allowable Settlement.

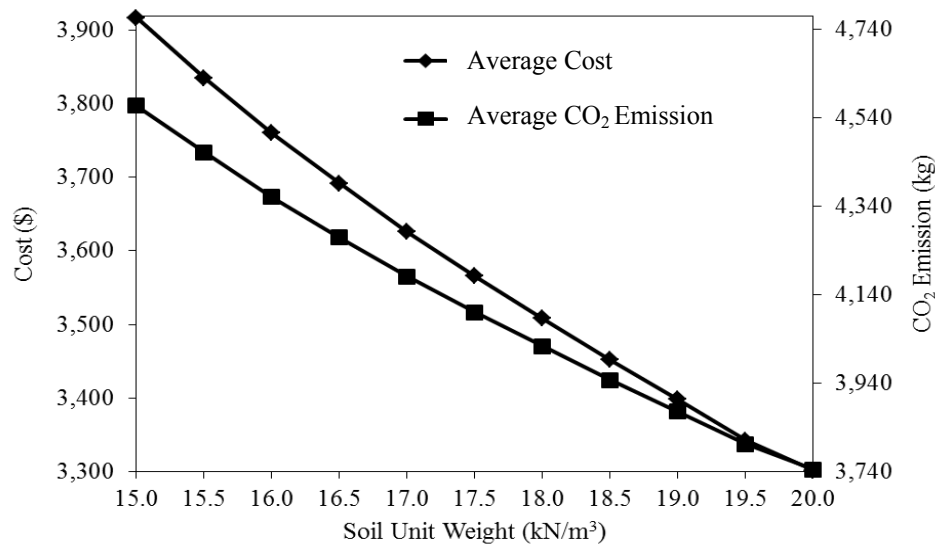


Figure 8. Average Cost and Average CO₂ Emissions as a Function of Soil Unit Weight.

CONCLUSIONS

A procedure is developed to minimize cost and CO₂ emissions for reinforced concrete strip footing designs. Evaluations are based on design optimizations using a cost and a CO₂ emission objective function developed with a hybrid multi-phase BB-BC algorithm. The objectives of this research are to develop low-cost and low-CO₂ emission designs of strip footings and to compare low-cost and low-CO₂ emission designs.

Both the cost and CO₂ objective functions are built using a weighted aggregate fitness function and have identical forms. Each of these objective functions are being minimized in order to provide low-cost and low-CO₂ emission designs while still adhering to appropriate geotechnical limit states. A sensitivity analysis shows a nearly linear increase in both cost and CO₂ emissions as the applied force is increased beyond 60 kN/m, with nearly constant values up to 60 kN/m. There is an increase in both cost and CO₂ emissions as the acceleration factor is increased. There is an increase in both cost and CO₂ emissions as the velocity is increased beyond 0.25 m/s, with nearly constant values up to 0.25 m/s. There is an increase in both cost and CO₂ emissions as the critical horizontal coefficient of acceleration is increased. There is an increase in both cost and CO₂ emissions as the factor of safety against seismic bearing failure is increased. There is a decrease in both cost and CO₂ emissions as the allowable settlement is increased. There is a decrease in both cost and CO₂ emissions as the soil unit weight is increased.

REFERENCES

- Camp, C. V. and Assadollahi, A. (2015). "CO₂ and Cost Optimization of Reinforced Concrete Footings Subjected to Uniaxial Uplift." *Journal of Building Engineering*, 3 171-183.
- Camp, C. V. and Assadollahi, A. (2013). "CO₂ and Cost Optimization of Reinforced Concrete Footings Using a Hybrid Big Bang-Big Crunch Algorithm." *Structural and Multidisciplinary Optimization*, 48(2) 411-426.
- Erol, O. K. and Eksin, I. (2006). "A New Optimization Method: Big Bang-Big Crunch." *Advances in Engineering Software*, Vol. 37, 106-111.
- Richards, R., Jr., Elms, D. G., and Budhu, M. (1993). "Seismic Bearing Capacity and Settlements of Foundations." *Journal of Geotechnical Engineering Division*, ASCE, 119(4), 662-674.
- United Nations Intergovernmental Panel on Climate Change (2007). *Climate Change 2007: Synthesis Report. Contribution of Working Groups I, II and III to the Fourth Assessment Report of the Intergovernmental Panel on Climate Change* [Core Writing Team, Pachauri, R.K and Reisinger, A. (eds.)]. IPCC, Geneva, Switzerland.
- Wang, Y. and Kulhawy, F.H. (2008). "Economic Design Optimization of Foundations." *Journal of Geotechnical and Geoenvironmental Engineering*, 134(8), 1097-1105.
- Yepes, V., González-Vidoso, F., Alcalá, J., and Villalba, P. (2012). "CO₂ Optimization Design of Reinforced Concrete Cantilever Retaining Walls based on a VNS-Threshold Acceptance Strategy." *Journal of Computing in Civil Engineering*, 26(3), 378-386.

Three-Dimensional Soil-Pile Group Interaction in Layered Soil with Disturbed Zone by the Boundary Element Analysis

Jeramy C. Ashlock, A.M.ASCE¹; and Zhiyan Jiang²

¹Associate Professor, Dept. of Civil, Construction and Environmental Engineering, Iowa State Univ., Ames, IA 50010. E-mail: jashlock@iastate.edu

²Ph.D. Student, Dept. of CCEE, Iowa State Univ., 497 Town Engineering Bldg, Ames, IA 50010. E-mail: zyjiang@iastate.edu

Abstract

As part of a current research project on dynamic soil-pile interaction, the parallelized boundary element method (BEM) code BEASSI was modified to enable analysis of three-dimensional dynamic behavior of pile groups surrounded by multiple multi-layered soil zones, with rigorous account of radiation and material damping. Dynamic soil-pile interaction was then analyzed in the frequency domain for a single pile and a 2×2 pile group, each surrounded by an inner disturbed-zone and an outer half-space zone. The layered inner zone enables effects of inhomogeneity, pile installation, and strain-dependent modulus and damping to be approximated, while the outer layered half-space zone can account for the far-field wave propagation in a vertically heter-ogeneous soil medium. The performance of the modified code is validated by comparison to static and dynamic benchmark solutions from the literature. A general formulation for analyzing the dynamic response of pile groups using impedance functions from the BEM analysis is also presented, with the above-ground pile segments modeled as beam-columns and the pile cap treated as a rigid body. For the present case of the 2×2 pile group, a 24×24 global stiffness matrix is formulated to capture the influence of each pile's six displacement degrees-of-freedom on the other piles due to pile-soil-pile interaction. The form and symmetries of the global stiffness matrix are verified by imposing displacements at the soil surface elevation for each pile cross-section separately, enabling future analyses to be performed more efficiently by specifying displacements at only one of the piles. Results of this study will lay the foundation for developing calibrated computational continuum models by analyzing upcoming full-scale vibration tests of pile groups.

INTRODUCTION

Dynamic soil-pile group interaction is an important issue in soil dynamics and geotechnical earthquake engineering for a wide range of pile applications. Compared to the dynamic soil-pile interaction for a single pile, several aspects of the problem become more complex for pile groups, such as the three dimensional nature of the underlying wave propagation phenomena, sensitivity of the foundation response to the in-situ and load-induced spatial variation of the soil's shear modulus and damping profiles, influence of the relative pile-soil material properties, interfacial contact conditions, and disturbance of the soil as a result of pile installation (e.g., Ashlock and Pak 2009). Methods of analysis for dynamic pile-soil interaction typically applied in research and practice include several based on generalized cyclic or dynamic Winkler (p-y curve) models (e.g., Matlock 1970; Novak 1974; Kagawa and Kraft 1980; Novak and El Sharnouby 1983; El Sharnouby and Novak 1990) and continuum-based analytical or numerical approaches such as those in Kuhlemeyer (1979), and Kaynia and Kausel (1982, 1991), for example.

Even under small strains, the soil inhomogeneity and variation of shear modulus and damping in a disturbed zone near the piles, which can result from pile installation as well as the nonlinear dependence of modulus and damping on both dynamic strain level and stress state, can have a significant impact on the dynamic response of piles. These issues have been examined to various degrees in the aforementioned studies.

In the present study, a three-dimensional continuum-based model with an inner disturbed zone and an outer semi-infinite half-space zone to differentiate the near- and far-field soil behavior is established. The BEM code BEASSI, which has been used in several previous studies of single piles, was modified in the present study to enable dynamic analysis of pile groups embedded in a disturbed inner zone and surrounded by a semi-infinite half-space zone. The piles and inner and outer soil zones enable an approximate account of horizontal heterogeneity, while both the inner and outer soil zones employ multilayered viscoelastic fundamental solutions (Pak and Guzina 2002) to handle vertical heterogeneities of density, Poisson's ratio, modulus, and damping. The program also features a regularized multi-domain formulation (Pak and Guzina 1999), families of singular and adaptive-gradient elements for treating stress singularities and discontinuities (Pak and Ashlock 2007), BEM compatible structural beam-column elements for the embedded portions of the piles, and an adaptive integration algorithm to ensure accuracy of the coefficient matrices (Ashlock 2006).

The accuracy of the modified BEASSI code is verified herein by comparison to benchmark studies involving a variety of shear modulus profiles, pile-to-pile spacings, and excitation frequencies. A sub-structuring method is used to formulate dynamic force-to-acceleration transfer functions for the case of a typical 2×2 pile group with unembedded pile segments above ground and a rigid pile cap. The impedance functions are obtained numerically from the traction solutions output by BEASSI, and verified with Betti's reciprocal theorem of elastodynamics. The impedance functions are then used as inputs to the transfer functions to examine the dynamic pile group response.

MODIFICATION OF BEASSI FOR PILE GROUP PROBLEM

The BEM code BEASSI was extended to handle cases of pile groups in multiple soil zones as described above. To generate the necessary 3D surface meshes and associated input files, new custom problem types and templates were also written for the pre/post-processing program GiD (www.gidhome.com). Each pile is modeled as a separate domain, and boundary conditions can be prescribed on either individual piles or the entire group. The performance of the modified code is validated herein by comparison to both static and dynamic benchmark solutions from the literature.

El Sharnouby and Novak (1990) calculated the static settlement of vertically loaded piles by treating the piles and soil as a composite continuum and specifying conditions of equilibrium for discrete nodes. The Poisson's ratio of the soil was 0.5, but that of the pile was not specified. The results were presented in the form of interaction factors as introduced by Poulos (1968), defined as:

$$\alpha = \frac{\text{settlement of one pile owing to adjacent pile load}}{\text{pile settlement under its own load}}$$

A corresponding case of two floating piles of diameter d in a homogenous half-space was analyzed by BEASSI for various spacing (s) and elastic modulus ratios. The length to diameter ratio of the piles was $L/d=25$ and the soil Poisson's ratio was set to $\nu_s=0.49$ to avoid numerical

instabilities. Analyses were conducted for two pile Poisson's ratios; $\nu_p=0.2$ and $\nu_p=0.49$, which had little effect on the results. The results from BEASSI follow the same trends as El Sharnouby and Novak (1990), with interaction factor decreasing with increasing pile spacing (Figure 1). For the lowest pile to soil modulus ratio $E_p/E_s=100$, the two analyses match very well, with a maximum difference of 0.036 which diminishes with increasing spacing. For higher modulus ratios, the differences are slightly greater but similar trends are observed. For the largest modulus ratio $E_p/E_s=10,000$ at a spacing of $S/d=2$, the interaction factors from BEASSI and the benchmark study are 0.638 and 0.706, respectively. In the benchmark study, piles were discretized into a limited number of elements with identical vertical shear stresses assumed. Additionally, surface loads as well as axial loads were reduced to point loads. These simplifications, which were not applied in BEASSI, may increase the stiffness of the soil-pile system and lead to the slightly higher interaction factors in the benchmark study.

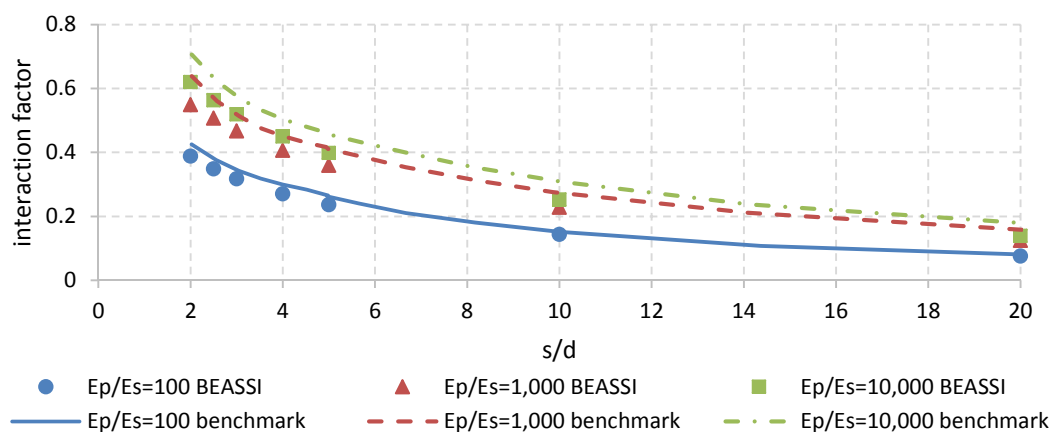


Figure 1. Comparison of interaction factors from present study and El Sharnouby and Novak (1990) for floating pile with Poisson's ratio 0.2 in homogeneous soil.

A dynamic case of a 2×2 fixed-head pile group in a homogeneous half-space from an often-referenced study by Kaynia and Kausel (1982) was also verified by the modified BEASSI program. The pile and soil parameters for this case were $E_p/E_s=100$, $\nu_s=0.4$, $\nu_p=0.25$, $L/d=15$ and $S/d=5$, with a mass density ratio of $\rho_s/\rho_p=0.7$. In BEASSI, the vertical, horizontal, rocking, and torsional impedances are obtained by prescribing unit displacements and rotations on top of the piles in the corresponding directions and appropriately integrating the resulting tractions. The real and imaginary parts of the impedances for the 2×2 pile group are presented in Figure 2. The damping coefficients reported in Kaynia and Kausel (1982) were converted to the corresponding imaginary parts of the impedance functions for comparison to the BEASSI results in this figure. As in Kaynia and Kausel (1982), the vertical impedance $k_{vv}(a_0)$ and rocking impedance $k_{mm}(a_0)$ were also normalized by the static values $Nk_{vv}^S(0)$ and $\sum_{i=1}^N x_i^2 k_{vv}^S(0)$, respectively, while the horizontal impedance $k_{hh}(a_0)$ and torsional impedance $k_{tt}(a_0)$ were normalized by $Nk_{hh}^S(0)$ and $\sum_{i=1}^N r_i^2 k_{hh}^S(0)$, where $N=4$ is the number of piles, x_i is the distance between the pile center and the rocking axis, r_i is the distance between the pile center and the center of rotation for torsion, and superscript S refers to the single pile's stiffness. The dimensionless frequency is defined as $a_0 = \omega d / C_s$ where C_s is the shear wave velocity of the soil and $\omega = 2\pi f$ is the circular frequency.

The results from BEASSI match the benchmark solution in Figure 2 well, especially at low frequencies. As the normalized frequency approaches zero, both methods tend to a similar value of static stiffness. When a_0 exceeds 0.6, the stiffness (real part of impedance) obtained by BEASSI is slightly lower than the benchmark and the damping (imaginary part of impedance) fluctuates near the benchmark values. From these benchmark comparisons, the modified BEASSI program is considered to be valid for solving pile group problems.

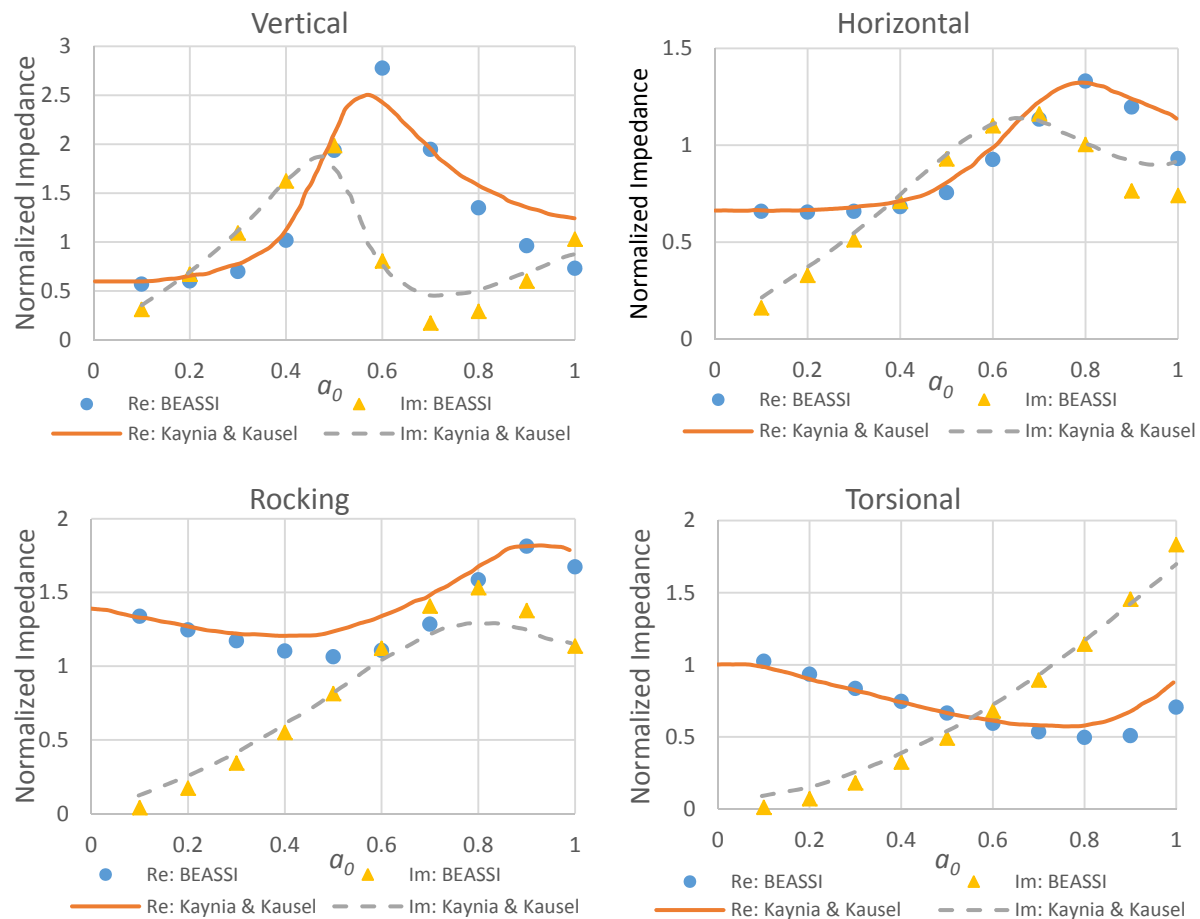


Figure 2. Comparison of normalized impedances for 2×2 pile group in homogeneous half space to results of Kaynia and Kausel (1982).

CASE STUDY OF A 2×2 PILE GROUP

In a previous study on dynamic soil-structure interaction for surface footings (Pak and Ashlock 2010), a near-field disturbed-zone and an outer zone were demonstrated to capture the observed multi-modal (simultaneous vertical plus coupled lateral-rocking) dynamic response of vibrating surface foundations from centrifuge tests better than the homogeneous half-space model. For a large centrifuge study of single piles tested in dry uniform sands, a similar disturbed-zone concept was also demonstrated in Ashlock (2006) to improve theoretical predictions relative to those for a pile in a homogeneous or even a square-root modulus half-space.

The disturbed-zone concept has been applied in various forms in several previous studies of piles. In the present 3D BEM study, it provides a method to account for many important physical phenomena related to pile installation and soil-pile interaction. Examples of such phenomena include spatial variations in soil modulus and damping owing to increased stresses

from the static foundation weight as well as the process of pile installation, changes in modulus and damping due to the imposed dynamic strain levels, and modified pile-soil contact conditions including separation due to pile installation and vibration. At the same time, the exterior zone allows the 3D free-field wave propagation to be captured in the far-field outside the disturbed zone. As demonstrated in Ashlock (2006), accounting for the near-field disturbance and far-field wave propagation via the disturbed-zone concept can significantly improve the accuracy by which multi-modal pile vibration can be modeled.

The disturbed-zone concept for 3D pile-soil interaction is extended herein to a typical case of a 2×2 pile group with $L/d=12.5$ and a spacing of $S/d=2$. The shear modulus, Poisson's ratio and density of the piles are assumed to be $133.33G_{ref}$, 0.2, and $1.11\rho_{ref}$, respectively, where G_{ref} and ρ_{ref} in BEASSI are arbitrary reference values with consistent units (e.g., shear modulus in units of N/m² and density in kg/m³ corresponding to a shear wave velocity $C_{s,ref} = \sqrt{G_{ref} / \rho_{ref}}$ in m/s and a corresponding dimensionless frequency $\bar{\omega} = a_0 / 2 = \omega d_{ref} / (2C_{s,ref})$). The Poisson's ratio and density in both the inner and outer soil zones are 0.25 and $1.00\rho_{ref}$ respectively, and are assumed to be unchanged during the pile installation process. The shear modulus and damping profiles for a generalized viscoelastic model having a square-root modulus profile in the outer zone, with modulus degradation and associated damping increase (due to pile installation and larger shear strains near the surface) were modeled as (Ashlock 2006):

$$\begin{aligned} \text{inner/disturbed-zone: } & \begin{cases} G^I(z) = G_{ref} \left[\beta + \alpha \left(1 - \frac{1}{1 + (z/z_d)^n} \right) \left(\left(\frac{z}{a} \right)^{0.5} - \frac{\beta}{\alpha} \right) \right] \\ \xi^I(z) = \xi_0 / [1 + (z/z_d)^n] \end{cases} \\ \text{outer zone: } & \begin{cases} G^O(z) = G_{ref} (z/a)^{0.5} \\ \xi^O(z) = 0 \end{cases} \end{aligned}$$

where $\alpha=1.1$, $\beta=0.1$, $z_d=5$, $n=3$, $\xi_0=0.3$, and $a=d/2$ is the pile radius. To examine the effect of the disturbed zone on the impedances, a model with the same soil profile for the outer half-space but without the disturbed-zone was also analyzed. The resulting impedances with and without the disturbed zone are plotted in Figure 3.

SUB-STRUCTURING METHOD FOR PILE GROUP

A general formulation for the dynamic response of a pile group in terms of transfer functions of directional pile-cap acceleration per unit applied force is developed herein by the method of sub-structuring. For this analysis, the pile cap is regarded as a rigid body and the unembedded pile segments are treated as Euler-Bernoulli beam-columns. These components form the superstructure and are treated analytically, while the embedded segments of the piles and the soil domain make up the soil-foundation substructure and are modeled computationally in BEASSI. Once the pile impedance functions at the soil surface elevation are obtained from BEASSI, they are input to the mathematical formulation to determine the theoretical acceleration/force transfer functions of the soil-pile-cap system. In a future study, such transfer functions will be evaluated against experimentally measured counterparts from pile-group vibration tests, to develop calibrated computational disturbed-zone models for multi-modal dynamic soil pile-group interaction.

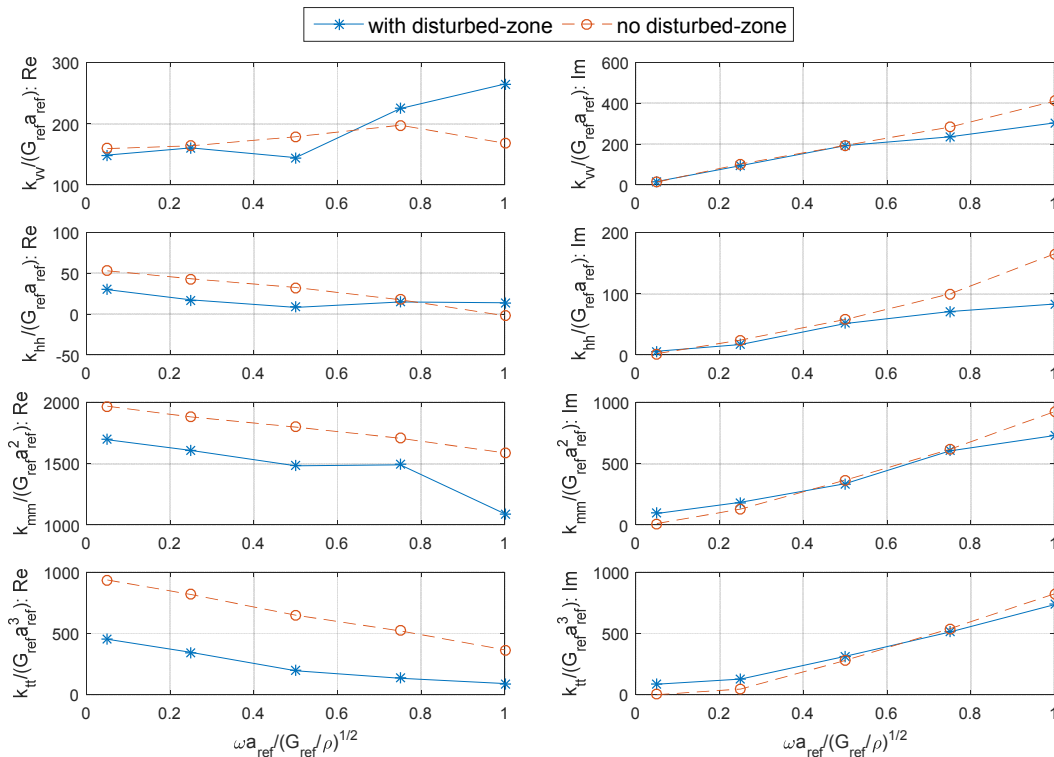


Figure 3. Comparison of impedance functions for 2×2 pile group in square-root half-space with and without disturbed-zone

Impedance matrix for pile-soil substructure. The geometry and notation for the 2×2 group subjected to either a dynamic horizontal force $q_H(t)$ or vertical force $q_V(t)$ at the pile cap is shown in Figure 4. For the viscoelastic soil-pile system under consideration, the pile group impedance may be obtained by linear superposition of the contributions of the single piles, by assembling the individual pile impedance submatrices into a global stiffness matrix.

A general elementary submatrix relating the force and moment resultants over the cross-section of pile i at the elevation of the ground-surface, due to 3D displacements and rotations of pile j (with the cross section of pile i fixed) can be expressed as:

$$\begin{bmatrix} F_x^i \\ F_y^i \\ F_z^i \\ M_x^i \\ M_y^i \\ M_z^i \end{bmatrix} = \begin{bmatrix} k_{xx}^{i-j} & k_{xy}^{i-j} & k_{xz}^{i-j} & k_{xr_x}^{i-j} & k_{xr_y}^{i-j} & k_{xr_z}^{i-j} \\ k_{yx}^{i-j} & k_{yy}^{i-j} & k_{yz}^{i-j} & k_{yr_x}^{i-j} & k_{yr_y}^{i-j} & k_{yr_z}^{i-j} \\ k_{zx}^{i-j} & k_{zy}^{i-j} & k_{zz}^{i-j} & k_{zr_x}^{i-j} & k_{zr_y}^{i-j} & k_{zr_z}^{i-j} \\ k_{m_x}^{i-j} & k_{m_y}^{i-j} & k_{m_z}^{i-j} & k_{m_x r_x}^{i-j} & k_{m_x r_y}^{i-j} & k_{m_x r_z}^{i-j} \\ k_{m_y}^{i-j} & k_{m_z}^{i-j} & k_{m_x r_x}^{i-j} & k_{m_y r_x}^{i-j} & k_{m_y r_y}^{i-j} & k_{m_y r_z}^{i-j} \\ k_{m_z}^{i-j} & k_{m_x r_x}^{i-j} & k_{m_y r_x}^{i-j} & k_{m_z r_x}^{i-j} & k_{m_z r_y}^{i-j} & k_{m_z r_z}^{i-j} \end{bmatrix} \begin{bmatrix} U_x^j \\ U_y^j \\ U_z^j \\ \Theta_x^j \\ \Theta_y^j \\ \Theta_z^j \end{bmatrix} \quad \text{or } \mathbf{F}^i = \mathbf{K}^{i-j} \mathbf{U}^j$$

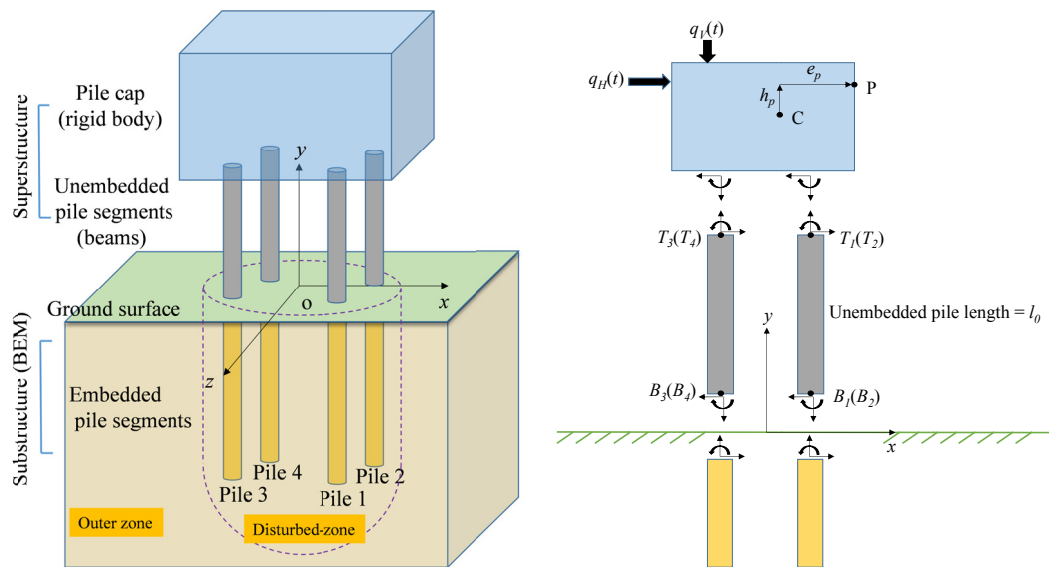


Figure 4. Sub-structuring method and notation for analysis of pile group

where the first subscript refers to force or moment in the x , y , or z directions, and the second subscript refers to translation or rotation with respect to the x , y , or z axes. For the four piles in the group, a 24×24 global stiffness matrix can thus be assembled using the 6×6 submatrices as follows:

$$\begin{bmatrix} \mathbf{F}^1 \\ \mathbf{F}^2 \\ \mathbf{F}^3 \\ \mathbf{F}^4 \end{bmatrix} = \begin{bmatrix} \mathbf{K}^{1-1} & \mathbf{K}^{1-2} & \mathbf{K}^{1-3} & \mathbf{K}^{1-4} \\ \mathbf{K}^{2-1} & \mathbf{K}^{2-2} & \mathbf{K}^{2-3} & \mathbf{K}^{2-4} \\ \mathbf{K}^{3-1} & \mathbf{K}^{3-2} & \mathbf{K}^{3-3} & \mathbf{K}^{3-4} \\ \mathbf{K}^{4-1} & \mathbf{K}^{4-2} & \mathbf{K}^{4-3} & \mathbf{K}^{4-4} \end{bmatrix} \begin{bmatrix} \mathbf{U}^1 \\ \mathbf{U}^2 \\ \mathbf{U}^3 \\ \mathbf{U}^4 \end{bmatrix}$$

where each of the 6×1 \mathbf{F}^i vectors contain the forces and moments at the ground surface elevation for pile i , and \mathbf{U}^i contains the corresponding displacements and rotations. Each of the 6×6 elementary stiffness matrices \mathbf{K}^{i-j} comprising the global stiffness matrix thus relates the force and moment resultants at pile i to the displacements and rotations of pile j .

The original global 24×24 matrix has 576 entries, making it impractical to analyze in practice. However, by imposing reasonable assumptions and taking advantage of symmetry of the 2×2 group, a more concise analysis can be used in which displacements need to be specified at only one of the piles in the BEM analysis. For simplification, the individual piles are all assumed to have the same dimensions and properties, and the soil profile is regarded as axisymmetric in both zones. By Betti's reciprocal theorem, all stiffness matrices of linear structures must be symmetric, thus the global stiffness matrix should be symmetric as well. Within the off-diagonal submatrices, the independent entries can be further reduced. For example, the influence of Pile 3 on Pile 1 is symmetric to that of Pile 2 on Pile 1, and the influence of Pile 4 on Pile 3 is equivalent to that of Pile 2 on Pile 1 due to symmetry about the $y-z$ plane. As a result, only the entries of four columns (a total of 96 entries) in the global matrix are independent, and the others can be obtained by symmetry with appropriate sign changes.

To verify the symmetry relations, several analyses were performed in BEASSI by imposing displacements and rotations of each pile independently, and analyzing the resultant

forces and moments on all piles to determine all entries of the global stiffness matrix numerically. It was found that the submatrices on and off the diagonal were exactly as predicted from the symmetry considerations. Therefore, all entries in the global matrix can be more efficiently determined by prescribing unit displacements and rotations at Pile 1 alone, then assembling the rest of the matrix using the symmetry relations.

Theoretical transfer functions for superstructure. In order to determine the dynamic response of the soil and pile-group system under general planar motion, three typical loading cases; vertically centric (VC), horizontally centric (HC), and vertically eccentric (VE) are considered, as discussed in Ashlock and Pak (2009). In the VC test, a vertical force is applied directly over the pile cap centroid, invoking a purely vertical response. In the VE test, a vertical force is applied in the vertical plane of the centroid, but offset horizontally to induce simultaneous vertical and coupled lateral-rocking motion. In the HC test, a horizontal force is applied in the vertical plane of the centroid, inducing coupled lateral-rocking motion, with no vertical motion resulting unless the pile cap centroid is not located above the center of the piles.

For the analysis, the acceleration response is desired at an arbitrary point of interest P located at (x_p, y_p, z_p) (Figure 4). For planar motion, the displacement and force vectors at any point P can be simplified to:

$$\mathbf{U}(P) = [U_y(x_p, y_p), U_x(x_p, y_p), \Theta_z(x_p, y_p)]^T \text{ and } \mathbf{F}(P) = [F_y(x_p, y_p), F_x(x_p, y_p), M_z(x_p, y_p)]^T$$

For rigid body motion of the pile cap, the displacement of point P can be related to that of the centroid C as $\mathbf{U}(P) = \mathbf{T}_{PC} \mathbf{U}(C)$, where $\mathbf{T}_{PC} = \mathbf{T}_{CP}^{-1}$ is a 3×3 kinematic transformation matrix containing the eccentricity $e_p = x_p - x_c$ and height $h_p = y_p - y_c$ of point P with respect to the centroid in Figure 4 (see Ashlock 2006). Eliminating $\mathbf{U}(C)$ by setting P as points T_1 and T_3 gives the displacement compatibility condition for rigid body motion of the pile cap as

$$\mathbf{T}_{T_1C}^{-1} \mathbf{U}(T_1) - \mathbf{T}_{T_3C}^{-1} \mathbf{U}(T_3) = 0 \quad (1)$$

Dynamic force and moment equilibrium for the pile cap then gives the three equations of motion:

$$\begin{aligned} -Q_V - F_y(T_1) - F_y(T_2) - F_y(T_3) - F_y(T_4) &= -m\omega^2 \ddot{U}_y(C) \\ Q_H - F_x(T_1) - F_x(T_2) - F_x(T_3) - F_x(T_4) &= -m\omega^2 \ddot{U}_x(C) \\ -Q_V e_v - Q_H h_H - [F_y(T_1) + F_y(T_2)]e_{T_1} - [F_y(T_3) + F_y(T_4)]e_{T_3} \\ &\quad - [F_x(T_1) + F_x(T_2)](-h_{T_1}) - [F_x(T_3) + F_x(T_4)](-h_{T_3}) - M_z(T_1) - M_z(T_2) - M_z(T_3) - M_z(T_4) \\ &= -J\omega^2 \ddot{\Theta}_z(C) \end{aligned}$$

where m and J are the mass and polar mass moment of inertia of the pile cap, and capital letters F , M , U , and Θ denote Fourier transforms of the force, moment, displacement, and rotation quantities at the top of the four piles. The three equations of motion shown above can be expressed in matrix-vector form as

$$\mathbf{Q} - \mathbf{T}_{T_1C}^T [\mathbf{F}(T_1) + \mathbf{F}(T_2)] - \mathbf{T}_{T_3C}^T [\mathbf{F}(T_3) + \mathbf{F}(T_4)] = -\omega^2 \mathbf{M} \mathbf{U}(C)$$

where $\mathbf{Q} = [-Q_V, Q_H, (-Q_V e_v - Q_H e_H)]^T$ is the forcing vector, $\mathbf{F} = [F_y, F_x, M_z]^T$, and \mathbf{M} is the mass/inertia matrix. By symmetry, $\mathbf{F}(T_1) = \mathbf{F}(T_2)$ and $\mathbf{F}(T_3) = \mathbf{F}(T_4)$, and the equilibrium equation can therefore be simplified to

$$-\omega^2 \mathbf{M} \mathbf{T}_{CT_1} \mathbf{U}(T_1) + 2\mathbf{T}_{T_1C}^T \mathbf{F}(T_1) + 2\mathbf{T}_{T_3C}^T \mathbf{F}(T_3) = \mathbf{Q} \quad (2)$$

Modeling the unembedded pile segments as beam-columns (assuming slenderness ratio criteria are satisfied), their partial differential equations of motion for axial deformation and bending in

the time domain become ordinary differential equations with parameter ω in the frequency domain, i.e.;

$$\frac{d^2 U_y(y, \omega)}{dy^2} + \left(\frac{\omega}{C_p} \right)^2 U_y(y, \omega) = 0, \text{ where } F_y(y, \omega) = E_p A_p \frac{dU_y(y, \omega)}{dy} \quad (3)$$

and

$$\frac{\partial^4 U_x(y, \omega)}{\partial y^2} - \beta^4 U_x(y, \omega) = 0 \quad (4)$$

where $C_p = \sqrt{E_p / \rho_p}$ and $\beta^4 \equiv \omega^2 \frac{\rho_p A_p}{E_p I_p}$. The solutions to the above two wave equations can be obtained in terms of six undetermined coefficients $\mathbf{C} = [C_1, \dots, C_6]^T$ (see Ashlock 2006), and written for any point $P = (x_p, 0 \leq y_p \leq l_0)$ along one of the piles as $\mathbf{S}(P)\mathbf{C} = [\mathbf{U}^T(P), \mathbf{F}^T(P)]^T$, where

$$\mathbf{S}(P) = \begin{bmatrix} \sin(\alpha y_p) & \cos(\alpha y_p) & 0 & 0 & 0 & 0 \\ 0 & 0 & \sin(\beta y_p) & \cos(\beta y_p) & e^{-\beta y_p} & e^{\beta(y_p - l_0)} \\ 0 & 0 & -\beta \cos(\beta y_p) & \beta \sin(\beta y_p) & \beta e^{-\beta y_p} & -\beta e^{\beta(y_p - l_0)} \\ E_p A_p \alpha \cos(\alpha y_p) & -E_p A_p \alpha \sin(\alpha y_p) & 0 & 0 & 0 & 0 \\ 0 & 0 & E_p I_p \beta^3 \cos(\beta y_p) & -E_p I_p \beta^3 \sin(\beta y_p) & E_p I_p \beta^3 e^{-\beta y_p} & -E_p I_p \beta^3 e^{\beta(y_p - l_0)} \\ 0 & 0 & E_p I_p \beta^2 \sin(\beta y_p) & E_p I_p \beta^2 \cos(\beta y_p) & -E_p I_p \beta^2 e^{-\beta y_p} & -E_p I_p \beta^2 e^{\beta(y_p - l_0)} \end{bmatrix}$$

The coefficients \mathbf{C} can be eliminated by applying the beam-column wave equation solutions at the top and bottom of the unembedded pile segments. For Pile 1 and Pile 2, this can be written as

$$\mathbf{S}^{-1}(T_1) \begin{bmatrix} \mathbf{U}(T_1) \\ \mathbf{F}(T_1) \end{bmatrix} = \mathbf{S}^{-1}(B_1) \begin{bmatrix} \mathbf{U}(B_1) \\ \mathbf{F}(B_1) \end{bmatrix} \quad (5)$$

Similarly, for Piles 3 and 4;

$$\mathbf{S}^{-1}(T_3) \begin{bmatrix} \mathbf{U}(T_3) \\ \mathbf{F}(T_3) \end{bmatrix} = \mathbf{S}^{-1}(B_3) \begin{bmatrix} \mathbf{U}(B_3) \\ \mathbf{F}(B_3) \end{bmatrix} \quad (6)$$

The pile force/moment vectors at the ground surface can be expressed in terms of the impedances:

$$\begin{cases} \mathbf{F}(B_1) = [\mathbf{K}^{1-1}(\omega) + \mathbf{K}^{1-2}(\omega)] \mathbf{U}(B_1) + [\mathbf{K}^{1-3}(\omega) + \mathbf{K}^{1-4}(\omega)] \mathbf{U}(B_3) \\ \mathbf{F}(B_3) = [\mathbf{K}^{3-1}(\omega) + \mathbf{K}^{3-2}(\omega)] \mathbf{U}(B_1) + [\mathbf{K}^{3-3}(\omega) + \mathbf{K}^{3-4}(\omega)] \mathbf{U}(B_3) \end{cases} \quad (7)$$

where only the impedances relevant to motion in the $x-y$ plane are included in the 3×3 \mathbf{K}^{i-j} matrices. Equations 1, 2, and 5–7 can be expressed as a 24×24 system of simultaneous equations:

$$\begin{bmatrix}
 S(B_1)S^{-1}(T_1) & \mathbf{0}_{6 \times 6} & -\mathbf{I}_{6 \times 6} & \mathbf{0}_{6 \times 6} \\
 \mathbf{0}_{6 \times 6} & S(B_3)S^{-1}(T_3) & \mathbf{0}_{6 \times 6} & -\mathbf{I}_{6 \times 6} \\
 \begin{bmatrix} -\omega^2 \mathbf{M} \mathbf{T}_{CT_1} & 2\mathbf{T}_{T_1C}^T \\ \mathbf{T}_{T_1C}^{-1} & \mathbf{0}_{3 \times 3} \end{bmatrix} & \begin{bmatrix} \mathbf{0}_{3 \times 3} & 2\mathbf{T}_{T_3C}^T \\ -\mathbf{T}_{T_3C}^{-1} & \mathbf{0}_{3 \times 3} \end{bmatrix} & \mathbf{0}_{6 \times 6} & \mathbf{0}_{6 \times 6} \\
 \mathbf{0}_{6 \times 6} & \mathbf{0}_{6 \times 6} & \begin{bmatrix} \mathbf{K}^{1-1}(\omega) + \mathbf{K}^{1-2}(\omega) & -\mathbf{I}_{3 \times 3} \\ \mathbf{K}^{3-1}(\omega) + \mathbf{K}^{3-2}(\omega) & \mathbf{0}_{3 \times 3} \end{bmatrix} & \begin{bmatrix} \mathbf{K}^{1-3}(\omega) + \mathbf{K}^{1-4}(\omega) & \mathbf{0}_{3 \times 3} \\ \mathbf{K}^{3-3}(\omega) + \mathbf{K}^{3-4}(\omega) & -\mathbf{I}_{3 \times 3} \end{bmatrix}
 \end{bmatrix}
 \begin{bmatrix}
 \mathbf{U}(T_1) \\
 \mathbf{F}(T_1) \\
 \mathbf{U}(T_3) \\
 \mathbf{F}(T_3) \\
 \mathbf{U}(B_1) \\
 \mathbf{F}(B_1) \\
 \mathbf{U}(B_3) \\
 \mathbf{F}(B_3)
 \end{bmatrix}
 =
 \begin{bmatrix}
 \mathbf{0} \\
 \mathbf{0} \\
 \mathbf{0} \\
 \mathbf{0} \\
 \mathbf{0} \\
 \mathbf{0} \\
 \mathbf{0} \\
 \mathbf{0}
 \end{bmatrix}
 +
 \begin{bmatrix}
 \mathbf{0} \\
 \mathbf{0} \\
 \mathbf{0} \\
 \mathbf{0} \\
 \mathbf{0} \\
 \mathbf{0} \\
 \mathbf{0} \\
 \mathbf{0}
 \end{bmatrix}
 = \mathbf{Q}$$

which can be solved for the unknown forces and displacements at the top (T) and bottom (B) points of the unembedded pile segments, per unit force applied to the pile cap in \mathbf{Q} . Using the resulting motion at the top of the piles, rigid body motion of the pile cap then provides the transfer functions of interest as the ratios of directional acceleration at any point P on the pile cap per unit applied force.

CONCLUSIONS

Preliminary results were presented from modification of the boundary element code BEASSI to handle 3D pile groups in a multilayered disturbed-zone surrounded by a multilayered half-space. The modified code was validated by comparison to static and dynamic benchmark solutions from the literature, and impedances for a 2×2 pile group in a disturbed-zone surrounded by a square-root modulus half-space were presented. A general formulation was presented that will enable computation of theoretical transfer functions of pile cap acceleration to applied force in the frequency domain. This formulation will be applied in subsequent publications to develop calibrated computational continuum models using results of upcoming full-scale vibration tests of a single pile and 2×2 pile group.

ACKNOWLEDGEMENTS

This material is based upon work supported by the National Science Foundation under Grant No. 1351828 entitled "CAREER: A Framework for Integrated Computational and Physical Simulation of Dynamic Soil-Pile Group Interaction". This support is gratefully acknowledged. Any opinions, findings, and conclusions or recommendations expressed in this material are those of the authors and do not necessarily reflect the views of the National Science Foundation.

REFERENCES

- Ashlock, J.C. (2006). "Computational and Experimental Modeling of Dynamic Foundation Interactions with Sand." Ph.D. Thesis, University of Colorado at Boulder, Boulder, CO.
- Ashlock, J.C. and Pak, R.Y.S. (2009). "Experimental Response of Piles in Sand under Compound Motion." *J. Geotech. Geoenviron. Eng.*, 10.1061/(ASCE)GT.1943-5606.0000038, 799-808.
- El Sharnouby, B., and Novak, M. (1990). "Stiffness Constants and Interaction Factors for Vertical Response of Pile Groups." *Can. Geotech. J.*, 27(6), 813-822.
- Kagawa, T. and Kraft, L. (1980). "Lateral load-deflection relationships of Piles Subjected to Dynamic Loadings." *Soils and Foundations*, 20(4), 19-36.
- Kaynia, A.M. and Kausel, E. (1982). "Dynamic behavior of pile groups." *Proc., 2nd International Conference on Numerical Methods of Offshore Piling*, Austin, TX, 509-532.

- Kaynia, A.M. and Kausel, E. (1991). "Dynamics of piles and pile groups in layered soil media." *Soil Dyn. Earthquake Eng.*, 10(8), 386–401.
- Kuhlemeyer, R. L. (1979) "Static and dynamic laterally loaded floating piles." *J. Geotech. Engrg. Div.*, 105(2), 289–304.
- Matlock, H. (1970). "Correlations for Design of Laterally Loaded Piles in Soft Clay." *Proc., Offshore Technology Conference*, Vol. 1 (1204), Houston, Texas, 577-94.
- Novak, M. (1974). "Dynamic stiffness and damping of piles." *Can. Geotech. J.*, 11(4), 574–598.
- Novak, M. and El Sharnouby, B. (1983) "Stiffness and damping constants of single piles. " *J. Geotech. Engrg. Div., ASCE*, 109(GT7), 961-974.
- Pak, R.Y.S. and Ashlock, J.C. (2007) "Method of adaptive-gradient elements for computational mechanics." *J. Eng. Mech.*, 133(1), 87–97.
- Pak, R.Y.S., and Ashlock, J.C. (2010). "A Fundamental Dual-zone Continuum Theory for Dynamic Soil-structure Interaction." *Earthquake Eng. Struct. Dyn.*, 40(9), 1011-1025.
- Pak, R.Y.S. and Guzina, B.B. (1999) "Seismic soil-structure interaction analysis by direct boundary element methods." *Int. J. Solids Struct.*, 36, 4743–4766.
- Pak, R.Y.S. and Guzina, B.B. (2002) "Three-dimensional Green's functions for a multilayered half-space in displacement potentials." *J.Eng. Mech.*, 128(4), 449–461.
- Poulos, H.G. (1968). "Analysis of the settlement of pile groups." *Géotechnique*, 18, 449-471.

Discussion of Concrete Pier Foundation Design for Transmission Structures

Haijian Shi, Ph.D., P.E., P.M.P.¹; and Drew Pizzo, P.E.²

¹Transmission and Substation Reliability, Pepco Holdings, 701 9th ST NW, Washington, DC 200001. E-mail: hshi@pepcoholdings.com

²Transmission and Substation Reliability, Pepco Holdings, 701 9th ST NW, Washington, DC 200001. E-mail: dpizzo@pepco.com

Abstract

Concrete pier foundations for transmission structures are widely used with high-voltage transmission lines. Current design practice focuses on strength design ensuring the foundation and top structures are safe. However, the performance design criteria for deflection and rotation on top of this kind of pier foundation are not well defined in any major code or guide resulting in utility firms and engineering companies adopting their own differing criteria. This article discusses the development of appropriate performance criteria for foundation design relating to transmission poles. Common pitfalls faced by geotechnical and structural engineers during the design and analysis and ways to avoid them are also discussed. Current common practices and procedures for transmission structure foundation design are discussed together with the importance of adopting appropriate performance criteria to ensure the safety, economic feasibility, and aesthetics of the foundation. Finally, three case studies—tangent pole, light angle pole, and dead end pole—are conducted using the software applications PLS CAISSON, MFAD, and LPILE. The results are compared in terms of shear distribution, moment distribution, and deflection along the length of the pile foundation to establish the ways and extent performance criteria can affect the design.

INTRODUCTION

Tubular steel poles have been used extensively in recent years to replace aging transmission structures. Drilled concrete pier foundations are widely used for high steel poles. Concrete pier foundations can also be constructed in a variety of subsurface condition including hard soil, soft soil, high groundwater tables, and rock with conventional access.

This article first discusses the design procedure for transmission tubular poles and popular design software. Common pitfalls and design criteria are presented next. Finally, three design examples using different design software are compared. Observations and a summary are presented at the end.

DESIGN PROCEDURE AND CRITERIA

Typically, the span and height of the steel tubular poles are controlled by the voltage and the environment of the lines such as the ground clearance. Once the parameters for the pole are determined, the foundation can be designed based on the loadings from the top structure and the soil conditions in the field. Subsurface investigation needs to be conducted to obtain the soil profile. After the pole manufacturer designs the pole and associated structures, the base reaction on top of the foundation is determined. Using top reaction loads and soil profile information, the

transmission pole foundation can be designed with the assistance of geo-structural software such as MFAD, LPILE, and PLS Caisson etc. Trial and error method can be used until the satisfactory size and depth of pier foundation is determined. For most of the cases, uncracked stiffness is used in the software.

DESIGN SOFTWARE

MFAD (User Guide for MFAD 5.0) is developed by Electric Power Research Institute (EPRI) after calibrating with full scale testing results. MFAD can analyze the pier foundation either directly embedded or using concrete pier foundation. Size and depth of the pile needs to be inputted into the model together with soil profile information. Performance criteria such as total deflection and rotation on top of the pier will be asked. At the end of the analysis, the capacity of the designed pier foundation will be revealed against the imputed load demand.

LPILE (User Guide for LPILE 2013) is developed by Ensoft, Inc and adopted different mechanism as compared to MFAD. Instead of checking the deformation of the pier foundation against input of allowable deflection and rotation, the pier foundation is analyzed using $p-y$ curve at each node of the pile. If the soil response is within the elastic range and the overall deflection is not significantly excessive, the design can pass the check. Therefore, in LPILE there are no specific requirements for foundation design performance criteria such as pile head deflection and rotation.

PLS Caisson (PLS Caisson-Version 11.0) is developed by Power Line Systems, Inc. The required input includes soil profile information, cross section dimension of the pier pile, and the loading on top of the pier. The analysis will recommend a depth of the pile that can meet the load requirement.

COMMON PITFALLS

There is a pitfall that some inexperienced engineers might fall when inputting parameters in different software. MFAD requires a parameter named Modulus of Deformation (E_p), which looks similar to another common parameter named Modulus of Subgrade Reaction (k). In some geotechnical reports, the parameter names are switched. This can lead to confusion and mistakes in the design.

These two parameters are essentially different in the following aspects:

1. Unit is different. The unit for E_p is ksi and the unit for k is pci.
2. Name should be different. E_p is called modulus of deformation and extensively used in MFAD. k is named modulus of subgrade reaction and can be used in LPILE.
3. Testing method is different. E_p is obtained by pressure meter test in the predrilled hole in the field (EPRI, 1982). k is obtained through plate bearing test. Due to the testing methods taken, the major purpose for E_p is for lateral loaded piles. k is for highway earthwork.
4. The detailed method of interpreting the parameters is different. E_p is categorized into two types based on the soil properties. If the soil is clay type, use User Guide for MFAD 5.0 Figure 3-2 “Modulus of Deformation for Cohesive Soils as a Function of Standard Penetration Resistance, Unconfined Compressive Strength and Soil Consistency” to relate SPT resistance value to determine the E_p . If the soil is not clay type, use SPT from soil report in Figure 3-4 “Modulus of Deformation as a Function of Standard Penetration

Resistance and Granular Soil Types” of User Guide for MFAD 5.0 to find the corresponding E_p . As for k , it is typically provided in the soils report.

DESIGN CRITERIA

Two criteria usually need to be met in order to ensure a satisfactory and safe foundation. The first criterion is strength criteria. It can be enforced by requiring the demands from factored load combinations not exceeding the factored strength of the foundation structure, which is the core of Load Resistance Factor Design (LRFD). The structural capacity is reduced or discounted by a strength Reduction Factor (RF) in the design to account for the uncertainty in material strength, precision level of estimating etc. On the other side of the equilibrium equation, the load is increased by Load Factor (LF). If the design follows $LF \times \text{Load Demand} < RF \times \text{Structural Capacity}$, the overall Safety Factor (SF) shall equal to LF/RF . This ensures the capacity of the structure is larger than the load demands for most of time even considering all the probabilistic distribution of loads, material strength, and geometry etc.

The other criterion is performance criteria, which includes the total deflection and rotation of pile head and non-recoverable deflection and rotation at the ground line. The non-recoverable deflection and rotation is deemed an aesthetic issue (EPRI Technical Report: Transmission Structure Foundation Design Guide, 2012). Usually the first criterion governs the design, and the second criterion serves as a supplement. But both criteria shall be met in order to reach a sufficient solution.

The issue in the foundation design is regarding the lack of appropriate performance design criteria. In ASCE 48-11, it is stated “...the owner shall include the following in the specification: ... design limit for foundation rotation and deflection, ...”. The performance design criteria for transmission structural foundation is not well defined in any major codes or standards such as NESC (2012) and ASCE 48-11 (2012). The major focus of the existing literature is regarding the strength design, which can prevent the structure from failure. Even though EPRI has conducted a survey among certain utility companies and consulting firms (EPRI Technical Report: Transmission Structure Foundation Design Guide, 2012) for the foundation design criteria, the root cause or the determining factor that affect the criteria is not clear. Different utility firms and engineering consulting companies are adopting their own criteria.

Referring to the performance criteria defined or described in other codes for other structures such as bridge and off shore platforms, it can be found that usually the requirement for the super structure determines the foundation performance criteria.

From AASHTO LRFD Bridge design specification (2013), section 10.5.2.2 stated “the tolerable movement criteria shall be established by either empirical procedure or structural analysis, or by consideration of both.” In addition, it is stated “Horizontal movement criteria should be established at the top of the foundation based on the tolerance of the structure to lateral movement, with consideration of column length and stiffness”.

From USACE 1110-2-2906 (1991), chapter 4, in the deformations session, it is stated that “Experience has shown that a vertical deformation of 1/4 inch and a lateral deformation of 1/4 to 1/2 inch at the pile cap are representative of long-term movements of structures such as locks and dams.” And “Operational requirements may dictate more rigid restrictions and deformations.”

From API (2012), section 6.3.3 stated “Deflections and rotations should not exceed serviceability limits which would render the structure inadequate for its intended function.”

The following performance criterion is recommended by Parrish, D.T. *et al* (2012). The other is based on the survey conducted by Electrical Power Research Institute (EPRI) for steel tangent pole drilled shaft foundation.

Table 1 Foundation Design Performance Criteria

Reference	Total Rotation (degree)	Non-recoverable Rotation (degree)	Ground line deflection/displacement (in)	Non-recoverable Ground line deflection (in)
Parrish, D.T. <i>et al</i> (2012)	2	1	4	2
EPRI, 1982	1.6	0.8	3.9	1.8

DESIGN EXAMPLES

To illustrate the application of the above described procedure and criteria, three examples are presented: one is intended for tangent pole, the other two for light angle pole and dead end poles. Three foundation design software packages including MFAD (version 5.1.1.18), LPILE, and PLS CAISSON have been used to analyze the performance of the drilled pier foundation.

All three foundations use round drilled reinforced concrete pier. The concrete compressive strength is 4 ksi. Details of the foundation and loading on top of foundation can be found in Table 2. The governing load cases used in the foundation analysis comes from the base reaction calculation, which originated from various load combinations. The soil profiles are picked from hundreds of soil profiles from the northeast coast. More details can be found in Figure 1.

Each of the three pole foundations have been modeled in the three software applications. The output of each software application is different. But most of software has moment, shear and deflection distribution along the depth of the pile. Therefore, these three indexes have been compared in charts to provide the insights between the different software applications.

Table 2 Details for the Pole Foundations

Pole Foundation	Tangent	Light Angle	Dead End
Diameter (ft)	9	10	14
Depth (ft)	21 or 22.5	26 or 36	35 or 49.5
Soil layer	6	4	4
Water table (ft)	6.5	6	22
Governing Shear (kips)	71	200	333
Governing Moment (kip-ft)	7,371	17,400	44,709

Where ML: inorganic silts and very fine sands; SM: silty sands and sand-silt mixtures; GM: silty gravels and gavel-sand-clay mixture; SP: poorly graded sands and gravelly sands; CL: inorganic clays of low to medium plasticity;

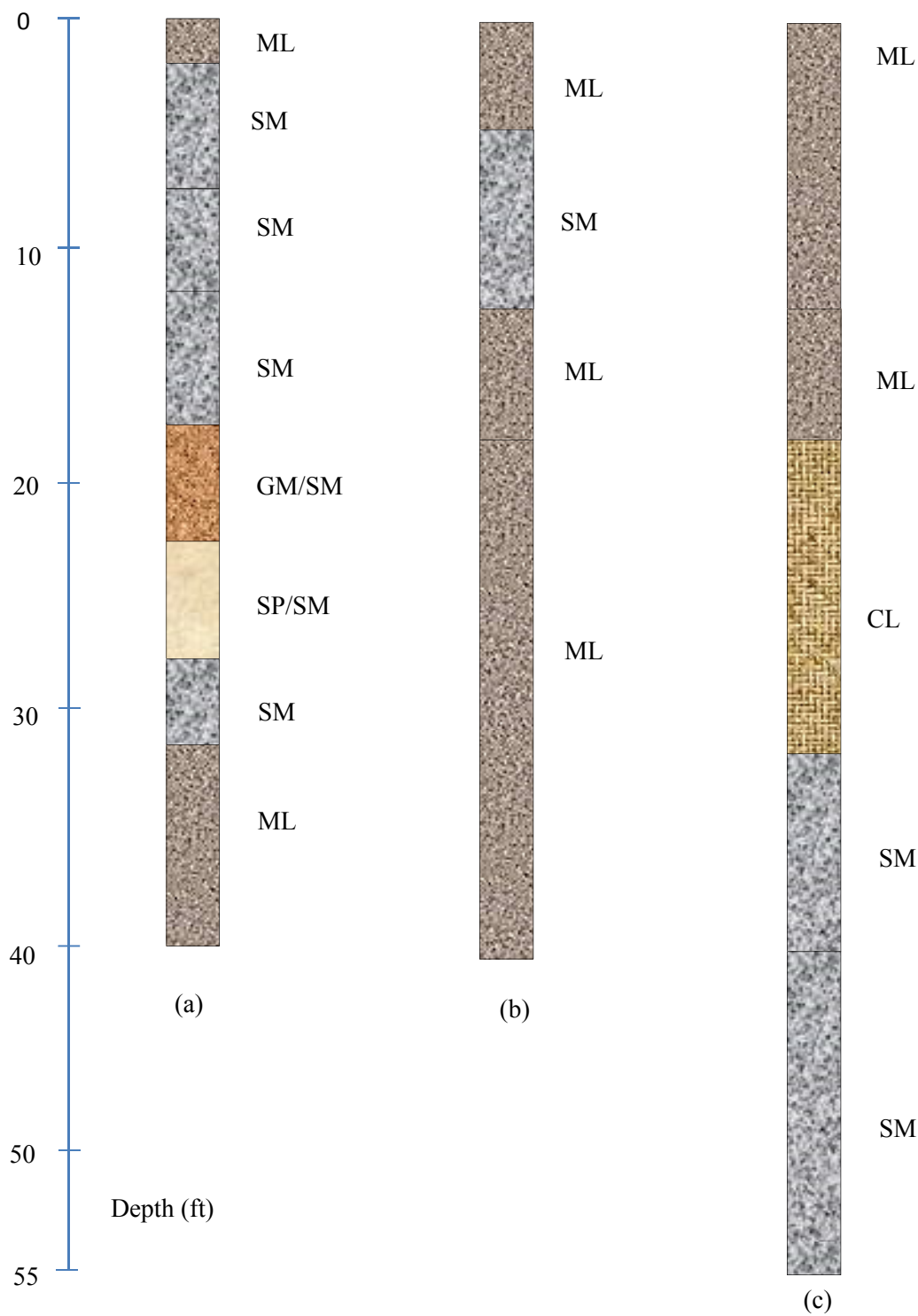


Figure 1 Soil Profiles (a) for the tangent pole (b) for the light angle pole (c) for the dead end pole

For each of three pole foundations, it has been modeled in the three software. The output of each software is different. But most of software has moment, shear, and deflection distribution along the depth.

For the tangent pole foundation, it can be seen that both shear distribution and moment distribution is close for all three software applications. MFAD requires a foundation with less depth than LPILE and PLS Caisson. The deflection from LPILE is much larger than the results from MFAD, which in turn requires a foundation with greater depth.

For the light angle pole foundation, it is found that PLS Caisson calculates a pile foundation more than 10 feet shorter than the rest of two software. The shear and moment distribution from MFAD and LPILE is close, however the deflection from LPILE is still higher than the results from MFAD.

For the dead end pole foundation, PLS Caisson recommended a foundation with less depth than MFAD and LPILE. The deflection from LPILE is still larger than the results from MFAD, but the difference between the two software applications is smaller compared with the light angle pole foundation.

The deflection from MFAD meets the performance criteria in Table 1 for all three cases. The deflection from LPILE, however, exceeds the criteria as in Table 1. Considering the working mechanism of LPILE is more focused on the $p-y$ curve to ensure the ultimate geotechnical capacity would not be exceeded, this can be acceptable.

The results from the three software packages are close for the tangent pole example, which has low loads from the top structure in terms of shear and overturning moment. The recommended depth of pier foundation from PLS Caisson can be different with the results of LPILE and MFAD when the overturning moment is relatively high. Such differences are most likely caused by the unique algorithm each software packages adopt. Therefore, the usage of two different software applications is recommended to provide a secondary check and achieve a conservative foundation design.

SUMMARY

Attention needs to be paid to the definition of important geotechnical parameters such as Modulus of Deformation (E_p) and Modulus of Subgrade Reaction (k) to avoid misuse. Even though most of the foundation can be designed safely and sufficiently only using the strength criteria, performance criteria is recommended to be adopted to eliminate the excessive movement and potential issues to the top attached conductors.

Using different geotechnical software for the same design usually leads to slightly different designs. To ensure the safety of the foundation, either using more than one software application or using manual checks is recommended to achieve a sound foundation design.

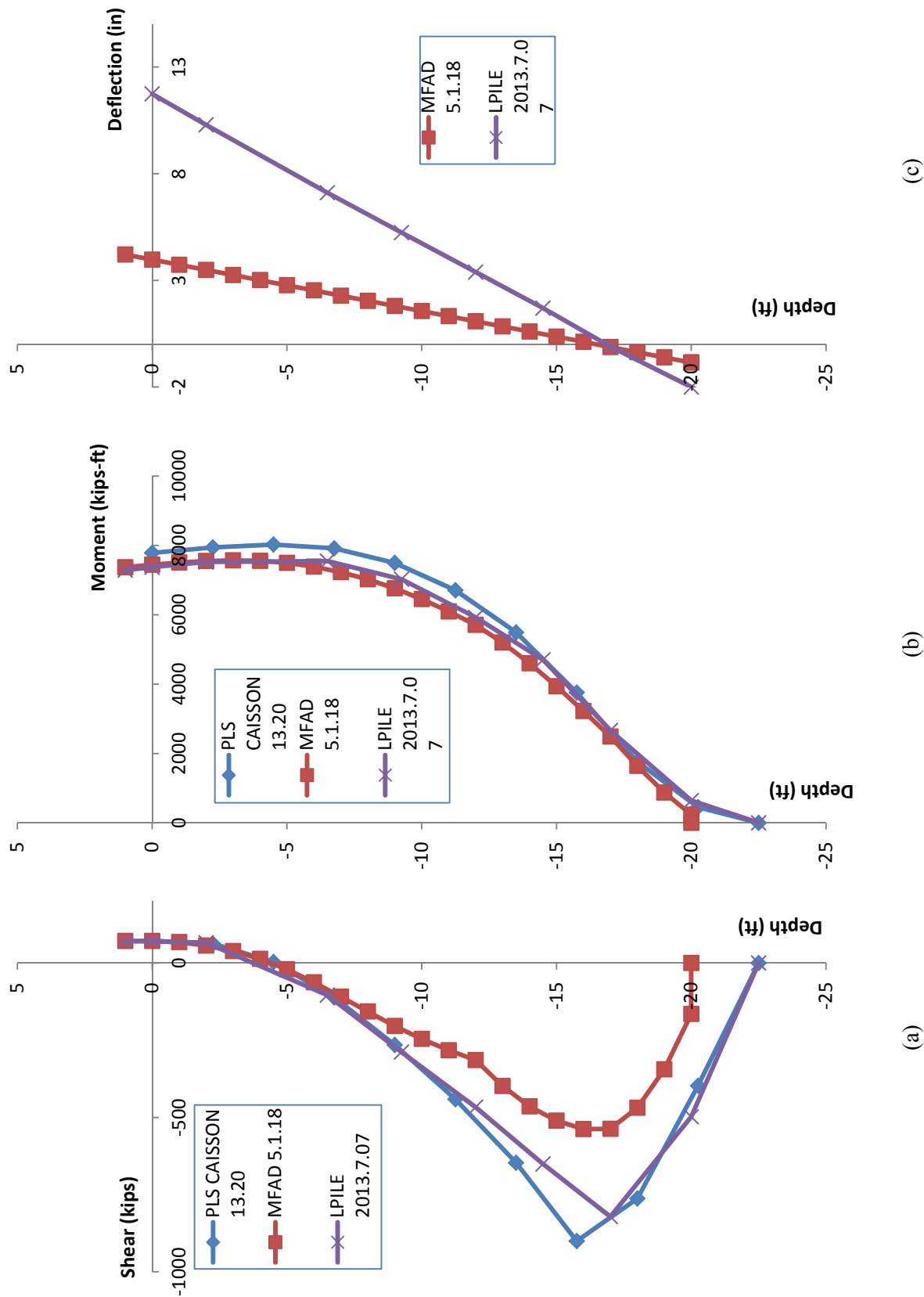


Figure 2 Tangent Pole Foundation (a) shear distribution along the depth (b) moment distribution along the depth (c) deflection along the depth

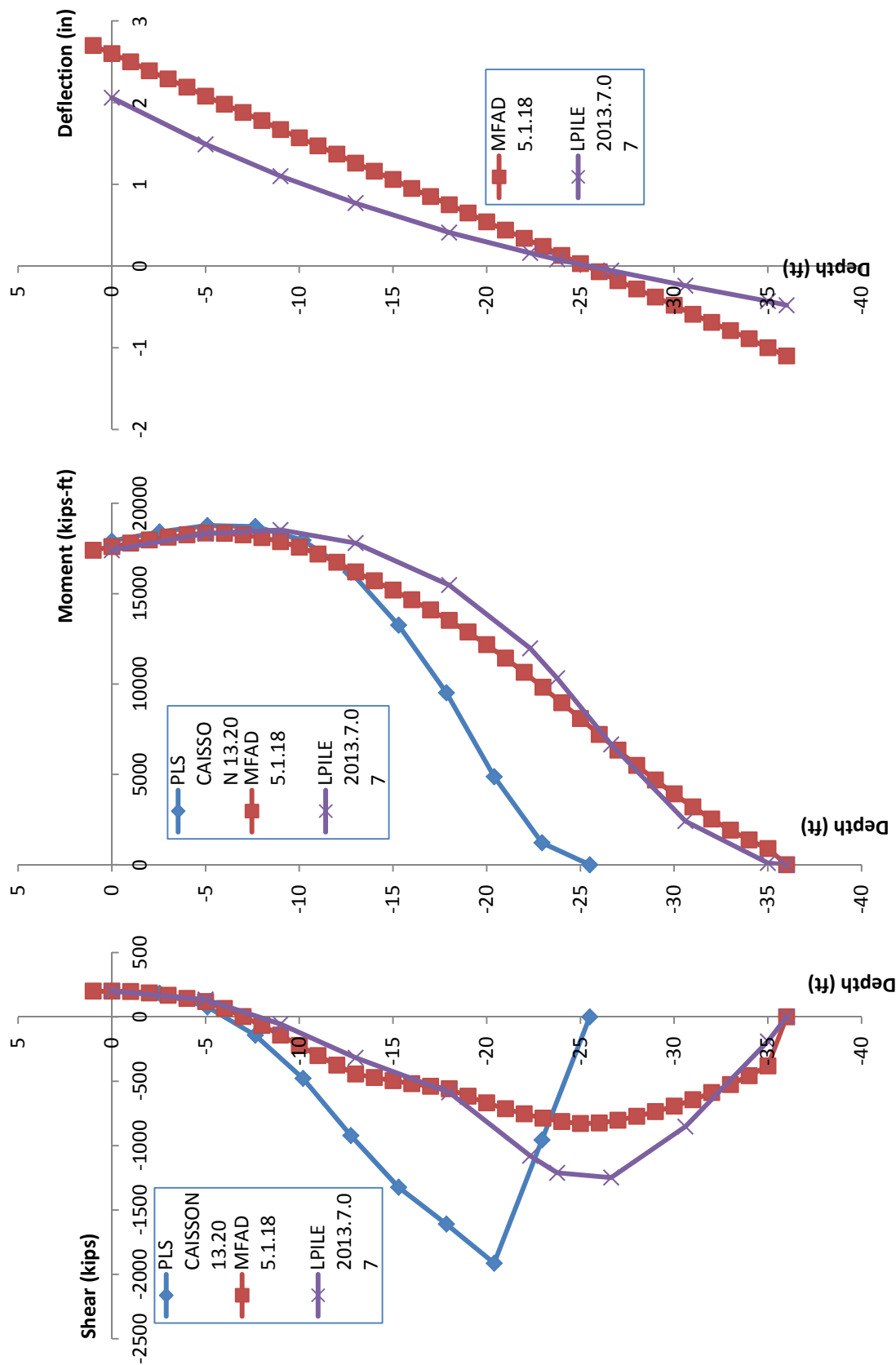


Figure 3 Light Angle Pole Foundation (a) shear distribution along the depth (b) moment distribution along the depth (c) deflection along the depth

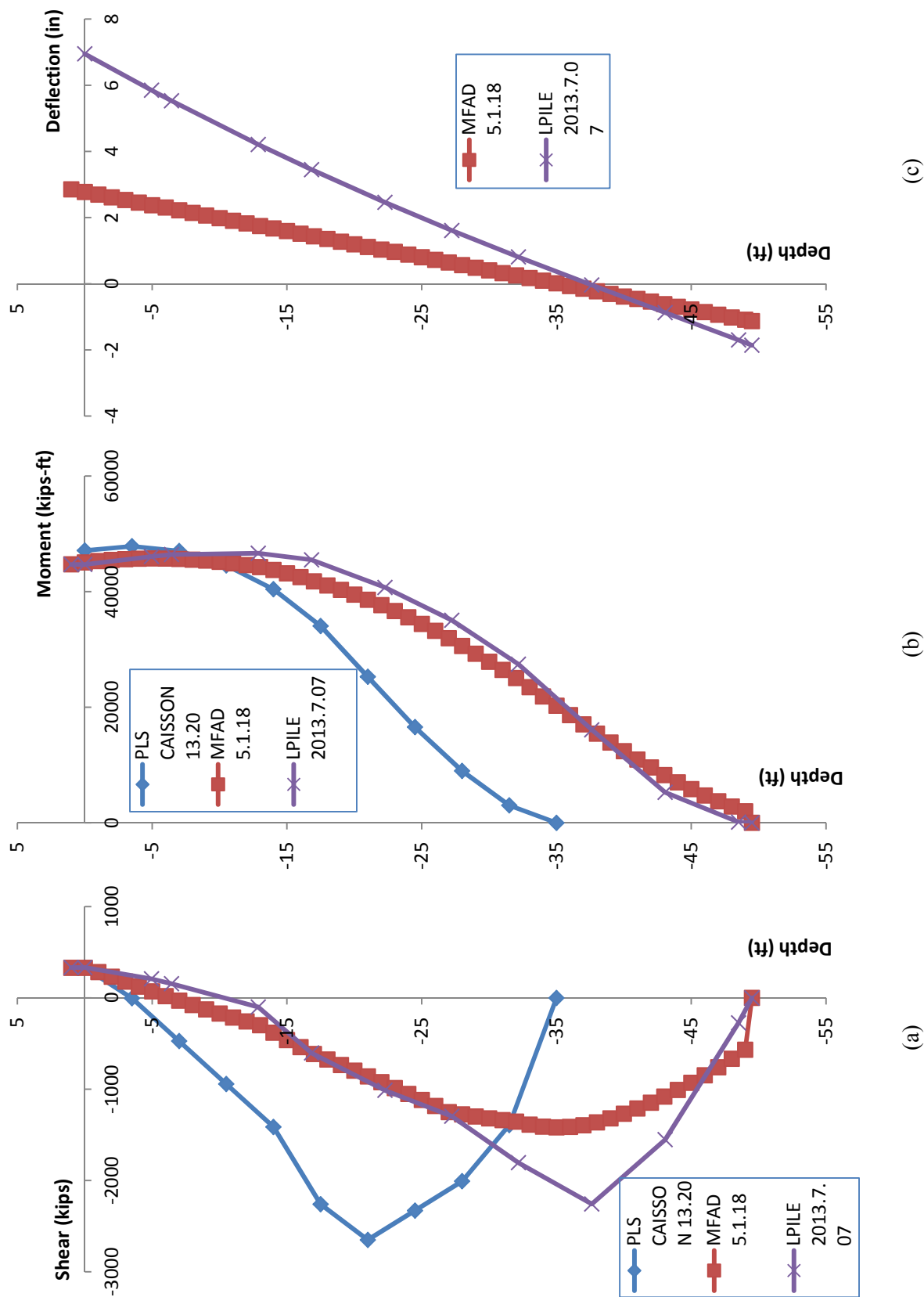


Figure 4 Dead End Pole Foundation (a) shear distribution along the depth (b) moment distribution along the depth (c) deflection along the depth

REFERENCE

- EPRI (Electric Power Research Institute). (2010) *User Guide for MFAD 5.0 (Moment Foundation Analysis and Design)*, Palo Alto, CA.
- Isenhower, W.M., and Wang, S. (2014). *User Guide for LPile 2013*, Enoft Inc.
- PLS (Power Line Systems, Inc.) (2011) *Caisson-Version 11.0*, Madison, WI.
- Electric Power Research Institute (EPRI). (1982) *Laterally Loaded Drilled Pier Research, Volume 2: Research Documentation. Product ID: EL-2197-V2*.
- EPRI (Electric Power Research Institute). (2012) *Transmission Structure Foundation Design Guide*, EPRI Technical Report, Palo Alto, CA.
- ASCE (American Society of Civil Engineers). (2012) *Design of Steel Transmission Pole Structures*, ASCE 48-11, ASCE, Reston, VA.
- IEEE (Institute of Electric and Electronics Engineers). (2012) *National Electrical Safety Code*, New York, NY.
- AASHTO (American Association of State Highway and Transportation Officials). (2013) *LRFD Bridge Design Specifications*, 6th Edition, Washington, DC.
- USACE (US Army Corps of Engineers). (1991), *Design of Pile Foundations*, Engineer Manual 1110-2-2906, Washington, DC.
- API (American Petroleum institute). (2012) *API Recommended Practice 2A-WSD Planning, Designing, and Constructing Fixed Offshore Platforms—Working Stress Design*, Dallas, TX.
- Parrish, T.D., Bledsoe, J.K., and DiGioia A.M. (2012) “Revealing Foundation Design Approaches”, *T&D World Magazine*, <<http://tdworld.com/overhead-transmission/revealing-foundation-design-approaches>> (Jan 1, 2012).

Case History of a Full Scale Axial Load Test of Sheet Piles

**Matthew B. Sylvain, M.S., S.M.ASCE¹; Miguel A. Pando, Ph.D., P.Eng., M.ASCE²;
Matthew J. Whelan, Ph.D., M.ASCE³; Corey D. Rice, M.S., S.M.ASCE⁴; Vincent O.
Ogunro, Ph.D., M.ASCE⁵; Youngjin Park, Ph.D., M.ASCE⁶; and Thomas Koch, P.E.⁷**

¹Ph.D. Student, Dept. of Civil and Environmental Engineering, Univ. of North Carolina at Charlotte, 9201 University City Blvd., Charlotte, NC 28223. E-mail: msylvain@uncc.edu

²Associate Professor, Dept. of Civil and Environmental Engineering, Univ. of North Carolina at Charlotte, 9201 University City Blvd., Charlotte, NC 28223. E-mail: mpando@uncc.edu

³Associate Professor, Dept. of Civil and Environmental Engineering, Univ. of North Carolina at Charlotte, 9201 University City Blvd., Charlotte, NC 28223. E-mail: M.Whelehan@uncc.edu

⁴Ph.D. Student, Dept. of Civil and Environmental Engineering, Univ. of North Carolina at Charlotte, 9201 University City Blvd., Charlotte, NC 28223. E-mail: cdrice@uncc.edu

⁵Associate Professor, Dept. of Civil and Environmental Engineering, Univ. of North Carolina at Charlotte, 9201 University City Blvd., Charlotte, NC 28223. E-mail: vogunro@uncc.edu

⁶EPIC Engineer, Dept. of Civil and Environmental Engineering, Univ. of North Carolina at Charlotte, 9201 University City Blvd., Charlotte, NC 28223. E-mail: Y.Park@uncc.edu

⁷Structures Management Unit, North Carolina Dept. of Transportation, 1100 New Bern Ave., Raleigh, NC 27601. E-mail: tkoch@ncdot.gov

Abstract

Short span bridges in the U.S. that are located near rivers and streams typically use sheet piles to defend the abutment against erosion and scour. In such bridges, the abutment axial load demands are usually carried by driven piles installed behind the scour protection sheet piles. An alternative bridge abutment design approach, successfully used for decades in Europe and in some projects in the U.S., involves installing sheet piles for the double function of scour protection and axial load bearing. This design paradigm shift has the potential to significantly reduce construction cost. However, widespread implementation and acceptance of this design approach requires full-scale axial load tests on instrumented sheet piles. This paper presents an axial load test program carried out at a test site in North Carolina that shows that the axial stiffness and load capacity of the sheet pile was comparable to the response recorded in the comparison H-pile when normalized for differences in the tip and surface areas.

INTRODUCTION

FHWA (2012) reported bridge abutment scour as one of the major causes of bridge failure in the United States. For short span bridges (i.e., spans less than 20 m) in the U.S., it is common to use sheet piles as an abutment scour protection measure in a typical configuration shown schematically in Figure 1. As shown in this figure, the sheet piles are located along the abutment face with a row of axial load bearing H-piles installed at some distance behind them. Any axial load bearing contribution from sheet piles used for scour protection is typically neglected in design. However, completely neglecting all axial load bearing contribution from the sheet piles may be overly conservative based on the several European bridge projects that have reported successful performance of bridge abutment designs with only sheet piles (McShane 1991;

Yandzio 1998). In addition to the successful European experience with this design approach, a few projects in the U.S. have also reported favorable performance of bridge abutments that utilized sheet piles as axial load bearing foundation elements. For example, Carle et al. (1989) reported the successful use of PZ 27 sheet piles as sole axial load bearing elements for the abutments of the Small Creek Bridge in Seward, Alaska. The abutment configuration for this bridge is shown schematically in Figure 2. As shown in this figure, the sheet piles are approximately 8.83 m in length with H-pile tips driven to bedrock. Another successful case history in the U.S. is the demonstration bridge project in Black Hawk County Iowa reported by Evans et al. (2010). A schematic illustrating the sheet pile abutment design used for this bridge is shown in Figure 3. This single span bridge is 11.89 m long and used PZ-22 sheet piles driven to bedrock. The authors of this study indicated the sheet piles provided considerable axial load capacity that translated to savings in construction time and cost.

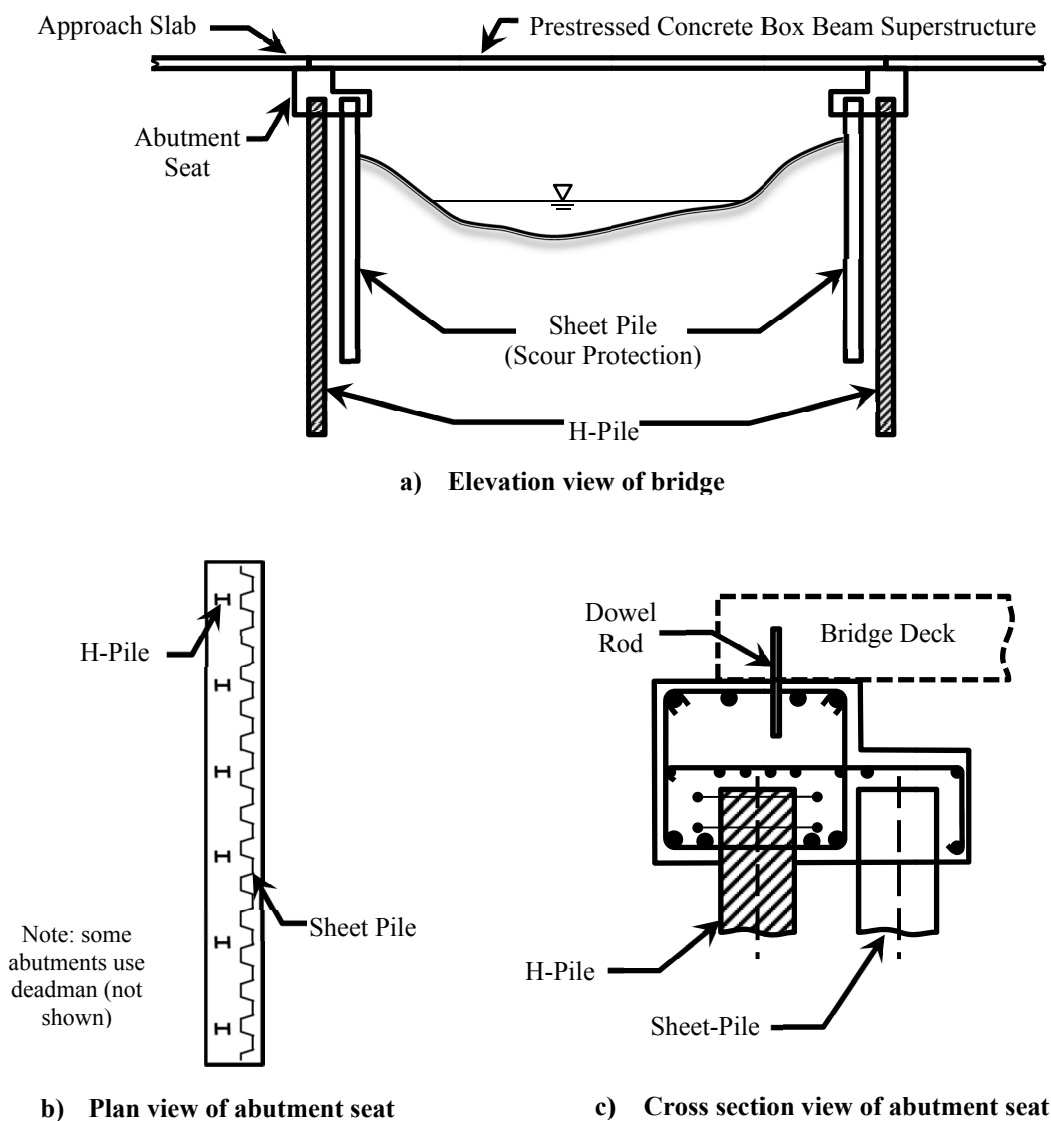


Figure 1. Drawing of typical short span bridge layout within the U.S.

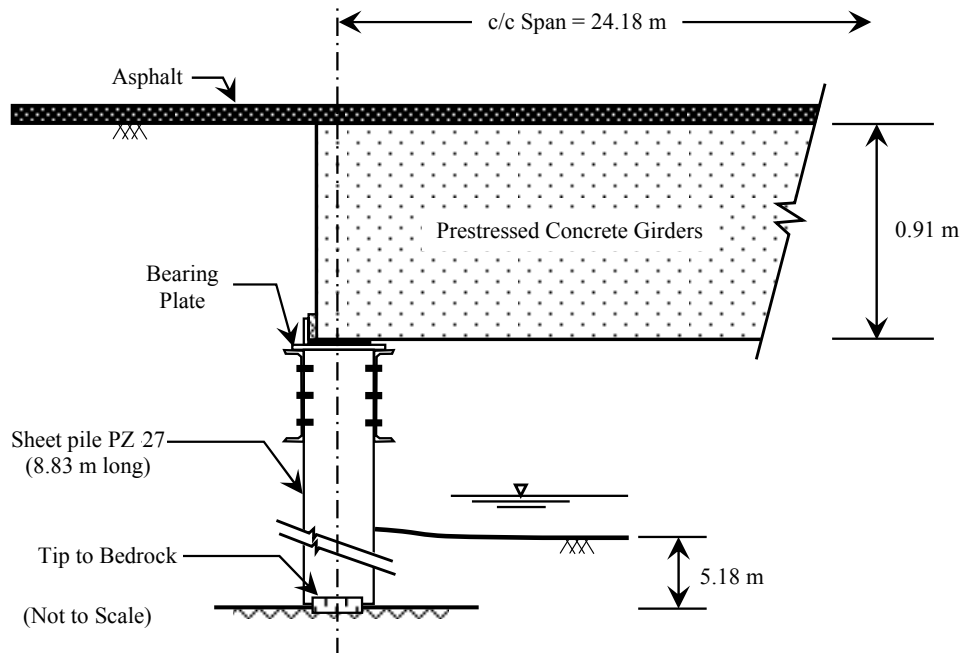


Figure 2. Abutment configuration of the Small Creek Bridge in Seward, Alaska (adapted from Carle et al. 1989).

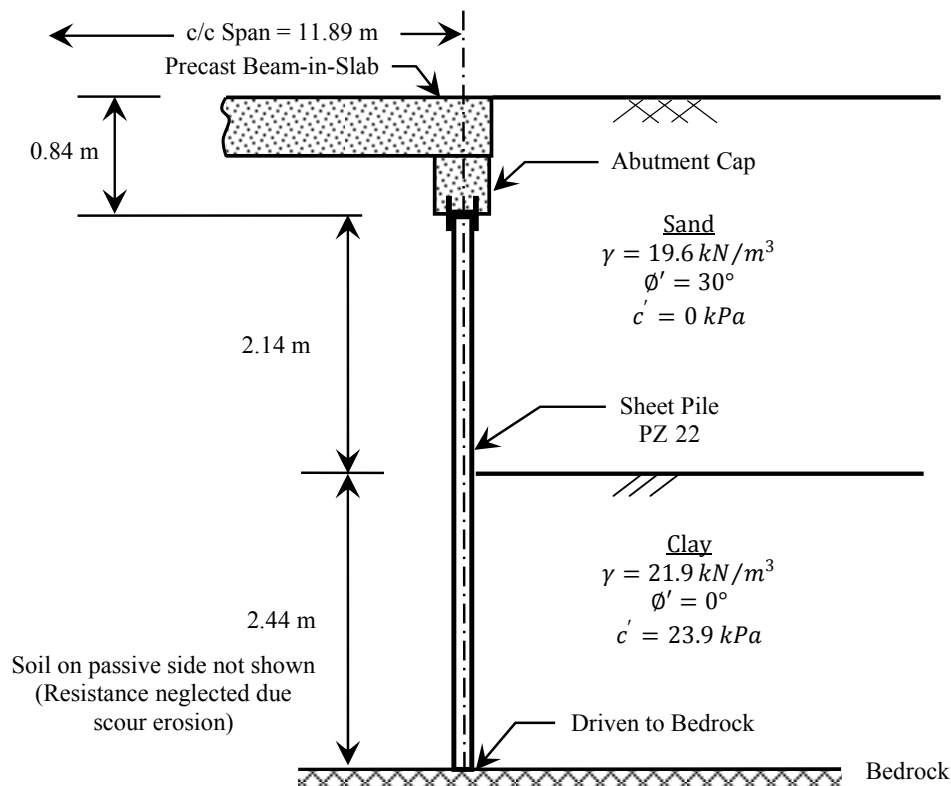


Figure 3. Sheet pile replacement bridge in Black Hawk Co., Iowa (adapted from Evans et al. 2010).

The ample experience in Europe evidenced by many successful case histories reported in the literature, coupled with the few case histories reported in North America, support the incorporation of the axial load bearing capacity offered by sheet piles in abutment design. Particularly for short span bridges, alternative abutment designs are not only feasible but may result in significant cost savings due to reduced construction time (due to fewer pile installations) and required materials (as this design may result in elimination or a reduction of the number of H-piles required for carrying design loads). However, despite empirical evidence of the potentially significant axial load capacity and stiffness provided by sheet piles in past bridge construction and research projects, bridge designers in the U.S. have yet to routinely adopt the use of the axial load bearing capacity of sheet piles for typical design of short span bridges. This is possibly in part due to the absence of well-documented case histories involving heavily instrumented, full-scale axial load tests on sheet piles and the lack of associated design guidance developed from such testing.

In this paper, the authors report the results of a full-scale field axial load test on an instrumented pair of sheet piles. Furthermore, this case history includes an axial load test on an H-pile installed a few meters from the sheet piles with similar embedment depth and geotechnical conditions. This case study serves to provide a valuable comparison between the axial load capacity and stiffness of these two pile types.

PROJECT DETAILS

Test site. The field site was located within the equipment yard of an International Construction Equipment (ICE) facility located in Matthews, N.C. The site is located in the Charlotte Belt of the Piedmont Physiographic Province of North Carolina. The soils in this region were typically developed from differential weathering of the underlying igneous or metamorphic rock. These soils are referred to as residuum and can have variable thicknesses depending on the degree of weathering.

The site investigation used to characterize the geotechnical conditions of the test site involved two conventional boreholes with SPT testing and sampling, two seismic CPTu soundings, and the installation of a standpipe for monitoring groundwater elevation. The location of the field tests, as well as the location of the test piles, which were installed approximately 5.6 m apart, are shown in Figure 4. A summary of the main geotechnical test results along with a generalized soil profile based on exploratory borings is provided in Figure 5. The general soil conditions at this site consists of a dense layer of gravel with sand fill to a depth of 0.15 m. The fill layer is underlain by a layer of medium dense clayey sand that extends to a depth of about 1.85 m. Beneath this sand layer, a layer of soft to medium stiff silt extends to a depth of about 2.60 m. Following the silt layer, a loose clayey sand extends to a depth of about 5.65 m, and is followed by a medium dense to dense silty sand extending to the final depth investigated of 10.15 and 14.48 m for boring SPT-1 and SPT-2, respectively. A CME 550 drill rig was used for the SPT field investigation and the maximum depths reached correspond to practical auger refusal for this rig.

Test piles. The load test program performed for this project involved axial load testing of a pair of PZ 27 sheet piles (referred to as simply sheet pile). In addition to the sheet pile, one HP 12x53 H-pile was installed for comparison purposes. The cross sectional details for these piles are shown in Figure 6 and summarized in Table 1. Both test piles had a total length of 6.1 m.

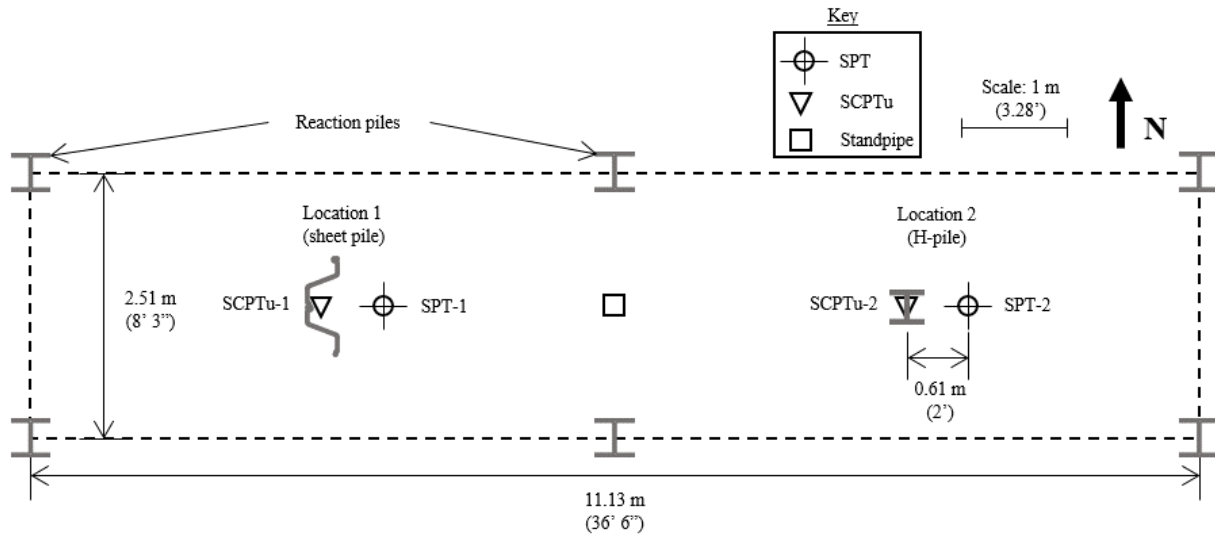


Figure 4. Location of field tests.

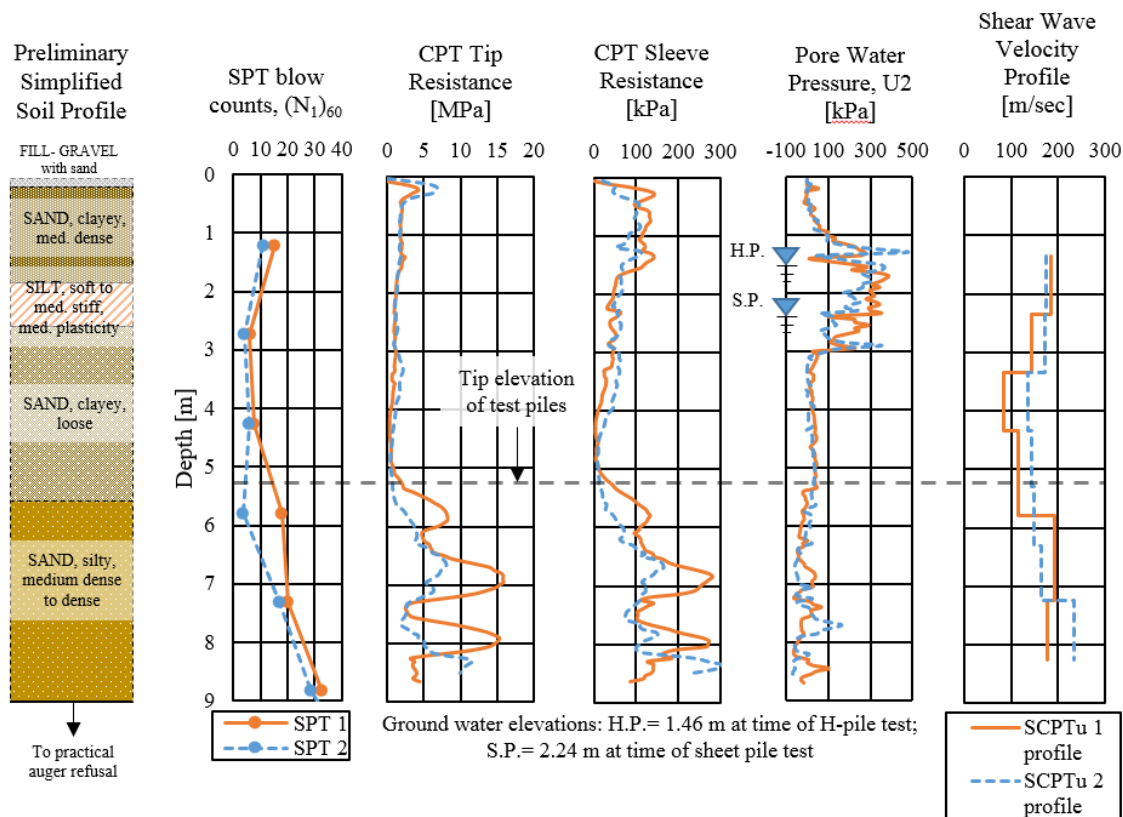


Figure 5. Preliminary generalized soil profile at field test site and field test results.

The test piles were installed using both a vibratory and impact hammer. Vibratory driving was performed using an ICE Model 28C hammer and impact driving was performed using an ICE Model I-12 hammer. Both hammers were used to simulate typical field installation practice. The test piles were first installed to an initial embedment depth of 2.4 m using the vibratory hammer and then driven to the final embedment depth of 5.2 m using the impact hammer. Figure 7 presents the driving record as well as images of pile installation. At the end of driving (EOD),

the driving resistance was measured as 19.7 and 9.8 blows per meter for the sheet pile and H-pile, respectively. Pile driving analysis (PDA) measurements were obtained on both piles during restrike performed 11 days after driving with the same impact hammer. The axial pile capacity estimates obtained from the PDA measurements using the Case method damping model with an RX7 damping (Goble et al. 1975) were 196 kN and 40 kN for the sheet pile and H-pile, respectively.

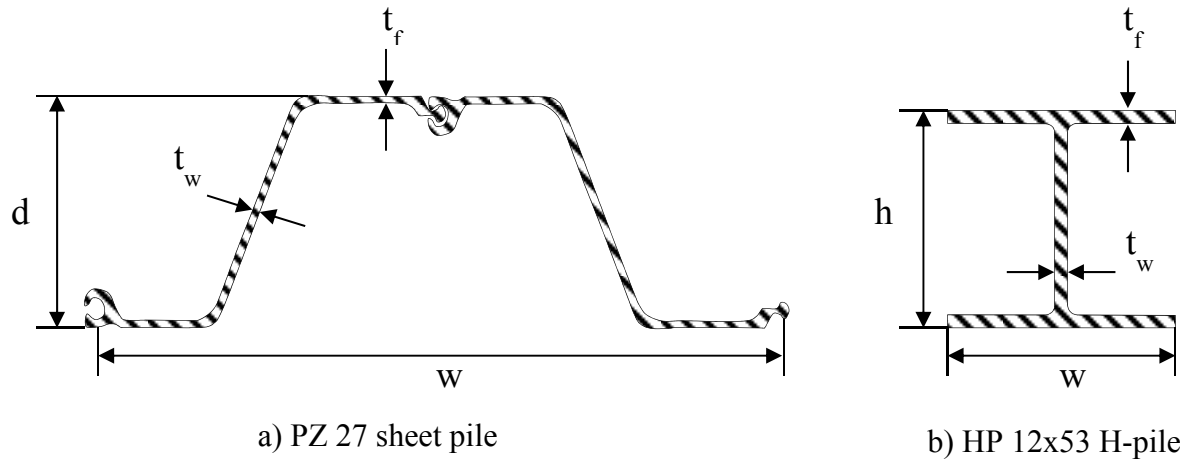


Figure 6. Cross section of test piles.

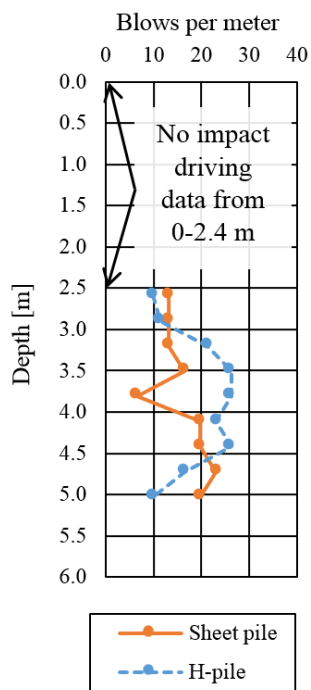
Table 1. Section dimensions for PZ 27 and HP 12x53 pile sections.

Test Pile Type	Pile Designation	Width, w (mm)	Depth, d (mm)	Thickness		Cross Sectional Area (cm ²)	Perimeter Surface Area (m ² /m)
				Flange, t_f (mm)	Wall, t_w (mm)		
Sheet pile	PZ 27	914	305	9.50	9.50	153.71 ¹	2.74
H-pile	HP 12x53	305	300	11.0	11.0	100.00	1.77

Note: (1): Area reported corresponds to the total cross sectional area that includes the pair of PZ 27.

STATIC LOAD TEST SETUP

The setup used for the static pile load testing of the sheet pile and H-pile was developed in general accordance with ASTM Standard D1143 (ASTM 2013). Six HP 14x73 piles were driven around the test piles and used to construct the reaction frame. Loads were applied using a model RCH-603 Enerpac hollow plunger cylinder with 533.8 kN capacity and 7.62 cm of stroke. The jack used to operate the piston was a model P-80 Enerpac hand pump. Displacement was measured at the four corners of the pile head using digital dial gauges with measurement resolution of 0.002 mm. A model TD175 Industrial Commercial Scales canister load cell with 444.8 kN full-scale range was used to measure the applied axial load at the pile head and was signal conditioned with a 24-bit PXI-4330 bridge input module. The displacement and load measurements were obtained concurrently by a digital data acquisition system. The static axial pile load test setup is shown in Figure 8.



a.) Driving record for pile installation



b.) Impact hammer and H-pile



c.) Instrumentation for PDA

Figure 7. Driving record and images of test pile installation.

AXIAL CAPACITY ESTIMATES USING STATIC LOAD METHODS

Prior to axial load testing, the axial load capacities of both test piles were estimated using static methods including the CPT-based LCPC method (Bustamante and Gianeselli 1982) and SPT-based Meyerhof method (Meyerhof 1976) assuming a no plugging condition at the tip. The axial load capacity estimates using these static methods for both test piles are presented in Table 2.

STATIC AXIAL LOAD TEST RESULTS

Static load testing was performed on both the sheet pile and H-pile in general accordance with ASTM Standard D1143 (ASTM 2013). Testing was performed using the constant rate of penetration as well as the quick load test procedures. However, for the sake of brevity, only the results from the constant rate of penetration testing are presented. Loading was applied to achieve a constant rate of penetration of about 0.13 mm/min. The axial load test results, presented as pile head displacement versus applied axial load, are provided in Figure 9. Each of these curves show a white dot with a black boarder that represent the axial load capacity for each test pile based on the Chin-Kondner failure criterion (Chin 1970). Using this failure criterion, the failure loads for the sheet pile and H-pile were found to be 158 and 101 kN, respectively. The axial load capacities can also be compared based on an arbitrary pile head displacement. For example, at a pile head displacement of 7 mm the axial load capacity for the sheet pile and the H-

pile were found to be 165 and 100 kN, respectively. The axial load capacities are also summarized in Table 2.



a.) Image of test pile and reaction frame



b.) Image of test H-pile prior to static load test

Figure 8. Image of test setup and axial load test.

Table 2. Results of static load testing and predicted load capacity.

Test Pile Type	Measured (Axial load test and PDA dynamic measurements)			Predicted (Static methods)	
	Load at 7 mm Displacement (kN)	Failure Load ¹ (kN)	Restrike PDA Capacity ² (kN)	LCPC ³ (kN)	Meyerhof ⁴ (kN)
Sheet pile	165	158	196	285	157
H-pile	100	101	40	189	76

Notes: ⁽¹⁾: Reported failure load is based on the Chin-Kondner failure criterion (Chin 1970).

⁽²⁾: Axial load capacity estimate based on PDA dynamic measurements during restrike (11 days after installation) and the CASE damping model (damping CRX 7).

⁽³⁾: LCPC based on Bustamante and Ganeselli (1982).

⁽⁴⁾: Based on Meyerhof (1976).

The static methods used to predict the axial load capacity of the test piles were compared to the failure load obtained based on the Chin-Kondner failure criteria. This resulted in load estimates that varied by as little as 0.6% under-prediction of capacity (as determined by the Meyerhof method compared to the failure load of the sheet piles) to as much as 87.1% over-prediction of capacity (as determined by the LCPC method compared to the H-pile failure load). Results indicate that the LCPC method over-predicted the axial load capacity by 80.4% and 87.1% for the sheet pile and H-pile, respectively. The Meyerhof method was found to under-predict the capacity of both the sheet pile and the H-pile by 0.6% and 24.8%, respectively. Pile

capacity estimates obtained from the restrike PDA testing over-predicted the capacity of the sheet pile pair by 24.1% and under-predicted the capacity of the H-pile by 60.2%.

In terms of axial stiffness of the two test piles, this was assessed in terms of the secant slope, computed by connecting the origin and the load-displacement responses at a prescribed pile head displacement (values of 0.5 and 7 mm were selected). For the prescribed pile head displacement of 0.5 mm the axial load secant stiffness values were found to be 128.9 and 116.27 kN/mm for the sheet pile and H-pile, respectively. The axial stiffness values obtained for a pile head displacement of 7 mm were 23.6 and 14.3 kN/mm for the sheet pile and H-pile, respectively. The higher axial load secant stiffness values of the sheet pile is as expected given its larger cross sectional area and skin friction surface area (see Table 1) compared to the H pile.

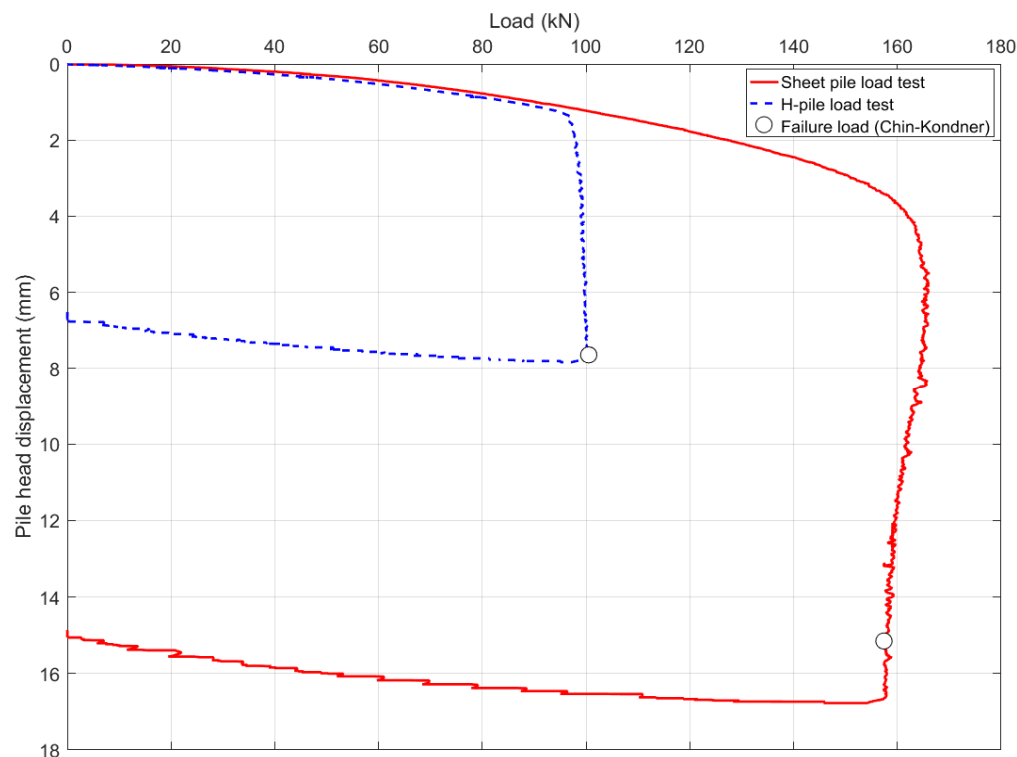


Figure 9. Load versus displacement results for static load testing of sheet pile and H-pile with failure loads.

It is important to point out that the total shaft area of the sheet pile, without consideration of cover plates, was 14.2 m^2 whereas the shaft area of the H-pile was 9.2 m^2 . Additionally, the area of the tip of the sheet pile was 153.7 cm^2 compared to a tip area of 100 cm^2 for the H-pile. In other words, the sheet pile had a total shaft area and an unplugged tip area that were 54.3% and 53.7% larger than the corresponding shaft and tip areas of the H-pile. The larger shaft area and tip area largely explain the larger observed axial capacity and stiffness for the sheet pile. However, the larger axial capacity measured for the sheet pile may also be attributed, likely to a lesser extent, to differences in soil conditions as reported in Figure 5. The main soil profile difference between the two test pile locations was found at the clayey sand layer near the elevation of the pile tips. At the location of the sheet pile this layer was denser, based on higher CPT tip and sleeve resistances and a higher SPT blow count recorded at 5.8 m, than the

conditions encountered in this same layer at the H-pile location. The somewhat denser layer near the tip of the sheet pile, as compared to H pile, is likely to have also contributed to the observed higher axial capacity of the sheet pile compared to the H-pile.

Overall the axial load testing results show that the axial stiffness and load capacity of the sheet pile was comparable to the response recorded in the comparison H-pile, particularly when normalized for differences in the tip and surface areas.

SUMMARY AND CONCLUSIONS

As mentioned above, the sheet pile was found to have comparable axial capacity and axial stiffness as compared to the H-pile, when normalized for differences in the tip and surface areas. However, to a lesser extent the observed larger axial capacity for the sheet pile may also be attributed to some differences in the soil conditions near the toe of this test pile (Figure 5). Despite these small differences, the results from this full scale axial load test program strongly suggests a good potential for sheet piles to be utilized for axial load bearing foundation elements for bridge abutments and other structures.

These tests present the results of full scale, well instrumented, axial load testing of both an H-pile and sheet pile. The axial load capacity of the sheet pile was found to exceed the axial load capacity of the H-pile. Therefore, there is strong potential for the axial load bearing capacity of sheet piles to be considered for bridge design. Based on the results presented in this paper, incorporation of the axial load bearing capacity of sheet piles could provide substantial savings in terms of time and money.

ACKNOWLEDGMENTS

The research presented in this paper is part of the ongoing research project sponsored by the North Carolina Department of Transportation (NCDOT). The financial support through this grant is greatly appreciated. The contents of this paper reflect the views of the authors and not necessarily the views of the University nor NCDOT. The authors are responsible for the fact and the accuracy of the data presented herein. Furthermore, the contents do not necessarily reflect the official views or policies of the NCDOT. Additionally, this paper does not constitute a standard, specification, or regulation.

The authors would like to express their special gratitude to ICE for the use of their yard, equipment, and personnel required for conducting this pile load test. Special gratitude also goes to Lee of the Carolinas for their assistance and support in several tasks of this project including assistance with providing steel for construction of the reaction frame. We also acknowledge the generous support by Skyline Steel (for test piles and reaction piles), S&ME, Inc. (for geotechnical drilling and testing), and GRL Inc. (for PDA services).

REFERENCES

- ASTM. (2013). *ASTM- D1143- Standard test methods for deep foundations under static axial compressive load*. ASTM International, 100 Barr Harbor Drive, PO Box C700, West Conshohocken, PA.
- Bustamante, M.G., and Gianceselli, L. (1982). *Pile Bearing Capacity Prediction by Means of Static Penetrometer CPT*. Proceedings of the 2nd European Symposium on Penetration Testing, ESOPTII, Amsterdam, 2, 493-500.

- Carle, R., and Whitaker, S. (1989). Sheet Piling Bridge Abutments. *Deep Foundations Institute Annual Meeting*, Maryland, 1-16.
- Chin, F.K., (1970). *Estimation of the ultimate load of pile not carried to failure*. Proceedings of the Second Southeast Asian Conference on Soil Engineering, Singapore, 81-90.
- Evans, R. (2010). *Modified sheet pile abutments for low volume road bridges*. MS thesis, Iowa State University.
- FHWA (Federal Highway Administration). (2012). *Evaluating Scour at Bridges*, FHWA Publication No. FHWA-HIF-12-003, HEC No. 18, April, 2012.
- Goble, G.G., Likins, G.E., and Rausche, F. (1975). *Bearing Capacity of Piles from Dynamic Measurements*. Final report, Department of Civil Engineering, Case Western Reserve University, Cleveland, Ohio.
- McShane, G. (1991). Steel sheet pile used in the combined role of bearing piles and earth retaining members. *4th International Conference on Piling and Deep Foundations*, Stresa, Italy, April 7-12.
- Meyerhof, G.G. (1976). *Bearing capacity and settlement of pile foundations*. American Society of Civil Engineers, ASCE, Journal of the Geotechnical Engineering Division, 195-228.
- Yandzio, E. (1998). *Design Guide for Steel Sheet Pile Bridge Abutments*. SCI Publication No. 187, ISBN 1859420648.

Load Testing and Performance of Instrumented ACIP Piles in Texas Clays

Nasser Massoudi, Ph.D., P.E., M.ASCE¹; and Kenneth R. Bell, Ph.D., P.E., F.ASCE²

¹Bechtel Corp., 12011 Sunset Hills Dr., Reston, VA 20190. E-mail: nmassoud@bechtel.com

²Bechtel Corp., 12011 Sunset Hills Dr., Reston, VA 20190. E-mail: krbell@bechtel.com

Abstract

A series of instrumented pile load tests was performed on augered cast in-place piles in an area northeast of Austin, Texas. The site soils primarily comprised of clays. The load test program included testing various pile diameters and lengths. Ten compression and tension load tests were performed. Five of the test piles were instrumented with internal strain gages at multiple levels. Load test results provided valuable insight on distribution of loads along the pile shaft and at the toe. This paper summarizes the site subsurface conditions, results of the pile load tests, observed load distribution in instrumented piles, and compares back-calculated skin friction and toe resistance factors from the load tests with those commonly used in pile design.

INTRODUCTION

There is abundant literature on load testing of deep foundations in general. However, well documented case histories on load testing of instrumented Augered Cast-in-Place (ACIP) piles, constructed using continuous flight augers (CFA), are limited. Perhaps the earliest and most comprehensive field study of instrumented ACIP piles in the U.S. was performed by O'Neill et al. (1999) on load testing of three 18-in. diameter, 30 – 50-ft long piles at 3 different sites in Texas, investigating load transfer in a variety of soils such as clay, sand, mixed soils, and much more. Lambert (2000) presented data, including one lateral test, for 15 instrumented piles, with diameters of 14 – 24 in. and lengths of 25 – 99 ft in mixed clays, sands, and rocks of the U.S. Midwest. Sorensen (2006) summarized the findings, including two lateral tests, from 7 instrumented 14-in. diameter, 40 – 60-ft long piles in a high seismic area in California, with soft-hard clays and silts. Another comprehensive document addressing the design and construction of ACIP piles was prepared by FHWA (2007); the testing reported in this paper predates the FHWA document. Beck and Harrison (2009) assessed load distribution of an instrumented 14-in. diameter, 87-ft long pile. Vipulanandan et al. (2012) investigated the load transfer mechanism, including residual forces, in a 30-in. diameter 39-ft long pile in hard clay.

This paper describes the findings from a series of load tests that were performed on ACIP piles installed using CFA. The load test program included testing various pile diameters and lengths. A total of 10 compression and tension tests was performed on piles ranging in diameters from 14 to 18 in. and lengths from 55 to 70 ft. Of the 10 test piles, 5 piles were instrumented with multiple strain gages and data were collected during the load testing. Of these 5 piles, only 2 experienced enough deformation from which failure could be discerned. From these, the collected information was used to assess the load distribution along the pile shaft and at the toe.

SUBSURFACE CONDITIONS

The subsurface conditions predominantly were comprised of clays, with sand and lignite interbeds. Three dominant layers were present, including man-made fill. Bedrock was not encountered. The soils were of marine origin, belonging to the Calvert Bluff Formation of the Wilcox Group (lower Eocene Age). A summary of the subsurface conditions is presented below.

- **Layer 1 (Fill Material and Sand):** clay, sand, and lignite of varying proportions, with an average SPT N-value of 20 blows/ft.
- **Layer 2 (Clay):** naturally occurring clay, sandy clay, and lignite, with an average SPT N-value of 68 blows/ft. Lignite zones of about 1.5 – 9 ft thick were present within the clay soils.
- **Layer 3 (Sand):** naturally occurring sand with varying amounts of clay and/or silt, with an average SPT N-value of 82 blows/ft.

Most clays indicated high plasticity (PI as high as 50), suggesting potentially expansive soils, particularly where lignite was present. Results of 8 swell tests indicated swell ratios in the range of 1.6 – 5.5%. The higher swell results were in soils at shallow depths.

Groundwater level, on average, was at a depth of about 7 ft below the ground surface. The soil and groundwater conditions at test pile locations are shown in Figure 1.

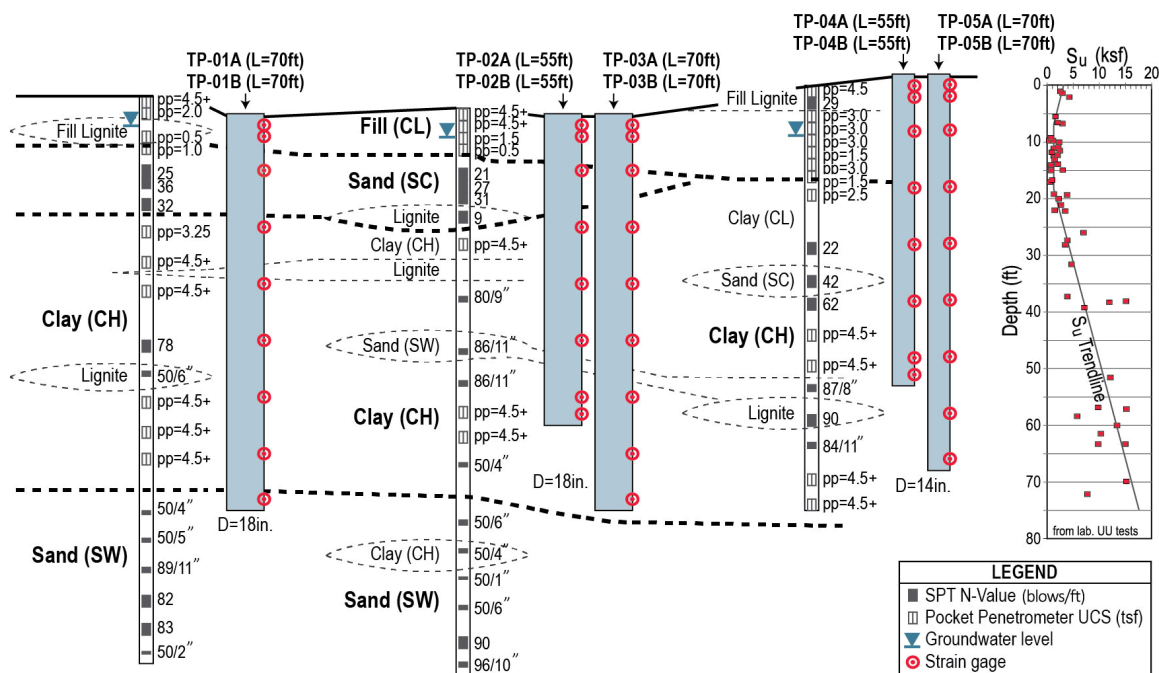


Figure 1. Test Piles and Subsurface Conditions

TEST PILE DETAILS

Of the 10 test piles, 5 were subjected to compression loading and 5 were tested in tension. The compression tests were performed per ASTM D1143 “standard” and “quick” loading procedures. The tension tests followed ASTM D3689. A calibrated load cell was used for load measurements. Pile top deflections were measured using 4 dial gages, equally spaced around the pile top. Information on test piles is summarized in Table 1.

Table 1. Summary of Test Piles and Load Testing Results

Test Pile Information			Load Test Type	DL (ton)	TL (ton)	Measured Movement at Top of Test Pile (in.)			Est. Pile Failure Load (ton)
Test No.	D (in.)	L (ft)				@ DL	@ TL	After Unload	
TP-01A	18	70	C, S	120	240	0.1	0.24	0.06	370*
TP-01B	18	70	T, S	70	140	0.03	0.15	0.08	150*
TP-02A	18	55	C, S	120	375	0.19	0.60	0.27	370
TP-02B	18	55	T, S	70	210	0.02	0.34	0.16	150
TP-03A	18	70	C, Q	120	240	0.09	0.22	0.04	370*
TP-03B	18	70	T, Q	70	140	0.03	0.14	0.06	150*
TP-04A	14	55	C, Q	70	300	0.06	1.46	1.05	230
TP-04B	14	55	T, Q	43	180	0.01	0.25	0.17	180
TP-05A	14	70	C, Q	70	140	0.06	0.17	0.02	230*
TP-05B	14	70	T, Q	43	90	0.02	0.08	0.05	180*

Note: D=Diameter, L=Length, C=Compression, T=Tension, S=Standard Loading, Q=Quick Loading, DL=Design Load, TL=Maximum Applied Test Load, *=Est. from Figure 2 by comparison with neighboring piles although TL did not reach these loads

All test piles had steel reinforcement. For the 14-in. diameter compression piles, reinforcement consisted of 4 #10 bars with #3 ties at 5-in. spacing; the rebars extended 26 ft into the piles. For the 18-in. diameter piles, 8 #10 bars with #4 ties at 6-in. spacing were included; the rebars extended 32 ft into the piles. Tension reinforcement consisted of one full length, 150 ksi Dywidag threaded bar with diameter ranging from 1.75 – 2.5 in., depending on the test load. For tension test piles, a 2-in. diameter PVC sleeve was placed around the upper 30 ft of the center bar, to mitigate concerns of premature failure of the rebar-grout bond.

TEST PILE INSTALLATION AND QUALITY CONTROL

Test piles were installed following the guidance and quality elements of the Deep Foundations Institute (DFI, 1994). Logs of piling installation were prepared manually, in addition to monitoring of the pile installation via a calibrated Pile Installation Recorder (PIR-A).

The specified minimum grout factor was 1.15. The actual measured grout factors ranged from 1.3 – 1.4. The specified minimum grout strength was 4,000 psi. Grout samples were taken from each delivery truck and tested for flow, density, and unconfined compressive strength (UCS). In general, the grout UCS exceeded the design requirements. Grout UCS values on the day of pile load testing are shown in Table 2.

Grout pressures were measured both at the pump and in-line, and are shown in Table 2. The measurements at the pump were via a pressure gage; whereas, the in-line measurements were by the PIR-A via a calibrated sensor. The grout pump was located approximately 150 ft from the drill rig. Grout pressures in Table 2 show that the piles experienced only 5 – 10%, or perhaps lower, of the pressures registered at the pump.

Integrity tests were performed on all test piles within 7 days of installation using the non-destructive pile integrity testing (PIT), per ASTM D5882. The PIT results showed significant damping of the stress waves from the surrounding soils, making it impossible to reliably identify the pile response from the toe. Amplifications with gains of x40 were also applied to the data,

which only amplified the background noise along with toe reflection. Typical length/diameter ratio of the test piles is in the 37:1 – 60:1 range; therefore, given the generally stiff soil profile and signal damping, lack of toe response is not unexpected. No defects were evident in the PIT results; however, they indicated significant changes in cross-section by bulging or necking in Layer 1 soils. A few piles indicated bulging in the 5 – 20 ft depth range, likely due to presence of the fill or sandy soils in these depth ranges. PIT results on test pile TP-04A indicated impedance increases below a depth of 40 ft, a likely indication of bulging or high friction at that depth.

Table 2. Grout Parameters and Properties

Test Pile Information			Load Test Type	Measured Grout Factor	GP.P (psi)	GP.PIR (psi)	Average UCS (psi)	E from UCS (psi)
Test No.	D (in.)	L (ft)						
TP-1A	18	70	C, S	1.30	280	24	4,293	3.7E6
TP-1B	18	70	T, S	1.29	280	18	5,430	4.2E6
TP-2A	18	55	C, S	1.40	300	27	3,820	3.5E6
TP-2B	18	55	T, S	1.35	280	30	4,947	4.0E6
TP-3A	18	70	C, Q	1.27	300	19	4,083	3.6E6
TP-3B	18	70	T, Q	1.35	280	19	5,590	4.3E6
TP-4A	14	55	C, Q	1.42	250	25	5,213	4.1E6
TP-4B	14	55	T, Q	1.39	250	27	5,267	4.1E6
TP-5A	14	70	C, Q	1.39	250	14	4,597	3.9E6
TP-5B	14	70	T, Q	1.40	250	12	4,193	3.7E6

Note: D=Diameter, L=Length, C=Compression, T=Tension, S=Standard Loading, Q=Quick Loading, GP.P=Avg. Grout Pressure at the Pump, GP.PIR=In-Line Avg. Grout Pressure Measured by PIR-A, UCS=Unconfined Compressive Strength of Grout, E=Est. Grout Elastic Modulus

PILE LOAD TEST RESULTS

Results of the 10 compression and tension load tests are shown in Figure 2; they are grouped by test type and pile diameter. The load test results are summarized in Table 1.

For estimating failure loads, compression failure was defined using the Davisson criterion, except the elastic shortening of the pile was estimated as half of PL/AE . Tension failure was defined as half the elastic shortening of the pile plus 0.1 in. at the pile top. Only the shorter 55-ft long piles experienced the necessary movements to reach “failure” condition.

Of all the test piles, test pile TP-04A experienced the greatest settlement under the maximum applied test load. Test pile TP-04A could be characterized as having truly “failed” under these load conditions given a final settlement of 1.46 in. at the top of the pile and more than 1 in. of irrecoverable movement upon unloading. The 1.46 in. movement matches well with 10% of the pile diameter, a common criterion for “failure” of a pile. Test pile TP-02A experienced a top movement of about 3% of the pile diameter. The remaining piles experienced much less movement, or about 1% of the pile diameter, as shown in Table 1 and Figure 2.

INSTRUMENTED PILE RESULTS

The five compression test piles were fitted with internal strain gages; they are identified in Table 1 with Test No. designation “A.” Strain gages were “sister bars” Model 4911, from Geokon, mounted in the factory on a No. 4 rebar with factory-installed cables, and factory-calibrated. Related accessories included a terminal box (with manual switch) for data collection. The positions of strain gages on the typical 55-ft and 70-ft long piles are shown in Figure 1.

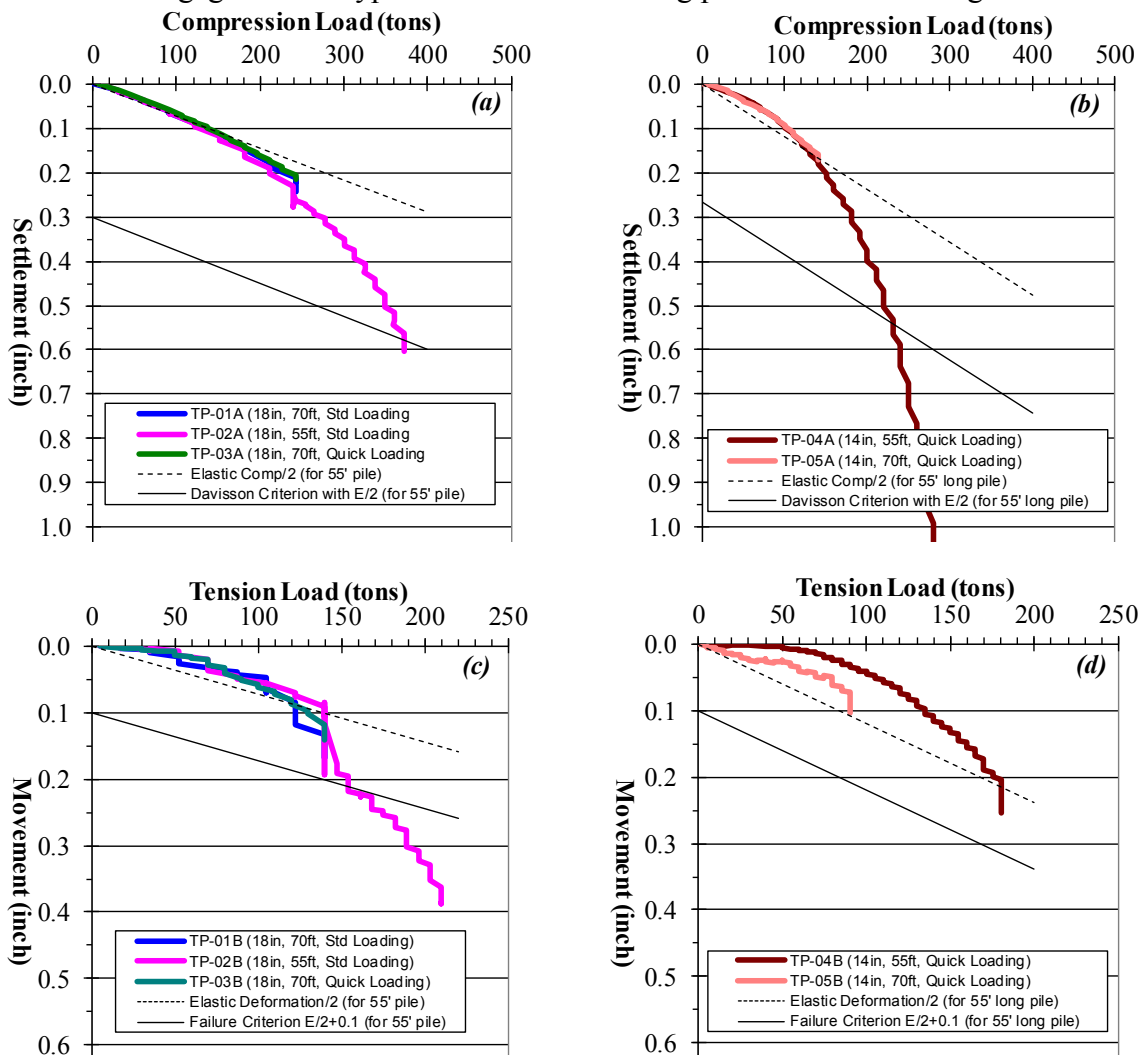


Figure 2. Compression and Tension Load Test Results

In evaluating loads from strain gages, the elastic modulus of the pile is significant. Variations in grout modulus directly impact estimating pile load and its distribution. The UCS of grout samples on the day of pile load testing are shown in Table 2. Based on UCS results, elastic modulus, E , was estimated from $E=57,000\sqrt{f'_c}$ (ACI, 2008), where f'_c =UCS. The E values are shown in Table 2. Moduli were also estimated from the strain gages. These values commonly vary from those estimated based on UCS. A comparison of interpreted loads based on the two moduli (UCS correlations vs. strain gages) indicated load discrepancies of about 15 – 20% in the upper 5 ft of the piles where moduli are reliably obtained from strain gages. The discrepancy is

only expected to increase with pile depth due to the expected increase in moduli from strain gages with increased depth. This difference is attributed to the strain level at which modulus is estimated from the two methods and the pile “composite” effects. Siegel (2010) reported load variations in the range of about 30 – 50% for a test case depending on the choice of E .

As noted previously, only test piles TP-02A and TP-04A experienced larger settlements. For this reason, results from these two test piles are used for evaluating the strain and load distribution. Test pile TP-04A is expected to have developed the maximum resistance of the soils for its settlement of about 10% of the pile diameter. Results for TP-04A are shown in Figure 3. It should be noted that in assessing the pile load distribution, residual loads were assumed to be negligible. Limited data on long-term behavior of ACIP piles indicate that the duration for onset and ultimate value of residual load development is in the range of about 7 – 58 days after pile installation (Siegel and McGillivray, 2009). Test piles TP-02A and TP-04A were tested 11 days and 22 days after their installation, respectively. Therefore, some residual loads are expected, as shown in Figure 3(b); however, they are small. Residual loads are discussed later in more detail.

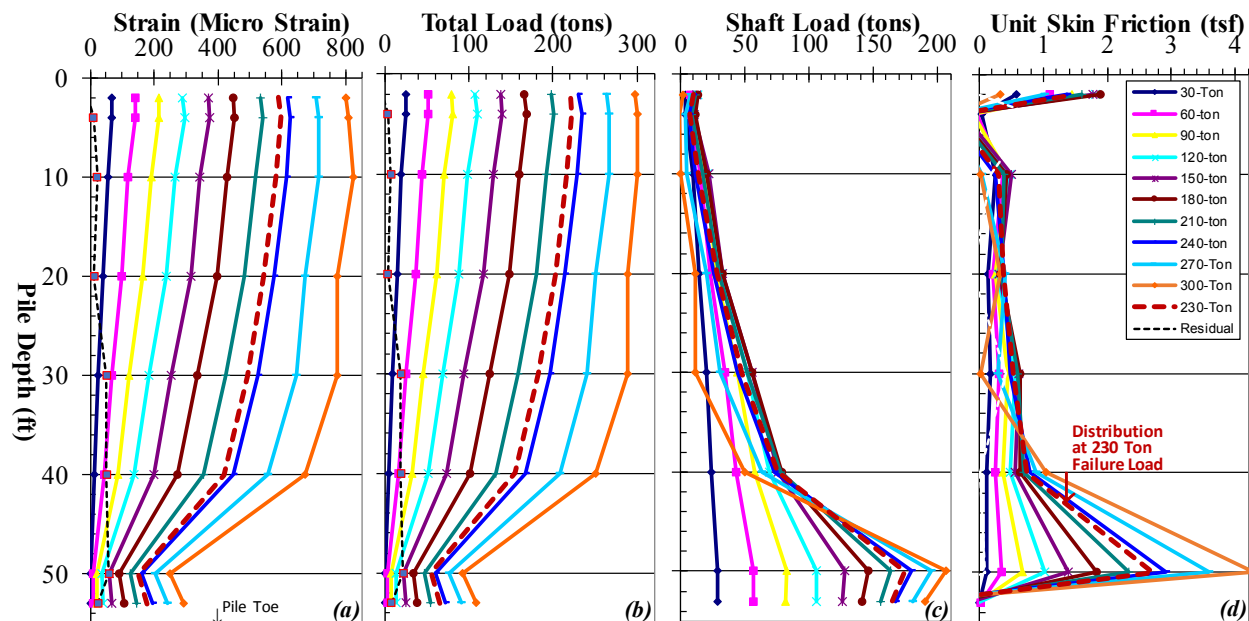


Figure 3. Strain and Load Distribution from Strain Gages in Test Pile TP-04A

Results in Figure 3(a) show higher strains near the pile top and progressively lower strains with depth, as expected. The load distribution in the pile follows a pattern similar to the strain distribution as shown in Figure 3(b). The test loads are shown to be dominantly counteracted by shaft resistance; and as the test load exceeds the shaft capacity, additional resistance ceases to mobilize. This is evident in the upper 40 ft of the pile in Figure 3(c) and (d) where skin friction is largely expended at the test load of about 150 tons, and no more increase is evident despite increasing test load. In fact, at the higher test loads of 270 or 300 tons, skin friction is so exhausted that the recorded shaft loads are even lower than those seen for the lower test loads of 30 or 60 tons. This is due to excessive straining of the soils and remolding of the bond zone at these higher loads, indicative of soil strengths post-peak or even near the residual state. These observations are more evident in Figure 4(a) and (b), not only indicating higher peak shaft resistance with increased depth, but also a reduction in shaft resistance after a certain measure of

settlement or straining. Additionally, whereas Figure 4(a) shows progressively larger pile top settlements are needed to mobilize the peak resistance at greater depth, Figure 4(b) shows that these peak values are developed at smaller strains with increased depth. Sorenson (2006) reported similar observations, i.e., peak side shear resistance was mobilized at different strains. Moreover, results in Figure 4 show that shaft resistance is completely exhausted in the upper 40 ft, whereas no such response is observed in deeper soils. At a depth of 50 ft, even the highest test loads are still being resisted with no apparent post peak indications.

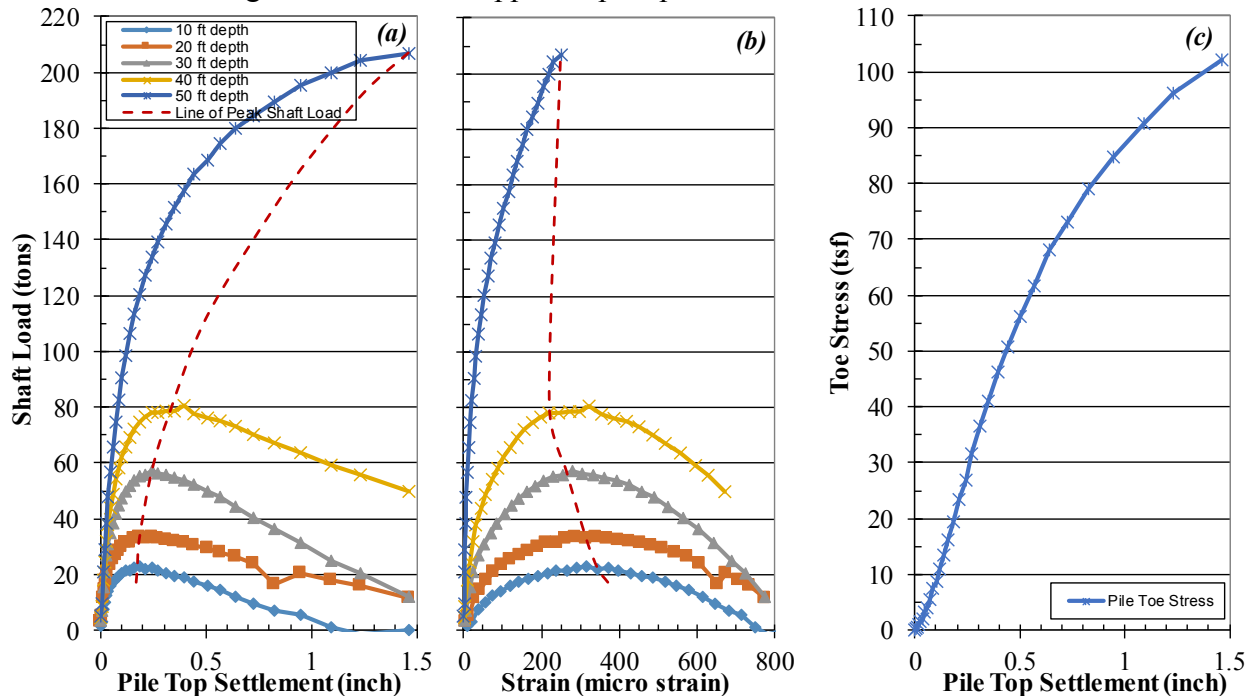


Figure 4. Shaft Load and Toe Stress Development in Test Pile TP-04A

Development of the unit skin friction follows the shaft load development, as shown in Figure 3(c) and (d). It is shown that skin friction is expended as stresses progressively exceed shaft capacity along the pile length. A uniformly increasing skin friction distribution is noted along most of the pile in the 10 – 40 ft range. At the 230-ton estimated failure load (which was determined independently based on pile top load-deformation characteristics), essentially no additional increase in skin friction is observed in the upper 40 ft despite increasing test loads. Below 40 ft, soils continue to offer resistance even at loads exceeding the pile failure load, and without experiencing much strain.

It should be noted that reasons for strains or loads suddenly increasing below a depth of 50 ft, as shown in Figure 3(a) and (b) are unclear; probably a manifestation of strain gage locations too close to the pile tip.

The load distributions show smaller toe contributions to pile capacity than the shaft. Development of the pile toe stress is shown in Figure 4(c). At the 230-ton failure load, corresponding to a pile top settlement of 0.55 in., the toe stress is about 60 tons/ft² (tsf).

Results from test piles TP-02A and TP-04A were normalized relative to the estimated failure load and pile diameter, as shown in Figure 5. Failure (as defined by the Davisson criterion, or Load Ratio=100%) occurs at a pile top settlement of 3.5 – 4% of the pile diameter, as shown in Figure 5(a). The results are similar to those on ACIP piles in Houston where failure

at 180 tons was defined at a settlement of 5% of the pile diameter (O'Neill et al., 1999). McVay et al. (1994) reported that 5% of pile diameter also favorably represented failure of ACIP piles in Florida sands; and that the Davisson criterion overpredicted compression capacity by about 24%. Results in Figure 5(b) show that peak shaft resistance is reached along most of the pile length at small pile top settlements of about 1 – 3% of the pile diameter up to a depth corresponding to about 35 diameter of the pile. It is also shown that significantly more settlement, up to about 10% of the pile diameter, is required thereafter to mobilize the shaft resistance at greater depths.

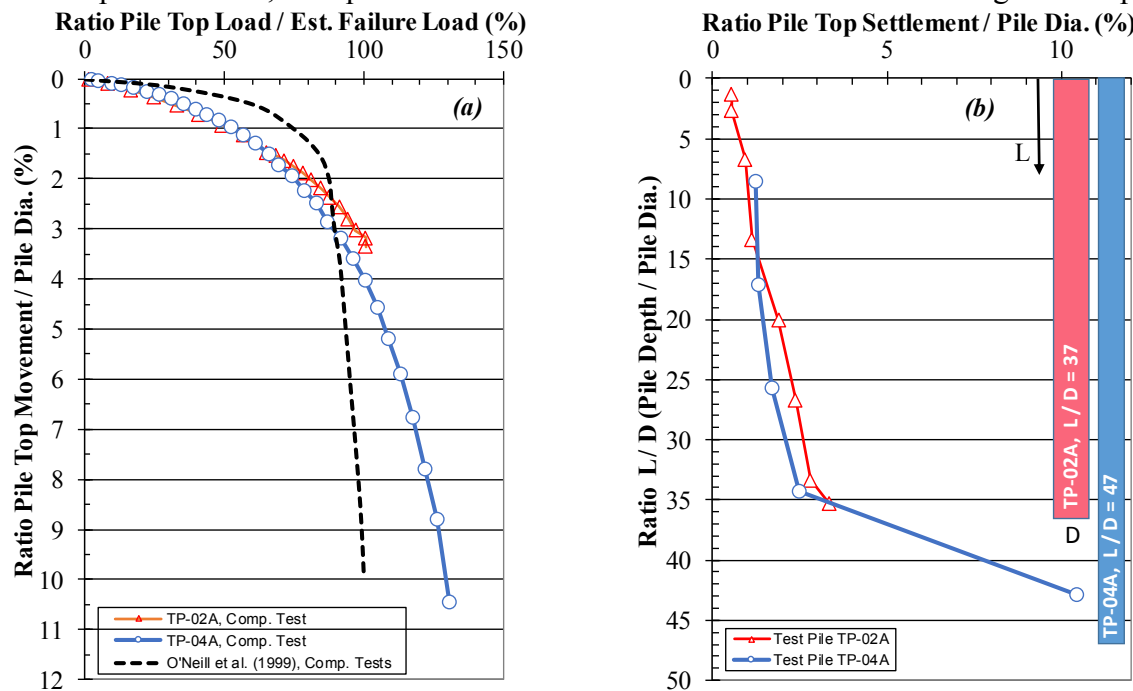


Figure 5. Development of (a) Pile Capacity and (b) Peak Shaft Resistance

RESIDUAL LOADS

Residual loads were measured in all instrumented test piles; results are shown in Figure 6. Also shown are pile diameters (D) as well as the duration (Days) after pile installation when residual loads were measured.

Typical pattern of residual load distribution is one that somewhat linearly increases with depth until reaching a transition point (sometimes referred to as the “critical depth”) and then reduces with depth, finally terminating at some value at the pile toe. The only pattern that is visible from the measurements in Figure 6(a) is one of initially increasing residual loads with depth. However, this pattern is not consistently displayed, as it is sometimes interrupted by sharp increases or decreases in the load. Additionally, no transition point is obvious with any degree of certainty. The reasons for such uncharacteristic patterns are unclear; however, significant changes in pile cross-section may be a factor, as discussed earlier.

Results from the two test piles TP-02A and TP-04A are shown separately in Figure 6(b) for they are discussed in more detail in this paper. Test pile TP-02A shows a rather constant residual load of about 12 tons in the upper 20 ft, which appears high for that interval, particularly near the ground surface. Test pile TP-04A shows a progressively increasing residual load to a

depth of about 30 ft, and reluctantly implies a transition zone in the 30 – 50 ft depth range; however, not so distinctly. Given the uncertainty in observed conditions, and for comparison with the measured values, an attempt was made to estimate the residual loads for this test pile, as shown in Figure 6(c). Figure 6(c) shows that the measured residual load is relatively small compared to the measured failure load. This is not unexpected of CFA type ACIP piles for which ground displacement is none or very small. Unlike driven piles where pile installation causes soil consolidation and changes the ground stresses, CFA type ACIP piles are considered low displacement piles, and are expected to cause little change in ground stresses during installation. For this reason, in estimating the residual toe load, it was assumed that this load was primarily caused by the weight of the fluid grout plus the grout pressure measured from the PIR-A (refer to Table 2, GP.PIR), or a force of about 6 tons. Residual loads for the upper 40 ft of the pile were estimated following the assumption that the “true” load distribution in a pile is represented by a curve similar to the “measured” load distribution, however, twice as steep as the measured values (Fellenius, 2002). Each increment of the measured load in the upper 40 ft was therefore steepened, as shown in Figure 6(c). Using the estimated load at the 40 ft level and at the toe, the residual load at the 50 ft level was interpolated. The difference in values between the two measured and the true curves is the residual load. As shown in Figure 6(c), the estimated and measured residual loads are reasonably comparable and very small. A transition zone, although not so distinct, may be visible in the estimated values at the 40 ft level.

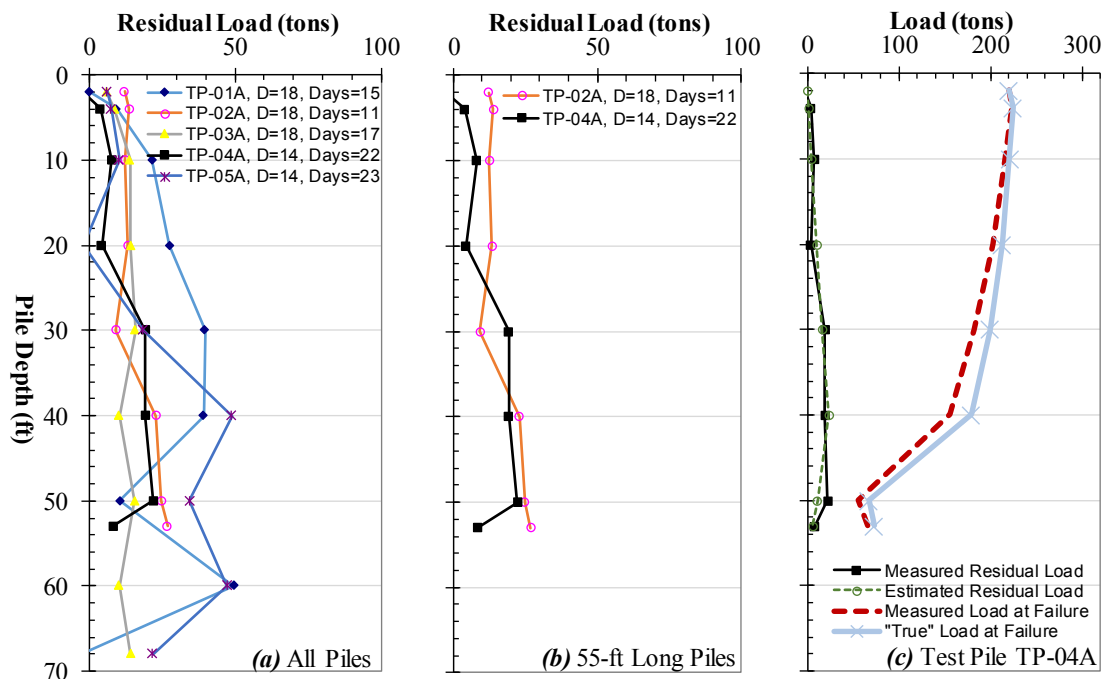


Figure 6. Residual Loads in Test Piles

BACK-CALCULATIONS FROM STRAIN GAGE RESULTS

Empirical skin friction factor α and bearing capacity factor N_c were back-calculated from the test results shown in Figures 3 and 4. Table 3 provides a summary of the observed values. The factor α was calculated as the ratio of skin friction and the soil undrained shear strength, S_u . The

N_c factor is commonly represented as the ratio of unit toe resistance and the soil shear strength at the pile toe, or 9 for clays. The N_c factor was also back-calculated using a relationship proposed in FHWA (2010) for sands where base resistance is taken as $0.60N_{60}$ and limited to ≤ 30 tsf, with N -value limited to 50 blows/ft. The sand relationship was investigated for the apparent presence of a sandy layer near the tip of test pile TP-04A as shown in Figure 1. N_{60} is the SPT N -value corrected for hammer efficiency. As shown in Figure 1, the pile toe is seated in materials with uncorrected N -value of about 90. Site specific hammer energy efficiency factors were not available. Typical values are in the range of 1.2 – 1.3; a value of 1.25 was assumed, resulting in a corrected N -value of 112 blows/ft. The proposed FHWA relationship yields a value for $N_c = 0.54$ (i.e., $60/112$) for test pile TP-04A. Sand is not shown at the toe of test pile TP-02A. However, when similar relationship and N -values are applied, a value of 0.61 is obtained for N_c (i.e., $68/112$) for test pile TP-02A. It should be noted that the toe resistance values of 60 and 68 exceed the upperbound value of 30 tsf, and the N -value of 90 exceeds the upperbound value of 50 blows/ft, in FHWA (2010). It is also noted that FHWA (2010) recognizes base resistance values higher than 30 tsf, and N -values higher than 50 blows/ft, recommending load testing for verification, as shown in this paper.

The back-calculated N_c factors of 9.2 and 9.4 in Table 3 are similar to the value of 9 typically used for clays based on theoretical considerations. Similarly, the back-calculated values of 0.54 and 0.61 are similar to the 0.60 value for sands suggested in FHWA (2010).

The back-calculated α values in Table 3 are also shown in Figure 7, superimposed for comparison on typical values available in the literature ((a). NAVFAC, 1982 and (b). Reese et al., 2006). These values fall within the range of those reported for similar soils. Additionally, the results suggest an increasing trend in α values for very hard soils. A similar trend appears to be somewhat suggested for a limited range of data in Reese et al. (2006).

Table 3. Back-Calculated α and N_c Factors from Strain Gages

Test Pile TP-02A							Test Pile TP-04A						
D	q_s	q_b	S_u	C_u/p_a	α	N_c	D	q_s	q_b	S_u	C_u/p_a	α	N_c
10	0.55	---	0.75	0.7	0.73	---	10	0.30	---	1.0	0.9	0.30	---
20	0.34	---	1.6	1.5	0.21	---	20	0.38	---	0.7	0.7	0.51	---
30	0.74	---	3.0	2.8	0.25	---	30	0.54	---	1.8	1.7	0.30	---
40	1.38	---	4.4	4.2	0.31	---	40	1.03	---	3.7	3.5	0.28	---
50	2.10	---	5.9	5.6	0.36	---	50	2.71	---	5.5	5.2	0.49	---
53	2.44	---	6.5	6.1	0.38	---	53	3.60	---	6.2	5.8	0.58	---
55	---	68	7.2	---	---	9.4	55	---	60	6.5	---	---	9.2

Note: D=Depth (ft), q_s =Max. Skin Friction (tsf), q_b =Max. Toe Resistance (tsf), $S_u=C_u$ =Undrained Shear Strength (tsf), p_a =Atm. Pressure (1.06 tsf)

It should be noted that Reese et al. (2006) states that materials with $C_u/p_a > 2.5$ fall in a Cohesive Intermediate Geomaterial category, defined as “weak rock” or similar materials with compressive strengths in the range of 73 – 725 psi (2.6 – 26 tsf), and its formulation accounts for rock “joint effects,” pile hole condition such as “smoothness,” etc. Although the materials in which test piles TP-02A and TP-04A were installed exhibited strengths that were in the range of those for Cohesive Intermediate Geomaterials, the Reese et al. (2006) formulation could not be justified and was not used in the back-calculation of α values for (1) “rock” was not present in the geology and (2) the materials could be readily sampled using conventional soil sampling tools including tube samples.

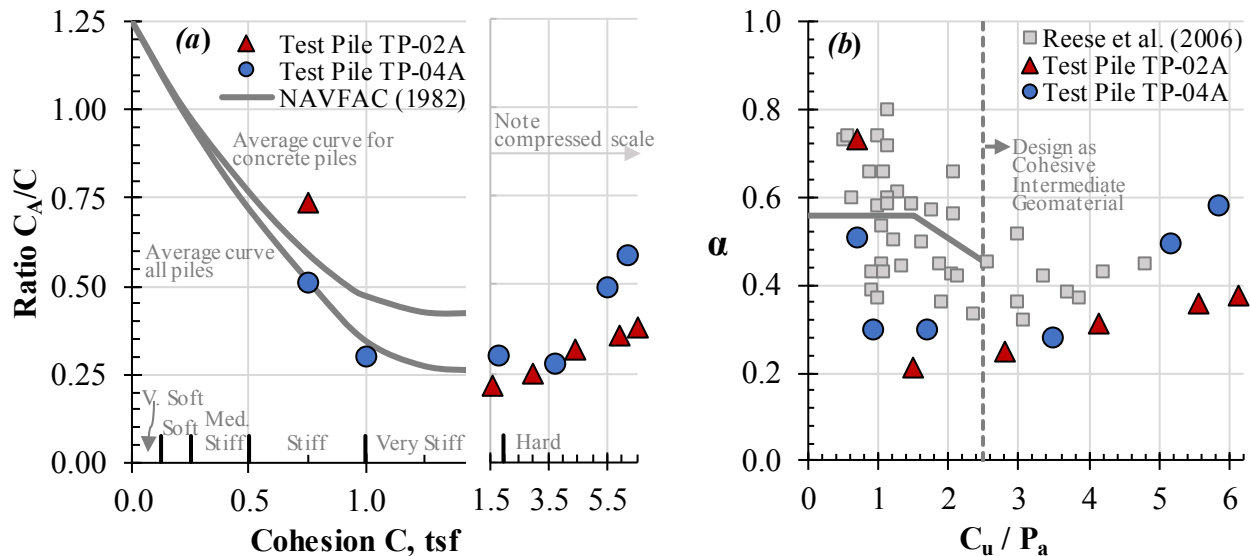


Figure 7. Back-Calculated α Factors from Strain Gages

CONCLUSIONS

Distribution of skin friction and toe resistance were examined from results of instrumented ACIP pile load tests. The results provide a case history on performance of CFA-type, ACIP pile application in predominately hard clay soils.

Results reinforce that measurements from internal strain gages provide enhanced understanding of pile behavior. They support the convention that larger pile top movements are needed to mobilize the resistance at greater depths. However, results also show that internal strains do not necessarily follow the same convention as pile top settlement, i.e., smaller strains can mobilize the maximum shaft resistance in deeper soils.

The peak shaft resistance of ACIP piles is shown to develop at relatively small pile top settlements of about 1 – 3% of pile diameter for lengths up to $L/D=35$. Significantly more settlements, up to about 10% of pile diameter, are required to mobilize the peak value for greater L/D .

Measured residual loads varied widely, without a consistent trend. Shorter piles exhibited comparatively small residual loads than larger piles, however, the reverse was also shown at isolated depths for some piles. Residual loads could be reasonably duplicated for one pile by relying on the measured load distribution in that pile.

Shaft resistance, α , and bearing capacity, N_c , factors deduced from the load test results compared well with those in the literature. It is concluded that the design of ACIP piles should not rely on the maximum undrained shear strength of soils alone; rather, soil strength should be modified commensurate with established α and N_c values.

Results also suggest a trend of increasing α values for very hard soils (geomaterials). This trend is not evident in NAVFAC (1982); however, it could be somewhat discerned in limited data in Reese et al. (2006).

Variations were noted in observed pile load distribution, particularly near the pile top and the toe. These could have been better explained had direct information on actual pile geometry been available. Although pile geometry can be derived from PIT results with some effort, more recent developments such as thermal integrity testing, which was not available in 2006 when the work in this paper was completed, would have added much more to a better understanding of the observed pile behaviors.

The cost of the strain gage instrumentation hardware was less than 5% of the cost of the pile load tests and less than 0.5% of the total piling cost, excluding engineering. (The strain gages were installed, data collected, and results interpreted by the principal author.) Valuable information is obtained when piles are instrumented, assisting tremendously with qualifying pile capacity, size, and length; as well as supporting value engineering, deviation assessments, and the overall confidence in knowing “where the loads are at every stage of the loading.”

REFERENCES

- American Concrete Institute (2008). *Building Code Requirements for Reinforced Concrete*. ACI 318. ACI, Farmington Hills, MI.
- Beck, W.K. and Harrison, P.J. (2009). “Load Test on Small Diameter Augered Cast-in-Place Piles through Fill.” ASCE Proceedings, Contemporary Topics in Deep Foundations, GSP 185, pp. 430-437.
- Deep Foundations Institute (1994). *Inspector’s Guide to Augered Cast-In-Place Piles*.
- Fellenius, B.H. (2002). “Determining the True Distribution of Load in Instrumented Piles.” Proceedings, ASCE International Deep Foundation Congress, Geotechnical Special Publication No. 116, Orlando, FL, February 2002, Vol. 2, pp. 1455-1470.
- FHWA (2007). *Design and Construction of Continuous Flight Auger (CFA) Piles*. Geotechnical Engineering Circular, GEC No. 8, FHWA-HIF-07-03, April 2007.
- FHWA (2010). *Drilled Shafts: Construction procedures and LRFD Design Methods*. Geotechnical Engineering Circular, GEC No. 010. May 2010.
- Lambert, T.L. (2000). “Instrumented Static Load Testing-Augur Cast-in-Place Piles.” DFI Proceedings, Augered Cast-in-Place Piles Committee Specialty Seminar, Deep Foundations Institute, May 12, 2000, St. Louis, Missouri, pp. 55-76.
- McVay, M., Armaghani, B., and Casper, R. (1994). “Design and Construction of Auger-Cast Piles in Florida.” *Transportation Research Record 1447*, Design and Construction of Auger Cast Piles and Other Foundation Issues. Transportation Research Board.
- NAVFAC 7.02 (1982). *Foundations and Earth Structures*. Department of the Navy, Naval Facilities Engineering Command.
- O’Neill, M.W., Vipulanandan, C., Ata, A., and Tan, F. (1999). *Axial Performance of Continuous-Flight-Auger Piles for Bearing*. Final Report to Texas Department of Transportation, Report No. 7-3940-2, August 1999.

- Reese, L.C., Isenhower, W.M., Wang, S-T (2006). *Analysis and Design of Shallow and Deep Foundations*. John Wiley & Sons, Inc. Hoboken, New Jersey.
- Siegel, T.C. and McGillivray, A. (2009). "Interpreted Residual Load in an Augered Cast-in Place Pile." DFI Proceedings, 34TH Annual Conference on Deep Foundations, Deep Foundations Institute, pp. 173-182.
- Siegel, T.C. (2010). "Load Testing and Interpretation of Instrumented Augered Cast-in-Place Piles." DFI Journal, Vol. 4, No. 2, December 2010. Deep Foundations Institute.
- Sorenson, K.G. (2006). "Instrumented Load Testing of Auger Cast Piles." DFI Proceedings, Augered Cast-in-Place Piles Committee Specialty Seminar, Deep Foundations Institute, May 5, 2006, Los Angeles, California, pp. 74-79.
- Vipulanandan, C., Vembu, K., and Guvener, O. (2012). "Monitoring Auger Cast in Place Pile Construction and Testing in Hard Clay." DFI Proceedings, 37TH Annual Conference on Deep Foundations, Deep Foundations Institute, October 16-19, 2012, Houston Texas.

Variability of Pile-Soil Interaction: A Comparison of Behavior Seen in Instrumented Pile Pairs at Three MnDOT Bridge Sites

Aaron S. Budge, Ph.D., P.E., M.ASCE¹; and
Derrick D. Dasenbrock, P.E., F.ASCE²

¹Dept. of Mechanical and Civil Engineering, Minnesota State Univ., Mankato, 205 Trafton Science Center East, Mankato, MN 56001. E-mail: aaron.budge@mnsu.edu

²Minnesota Dept. of Transportation, 1400 Gervais Ave., Maplewood, MN 55109. E-mail: derrick.dasenbrock@state.mn.us

Abstract

The Minnesota Department of Transportation has instrumented several driven pile bridge foundations with the intent of gaining an improved understanding of complex pile-soil interaction given various construction layouts, structural and earth fill loading sequences, and geotechnical site conditions. Axial pile loading behavior was examined throughout construction and into bridge service as part of a bridge performance monitoring program. Three similar case studies of instrumented pile pairs at bridge abutments are examined: a comparison of the behavior of a pile within an existing roadway footprint and a pile installed in a widened side-hill fill on a bridge reconstruction project; a comparison of interaction between leading and trailing row piles in a 3-row pile group; and a comparison of pile loads seen on a pile in an integral abutment and a structurally unloaded pile positioned outside the pile cap. These sites have allowed unique observations and interesting conclusions relative to pile-soil interaction.

INTRODUCTION

The Minnesota Department of Transportation (MnDOT) has conducted several driven pile performance monitoring projects to investigate and assess the practical impact of pile-soil interaction, including the phenomenon of downdrag and the resulting dragload, on driven pile design and construction practice. (For various projects, see Budge and Dasenbrock (2011, 2010a, 2010b); Budge, Dasenbrock and Mattison (2015); Dasenbrock, Borree and Budge (2011); Dasenbrock, Mattison and Budge (2012)). While current design guidance addresses pile-soil interaction, downdrag and its associated dragload, there has been significant discussion by MnDOT personnel and the engineering community as to when negative skin friction can be expected, how to predict the magnitude of the dragload to be considered in design, and what scenarios, if any, exist when dragload may be safely ignored. This paper presents observations from three projects in Minnesota where pairs of driven production piles were instrumented and monitored over periods of months to years, through construction and initial service, including lessons learned on those projects relative to the pile-soil interaction.

Initial work performed on other projects proved that dragload existed, was measurable and permanent, and the behavior and observed magnitudes appeared consistent with predictions given geotechnical site conditions and structural loading (Budge, Dasenbrock and Mattison, 2015). Monitoring “pile pairs” has provided additional insight into the pile-soil behavior, in otherwise similar soil conditions, based on differences in pile geometry, position, or loading.

This paper presents the results of three MnDOT pile monitoring projects. For each project, a pair of instrumented driven piles was installed and the behavior of each was monitored and compared. The three projects are described in limited detail and observations and overall conclusions are discussed. These three projects include:

- (1) Bridge 82587: One pile in former embankment area; one in newly placed side-hill fill,
- (2) Bridge 27V97: One pile in row 1 and second pile in row 3 of a bridge abutment foundation,
- (3) Bridge 83040: One pile in a single row abutment cap and a second non-structurally loaded pile placed slightly outside the cap.

FOREST LAKE INTERCHANGE AT WASHINGTON COUNTY 82 & CSAH 2, BR 82527

Collaboration between Washington County and the State of Minnesota (MnDOT) led to mutual benefit on this partnering project where the state provided additional design review and the county agreed to help fund and support a performance evaluation program that included stress, strain, and deformation monitoring. The Forest Lake Interchange bridge used 16-inch cast-in-place-concrete (CIPC) piles (closed-end steel pipe piles infilled with concrete) for support of the west abutment. Two production piles were instrumented using vibrating wire strain gages attached to sister bars and installed after driving but prior to placement of concrete in the piles. In addition, several earth pressure cells were placed along the back row of piling and a horizontal ShapeAccelArray (SAA) was positioned along the back row of piling to monitor embankment settlement. At this site, a narrow existing bridge was to be removed and the approach embankment widened for a new wider bridge. The work included an embankment soil pre-load and surcharge near the west bridge abutment, as shown in Figure 1.

The point of interest for this project was to determine if a new pile installed in the center of the roadway, where the roadway embankment had been in-place previously, would perform differently than a new pile at the exterior of the abutment where the new soil and surcharge would be placed as part of the construction sequence. Both instrumented piles were plumb piles in the rear row of the pile group. The site was characterized by a layer of compressible clay soils extending from near the ground surface to a depth of about 40 feet, at which point dense sandy soils were encountered.

The pile cap was constructed at an elevation near the lower highway grade, with new side-hill fill material for the bridge approach, and the surcharge soil, being placed after pile driving and abutment stem-wall construction. Both the south instrumented pile (along the former and future centerline, in the middle of the embankment, designated as “Test Pile No. 2” in Figure 2) and the northern instrumented pile (at the northern edge of the pile group, designated as “Test Pile No. 1” in Figure 2) were subjected to the soil surcharge as part of the project design. The locations of the two instrumented piles are shown on Figure 2, which is a plan view of the pile group. The horizontal SAA showed soil settlement near the center of the bridge foundation (in the footprint of the former bridge embankment) was about 0.5 inches. Soil settlement near the north end of the pile group (under the new fill material) was about 2.5 inches. Somewhat contrary to expectations, both instrumented piles showed similar response during and post-construction, with measured service loads slightly exceeding factored design loads. These design loads incorporated anticipated dragload for each pile.

Figure 3 shows the response of the piles during and after construction. The maximum measured loads were approximately 500 kips (250 tons), which was approaching the predicated factored geotechnical resistance for the piles. While this load was less than the nominal geotechnical capacity, the measured load exceeded the factored Strength I Design Load (per AASHTO) and certainly exceeded the unfactored Dead Load (DL) plus predicted Dragload (DD) load combination. As mentioned, the results were surprisingly similar given one pile in a ‘preloaded’ position (South Pile) and the second in an area of new fill material (North Pile). One may have expected more dragload to exist in the pile positioned in the area of new fill.

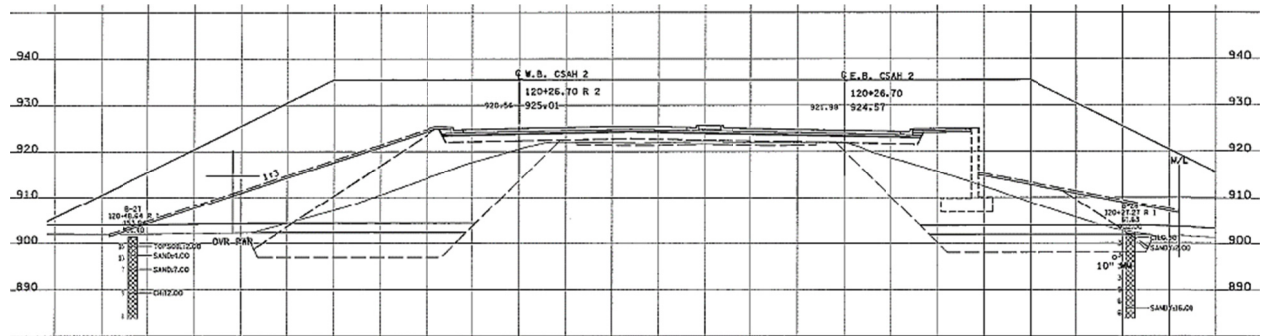


Figure 1. Compressible soils at the site were preloaded with a soil surcharge to reduce future roadway settlement in the vicinity of the west abutment of Bridge 82527.

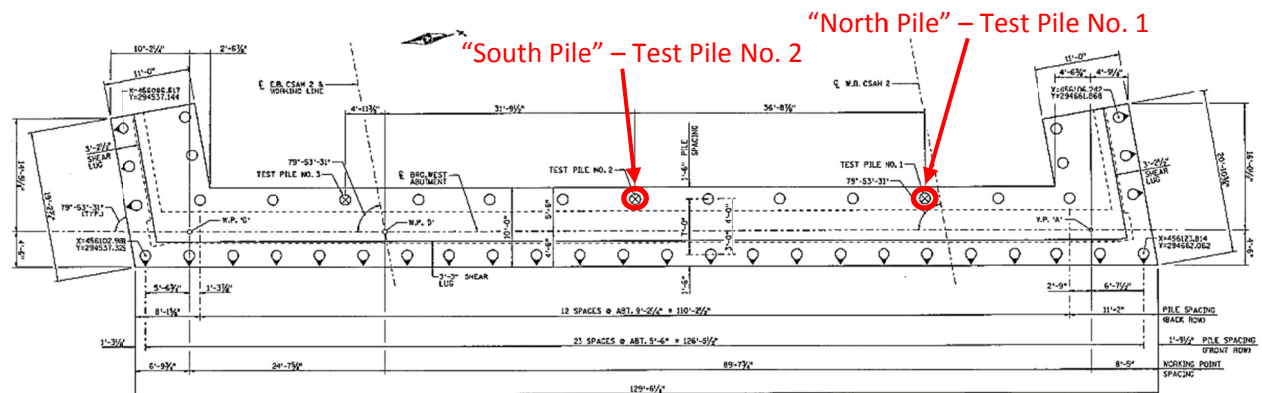


Figure 2. Plan view of the west abutment of Bridge 82527, showing the location of the two instrumented piles (“South Pile” – Test Pile No. 2 and “North Pile” – Test Pile No. 1) monitored on this project.

HIGHWAY 169/I-494 INTERCHANGE, BR 27V97

The second pile-pair instrumentation project was located at the interchange of highways US 169 and I-494 seven miles southwest of Minneapolis, Minnesota. Test Pile #5 (North Pile) and Test Pile #6 (South Pile), two 12.75-inch CIPC pipe piles in the abutment foundation, were instrumented using sister bar strain gages after driving. One pile (South Pile – Test Pile #6) was

located in the front row of piling and the second (North Pile – Test Pile #5) was located in the rear row. The front row of piles was offset from the rear row by about 11.5 feet and in the shadow of the central row of piling. Figure 4 shows the pile layout. This site was characterized by medium-dense, plastic, compressible soils overlying stronger sandy soils. The stronger bearing soils were not exceptionally strong or dense; SPT blow counts ranged from 15 to 39.

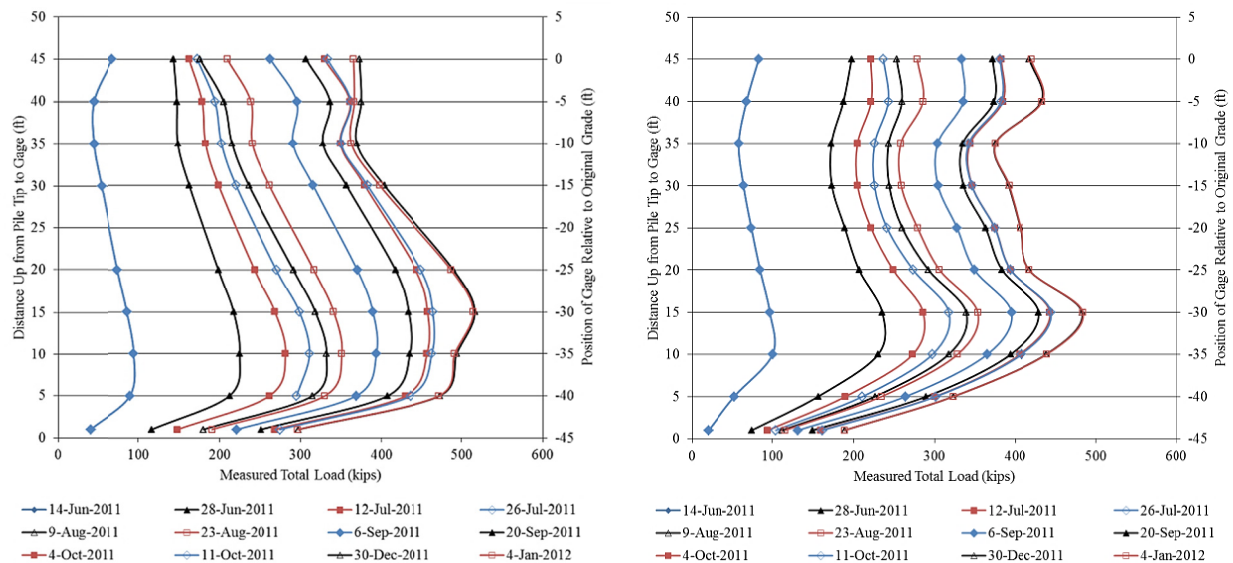


Figure 3. Results from the North Pile (left) and South Pile (right) at the Forest Lake Interchange at Washington County 82 and CSAH 2 project.

The factored design load for the structure (Strength I Load Combination) was 90.6 tons/pile. Significant loads were measured in the piles. The footing, abutment wall, and wing walls were constructed quickly, and with different gaps and arrangements of falsework (see Figure 5); the type of loading and associated pile response was somewhat more difficult to separate during the construction sequence at this site. Graphs of the pile strain behavior observed during construction are shown in Figure 6. The pile response data show a distinct ‘neutral plane,’ the point of reversal from negative to positive skin friction. This is also the point of maximum pile load near the middle of both instrumented piles. The added loads measured at this sites are significant (similar to the magnitude of other types of structural design loads), but not to the point of concern for geotechnical or structural failure. It is believed that the higher loads and the more distinct neutral plane seen in Test Pile #5 (North Pile) are due to that pile’s proximity to the backfill placed behind the abutment. There was much less fill placed near the footing toe, in the vicinity of Test Pile #6 (South Pile). The neutral plane location appears to be about 10 feet different between the two piles. A higher neutral plane, and earlier load shedding, seems consistent with the physical conditions of less fill being placed near Test Pile #6.

BUTTERFIELD BRIDGE ADDITION, BR 83040

The third project was located in Butterfield, Minnesota, where a bridge was constructed for the widening of Minnesota Highway 60 over a railroad. A static load test was performed on a pile in

the single-row pile group on the west abutment. The load test pile (designated as SLT-5) and two of the four reaction piles were production piles. Two additional reaction piles, one behind the pile row and one in front of the pile row (designated as SRP-2) were installed for the load test (see Figure 7) but were not part of the pile group supporting the structure. The instrumented piles were 12.75-inch diameter, 0.25-inch wall, closed-end pipe piles with an embedded length of about 72 ft, driven into dense sandy soils. As with the previously discussed projects, the steel pipes were subsequently filled with concrete. This project was unique in that one of the two instrumented piles (the reaction pile SRP-2) remained outside the pile cap (see Figure 8) and was never subjected to structural top loading, allowing an assessment of pile-soil interaction for an ‘unloaded’ pile relative to a structurally loaded pile.

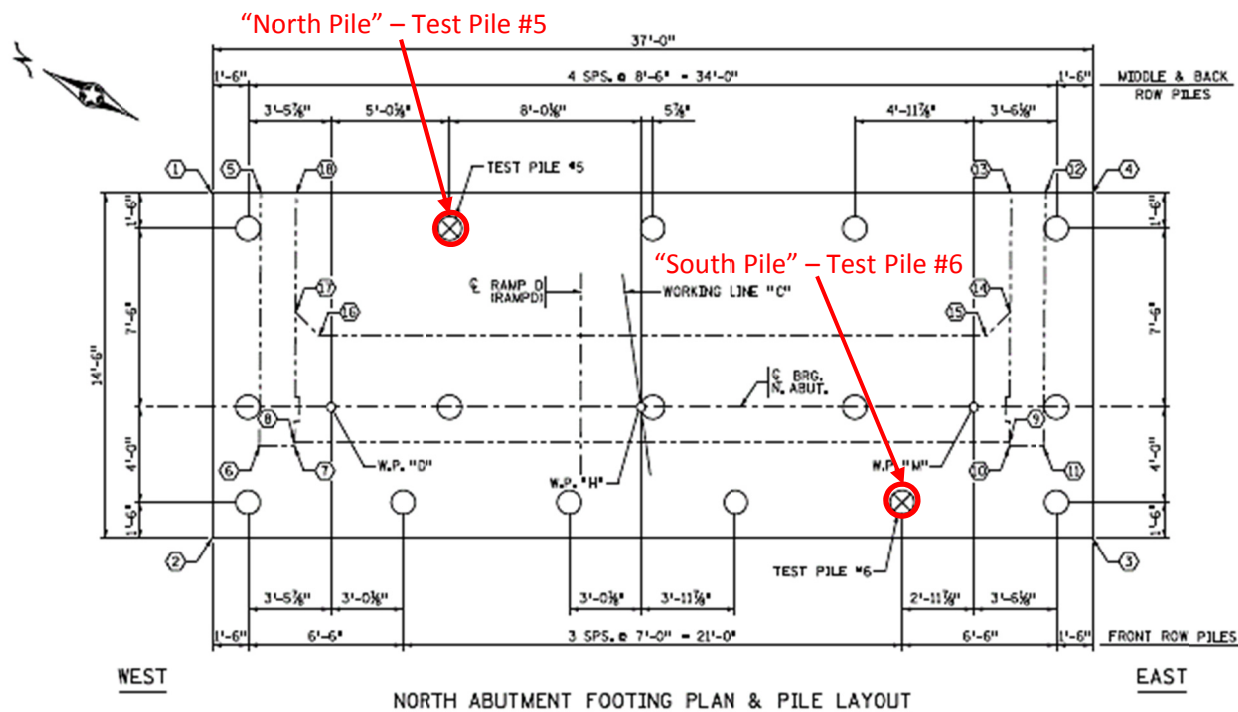


Figure 4. Footing plan showing the pile layout in the north abutment of BR 27V97 showing the location of instrumented piles Test Pile #5 and Test Pile #6.

The factored design loads for the structure (Strength I Load Combination) was 125.0 tons/pile. As seen in the left plot of Figure 8, the ‘unloaded’ instrumented pile, SRP-2, shows an increase in the load as a function of time at the gage locations, with no structural top-loading applied to the pile. The increased load in the uppermost 20 ft of the pile is relatively uniform, presumably due to the earth load applied as the abutment was constructed. At greater depths, dragload (load accrual) becomes more notable, with a maximum increase in load at the neutral plane, in this case approximately 10 ft from the pile toe, where load then begins to shed. Load accrual of about 50 kips, from a depth of 10 feet above toe to about 50 feet above the toe, was observed on the pile without structural load.

The data from the instrumented static load test pile, designated as SLT-5, is shown in the right plot of Figure 9. The difference seen between the ‘unloaded’ pile (SRP-2) and ‘loaded’ pile (SLT-5) is that only soil-induced loads (earth loads and dragload) are present in pile SRP-2 (left)

while SLT-5 (right) includes both soil-induced loads and structural top loads. Notably, the shape and magnitude of increased total load in both plots (from about 20 feet below the pile head to the pile toe) is very similar. Due to the dragload influence, the load distribution is biased toward load shedding only in the lower 10 feet of the pile length and the maximum measured load in the loaded pile is approximately 170 kips (higher than the measured top load of 120 kips). This is, however, still well below the factored design load of 250 kips (125 tons).



Figure 5. The BR 27V97 north abutment pile cap has been cast; formwork is in place to cast the abutment stem; a portion of the north retaining wall is in place.

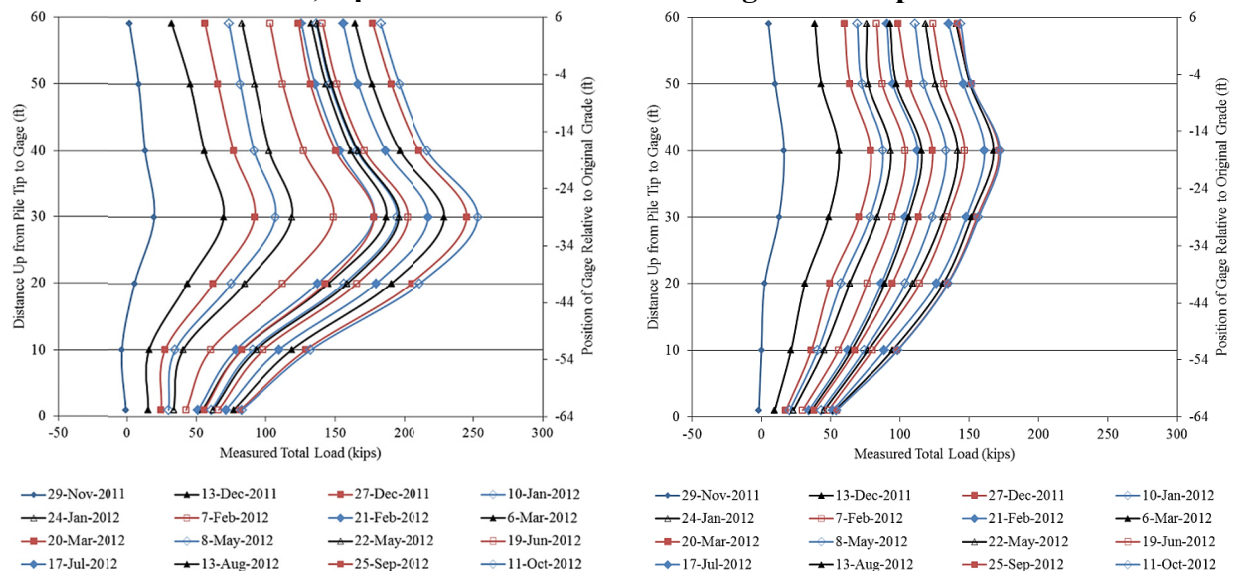


Figure 6. Results from the instrumented north pile, Test Pile #5 (left) and south pile, Test Pile #6 (right), at the BR 27V97 at the US169/I-494 Interchange.

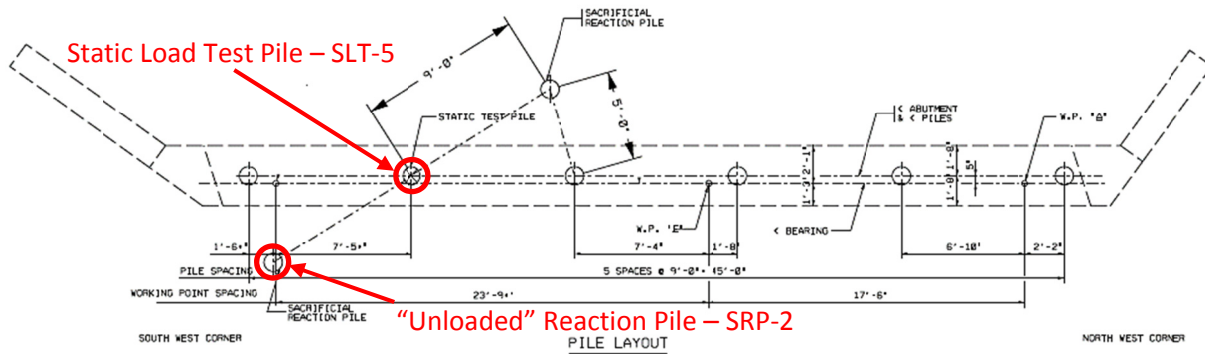


Figure 7. A load test performed on BR 83040 provided a monitoring opportunity for dragload comparisons between a structural loaded pile and a pile without top loads. A sacrificial pile on the exterior of the abutment was needed for the load test; when it was abandoned, it was outfitted with strain gages at the same elevations as the load test pile and filled with concrete.



Figure 8. One of the two sacrificial reaction piles (SRP-2) from a load test at this site can be seen in front of the west integral-abutment pile cap. A set of gages in the same arrangement as in the test pile was installed to repurpose this pile for dragload characterization at the site.

In theory, the difference in the load distribution from the loaded pile (SLT-5) and the unloaded pile (SRP-2) should equal the structural load applied to the pile. In other words, the unloaded pile should show the loads developed due to pile-soil interaction (both earth loads and dragloads). The loaded pile includes the soil loads (earth loads and dragloads) and the structural loads, such that the difference in the two should provide insight on the structural load distribution in the pile. Figure 10 shows the difference in the measured loads in the two piles, which shows a fairly uniform structural load of approximately 60-80 kips through much of the pile. This

behavior would also be consistent with an end-bearing pile where the structural load is transmitted to the pile toe with minimal load shedding along the pile length.

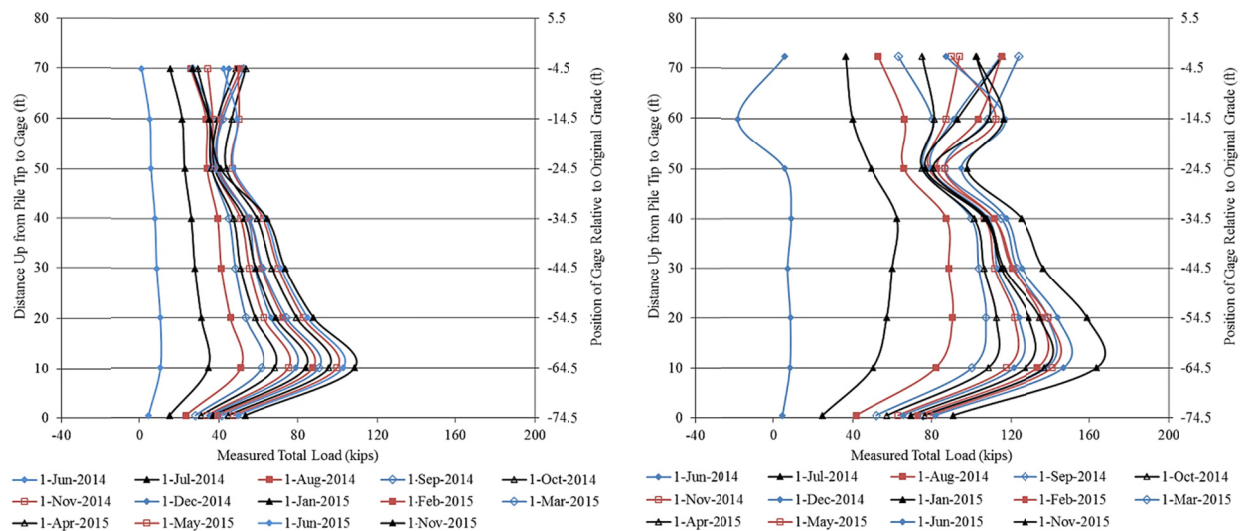


Figure 9. Results from the instrumented ‘unloaded’ pile (reaction pile SRP-2 – left plot) and the ‘loaded’ pile (static load test pile SLT-5 – right plot) at BR 83040.

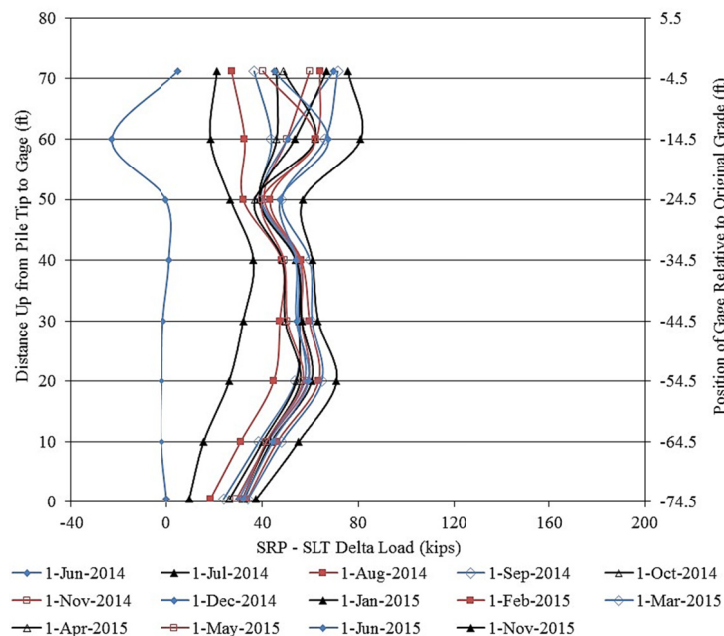


Figure 10. Plot showing the difference in measured values from the instrumented ‘unloaded’ pile (reaction pile SRP-2) and the ‘loaded’ pile (static load test pile SLT-5) at Bridge 83040.

CONCLUSIONS

Each of the three “pile pair” sites demonstrated pile behavioral responses that confirmed the presence of dragload in each case, and allowed for a side-by-side evaluation of pile performance where geotechnical site character was similar - but other factors, such as preloading, pile placement, and pile loading were different. The overall shape of the load distribution curves was different, by inspection, between the two piles at each site, but still comparable. Summarizing the conclusions reached, based on the three projects, the following points are of interest:

- Each project showed measureable dragload, with load distributions in the instrumented piles indicating maximum loads at depths well below the pile head.
- All six piles each showed a distinct neutral plane, where a reversal of skin friction indicates the transition from negative skin friction to positive skin friction.
- The location of piles within the pile group appears to impact the load imparted to the piles from dragload effects. It is likely piles in a pile group which are closer to earth loads (the heel of a footing) in the structural backfill see greater influence of consolidation effects than piles in outer rows of piling (near the toe) where new fill has not been placed.
- During loading, at all sites, the location of the neutral plane appeared relatively constant, suggesting that, at these sites, the soil conditions and loading were such that load accrual and shedding occurred in similar mechanisms as new soil loads and structural loads were applied. As the neutral plane did not move during the observations, it appears that the piles were loaded well below geotechnical failure.
- In each case the overall pile load, as measured on the strain gages, increased. This suggests that dragload should be treated as a permanent load that must be considered in the evaluation of the structural pile capacity.
- In each of these case histories, and in additional MnDOT projects of a similar nature, a clearly established neutral plane was evident in the data collected. This would lend credence to application of the neutral plane approach, as allowed by AASHTO design guidelines, when accounting for dragload effects on driven piles.

In general, while progress is being made with respect to understanding of pile-soil interaction, there is still much left to learn relative to the phenomenon and its impact on pile design. As additional case histories collect more information and further studies refine the present understanding, improvements to the design process will be possible.

REFERENCES

- Budge, A.S., Dasenbrock, D.D., and Mattison, D.J. “*A Synthesis of Pile Performance Monitoring Projects in Downdrag Environments in Minnesota*”, ASCE Geotechnical Special Publication No. 256 – Proceedings of the International Foundations Congress and Equipment Expo 2015 (March 2015.)
- Budge, A.S. and D.D. Dasenbrock, “*Performance Data Collected from Instrumentation on a MnDOT Bridge Abutment Foundation Subject to Downdrag*”, ASCE Geotechnical Special Publication No. 211 – GeoFrontiers 2011 (March 2011.)
- Budge, A.S., and D.D. Dasenbrock, “*Installation of Downdrag Instrumentation on a Bridge Abutment Foundation: Lessons Learned*”, ASCE Geotechnical Special Publication No. 199 – GeoFlorida 2010 (February 2010.)

- Budge, A.S. and D.D. Dasenbrock, "*Downdrag monitoring on the Crosstown Commons reconstruction*", Proceedings of the University of Minnesota's 58th Annual Geotechnical Engineering Conference, Minneapolis, MN, February 2010.
- Dasenbrock, D.D., B.R. Borree and A.S. Budge, "*Behavior of a Mn/DOT Bridge Foundation Subject to Downdrag*", Proceedings of the University of Minnesota's 59th Annual Geotechnical Engineering Conference, Minneapolis, MN, February 2011.
- Dasenbrock, D.D., D.J. Mattison and A.S. Budge, "*Measured Live Load Effects on Driven Pipe Piles with Established Dragload*", Proceedings of the University of Minnesota's 60th Annual Geotechnical Engineering Conference, Minneapolis, MN, February 2012.